

## Rock Mechanics Forsmark

### Site descriptive modelling Forsmark stage 2.2

Rune Glamheden, Anders Fredriksson  
Golder Associates AB

Kennert Röshoff, Johan Karlsson  
Berg Bygg Konsult AB

Hossein Hakami, Itasca Geomekanik AB

Rolf Christiansson, Svensk Kärnbränslehantering AB

December 2007

#### **Svensk Kärnbränslehantering AB**

Swedish Nuclear Fuel  
and Waste Management Co  
Box 250, SE-101 24 Stockholm  
Tel +46 8 459 84 00



# **Rock Mechanics Forsmark**

## **Site descriptive modelling Forsmark stage 2.2**

Rune Glamheden, Anders Fredriksson  
Golder Associates AB

Kennert Röshoff, Johan Karlsson  
Berg Bygg Konsult AB

Hossein Hakami, Itasca Geomekanik AB

Rolf Christiansson, Svensk Kärnbränslehantering AB

December 2007

# Preface

This report describes the results of the rock mechanics site modelling for the Forsmark area during modelling stage 2.2. The overall aim of the report is to provide the Repository Design and the Safety Assessment working groups with rock mechanics properties that are typical for the Forsmark area. The rock mechanics report is one of four reports from the site modelling stage 2.2.

In addition to the authors, the following people have contributed to the rock mechanics modelling work at Forsmark, stage 2.2:

Hanna Bohlin – Compilation of primary data of intact rock.

Malin Johansson – Development of tables and figures regarding the in situ stress.

Ulrika Lindberg – Visualisation of rock mechanics data.

Lars Persson – Compilation of primary data of fractures and assistance in the theoretical modelling of rock mass properties.

The authors acknowledge Philip Curtis, Thomas Doe, John Hudson, Harald Hökmark, Flavio Lanaro, Derek Martin, Roland Pusch and Jonny Sjöberg for examination of the manuscript.

# Abstract

The Swedish Nuclear Fuel and Waste Management Company (SKB) is undertaking site characterisation at two different locations, Forsmark and Laxemar/Simpevarp, with the objective of siting a geological repository for spent nuclear fuel. The characterisation of a site is an integrated work carried out by several disciplines including geology, rock mechanics, thermal properties, hydrogeology, hydrogeochemistry and surface systems. This report presents the rock mechanics model of the Forsmark site up to stage 2.2.

The scope of work has included compilation and analysis of primary data of intact rock and fractures, estimation of the rock mass mechanical properties and estimation of the in situ state of stress at the Forsmark site.

The laboratory results on intact rock and fractures in the target volume demonstrate a good quality rock mass that is strong, stiff and relatively homogeneous. The homogeneity is also supported by the lithological and the hydrogeological models.

The properties of the rock mass have been initially estimated by two separate modelling approaches, one empirical and one theoretical. An overall final estimate of the rock mass properties were achieved by integrating the results from the two models via a process termed "Harmonization".

Both the tensile tests, carried out perpendicular and parallel to the foliation, and the theoretical analyses of the rock mass properties in directions parallel and perpendicular to the major principal stress, result in parameter values almost independent of direction. This indicates that the rock mass in the target volume is isotropic.

The rock mass quality in the target volume appears to be of high and uniform quality. Those portions with reduced rock mass quality that do exist are mainly related to sections with increased fracture frequency. Such sections are associated with deformation zones according to the geological description. The results of adjacent rock domains and fracture domains of the target volume show that all rock domains covered by the empirical analysis have rock of good competent quality. The evaluated mechanical properties of the deterministic deformation zones are on the whole relatively close to the properties evaluated for the fracture domains.

The in situ state of stress at the Forsmark site has been estimated based on direct measurements including overcoring and hydraulic fracturing, as well as indirect observations including borehole breakout, core diskings and micro crack porosity. The results were utilised as input data to a numerical model for evaluation of stress variability caused by deformation zones as well as the discrete fracture network. Both direct and indirect measurements of the in situ stresses end up with a stable and constant orientation of the major horizontal stress in NW-SE direction. The magnitude of the major principal stress is constrained by indirect observations of core and borehole damage along with stress measurements.

Fracture domains FMM01 and FFM06 are presumed to have the same stress gradient. The adopted model results in a mean magnitude of the major horizontal stress of around 41 MPa and of the minor horizontal stress around 23 MPa at 500 m depth in FFM01. Compared to the previous model version, the present estimate corresponds to a slight reduction in situ stress magnitudes.

Results from numerical modelling with respect to deformation zones, show that the stress field in the target volume is relatively homogeneous, and that it is mainly the gently dipping deformation zone ZFMA2 that has importance for the stress field in the target volume.

For the rock mass conditions at Forsmark numerical modelling, regarding local stress spatial variability due to discrete fractures, indicates that the major principal stress could be expected to vary spatially by  $\pm 5$  MPa in magnitude and  $\pm 9$  degrees in orientation.

# Sammanfattning

Svensk Kärnbränslehantering AB genomför platsundersökningar inom två olika områden, Forsmark och Laxemar/Simpevarp, i syfte att lokalisera ett slutförvar för använt kärnbränsle. De platsbeskrivande modellerna tas fram som ett integrerat arbete och involverar flera olika ämnesområden såsom geologi, bergmekanik, termiska egenskaper, hydrogeologi, hydrokemi och ytnära system. Denna rapport redovisar den bergmekaniska modellen för Forsmark till och med steg 2.2.

Arbetet har omfattat sammanställning och analys av primär data för intakt berg och sprickor, uppskattning av bergmassans mekaniska egenskaper samt uppskattning av in situ spänningarna i Forsmark.

Laboratorieresultaten på intakt berg och sprickor i bergvolymen för ett tilltänt förvar uppvisar en bergmassa med god kvalitet som är stark och styv och relativt homogen. Att bergmassan är homogen stöds också av den litologiska och den hydrogeologiska modellen.

Bergmassans mekaniska egenskaper har uppskattats med hjälp av två olika metoder, en empirisk och en teoretisk metod att uppskatta bergmassans egenskaper. En slutgiltig uppskattning av bergmassans egenskaper har erhållits genom att förena resultaten från de två metoderna via en process benämnd ”Harmonisering”.

Laboratorieförsök av draghållfastheten vinkelrät och parallellt mot foliationen samt teoretiska analyser av bergmassans egenskaper parallell och vinkelrät mot största huvudspänningen resulterar i värden som i princip är oberoende av riktning. Resultaten indikerar att bergmassan i den tilltänkta förvarsvolymen är isotropisk.

Bergmassans kvalitet i den tilltänkta förvarsvolymen verkar utgöras av hög och enhetlig kvalitet. Den andel av bergmassan som har reducerad hållfasthet är i första hand relaterad till avsnitt med ökad sprickfrekvens. Den geologiska modellen påvisar att dessa avsnitt är förbundna med deformations zoner. Resultaten för bergdomän och sprickdomän som omger den tilltänkta förvarsvolymen visar att samtliga bergdomän som omfattas av den empiriska analysen utgörs av kompetent berg av god kvalitet. De mekaniska egenskaperna som utvärderas för deterministiska deformations zoner är i huvudsak jämförbara med egenskaperna som utvärderats för sprickdomänen.

In situ spänningarna i Forsmark har uppskattats baserat på direkta mätningar, såsom överborrning och hydrauliskspräckning, samt indirekta metoder, såsom utfall i borrhål, spjälkning i borrhärnor och utvärdering av mikrospickvolymen. Resultaten har använts som input i en numerisk modell för utvärdering av spänningarnas variabilitet på grund av deformations zoner och diskreta spricknätverk. Både direkta och indirekt bestämningar av in situ spänningen resulterar i en stabil och konstant orientering av största horisontella spänningen i NW-SE riktning. Största huvudspänningens magnitud har kunnat gränssättas genom indirekta observationer av skador på borrhärnor och i borrhål samt direkta spänningsmätningar.

Sprickdomänen FFM01 och FFM06 antas ha samma spänningsgradient. Den antagna modellen resulterar i ett medelvärde för störst horisontella huvudspänningen på ungefär 41 MPa och för minsta horisontella huvudspänningen som är ungefär 23 MPa på 500 m djup i FFM01. Jämfört med tidigare modellversioner motsvarar den aktuella uppskattningen en viss reducering av spänningsmagnituden.

Resultat från numerisk modellering avseende deformationszonerna i modellområdet visar att spänningsfältet i den tilltänkta lagervolymen är relativt homogent och att det i första hand är deformationzon ZFMA2 som inverkar på spänningsfältet i volymen.

Numerisk modellering avseende enskilda sprickors inverkan på in situ spänningarnas rumsliga variabilitet tyder på att i Forsmark kan största huvudspänningens magnitud förväntas variera  $\pm 5$  MPa och dess riktning  $\pm 9$  grader.

# Contents

<b>1</b>	<b>Introduction</b>	11
1.1	Background	11
1.2	Objective and scope	12
1.3	Strategy for the site investigations	12
	1.3.1 Parameters to determine	12
	1.3.2 Sampling strategy	12
1.4	Modelling methodology	14
1.5	Settings of the Forsmark area	15
1.6	Boreholes available in model stage 2.2	16
	1.6.1 Location of the drill sites	16
	1.6.2 Borehole orientation data	17
1.7	Overview of previous model versions	18
1.8	Nomenclature	19
1.9	Abbreviations and symbols	20
	1.9.1 Geological and rock mechanics abbreviations	20
	1.9.2 Other abbreviations	20
	1.9.3 SKB code identity of tested rock types	21
1.10	Structure of this report	21
<b>2</b>	<b>Input from other disciplines</b>	23
2.1	Geological model overview	23
	2.1.1 Bedrock in the Forsmark area	23
	2.1.2 Rock domain model	23
	2.1.3 Model for deterministic deformation zones	26
	2.1.4 Fracture domain model	30
	2.1.5 Discrete fracture network model	32
2.2	Hydrogeological input	33
<b>3</b>	<b>Mechanical properties of intact rock</b>	35
3.1	Overview of the primary data	35
3.2	Strength properties of intact rock	36
	3.2.1 Uniaxial compressive strength	37
	3.2.2 Crack initiation stress	38
	3.2.3 Tensile strength	39
	3.2.4 Triaxial compressive strength	41
3.3	Deformation properties of intact rock	44
	3.3.1 Young's modulus	44
	3.3.2 Poisson's ratio	44
3.4	Microcrack volume measurements	45
3.5	Variability and trends in results	46
	3.5.1 Spatial variability in relation to geological features	47
	3.5.2 Depth dependency	48
	3.5.3 Variability in results between modelling steps	50
3.6	Summary of intact rock mechanical properties	52
	3.6.1 Uncertainties	52
	3.6.2 Evaluated properties for intact rock	52
<b>4</b>	<b>Mechanical properties of fractures</b>	55
4.1	Overview of the primary data	55
4.2	Tilt test results	56
4.3	Direct shear test results	58
	4.3.1 Description of parameter evaluation	59

4.3.2	Tests on open fractures	59
4.3.3	Tests on sealed fractures	61
4.4	Variability and trends in test results	62
4.4.1	Spatial variability in relation to geological features	62
4.4.2	Influence of fracture sets on mechanical properties	62
4.4.3	Depth dependency	62
4.4.4	Variability in results between modelling steps	64
4.5	Summary of mechanical properties of fractures	65
4.5.1	Uncertainties	65
4.5.2	Evaluated mechanical properties of fractures	65
<b>5</b>	<b>Rock mass mechanical properties</b>	<b>71</b>
5.1	Empirical approach using classification systems	71
5.1.1	Strength and deformation properties for the rock domains	72
5.1.2	Strength and deformation properties for the fracture domains	77
5.1.3	Strength and deformation properties for the deformation zones	79
5.1.4	Summary of the results from the empirical model	81
5.2	Theoretical approach using numerical models	83
5.2.1	Strength and deformation properties for the fracture domains	83
5.2.2	Strength and deformation properties of the deformation zones	88
5.2.3	Summary of the results from the theoretical model	90
5.3	Harmonized rock mass mechanical properties	91
5.3.1	Harmonization of results for fracture domains	92
5.3.2	Harmonization of results for deformation zones	93
5.4	Summary of the results after harmonization	93
<b>6</b>	<b>In situ state of stress</b>	<b>95</b>
6.1	Regional stress state	95
6.1.1	Plate tectonics and the Scandinavian Shield	95
6.1.2	Crustal stresses and seismic activity	95
6.1.3	Stress measurements in the Forsmark region	95
6.1.4	Expected stress magnitudes and directions	97
6.2	Geological overview	97
6.2.1	General geology and tectonics in the Forsmark area	97
6.2.2	Deterministic deformation zone model	98
6.2.3	Fracture domain model	101
6.3	Stress model from primary data	102
6.3.1	Primary data	102
6.3.2	Measurement locations and deformation zones	105
6.3.3	Stress magnitudes at repository level in the target volume	106
6.4	Evaluation of stress variability caused by deformation zones	112
6.4.1	Modelling approaches	112
6.4.2	In situ stress issues addressed by modelling stage	112
6.4.3	Findings from the numerical stress modelling	116
6.4.4	Summary	125
6.5	Evaluation of local stress spatial variability	125
6.5.1	Stress variability with depth due to varying modulus	126
6.5.2	Stress variability due to discrete fractures	127
6.6	Assessment of in situ stress state at repository depth	129
6.6.1	Uncertainty and spatial variability in the stress model	130
6.6.2	Proposed in situ stress models	131
<b>7</b>	<b>Summary of the rock mechanics model</b>	<b>135</b>
7.1	Intact rock properties	135
7.2	Fracture properties	135
7.3	Rock mass properties	136
7.4	In situ state of stress	137
7.5	Overall confidence	138

<b>8</b>	<b>Conclusions</b>	139
<b>9</b>	<b>References</b>	141
<b>Appendix 1</b>	Intact rock mechanical properties	147
<b>Appendix 2</b>	Mechanical properties of fractures	165
<b>Appendix 3</b>	Results from empirical modelling	175
<b>Appendix 4</b>	Results from theoretical modelling	199
<b>Appendix 5</b>	WellCad plots stress observations	217
<b>Appendix 6</b>	Evaluated principal stresses	243
<b>Appendix 7</b>	Numerical modelling of in situ stresses	245
<b>Appendix 8</b>	Visualization of rock mechanics data	251
<b>Appendix 9</b>	Rock mechanics symbols	275
<b>Appendix 10</b>	Delivery date of primary data from SICADA	277



# 1 Introduction

## 1.1 Background

The Swedish Nuclear Fuel and Waste Management Company (SKB) is undertaking site characterization at two different locations, the Forsmark and Laxemar/Simpevarp areas, with the objective of siting a geological repository for spent nuclear fuel. The investigations are conducted in campaigns with the help of data freezes. After each data freeze, the site data are analysed and modelling work is carried out. A site descriptive model (SDM) is an integrated model for geology, rock mechanics, thermal properties, hydrogeology, hydrogeochemistry along with a description of the surface system.

So far, three versions of a site descriptive model (SDM) have been completed in the Forsmark area. Version 0 /SKB 2002/ established the state of knowledge prior to the site investigation. Version 1.1 /SKB 2004/ was completed during 2004 and version 1.2 in June 2005 /SKB 2005a/. Version 1.2 of the SDM concluded the initial site investigation work (ISI). It formed the basis for a preliminary repository layout (layout D1), a preliminary safety evaluation (PSE) /SKB 2005b/ and a safety assessment (SR-Can) /SKB 2006a/.

Three analytical and modelling stages have been carried out during the Complete Site Investigation work (CSI). An important component of each of these stages is to address and continuously try to resolve uncertainties of importance for repository engineering and safety assessment. Model stage 2.1 /SKB 2006b/ included an updated geological model for Forsmark and aimed to provide a feedback from the modelling working group to the site investigation team to enable completion of the site investigation work. Model stages 2.2 and 2.3 have established the different discipline-specific models which are synthesized into the framework of the integrated site descriptive model SDM-Site.

The working model and the results of the rock mechanics work in model stage 2.2 for the Forsmark site are compiled in this report. This is one out of four reports from stage 2.2, the other reports conclude the current understanding of geology, thermal properties and hydrogeological conditions. An outline of the main reference to the SDM-site for Forsmark is presented in Figure 1-1. The thermo-mechanical data are to be found in the main reference regarding thermal properties /Back et al. 2007/.

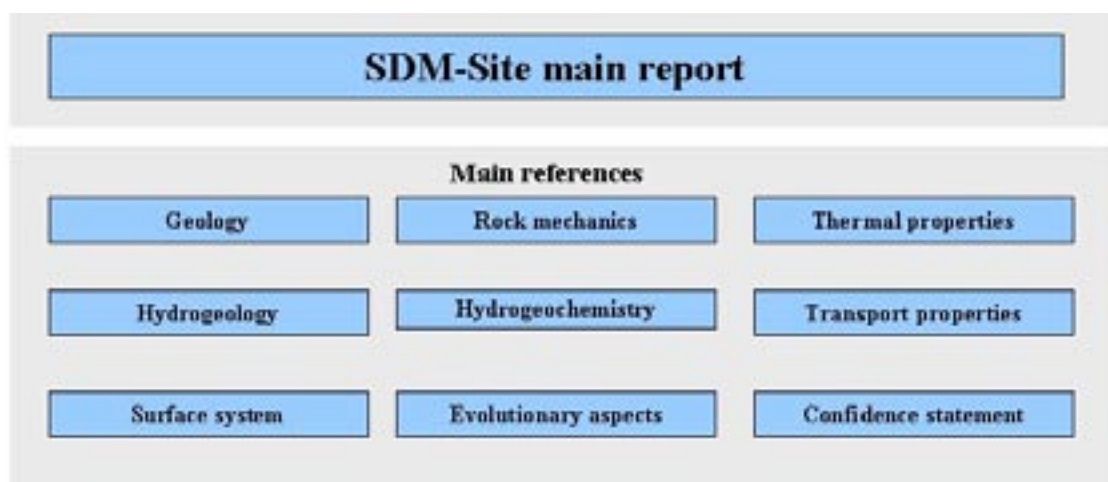


*Figure 1-1. Outline of main references to SDM-site for Forsmark.*

## 1.2 Objective and scope

This report synthesizes the mechanical properties of the rock mass at the Forsmark site up to modelling stage 2.2. The overall aim is to provide the rock mechanics parameters that may impact design and safety assessments. In addition to this the report demonstrates that SKB has developed a good understanding of the site. The current data freeze 2.2 includes almost all rock mechanics data that will be available, so this report can be considered as a draft final report on rock mechanics as an input to the integration with SDM-Site.

The specific objectives of the rock mechanics study stage 2.2 are to:

- Finalise the assigned mechanical properties for rock types and geological domains described in the geology stage 2.2 report, as well as assessing the confidence in the model.
- Examine to what degree the mechanical properties are representative for the volume of rock that may host a final repository.
- Present the current understanding of the state of stress, its possible variability and dependence on geological heterogeneities, as well as the confidence in the model.
- Incorporate feedback from SR-Can /SKB 2006a/ that is of relevance to the rock mechanics modelling work, thereby further reducing the uncertainties in stress and rock mechanics properties.

The feedback from SR-Can has also been taken into account by further stress modelling and 3D visualisation of the uniaxial compressive strength of laboratory results within the target volume.

## 1.3 Strategy for the site investigations

### 1.3.1 Parameters to determine

The site investigations should provide the necessary data for design and assessment of long-term safety of a deep repository /Andersson et al. 2000, SKB 2006c/. The rock mechanics model shall describe the distribution of the rock mechanics properties and the in situ stresses of a candidate area. The model shall also describe the rock quality with regard to constructability /SKB 2000, SKB 2001/. For example rock mechanics data are used in the design to estimate the risk for stability problems and assessment of rock support needs /Brantberger et al. 2006/, while the safety assessment employ rock mechanics data for the analysis of thermo-mechanically induced changes in the repository near field /Hökmark et al. 2006/ along with seismically induced slip on fractures /Fälth and Hökmark 2006/.

A compilation of the parameters that are required by different end users and included in the rock mechanics site descriptive model are presented in Table 1-1. The thermal expansion of the rock is not included in the table since this parameter is reported in the thermal site descriptive model /Back et al. 2007/. Neither is the information from geology, needed to prepare the rock mechanics description, listed in the table.

### 1.3.2 Sampling strategy

The overall strategy in sample selection for testing in the SKB site investigation programme is based on:

- consultation with site geologists on the representativeness of potential test objects,
- collection of samples in batches at a depth with a number of specimens as close to each other as practically achievable,
- avoidance of samples with presumed planes of weakness in the loading direction, such as uniaxial testing of foliated rock with the plane of foliation at an acute angle to the core axis.

**Table 1-1. Compilation of rock mechanical parameters included in the site descriptive model with specified end user. Modified after /SKB 2001/.**

Parameter group	Parameter	End user <sup>1,2,3,4</sup>
Intact rock	Elastic properties ( $E, \nu$ )	SA
	Crack initiation stress ( $\sigma_{ci}$ )	D, SA
	Compressive strength ( $c, \phi, \psi$ )	D, SA
	Tensile strength ( $\sigma_t$ )	SA
	Micro crack volume	SA (HgC, TP)
Fractures	Deformation properties ( $K_N, K_S$ )	SA
	Shear strength ( $c_{p,r}, \phi_{p,r}, \psi_{0.5,5,20}$ )	D, SA
Rock mass	Elastic properties ( $E_m, \nu_m$ )	D
	Compressive strength ( $c_m, \phi_m, \psi_m$ )	D
	Tensile strength ( $\sigma_{tm}$ )	D
In situ stresses	Orientation	D, SA
	Magnitude	D, SA

<sup>1</sup> D – Design

<sup>2</sup> SA – Safety Assessment

<sup>3</sup> HgC – Hydrogeochemistry

<sup>4</sup> TP – Transport properties

During the Initial Site Investigations, the focus was to sample boreholes at roughly 300 m, 500 m and 700 m depth to get a first indication of spatial variability in the target volume. During the Complete Site Investigations, the focus has been more on testing mechanical properties at a tentative depth of 400–500 m within the target volume FFM01 and FFM06.

In addition, secondary rock types and the altered granite in FFM06 have been tested in a later stage. Here the actual location, rather than a specific depth interval, has been of importance for the sampling.

Compared to sample criteria set up initially, the number of samples has been gradually reduced since the results indicated homogeneous conditions within the target volume.

A batch for uniaxial testing has normally included 5 samples. The applied standard for indirect tensile strength prescribes 10 tests, and for triaxial testing at least two samples for each confinement stress level have been tested from nearby locations. Samples for the different mechanical tests have been selected from nearby locations, together with samples for testing of thermal properties. Typically all samples from a test level have been selected from two nearby core boxes (less than 10 m spacing).

The sampling strategy for the tilt tests was to perform the testing in the core shed during core logging. Fractures with a relative angle to the core axis in intervals  $0^\circ$ – $30^\circ$ ,  $30^\circ$ – $60^\circ$  and  $> 60^\circ$  were tested. The ambition was to test an even distribution of fractures along each drill core, but due to the locally very low fracture frequency tilt testing was not carried out along many borehole sections.

Samples for the testing of normal stiffness and shear stress were intended to be collected from the same depth intervals as for testing of intact rock. However, during the Initial Site Investigation since the boreholes were drilled sub-vertically there were long sections with no open or broken fractures available for testing due to low fracture frequency. Samples were typically taken from either gently dipping fractures, or steeply dipping fractures with a small angle to the core axis. In the latter case two to three samples could be taken from the same fracture. During the Complete Site Investigations the cored boreholes were typically drilled inclined, which allowed a greater possibility to select fractures for testing. However, the low fracture frequency at depth still limited the flexibility in selecting fractures.

The results of mechanical testing have to be critically reviewed with particular focus on test results that appeared anomalous compared to the majority. Local heterogeneities may have a large influence on test results because of the small volume of rock involved in the testing methods. Such results are included in the following sections and their impacts on the mean values of mechanical properties are commented upon. Because of the obvious impact of minor heterogeneities on strength parameters of small samples of crystalline rock, only a limited number of mechanical tests of intact rock within deformations zones have been carried out.

### 1.4 Modelling methodology

The strategy for development of a Rock Mechanics Site Descriptive Model is stated in /Andersson et al. 2002/. Figure 1-2, which is adopted from this report, illustrates the components of the Rock Mechanics Site Descriptive Model, as well as the proposed flow chart for the work.

The mechanical properties of the rock are partly dependent on the properties of the intact rock, and partly on the frequency and properties of fractures. The primary data of intact rock and fractures is utilised by two modelling approaches, one empirical and one theoretical, to estimate the properties of the rock mass. The empirical approach estimates the rock mass properties based on classification indexes and empirical relationships, while the theoretical approach estimates the properties of the rock mass using numerical models. Inputs to the theoretical model are the mechanical behaviour of the intact rock and the fractures, along with fracture geometry. The final estimate of the rock mass properties is achieved by integrating the results from the two models via a process termed “Harmonization”.

The in situ stresses are analysed in a separate numerical model. Input data to this model are the stress measurements along with the geometrical and mechanical characterisation model. The numerical model gives the distribution of stress magnitudes and the orientation in the model volume.

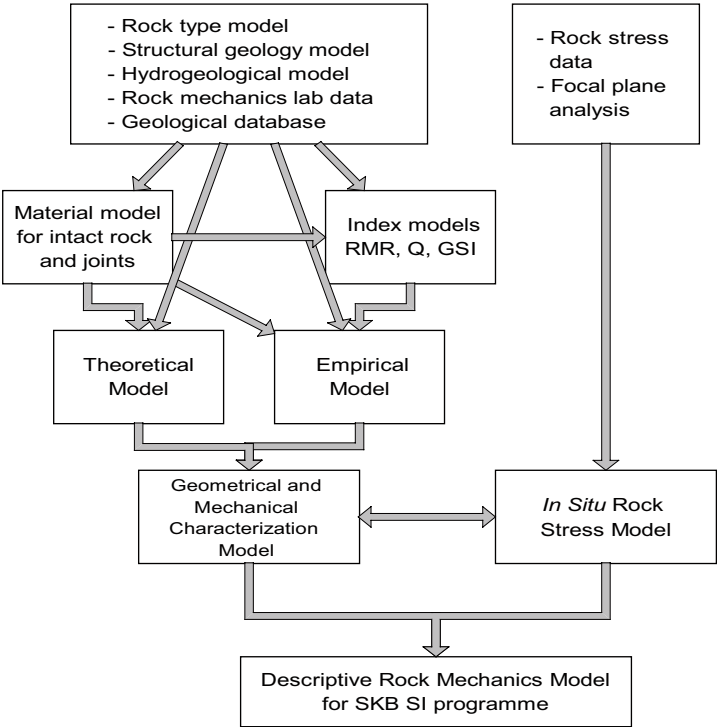
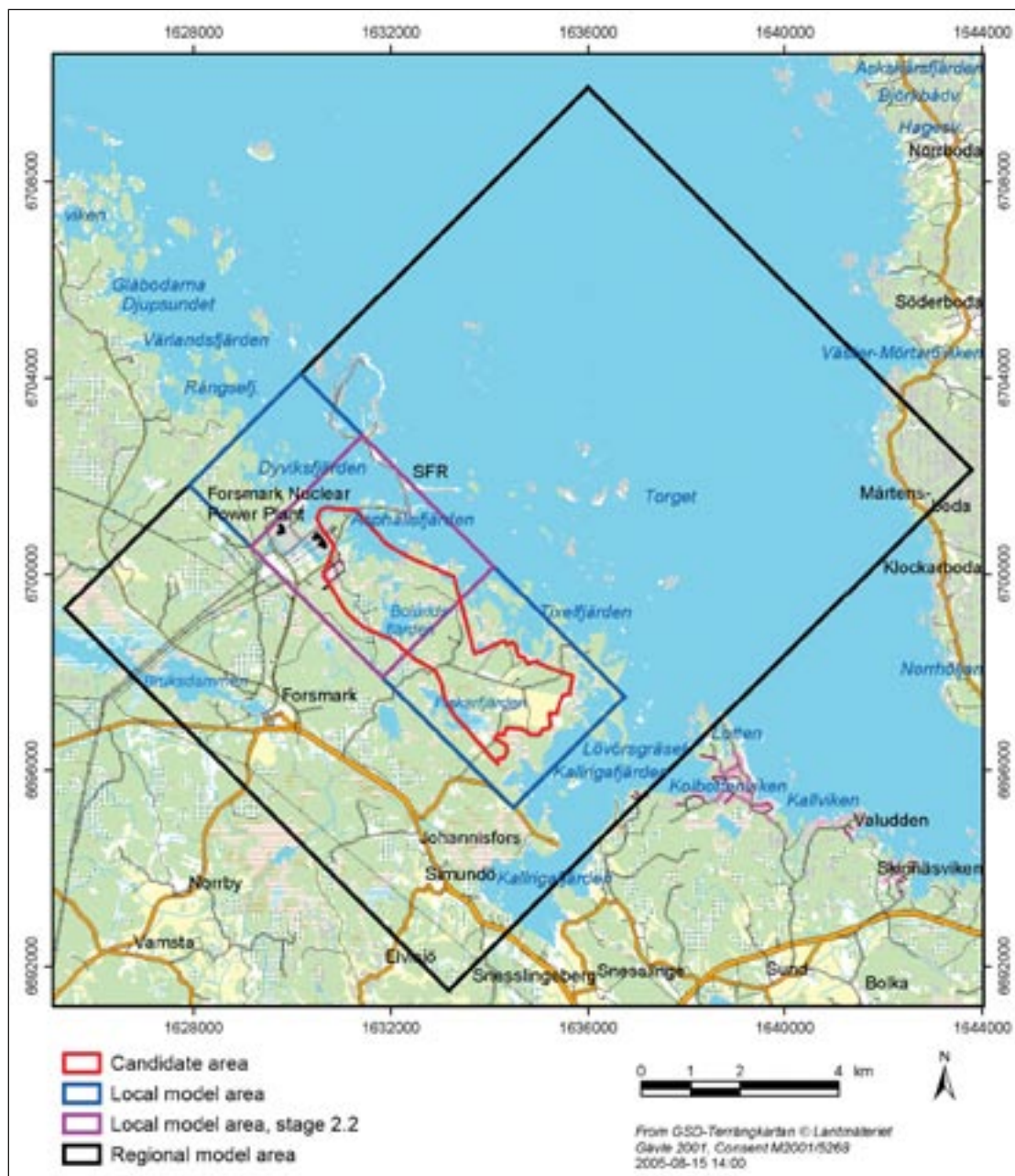


Figure 1-2. Flowchart for the rock mechanics site descriptive model /Andersson et al. 2002/.

## 1.5 Settings of the Forsmark area

The Forsmark site is located in northern Uppland within the municipality of Östhammar, about 170 km north of Stockholm. The candidate area at Forsmark is located along the shoreline of Öregrundsgrepen. It extends from the Forsmark nuclear power plant and SFR-facility access road in the north-west to Kallrigafjärden in the south-east (Figure 1-3). The candidate area is approximately 6 km long and 2 km wide. The north-western part of the candidate area has been selected as the target area for the complete site investigation work /SKB 2005c/.



**Figure 1-3.** Regional and local model areas at Forsmark. The local model area used during model stage 2.2 is marked in purple. It covers the north-western part of the candidate area that has been selected as a target area for a potential repository. Coordinates are provided using the RT90 (RAK) system /Stephens et al. 2007/.

## 1.6 Boreholes available in model stage 2.2

### 1.6.1 Location of the drill sites

Figure 1-4 presents the candidate area with the locations of drill sites and boreholes, from which data were available in model stage 2.2 /Stephens et al. 2007/. A list of the boreholes used in the rock mechanics modelling is provided in Table 1-2.



**Figure 1-4.** Location of drill sites and boreholes, from which data were available for model stage 2.2, at the Forsmark site /Stephens et al. 2007/.

**Table 1-2. List of the boreholes used in the rock mechanics modelling.**

	Laboratory testing	Rock mass characterisation	Borehole overcoring	Hydraulic methods	Borehole breakout	Core dinking
KFM01A	x	x		x	x	
KFM01B		x	x	x	x	x
KFM01C	x					
KFM01D	x					x
KFM02A	x	x		x	x	
KFM02B	x		x			
KFM03A	x	x			x	
KFM04A	x	x		x	x	x
KFM05A	x				x	x
KFM06A	x	x <sup>1</sup>			x	x
KFM06B						
KFM06C		x <sup>1</sup>				
KFM07A	x			x		x
KFM07B			x			
KFM07C		x	x	x	x	x
KFM08A	x			x		x
KFM08B						x
KFM08C		x <sup>1</sup>				
KFM08D						x
KFM09A	x	x		x		x
KFM09B		x		x		
KFM09C						
KFM10A						x
KFM11A						x
KFK001 (DBT1)			x	x		
KFK003 (DBT3)			x			

<sup>1</sup> Only that part of the borehole that pass rock domain RFM045.

### 1.6.2 Borehole orientation data

As a result of an extensive quality check by SKB, the Sicada database was updated with regards to borehole geometries and orientation data in March 2007 and in October 2007 /Munier and Stigsson 2007/. Data utilised in the rock mechanics model regarding strength and deformation properties were delivered from SICADA before March 2007 with the exception of primary data in KFM06A, KFM06C and KFM08C used for the empirical modelling (cf. Appendix 10). Furthermore, the primary data used for analysis of the in situ stress measurements were delivered after March 2007 with the exception of the borehole breakout results. This means that some modelling results are based on orientation data that include larger errors than the current data in SICADA. The possible impact due to this situation is accounted for here.

The identified main sources of uncertainties and errors are the following:

- uncertainty in the orientation of the borehole,
- uncertainty in the orientation obtained from the BIPS image,
- errors due to the use of different calculation procedures in BOREMAP and SICADA.

Uncertainties in orientation of data for the rock mechanics modelling may influence the stress measurement results, primarily the orientation of stress components and consequently the calculation of stress magnitudes. The results from overcoring are influenced by errors in the measurement of borehole deviation, while the results from HTPF are sensitive to uncertainties in BIPS measurements. The study of borehole breakout is only influenced by uncertainties in the orientation of the televiewer.

Uncertainties in the orientation of fractures are of importance if the subdivision into fracture sets is changed. The normal and shear strength of fractures are correlated to fracture sets and the number of fracture sets is also a parameter used in the empirical modelling of rock mass mechanical properties. Moreover, a change in the number of fracture sets may lead to changes of the evaluated anisotropy in the theoretical modelling.

Evaluation and quantifying of uncertainties in orientation data have been carried out for sixteen boreholes in Forsmark. After the latest update in October 2007, the evaluated orientation uncertainty of objects in most boreholes has a mean around 10 degrees. Borehole KFM02A shows the largest orientation uncertainty (mean 14.5 degrees) followed by KFM01A, KFM01B and KFM07C /Munier and Stigsson 2007/.

The influence on the rock mechanics modelling, on account of not using the latest updated orientation data, have been checked by comparing modelling results based on orientation data in SICADA before March 2007 and after October 2007. The influence of the in situ stress orientation is within one or two degrees and the influence of the magnitude is hardly noticeable. The overall judgment from this comparison is that the performed correction of the orientation data has a very limited influence on the rock mechanics modelling. A more comprehensive examination of the possible effects on the rock mechanics modelling will be performed during modelling stage 2.3.

## 1.7 Overview of previous model versions

Model version 0 /SKB 2002/, established the state of knowledge prior to the site investigation. This rock mechanics model was based on information from boreholes and tunnels of the Forsmark nuclear power plant and the SFR repository.

Model version 1.1 /SKB 2004/, was the first model to include data from the site investigation. However, this model was still based mainly on information from Forsmark nuclear power plant and the SFR repository. Additional information comprised empirical characterization of borehole KFM01A (RFM029) together with new outcrop surveys (RFM017, RFM018, RFM032 and RFM033).

The first new laboratory testing campaign was carried out on samples from four boreholes: KFM01A, KFM02A, KFM03A and KFM04A, presented in model version 1.2 /SKB 2005a/. The amount of available laboratory tests increased significantly and included samples of the two dominant rock types and several natural fractures. The rock mass mechanical properties were estimated by means of empirical and theoretical methods. The state of stress in the rock mass was estimated based on measurements in KFM01A, KFM01B, KFM02A and KFM04A besides previous measurements in the Forsmark area.

Modelling stage 2.1 included new data from sampling of boreholes KFM05A and KFM06A. Although the rock mechanics properties in the target volume were stated to be rather well known a need for additional sampling of the subordinate rock types was identified. The stress modelling carried out so far indicated that the in situ stresses at Forsmark were of high magnitude. However, the uncertainties of the evaluated state of stress were considerable. Further stress measurements and analysis of stress by indirect methods were suggested. A need for numerical stress modelling of gently dipping deformation zones was also identified.



All of the previous rock mechanics model versions were based on a previous version of the geological model. From the viewpoint of rock mechanics, important changes that distinguish the current model from the previous are the larger extension of rock domain RFM045 and the introduction of fracture domains. Moreover, a new DFN-model has also been developed.

The gradual development of the deformation zone (DZ) model, through the modelling stages has been considered with respect to the tentative perturbation of the state of stress at the site. The DZ model within the target volume has been relatively robust since SDM version 1.2, although details in orientation have been modified, primarily due to new high resolution data /Stephens et al. 2007/.

## 1.8 Nomenclature

Definitions for some important geological terms that are used frequently in the report are presented below. The definitions given are adopted from /Stephens et al. 2007/, however, most of the definitions are based on the guidelines provided in /Munier and Hermanson 2001/ and /Munier et al. 2003/.

- Rock unit (RU). A rock unit is defined on the basis of one or several combined properties including rock composition, grain size, degree of bedrock homogeneity, degree and style of ductile deformation, early-stage alteration (albitization) and fracture frequency. Both dominant and subordinate rock types are defined for the rock units.
- Rock domain (RD). A rock domain refers to a rock volume in which rock units show a similar composition, grain size, degree of bedrock homogeneity and style of deformation. The term rock domain is used in the 3D geometric modelling work and different rock domains at Forsmark are referred to as RFMxxx.
- Deformation zone (DZ). A deformation zone is a general term referring to an essentially 2D structure along which there is a concentration of brittle, ductile or combined brittle and ductile deformation.

Bearing in mind the resolution scale of the current modelling work, a distinction is made between:

1. Deformation zones, which have surface traces longer than 1,000 m and are modelled deterministically. These are referred to as ZFMxxx and are included in the DZ block model.
  2. Minor deformation zones, which have trace lengths shorter than 1,000 m and are modelled deterministically. These are referred to as ZFMxxx, but are not included in the DZ block model(s).
  3. Possible deformation zones, which have been recognised in the single hole interpretations, but have not been linked to other features (e.g. a low magnetic lineament, a seismic reflector) that provide a basis for modelling in 3D space. For this reason, these structures are not modelled deterministically.
- Fracture domain (FD). A fracture domain refers to a rock volume outside deformation zones in which rock units show similar fracture frequency characteristics. The term is used in the first hand as a basis for the discrete fracture network modelling work (geological DFN) and different fracture domains at Forsmark are referred to as FFMxxx.
  - Discrete fracture network (geological DFN). The fracturing in the bedrock is described on the basis of a standardized statistical procedure, which provides geometries, directions and spatial distributions for the fractures within defined fracture domains.
  - Candidate area/volume. The area at the ground surface, and its extension at depth, in a municipality that was recognised as suitable for a site investigation, following the feasibility study work /SKB 2000/.

- Target volume. The target volume includes the rock volume that has been identified as suitable for the excavation of the waste repository /SKB 2005c/. In connection with the stage 2.2 modelling work, this volume is defined as the parts of rock domains RFM029 and RFM045 that are situated north-west of the steeply dipping zone ZFMNE0065 and beneath the gently dipping zones ZFMA2, ZFMA3 and ZFMF1. The target volume defines the boundaries of the volume in which geological DFN modelling work will be carried out during stage 2.2 and is the focus for this report.

## 1.9 Abbreviations and symbols

The most important abbreviations employed in the report are put together in this section. Rock mechanics symbols utilised in the report are listed in Appendix 9.

### 1.9.1 Geological and rock mechanics abbreviations

DFN	Discrete fracture network
DZ	Deformation zones > 1,000 m and modelled deterministically
HF	Hydraulic Fracturing
HTPF	Hydraulic Tests on Pre-existing Fractures
MDZ	Minor deformation zone < 1,000 m and modelled deterministically
P <sub>10</sub>	Number of fractures per unit length of scan line (borehole)
P <sub>21</sub>	Length of fractures traces per unit sampling area (outcrops)
P <sub>32</sub>	Area of fractures per unit volume of rock mass
PDZ	Possible deformation zone
FFMxx	Fracture domain Forsmark model
Q	Rock Mass Quality index
RU	Rock Unit
RD	Rock domain
RMR	Rock Mass Rating
RQD	Rock Quality Designation
RFMxx	Rock domain Forsmark model
ZFMxx	Deformation zone Forsmark model

### 1.9.2 Other abbreviations

CANMET	Mining and Mineral Sciences laboratories of Canada
CSI	Complete site investigation
HUT	Helsinki University of Technology
ISRM	International Society of Rock Mechanics
ISI	Initial site investigation
NGI	Norwegian Geotechnical Institute
PSE	Preliminary safety assessment
SDM	Site descriptive model
SI	Site investigation phase
SP	Swedish National Testing and Research Institute
3DEC	3 Dimensional Distinct Element Code

### 1.9.3 SKB code identity of tested rock types

Code	Rock type name
101051	Granite, granodiorite and tonalite, metamorphic, fine- to medium-grained
101054	Tonalite to granodiorite, metamorphic
101056	Granodiorite, metamorphic
101057	Granite to granodiorite, metamorphic, medium-grained
101058	Granite, metamorphic, aplitic
101061	Pegmatite, pegmatitic granite

## 1.10 Structure of this report

The modelling work reported here is divided into several sections. Section 2 presents a short overview of the geological model together with input from other disciplines that are of importance for the rock mechanics model.

The primary data on intact rock and fractures available at data freeze 2.2 are compiled in Sections 3 and 4, respectively.

Section 5 provides the estimated rock mass strength and deformation moduli based on empirical and theoretical modelling, and presents the harmonised rock mass properties.

The in situ state of stress, based on in situ stress observations and stress modelling attempts is described in Section 6.

Section 7 summarises the rock mechanics model and finally some conclusions are drawn in Section 8 of the report.

The report is completed with a number of appendices (1–10) that are linked to various sections. Appendix 1 addresses the intact rock mechanical properties. Appendix 2 presents mechanical properties of fractures. Appendices 3 and 4 include results from the empirical and theoretical modelling, respectively. WellCad-plots of the stress observations are presented in Appendix 5. The evaluated principal stresses are presented in Appendix 6. Deformation zones included in the numerical modelling of in situ stresses and results from the modelling are shown in Appendix 7. Visualizations of rock mechanics data are presented in Appendix 8. Rock mechanics symbols utilised in the report are listed in Appendix 9. Finally, Appendix 10 presents the date of delivery of primary data from SICADA used in the rock mechanics modelling.

## 2 Input from other disciplines

### 2.1 Geological model overview

The geology of the Forsmark site based on modelling stage 2.2 is described in /Stephens et al. 2007/ and according to previous model versions in /SKB 2006b/ and /SKB 2005a/. A short description of the geological model with its rock types, rock domains, fracture domains and deformation zones is provided here. Furthermore, conditions in the geology model judged to have high importance for the rock mechanics model are also discussed.

#### 2.1.1 Bedrock in the Forsmark area

A simplified bedrock map developed within the site investigation program, with focus on the candidate area, is shown in Figure 2-1 /Stephens et al. 2007/. The colour for each rock unit on the map corresponds to the dominant rock type in that part of the map.

The dominant rock type within the candidate area is metamorphic medium grained granite to granodiorite that belongs to group B, see Figure 2-1. Although dykes of amphibolite and pegmatite occur, the bedrock in the central part of the candidate area is relatively homogeneous /SKB 2005a/. In contrast to this, inhomogeneous bedrock that displays high ductile strain is present in the south-west and north-east of the candidate area. Rocks that are tonalitic and granodioritic in composition dominate to the south-west and aplitic metamorphic granite dominates in a 1 km wide belt to the south-east.

#### 2.1.2 Rock domain model

Rock domains are defined using a combination of the composition, grain size and homogeneity along with the style and inferred degree of ductile deformation of various rock units /Stephens et al. 2007/. A regional model for rock domains was firmly established in model version 1.2 /SKB 2005a/. A local model for rock domains with focus on the so called target volume was introduced in modelling stage 2.1. Only minor revisions of the boundaries between rock domains in both these models have been carried out during modelling stage 2.2 /Stephens et al. 2007/. The distribution of rock domains at the surface in the local model area based on modelling stage 2.2 are shown in Figure 2-2. A three dimensional model for rock domains inside the target volume, in the north-western part of the candidate volume, is presented in Figure 2-3.

Fourteen rock domains are recognised inside the local model volume. The target volume is on the whole composed of two rock domains, RFM029 and RFM045, which are surrounded by various other rock domains. In general, the rock in the surrounding domains displays significantly more ductile deformation relative to that observed in the domains inside the target volume. All domains in the marginal volumes dip steeply towards the south-west.

Compared to the previous modelling stage 2.1 /SKB 2006b/, the position of the boundaries between rock domain RFM029 and the margin domains have been modified and the volume of rock domain RFM045 has increased somewhat /Stephens et al. 2007/.

Rock domain RFM029 has a synform geometry, which is constrained by the marginal domains RFM032 and RFM044. The integrated surface and borehole data from the local model volume indicate a fold axis that plunges 170/55. The orientation of the mineral lineation is basically sub-parallel with the folding geometry inside rock domain RFM029 /Stephens et al. 2007/.

The dominant rock type in rock domain RFM029 is medium-grained metamorphic granite (101057), which constitutes approximately 75% of the domain. Subordinate rock types in rock domain RFM029 include pegmatite and pegmatic granite (13%, 101061), fine to medium-grained metagranitoid (5%, 101051) and amphibolite (4%, 102017).

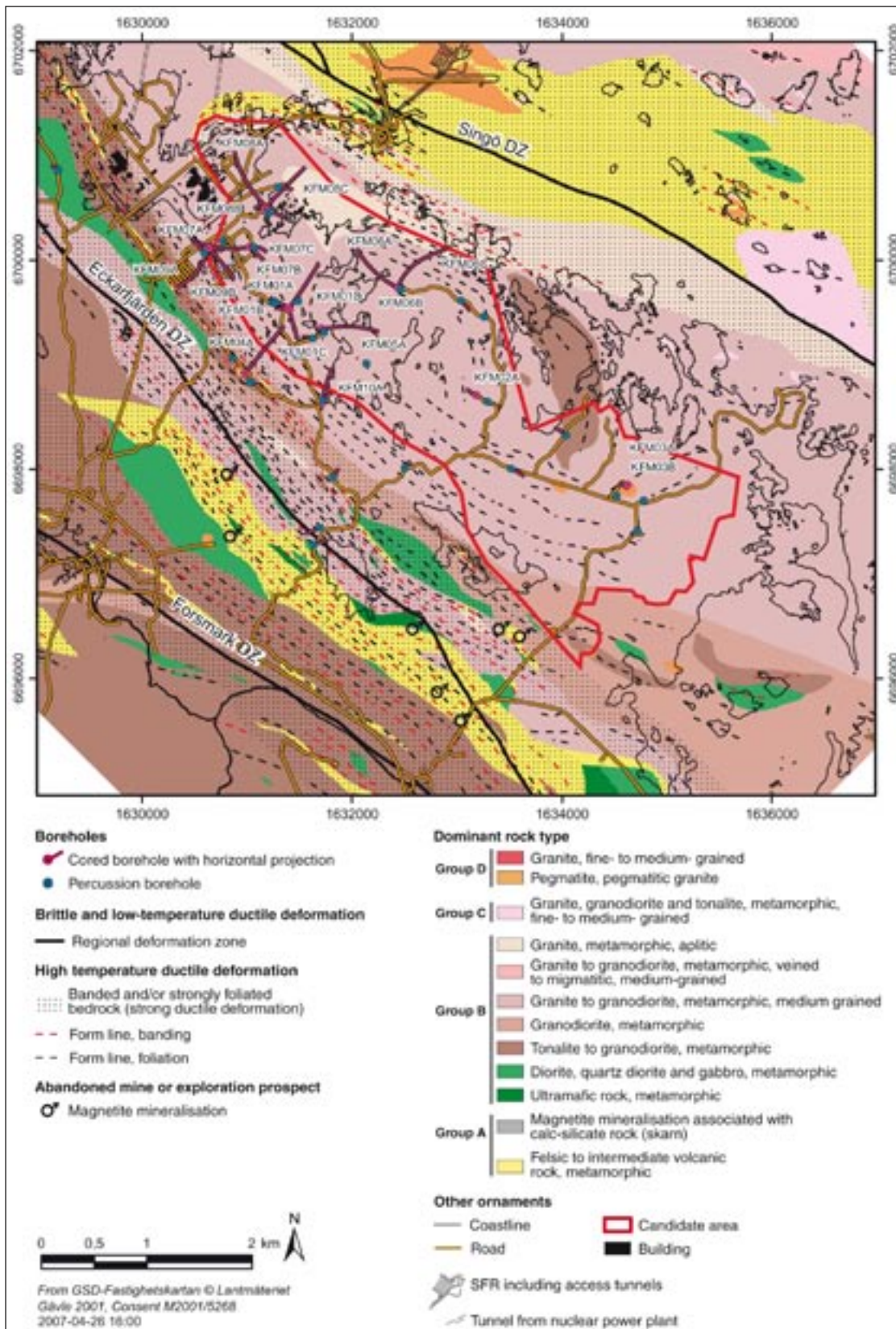
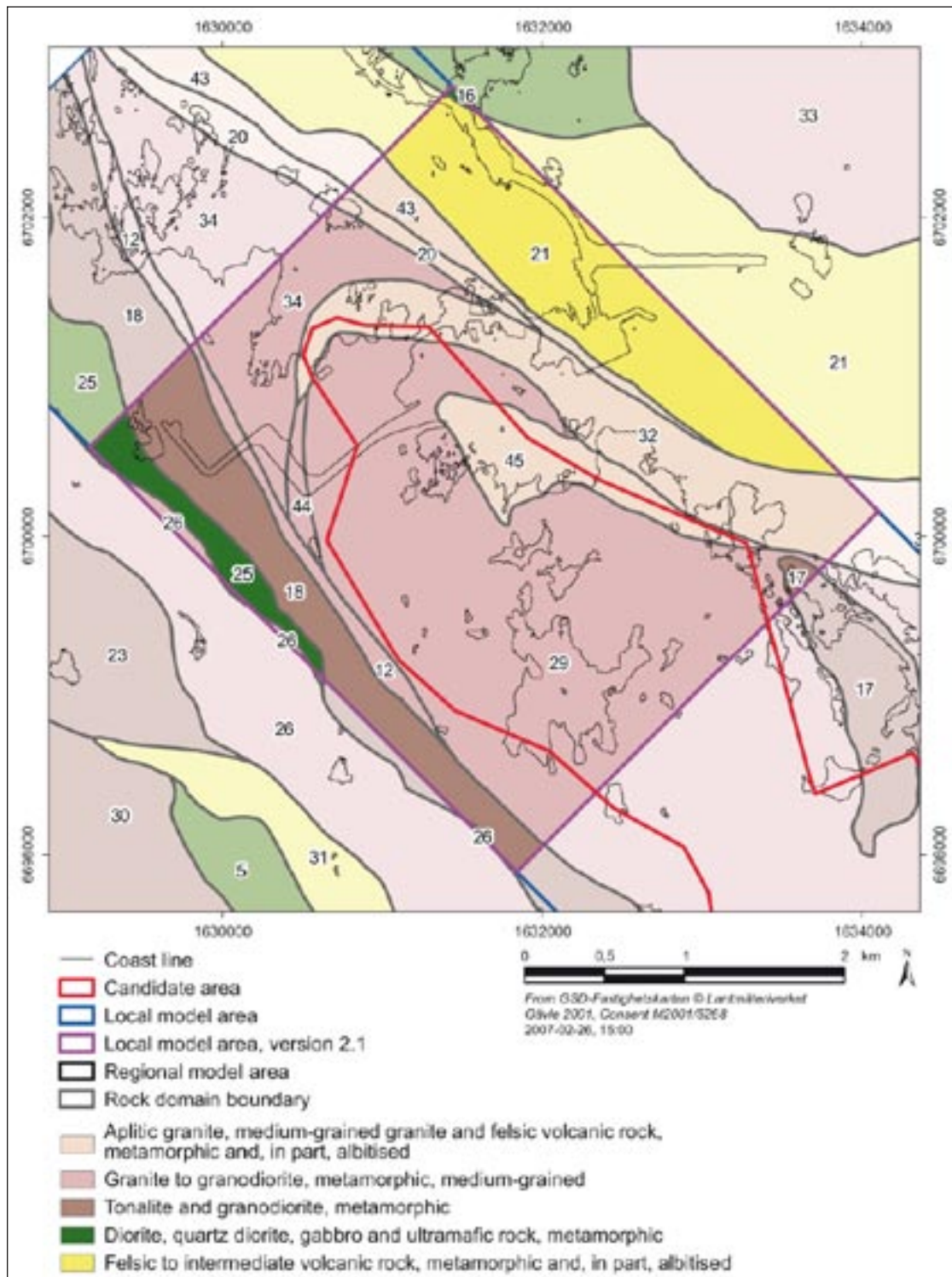
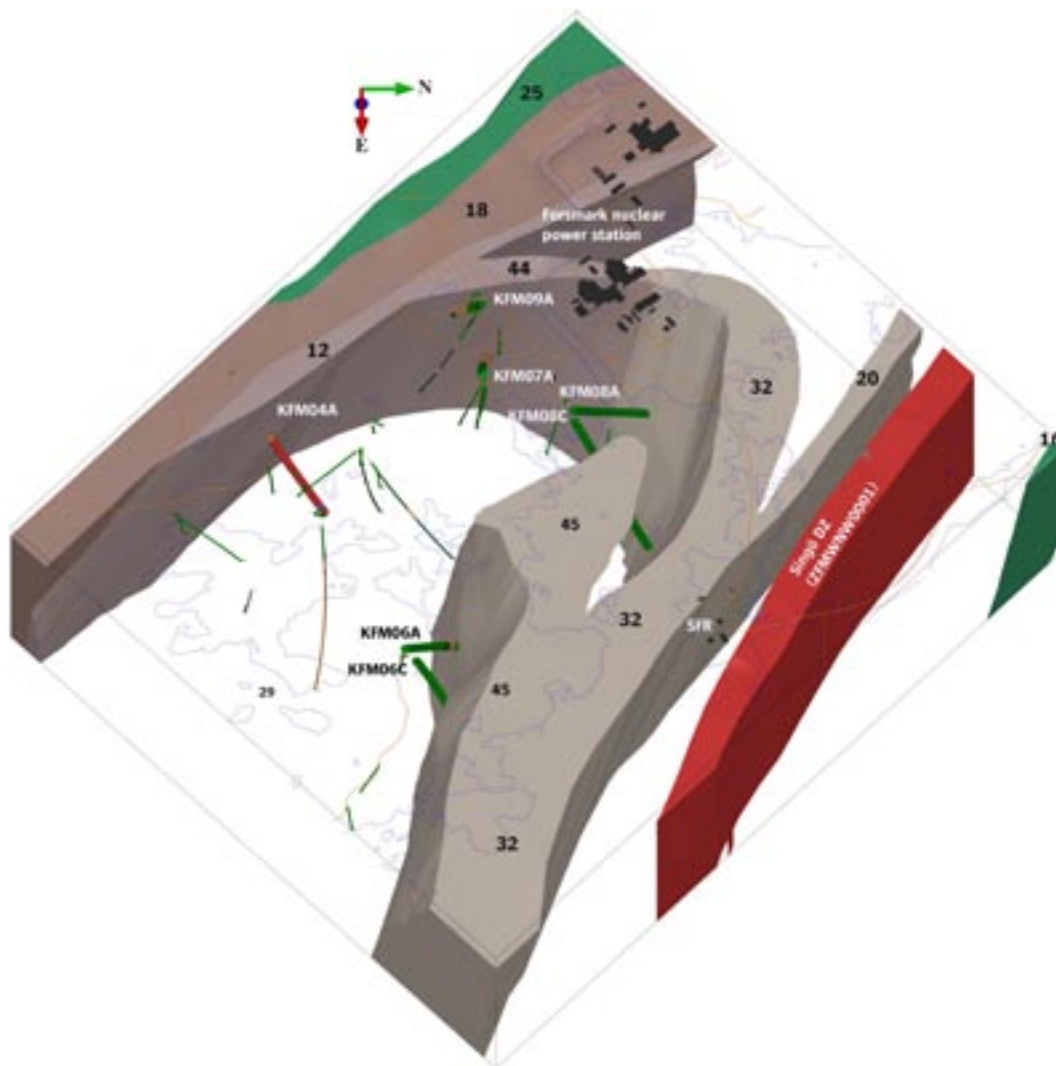


Figure 2-1. Bedrock geological map (version 2.2) including regional deformation zones with focus on the candidate area at the Forsmark site. The locations of the cored drillholes up to modelling stage 2.2 are also shown. Coordinates are provided using the RT90 (RAK) system /Stephens et al. 2007/.



**Figure 2-2.** Two dimensional model, version 2.2, at the surface of rock domains a) inside (darker colours) and immediately around (paler colours) the local model area. b) inside the regional model area. The colours represent the dominant rock type in each domain /Stephens et al. 2007/.



*Figure 2-3. Three dimensional model of rock domains inside the target volume, in the north-western part of the candidate volume /Stephens et al. 2007/. The model is viewed to the west from approximately the position of SFR.*

Rock domain RFM045 has a constricted rod-like geometry that plunges moderately to steeply to the south-east, see Figure 2-2 and Figure 2-3. The dominant rock types in this domain are aplitic granite (101058) and medium-grained metamorphic granite (101057), which represent approximately 51% and 18% of the rock domain respectively. Both these rocks are commonly affected by Na-K alteration (albitization). Modal analyses indicate that Na-K alteration gives rise to an increase in the quartz content with contemporary decrease in the content of K-feldspar, relative to unaltered rocks /Stephens et al. 2007/.

Subordinate rock types in rock domain RFM045 are essentially the same as in domain RFM029 and include pegmatite and pegmatitic granite (14%, 101061), fine to medium-grained meta-granitoid (9%, 101051) and amphibolite (6%, 102017).

### **2.1.3 Model for deterministic deformation zones**

The deterministic modelling work addresses zones that vary in length from  $L > 1,000$  m and upwards. The prime difference between the model stage 2.2 and previous models concerns the increased frequency of borehole intersections along deformation zones and the improved understanding of the character of the zones.

A conceptual geometric model for a brittle deformation zone at Forsmark is presented in Figure 2-4. The deformation zones are subdivided into a transition zone and a core. The transition zone, which normally ranges from a few metres up to several tens of metres in Forsmark, contains a fracture frequency and commonly also an alteration that is anomalous with respect to that observed in the host rock. If the deformation zone includes a core its thickness may vary from a few centimetres up to a few metres. The core is normally composed of a high frequency of sealed fractures, commonly in the form of a complex sealed fractured network, in combination with rock alteration. Fault gouge has not been encountered in the deformation zones in the local model /Stephens et al. 2007/.

To illustrate the condition of a typical deformation zone in the local model, Figure 2-5 presents a compilation of the fracture frequency of sealed and open fractures in a drill core intersecting ZFMENE0062A, together with two photographs at different scales from surface excavation of ZFMENE0062A, Figure 2-6. As can be observed in the figure, the zone consists mainly of sealed fractures in combination with rock alteration.

Sixty deformation zones were modelled deterministically in the local model in the current modelling stage 2.2 /Stephens et al. 2007/. Vertical and steeply dipping deformation zones dominate the picture and comprise 48 zones whereas a further 12 zones are gently dipping. All deformation zones that were modelled deterministically within the local model are presented in a horizontal section at 500 m depth in Figure 2-7.

The gently dipping zones occur mostly in the south-eastern part of the candidate volume. The reason for this is probably related to the gentle south-east dip of the amphibolites, tectonic foliation and mineral stretching lineation in this part of the candidate volume /Stephens et al. 2007/.

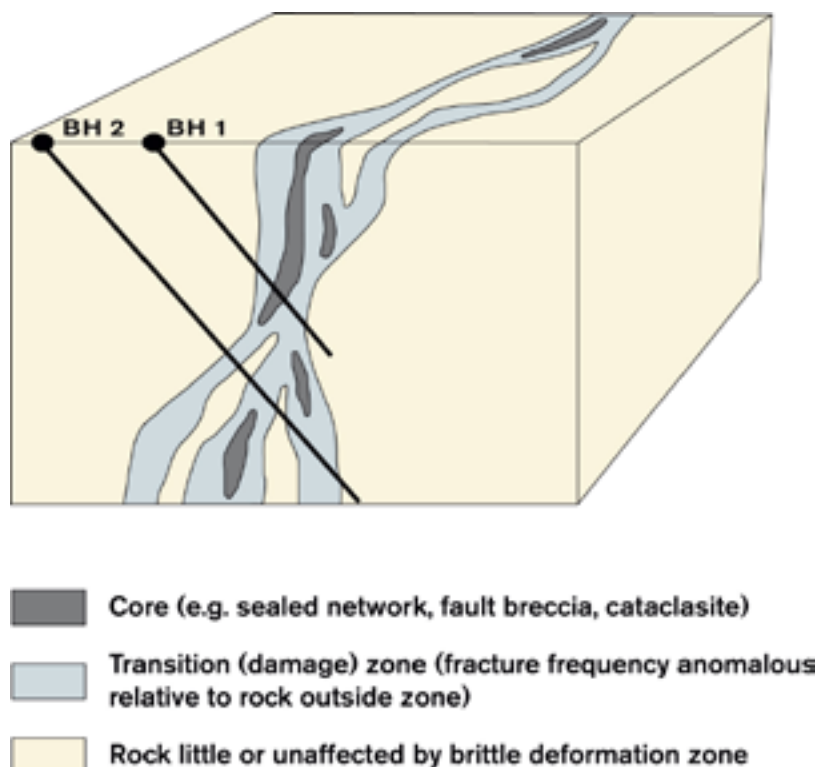


**Figure 2-4.** Three-dimensional cartoon illustrating a conceptual geometric model for a brittle deformation zone at Forsmark /Stephens et al. 2007/.



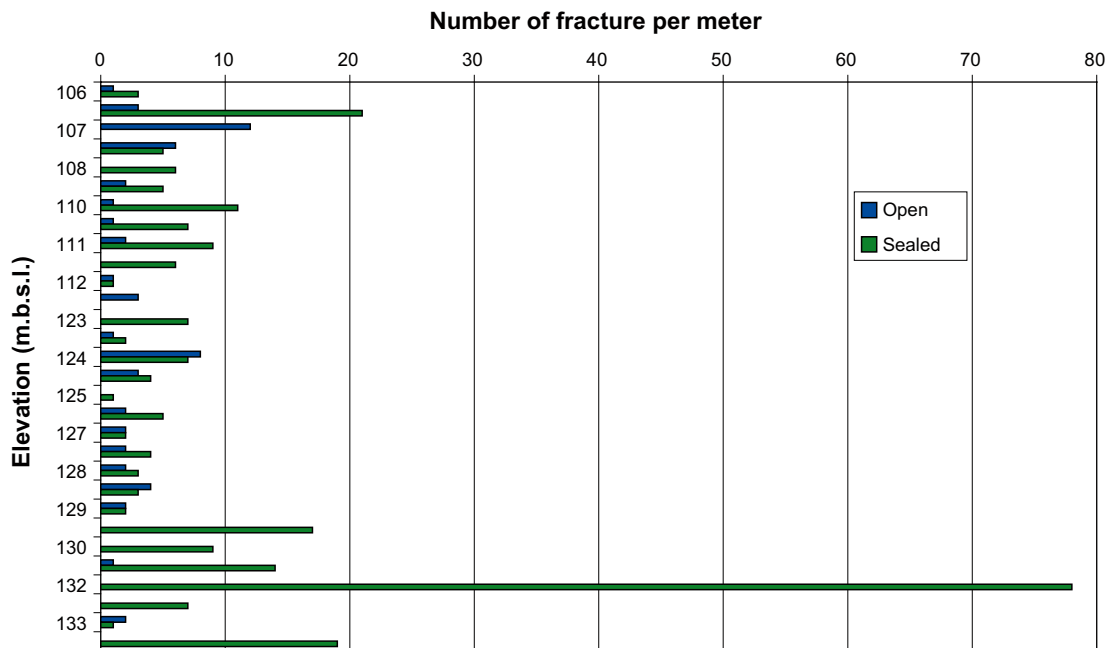


*Figure 2-5. Compilation of the fracture frequency of sealed and open fractures in a drill core intersecting deformation zone ZFMENE0062A.*



*Figure 2-6. Shows two photographs at different scales from a surface excavation of ZFMENE0062A /Stephens et al. 2007/.*

Four sets of deformation zones can be distinguished at the Forsmark site /Stephens et al. 2007/. In the local model volume, 30 vertical steeply dipping deformation zones referred to as ENE and NNE occur. 14 deformation zones referred to as SW steeply dipping zones with strike WNW and NW are present. A few steeply dipping deformation zones that strike NNW and EW are also present. The orientation of the deformation zones included in the local model is presented in a stereographic projection in Figure 2-8.

The character of the deformation zones, sorted on orientation with concise descriptions adapted from /Stephens et al. 2007/, is presented below:

Steeply dipping deformation zones striking ENE and NNE are formed in the brittle regime and are dominated by sealed fractures and sealed fracture network. Hematite-stained adularia, laumontite, chlorite and calcite are frequent in fractures of these zones.

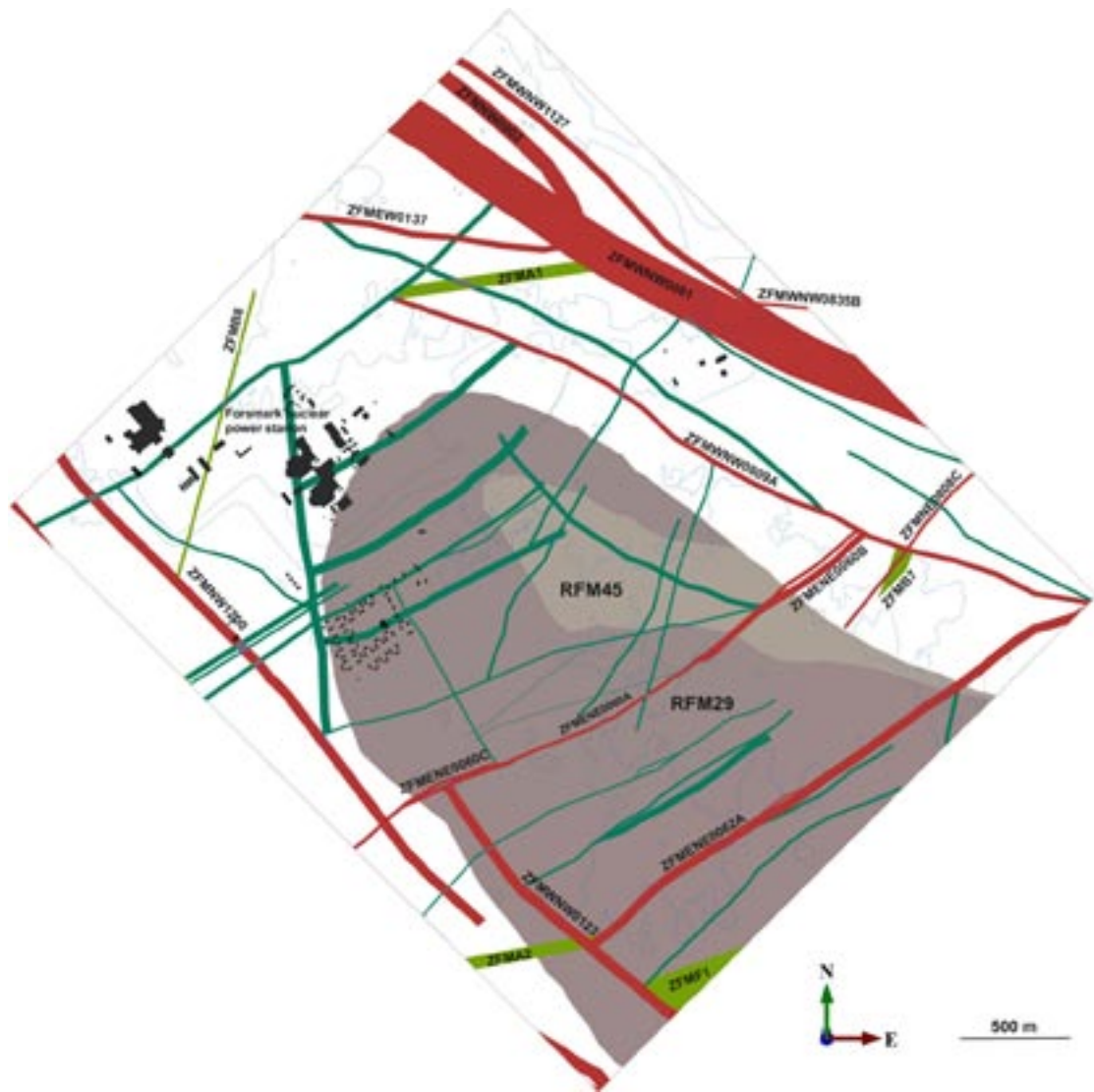


**Figure 2-7.** All deformation zones with  $L > 1,000$  m, presented together with the distribution of the rock domains RFM029 and RFM045, in a horizontal section at 500 m depth within the local model. The model is viewed to the north. Zones marked in red are steeply dipping or vertical and have a trace length at the surface longer than 3,000 m. Zones marked in blue-green are steeply dipping or vertical and are less than 3,000 m in length. Zones marked in green are gently dipping /Stephens et al. 2007/.

SW steeply dipping deformation zones with strike WNW and NW subsets are composite structures that contain mylonites, cataclastic rocks and cohesive breccias. The deformation zones are dominated by sealed fractures, which frequently include epidote, quartz, chlorite and calcite.

Steeply dipping deformation zones striking NNW are formed in the brittle regime and are dominated by sealed fractures. The fracture minerals in these zones are similar to those observed in the ENE to NNE set.

Gently dipping deformation zones are, as the other sets, also formed in the brittle regime. However, relative to the other sets they contain a higher frequency of open fractures and disconnected crush material. Chlorite, calcite and clay minerals are common fracture fillings in these zones.

Geological properties of each of the sixty zones that are included in the local model can be found in /Stephens et al. 2007/.

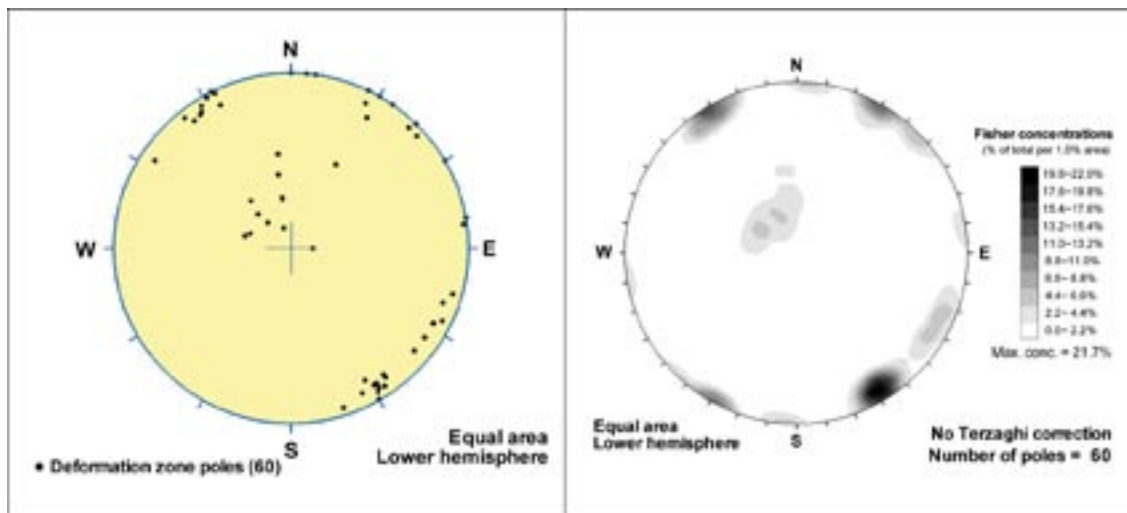


**Figure 2-8.** Orientation of deformation zones included in the local model. The orientation of the zones is shown as poles to planes in a stereographic equal-area, lower hemisphere projection /Stephens et al. 2007/.

#### 2.1.4 Fracture domain model

A fracture domain refers to a rock volume outside deformation zones in which rock units show similar fracture frequency characteristics. Fracture domains at Forsmark are defined on the basis of the single-hole interpretation work, and the results of the initial statistical treatment of fractures /Olofsson et al. 2007/. The fracture domain model captures both open and sealed fractures, and altered albitized granitic rock is also considered.

The analysis in /Olofsson et al. 2007/ concluded that six separate fracture domains were distinguished within the local model volume. The target volume comprises four of these fracture domains, namely FFM01, FFM02, FFM03 and FFM06. Figure 2-9 shows a three-dimensional image of the fracture domain model with the deterministic deformations zones in the target volume.

Fracture domain FFM01 dominates the lower part of the target volume. The bedrock in this domain can be described as sparsely fractured with low frequency of open and partly open fractures.

Fracture domain FFM02 dominates the upper north-western part of target volume. This fracture domain is characterized by a high frequency of gently dipping and sub-horizontal, open and partly open fractures.

Fracture domain FFM03 is situated in the south-east part of the target volume directly above the gently dipping zones ZFMA2 and ZFMF1. The domain is characterized by a high frequency of gently dipping deformation zones, containing both open and sealed fractures.

The dark grey volume in Figure 2-9 shows the position of fracture domain FFM06. The domain volume coincides with rock domain RFM045. It is distinguished by the widespread occurrence of fine-grained, altered (albitized) granitic rock, with a higher content of quartz compared to unaltered granitic rock.

The two remaining fracture domains FFM04 and FFM05, situated along the south-west and north-western/north-eastern margins respectively, outside the target volume, are shown in Figure 2-10. FFM04 includes rock domains RFM012 and RFM018, while FFM05 includes RFM032 and RFM044.

The rock mechanical modelling is concentrated on fracture domains FFM01 and FFM06, located in the target volume, at an applicable repository depth.

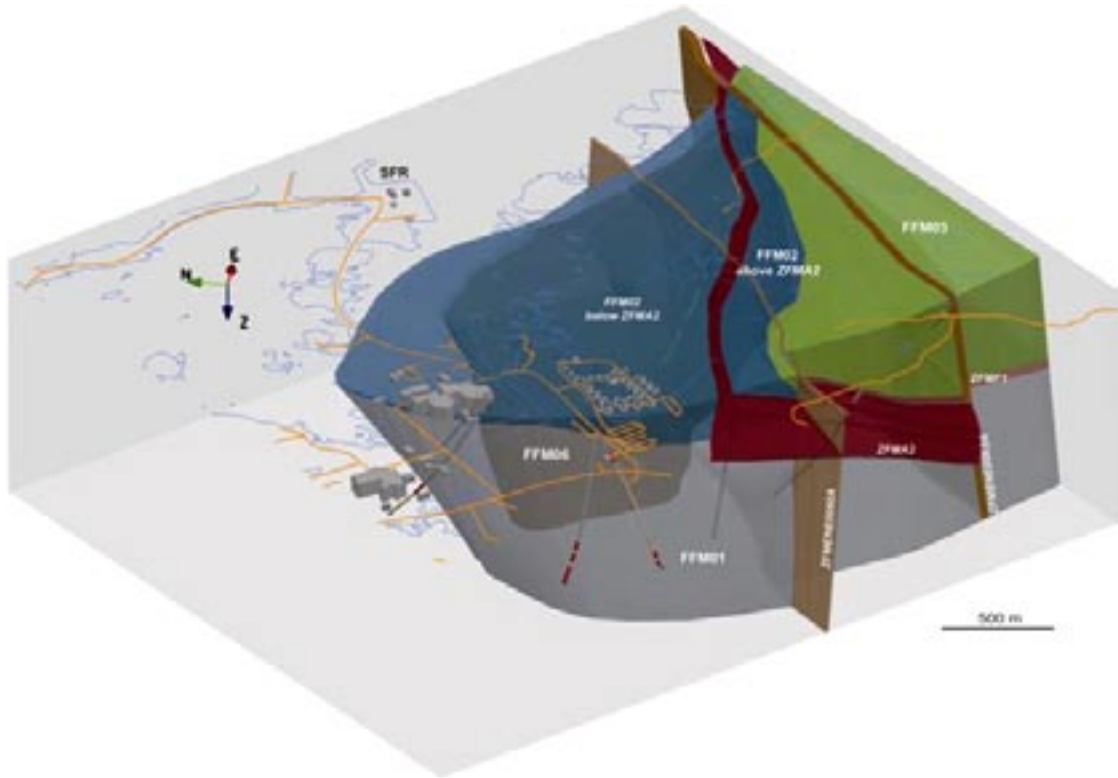


**Figure 2-9.** Three dimensional model of the fracture domain model showing the fracture domains together with the deterministic deformations zones that are encountered in the target volume /Olofsson et al. 2007/.

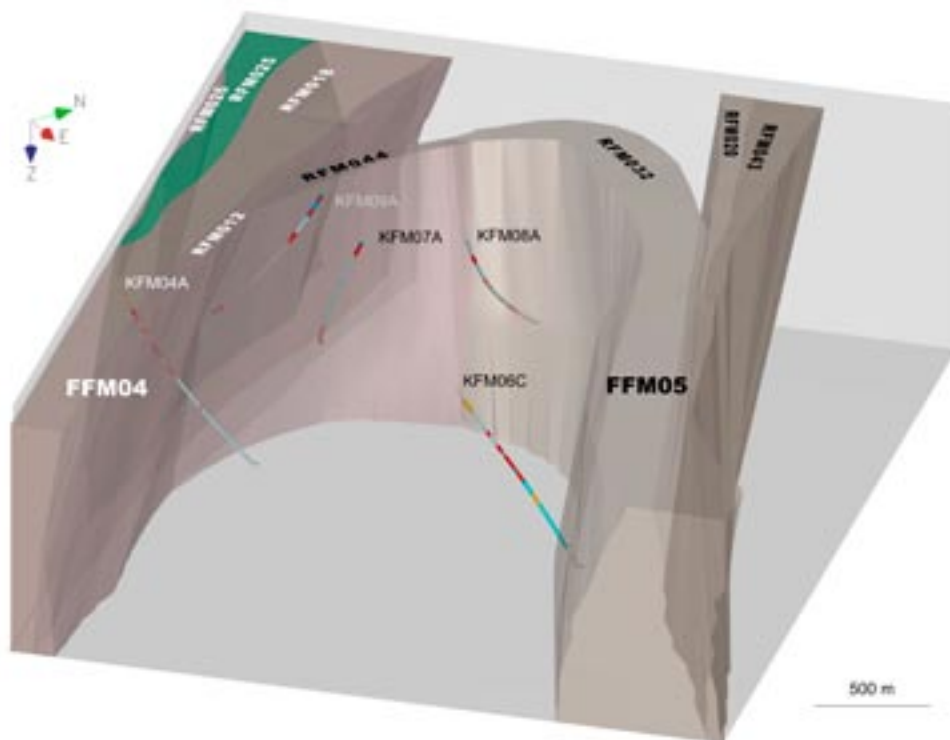


**Figure 2-10.** Three dimensional model of the fracture domain model showing the relationship between FFM04 and FFM05 and rock domains located outside the target volume.

### 2.1.5 Discrete fracture network model

The Discrete Fracture Network model (DFN-model) deals with fractures of a size range between 0.5–564 m. A DFN-model embraces separate models for fracture orientation, fracture size and fracture intensity. The current DFN-model, version 2.2 /Fox et al. 2007/, is valid within the target volume in fracture domains FFM01, FFM02, FFM03 and FFM06. A draft of this model was presented in June 2007 and the final report was presented in October 2007.

The fracture set orientation model was developed from the mapping of nine outcrops at the Forsmark site. The fracture sets have been divided into Global sets (visible in nearly all mapped outcrops) and Local sets (visible only in a subset of the mapped outcrops). The data available from surface outcrops lies entirely within fracture domains FFM02 and FFM03. Borehole data comes from FFM01, FFM02 and FFM03.

To illustrate the conditions in Forsmark, the mapped fracture sets in two bore holes KFM06A and KFM08A intersecting fracture domain FFM01, are presented in stereographic projections in Figure 2-11. The pole plots indicate 3–4 steeply dipping fracture sets and one sub-horizontal fracture set.

The intensity values have been derived from outcrops ( $P_{21}$ ) and borehole data ( $P_{10}$ ). (See Section 1.9 for definitions  $P_{10}$ ,  $P_{21}$  and  $P_{32}$ .) Fractures identified as belonging to DZs and MDZs were removed from the data used in the derivation. The fracture intensity ( $P_{32}$ ) as a function of elevation based on all mapped fractures in FFM01 is presented in Figure 2-12. The diagram clearly shows that the open fractures only represents a small portion of the total number of fractures and at the same time indicate a decreasing intensity with depth.

The DFN model comprises alternative models on size and intensity scaling. Adjustment factors for spatial variations in fracture intensity based on lithology or depth are also included.

The rock mechanics modelling employs the DFN-model for theoretical modelling of the rock mass properties, see Section 5.2. The results of theoretical modelling accounted for in this report were based on the draft DFN-model presented in June 2007. To check what influence the changes in the final DFN-model have had on the theoretical modelling, comparative studies have been performed using the final DFN-model as input, see Appendix 4. The results from these studies clearly show that the changes between the draft and the final DFN-model, have not had any significant influence on the outcome of the theoretical modelling.

Further details concerning the DFN model are to be found in /Fox et al. 2007/.

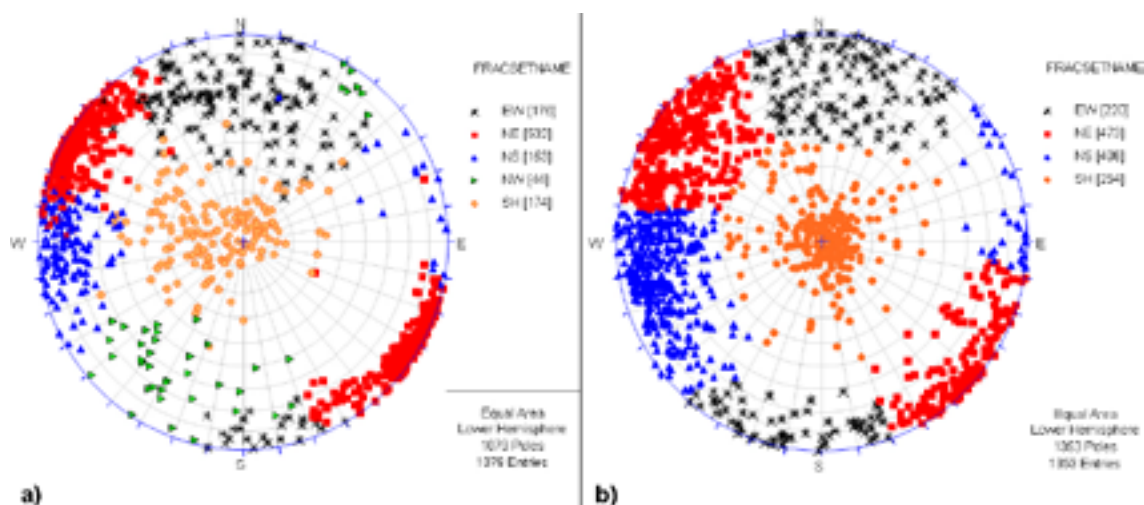


**Figure 2-11.** Observed fracture sets in two boreholes a) KFM06A and b) KFM08A intersecting fracture domain FFM01. The orientation of the fractures is shown as poles to planes in a stereographic equal-area, lower hemisphere projection /Fox et al. 2007/.

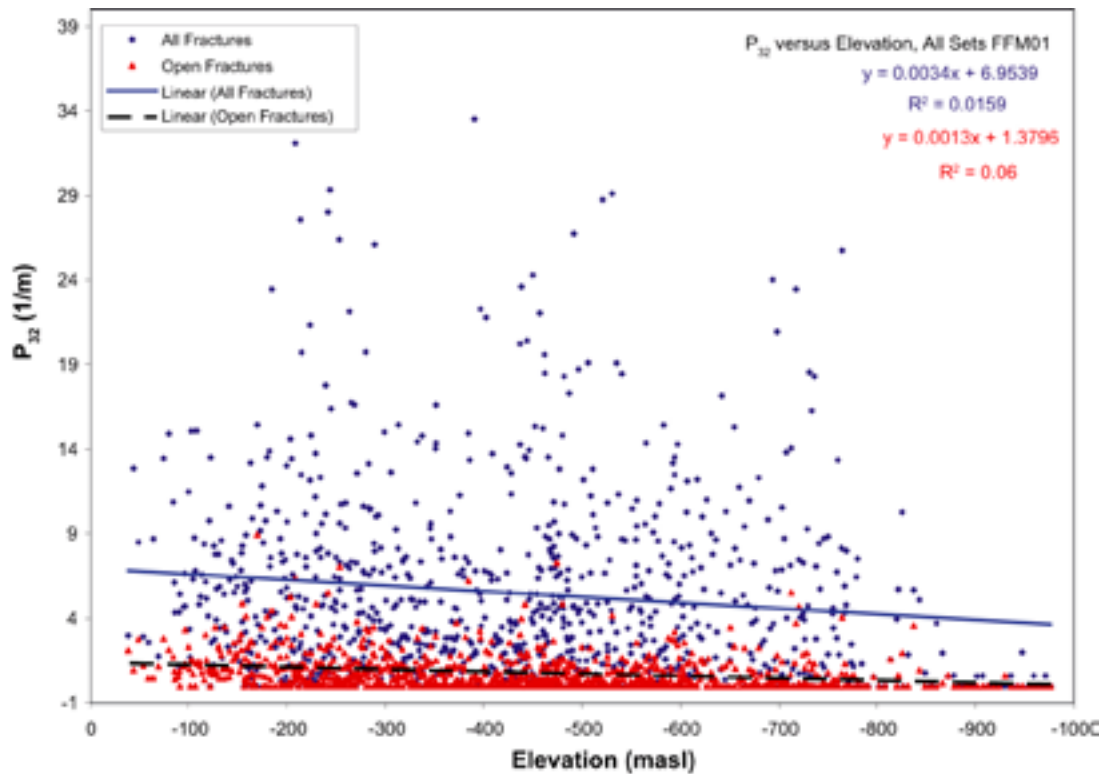


**Figure 2-12.** Fracture intensity ( $P_{32}$ ) as a function of elevation based on all fractures mapped in FFM01 /Fox et al. 2007/.

## 2.2 Hydrogeological input

The hydrogeological model of the Forsmark site accounts for highly transmissive fractures in the near surface bedrock in the north-west part of the tectonic lens, corresponding to FFM02, and sparsely fractured low transmissive bedrock below 400 m elevation, corresponding to bottom part of FFM01, /Follin et al. 2007/. Within FFM02, most of the flow occurs on sub-horizontal or gently dipping fractures, which maybe hydraulically connected for several hundreds of metres.

## 3 Mechanical properties of intact rock

### 3.1 Overview of the primary data

In this chapter, the mechanical properties from laboratory tests on intact rock are presented and discussed. The presentation here is supported by /Olofsson et al. 2007/, which includes a comprehensive compilation of the primary data from laboratory tests on intact rock and field tests in boreholes.

The presentation concentrates on tests performed in the target volume in rock domains RFM029 and RFM045, with subdivision into fracture domains FFM01, FFM02, FFM03 and FFM06. The section also covers a brief account of data from the adjacent rock domains RFM017, RFM018 and RFM034. A compilation of the results, including the adjacent rock domains, is assembled in Appendix A1.2 to A1.6. Three dimensional visualisation of the sampling locations in relation to fracture domains and deformation zones is presented in Appendix 8. The results in relation to geological features are supported by WellCad plots in /Olofsson et al. 2007/.

The dominant rock type in rock domain RFM029 is metamorphic, medium-grained granite to granodiorite, (101057), while rock domain RFM045 is comprised mainly of aplitic granite (101058). Other mapped rock types in the target volume are tonalite to granodiorite, pegmatite and amphibolite. Detailed information of the rock domain and the fracture domain model is presented in Sections 2.1.2 and 2.1.4.

The majority of the laboratory tests on intact rock were performed at SP (Swedish National Testing and Research Institute). P-wave velocity tests on core samples were performed by NGI (Norwegian Geotechnical Institute).

The methodology, standards and performance used for the testing are described in the following SKB Method Descriptions:

- Uniaxial Compression: SKB MD 190.001e, ver. 4.0 (2006-10-31).
- Triaxial Compression: SKB MD 190.003e, ver. 3.0 (2006-10-31).
- Indirect Tensile Tests: SKB MD 190.004e, ver. 3.0 (2006-10-31).
- P-wave Velocity on core samples: SKB MD 190.002, ver. 3.0 (2006-10-31).
- Direct Tensile Test: SKB P-07-76.

To gain information about measurement quality inter-laboratory experiments were performed. Repeated measurements with different measurement systems (i.e. different instruments, observers, environment etc) will give an estimate of reproducibility. Inter-laboratory comparisons are organized in such a way that the pilot laboratory sends out the same test item (or a sample of it) to different laboratories, which have to report back their results. However, this could not be carried out for mechanical testing. Instead, nearby samples were sent to Helsinki University of Technology (HUT) for comparative uniaxial, triaxial and indirect tensile strength testing /Sandström 2005/. In addition, Mining and Mineral Sciences Laboratories of Canada (CANMET) tested both indirect and direct tensile strength /Gorski et al. 2007/. The laboratory tests by HUT and NGI have been reported by /Lanaro and Fredriksson 2005/. The inter-laboratory tests included in this report are the tests by CANMET, and the indirect tests by HUT.

Except for laboratory tests of P-wave velocity, which are compiled in Appendix A1.1, the number and type of laboratory tests on intact rock carried out in each rock domain are listed in Table 3-1. The performed test program on intact rock includes in total 97 uniaxial compressive tests, 94 triaxial compressive tests and 205 tensile tests. The total amount of compressive tests is divided into 63 tests in FFM01, 21 tests in FFM03 and 5 tests in FFM06. The distribution of

**Table 3-1. Number of tests with each testing method performed in rock domain RFM017, RFM018, RFM029, RFM034, RFM044 and RFM045.**

Borehole	Rock domain	Fracture domain	Uniaxial compressive	Triaxial compressive	Tensile tests
KFM01A	RFM029	FFM01	14	14	30
KFM01A				6 <sup>1</sup>	
KFM01C	RFM029	FFM01	–	5	–
KFM01D	RFM029	FFM01	–	4	20 (20 <sup>2</sup> )
KFM02A	RFM029	FFM01	5	4	10
KFM02A	RFM029 PDZ	–	4	4	10
KFM02A	RFM029	FFM03	5	4	10
KFM02B				6 <sup>1</sup>	
KFM03A	RFM029	FFM03	12	12	30
KFM03A	RFM017	FFM03	4	4	10
KFM04A	RFM018 DZ	–	4		11
KFM04A	RFM029	FFM01	10	8	22
KFM05A	RFM029	FFM01	10	8	20
KFM06A	RFM029	FFM01	10	–	5
KFM06A	RFM045	FFM06	5	–	–
KFM07A	RFM029	FFM01	8	4	6
KFM08A	RFM029	FFM01	–	6	1
KFM09A	RFM034	FFM01	6	3	14
KFM09A	RFM044	FFM05	–	2	6
Total			97	94	205

<sup>1</sup> Microcrack volume measurements /Jacobsson 2007/.

<sup>2</sup> Direct tests from Canada, CANMET-MMSL /Gorski et al. 2007/.

the tests in the investigated volume follows the sampling strategy, cf. Section 1.3.2. The focus during the Complete Site Investigations has been on testing mechanical properties at a tentative depth of 400–500 m within the target volume FFM01 and FFM06.

The test results are mainly of intact, unaltered and unfractured rock. Four samples in rock domain RFM018 from borehole KFM04A were taken in a deformation zone (ZFMNW1200) and four samples in rock domain RFM029 were taken in a “possible deformation zone”. However, most test samples are on the whole without imperfections. The strategy for the site investigation is outlined in Section 1.3.

Laboratory testing in addition to that presented in Table 3-1, including uniaxial compressive and indirect tensile tests, has been performed on samples from fracture domain FFM06. A test series for determination of elastic parameters including sealed fracture networks (ZFMENE0060) has also been performed, as well as additional microcrack volume measurements. The results from these new tests will be presented in a complementary report under modelling stage 2.3.

## 3.2 Strength properties of intact rock

In this section the strength properties of intact rock, determined on samples taken in the target volume rock domain RFM029 and RFM045, are discussed. The results include Uniaxial compressive strength ( $\sigma_c$ ), Crack initiation stress ( $\sigma_{ci}$ ), Triaxial strength and Tensile strength ( $\sigma_t$ ).



### 3.2.1 Uniaxial compressive strength

Uniaxial compressive strength is an important parameter for design and the assessment of a repository. The parameter is used to evaluate the potential risk for excavation and thermal induced spalling in deposition holes, cf. Table 1-1, Section 1.3.1.

The location and the results of the uniaxial compressive tests are presented in a three dimensional view in Figure 3-1. The uniaxial compressive strength is indicated by different colours with subdivisions of intervals according to the legend. It should be noted that since the sampling for rock mechanics tests are conducted on core samples that are situated close to one another some sample locations are hidden.

#### **Samples from fracture domains**

The test results from fracture domain FFM01 of the main rock type, granite to granodiorite (101057), range from 157 MPa to 289 MPa with a corresponding mean value of approximately 225 MPa based on 47 tests. The pegmatite (101061) gives a similar result with a mean value of approximately 230 MPa, cf. Figure 3-2.

From fracture domain FFM03, 13 samples of the main rock type, granite to granodiorite (101057) were tested. The results range from 200 to 250 MPa with a mean value of 220 MPa. 4 samples of tonalite (101054) were also tested, giving values in the range of 143 to 152 MPa with a mean of 150 MPa.

Only five samples from fracture domain FFM06 were tested, all of metamorphic aplitic granite (101058). The results show values in the range of approximately 230 to 371 MPa with a mean value of 310 MPa.

The analyses of the results of the uniaxial compressive strength indicate that nine tests gave values of less than 160 MPa. The test results of these samples are listed in detail in Appendix A1.2 including sample depth and borehole information. The cause of failure has been analysed and in five cases the low value is due to failure along foliation planes or along sealed fractures in the core. These samples are included in the dataset used for calculation of test results and lower the total UCS mean value by 2.8% compared to if they were omitted.

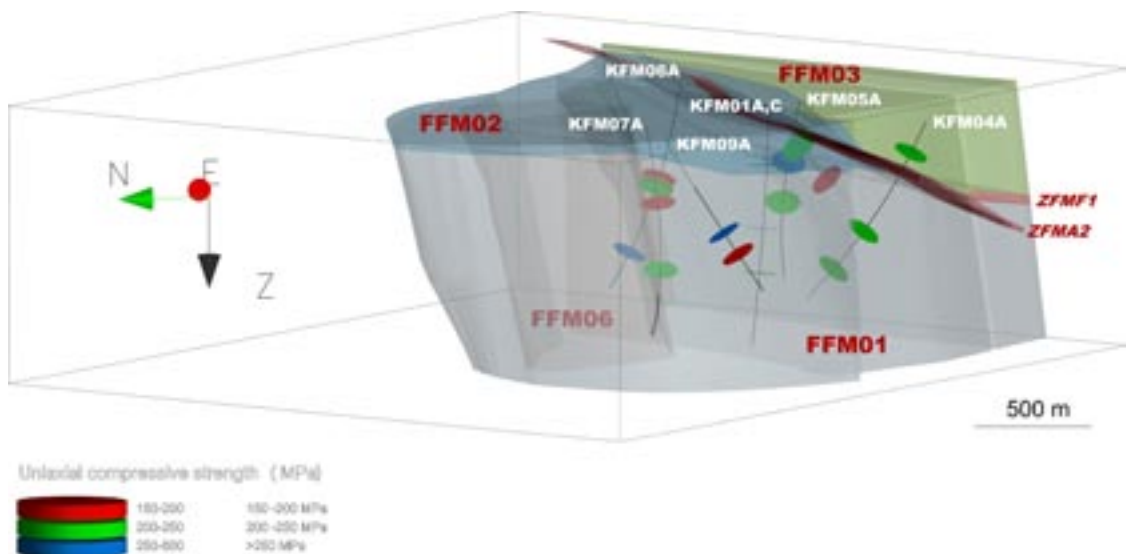


**Figure 3-1.** Location and results of the uniaxial compressive tests. Since the samples are situated close to one another some sample locations are hidden.

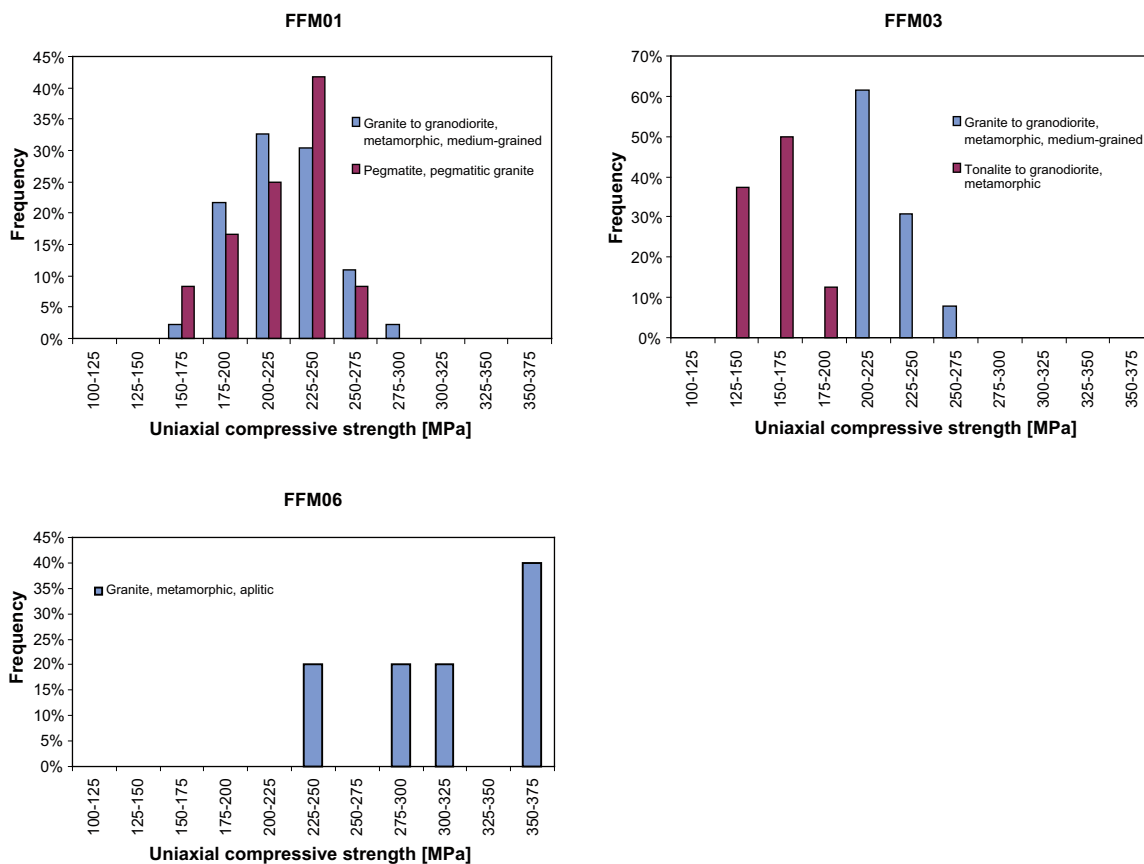


Figure 3-2. The frequency distribution of the test results from the uniaxial test, including all samples.

### Samples from deformation zones

The number of uniaxial compressive tests performed on samples within deformation zones is limited to four in KFM02A from a “possible deformation zone” (PDZ) and four in KFM04A from deformation zone ZFMNW1200.

The test results from deformation zone ZFMNW1200, in rock domain RFM018, on metamorphic granodiorite (101057) have a higher mean value of uniaxial compressive strength (6%) than intact rock of the same rock type in RFM029. However, since the specimens from the deformation zones are classified and sampled as intact rock, the difference in UCS is not expected to be large. The samples from borehole KFM02A in a PDZ in rock domain RFM029 display lower values than the results from deformation zone ZFMNW1200, see Appendix A1.2.

### 3.2.2 Crack initiation stress

The Crack Initiation Stress ( $\sigma_{ci}$ ) as the uniaxial compressive strength is a parameter that is used to evaluate the potential risk for excavation induced and thermal induced spalling in deposition holes, cf. Table 1-1, Section 1.3.1.

The crack initiation stress has been evaluated from the uniaxial compressive strength tests according to the procedure presented by /Martin et al. 2001/. The value is a measure of the stress required to initiate tensile cracking in laboratory samples. /Andersson 2007/ showed that this stress level could be used as a lower bound estimate to assess the onset of spalling around circular openings subjected to thermal-mechanical loading. The results of all samples are presented in Figure 3-3.

For granodiorite (101057) and pegmatite (101061) in rock domain RFM029, the crack initiation starts around 120 MPa. The crack initiation stress for granite (101058) in rock domain RFM045 is higher and has a mean of 170 MPa, see Table 3-2. The higher value of the tested rock types in rock domain RFM045 might be due to alteration (albitization) which increases the quartz content /Stephens et al. 2007/.

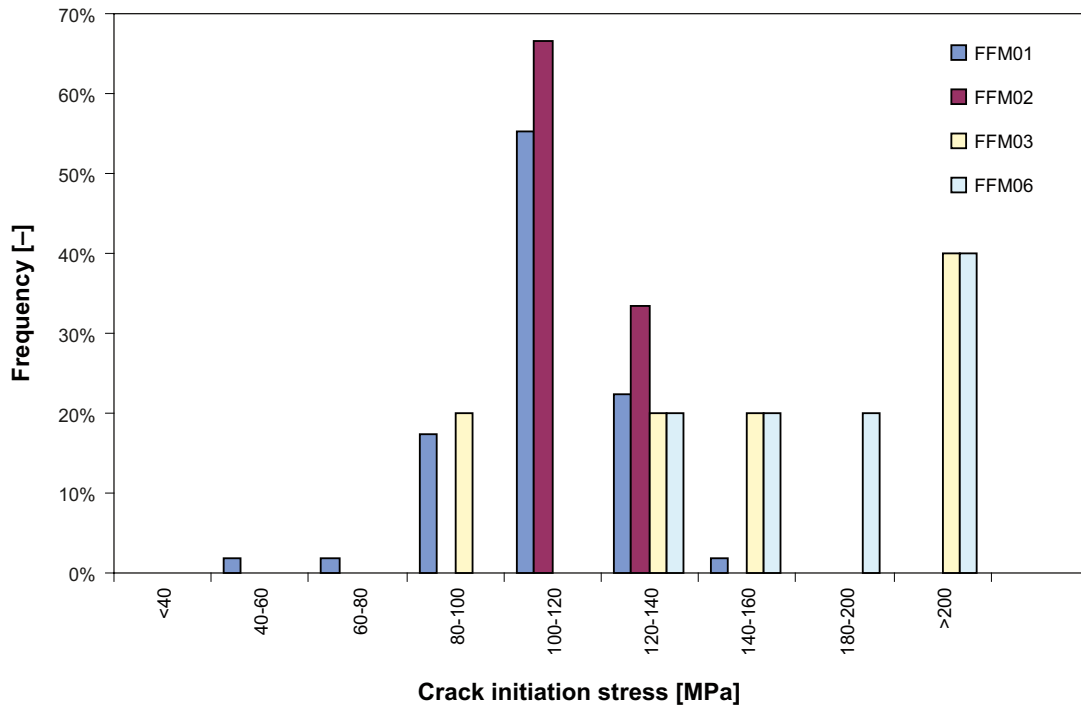


**Figure 3-3.** The crack initiation stress versus frequency for samples in fracture domain FFM01, FFM02, FFM03 and FFM06.

**Table 3-2.** Crack initiation stress evaluated of samples in domains RFM029 and RFM045.

Rock domain	Rock type	No. of samples	Minimum (MPa)	Mean (MPa)	Median (MPa)	Maximum (MPa)	Std. dev. (MPa)
RFM029	Granite to granodiorite, metamorphic, medium-grained	63	60	115	115	187	21
RFM029	Pegmatite, pegmatitic granite	10	100	121	123	140	12
RFM045	Granite, metamorphic, aplitic	5	125	169	170	200	29

### 3.2.3 Tensile strength

The tensile strength of intact rock is one of several rock mechanics parameter established for the repository safety assessment, see Table 1-1, Section 1.3.1. Indirect tensile tests, performed by the Brazilian test method, were conducted on 185 samples in parallel and perpendicular direction to the foliation. The location of the sampling for indirect testing is presented in Figure 3-4. The statistics of the test results for each of the main rock types, sorted into fracture domains, are presented in Appendix A1.5.

In addition to the indirect tests, a comparative test series of direct tensile tests were performed by CANMET on 20 samples of granite to granodiorite (101057). These samples were collected in fracture domain FFM01 from borehole KFM01D at 387 to 400 m depths. The direct tests were performed according to split-grip test set up where the sample is ground to a smaller diameter along the central part.

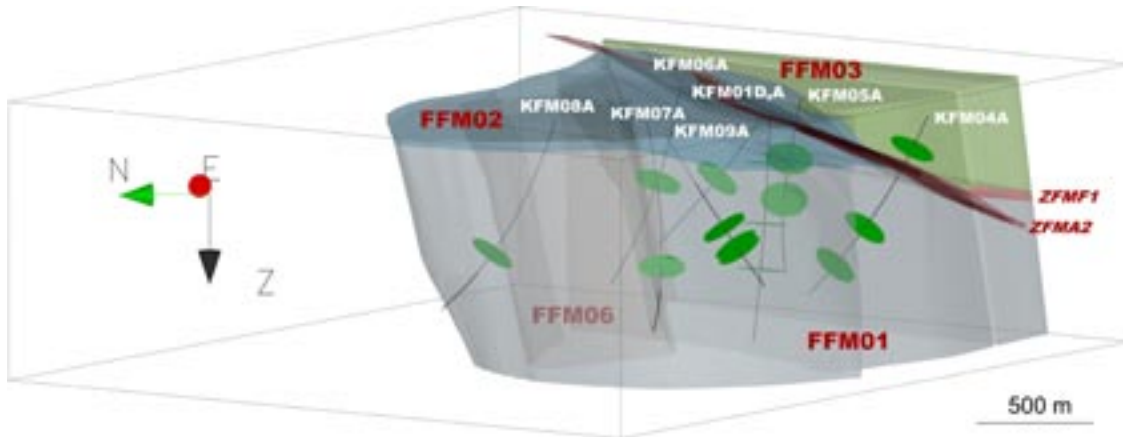


**Figure 3-4.** Location of sampling for the indirect tests. Since the samples are situated close to one another some sample locations are hidden.

The evaluated mean values of the indirect tests sorted into fracture domains, the influence of loading direction and the mean of the direct tensile tests are shown in Figure 3-5. A frequency distribution of the indirect tests in relation to tested rock types is also included in the diagram.

The mean values of tensile strengths for fracture domains from the indirect tests range between 13 and 16 MPa independent of rock type, cf. Figure 3-5a. The difference between test results carried out perpendicular and parallel to the foliation is only about 1 MPa, which indicates isotropic tensile strength. As expected, the 11 MPa mean value of the direct tensile test is consistently less than the mean value of indirect test.

A compilation of the tensile tests performed by SP, HUT and CANMET on the main rock type is presented in Table 3-3. The indirect tests by CANMET show the largest strength, while the direct tests show the lowest strength value. The difference in mean between the indirect tests performed by SP and by CANMET is approximately 40%.

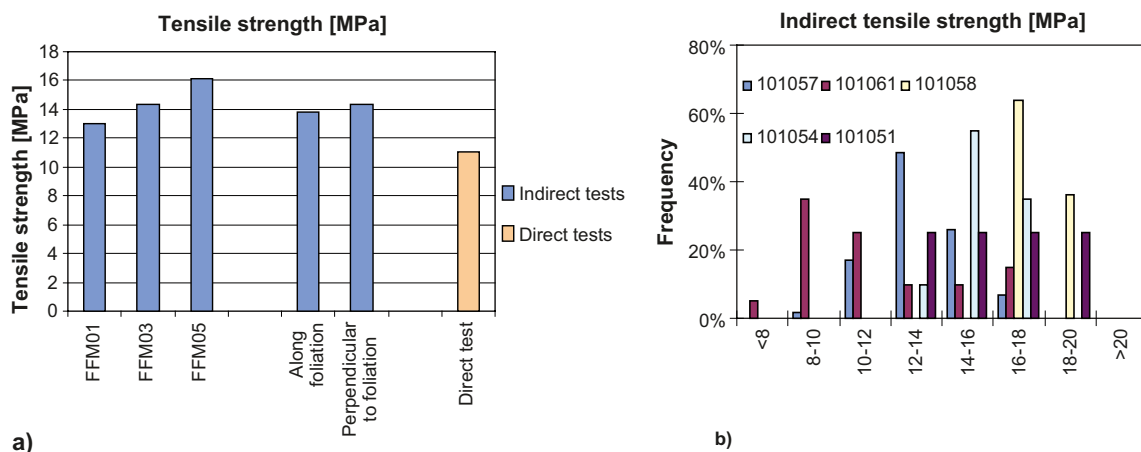


**Figure 3-5.** Results of the indirect and direct tensile strength tests. a) Comparison of mean values of fracture domains, influence of applied loading direction and the mean of the direct tests performed in Canada. b) Frequency distribution of tensile strength for all samples, rock types and location of sampling for the indirect tests.

**Table 3-3. Indirect- and direct tensile tests performed on samples in RFM029 and RFM034 by SP, and by HUT and CANMET in RFM029. All samples are rock type (101057).**

Institute Testing method	Rock domain	No. of samples	Minimum (MPa)	Mean (MPa)	Mode (MPa)	Maximum (MPa)	St. dev. (MPa)
<b>SP-testing</b>							
Indirect tensile strength	RFM029	122	9.7	13.3	13.5	17.9	1.63
Indirect tensile strength	RFM034	8	14.0	15.6	15.3	17.7	1.19
<b>HUT-testing</b>							
Indirect tensile strength	RFM029	10	14.1	15.3	15.0	16.2	0.62
<b>CANMET-testing</b>							
Indirect tensile strength	RFM029	20	15.5	19.0	18.5	20.9	1.47
Direct tensile strength	RFM029	20	7.9	11.1	11.2	13.2	1.55

The ratio between the mean values of the direct and indirect tests was calculated based on the samples tested by CANMET in Canada. Here the direct and indirect tests were performed over the same core length. The calculated ratio between the direct- and the indirect tensile strength is  $r = 0.58$ . A common explanation to the observed smaller strength values from the direct tensile test, is that there are less critically stressed volumes involved in the indirect tests.

### 3.2.4 Triaxial compressive strength

In the following section the results of triaxial compressive strength are presented. In addition the evaluated Hoek-Brown's and Mohr-Coulomb's failure envelopes for intact rock are also presented. The failure envelopes are used in the theoretical approach to estimate rock mass properties.

The locations of sampling for triaxial testing are presented in Figure 3-6. No data from rock domain RFM045 are available since no triaxial tests were performed on samples from that rock domain.

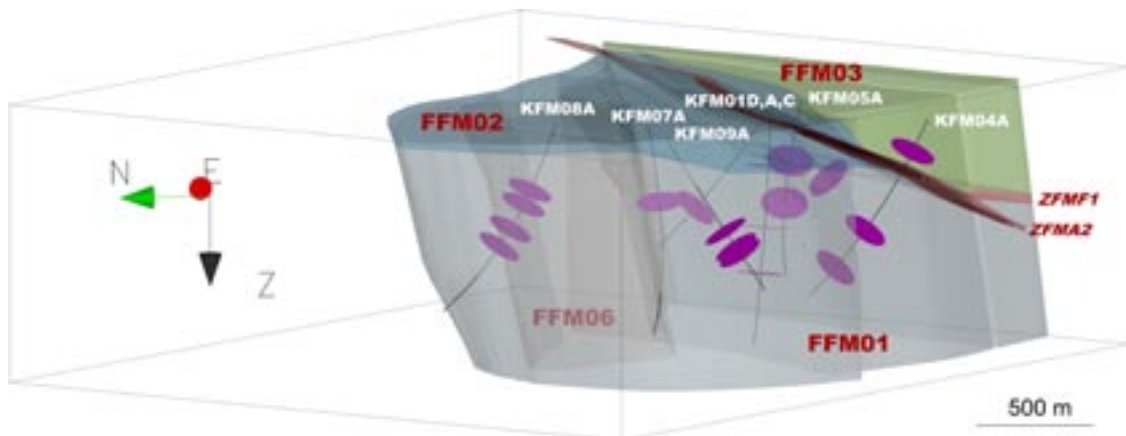


**Figure 3-6.** Location of sampling for the triaxial tests. Since the samples are situated close to one another some sample locations are hidden.

The Hoek-Brown criterion is given by the following equation /Hoek et al. 2002/:

$$\sigma'_1 = \sigma'_3 + \sigma_c \left( m_i \frac{\sigma'_3}{\sigma_c} + s \right)^{0.5} \quad \text{Equation 3-1}$$

where,  $\sigma'_1$  and  $\sigma'_3$  are maximum and minimum principal stress,  $\sigma_c$  uniaxial compressive strength of intact rock and  $m_i$  and  $s$  are constants which depends upon the characteristics of the rock. For intact rock of unaltered condition  $s$  equals 1. The failure envelope is developed as the best fit of the results from the uniaxial and triaxial compressive tests. The Mohr-Coulomb's linear approximations of the Hoek-Brown's Criterion were also calculated for a certain stress interval (0 to 15 MPa).

Figure 3-7 shows the evaluated Hoek-Brown's and Mohr-Coulomb's failure envelopes based on uniaxial and triaxial tests on granite to granodiorite (101057). The mean triaxial strength increases roughly by 10 MPa per 1 MPa increase in confining pressure within a 2–20 MPa range. A complete compilation of the results from the triaxial testing of all rock types is presented in Appendices A1.3 and A1.6.

The diagram also provides an estimation of the tensile strength of the intact rock that can be compared with the laboratory results in Section 3.2.3. However, the measurements of the tensile strength included in the figure were not used for evaluation of the failure envelopes. The tensile strength evaluated from the Hoek-Brown's and Mohr-Coulomb's envelopes shows good agreement with the test data for the rock types pegmatite and tonalite, whereas the test values obtained are larger for granite to granodiorite.

The evaluated compressive strength at zero confinement (UCS) and the constant  $m_i$  included in Hoek-Brown's criterion, sorted by rock type, is presented in Table 3-4. The UCS values evaluated from the triaxial tests are in rather good agreement with the values obtained from standard uniaxial tests. The mean value of  $m_i$  varies between 13 and 46, depending on rock type and rock properties. The lowest value  $m_i = 13$  was obtained for Tonalite. In /Hoek 2007/ a mean value of  $m_i$  on intact samples of granites is reported to be  $32 \pm 3$  compared to  $29 \pm 3$  for granite to granodiorite (code 101057) in Forsmark.

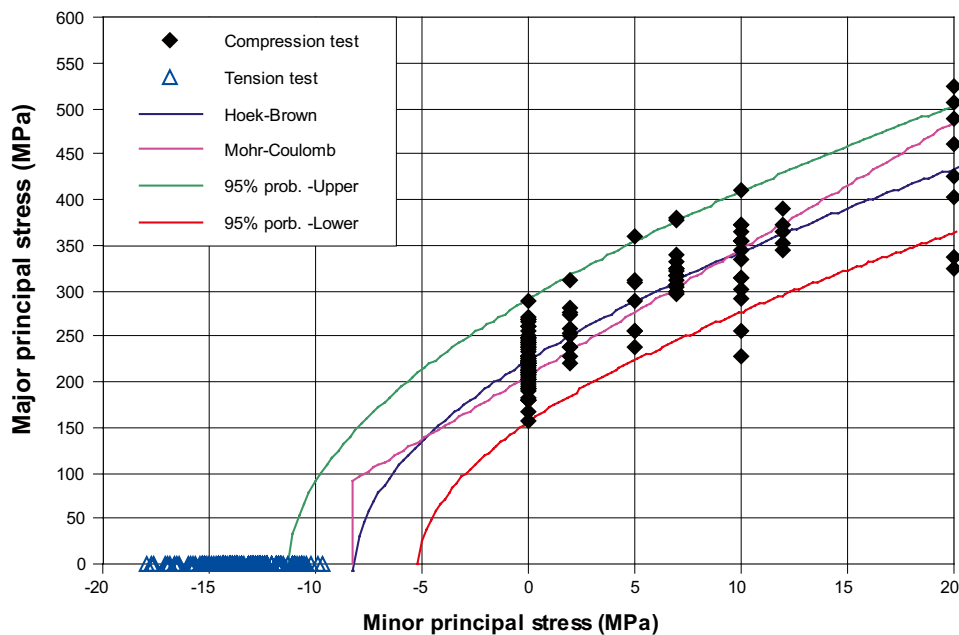


**Figure 3-7.** Hoek and Brown's and Coulomb's failure envelopes based on uniaxial and triaxial tests on metamorphic, medium-grained granite to granodiorite. Tensile strength from test data are included in the diagram but not used for the evaluation of the failure envelopes.

**Table 3-4. Evaluated compressive strength at zero confinement (UCS) and the constant  $m_i$  for Hoek-Brown's criterion. The results are based on samples of intact rock from rock domain RFM029. Since FFM02 and FFM06 only include uniaxial tests, they are not represented here.**

Fracture domain	Rock type	Number of samples	Min strength <sup>1</sup>		Mean		Max strength <sup>2</sup>	
			UCS (MPa)	$m_i$	UCS (MPa)	$m_i$	UCS (MPa)	$m_i$
FFM01	Granite to granodiorite, metamorphic, medium-grained	86	149	31	225	28	299	26
FFM01	Granite, granodiorite and tonalite, metamorphic, fine- to medium-grained	4	136	50	165	46	194	42
FFM01	Pegmatite, pegmatitic granite	15	165	19	227	18	289	17
FFM03	Granite to granodiorite, metamorphic, medium-grained	25	196	29	221	28	246	28
FFM03	Tonalite to granodiorite, metamorphic	8	142	13	151	13	160	13

<sup>1</sup> Lower envelope, 95% probability.

<sup>2</sup> Upper envelope, 95% probability.

The evaluated cohesion,  $c$ , and the friction angle,  $\phi$ , for the Mohr-Coulomb's criterion based on the results on intact rock sampled are presented in Table 3-5. Since FFM02 and FFM06 only include uniaxial tests, they are not represented here. The cohesion and the angle of friction evaluated according to Mohr-Coulomb's Criterion, varies between 17–42 MPa and 51–63 degrees respectively. The lowest value of the friction angle was obtained for Tonalite, see Table 3-5.

**Table 3-5. Evaluated cohesion and friction angle for the Mohr-Coulomb's criterion. The results are based on samples of intact rock from rock domain RFM029. Since FFM02 and FFM06 only include uniaxial tests, they are not represented here.**

Fracture domain	Rock type	Number of samples	Min strength <sup>1</sup>		Mean		Max strength <sup>2</sup>	
			$c$ (MPa)	$\phi$ (°)	$c$ (MPa)	$\phi$ (°)	$c$ (MPa)	$\phi$ (°)
FFM01	Granite to granodiorite, metamorphic, medium-grained	86	19	59	28	60	36	61
FFM01	Granite, granodiorite and tonalite, metamorphic, fine- to medium-grained	4	17	62	19	63	22	63
FFM01	Pegmatite, pegmatitic granite	15	24	55	33	56	42	56
FFM03	Granite to granodiorite, metamorphic, medium-grained	25	24	60	27	60	30	61
FFM03	Tonalite to granodiorite, metamorphic	8	24	51	25	51	26	51

<sup>1</sup> Lower envelope, 95% probability.

<sup>2</sup> Upper envelope, 95% probability.

### 3.3 Deformation properties of intact rock

The elastic properties Young's modulus and Poisson's ratio presented in this section are employed in the safety assessment to analyse thermo-mechanically induced changes in the repository near field, cf. Table 1-1, Section 1.3.1.

#### 3.3.1 Young's modulus

The modulus may be calculated in a number of ways: tangent Young's modulus  $E_t$ , mean Young's modulus  $E_{av}$  and secant Young's modulus  $E_s$ . The modulus presented here is based on the tangent Young's modulus evaluated at 50% of the compressive strength.

Young's Modulus is determined from the uniaxial and triaxial compressive tests. The sampling locations are shown in Figure 3-1 and Figure 3-5 respectively, and in Appendix 8. The frequency distribution of Young's modulus from the uniaxial tests is presented in Figure 3-8a. Figure 3-8b shows a comparison between Young's modulus determined by uniaxial and triaxial compressive tests for granite to granodiorite.

For rock domain RFM029, Young's modulus from uniaxial compressive tests gives a mean of approximately 75 GPa with a standard deviation of only 3 MPa and is independent of rock type, cf. Appendix A1.6. In rock domain RFM045 the value is higher with a mean of 83 GPa for metamorphic aplitic granite (101058).

Young's modulus evaluated from the triaxial compressive strength in rock domain RFM029 ranges between 70 and 74 GPa with the exception of granite, granodiorite, (101051) which has a mean value of 68 GPa. No triaxial tests were performed on rock samples in rock domain RFM045. Figure 3-8b indicates that there is no significant difference in Young's modulus evaluated from the uniaxial or triaxial tests in Forsmark.

#### 3.3.2 Poisson's ratio

Poisson's ratio is evaluated from the testing of uniaxial and triaxial compressive strength tests. The sampling locations are presented in Figure 3-1 and Figure 3-5, and in Appendix 8. The frequency distribution of Poisson's ratio from the uniaxial tests is presented in Figure 3-9a, whilst Figure 3-9b shows a comparison between Poisson's ratio determined by uniaxial and triaxial compressive tests for granite to granodiorite.

The mean value of Poisson's Ratio in rock domain RFM029 ranges from 0.14 to 0.35 in uniaxial compressive tests. The lower value is from granite to granodiorite (101057) and the higher value is obtained from pegmatite (1010061) cf. Appendix A1.6.

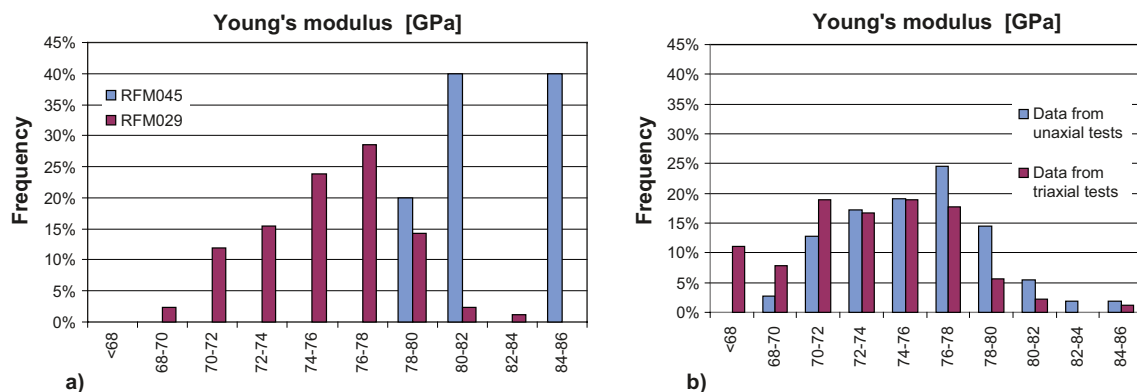
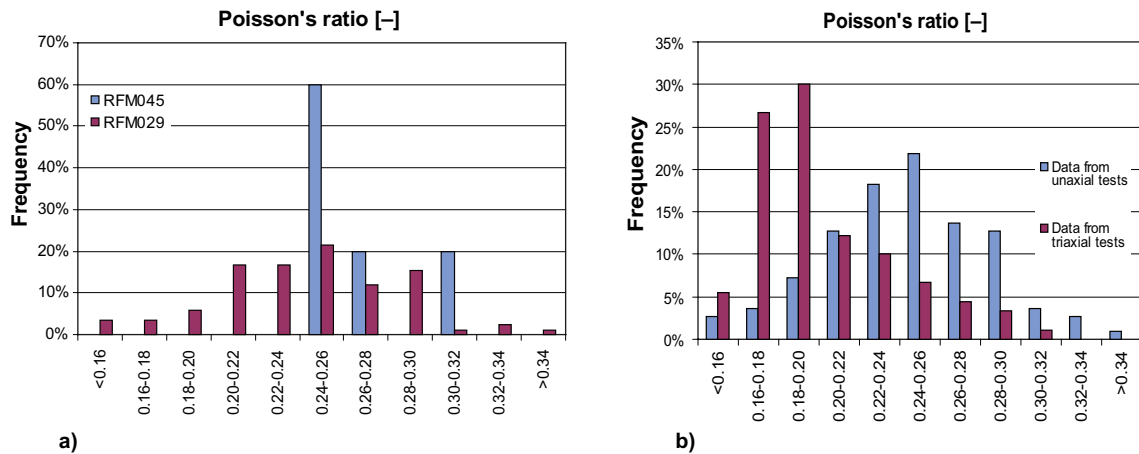


Figure 3-8. a) Frequency distribution of Young's modulus from uniaxial tests on intact rock in domains RFM029 and RFM045. b) Comparison of Young's modulus for granite to granodiorite evaluated from uniaxial- and triaxial tests.





**Figure 3-9.** a) Frequency distribution diagram of Poisson's Ratio for tests performed in rock domains RFM029 and RFM045. b) Comparison of Poisson's ratio for granite to granodiorite evaluated from uniaxial and triaxial tests.

The triaxial tests give mean values in the range of 0.19 to 0.24 with the higher value for granite to granodiorite (101051) cf. Appendix A1.6. The triaxial tests are expected to show lower values of Poisson's ratio than the uniaxial tests, since the confinement stress inhibits lateral dilation of the samples.

In rock domain RFM045, the uniaxial testing resulted in Poisson's Ratio ranging from 0.25 to 0.31. No triaxial tests were performed in this rock domain.

### 3.4 Microcrack volume measurements

/Martin and Stimpson 1994/ showed that the coring of granite at depth could induce microcracking. The microcracking originates from stress relaxation and mechanical effects from the drilling. The drill core sample is under no confining stress in laboratory while the rock in situ is under a certain confining stress depending on depth and location. Moderate microcracking influences the porosity of the intact sample, while significant microcracking may also affect the mechanical properties of laboratory samples.

The microcrack volume measurements are aimed at a refined estimation of the intact rock in situ porosity. The results are used by Hydrogeochemistry to calculate the precise composition of the natural matrix pore water. However, the results are also of interest in the determination of the Transport properties of the intact rock. Furthermore, the microcrack volume measurements can help indicate differences in stress state between boreholes or sites and differences in deformation behavior between rock types.

One method to estimate the amount of microcracking is to measure the amount of nonlinear volumetric strain recorded in hydrostatic triaxial compression tests, as illustrated in Figure 3-10 /Jacobsson 2007/. Based on this a test series of 12 samples from bore holes KFM01A and KFM02B was performed in order to evaluate the microcrack volume in samples of granite to granodiorite (101057). The specimens were taken at borehole lengths ranging from 232–491 m in KFM01A and 197–570 m in KFM02B. The results are shown in Figure 3-11.

The estimated microcrack volume for samples in KFM01A and KFM02B is in the range of 0.035–0.078% and 0.021–0.041% respectively. The results indicate a microcrack volume that corresponds to 5–10% of the measured mean porosity (0.4%) for the present rock type.

The results show a linear increase of crack volume with depth in the samples from borehole KFM01A, while depth dependency is indistinct for samples from borehole KFM02B. However, the estimated crack volume in the samples from Forsmark is considerably less than the crack

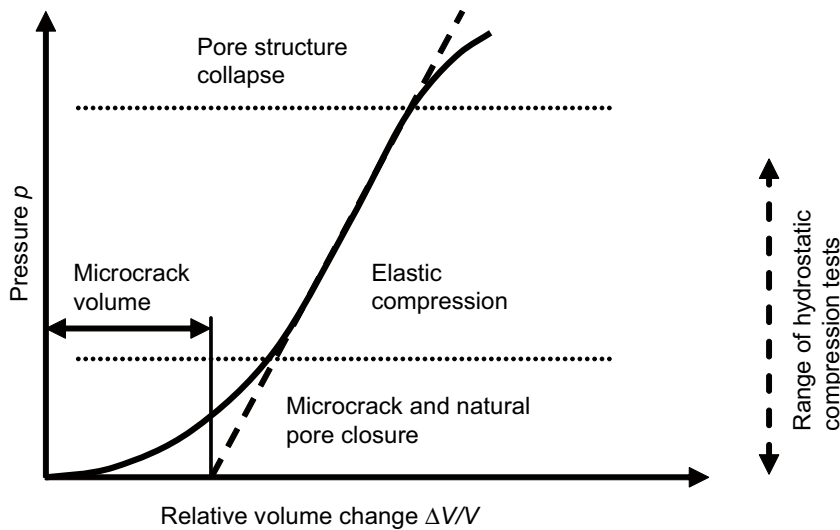


Figure 3-10. Schematic deformation phase during a hydrostatic compression test with the definition of the micro crack volume /Jacobsson 2007/.

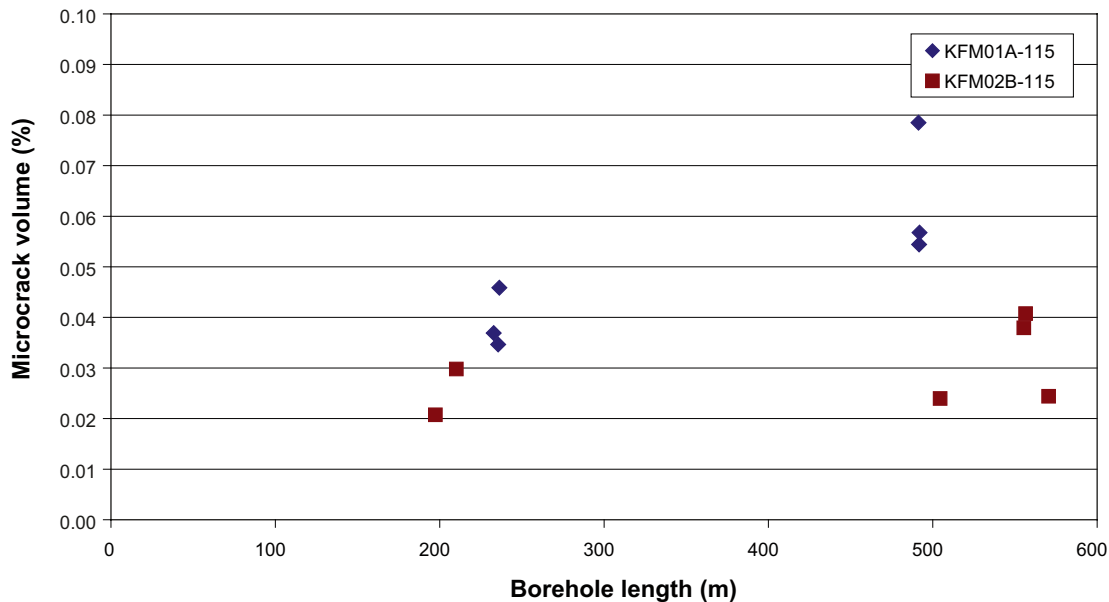


Figure 3-11. Measured micro crack volume versus sampling level (borehole length) /Jacobsson 2007/.

volumes recorded in samples investigated by /Martin and Stimpson 1994/. The impact on the mechanical properties is most likely minor.

### 3.5 Variability and trends in results

The spatial variability of the intact rock has been evaluated by analysing the size of the statistical spread and by comparing the results from the current modelling step 2.2 with the results from the previous modelling steps /SKB 2006b and SKB 2005a/. A small statistical spread and an insignificant change of the parameters between the modelling steps are indications of homogeneous conditions. However, one should bear in mind that the core sections used for specimens have been selected avoiding sections with sealed fractures or other imperfections in the core

with an acute angle to the direction of the axial load. In addition several specimens were also taken close to each other and both issues mean that the spatial variability of the intact rock must be assumed to be greater than predicted from the laboratory results.

### 3.5.1 Spatial variability in relation to geological features

The locations of uniaxial compressive tests are presented in Figure 3-12. The picture shows the results in relation to the geological features in the local area. Additional maps are to be found in Appendix 8. The results in relation to geological features are also supported by WellCad plots in the report by /Olofsson et al. 2007/.

The geological features that occur in the target area seem to have little influence on the strength and deformation properties of the intact rock. The laboratory tests, as well as the measurements of P-wave velocities in boreholes, indicate that the mechanical properties of the target area are

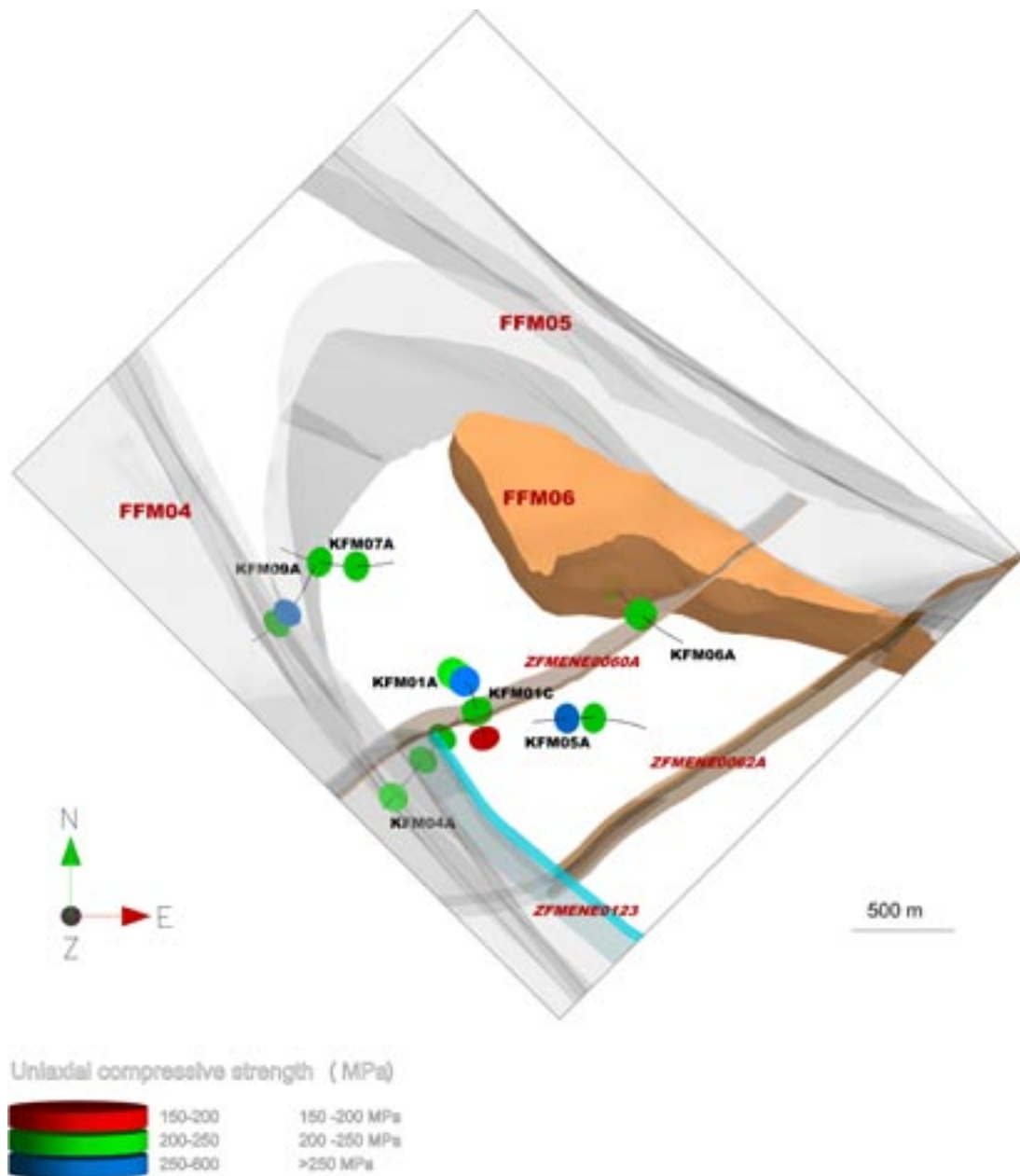


**Figure 3-12.** Location and results of the uniaxial compressive tests. Since the samples are situated close to one another some sample locations are hidden.

rather stable and homogeneous. In general there are only small changes in the P-wave velocity when passing the deformation zones. Moreover, the laboratory results on samples inside or in the vicinity of deformation zones are in the same range as the results on samples taken in the host rock outside deformation zones.

The small influence on the mechanical properties by the deformations zone has support in the geological description of the deformation zones being composed mainly of sealed fractures, cf. Section 2.1.3. However, the sampling strategy may involve some bias in the results leading to a description of the site that is too uniform.

### 3.5.2 Depth dependency

Some trends are observed when the properties of the intact rock samples are plotted with depth. Since the subject has been treated previously in /SKB 2005a, SKB 2006b/ and in /Olofsson et al. 2007/, only a brief account is given here. Further graphs that complete the presentation are presented in Appendix A1.8.

#### Uniaxial compressive strength and indirect tensile strength

In Figure 3-13a the depth dependence of uniaxial compressive strength is plotted for all rock samples, while Figure 3-13b shows the samples of the main rock type sorted by borehole. The main rock type (metamorphic, medium-grained granite to granodiorite) displays a gentle trend of decreasing uniaxial compressive strength with depth, especially clear when looking at the boreholes separately. For the other rock types the number of samples is too small to show a clear trend with depth.

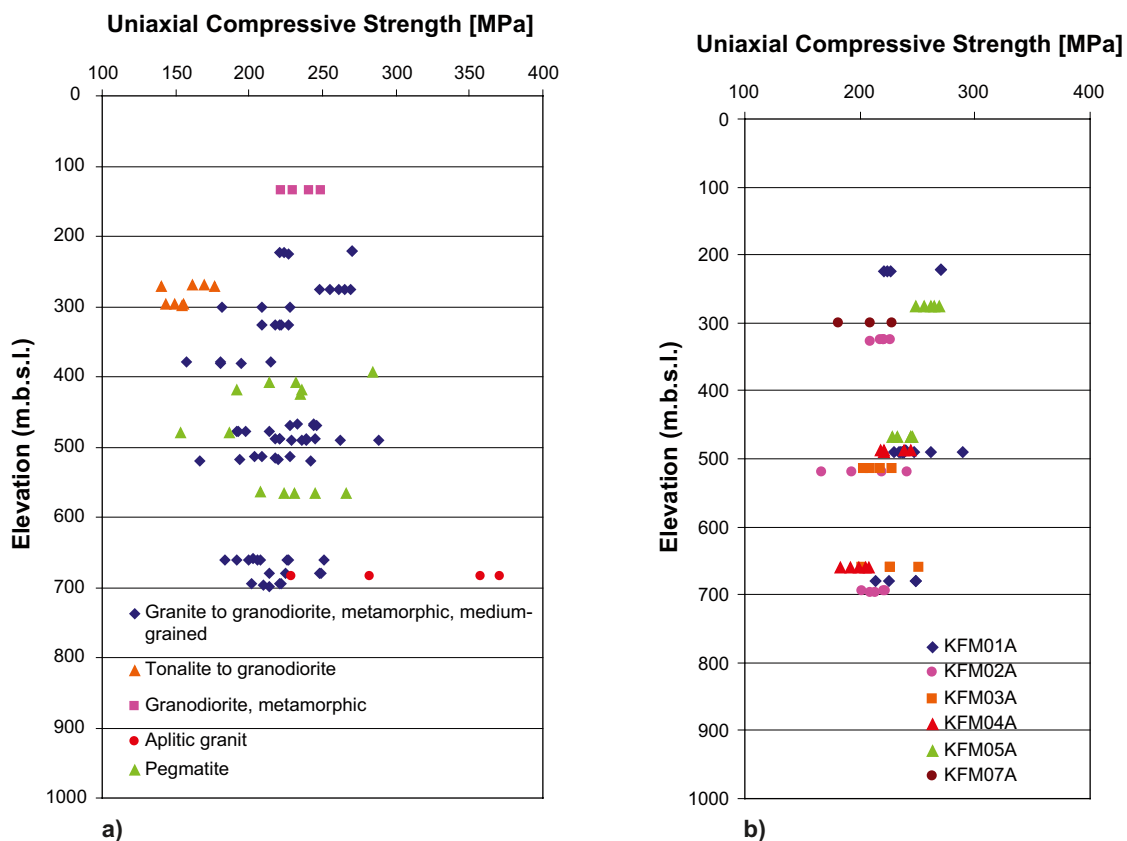


Figure 3-13. a) The uniaxial compressive strength versus depth for all rock types. b) The uniaxial compressive strength of the main rock type (101057) sorted by borehole.

Similar observations can be made regarding the tensile strength in Figure 3-14 where the tensile strength is plotted versus depth. The CANMET samples were not included in this figure. The main rock type displays a gentle trend of decreasing tensile strength with depth, whereas the other rock types show no clear trend with depth.

The slight decrease in compressive and tensile strength with depth may result from stress-induced microcracking during coring. These findings are consistent with the results from the microcrack volume measurements as discussed in Section 3.4.

The assumption that the coring at depth induces microcracks in the samples is also supported by measurements of the P-wave of laboratory samples. As an illustration, the measurements of the P-wave velocity along KFM01A and KFM04A are shown in Figure 3-15. The plots that gives the results from in situ measurements and laboratory measurements on samples from the boreholes, show a clear decreasing trend in the P-wave velocity in the samples below 500 depth, while a stable trend in the in situ measurements, especially for KFM01A.

It may also be noted in the figures that the P-wave velocity determined on laboratory samples indicates some anisotropy of the intact rock, particularly along KFM01A. However, the anisotropic conditions indicated by the P-wave are not supported by the measurements of tensile strength, which were performed parallel and perpendicular to the foliation on laboratory samples, cf. Section 3.2.3.

### Young's Modulus and Poisson's Ratio

It's also possible to observe a slight reduction in Young's Modulus with depth, see Figure 1-11 in Appendix A1.8. This observation is made for granite to metamorphic, medium-grained granodiorite. The decrease is most pronounced down to about 300 m depth. A similar behaviour is not seen in Poisson's Ratio, see Appendix A1.8.

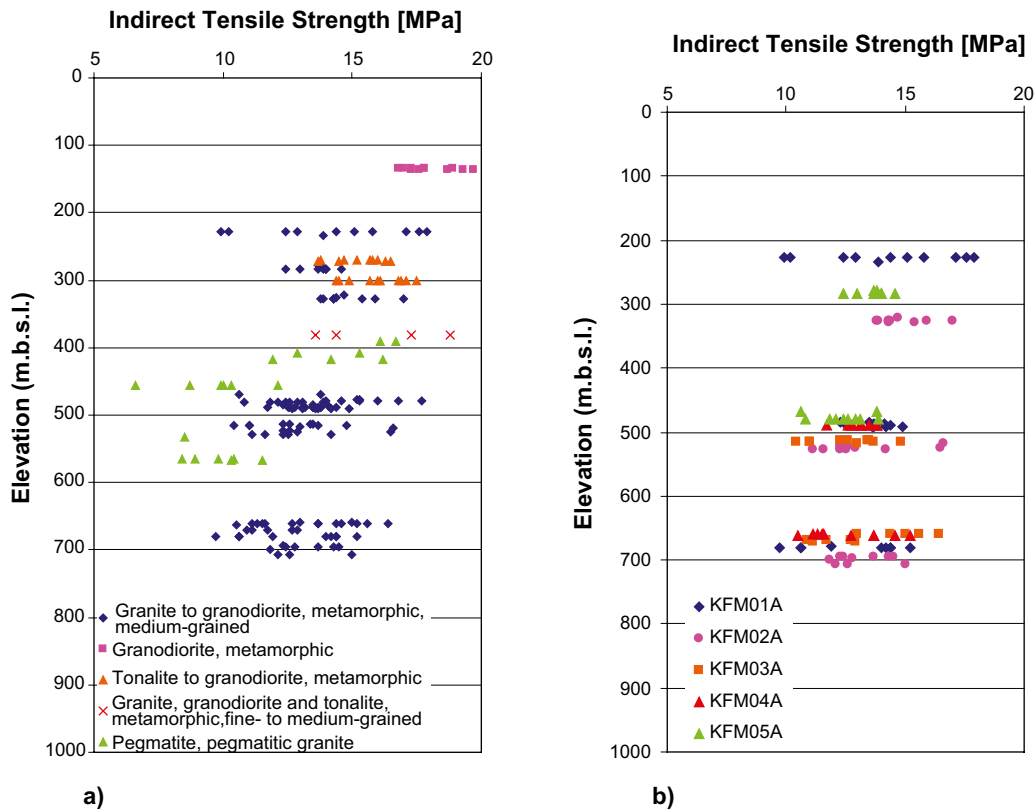


**Figure 3-14.** a) Indirect tensile strength versus depth for all rock types. b) Indirect tensile strength of the main rock type (101057) sorted by borehole. The CANMET results are not included in the diagrams.

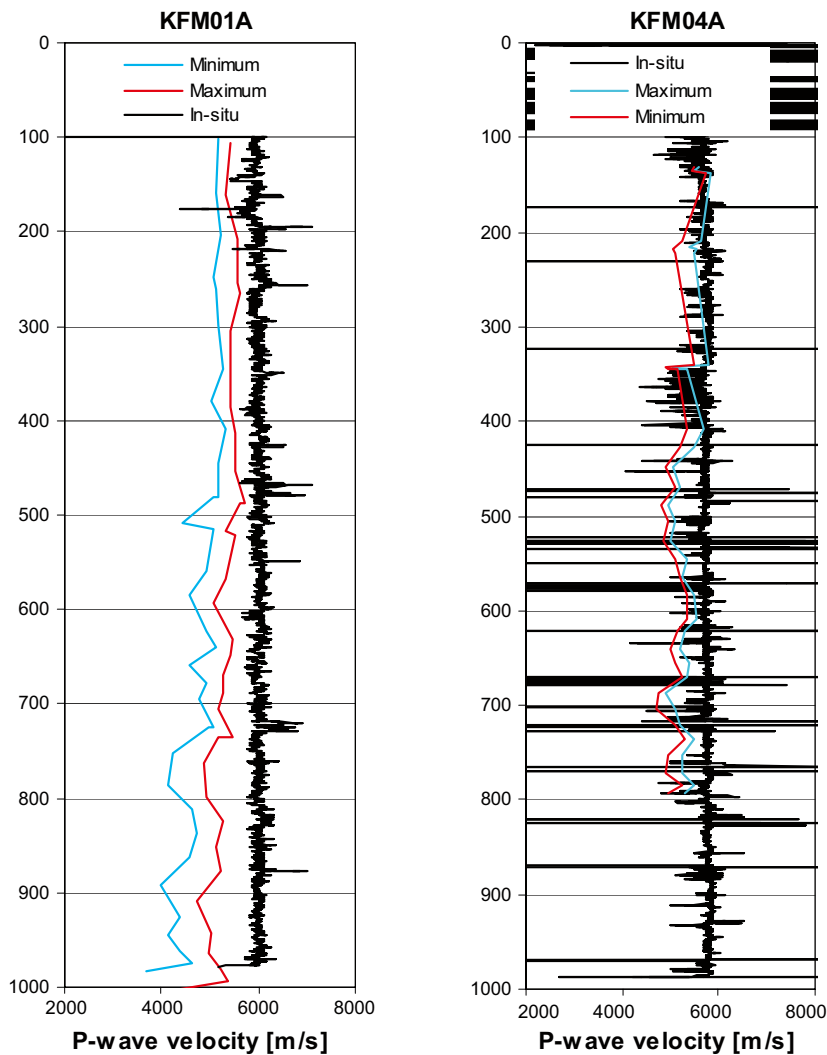


**Figure 3-15.** Plot of the P-wave velocity versus depth measured in situ and on samples from KFM01A and KFM04A /Lanaro and Fredriksson 2005/.

### 3.5.3 Variability in results between modelling steps

In Table 3-6 to Table 3-9, a comparison is made between the results from modelling version 1.2 and modelling stages 2.1 and 2.2 for the parameters of the main rock type granite to granodiorite. The sample population included in the evaluation of the compressive strength for the main rock type has increased by approximately 30% between model version 1.2 and the current modelling stage. In a similar way, the number of samples for determination of tensile strength has increased by about 25% and for Young's modulus by about 50% since model version 1.2.

No major changes can be seen in the results. The mean values of uniaxial compressive strength, cohesion, friction angle, tensile strength and Young's modulus are rather constant. However, the range between the minimum and maximum of the compressive strength has increased by about 40%. In summary, the following conclusions can be drawn: the variability of the selected samples is small; the increasing number of tests has not changed the evaluated mean values that seem to be representative for the studied rock; and the number of tests seems to be sufficient within the different rock types of intact, undisturbed material.

**Table 3-6. Comparison of the compressive strength and constant  $m_i$  for Hoek-Brown's Criterion obtained for Forsmark SDM 1.2 and modelling stages 2.1 and 2.2.**

Rock type	Number of samples	Min strength		Mean		Max strength	
		$\sigma_c$ [MPa]	$m_i$	$\sigma_c$ [MPa]	$m_i$	$\sigma_c$ [MPa]	$m_i$
Granite to granodiorite, Forsmark 1.2	99	178	28.6	227	27.0	275	26.0
Granite to granodiorite, Forsmark 2.1	123	176	30.5	227	28.6	279	27.4
Granite to granodiorite, Forsmark 2.2	130	156	30.0	223	27.2	291	25.6

**Table 3-7. Comparison of the indirect tensile strength obtained for Forsmark SDM 1.2 and modelling stages 2.1 and 2.2.**

Rock type	Number of samples	Minimum [MPa]	Mean [MPa]	Maximum [MPa]
Granite to granodiorite, Forsmark 1.2	112	10	13.5	17.5
Granite to granodiorite, Forsmark 2.1	132	9.7	13.5	17.9
Granite to granodiorite, Forsmark 2.2	140	9.7	13.6	17.9

Note: This comparison also includes the tensile tests performed by HUT.

**Table 3-8. Comparison of the results of Young's modulus from uniaxial tests obtained for Forsmark SDM 1.2 and modelling stages 2.1 and 2.2.**

Rock type	Number of samples	Minimum [GPa]	Mean [GPa]	Maximum [GPa]	St dev. [GPa]
Granite to granodiorite, Forsmark 1.2	52	69	76	82	3
Granite to granodiorite, Forsmark 2.1	68	69	76	83	3
Granite to granodiorite, Forsmark 2.2	77	70	76	83	3

**Table 3-9. Comparison of the cohesion and friction angle for Mohr-Coulomb's Criterion obtained for Forsmark SDM 1.2 and modelling stages 2.1 and 2.2.**

Rock type	Number of samples	Minimum		Mean		Maximum	
		c [MPa]	$\phi$ [°]	c [MPa]	$\phi$ [°]	c [MPa]	$\phi$ [°]
Granite to granodiorite, Forsmark 1.2	99	22.5	59.4	28.1	60.0	33.7	60.4
Granite to granodiorite, Forsmark 2.1	123	21.9	59.9	27.6	60.5	33.5	61.0
Granite to granodiorite, Forsmark 2.2	130	20.0	59.2	27.6	60.0	35.6	60.5

Note: The cohesion and friction angle are determined for a confinement stress between 0 and 15 MPa.

## 3.6 Summary of intact rock mechanical properties

### 3.6.1 Uncertainties

The uncertainties in the estimation of the rock mass mechanical properties may originate from uncertainties in the methods used for estimating the properties as well as uncertainties in spatial variation in the input data. The spatial variability has been discussed in the previous Section 3.5. Regarding the uncertainty that originates from the methods used for estimation the properties of the intact rock the following sources are judged to be the most important:

- Sample and sampling strategy.
- Testing facilities and testing methods.
- Measurement uncertainty.
- Conceptual model uncertainty.
- Influence of sample size.

The listed sources of uncertainties are not treated further in this report. However, specifications of the uncertainties in the laboratory methods used are to be found in SKB's Method Descriptions and the underlying P-reports presenting the laboratory results. Here, the uncertainty of the mechanical properties of the intact rock is expressed statistically only by means of a range of variation in the evaluated mean values.

The uncertainty of the mean was quantified according to the "Central Limit Theorem" /Peebles 1993/ for a 95% confidence interval. Minimum and maximum truncation values given in the tables below are based on the observed minimum and maximum for the tested population. The estimated amount of statistical spread as a range of variation of the possible mean value for each rock type and parameter is presented in Appendix A1.9.

### 3.6.2 Evaluated properties for intact rock

Evaluated intact rock mechanical properties for the main rock type and some subordinate rock types in rock domains RFM029 and RFM045 are presented in Table 3-10. Table 3-11 and presents a comparison of results from rock domains RFM017 and RFM034 whilst rock domain RFM029 is presented in Table 3-12.

The number of tests within fracture domain FFM01 is much larger than for FFM06. This fact makes the uncertainty of the results for FFM06 larger than for FFM01. For example the uncertainty of the mean compressive strength is estimated to only  $\pm 4\%$  for the main rock type in RFM029, whereas  $\pm 21\%$  for the main rock type in RFM045. However, the difference in estimated uncertainty is larger concerning the strength properties than the deformation properties.

Although there is a larger uncertainty the available data without doubt indicate a much higher compressive strength and crack initiation stress in FFM06 than in FFM01. Moreover, the Young's modulus of the rock in FFM06 is also slightly stiffer than the rock in FFM01, cf. Table 3-10. The evaluated compressive strength for the dominant rock type in FFM01 corresponds to values of very strong rock, while the dominant rock type in FFM06 corresponds to values of extremely strong rock /Hoek 2007/. The consistent higher values of the rock types in domain FFM06 is supposed to be caused by albitization of the rock, which increases the quartz content /Stephens et al. 2007/.

The strength evaluated from the adjacent rock domains RFM017 and RFM034 are consistently somewhat lower than the strength from RFM029, while Young's modulus and Poisson's ratio mainly correlate with data from RFM029, Table 3-12.



**Table 3-10. Summary of strength and deformation properties for intact rock in domains RFM029 and RFM045.**

RFM FFM Rocktype	Number of samples	E [GPa]	$\nu$	$\sigma_c$ [MPa]	$\sigma_{ci}$ [MPa]	Number of samples	$\sigma_t$ [MPa]
		Mean/st dev Min-max Uncertainty of mean <sup>1</sup>	Mean/st dev Min-max Uncertainty of mean <sup>1</sup>	Mean/st dev Min-max Uncertainty of mean <sup>1</sup>	Mean/st dev Min-max Uncertainty of mean <sup>1</sup>		Mean/st dev Min-max Uncertainty of mean <sup>1</sup>
RFM029 FFM01 101057	47	76/3 69–83 ± 1%	0.23/0.04 0.14–0.30 ± 4%	226/28 157–289 ± 4%	116/23 60–187 ± 7%	82	13/2 10–18 ± 2%
RFM029 FFM01 101061	10	75/3 71–80 ± 3%	0.30/0.03 0.26–0.35 ± 6%	228/21 192–266 ± 6%	121/12 100–140 ± 9%	11	12/3 8–16 ± 13%
RFM029 FFM03 101057	13	75/3 71–80 ± 2%	0.23/0.03 0.16–0.27 ± 7%	220/13 203–251 ± 3%	118/7 105–127 ± 4%	30	14/2 10–17 ± 5%
RFM029 FFM03 101054	4	72/3 70–76 ± 4%	0.29/0.04 0.25–0.34 ± 13%	150/6 143–155 ± 4%	–	10	16/1 14–18 ± 4%
RFM029 PDZ 101057	4	77/1 77–79 ± 1%	0.22/0.02 0.20–0.24 ± 8%	205/33 166–242 ± 16%	105/22 85–134 ± 35%	10	13/2 11–17 ± 9%
RFM045 FFM06 101058	5	83/3 80–86 ± 3%	0.27/0.03 0.25–0.31 ± 8%	310/58 229–371 ± 16%	169/29 125–200 ± 15%	–	18 <sup>2</sup>

<sup>1</sup> The uncertainty of the mean was quantified for a 95% confidence interval.

<sup>2</sup> Estimated value based on results from adjacent domains.

In Table 3-10, the given values of the tensile strength, are based entirely of results from indirect tests. The results from direct measurements are expected to be smaller. By multiplying the given numbers with a factor of 0.6 gives an approximation of what the values would have been in case of direct measurements.

Table 3-11 gives the evaluated values of the constant  $m_i$  included in Hoek-Brown's failure criterion and evaluated cohesion and friction angle based on Mohr-Coulomb's criterion. The values given for the constant  $m_i$  correspond to normal values for granite, while the cohesion and friction angle correspond to values of very strong rock /Hoek 2007/.

The estimated microcrack volume for samples of the main rock type indicates that the microcracking due to stress relaxation and mechanical effects during the drilling is moderate in Forsmark. The evaluated microcrack volume corresponds to 5–10% of the measured mean porosity. Furthermore, the results show a linear increase of the crack volume with depth in the samples from borehole KFM01A, while the depth dependency is indistinct for samples from borehole KFM02B. However, the estimated crack volume in the investigated samples is considered to have only minor or insignificant impact of the mechanical properties.

The geological features that occur in the target area seem to have little influence on the strength and deformation properties of the intact rock. The laboratory results on samples inside or in the vicinity of deformation zones are in the same range as the results on samples taken in the host rock outside deformation zones. These findings are in accordance with the geological description of the deformation zones being composed of mainly sealed fractures.

**Table 3-11. Evaluated mean values of constant  $m_i$  included in Hoek-Brown's criterion and mean values of the cohesion and friction angle of Mohr-Coulomb's criterion for intact rock in domain RFM029 and RFM045.**

Rock domain	Fracture domain	Rock type	Number of samples	$m_i$	c [MPa]	$\phi$ [°]
RFM029	FFM01	Granite to granodiorite, metamorphic, medium-grained 101057	86	28	28	60
RFM029	FFM01	Pegmatite, pegmatitic granite 101061	15	18	33	56
RFM029	FFM01	Granite, granodiorite and tonalite, metamorphic, fine- to medium-grained 101051	4	46	19	63
RFM029	FFM03	Granite to granodiorite, metamorphic, medium-grained 101057	25	28	27	60
RFM029	FFM03	Tonalite to granodiorite, metamorphic 101054	8	13	25	51
RFM029	PDZ	Granite to granodiorite, metamorphic, medium-grained 101057	4	37	24	62
RFM045	FFM06	Granite, metamorphic, aplitic 101058	5	29 <sup>1</sup>	30 <sup>1</sup>	60 <sup>1</sup>

<sup>1</sup> Estimated value based on results from adjacent fracture domains.

**Table 3-12. Comparison of results for intact rock in domain RFM017 and RFM034 with results in RFM029 related to mean and its uncertainty.**

Rock domain	Rock type	$\sigma_c$ [MPa]	$\sigma_t$ [MPa]	$m_i$	$\phi$ [°]	c [MPa]	E [GPa]	$\nu$
RFM029	101057	222 ± 26	14 ± 2	27.2	60	27.6	78 ± 3	0.24 ± 0.03
RFM034	101057	195 ± 10	15 ± 1				73 ± 2	0.27 ± 0.02
RFM029	101061	231 ± 21	11 ± 3	19.5	57	32.3	76 ± 3	0.30 ± 0.03
RFM034	101061	170 ± 24	10 ± 2				72 ± 1	0.26 ± 0.10
RFM029	101054	152 ± 6	16 ± 1	9.4	47	29.4	70 ± 3	0.29 ± 0.04
RFM017	101054	166 ± 16	15 ± 1				72 ± 4	0.25 ± 0.03

Note: The uncertainty of the mean was quantified for a 95% confidence interval.

The main rock type displays a gentle trend of decreasing compressive and tensile strength with depth, whereas the other rock types show no clear trend with depth. The decrease is in the range of 10–15% for compressive and tensile strength at depths larger than 500 m, may result from stress-induced microcracking during coring. These findings are consistent with the results from the microcrack volume measurements and the P-wave measurements.

The variability in results between modelling steps is small. The increasing number of tests has not changed the evaluated mean values that seem to be representative for the studied main rock type. Thus, the number of tests of intact rock seems to be sufficient within the target volume.

## 4 Mechanical properties of fractures

### 4.1 Overview of the primary data

In this chapter the laboratory strength and deformation properties of discrete fractures are presented and discussed. The presentation here is supported by /Olofsson et al. 2007/, which includes a comprehensive compilation of the tilt and direct shear tests available by data freeze 2.2. This report also included WellCad plots that show the results in relation to geological features.

The results are of samples taken from the target volume in rock domain RFM029 and RFM045, and some of the adjacent rock domains RFM012, RFM034 and RFM044. The available tests on fractures for the selected rock domains are listed in Table 4-1. A complete compilation of the results, including data from the adjacent rock domains, is assembled in Appendix 2. Three dimensional visualisation of the sampling locations, in relation to fracture domains and deformation zones, is presented in Appendix 8.

**Table 4-1. Number of tested fractures for each testing method performed in rock domain RFM012, RFM029, RFM034 and RFM044 (DZ= Deformation zone).**

Borehole	Rock domain	Fracture domain	Tilt tests on fractures	Shear tests on open fractures	Shear tests on sealed fractures
KFM01A	RFM029	FFM01	20	1	
KFM01A	RFM029	FFM02	11	4	
KFM01A	RFM29DZ		10	1	
KFM01D	RFM029	FFM01			4
KFM02A	RFM029	FFM01	13	4	
KFM02A	RFM029	FFM03	9	1	
KFM02A	RFM029DZ		18	2	
KFM03A	RFM029	FFM03	30	8	
KFM03A	RFM029DZ		5		
KFM03B	RFM029	FFM03	2		
KFM03B	RFM029DZ		1		
KFM04A	RFM029	FFM01	22	2	
KFM04A	RFM029	FFM04	2		
KFM04A	RFM029DZ		2	4	
KFM05A	RFM029	FFM01	4	8	
KFM05A	RFM029DZ		5		
KFM06A	RFM029	FFM01		6	
KFM07A	RFM029	FFM01		5	
KFM08A	RFM029	FFM01		2	
KFM08A	RFM029DZ			3	
KFM09A	RFM044	FFM05	5	2	
KFM09A	RFM44DZ		1		
KFM09A	RFM034	FFM01		1	
KFM09A	RFM012	FFM04		3	
KFM09A	RFM029	FFM01	1		
KFM09A	RFM029DZ		2		
Total			163	57	4

The mechanical properties of fractures are used in the safety assessment of a repository to analyse seismically induced slip on fractures /Fälth and Hökmark 2006/, cf. Section 1.3. The results are also used in the theoretical approach to estimate the strength and deformation properties of the rock mass.

The strength and deformability of the natural rock fractures was determined in two ways:

1. To get an overview of the variation in fracture properties along the boreholes tilt tests were performed, where shearing is induced by the self-weight of the upper block as the fracture is progressively tilted.
2. To get more detailed information on strength and deformability of the fracture, direct shear tests were performed on fractures from selected locations where shearing is induced by actuators that apply a load perpendicular and parallel to the fracture plane. Three different types of shear test configuration were used; these are referred to as Type I, Type II and Type III. The main differences between the different shear test configurations are explained in Section 4.3.

The methodology, standard and performance used for the laboratory testing are described in SKB's Method Description for each test:

- Tilt tests on fractures: SKB MD 190.006, ver 2.0 (2002-04-16).
- Shear tests on fractures: SKB MD 190.005e, ver 4.0 (2006-11-07).

Tilt tests were performed on 163 fracture samples. The tests are based on a sample size of 100 mm. All tilt tests were performed by the Norwegian Geological Institute Laboratory (NGI).

Direct shear tests were performed on 57 open fracture samples and 15 tests were performed on sealed fractures. The sample size for direct shear tests was about 55 mm. All samples were tested by the Swedish National Testing and Research Institute (SP).

The samples for the direct shear tests were intended to be collected from the same depth intervals as for testing of intact rock. However, the low fracture frequency at depth limited the possibility of collecting appropriate fractures for testing.

The focus during the Complete Site Investigations has been on testing samples within the target volume (cf. Section 1.3.2). No samples were taken in FFM06, since the sampling of fractures was already complete when this fracture domain was added to the geological model. However, the fractures of FFM06 are expected to have similar properties as fractures in fracture domain FFM01.

An inter-laboratory test series to check the quality in the direct shear tests by SP have been performed by NGI, cf. Section 3.1. These laboratory tests have been reported by /Lanaro and Fredriksson 2005/ and are not included here.

## 4.2 Tilt test results

A number of tilt tests were performed on natural fractures in order to evaluate the strength of the fractures. The tilt tests are designed to allow the fracture parameter determination according to /Barton and Bandis 1990/. The shear strength of the fracture is a function of the normal stress  $\sigma_n$  as:

$$\tau = \sigma_n \tan \left[ \phi_b^{BB} + JRC \log \left( \frac{JCS}{\sigma_n} \right) \right] \quad \text{Equation 4-1}$$

$JRC$  is the Joint Roughness Coefficient that quantifies roughness,  $JCS$  is the Joint Wall Compression Strength of the rock surfaces, and  $\phi_b^{BB}$  is the basic friction angle on dry saw-cut

surfaces. The residual friction angle  $\phi_r^{BB}$  is used instead of  $\phi_b^{BB}$  if the strength of wet surfaces is considered. The index notation *BB* is used to emphasize that the parameters relate to the Barton-Bandis model, to differentiate them from parameters in the Mohr-Coulomb model, discussed later. /Barton and Bandis 1990/ also suggested truncating the strength envelope as follows:  $\tau/\sigma$  should always be smaller than  $\tan(70^\circ)$  and, in this case, the envelope should go through the origin ( $\sigma_n = \tau = 0$  MPa), in other words the cohesion is zero.

The *JRC* and *JCS* parameters are dependent on fracture length. The measured *JRC*<sub>0</sub> and *JCS*<sub>0</sub> values relate to fracture specimens of different lengths. Therefore, the measured values are normalised and extrapolated to values that relate to a standard fracture length of 100 mm, and hereafter referred to as *JRC*<sub>100</sub> and *JCS*<sub>100</sub> values.

For a certain level of stresses, the relation in Equation 4-1 can be linearly approximated to determine the peak friction angle and cohesion of the Mohr-Coulomb Strength Criterion as:

$$\tau = c_p^{MC} + \sigma_n \tan(\phi_p^{MC}) \quad \text{Equation 4-2}$$

where  $c_p^{MC}$  and  $\phi_p^{MC}$  are peak cohesion and peak friction angle. Similarly, the residual cohesion  $c_r^{MC}$  and peak friction angle,  $\phi_r^{MC}$  can be fitted by the Mohr-Coulomb residual envelope. The determined Mohr-Coulomb model parameters based on all tilt tests are presented in Table 4-2. The linear Mohr-Coulomb envelope has been fitted to the curved *BB* envelope in the stress range from 0–20 MPa, i.e. the same stress range as the direct shear stress envelope is fitted to the measured data. Calculated results from tilt tests in fracture domain FFM01 and in the deformation zones are presented in Table 4-3 and Table 4-4 respectively. The results show a very small difference in the evaluated friction angles and cohesion between FFM01 and DZ. Calculated results from tilt tests in other fracture domains are presented in Appendix A2.1.

**Table 4-2. Calculated results from all tilt tests, total 163 tests.**

Test	Minimum	Mean	Median	Maximum	Std. dev.
Peak friction angle, $\phi_p^{MC}$ [°]	25.8	33.8	33.9	37.7	1.9
Peak cohesion, $c_p^{MC}$ [MPa]	0.2	0.5	0.5	0.8	0.1
Residual friction angle, $\phi_r^{MC}$ [°]	20.3	29.4	29.6	37.9	3.0
Residual cohesion, $c_r^{MC}$ [MPa]	0.2	0.4	0.4	0.7	0.1

**Table 4-3. Calculated results from tilt tests in FFM01, total 64 tests.**

Test	Minimum	Mean	Median	Maximum	Std. dev.
Peak friction angle, $\phi_p^{MC}$ [°]	29.5	33.9	33.9	36.6	1.7
Peak cohesion, $c_p^{MC}$ [MPa]	0.2	0.4	0.4	0.7	0.1
Residual friction angle, $\phi_r^{MC}$ [°]	22.6	29.7	30.1	37.9	2.9
Residual cohesion, $c_r^{MC}$ [MPa]	0.2	0.4	0.4	0.6	0.1

**Table 4-4. Calculated results from tilt tests in deformation zones, total 34 tests.**

Test	Minimum	Mean	Median	Maximum	Std. dev.
Peak friction angle, $\phi_p^{MC}$ [°]	28.5	33.3	33.4	36.4	2.0
Peak cohesion, $c_p^{MC}$ [MPa]	0.3	0.5	0.5	0.8	0.1
Residual friction angle, $\phi_r^{MC}$ [°]	21.5	29.5	29.4	37.2	3.1
Residual cohesion, $c_r^{MC}$ [MPa]	0.3	0.4	0.4	0.7	0.1

### 4.3 Direct shear test results

Direct shear tests were performed on specimens containing a natural fracture from boreholes KFM01A to KFM09A. The locations of sampling for direct shear tests are presented in Figure 4-1. No samples were taken from fracture domain FFM06. However, the mechanical properties of fractures in FFM06 are judged to be similar to those in fracture domain FFM01.

In the normal loading tests, the joints were loaded and unloaded twice up to a normal stress of 10 MPa (20 MPa on specimens from borehole KFM05A). Direct shear tests with constant normal loading were carried out after the normal loading tests. Each fracture sample was sheared three times, at the normal stress levels 0.5, 5 and 20 MPa.

To examine how the clamping of rock specimens in the laboratory test apparatus may influence test results, three different techniques were used. The main difference between the different methods is the casting material and size of the steel holders that are used to hold the specimen in the shear test apparatus. The three different test configurations denoted Type I, Type II, and Type III are briefly described below.

**Type I:** The aim was to use maximum fracture length resulting in various fracture lengths depending on the formation. The specimens were cast into specimen holders using a fast hardening anchoring grout. The normal deformation was measured using an indirect measurement method. A correction of the normal deformation values due to the cement deformation were subsequently carried out based on results from reference tests on steel specimens. The shear test started from an initial state corresponding to a matching fracture at the 0.5 and the 20 MPa normal stress level, but not on the 5 MPa level. This test type was used on samples from boreholes KFM01A, KFM02A, KFM03A and KFM04A.

**Type II:** The aim was to use similar fracture areas in the different specimens and the fractures were therefore cut to a length between 50–60 mm. The specimens were also cut parallel to the fractures to obtain equal total heights. The specimens were cast into smaller specimen holders using an epoxy material. A correction of the normal deformation values due to the epoxy deformation were carried out based on results from reference tests on steel specimens. The shear test started from the initial state corresponding to a matching fracture at respective normal stress level. This test type was used on samples from borehole KFM05A.

**Type III:** The aim was to use similar fracture areas in the different specimens and the fractures were therefore cut to a length between 50–60 mm. The specimens were also cut parallel to the fractures to obtain equal total heights. The specimens were partially cast into fast hardening anchoring grout for the normal loading test. A direct measurement of the normal deformation

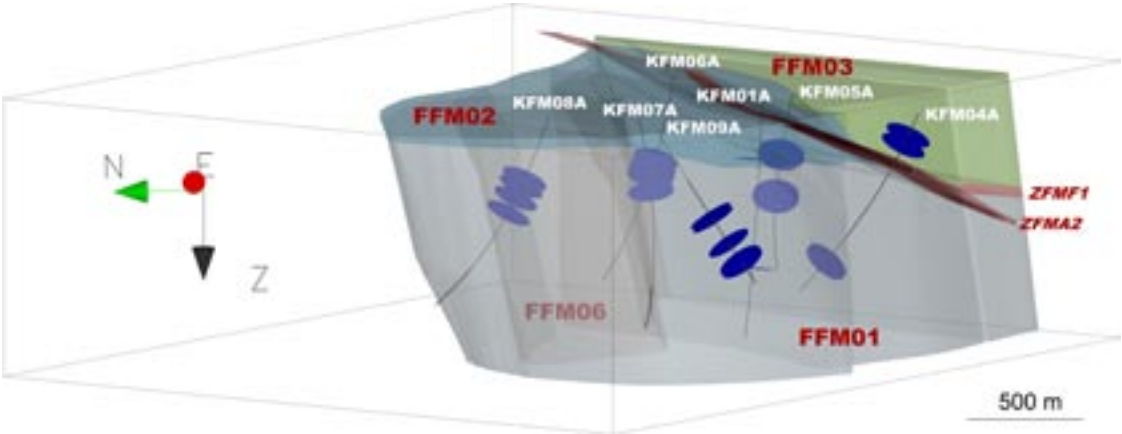


Figure 4-1. Location of samples for shear tests on open fractures. Since the samples are situated close to one another some sample locations are hidden.

over the fracture was used. The specimens were removed from the holders after the test and cast into another set of specimen holders using an epoxy material. This configuration was used during the shear tests. The shear test started from an initial state corresponding to a matching fracture at respective normal stress level. This test type was used on samples from boreholes KFM05A, KFM06A, KFM07A, KFM08A and KFM09A.

#### 4.3.1 Description of parameter evaluation

The secant normal stiffness  $K_N$  is determined as the secant evaluated between the unloaded state and full loading of the second load cycle.

The secant shear stiffness  $K_S$  is determined as the secant evaluated between 30% and 50% of the peak shear stress  $\sigma_{s,max}$  at each of the three normal stress levels, 0.5, 5 and 20 MPa. The secant dilatancy angle  $\Psi$  is determined between 0.3 and 1.3 mm shear deformation at the 0.5 MPa normal stress level, between 0.5 and 1.9 mm shear deformation at the 5 MPa normal stress level and between 0.7 and 2.1 mm shear deformation at the 20 MPa normal stress level. Small modifications of the evaluation criteria were done in some cases. This is noted in conjunction with the result presentations.

The peak friction angle  $\phi_p$  and cohesion  $c_p$  and the residual friction angle  $\phi_r$  and cohesion  $c_r$  were determined by linear regression (least square fit) to the measured peak and residual shear stresses at the three normal stress levels.

#### 4.3.2 Tests on open fractures

The influence of the deformation in the holder, in the anchoring grout and rock outside the fracture on the evaluated normal stiffness,  $K_{NM}$ , of the fracture can be expressed as:

$$K_{NM} = \frac{\sigma_n}{\delta_F + \delta_T} \quad \text{Equation 4-3}$$

where,  $\delta_F$  is the normal deformation of the fracture,  $\delta_T$  the deformation in the holder, the grout and the rock outside the fracture and  $\sigma_n$  is the normal stress. By rearranging Equation 4-3 the real normal stiffness,  $K_{NF}$ , of the fracture can be calculated if the stiffness of the holder and grout,  $K_{NT}$ , is known.

$$\frac{1}{K_{NF}} = \frac{1}{K_{NM}} - \frac{1}{K_{NT}} \quad \text{Equation 4-4}$$

The type III test gives the normal stiffness of the fracture,  $K_{NF}$ , as the deformation is measured directly over the fracture. By assuming that the mean real normal stiffness for the fractures tested by type I and type II tests shall be the same as measured by the type III test, the stiffness of the holder and grout,  $K_{NT}$ , can be calculated, see Table 4-5.

**Table 4-5. Mean real normal stiffness and calculated stiffness of the holder and grout.**

Test type	Measured mean normal stiffness, $K_{NM}$ , (MPa/mm)	Normal stiffness, $K_{NF}$ , (MPa/mm)	Stiffness of holder, grout and rock, $K_{NT}$ , (MPa/mm)
I	130	1,010	149.2
II	340	1,010	512.5
III	1,010	1,010	

The measured normal stiffness,  $K_{NM}$ , by the type I and type II tests can be corrected by using Equation 4-3. The measured shear stiffness and friction angle by the type I and type II tests can also be corrected. The evaluated corrected parameters with respect to normal stiffness, peak friction angle and peak cohesion are presented in Table 4-6 to Table 4-8. The variation of the normal stiffness,  $K_N$ , is high compared with the variation in other parameters. The results show a significant lower stiffness in FFM02 and FFM03, i.e. the fracture domains that include more fractures. The different test configurations may have influenced the results even if an attempt to correct for this difference was made. Besides this, the difference in the examined properties seems to be small between the fracture domains. Evaluated shear stiffness, dilatation angle, residual friction angle and cohesion are reported in Appendix A2.2 and Section 4.5.2.

**Table 4-6. The result of Normal stiffness  $K_N$  from each fracture domain, 57 tests. Values from test type I and type II are converted to test type III.**

FFM	Number of samples	Minimum $K_N$ (MPa/mm)	Mean $K_N$ (MPa/mm)	Median $K_N$ (MPa/mm)	Maximum $K_N$ (MPa/mm)	Std. dev. $K_N$ (MPa/mm)
FFM01	29	159	656	589	1,833	396
FFM02	4	115	248	197	483	165
FFM03	9	152	293	208	734	193
FFM04	3	1,072	1,385	1,458	1,624	283
FFM05	2	559	599	599	639	57
DZ	10	167	662	367	2,445	729
All	57	115	607	513	2,445	483

**Table 4-7. The result of peak friction angle,  $\phi_p$  from each fracture domain, 57 tests. Values from test type I and type II are converted to test type III.**

FFM	Number of samples	Minimum $\phi_p$ (°)	Mean $\phi_p$ (°)	Median $\phi_p$ (°)	Maximum $\phi_p$ (°)	Std.dev. $\phi_p$ (°)
FFM01	29	29.3	36.6	36.3	42.0	2.9
FFM02	4	34.4	36.4	35.5	40.0	2.5
FFM03	9	34.2	37.0	37.5	39.0	1.7
FFM04	3	28.5	32.0	32.5	35.0	3.3
FFM05	2	35.7	37.0	37.0	38.2	1.8
DZ	10	32.5	35.3	34.8	38.4	2.4
All	57	28.5	36.2	36.2	42.0	2.8

**Table 4-8. The result of peak cohesion,  $c_p$  from each Fracture domain, 57 tests.**

FFM	Number of samples	Minimum $c_p$ (MPa)	Mean $c_p$ (MPa)	Median $c_p$ (MPa)	Maximum $c_p$ (MPa)	Std.dev. $c_p$ (MPa)
FFM01	29	0.2	0.8	0.7	1.3	0.3
FFM02	4	0.2	0.5	0.4	1.0	0.4
FFM03	9	0.3	0.6	0.5	0.9	0.2
FFM04	3	0.6	0.9	0.7	1.4	0.4
FFM05	2	0.7	0.8	0.8	0.9	0.2
DZ	10	0.0	0.8	0.7	1.7	0.5
All	57	0.0	0.7	0.7	1.7	0.4



### 4.3.3 Tests on sealed fractures

Shear tests on sealed fractures were performed on four sealed fractures from borehole KFM01D. Three specimens were prepared from each fracture and tested at three different normal stress levels. The initial test was followed by three shear cycles, at the normal stress levels 0.5 MPa, 5 MPa and 20 MPa, on the open fracture that was created after breaking the sealed joint. The results from tested fractures at elevation 459.0 m are shown as an example in Figure 4-2. The results from two other sealed fractures are presented in Appendix A2.3. (The results from one fracture have been excluded since the failure occurred in the grout and the intact rock.) The evaluated strength parameters are given in Table 4-9. The measured friction angles of the sealed fracture are slightly lower than that of intact rock, 53° compared to 60° for intact rock. The measured cohesion is considerably lower, 4 MPa compared with 28 MPa for intact rock. The results from the shear tests after breaking the sealed fracture are similar to the results for the tests on open fractures, as seen in Table 4-7 and Table 4-8.

**Table 4-9. Test results from tests on sealed fractures**

Parameter	Minimum	Mean	Median	Maximum	Std. dev.
Peak friction angle of sealed fractures [°]	48.3	52.6	51.6	57.9	4.9
Peak cohesion of sealed fractures [MPa]	2.21	4.06	2.46	7.50	2.99
Peak friction angle of broken fractures [°]	34.4	37.5	36.9	41.1	3.4
Peak cohesion of broken fractures [MPa]	0.44	0.54	0.49	0.71	0.15
Residual friction angle of broken fractures [°]	30.7	32.1	31.8	33.7	1.5
Residual cohesion of broken fractures [MPa]	0.43	0.52	0.51	0.61	0.09

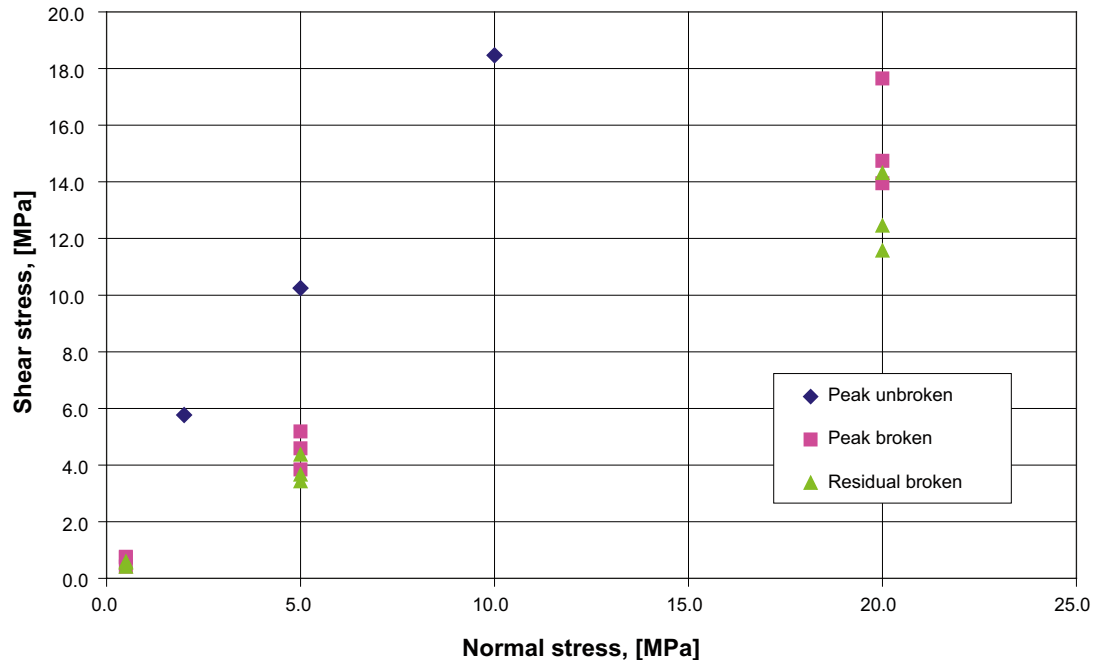


*Figure 4-2. Shear test on sealed fracture from borehole KFM01D, elevation 459.0 m.*

## 4.4 Variability and trends in test results

The spatial variability of the fracture mechanical properties has been dealt with in a similar way as for the mechanical properties of intact rock, Section 3.3. By analysing the size of the statistical spread and by comparing the results from the current modelling stage 2.2 with the results from the previous modelling steps /SKB 2006b and SKB 2005a/ an appreciation of the spatial variability was obtained. A small statistical spread and an insignificant change in the parameters between the modelling steps are indications of homogeneous conditions.

### 4.4.1 Spatial variability in relation to geological features

The locations of sampling for direct shear tests are presented in Figure 4-1. The picture shows the sampling in relation to the geological features in the area. The results in relation to geological features are also presented by WellCad plots in the report by /Olofsson et al. 2007/.

The number of tested fractures in different fracture domains is shown in Table 4-10. No fractures were tested from fracture domain FFM06.

Both tilt tests and direct shear tests in FFM01 and FFM03 indicate rather stable measured strength parameters. In other fracture domains the numbers of samples are too small to give information about the variation within the domains. The measured values in deformation zones are in the same range as measured values in the rock mass outside deformation zones.

### 4.4.2 Influence of fracture sets on mechanical properties

In modelling stage 2.1 the potential influence of fracture sets on the mechanical properties determined by tilt and shear test were studied /SKB 2006b/. The study showed that the discrepancies observed between the different fracture sets were insignificant. Thus, in the current modelling stage the mechanical properties have not been separated on fracture sets. The study has instead concentrated on the difference between the fracture domains.

### 4.4.3 Depth dependency

All parameters evaluated from tilt tests and direct shear tests are presented as a function of elevation in Appendix A2.4 and Appendix A2.5, respectively. The evaluated friction angle versus depth based on tilt tests is shown in Figure 4-3 and based on directed shear tests in Figure 4-4. Furthermore, normal stiffness and shear stiffness (0.5 MPa) versus depth are shown in Figure 4-5. The depth dependency of the parameters evaluated from the tilt tests and direct shear tests has been treated previously in /SKB 2006b/ and in /Olofsson et al. 2007/.

**Table 4-10. Number of samples in different fracture domains.**

Fracture domain	Tilt tests	Direct shear tests on open fractures	Direct shear tests on sealed fractures <sup>1</sup>
FFM01	64	29	4 <sup>2</sup>
FFM02	7	4	
FFM03	41	9	
FFM04	2	3	
FFM05	5	2	
DZ	34	10	
Affected by DZ	10		
All	163	57	4

<sup>1</sup> Each fracture include three specimens.

<sup>2</sup> The test of one fracture resulted in failure in the grouting and in the intact rock instead of the sealed fracture.

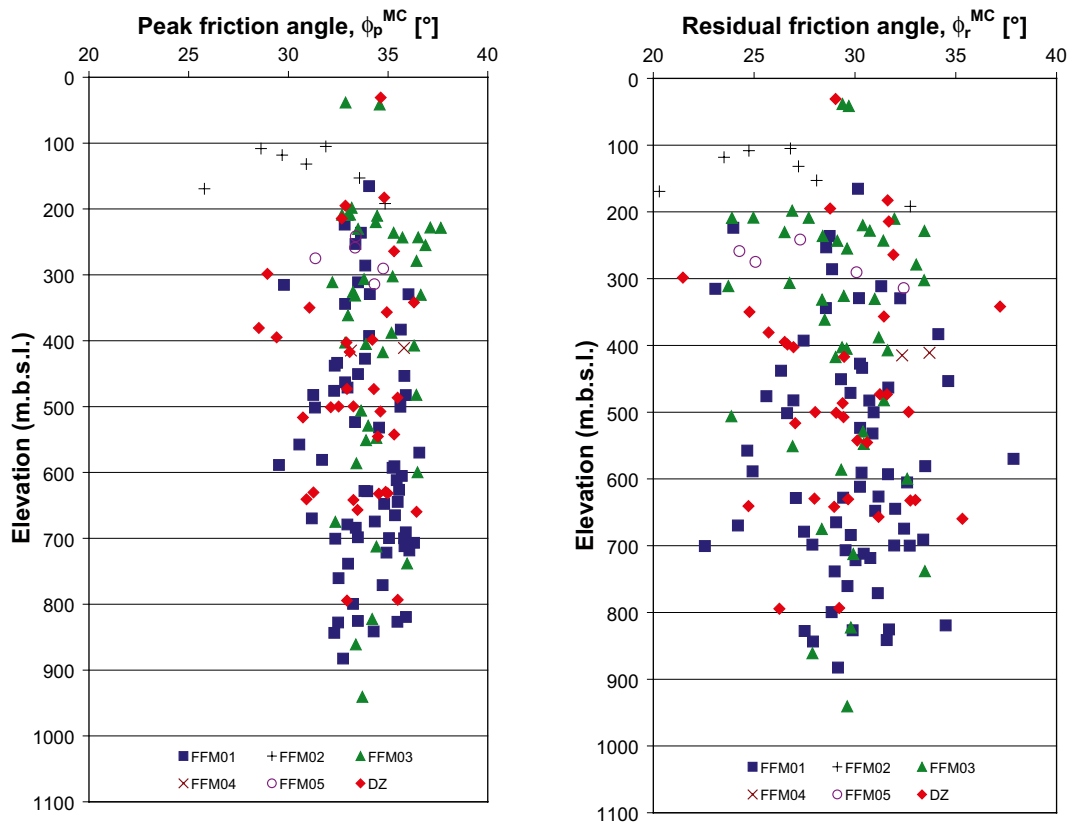


Figure 4-3. Peak friction angle  $\phi_p^{MC}$  and residual friction angle  $\phi_r^{MC}$  versus depth based on tilt tests.

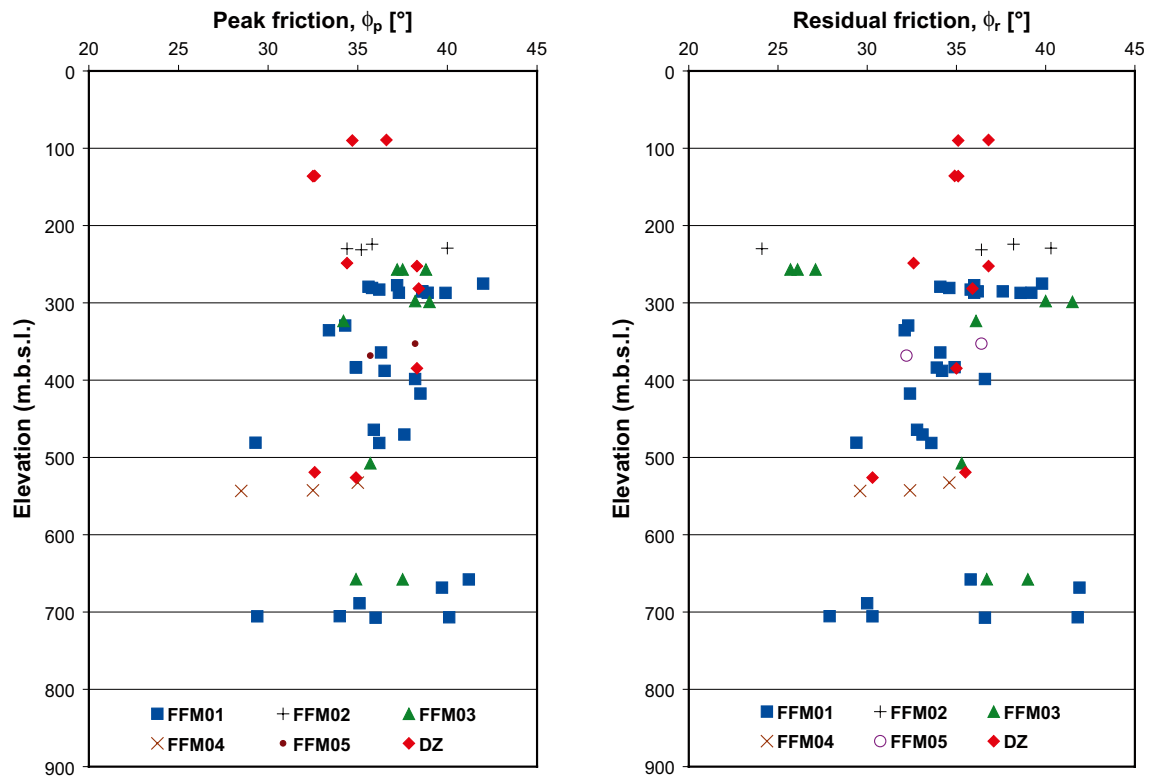


Figure 4-4. Peak and residual friction angle versus depth based on direct shear tests on open fractures.

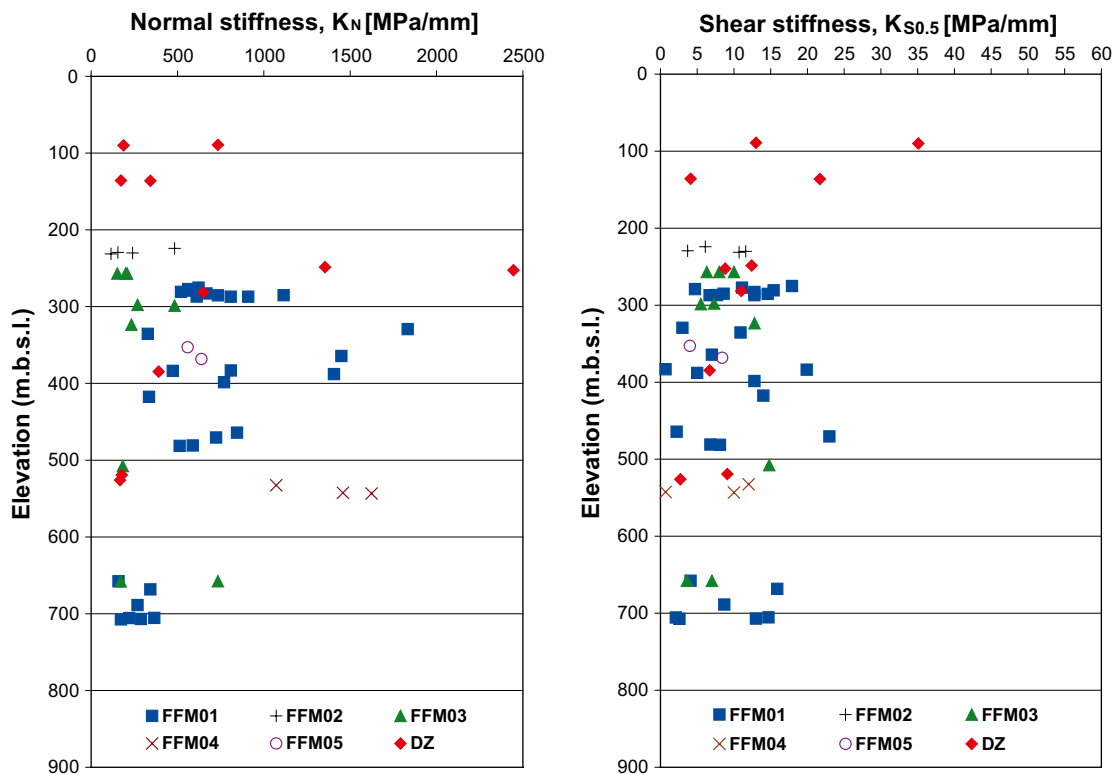


Figure 4-5. Normal stiffness  $K_N$  and shear stiffness  $K_{S0.5}$  versus depth based on direct shear tests on open fractures.

It is difficult to see any clear trends. The evaluated friction angle from tilt tests in fracture domain FFM02 seems however to be smaller than in other domains. The scatter in measured friction angle from tilt tests and direct shear tests are similar, however, the magnitude of the friction angle is slightly higher for the direct shear tests. The scatter in measured normal and shear stiffness is high as well.

#### 4.4.4 Variability in results between modelling steps

In Table 4-11 and Table 4-12, a comparison is made between the results from modelling versions 1.2 and modelling stages 2.1 and 2.2 of the parameters for peak strength determined from tilt and direct shear tests. All tests have been re-evaluated after the modification of the testing procedure for the direct shear tests.

No changes can be seen in the results from the tilt tests. The mean values along with the minimum and maximum are constant.

The results from the direct shear tests show a small increase in the peak cohesion, the standard deviation for the peak cohesion and a small increase in the span between the minimum and maximum with the number of tests. The direct shear test procedure has been modified between version 1.2 and stage 2.1, which may have some influence on the results.

In summary, the following conclusions are drawn: the variability of the selected samples is small; the increasing number of tests has not changed the evaluated mean values that seem to be representative for the studied fractures; and the number of tests seems to be sufficient.

**Table 4-11. Comparison of the parameters for the Coulomb's Criterion based on the results of tilt tests for Forsmark SDM 1.2, 2.1 and 2.2.**

	Number of samples	Minimum		Mean/std. dev		Maximum	
		$c_p$ [MPa]	$\phi_p$ [°]	$c_p$ [MPa]	$\phi_p$ [°]	$c_p$ [MPa]	$\phi_p$ [°]
Forsmark 1.2	142	0.17	25.8	0.46/0.14	33.8/2.0	0.83	37.7
Forsmark 2.1	151	0.17	25.8	0.46/0.13	33.8/2.0	0.83	37.7
Forsmark 2.2	163	0.17	25.8	0.46/0.13	33.8/2.0	0.83	37.7

Note: The cohesion and friction angle are determined for a confinement stress between 0 and 20 MPa. Minimum and maximum are limits of measured data.

**Table 4-12. Comparison of the parameters for the Coulomb's Criterion based on the results of direct shear tests for Forsmark SDM 1.2, 2.1 and 2.2.**

	Number of samples	Minimum		Mean/std. dev		Maximum	
		$c_p$ [MPa]	$\phi_p$ [°]	$c_p$ [MPa]	$\phi_p$ [°]	$c_p$ [MPa]	$\phi_p$ [°]
Forsmark 1.2	27	0.00	29.4	0.58/0.28	36.2/2.8	1.11	41.2
Forsmark 2.1	41	0.00	29.3	0.68/0.34	36.2/2.8	1.29	42.0
Forsmark 2.2	57	0.00	28.5	0.73/0.36	36.2/2.8	1.69	42.0

Note: The cohesion and friction angle are determined for a confinement stress between 0 and 20 MPa. Minimum and maximum are limits of measured data.

## 4.5 Summary of mechanical properties of fractures

### 4.5.1 Uncertainties

The uncertainties in the estimation of the fracture mechanical properties have been dealt with in a similar way as the mechanical properties for intact rock. The spatial variability has been discussed in the previous Section 4.4. The uncertainty that originates from the methods used to determine the fracture properties are on the whole the same as those dealt with regarding the properties of the intact rock, see Section 3.6.1. However, the effect of the different sources of uncertainty is not the same in the case of the fracture properties. Specifications of the uncertainties in the used laboratory methods are to be found in SKB's Method Descriptions and the underlying P-reports that present the laboratory results. Here, the uncertainty of the mechanical properties of fractures is expressed statistically only by means of a range of variation in the evaluated mean values.

The uncertainty of the mean was quantified according to the "Central Limit Theorem" /Peebles 1993/ for a 95% confidence interval. Minimum and maximum truncation values given in the tables below are based on the observed minimum and maximum for the tested population.

### 4.5.2 Evaluated mechanical properties of fractures

A summary of the results from laboratory tests for the different fracture domains are shown in Table 4-13 to Table 4-16. The number of tests within fracture domains FFM01 and FFM03 are larger than in the other domains, which makes the uncertainty in these domains smaller. No tests have been performed on fractures from fracture domain FFM06. The reason being that the sampling of fractures was already complete prior to the definition of this fracture zone. However, the mechanical properties of fractures in FFM06 are judged to be similar to those of fracture domain FFM01.

On the whole, the results for samples from various fracture domains and examined fracture zones are similar. The differences that exist chiefly concern the normal stiffness, which is lesser in fracture domains FFM02 and FFM03, and higher in fracture domain FFM04.

**Table 4-13. Summary of properties from tilt tests for the fracture domains.**

Fracture domain	Peak friction (°)	Peak cohesion (MPa)	Residual friction (°)	Residual cohesion (MPa)
	Mean/std. dev.	Mean/std. dev.	Mean/std. dev.	Mean/std. dev.
	Min-max <i>Uncertainty of mean</i>	Min-max <i>Uncertainty of mean</i>	Min-max <i>Uncertainty of mean</i>	Min-max <i>Uncertainty of mean</i>
FFM01	33.9/1.7 29.5–36.6 ± 1.2%	0.4/0.1 0.2–0.7 ± 6.2%	29.7/2.9 22.6–37.9 ± 2.4%	0.4/0.1 0.2–0.6 ± 6.2%
FFM02	30.8/3.1 25.8–34.9 ± 7.5%	0.5/0.1 0.2–0.7 ± 14.8%	26.2/3.9 20.3–32.8 ± 11.0%	0.4/0.1 0.2–0.6 ± 18.5%
FFM03	34.5/1.5 32.2–37.7 ± 1.3%	0.5/0.1 0.2–0.8 ± 6.1%	29.3/2.5 23.7–33.5 ± 2.6%	0.4/0.1 0.2–0.7 ± 7.7%
FFM04	34.5/1.9 33.1–35.8 ± 7.6%	0.5/0.2 0.3–0.6 ± 55.4%	33.0/1.0 32.3–33.7 ± 4.2%	0.5/0.2 0.3–0.6 ± 55.4%
FFM05	33.4/1.3 31.4–34.8 ± 3.4%	0.4/0.1 0.3–0.6 ± 21.9%	27.8/3.2 24.3–32.3 ± 10.7%	0.4/0.1 0.2–0.5 ± 21.9%
DZ	33.3/2.0 28.5–36.4 ± 2.0%	0.5/0.1 0.3–0.8 ± 6.7%	29.5/3.1 21.5–37.2 ± 3.5%	0.4/0.1 0.3–0.7 ± 3.4%

Note: The uncertainty of the mean is quantified for a 95% confidence interval. Minimum and maximum truncation values are based on the observed min' and max' for the tested population.

**Table 4-14. Summary of properties from direct shear tests for the fracture domains.**

Fracture domain	Peak friction (°)	Peak cohesion (MPa)	Residual friction (°)	Residual cohesion (MPa)
	Mean/std. dev.	Mean/std. dev.	Mean/std. dev.	Mean/std. dev.
	Min-max <i>Uncertainty of mean</i>	Min-max <i>Uncertainty of mean</i>	Min-max <i>Uncertainty of mean</i>	Min-max <i>Uncertainty of mean</i>
FFM01	36.6/2.9 29.3–42.0 ± 2.9%	0.8/0.3 0.2–1.3 ± 13.7%	34.9/3.4 27.9–41.9 ± 3.6%	0.3/0.2 0.1–0.8 ± 24.3%
FFM02	36.4/2.5 34.4–40.0 ± 6.7%	0.5/0.4 0.2–1.0 ± 78.4%	34.8/7.3 24.1–40.3 ± 20.6%	0.4/0.6 0.1–1.3 ± 147.0%
FFM03	37.0/1.7 34.2–39.0 ± 3.0%	0.6/0.2 0.3–0.9 ± 21.8%	34.2/6.2 25.7–41.5 ± 11.8%	0.5/0.4 0.2–1.1 ± 52.3%
FFM04	32.0/3.3 28.5–35.0 ± 11.7%	0.9/0.4 0.6–1.4 ± 50.3%	32.2/2.5 29.6–34.6 ± 8.8%	0.3/0.1 0.2–0.4 ± 37.7%
FFM05	37.0/1.8 35.7–38.2 ± 6.7%	0.8/0.2 0.7–0.9 ± 34.7%	34.3/3.0 32.2–36.4 ± 12.1%	0.4/0.1 0.4–0.5 ± 34.7%
DZ	35.3/2.4 32.5–38.4 ± 4.2%	0.8/0.5 0.0–1.7 ± 38.7%	34.8/2.0 30.3–36.8 ± 3.6%	0.3/0.2 0.0–0.6 ± 41.3%

Note: The uncertainty of the mean is quantified for a 95% confidence interval. Minimum and maximum truncation values are based on the observed min' and max' for the tested population.

**Table 4-15. Summary of properties from direct shear tests for the fracture domains.**

Fracture domain	Normal stiffness, $K_N$ (GPa/m)	Shear stiffness, $K_{S0.5}$ (GPa/m)	Shear stiffness, $K_{S5.0}$ (GPa/m)	Shear stiffness, $K_{S20.0}$ (GPa/m)
	Mean/std. dev.	Mean/std. dev.	Mean/std. dev.	Mean/std. dev.
	Min-max <i>Uncertainty of mean</i>	Min-max <i>Uncertainty of mean</i>	Min-max <i>Uncertainty of mean</i>	Min-max <i>Uncertainty of mean</i>
FFM01	656/396 159–1,833 ± 22.0%	10/6 1–23 ± 21.8%	26/9 7–46 ± 12.6%	34/10 18–52 ± 10.7%
FFM02	248/165 115–483 ± 65.2%	8/4 4–12 ± 49.0%	26/4 21–31 ± 15.1%	33/8 25–41 ± 23.8%
FFM03	293/193 152–734 ± 43.0%	8/4 4–15 ± 32.7%	31/7 23–43 ± 14.8%	35/10 20–49 ± 18.7%
FFM04	1,385/283 1,072–1,624 ± 23.1%	8/6 1–12 ± 84.9%	16/5 12–22 ± 35.4%	23/5 18–29 ± 24.6%
FFM05	599/57 559–639 ± 13.2%	6/3 4–8 ± 69.3%	20/7 14–25 ± 48.5%	25/2 23–26 ± 11.2%
DZ	662/729 167–2,445 ± 68.3%	12/10 3–35 ± 51.7%	26/9 7–41 ± 21.5%	31/8 19–44 ± 16.0%

Note: The uncertainty of the mean is quantified for a 95% confidence interval. Minimum and maximum truncation values are based on the observed min' and max' for the tested population.

**Table 4-16. Summary of properties from direct shear tests for the fracture domains.**

Fracture domain	Dilatancy angle, $\psi_{0.5}$ (°)	Dilatancy angle, $\psi_5$ (°)	Dilatancy angle, $\psi_{20}$ (°)
	Mean/std. dev.	Mean/std. dev.	Mean/std. dev.
	Min-max <i>Uncertainty of mean</i>	Min-max <i>Uncertainty of mean</i>	Min-max <i>Uncertainty of mean</i>
FFM01	14.6/4.1 7.8–27.1 ± 10.2%	7.7/2.7 2.5–13.7 ± 12.8%	3.2/2.1 0.2–9.6 ± 23.9%
FFM02	15.2/2.9 11.5–17.6 ± 18.7%	2.2/0.5 1.6–2.6 ± 22.3%	2.1/2.2 0.2–4.3 ± 102.7%
FFM03	16.4/2.2 14.0–20.2 ± 8.8%	3.1/2.1 0.5–6.3 ± 44.3%	2.3/1.7 0.2–6.1 ± 48.3%
FFM04	10.1/0.7 9.5–10.9 ± 7.8%	6.6/1.3 5.4–7.9 ± 22.3%	1.3/1.0 0.3–2.2 ± 87.1%
FFM05	14.7/0.4 14.4–15.0 ± 3.8%	8.8/0.1 8.7–8.8 ± 1.6%	2.3/0.5 1.9–2.6 ± 30.1%
DZ	14.4/6.4 0.3–22.8 ± 27.6%	5.7/4.3 1.0–13.0 ± 46.8%	3.0/1.3 0.5–4.6 ± 26.9%

Note: The uncertainty of the mean is quantified for a 95% confidence interval. Minimum and maximum truncation values are based on the observed min' and max' for the tested population.

### **Normal and shear stiffness**

The change in testing procedure for the direct shear tests could influence the results by increasing uncertainty in these tests, principally of the normal stiffness, although an attempt to correct the results has been made.

To get an appreciation of the stiffness determined in the present work, in relation to previously investigations, the results have been compared to tests performed by /Lanaro 2001/. Lanaro has reported normal and shear stiffness from fracture sets in the Äspö laboratory. It should be noted that in the investigation carried out by Lanaro the deformation of the intact rock was subtracted from measured deformation over fracture when determining the normal stiffness. The results from /Lanaro 2001/ are compared with the results from the present work in Table 4-17.

The comparison shows that the normal stiffness for Forsmark 2.2 is higher, up to a double magnitude, while the shear stiffness is in the same order of magnitude. The standard deviation for the normal stiffness is high both in Lanaro's investigation and in the current investigation. The divergence in the results is most likely caused by differences in the method of determining the normal stiffness.

### **Recommendation regarding results from tilt and direct shear tests**

The results from the tilt tests in fracture domain FFM01 have been recalculated for the same sample size (~ 55 mm) and stress interval as for the direct shear tests. The peak friction angle and peak cohesion evaluated from tilt tests and direct shear tests are compared in Figure 4-6 and Figure 4-7. Both the peak friction and the peak cohesion evaluated from direct shear tests are higher than from tilt tests.

For use in design and in the theoretical approach it is recommended to use the values from direct shear tests, Table 4-14 to Table 4-16, since they are based on direct measurements with a stress magnitude comparable to what is expected to be found at tentative repository depth in the Forsmark target volume.

It should be noted that the large-scale mechanical properties of fractures are expected to deviate from the results reported here on small specimens of 50–60 mm in size. Due to reduction in the effective roughness of the surface, JRC, most likely the shear strength of the large-scale fractures will be reduced as compared to the results from the tested samples /Bandis 1980/. Due to the greater possibility of weakness in a large surface, it is also likely that the mean joint wall compressive strength, JCS, decreases with increasing scale /Barton and Bandis 1982/. There is also a possibility that the large-scale fractures will show differences between the fracture sets, although the differences in the small scale were insignificant, cf. Section 4.4.2.

**Table 4-17. Comparison of normal and shear stiffness determined in the present work with investigations performed by /Lanaro 2001/.**

	Mean (GPa/m)	Std. dev (GPa/m)	Min (GPa/m)	Max (GPa/m)
<b>/Lanaro 2001/</b>				
$K_N$ , Secant normal stiffness 0.5–10 MPa	348	401	67	1,399
$K_S$ , $\sigma_n = 10$ MPa	31	7	21	44
<b>Forsmark 2.2</b>				
$K_N$ , Secant normal stiffness 0.5–10 MPa	607	483	115	2,445
$K_S$ , $\sigma_n = 20$ MPa	33	10	18	52



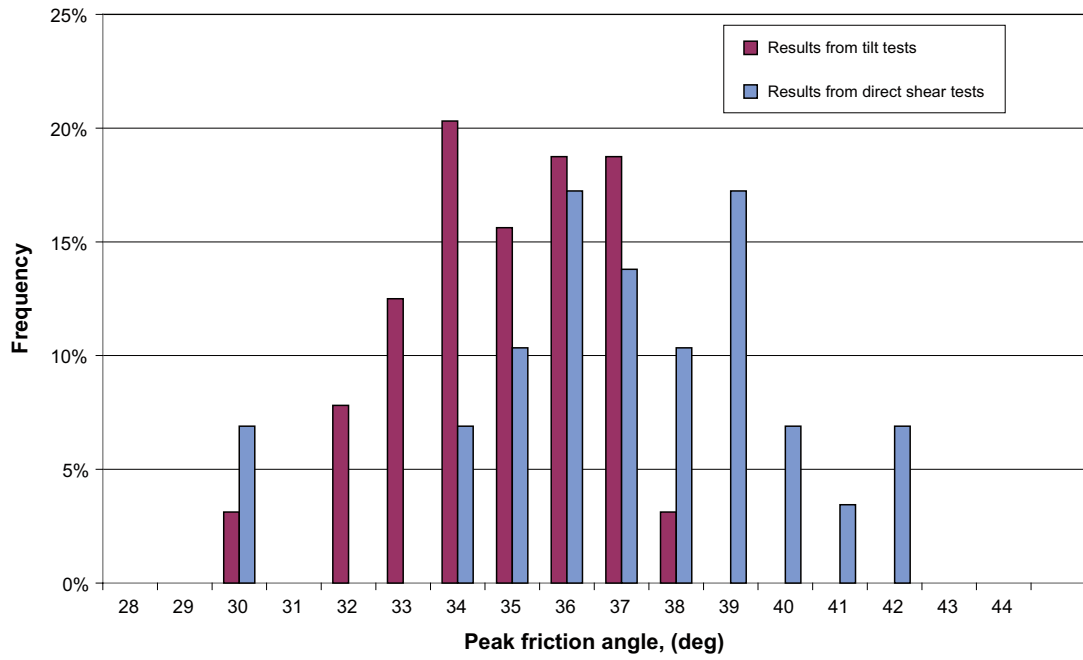


Figure 4-6. Comparison of the peak friction angle from tilt tests and from direct shear tests.

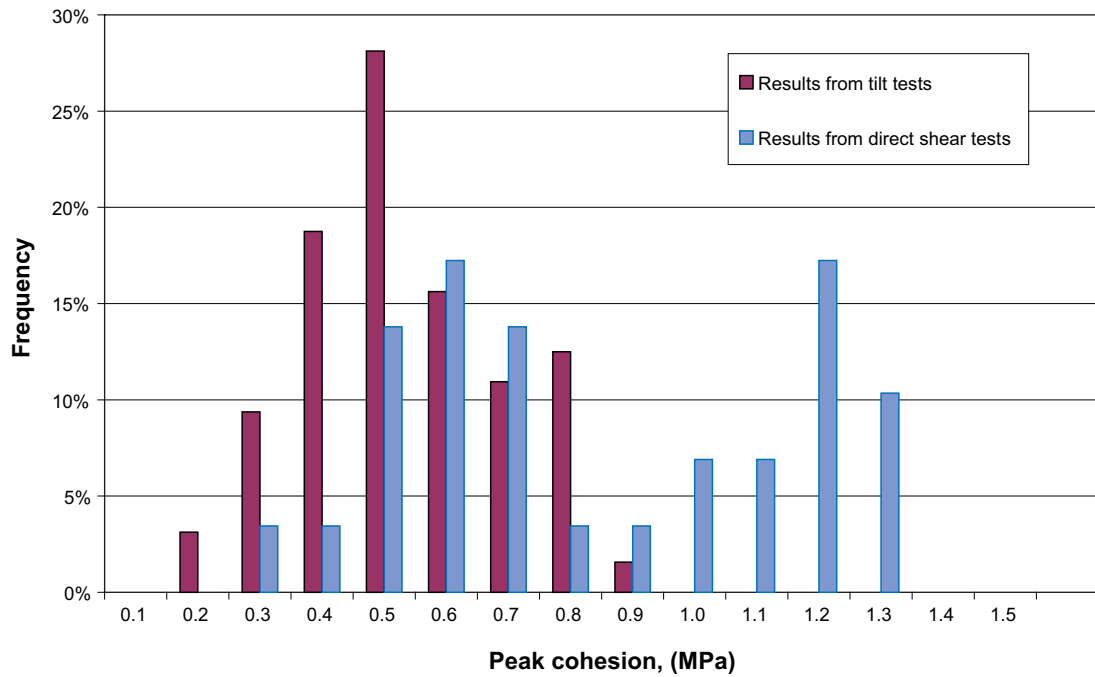


Figure 4-7. Comparison of the peak cohesion from tilt tests and from direct shear tests.

## 5 Rock mass mechanical properties

In this section the rock mass strength and deformation properties are estimated. The rock mass quality with regard to constructability is used in the design of a repository to estimate the risk for stability problems and assessment of the rock support requirements, cf. Section 1.3.1.

Two modelling approaches are utilised to estimate the rock mass properties, an empirical and a theoretical approach. The empirical approach estimates the rock mass mechanical properties based on classification systems and empirical relationships, while the theoretical approach estimates the properties of the rock mass by using numerical models. The final estimate of the rock mass properties is achieved by weighting the results from the two models together, a process termed “Harmonization”. The modelling methodology of the rock mechanics site description is presented with additional details and a flowchart in Section 1.4.

### 5.1 Empirical approach using classification systems

This section summarises the results of the rock mechanics characterization of the rock domains RFM029 and RFM045 by means of empirical methods based on seven new characterized boreholes as well as old data from the previous Forsmark site description version 1.2. /SKB 2005a/. The new boreholes are KFM01B, KFM07C, KFM09A, KFM09B, KFM06A, KFM06C and KFM08C reported by /Bäckström and Lanaoro 2007/. In KFM06A, KFM06C and KFM08C only the part of the borehole passing rock domain RFM045 was characterized.

The characterizations were performed for borehole sections of 5 m according to the empirical methods of the Q-system, RMR (Rock Mass Rating) and the methodology developed for the Äspö Test Case /Andersson et al. 2002, Röshoff et al. 2002/. The influence of the characterization scale has been examined by the comparison of results obtained for characterization at 1 and 5 m sections /Bäckström and Lanaoro 2007/. The comparison shows that a difference in scale has an insignificant impact on the results, see Appendix A3.1.

The well established formulae for RMR /Bieniawski 1989/ and Q /Barton 2002/ are reported here for the convenience of the reader. The basic equation for the RMR /Bieniawski 1989/ is:

$$RMR = RMR_{strength} + RMR_{RQD} + RMR_{spacing} + RMR_{conditions} + RMR_{water} + RMR_{orientation} \quad \text{Equation 5-1}$$

where the subscripts refer to the strength of the intact rock; Rock Quality Designation; conditions and spacing of the fractures; groundwater conditions and the orientation of the fracture sets with respect to the hypothetical tunnel orientation.

The basic equation for Q /Barton 2002/ is:

$$Q = \frac{RQD}{J_n} \times \frac{J_r}{J_a} \times \frac{J_w}{SRF} \quad \text{Equation 5-2}$$

where,  $J_n$  depends on the number of fracture sets;  $J_r$  and  $J_a$  on the roughness and alteration of the fractures;  $J_w$  on the groundwater conditions and SRF (Stress Reduction Factor) takes into account the stresses in the rock mass. The classification systems have been applied for obtaining the ratings independently on the water pressure ( $J_w = 1$ ,  $RMR_{water} = 15$ ) and possible orientation of the excavation ( $RMR_{orientation} = 0$ ) /Andersson et al. 2002/. The effect of the stress state has been taken into account by assigning  $SRF = 1$  for rock mass outside deformation zones and  $SRF = 2.5$  in deformation zones with markedly reduced RQD values.

Several empirical correlations between Q and RMR ratings have been reported in the literature. Since such correlations are to a certain degree site sensitive, a site-specific correlation has been examined for the rock mass in rock domain RFM029 and RFM045. The results are shown together with some of the relations presented in the literature in Appendix A3.2. The correlation that seems to fit results best is one published by /Cameron-Clarke and Budavari 1981/:

$$RMR = 5 \ln Q + 60.8 \quad \text{Equation 5-3}$$

The mechanical properties of the rock mass were estimated from the characterization of the rock mass quality. In particular, focus was given to:

- The deformation modulus ( $E_m$ ) and Poisson's ratio ( $\nu_m$ ) of the rock mass calculated by means of *RMR*.
- The equivalent uniaxial compressive strength ( $UCS_m$ ) and tensile strength ( $T_m$ ) of the rock mass determined by means of *RMR*, through *GSI*, and the Hoek-Brown's Failure Criterion.
- The friction angle ( $\phi_m$ ), cohesion ( $c_m$ ) and apparent uniaxial compressive strength of the rock mass according to the Coulomb's Criterion also determined by means of *RMR*, through *GSI*, and the Hoek-Brown's Failure Criterion.

The empirical characterization of the rock mass does not consider sealed or partly open fractures. Empirical methods are designed based on the occurrence of open fractures, which are the weakest component of the rock mass. However, since natural rocks often contain a mixture of open and sealed or partly open fractures, this does not mean that the empirical methods ignore their presence. In fact, the empirical methods build on databases of real case histories where sealed or partly open fractures are present. Therefore, such fractures are at least implicitly considered, even if they are not directly analysed. However, the rock mass in Forsmark is dominated by sealed fractures, open fractures only constitute a small portion of the total (cf. Section 2.1.3) therefore the rock mass quality determined by Q and RMR may be overestimated since sealed fractures are not considered explicitly.

The analysed boreholes were subdivided into rock domains (RFM), fracture domains (FFM) and deterministic deformation zones (DZ) according to the geological model presented by /Stephens et al. 2007/. Furthermore, the deterministic deformation zones were also divided into major deformation zones (> 1,000 m), minor deformation zones (< 1,000 m) and possible deformation zones. The properties for each component of geological model were evaluated empirically.

The following section presents the mechanical properties for rock domains, fracture domains and deformation zones. In addition, variations of the rock mechanics properties per borehole and along the boreholes are presented in the Appendix A3.3.

## 5.1.1 Strength and deformation properties for the rock domains

### ***Rock domains in the target volume, RFM029 and RFM045***

The empirical modelling focuses on rock domain RFM029 and RFM045, which is the planned target volume. The total length of studied core includes 4,869 m for rock domain RFM029 and 945 m for rock domain RFM045.

The results of the Q- and RMR-rock mass characterizations are presented in Figure 5-1 and Figure 5-2, respectively. Further plots are to be found in Appendix 8. The rock mass quality in the two rock domains is commonly classified as "very good" according to the empirical Q-system /Barton 2002/ and RMR-system /Bieniawski 1989/. The rock mass in RFM045 presents a slightly higher occurrence of high quality rock compared to RFM029, but the differences are judged to be insignificant from a rock mechanical point of view.

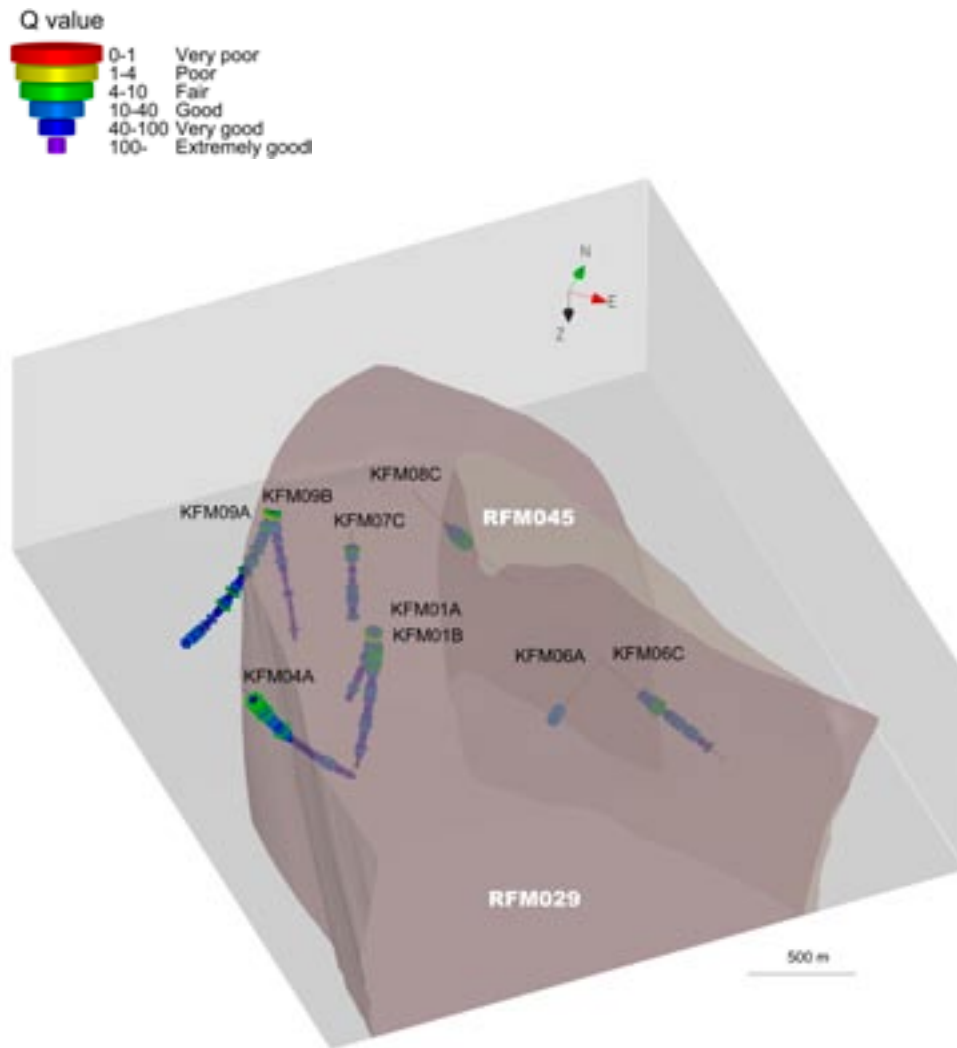


**Figure 5-1.** *Q value (mode) for each 5 m interval, viewed towards north. In KFM06A, -06C and -08C, only the sections in RFM045 were characterized.*

The evaluated rock mass properties in rock domains RFM029 and RFM045, outside the deformation zones, are presented with frequency distributions in Figure 5-4. For the largest rock domain, RFM029, the equivalent uniaxial compressive strength ( $UCS_m$ ) and the deformation modulus ( $E_m$ ) is estimated to a mean value of 83 MPa and 69 GPa, respectively. This can be compared with a mean value of Young's Modulus of the intact of 75 GPa within the same rock domain, see Section 3.3.1.

Compared to rock domain RFM029 the values for the same properties in RFM045 are 95 MPa ( $UCS_m$ ) and 70 GPa ( $E_m$ ) respectively. The estimated mean of Young's modulus for intact rock in RFM045 is 83 GPa.

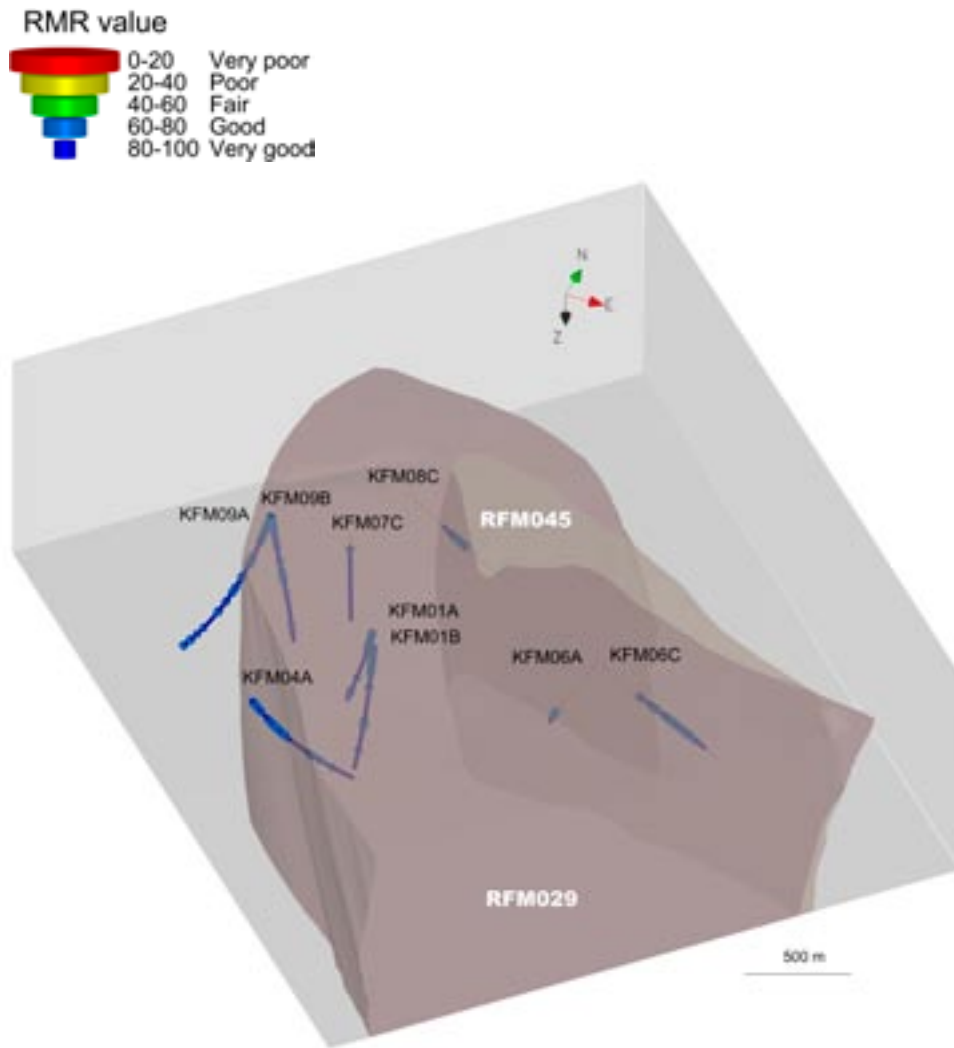


*Figure 5-2. RMR value for each 5 m interval, viewed towards north. In KFM06A, -06C and -08C, only the sections in RFM045 were characterized.*

It may be noted in Figure 5-3 that the frequency distribution of Young's modulus is unequally distributed around the mean. This is due to the empirical formula used in the computation, which has a cut-off at the value of the intact rock. Poisson's ratio shows a similar distribution since it is directly evaluated based on the relationship between Young's modulus of intact rock and the value for the rock mass.

As shown above in Table 5-1 the results from modelling stage 2.2 are in good agreement with the results from Forsmark version 1.2. The same empirical formulae have been used for both stages. The current modelling stage 2.2 includes about 36% more data (1,743 borehole metres) than Forsmark version 1.2, yet the resulting differences are on the whole insignificant.

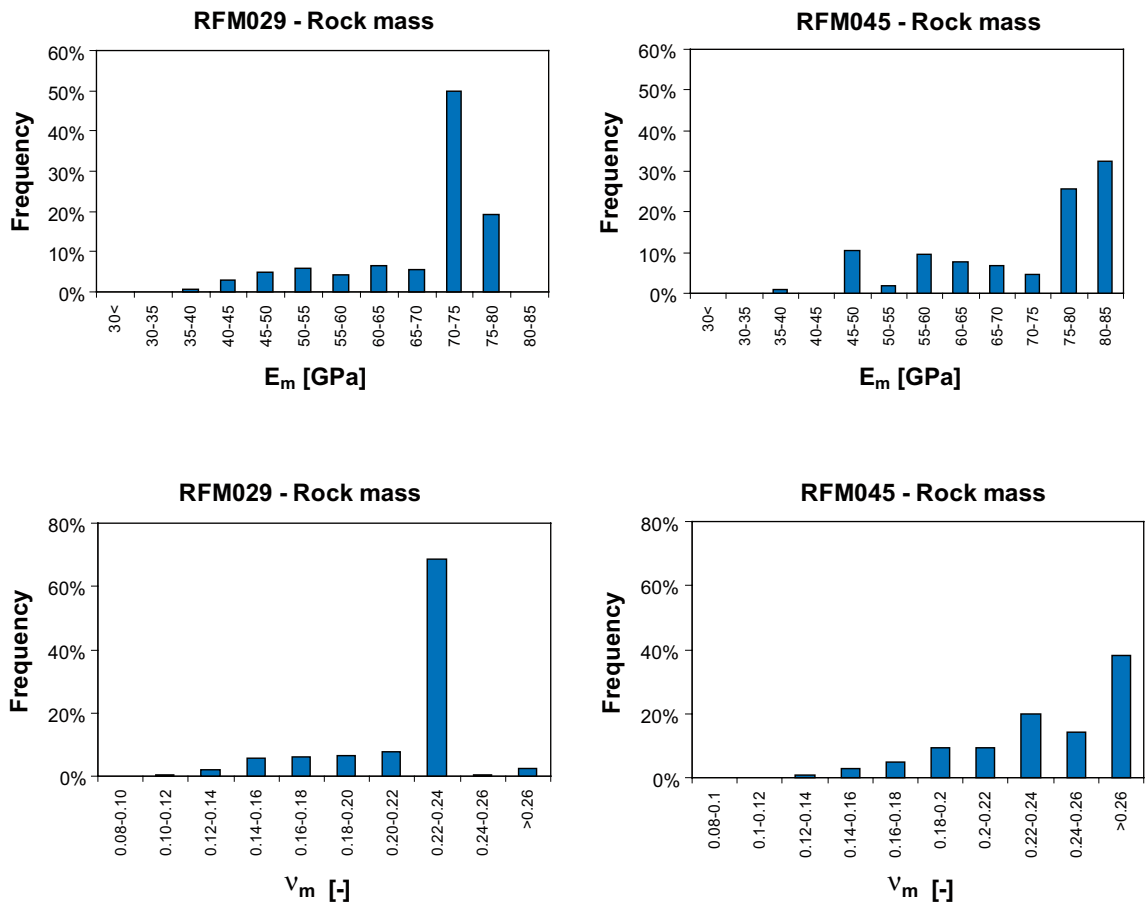


Figure 5-3. Frequency distribution of evaluated deformation properties of the rock mass outside deformation zones in rock domains RFM029 and RFM045.

Table 5-1. Comparison of the results from SDM 1.2 and modelling stage 2.2 for the rock mass outside deformation zones in domain RFM029.

Rock mass parameter	Forsmark 1.2			Forsmark 2.2		
	Min	Mean/std dev	Max	Min	Mean/std dev	Max
$Q^*$	7	370 [86]	2,133	2	363 [100]	2,133
RMR	73	87/6	98	71	87/6	98
$E_m$ [GPa]	37	69/10	75	34	69/10	76
$v_m$	0.12	0.22/0.03	0.27	0.11	0.22/0.03	0.30
UCS <sub>m</sub> (H-B) [MPa]	18	80/29	153	23	84/28	153
$\phi_m$ [°]	40	49/2	51	32	49/2	52
$c_m$ [MPa]	15	25/4	35	12	26/4	35
UCS <sub>m</sub> (M-C) [MPa]	63	134/26	196	44	138/25	196
$T_m$ [MPa]	0.3	2/1	5	0.5	2/1	5

\* Mode values are shown in brackets.

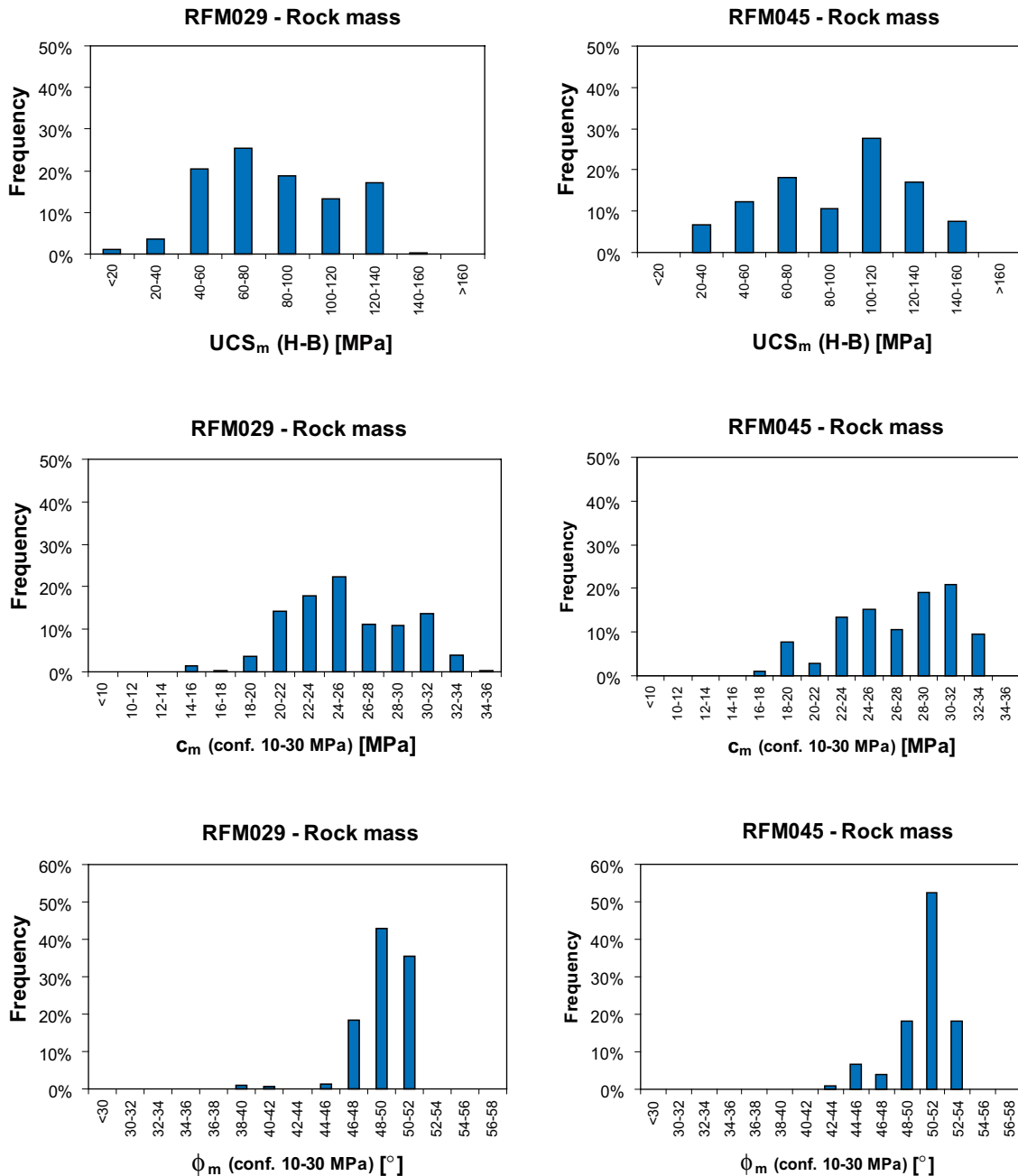
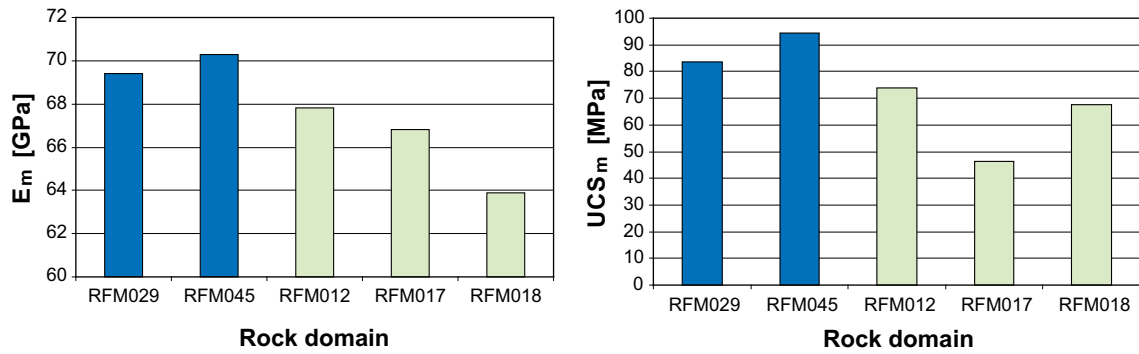


Figure 5-4. Frequency distribution of evaluated strength properties of the rock mass outside deformation zones in rock domains RFM029 and RFM045.

#### Adjacent rock domains, RFM012, RFM017 and RFM018

The target volume is surrounded by rock domains RFM012, RFM017 and RFM018. A comparison of the rock mass properties outside the deformation zones in these domains and the target volume is shown in Figure 5-5.

Rock domains RFM029 and RFM045 have higher mean values for both the rock mass deformation modulus and the uniaxial compressive strength compared to the adjacent rock domains RFM012, RFM017 and RFM018. The mean uniaxial compressive strength of RFM017 is 46 MPa, which is 51% lower than the mean value in RFM045. The mean deformation modulus in rock domain RFM018 is 64 GPa, which is 9% lower than the mean value in domain RFM045. However, even the estimated minimum values,  $E_m = 64$  GPa in RFM018 and  $UCS_m = 46$  MPa in RFM017, indicate that the rock mass in all analysed rock domains is of good quality, close to the mechanical properties of the intact rock.



**Figure 5-5.** Comparison of mean deformation modulus and mean uniaxial compressive strength for the rock mass outside deformation zones in the rock domains of the tested target volume with the adjacent domains.

### 5.1.2 Strength and deformation properties for the fracture domains

The fracture domains (FFM) refer to a rock volume outside deformation zones in which rock units display a similar fracture frequency. Fracture domains FFM01, FFM02 and FFM03 represent the rock mass of rock domain RFM029 while FFM06 equals the rock mass of RFM045. The evaluated rock mass properties in fracture domain FFM01 are presented with frequency distribution in Figure 5-6 and Figure 5-7. A comparison of the mean rock mass properties subdivided into fracture domains is shown in Figure 5-8 and Figure 5-9. Once again the frequency distribution of Young's modulus and Poisson's ratio are unequally distributed around the mean, mainly due to the high quality rock and the cut-off in the empirical formulas used in the computation.

Fracture domains FFM01 and FFM06 generally show the highest values of rock mass mechanical properties and fracture domain FFM02 the lowest.

Fracture domain FFM06 in the target volume represents a stiff and strong rock mass with a deformation modulus ( $E_m$ ) of 70 GPa (Figure 5-8), a uniaxial compressive strength ( $UCS_m$ ) of 95 MPa, and a tensile strength ( $T_m$ ) of 2.3 MPa (Figure 5-9). The higher quality is mainly due to the high strength of the intact rock, compared to the other fracture domains.

Fracture domain FFM01 represents a quality comparable to FFM06 both regarding the deformation modulus (72 GPa), the uniaxial compressive strength (92 MPa) and the cohesion. The apparent angle of friction is somewhat less, Figure 5-9.

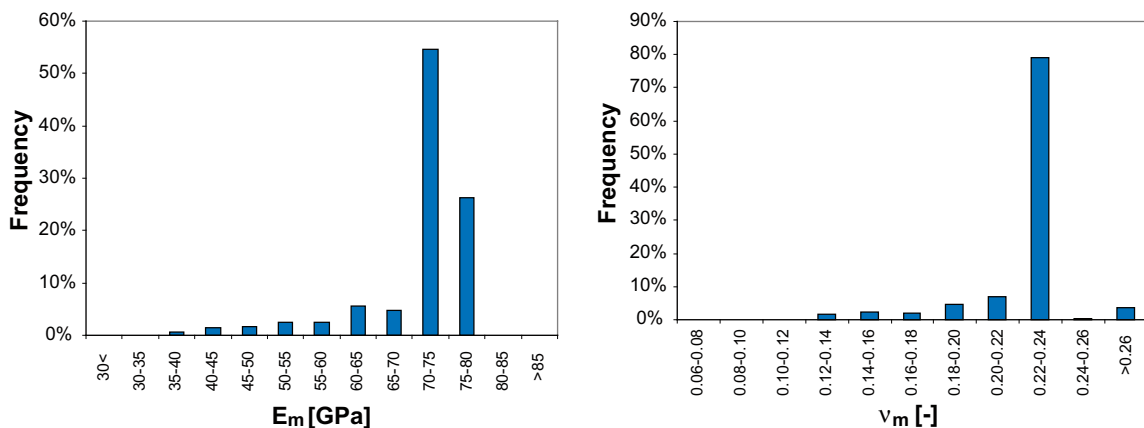


**Figure 5-6.** Frequency distribution of deformations properties evaluated for the rock mass in fracture domain FFM01.



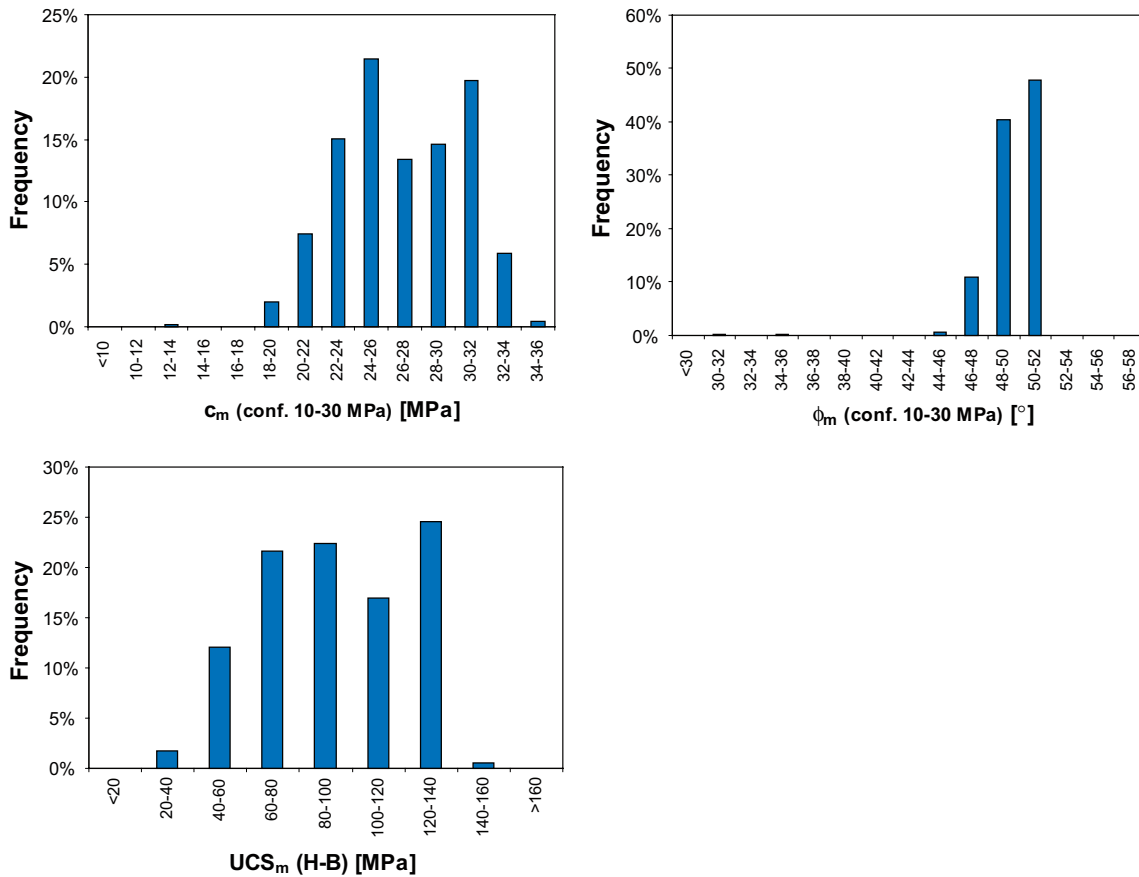


Figure 5-7. Frequency distribution of strength properties evaluated for the rock mass in fracture domain FFM01.

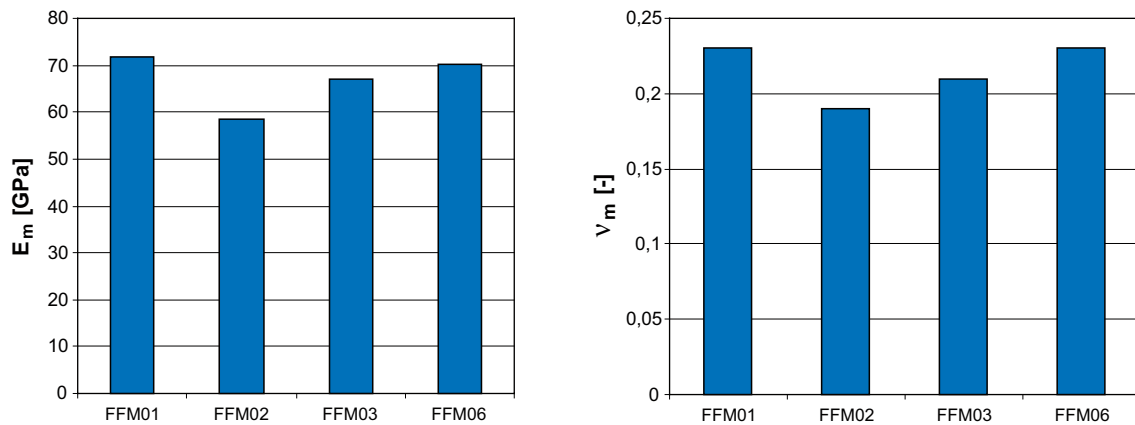
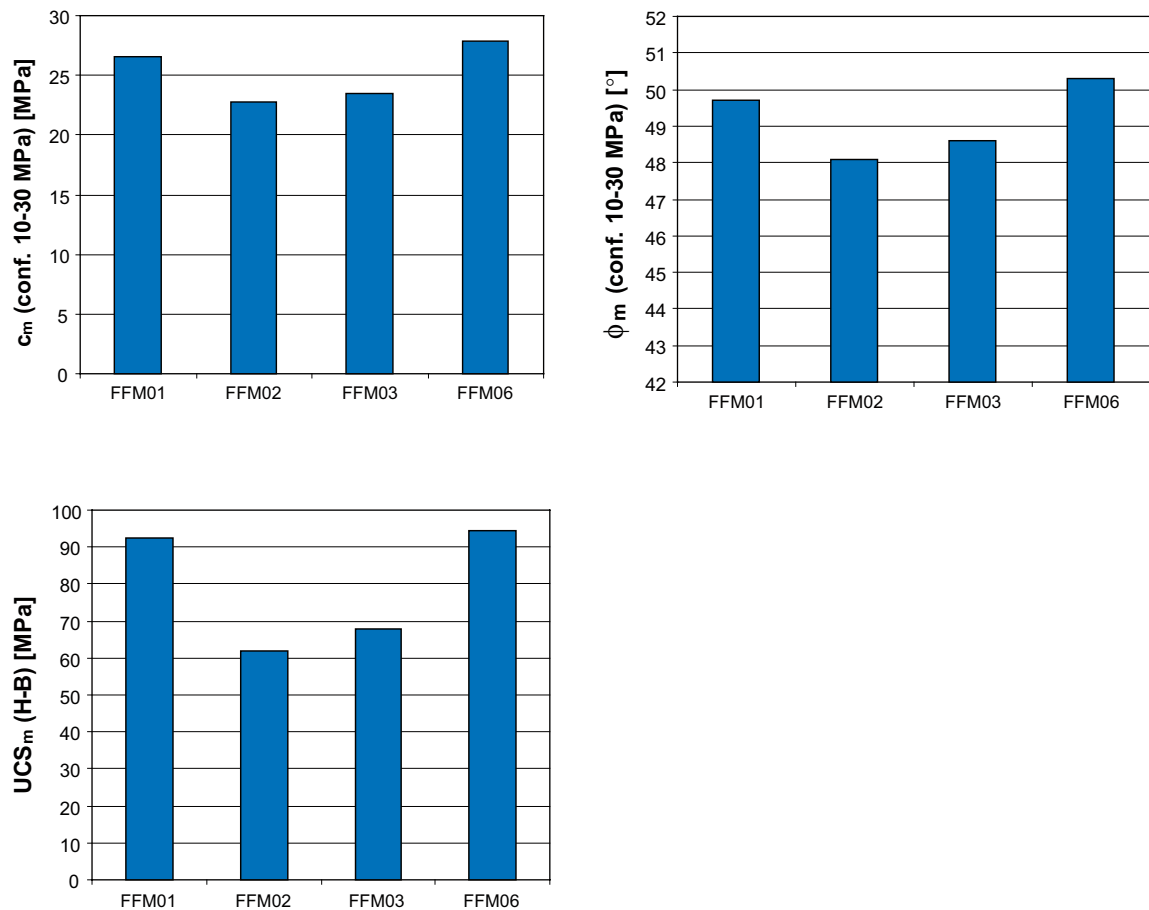


Figure 5-8. Comparison of the mean values of the rock mass deformation properties subdivided into fracture domains.

Fracture domain FFM02 represents the worst part of the rock mass in RFM029. The deformation modulus (59 GPa), the uniaxial compressive strength (62 MPa) and tensile strength (1.4 MPa) are all lower compared to fracture domains FFM01 and FFM06.

In summary it can be stated that the evaluated mechanical properties indicate, independent of fracture domain, that the rock mass in the target volume is stiff and strong and the differences are judged to be of minor importance in the assessment of the rock support needed for a tentative repository.



**Figure 5-9.** Comparison of the mean values of the rock mass strength properties subdivided into fracture domains.

### 5.1.3 Strength and deformation properties for the deformation zones

The deformation zones are subdivided into three groups based on size according /Andersson et al. 2000/, cf. Section 2.1.3:

- Deformation zones which are longer than 1,000 m and modelled deterministically.
- Deformation zones which are shorter than 1,000 m and modelled deterministically.
- Possible deformation zones which are probably shorter than 1,000 m and not modelled deterministically.

The studied rock volume includes 23 deterministic deformation zones that intercept the boreholes in rock domains RFM029 and RFM045. The deformation zones are subdivided into the following groups based on orientation and dip:

- Vertical and steeply-dipping brittle deformation zones with ENE, NNE and NE strike.
- Vertical and steeply-dipping brittle deformation zones with NNW strike.
- Vertical and steeply-dipping to SSW and SW deformation zones with WNW and NW strike.
- Gently-dipping brittle deformation zones.

As shown in Figure 5-10, the deformation zones with a gentle dip in general have slightly lower strength and deformation properties than the ENE- and NNE-oriented zones. As described in Section 2.1.3 the steeply-dipping brittle deformation zones are dominated by sealed fractures, which were not considered explicitly in the empirical characterization. The gently-dipping brittle deformation zones on the other hand contain a higher frequency of open fractures which explains the slightly lower values from these zones.

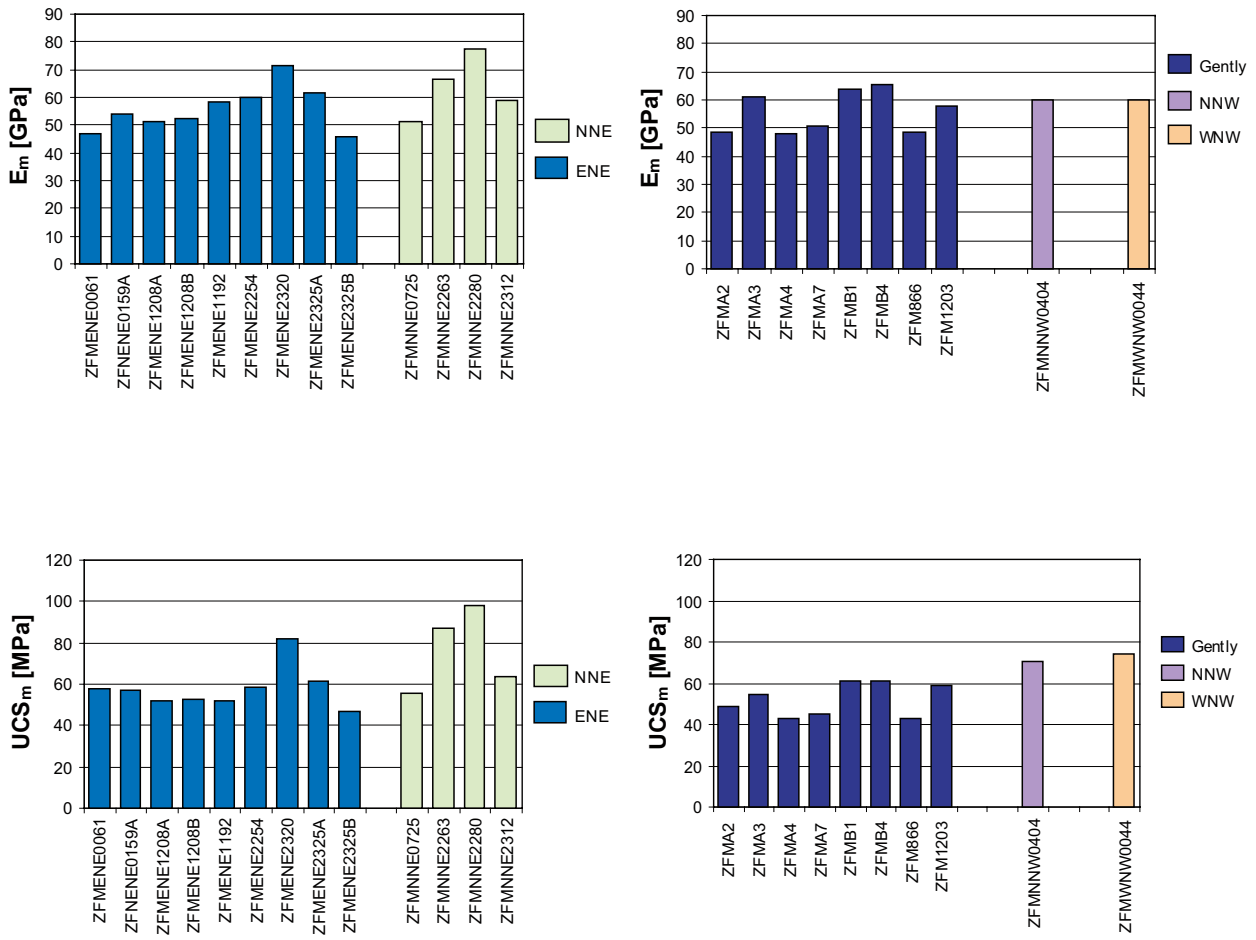


Figure 5-10. Deformation modulus and uniaxial compressive strength of the rock mass within deformation zones. The figure shows the evaluated mean values.

In Figure 5-11 a comparison between the three types of zones and the fracture domains is presented showing that FFM02 has values equal to the values of the deformation zones.

The spread of the mechanical properties of the deformation zones could not be correlated either with orientation or type of deformation nor with the thickness of the zones. No clear trends were observed but the gently dipping zones tend to have lower values of uniaxial compressive strength. The mean uniaxial compressive strength ranges from 43 to 98 MPa and the mean deformation modulus from 46 to 77 GPa.

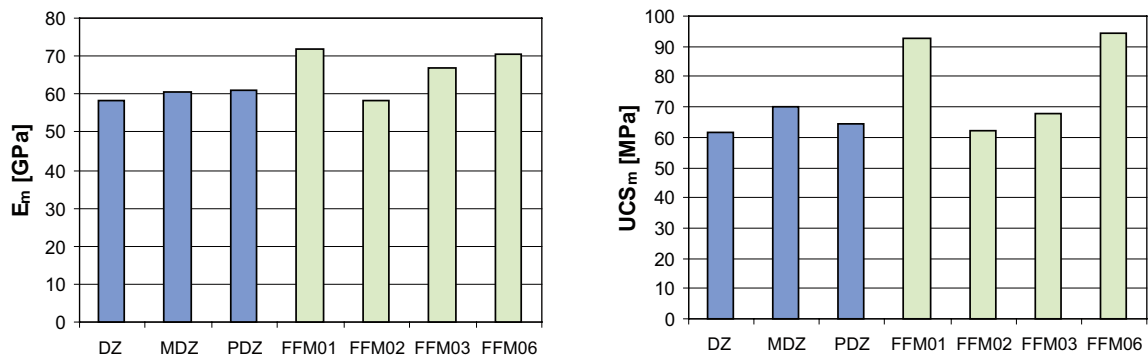


Figure 5-11. Comparison of rock mass strength and deformation properties for deformation zones and fracture domains. The figure shows the evaluated mean values.

Considered as a group, the rock mass quality of the deterministic deformation zones in general is classified as “very good rock” by the empirical systems. However, some sections of “poor rock” were observed. As an example, a 5 m section with a Q-value of 1.8 was observed in deformation zone ZFMA7 and a 5 m section with a Q-value of 2.3 in ZFMENE1208A, see Appendix A3.8

The mean deformation modulus in the deformation zones is around 59 GPa, 14% lower than the deformation modulus of the rock mass outside the deformation zones in domain RFM029. As a mean value, the equivalent uniaxial compressive strength of the rock mass in the deformation zones is 64 MPa, which is 22% lower than for the rock mass outside the deformation zones in domain RFM029.

#### **5.1.4 Summary of the results from the empirical model**

##### ***Uncertainties***

The empirical approach estimates of the rock mass mechanical properties are affected by the uncertainties in the geological parameters and intrinsic uncertainties due to the structure of the empirical systems themselves /Bäckström and Lanaro 2007/. The range of variation in the evaluated parameters depends on uncertainty in the input data; size of the sample population and the opinion of different operators characterising the rock mass.

The empirical approach assumes no explicit stress dependence of any parameter. The strength, deformation modulus and Poisson’s ratio, which depend on the confining stress, are thus valid under the conditions the empirical relationships were developed, namely shallow depth and low confining pressure. This fact leads to the incorporation of uncertainties since the empirical correlations are used to estimate strength and deformability of a rock mass, at a depth of 500 m, affected by a plain confining pressure.

The rock mass deformation modulus has been estimated based on the relationship between  $E_m$  and *RMR* developed by /Serafim and Pereira 1983/. The equation is based on the analyses of a number of case histories, mostly shallow depth facilities such as dam foundations, for which the deformation modulus was evaluated by back analysis of measured deformation /Hoek et al. 1995/.

The correlation assumes that the rock mass is isotropic. Furthermore, in the application of the formula using data from Forsmark, the formula has a cut-off at the value of the intact rock, which results in an unequal distribution of Young’s modulus around the mean. It should also be noted that most of the projects included in the database are of rock masses that had a quality corresponding to *RMR* < 75. The applicability of the equation to a repository constructed in a massive, high quality rock mass of *RMR* > 75, at 500 m depth, is consequently somewhat uncertain and it is likely that the estimated Young’s modulus of the rock mass is somewhat over estimated.

The uncertainty in the empirical approach of estimating rock mass properties has been treated in a similar way as for the intact rock and was expressed statistically by means of a range of variation in the evaluated mean values (cf. Section 3.6.1). The uncertainty of the mean was quantified according to the “Central Limit Theorem” /Peebles 1993/ for a 95% confidence interval. Minimum and maximum truncation values given in the table below are based on the observed minimum and maximum in the empirical model.

The mechanical properties of fracture domain FFM01 have least uncertainties, since calculated from the largest data set. Further details concerning the estimated uncertainties in the empirical approach are to be found in Appendix A3.6.

##### ***Estimated rock mass mechanical properties***

The rock mass quality of the site is in general classified as “very good rock” using either the Q or *RMR* rock mass rating systems. The statement is on the whole valid also for the rock mass in deformation zones. However, some sections of “poor rock” were observed in a few deformation zones.

The estimated rock mass strength and deformation properties and their variation in FFM01 and FFM06 based on the empirical approach are presented in Table 5-2. Similar tables with the estimated properties for fracture domains FFM02 and FFM03 and several deformation zones are provided in Appendices A3.7 and A3.8.

The results from modelling stage 2.2 are in good agreement with the results from previous SDM 1.2. Even though the current modelling stage 2.2 includes about 36% more data than SDM 1.2, the resulting differences are on the whole insignificant.

For fracture domain, FFM01, the equivalent uniaxial compressive strength ( $UCS_m$ ) and the deformation modulus ( $E_m$ ) is estimated to a mean value of 92 MPa and 72 GPa, respectively. The values for the same properties in FFM06 are 95 MPa ( $UCS_m$ ) respectively 70 GPa ( $E_m$ ). The rock mass quality in fracture domain FFM01 and FFM06 consequently are comparable and the mechanical properties of the rock mass are close to those of intact rock.

Fracture domain FFM02 shows properties very close to the mean properties estimated for the deformation zones and differs significantly from FFM01 and FFM06. The results for FFM03 correspond to properties between FFM01 and FFM02.

The evaluated mechanical properties, independent of fracture domain, indicate that the rock mass in the target volume is stiff and strong and the differences are judged to be of minor importance in the assessment of the rock support needed for tentative repository.

**Table 5-2. Estimated rock mass properties in fracture domain FFM01 and FFM06 based on the empirical modelling.**

Rock domain	FFM01	FFM06
Properties of the rock mass	Mean/std. dev. Min–max <sup>2</sup> Uncertainty of mean <sup>1</sup>	Mean/std. dev. Min–max <sup>2</sup> Uncertainty of mean <sup>1</sup>
Deformation modulus <sup>3</sup> [GPa]	72/8 39–76 ± 1%	70/12 40–81 ± 3%
Poisson's ratio <sup>3</sup>	0.23/0.03 0.12–0.30 ± 1%	0.23/0.04 0.12–0.33 ± 3%
Uniaxial compressive strength (Hoek-Brown) <sup>4</sup> [MPa]	92/27 23–153 ± 3%	95/32 30–149 ± 7%
Friction angle <sup>5</sup> [°]	50/2 32–52 ± 0%	50/2 43–53 ± 1%
Cohesion <sup>5</sup> [MPa]	27/4 12–35 ± 1%	27/4 18–34 ± 3%
Uniaxial compressive strength (Mohr-Coulomb) <sup>5</sup> [MPa]	146/24 44–196 ± 1%	151/30 82–201 ± 4%
Tensile strength <sup>4</sup> [MPa]	2.4/1.0 0.6–5.0 ± 3%	2.3/1.0 0.6–4.0 ± 8%

<sup>1</sup> The uncertainty of the mean is quantified for a 95% confidence interval.

<sup>2</sup> Minimum and maximum truncation values are based on the observed min' and max' for the tested population.

<sup>3</sup> The deformation modulus and the Poisson's ratio of the rock mass are assumed to be independent of the state of stress due to their high values.

<sup>4</sup> The uniaxial compressive and tensile strength are obtained from the Hoek-Brown's envelope of the rock mass.

<sup>5</sup> The apparent uniaxial compressive strength, cohesion and friction angle are obtained from the Coulomb's Strength Criterion with a 10 to 30 MPa confinement stress.

## 5.2 Theoretical approach using numerical models

The approach used in this activity is based on numerical simulations with the use of the 3DEC software /Itasca 2003/. The methodology has been developed for the purpose of the Site Investigations and is built upon three different models: the DFN model which is used to simulate the fracture network in the rock mass, the 3DEC mechanical model which is used to calculate the rock mass mechanical properties, and a statistical model for estimation of combined variability.

The modelling procedure is described in detail in /Olofsson and Fredriksson 2005/. The work was conducted according to the Activity Plan for “Establishment of a rock mechanics model for Forsmark 2.2”.

### 5.2.1 Strength and deformation properties for the fracture domains

The input to the DFN simulations is taken from the Draft presented in June 2007 by /Fox et al. 2007/. The primary geological DFN model (‘Base Case’) has been used. The input parameters for the DFN simulations in fracture domain FFM01 and FFM06 are shown in Appendix 4. The intensity,  $P_{32}$ , (total area of fractures/unit volume) in the “Base model” is corrected for lithology and for the ratio (open and partly open)/(total number of fractures), for further details see Appendix 4. Comparisons have been made with the final DFN-model presented in October 2007 and the changes in the DFN-model do not have any significant influence on the outcome of the theoretical approach, cf. Appendix 4.

Lithology corrections were made according to the main rock type metamorphic, medium-grained granite to granodiorite in FFM01 and metamorphic aplitic granite, in FFM06. The generated DFN simulations are valid for a depth of 400–600 m. Only open and partly open fractures are generated. In each fracture domain, 20 simulations of the fracture network have been generated in a 20×20×20 m block.

For each DFN-realisation the mean value of  $P_{10}$  (number of intersecting fracture/length) has been calculated along nine vertical boreholes evenly distributed in the model box. In Figure 5-12 the variation of  $P_{10}$  in the DFN simulations with variations along nine boreholes per realisation, is compared with the  $P_{10}$  recorded in boreholes in the fracture domains FFM01 and FFM06. The calculated  $P_{10}$  from the boreholes is the mean value for open and partly open fractures in each section of the fracture domain along the boreholes. The  $P_{10}$  variation from the DFN simulations is in accordance with the values from the boreholes. The DFN simulations are only valid for the main rock type in each fracture domain while data from the boreholes includes all rock types. The  $P_{10}$  in fracture domain FFM06 from the DFN-model is about 50% higher than in FFM01. The amount of data from boreholes in FFM06 is small in the depth interval 400–600 m.

From each block, two vertical thin slices, parallel to the maximum and minimum horizontal stresses are extracted. The fracture traces in these slices are converted to fractures in the 3DEC model. The 3DEC model is loaded under plane strain conditions and the stresses and strains during loading are recorded. From these curves the deformation modulus, Poissons ratio and failure load are evaluated assuming that the rock mass is a linear-elastic isotropic perfectly-plastic material. Each model has been tested at three different horizontal stresses. One model with the horizontal stress equal the horizontal in situ stress parallel to the model, one model with horizontal stress equal to 25% of the horizontal in situ stress parallel to the model, and lastly with a horizontal stress equal to 2 MPa. The cohesion and friction angle has been evaluated by fitting a linear envelope to the results from these three tests.

The different DFN simulations were analysed with mean values of all material data. The resulting variation of evaluated parameters is only affected by the variation of the geometry of the fracture network, see left side of Figure 5-13, which shows the resulting distribution of deformation modulus. The deformation modulus varies from 64 to 73 GPa.

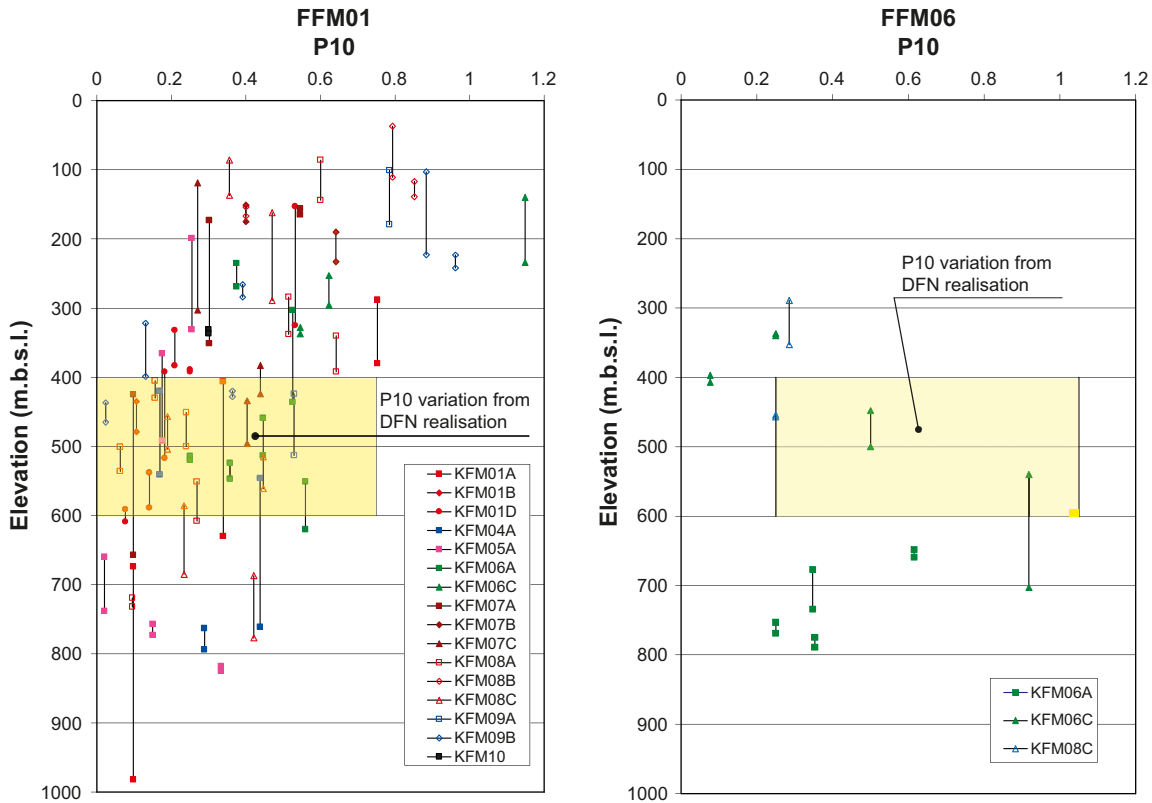


Figure 5-12. Comparison between  $P_{10}$  from DFN simulations and from boreholes.

To assess the influence of the variation in the material data one simulation was analysed with 40 combinations of the material data. The material data were taken at random from the given distributions of material data for intact rock and fractures. The distributions of all the input parameters are assumed to have a truncated normal distribution and it follows that the results are also expected to have a truncated normal distribution.

The resulting distribution of the deformation modulus is given in Figure 5-13, right side. The deformation modulus varies from 62 to 75 GPa. The variation in material data gives a larger variation in the resulting deformation modulus than the variation in geometry of the fracture network.

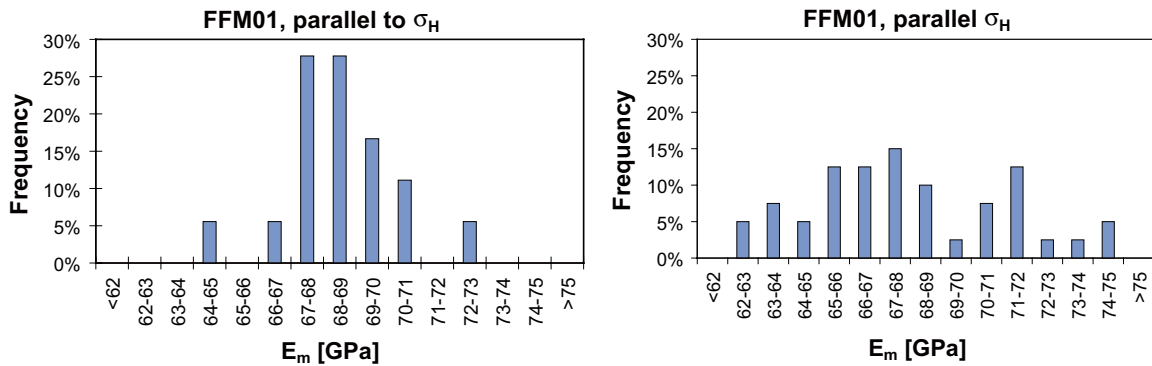


Figure 5-13. Evaluated rock mass deformation modulus, to the left influence of the DFN variation and to the right influence of variation in material data.

The combined effect of DFN variation and variation of material data has been calculated assuming that the variation in material data will have the same effect on all DFN simulations. For more details regarding the simulation see Appendix 4. The resulting distributions of all evaluated rock mass parameters are shown for fracture domain FFM01 and FFM06 in Figure 5-14 to Figure 5-23. The statistical parameters for the distributions are given in Table 5-3 to Table 5-6.

The stress level of  $\sigma_H$  and  $\sigma_h$  is 39 MPa respective 26 MPa in the diagrams presented below. Young's modulus and Poisson's ratio at other stress levels are provided in Appendix 4. The general tendency of the modelling results is an increase in Young's modulus and a decrease in Poisson's ratio with increased stress level.

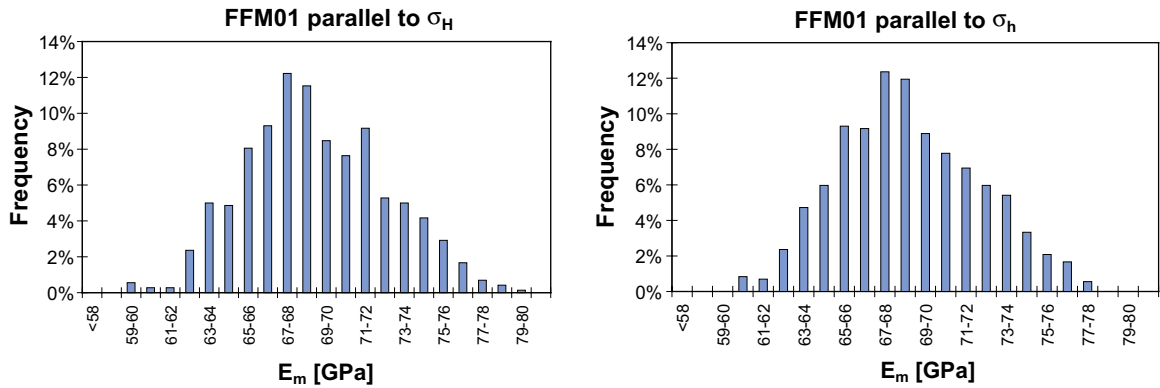


Figure 5-14. Frequency distribution of rock mass deformation modulus in domain FFM01.

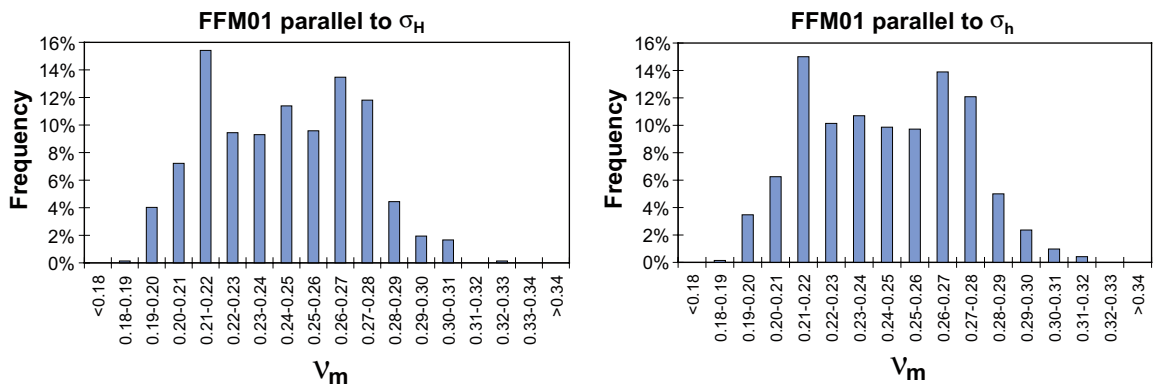


Figure 5-15. Frequency distribution of rock mass Poisson's ratio in domain FFM01.

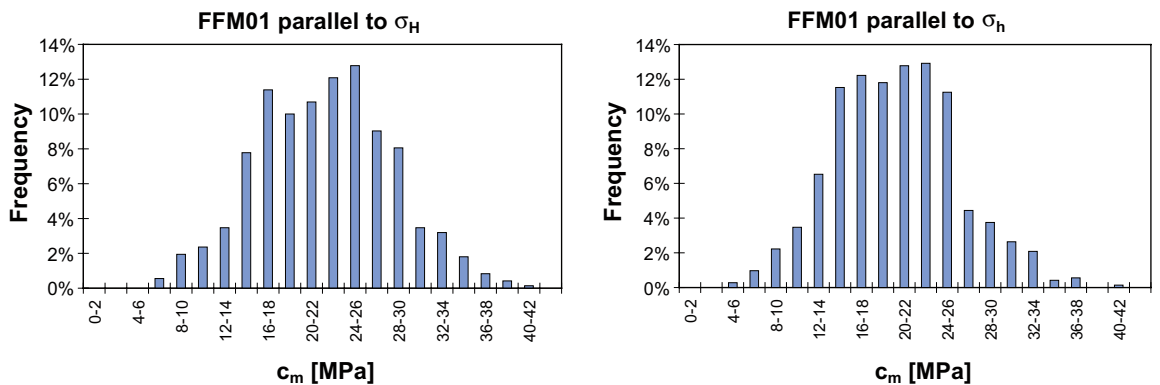


Figure 5-16. Frequency distribution of rock mass cohesion in domain FFM01.



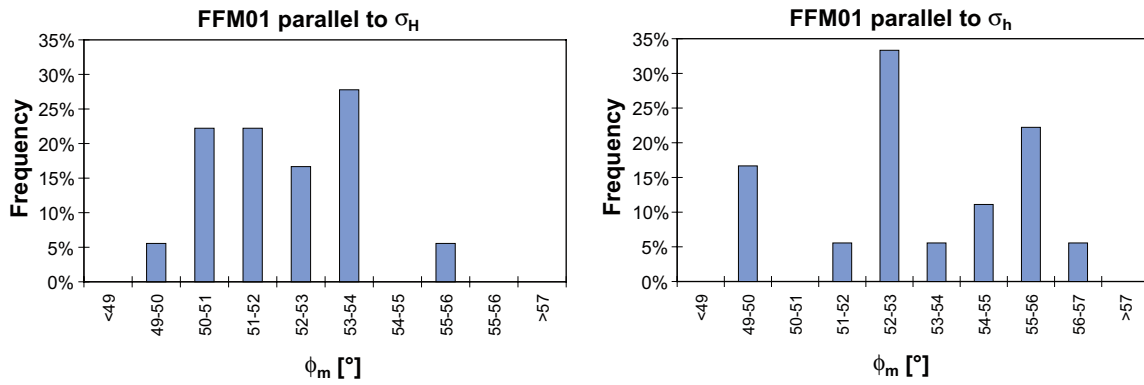


Figure 5-17. Frequency distribution of rock mass friction angle in domain FFM01.

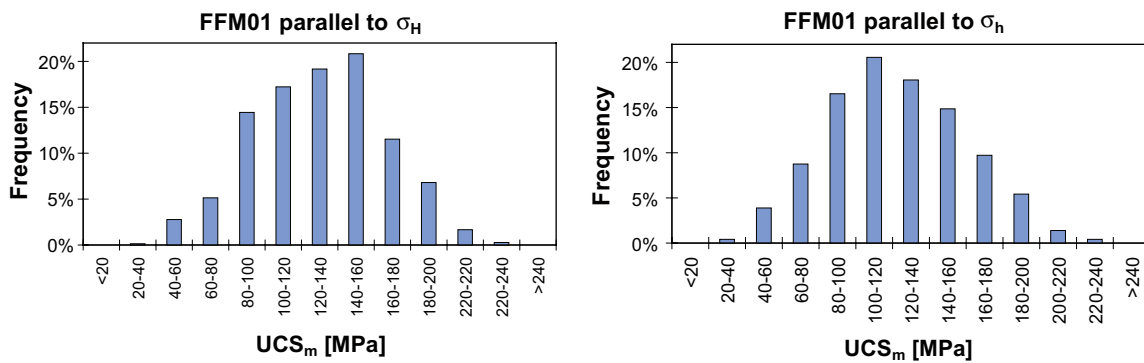


Figure 5-18. Frequency distribution of rock mass uniaxial compressive strength (Mohr-Coulomb) in FFM01.

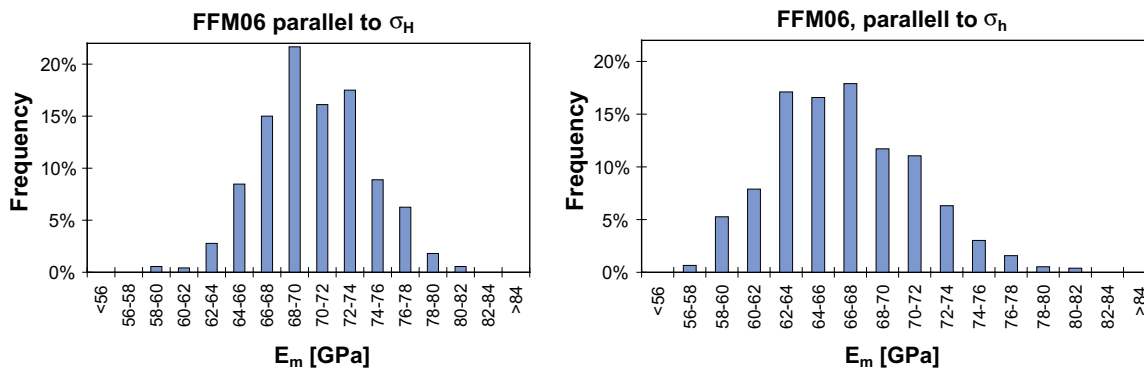


Figure 5-19. Frequency distribution of rock mass deformation modulus in domain FFM06.

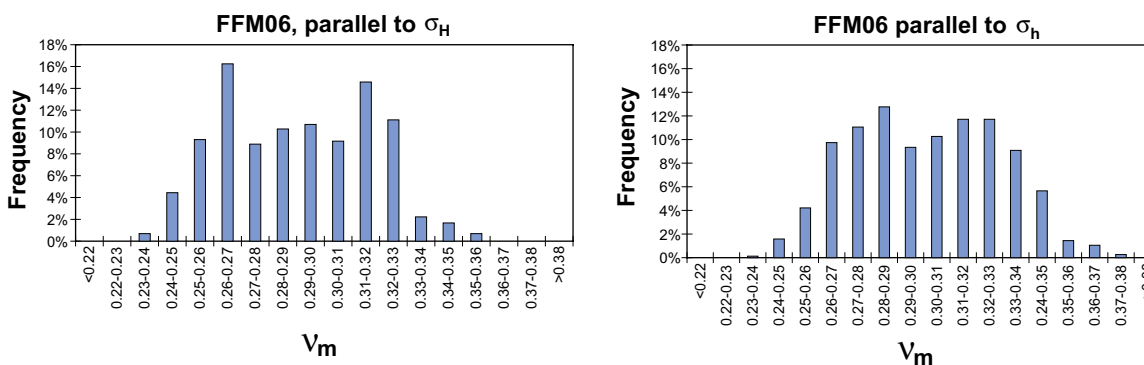


Figure 5-20. Frequency distribution of rock mass Poisson's ratio in domain FFM06.

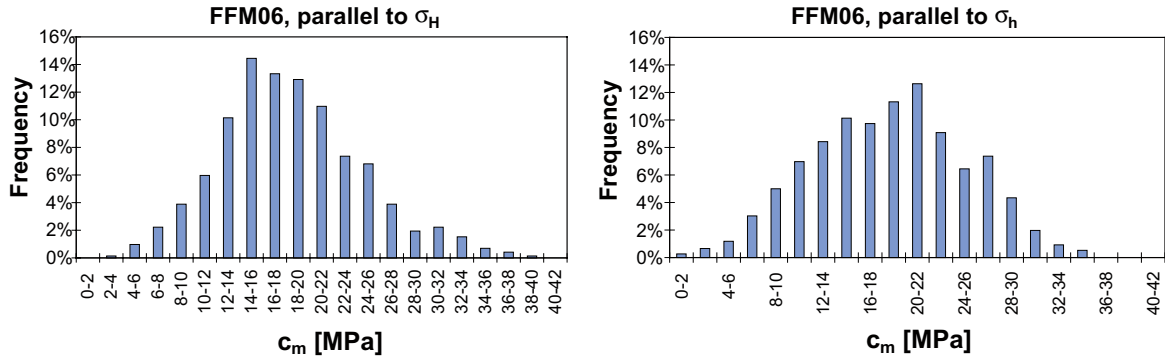


Figure 5-21. Frequency distribution of rock mass cohesion in domain FFM06.

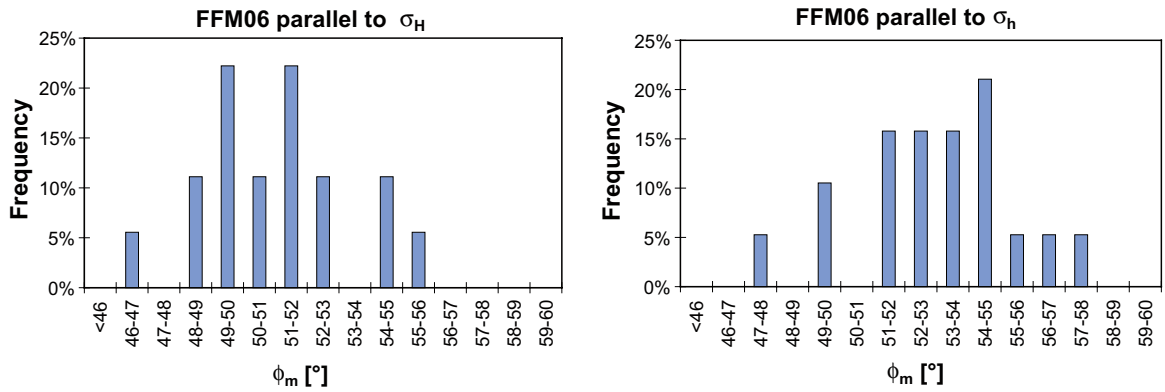


Figure 5-22. Frequency distribution of rock mass friction angle in domain FFM06.

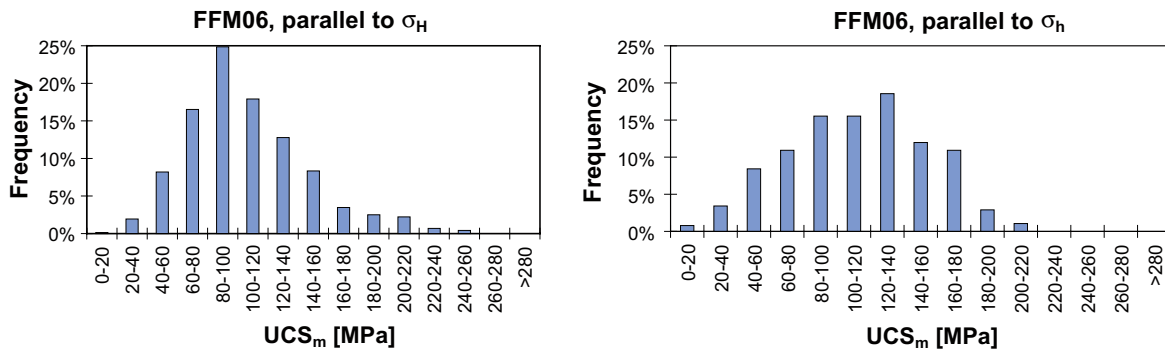


Figure 5-23. Frequency distribution of rock mass uniaxial compressive strength (Mohr-Coulomb) in FFM06.

Table 5-3. Statistical data for evaluated parameters in FFM01 parallel to  $\sigma_H$ .

FFM01	Unit	Mean	Std dev.	Minimum	Maximum
Deformation-modulus, $E_m$	[GPa]	68.9	3.6	59.3	79.4
Poisson's ratio, $\nu_m$		0.24	0.03	0.19	0.33
Cohesion, $c_m$	[MPa]	22.2	6.1	6.8	41.8
Friction angle, $\phi_m$	[°]	52.2	1.5	49.7	55.1
Uniaxial compressive strength, $UCS_m$	[MPa]	129.7	35.8	37.8	232.7

**Table 5-4. Statistical data for evaluated parameters in FFM01 parallel to  $\sigma_H$ .**

FFM01	Unit	Mean	Std dev.	Minimum	Maximum
Deformation-modulus, $E_m$	[GPa]	68.7	3.5	60.3	77.9
Poission's ratio, $\nu_m$		0.24	0.03	0.19	0.32
Cohesion, $c_m$	[MPa]	20.2	5.7	5.4	40.3
Friction angle, $\phi_m$	[°]	53.3	2.1	49.5	56.0
Uniaxial compressive strength, $UCS_m$	[MPa]	122.1	36.9	29.4	235.4

**Table 5-5. Statistical data for evaluated parameters in FFM06 parallel to  $\sigma_H$ .**

FFM06	Unit	Mean	Std dev.	Minimum	Maximum
Deformation-modulus, $E_m$	[GPa]	70.4	3.8	59.4	80.7
Poission's ratio, $\nu_m$		0.29	0.03	0.23	0.35
Cohesion, $c_m$	[MPa]	18.4	6.0	2.4	39.8
Friction angle, $\phi_m$	[°]	50.9	2.3	47.0	55.6
Uniaxial compressive strength, $UCS_m$	[MPa]	105.1	40.0	12.3	257.1

**Table 5-6. Statistical data for evaluated parameters in FFM06 parallel to  $\sigma_H$ .**

FFM06	Unit	Mean	Std. dev.	Minimum	Maximum
Deformation-modulus, $E_m$	[GPa]	66.6	4.4	56.4	81.3
Poission's ratio, $\nu_m$		0.30	0.03	0.24	0.37
Cohesion, $c_m$	[MPa]	26.1	6.5	1.1	35.7
Friction angle, $\phi_m$	[°]	53.0	2.3	47.5	57.0
Uniaxial compressive strength, $UCS_m$	[MPa]	112.8	42.0	5.6	219.7

### 5.2.2 Strength and deformation properties of the deformation zones

In the stress modelling, see Section 6.4, the deformation zones are modelled as fractures, with equivalent properties expressed by normal and shear stiffness together with the strength parameters cohesion and friction angle. To estimate typical properties of the deformation zones for use in the regional stress model, a theoretical approach has been used. The estimations are only made for deformation zones where data are available from boreholes and for zones that are to be used in the stress modelling. For the Singö deformation zone (ZFMWNW0001) the given properties were collected from /Glamheden et al. 2007/.

As described in Section 2.1.3, the deformation zones in the Forsmark area are mainly composed of sealed fractures. Only about 20–25% of the fractures are open or partly open. When the deformation zones were modelled only open fractures have been considered. However, the effect of sealed fractures has been considered by reducing the strength of the intact rock based on shear tests on sealed fractures. For more details about the procedure, see Appendix 4. A summary of the estimated properties is given in Table 5-7.

**Table 5-7. Summary of estimated properties for most of the deformation zones used in the stress modelling.**

ZFM	Borehole	DZ	Max <sup>1</sup> [fracture/m]	t <sup>2</sup> [m]	K <sub>N</sub> [MPa/mm]	K <sub>S</sub> [MPa/mm]	c [MPa]	φ [°]
<b>Vertical and steeply dipping fracture zones that trend ENE (NE)</b>								
ENE1061A	KFM08C	DZ4	30	2.3	78	23	0.7	36
		DZ5	0	2.4	90	31	4.3	53
	KFM08A	DZ1	8	58.1	83	23	0.8	36
ENE0062A	HFM25		12	28.4	84	24	0.7	36
ENE2248	KFM08A	DZ5	5	46.5	85	26	1.1	36
<b>Vertical and steeply dipping fracture zones that trend NNE</b>								
NNE2312	KFM08C	DZ2,DZ3	13	101.4	83	23	0.7	36
	HFM38	DZ1	20	15.0	80	16	0.7	36
<b>Vertical and steeply, SW-dipping deformation zones referred to as WNW and NW</b>								
WNW0001	Singö deformation zone				0.2 <sup>3</sup>	0.01 <sup>3</sup>	0.4 <sup>3</sup>	31.5 <sup>3</sup>
NW0003	HFM12	DZ1	6	58.4	87	27	1.0	36
	HFM13	DZ1	2	51.2	88	29	1.5	36
NW0017	HFM30	DZ1	20	8.0	79	13	0.7	36
WNW0123	KFM10A	DZ1	24	61.1	81	17	0.7	36
	KFM04A	DZ5	7	6.2	83	23	0.9	36
	HFM24	DZ1	10	11.8	81	20	0.7	36
	HFM24	DZ2	6	18.2	84	24	1.0	36
	HFM24	DZ3	9	31.8	85	24	0.7	36
	HFM29	DZ1	1	5.2	89	29	1.6	36
	HFM29	DZ2	7	17.2	84	24	0.9	36
	HFM29	DZ3	6	3.8	83	23	1.0	36
<b>Vertical and steeply dipping fracture zones that trend NNW</b>								
NNW0100	KFM09A	DZ3	18	52.0	82	22	0.7	36
	KFM07A	DZ4	12	58.7	84	24	0.7	36
	HFM23	DZ2	8	5.7	82	22	0.8	36
<b>Gently dipping fracture zones</b>								
A2	KFM10A	DZ2,DZ3	18	34.9	82	20	0.7	36
	KFM05A	DZ1	13	9.6	80	16	0.7	36
	KFM04A	DZ2,DZ3	23	33.9	82	14	0.7	36
	KFM02A	DZ6	13	23.9	84	22	0.7	36
	KFM01C	DZ1,DZ2	100	56.9	79	16	0.7	36
	KFM01B	DZ1	37	46.1	80	15	0.7	36
A3	KFM03A	DZ4	11	12.9	84	24	0.7	36
	KFM02A	DZ3	7	23.9	83	23	0.9	36
	HFM04	DZ2	4	3.8	81	22	1.2	36
B4	KFM02A	DZ8	3	11.9	84	25	1.3	36
F1	KFM02A	DZ6	16	43.8	85	24	0.7	36

<sup>1</sup> Number of open fractures.

<sup>2</sup> Borehole length.

<sup>3</sup> Data from /Glamheden et al. 2007/.

### 5.2.3 Summary of the results from the theoretical model

#### **Uncertainties**

The variability was studied in two steps, firstly by analysing the influence of the fracture pattern and by studying the influence of the variation of the input parameters, secondly by a subsequent combined analysis of the effects. The influence of input parameters on the rock mass properties was examined for one simulation with 40 combinations of the material data in fracture domain FFM01.

Stochastic variability in fracture properties among fractures in DFN simulations has not been examined. Instead, all fractures within a DFN simulation have been assigned the same values. This will probably overestimate the effect of the fracture input parameter variability on rock mass properties.

Assuming that the estimated variations of the properties correspond to the real variations, the uncertainty in the evaluated mean values can be calculated according to the “Central Limit Theorem” /Peebles 1993/ for a 95% confidence interval. Minimum and maximum truncation values given in the table below are based on the observed minimum and maximum in the theoretical model.

#### **Estimated rock mass mechanical properties**

The two analysed sections parallel to the maximum and minimum horizontal stresses gave the same deformation and strength properties in fracture domain FFM01. Thus, the results indicate that the rock mass is isotropic in this domain.

In fracture domain FFM06 the two analysed sections show a difference in deformation modulus of approximately 4 GPa in the mean values. Thus, the difference is small also in case of fracture domain FFM06 and has no practical importance. The results from the two sections in relation to the in situ stress conditions have consequently been combined to a single value. The estimated rock mass mechanical properties and their variation in FFM01 and FFM06, based on the theoretical approach, are presented in Table 5-8.

**Table 5-8. Estimated rock mass mechanical properties in fracture domain FFM01 and FFM06 based on the theoretical modelling.**

Properties of the rock mass	FFM01	FFM06
	Mean/std. dev. Min-max <i>Uncertainty of mean</i>	Mean/std. dev. Min-max <i>Uncertainty of mean</i>
Deformation modulus [GPa]	68.8/3.6 59.3–79.4 ± 2%	68.5/4.6 56.4–81.3 ± 3%
Poisson's ratio	0.24/0.03 0.19–0.33 ± 5%	0.3/0.03 0.23–0.37 ± 4%
Friction angle [°]	52.6/1.8 49.5–56.0 ± 2%	52.0/2.5 47.0–57.0 ± 2%
Cohesion [MPa]	21.2/6.1 5.4–41.8 ± 13%	18.5/6.3 1.1–39.8 ± 15%
Uniaxial compressive strength (Mohr-Coulomb) [MPa]	125.9/36.6 29.4–235.4 ± 14%	109.0/41.2 5.6–257.1 ± 18%

Note: The uncertainty of the mean is quantified for a 95% confidence interval. Minimum and maximum truncation values are based on the observed min' and max' for the tested population.

The difference in deformation properties between fracture domains FFM01 and FFM06 is small. The mean deformation modulus in FFM01 is 69 GPa and 70 GPa in FFM06. The higher fracture density in FFM06 is compensated for by a higher deformation modulus and higher strength of the intact rock.

The mean uniaxial compressive strength (M-C) in fracture domain FFM01 is 126 MPa and 109 MPa in FFM06. The higher fracture density in FFM06 reduces the rock mass strength in spite of the higher strength of the intact rock.

Compared with the previous estimation of the deformation and strength properties of the rock mass /Fredriksson and Olofsson 2005/ the deformation modulus is in the same range, 69–70 GPa, while the rock mass strength is higher in FFM01 and lower in FFM06, compared to the previous result of 119 MPa.

The uncertainty of the evaluated mean of cohesion is significantly higher than for other parameters.

### **5.3 Harmonized rock mass mechanical properties**

In this section the results from the empirical and theoretical approaches are compared to achieve a “harmonized” description of the rock mass. The two approaches provide estimates of the rock mass properties that on the whole are completely independent from one another. Both methods involve elements of subjective judgement and assumptions which motivate a subsequent harmonization step to guarantee the quality of the modelling results.

When performing the harmonization there are some modelling parameters that differ between the two approaches and which must be placed on level terms. There are also some factors regarding the deformation zones that limit the possibility to perform a harmonization.

Parameters that must be normalized are:

- Modelling scale. The empirical approach utilises borehole data divided into 5 m sections, whereas the theoretical approach is based on numerical modelling of blocks of 20×20×20 m.
- Confining stress. The empirical approach assumes no explicit stress dependence for the deformation modulus and Poisson’s ratio while the confining stress is taken into account in the theoretical approach.
- Fracture frequency. The empirical approach uses a mean value based on 5 m sections whereas the theoretical model is based on a mean value for the entire section of a borehole that intersects the same fracture domain.
- Poisson’s ratio. In the empirical approach Poisson’s ratio is limited to the value of intact rock while Poisson’s ratio might be larger than the intact value in the theoretical approach.

Factors that limit the possibility to perform a complete harmonization for the deformations zones are:

- Sealed fractures are not treated explicitly by the empirical approach whereas they are considered in the theoretical modelling of the deformations zones.
- The properties of the deformation zones are treated in an isotropic mode by the empirical approach while evaluated in parallel and perpendicular directions to the zone by the theoretical approach.

These differences regarding the deformation zones result in a parameter outcome from the two modelling approaches being in different classes.

### 5.3.1 Harmonization of results for fracture domains

The harmonization of the results for the fracture domains were carried out essentially in accordance with the methodology used in the Forsmark 1.2 model /SKB 2005a/. The harmonization only includes fractures domain FFM01 and FFM06, since its only these domains that are covered by the two approaches. The rock mass properties were assigned by making the following overall assumptions:

- The differences in modelling scale between the empirical and the theoretical approach were compensated for by enlarging the evaluated distribution. The minimum and maximum truncation values were assigned based on the smallest and the largest value estimated by both approaches. The standard deviation and uncertainty of mean were selected as the largest value presented by both approaches.
- The rock mass deformation modulus and Poisson's ratio was determined by averaging being applied to the mean values estimated by the two approaches without weighting.
- The uniaxial compressive strength was assumed based on the empirical approach which is evaluated on Hoek-Brown failure criterion. The theoretical approach makes use only of Mohr-Coulomb failure criterion.
- The apparent cohesion and friction angle based on Mohr-Coulomb failure criterion were assumed to be directly comparable for 10–30 MPa confining pressure. Averaging was applied to the mean values estimated by the two approaches without weighting.
- The rock mass tensile strength is reported based on the empirical approach, since no value is evaluated from the theoretical approach.

The suggested rock mechanical properties after the harmonization are presented in Table 5-9. The harmonized values in the table indicate parameter values recommended to be used for the rock mass outside deformation zones in the design and the safety assessment work.

**Table 5-9. Suggested rock mechanics properties of the rock mass in FFM01 and FFM06 after harmonization.**

Rock domain Properties of the rock mass	Empirical approach		Theoretical approach		Harmonized values	
	Mean/std. dev.		Mean/std. dev.		Mean/std. dev.	
	Min-max		Min-max		Min-max	
	Uncertainty of mean		Uncertainty of mean		Uncertainty of mean	
	FFM01	FFM06	FFM01	FFM06	FFM01	FFM06
Deformation modulus [GPa]	72/8 39–76 ± 1%	70/12 40–81 ± 3%	69/4 59–79 ± 2%	68/5 56–81 ± 3%	70/8 39–79 ± 2%	69/12 40–81 ± 3%
Poisson's ratio	0.23/0.03 0.12–0.30 ± 1%	0.23/0.04 0.12–0.33 ± 3%	0.24/0.03 0.19–0.33 ± 5%	0.3/0.03 0.23–0.37 ± 4%	0.24/0.03 0.12–0.33 ± 5%	0.27/0.04 0.12–0.37 ± 4%
Uniaxial compressive strength (Hoek and Brown) [MPa]	92/27 23–153 ± 3%	95/32 30–149 ± 7%	No values	No values	92/27 23–153 ± 3%	95/32 30–149 ± 7%
Friction angle (Mohr-Coulomb) [°]	50/2 32–52 ± 0%	50/2 43–53 ± 1%	53/2 50–56 ± 2%	52/2 47–57 ± 2%	51/2 32–56 ± 2%	51/2 43–57 ± 2%
Cohesion (Mohr-Coulomb) [MPa]	27/4 12–35 ± 1%	27/4 18–34 ± 3%	21/6 5–42 ± 13%	18/6 1–40 ± 15%	24/5 6–42 ± 13%	23/5 1–40 ± 15%
Tensile strength [MPa]	2.4/1.0 0.6–5.0 ± 3%	2.3/1.0 0.6–4.0 ± 8%	No values	No values	2.4/1.0 0.6–5.0 ± 3%	2.3/1.0 0.6–4.0 ± 8%

Note: The uncertainty of the mean is quantified for a 95% confidence interval. Minimum and maximum truncation values are based on the observed min' and max' for the tested population.

### **5.3.2 Harmonization of results for deformation zones**

The properties of the deformation zones estimated by the two approaches that are possible to compare and harmonize are the apparent cohesion and friction angle. However, the difference between the two approaches concerning the isotropic way (empirical approach) and anisotropic way (theoretical approach) of evaluating the mechanical properties, lead to a judgement being made that such a harmonization was unfounded. Further justification for not performing a harmonization for the deformation zones, is that the comparison reported in model stage 2.1 /SKB 2006b/ concluded that the difference is small when both approaches make use of an isotropic way to evaluate the properties of the deformation zones.

It is recommended that users who apply the results evaluated for the deformation zones should consider which one of the two approaches is the most appropriate for the case being analysed (cf. Section 5.1.3 and 5.2.2).

### **5.4 Summary of the results after harmonization**

The rock mass strength and deformation properties estimated from the empirical approach were in reasonable agreement with the strength and deformation properties estimated using the theoretical (numerical modelling) approach. Fracture domains FFM01 and FFM06, which show the highest rock mass quality of the examined domains, have almost equal evaluated mechanical properties. The higher fracture density in FFM06 is compensated for by higher strength and deformation modulus of the intact rock compared to FFM01.

The mechanical properties of the deformation zones were evaluated in an isotropic manner in the empirical approach and in an anisotropic manner in the theoretical approach. This means that the parameter outcome from the two approaches is not fully comparable. It is therefore recommended that users who apply the results evaluated for the deformation zones should consider which one of the two approaches is the most appropriate for the case being analysed.



## 6 In situ state of stress

### 6.1 Regional stress state

In this section the regional boundary conditions for the Forsmark area are presented based on the geological model for the site given by /Stephens et al. 2007/ and a review of the regional stresses given in /Martin 2007/ and /Sjöberg et al. 2005/.

#### 6.1.1 Plate tectonics and the Scandinavian Shield

It is generally accepted that the regional stresses within the plates are caused by relative plate motion. In Scandinavia today a general WNW-ESE compression is expected based on plate tectonics. Compilations by the World Stress Map Project /Reinecker et al. 2005/ show that the regional stress field in the southern part of Sweden is characterised by a general orientation of the major horizontal stress in the range of N130–150°, see Figure 6-1. The stress directions indicated on the map are based on information from focal mechanism, borehole breakouts as well as direct measurements by overcoring and hydraulic fracturing.

#### 6.1.2 Crustal stresses and seismic activity

Seismic activity is an excellent indicator of bedrock deformation and the regional orientation of the maximum horizontal stress. Both plate tectonics and glacial isostatic adjustment contribute to bedrock deformation in Fennoscandia /Martin 2007/.

According to a compilation by /Ojala et al. 2004/ the majority of the recorded seismic activity is concentrated near the western coastline of Norway and south-western Sweden. According to /Kinck et al. 1993/ the concentration of seismic events correlates with the thickness of the Scandinavian crust, i.e. the thicker the crust the fewer the number of seismic events. In the East-central part of Sweden, in the Forsmark region, where few events have occurred, the crust is uniform and thick /Kinck et al. 1993/. /Slunga 1991/ analysed approximately 200 seismic events in Fennoscandia, and found that the seismic events in southwest Sweden indicate strike-slip faulting regime, whereas the seismic events in central and northern Sweden indicated a thrust fault regime. Regardless of the faulting regime /Slunga 1991/ concluded that the seismic events indicated a regional maximum horizontal stress in the direction of N120°. A similar horizontal stress direction was reported by /Hicks et al. 2000/.

#### 6.1.3 Stress measurements in the Forsmark region

Measurements of the in situ stress from overcoring and hydraulic fracturing in the region around Forsmark have been performed at Finnsjön, in Stockholm city, at the Björkö Island and at Olkiluoto in Finland. The results from these measurements were given by /Sjöberg et al. 2005/ and briefly summarised below.

##### *Finnsjön*

The measurements at Finnsjön consist of hydraulic fracturing in a borehole about 15 km west of Forsmark. The minimum horizontal stress is close to the theoretical vertical stress of the overburden pressure. The orientation of the maximum horizontal stress is trending N110–150°, with a mean around N140°.

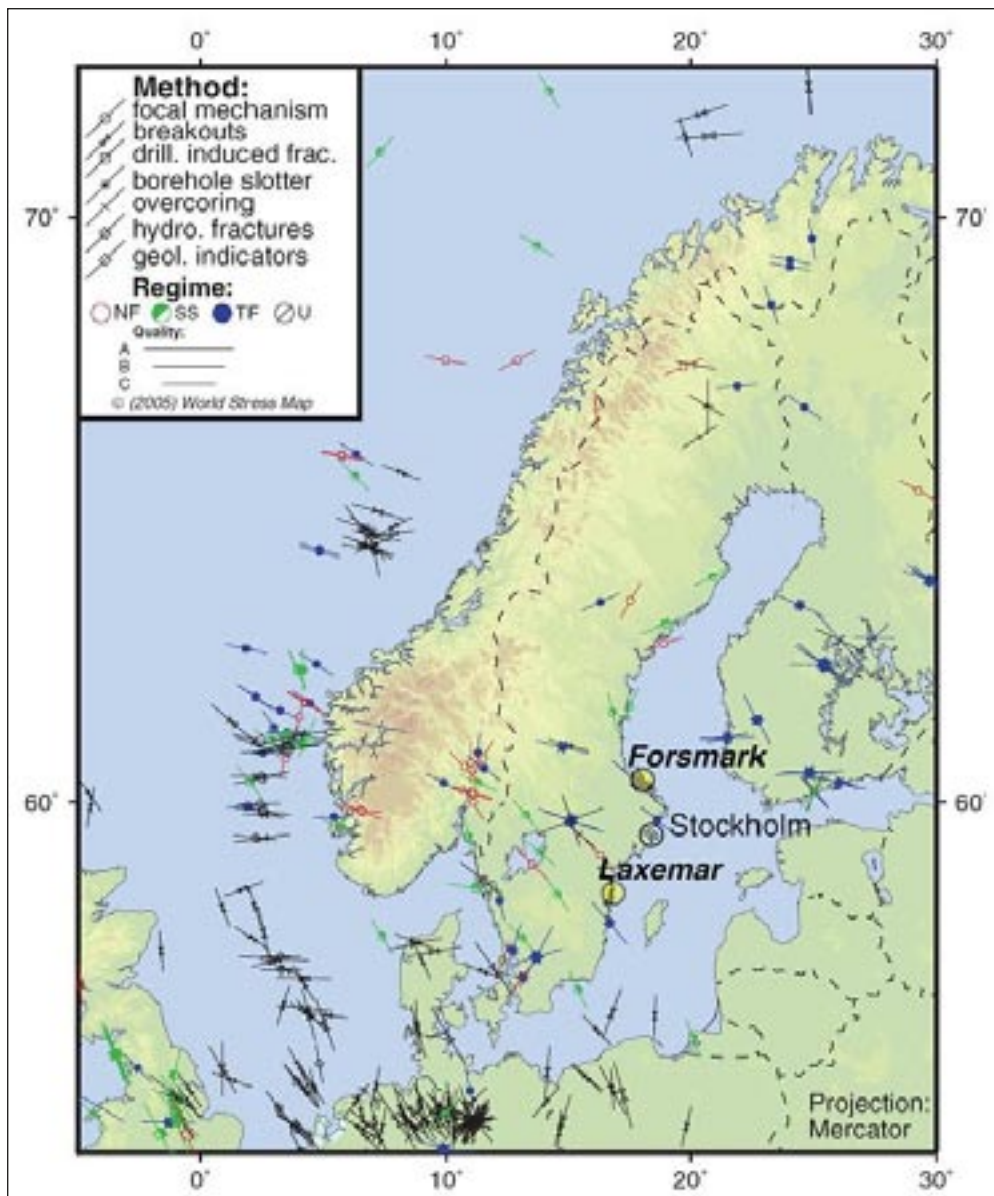


**Figure 6-1.** Orientation of the major principal stress based on data from the World Stress Map Project /Reinecker et al. 2005/. The numbers of the figure frame indicate degree latitude (vertical frame) and degree longitude (horizontal frame) /Martin 2007/.

### **Stockholm city**

The measurements in Stockholm city are from various infrastructure projects at shallow depths of generally less than 50 m below the ground surface. The data comprise several overcoring measurements and a single hydraulic fracturing measurement. The reported stress magnitudes vary significantly. However, most data indicate a maximum horizontal stress around 5 MPa. The orientation of the maximum in situ stress has a generally E-W to NW-SE trend.

### **Björkö Island**

At Björkö Island, in Lake Mälaren, the stress measurements include both hydraulic fracturing as well as hydraulic tests on pre-existing fractures. Measurements were carried out down to 875 m depth below the ground surface. The results show a maximum horizontal stress that is 1.5 to 2 times the minimum horizontal stress. The minimum horizontal stress is equal or lower than

the overburden weight. The most likely prevailing orientation of the maximum horizontal stress is N160°.

### ***Olkiluoto***

Stress measurements at Olkiluoto, the planned location of a Finnish nuclear waste repository, have been performed for depths between 300–800 m. The measurements include overcoring and hydraulic fracturing in a number of vertical boreholes. The results indicate that the vertical and the minimum horizontal stress are almost equal in magnitude, while the maximum horizontal stress is considerably larger around 25 MPa at 500 m depth. The recorded orientation varies significantly. However, the data indicate that the maximum horizontal stress is oriented in an E-W to ENE-WSW direction.

#### **6.1.4 Expected stress magnitudes and directions**

Information from focal mechanism, borehole breakouts as well as direct measurements by overcoring and hydraulic fracturing all indicate a general orientation of the major principal stress in the range of N130–150° in the region around Forsmark.

The data from direct measurements in the region around Forsmark, described in the previous section, show that the calculated vertical stress and the minimum horizontal stress, based largely on hydraulic fracturing data, are approximately equal in magnitude. Where overcoring data is available the maximum horizontal stress is considerably larger than the minimum horizontal stress.

## **6.2 Geological overview**

This section presents a brief overview of the geology of the Forsmark area with focus on conditions that are of importance for the stress modelling. The section is complementary to the overview given in Section 2.1. A complete description of the geology of the Forsmark site is to be found in /Stephens et al. 2007/.

### **6.2.1 General geology and tectonics in the Forsmark area**

The coastal deformation belt in northern Uppland, where Forsmark is situated, has a width that extends several tens of kilometres across the rocks in this part of the Fennoscandian Shield. The area is formed by high-strain belts surrounding tectonic lenses with lower ductile strain. Major regional deformation zones are situated within the broader, high-strain belts around the tectonic lenses. The Singö, Eckarfjärden and Forsmark deformation zones are the most well-known of these structures, see Figure 6-2.

The target volume is situated within the north-western part of one of the tectonic lenses, the Forsmark lens. The latter extends along the Uppland coast, from north-east of the nuclear power plant, south-eastwards to Öregrund, see Figure 6-2. The bedrock inside the Forsmark lens at 400–500 m depth is relatively homogeneous, while the rocks that surround the lens are more variable and affected by a generally higher degree of ductile strain.

The observation that the tectonic lens, confined in between the Forsmark and the Singö deformation zones, has homogenous properties of slightly better quality than the rock outside the lens, might be a cause for presumably higher principal stresses within it. This hypothesis has been checked by a numerical model presented in Section 6.4.

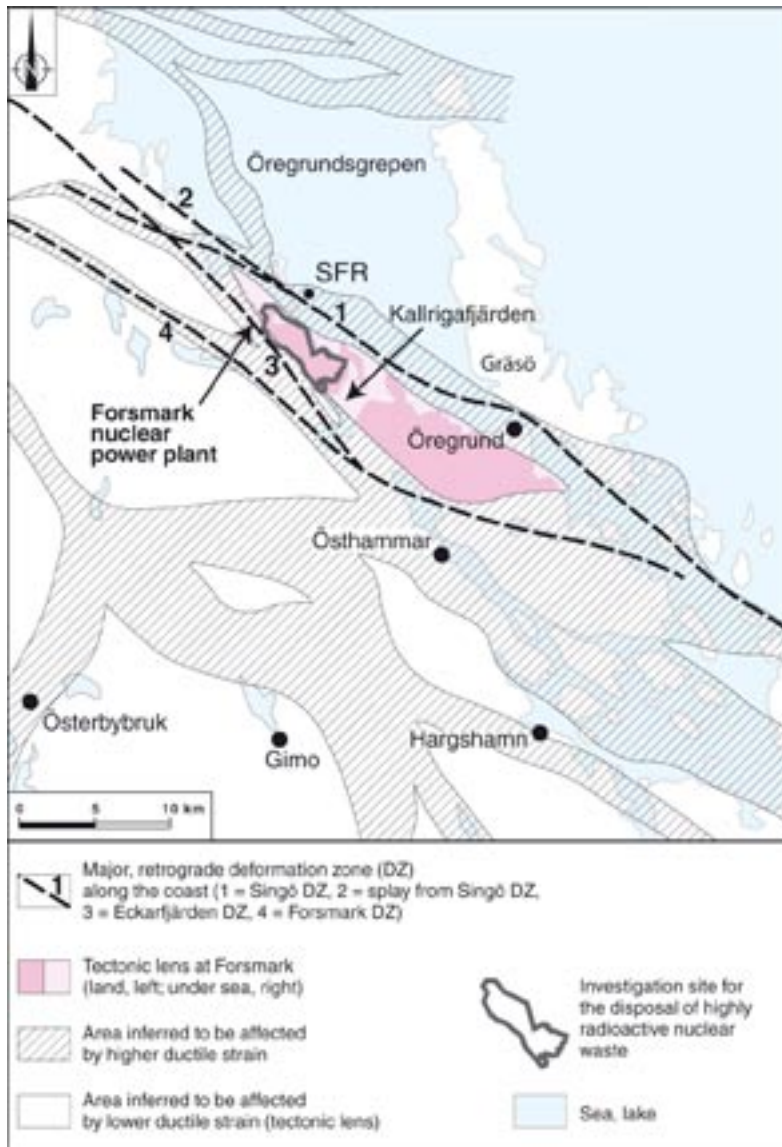


**Figure 6-2.** Map showing the structural geology in the Forsmark area with ductile high-strain belts that surround tectonic lenses with lower ductile strain. Only the major deformation zones in the Forsmark are included on this map /Stephens et al. 2007/.

### 6.2.2 Deterministic deformation zone model

The deterministic structural geological model includes zones of length  $L > 1,000$  m. Four sets of deformation zones can be distinguished at the Forsmark site:

- 1) Steeply dipping deformation zones striking ENE and NNE.
- 2) SW steeply dipping deformation zones with strike WNW and NW subsets.
- 3) Steeply dipping deformation zones striking NNW.
- 4) Gently dipping deformation zones.

Section 2.1.3 outlines all the deterministic deformation zones included in the local model and presents a horizontal section at 500 m depth in Figure 2-7. The orientation of the deformation zones presented, are also shown in a stereographic projection plot in Figure 2-8.

Figure 6-3 shows a structural geological map of the Forsmark area. All major structures, with a thickness equal or greater than 35 m, are shown on the map. The area inside the rectangle was selected to be included in the numerical model pertaining to Forsmark 2.2, see under Section 6.4.

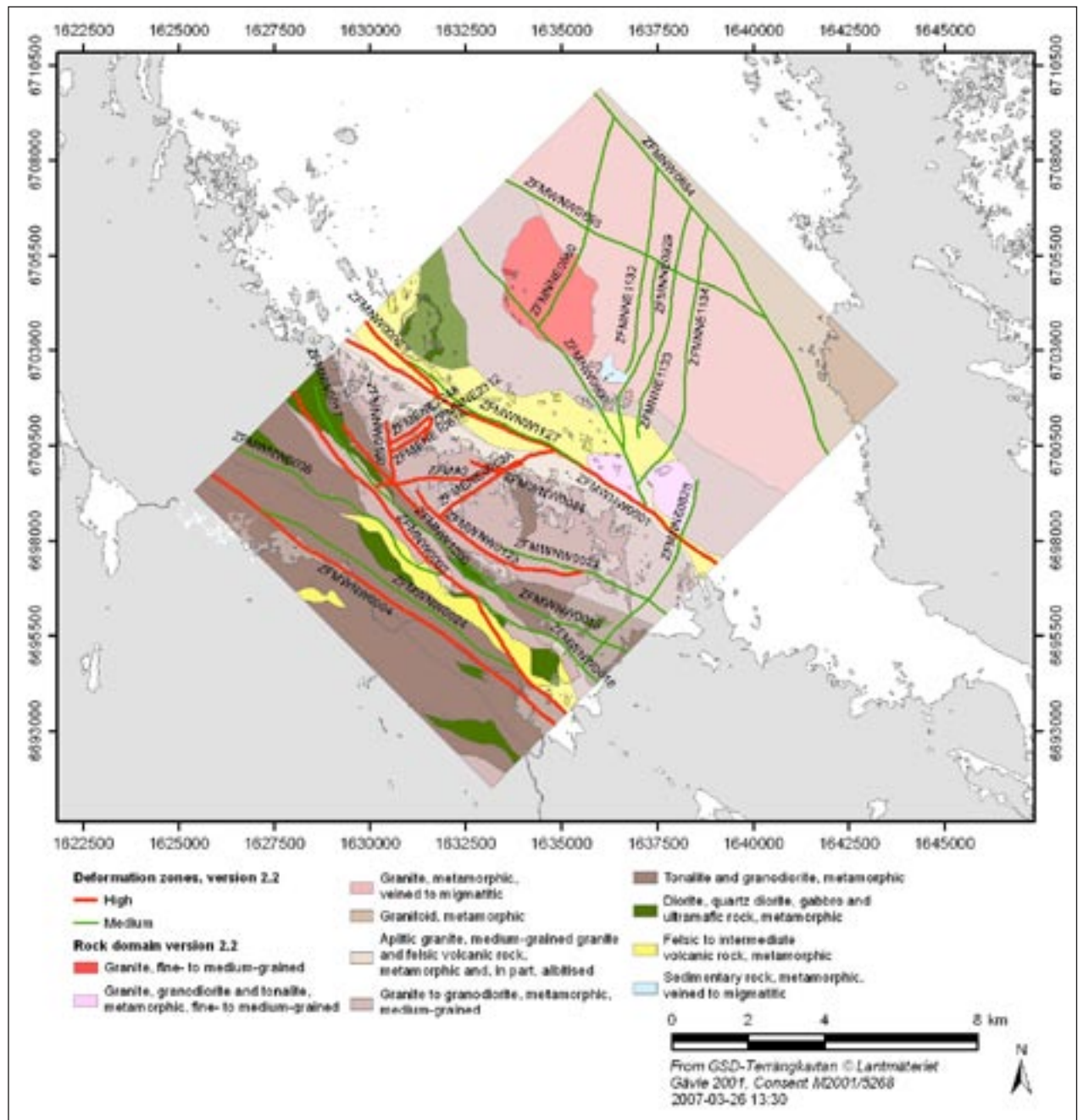


**Figure 6-3.** A structural geological map of the Forsmark area showing deformation zones that have a thickness greater than 35 m and/or a length that is greater than 1,500 m, see Appendix 7; The black square shows the outer limits of the numerical model pertaining to Forsmark 2.2, see Section 6.4.

Figure 6-4 shows a perspective view of the major deformation zones, all inclined at angles close to vertical, which were incorporated into the model block Forsmark 2.2. Other deformation zones, occurring at low to very low inclination angles, are not shown in this figure. A list of the deformation zones that were included in the model block is given in Appendix 7.

Gently dipping deformation zones occur most frequently in the south-eastern part of the target volume. Deformation zones ZFMA2 and ZFMF1 are the most important of these structures in the local model. The locations of ZFMA2 and ZFMF1 are indicated in two parallel vertical cross sections through the area in Figure 6-5.

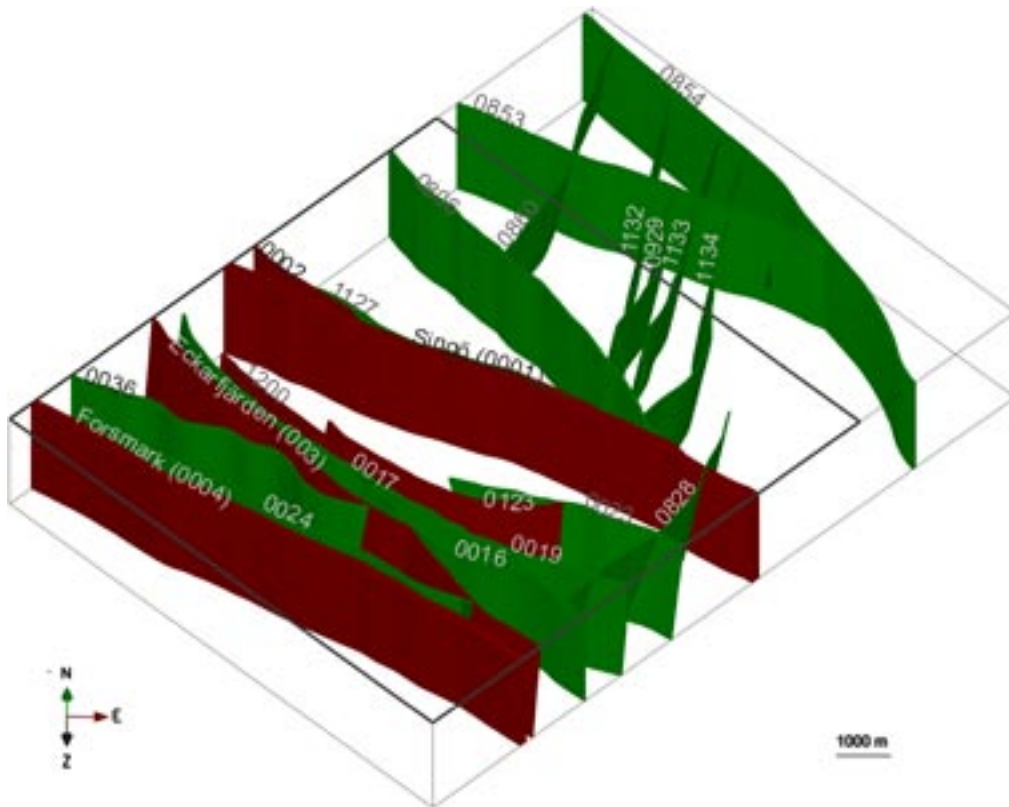


Figure 6-4. A perspective view of the deformation zones shown in Figure 6-3, which were incorporated into the model block, Forsmark 2.2. Not all deformation zones included the model are shown in this figure.

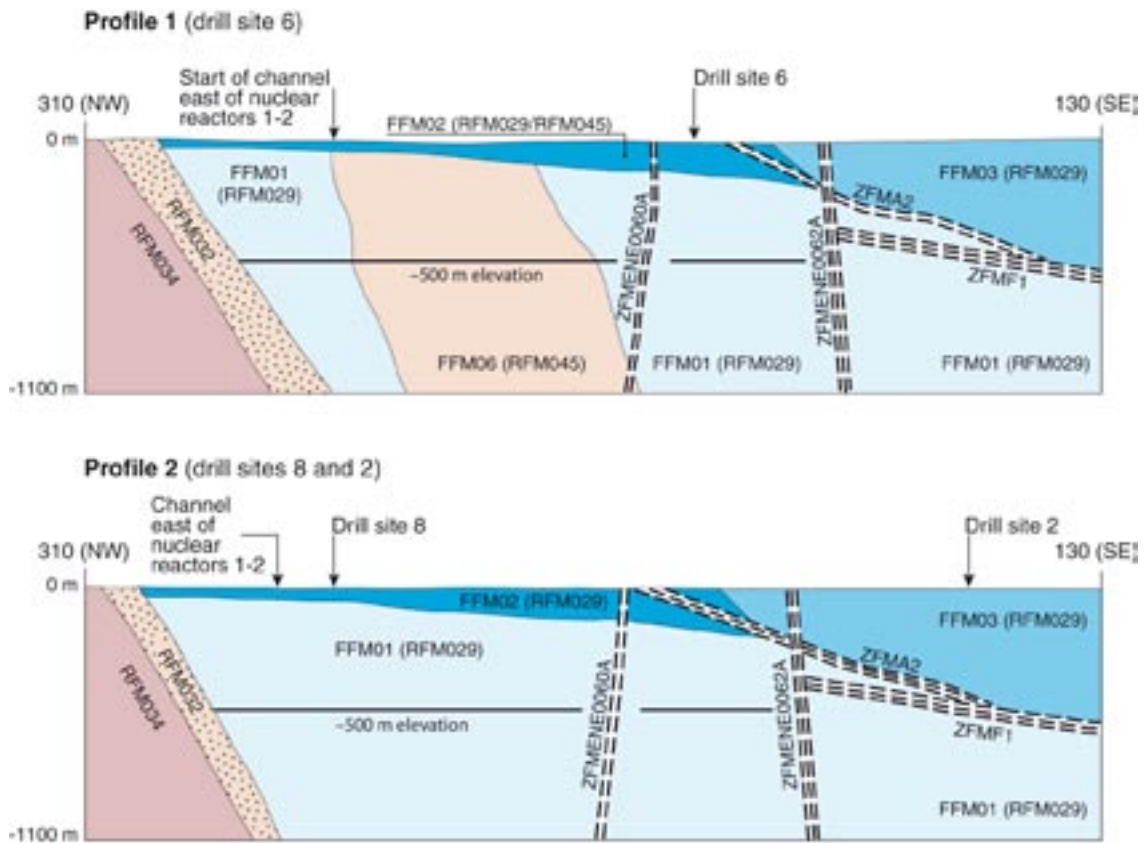


Figure 6-5. A NW-SE vertical section showing ZFMA2, ZFMENE062A and ZFMF1 and the fracture domains /Olofsson et al. 2007/.

### 6.2.3 Fracture domain model

The fracture domain model is based on both open and sealed fractures; altered albitized granitic rock is also considered. /Olofsson et al. 2007/ distinguish six separate fracture domains within the local model volume. The target volume comprises four of these fracture domains, namely FFM01, FFM02, FFM03 and FFM06. Section 2.1.4 presents a three-dimensional image of the fracture domain model, see Figure 2-9.

Figure 6-6 shows the frequency with depth below ground surface of 10,351 open fractures encountered in the Forsmark site characterisation boreholes. The fracture frequencies in the figure clearly show a significant reduction below a depth of 150 m and support the notion that there is a significant contrast between fracture domains FFM01 and FFM02/FFM03 /Martin 2007/.

A regional seismic survey was carried out as part of the Forsmark site characterisation program. About 16 km of high resolution seismic data were acquired along five separate profiles varying in length from 2 to 5 km. The nominal source and receiver spacing was between 10 m and 100 m /Juhlin et al. 2002/. The results from the seismic survey were reported by /Juhlin et al. 2002/ and are summarised in Figure 6-7. Those results show significantly lower P-wave velocities between 0 and 100 m depth and a gradual increase in seismic velocity below 100 m depth (Figure 6-7).

The seismic wave velocities are sensitive to open fractures and hence provide an indirect measure of rock mass quality and stiffness. According to /Jaeger et al. 2007/, the dynamic shear modulus ( $G_d$ ) of the material is related to the shear-wave velocity ( $V_s$ ) by:

$$G_d = V_s^2 \gamma \quad \text{Equation 6-1}$$

where,  $\gamma$  is the unit weight of the material.

/Juhlin 2006/ noted that the average ratio between the P-wave and S-wave in the Forsmark seismic survey was 1.72 below a depth of 100 m. Between 0 and 100 m depth /Juhlin 2006/ noted that the ratio is likely higher. The P-wave profile with depth and the P/S ratio of 1.72 was used to establish the shear modulus as a function of depth, see Figure 6-7. The results from the P-wave survey and the corresponding calculated dynamic shear modulus support the notion that rock mass quality gradually improves below a depth of 100 m. Below a depth of 400 m the improvement in rock mass quality is marginal. The observations discussed here have been used as basis for a numerical analysis that investigated the effect of a depth dependent deformation modulus on the in situ stress magnitudes, see Section 6.5.1.

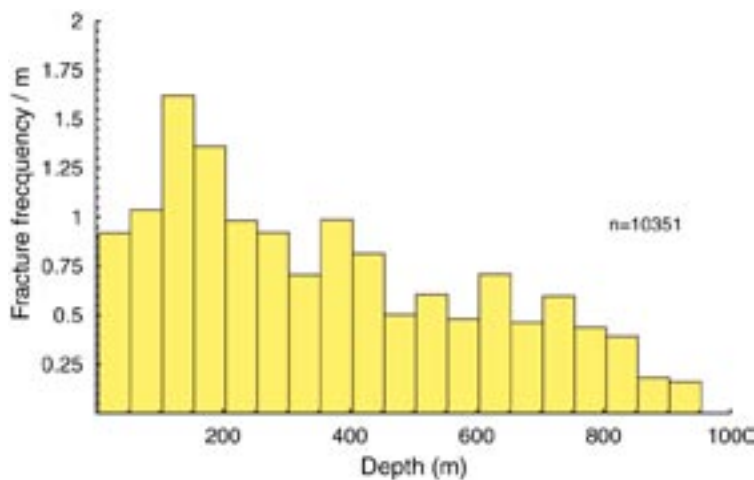


**Figure 6-6.** All open fractures from Forsmark boreholes that are visible on the BIPS log. Data obtained from SICADA (2007-04-23). From /Martin 2007/.

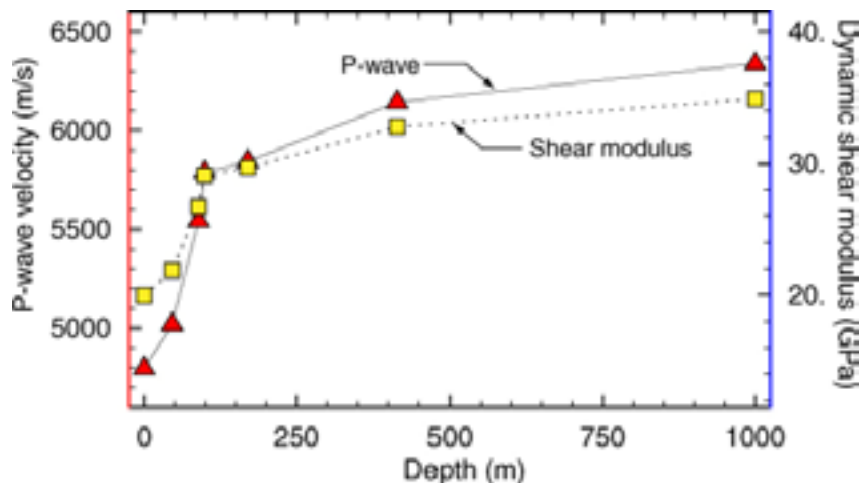


**Figure 6-7.** Seismic P-wave velocities from a 16 km long, high resolution regional seismic survey, conducted within the candidate area in 2002, data from /Juhlin et al. 2002/. The dynamic shear modulus was determined assuming a P/S wave ratio of 1.72.

## 6.3 Stress model from primary data

### 6.3.1 Primary data

/Stephansson et al. 1991/ summarised the state of stress in Fennoscandia using a rock stress database containing about 500 entries from more than 100 sites in Finland, Norway and Sweden. /Stephansson et al. 1991/ concluded that in the Fennoscandia shield there is a large horizontal stress component in the uppermost 1,000 m of bedrock, and that the maximum and minimum horizontal stresses exceed the vertical stress, assuming the vertical stress is estimated from the weight of the overburden.

The observations of the in situ state at the Forsmark site included both direct measurement and indirect observations. A comprehensive compilation and analysis of all observations from the site is reported in /Martin 2007/.

Methods used for direct measurements at the site were borehole Over Coring (OC), Hydraulic Fracturing (HF) and Hydraulic Tests on Pre-existing Fractures (HTPF). Indirect observations of the in situ stress included Borehole Breakout studies (BB), Core Disking (CD) and Micro Crack Porosity (MCP) in laboratory samples. The boreholes that have been utilised by each separate observation method are listed in Table 6-1.

The boreholes included in the overcoring and hydraulic fracturing are presented in three dimensional images in Figure 6-8 and Figure 6-9, respectively.

The primary data available in the SKB database, SICADA, have been displayed in a series of WellCad plots, one for each cored borehole, see Appendix 5. These plots provide a visual means of correlating in situ stress with geological features. The WellCad plot for borehole KFM07C, which is situated in the north-western part of the target volume (Figure 1-3), is provided here as an example, see Figure 6-10. A short description to facilitate the reading and understanding of these plots is given in Appendix 5.

Individual values from the overcoring measurements, hydraulic fracturing and hydraulic tests on pre-existing fractures are provided in /Martin 2007/.



**Table 6-1. Boreholes utilised for each in situ measurement and indirect observation method (Over Coring (OC), Hydraulic Fracturing (HF) and Hydraulic Tests on Pre-existing Fractures (HTPF). Indirect observations of the in situ stress included Borehole Breakout studies (BB), Core Disking (CD) and Micro Crack Porosity (MCP) in laboratory samples).**

Borehole name	Measurement method		Observation method		
	OC	HF/HTPF	BB	CD	MCP
KFM01A		x	x		x
KFM01B	x	x	x	x	
KFM01D				x	
KFM02A		x	x		
KFM02B	x			x	x
KFM03A			x		
KFM03B			x		
KFM04A		x	x	x	
KFM05A			x	x	
KFM06A			x	x	
KFM06B				x	
KFM06C				x	
KFM07A		x		x	
KFM07B	x				
KFM07C	x	x	x	x	
KFM08A		x	x	x	
KFM08B				x	
KFM08D				x <sup>1</sup>	
KFM09A		x	x	x	
KFM09B		x		x	
KFM10A				x	
KFM11A				x	
KFK001 (DBT1)	x	x			
KFK003 (DBT3)	x				

<sup>1</sup> The observations in this borehole are classified as uptake diskings not presented in wellcad plots.

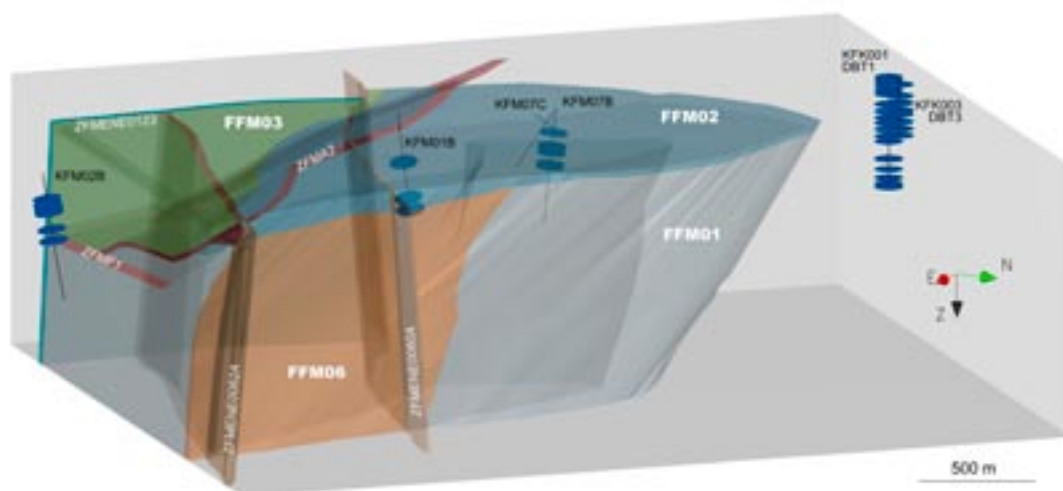


**Figure 6-8.** Three-dimensional image of the boreholes and the positions (blue discs) subjected to rock stress measurements by the overcoring method, viewed towards west.

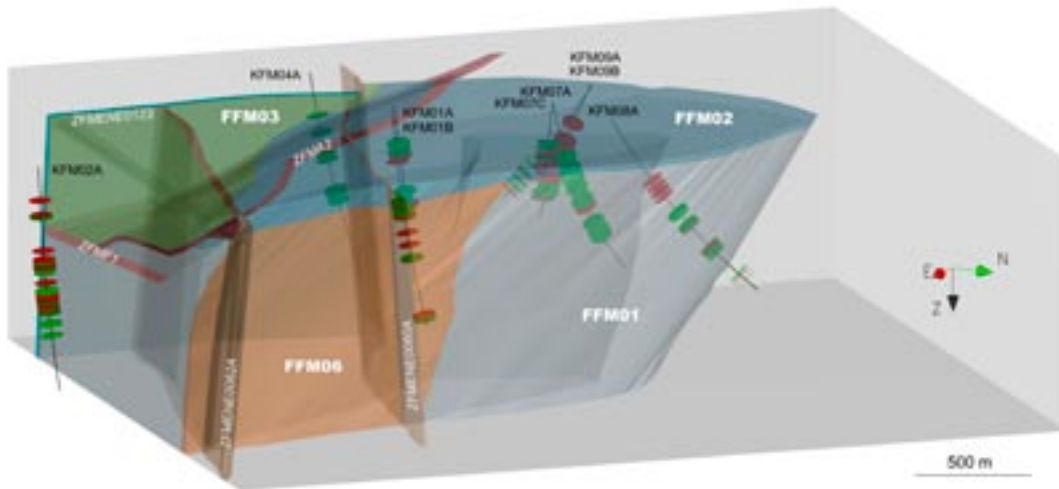


Figure 6-9. Three-dimensional image of the boreholes and the positions (green and red discs) subjected to rock stress measurements by the hydraulic fracturing method, viewed towards west. The green discs indicate successful attempts and the red ones failed attempts.

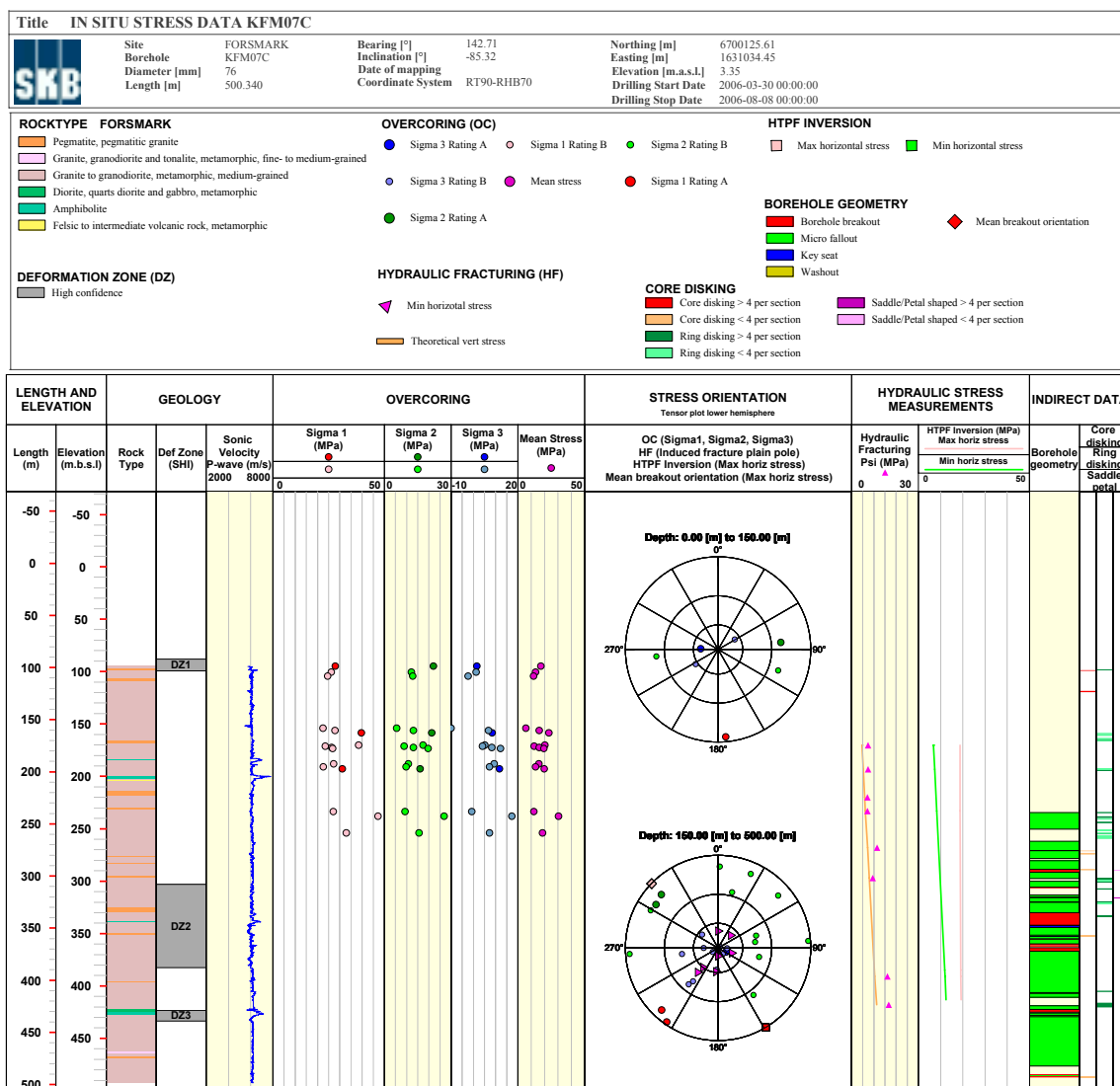


Figure 6-10. Example of a WellCad diagram for borehole KFM07C, showing selected geological data together with observations of the state of stress.

### 6.3.2 Measurement locations and deformation zones

In the relatively uniform crystalline rock conditions at Forsmark, the expected major cause for variation in stress magnitudes and orientations at the repository depth are the influence of the major deformation zones /Hakami et al. 2002/. Therefore it is of interest to study the location of measurements with respect to these zones. In Figure 6-8 and Figure 6-11 the boreholes with overcoring measurement data are shown together with the deformation zone model. The boreholes with hydraulic fracturing and the deformation zones are shown in Figure 6-9 and Figure 6-12. From these figures we can conclude that the most probable cause for stress variation is the gently dipping zone ZFMA2. Four of the overcoring holes (KFM01B, KFM07C, KFK001, KFK003) give data from below and to the north west of this zone, this volume being equal to fracture domain FFM01 at depth, and FFM02 in the upper part. The target volume for the repository is located in fracture domains FFM01 and FFM06.

Only one borehole, KFM02B, contains overcoring data from above and to the south east of the zone ZFMA2, in fracture domain FFM03 (see Sections 2.1.3 and 2.1.4).

Hydraulic fracturing data are available from six locations in FFM01 and FFM02 (KFM01A, KFM01B, lower KFM02A, KFM04A, KFM07A, KFM07C, KFM08A, KFM09A, KFM09B) and from one borehole in FFM03 (KFM02A).

This geographical distribution of the data with respect to the ZFMA2 gently dipping zone is the reason why the results for this group of four boreholes are presented together in the following plots. The upper parts of the boreholes belong to the more fractured domain FFM02. The depth of this domain varies slightly between boreholes but is about 150 m. Below this depth, the data is expected to show stresses from a fairly homogeneous stress domain.

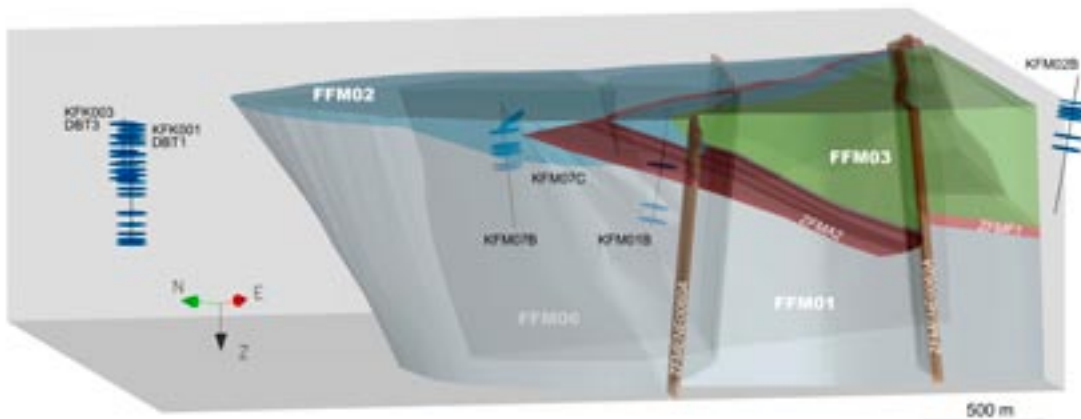


**Figure 6-11.** Three-dimensional image of the positions (blue discs) subjected to rock stress measurements by the overcoring method, viewed towards north-east.

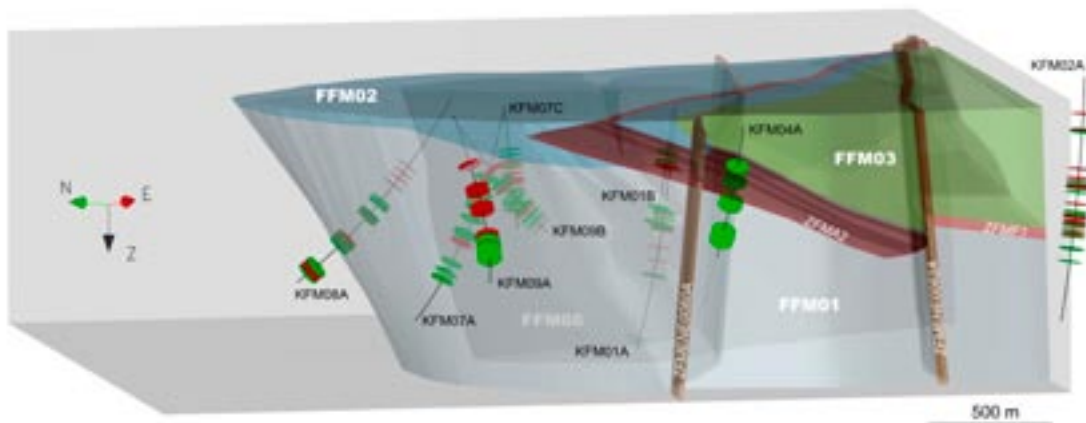


**Figure 6-12.** Three-dimensional image of the positions subjected to rock stress measurements by the hydraulic fracturing method, viewed towards north-east. The green discs indicate successful attempts and the red ones failed attempts.

### 6.3.3 Stress magnitudes at repository level in the target volume

As noted previously, two types of measurements were used in the Forsmark stress measurement campaigns: hydraulic fracturing (HF) combined with hydraulic testing of pre-existing fractures (HTPF) and overcoring using the Borre Probe. The results from these campaigns are briefly described below.

#### **Interpretation using hydraulic fracturing and HTPF measurements**

Hydraulic fracturing measurements were performed in borehole KFM01 (A and B) during the first stress measurement campaign /Klee and Rummel 2004/. The stress magnitudes derived from inversion calculation using the PSI method are presented in Figure 6-13. It may be noted from these measurements that the minor horizontal stress at 500 m depth is estimated to be about 14 MPa and the maximum horizontal stress is estimated to about 22 MPa.

Stress measurements using the HF and HTPF methods were also carried out in boreholes KFM09A, KFM09B, KFM08A, KFM07A, and KFM07C, in a second stress measurement campaign. /Ask et al. 2007/ used a total of 85 hydraulic fracturing tests and hydraulic tests on pre-existing fractures performed in boreholes KFM07A (13 tests), KFM07C (15 tests), KFM08A (23 tests), KFM09A (16 tests), and KFM09B (18 tests) to establish the most likely stress magnitudes. Of the 85 tests conducted, 46 involve unambiguous data, i.e. have a reliable normal stress and well-defined fracture geometry, though only nine of them exhibit a single fracture plane. The primary reason for the reduced success rate was that majority of the fractures tested were sub-horizontal /Ask et al. 2007/. This implies that the normal stress to the fractures would be expected to be only slightly larger than the weight of overburden.

In the absence of both reliable hydraulic fracturing data and hydraulic tests on pre-existing fractures from each drill site (only available at drill site 7), the resolution of the stress field was not always optimal. In addition, because the stress field appeared to be non-linear with depth interpolation of results over long depth intervals was not justified.

Despite the difficulties in collecting unambiguous data in certain cases, the state of stress was determined for all investigated boreholes. All solutions obtained from all boreholes, in terms of magnitude for the maximum horizontal stress, are summarised in Figure 6-14.

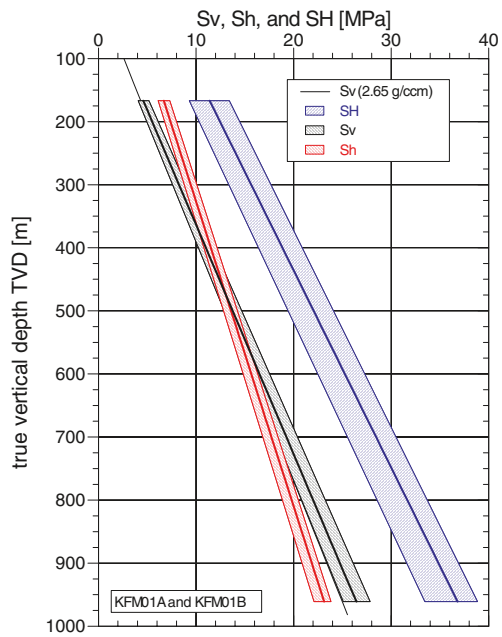


**Figure 6-13.** Principal stresses derived from inversion calculations according to the PSI method in boreholes KFM01A and KFM01B. The dashed area represents the scatter of the 10 best models,  $S_v$  (2.65 g/cm<sup>3</sup>) marks the vertical stress calculated for an average rock mass density of 2.65 g/cm<sup>3</sup> /Klee and Rummel 2004/.

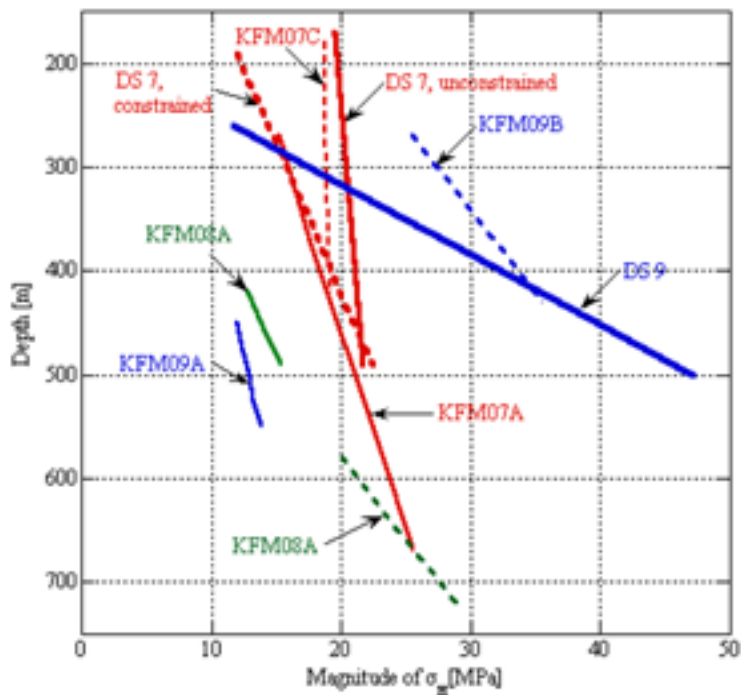


**Figure 6-14.** Summary plot of solutions for individual boreholes and drill sites with respect to magnitude of maximum horizontal stress /Ask et al. 2007/.

/Ask et al. 2007/ concluded that the stress determination for drill site 7 was the most reliable in terms of resolution of the stress field and for establishing the state of stress at 400 m and 500 m depths. In borehole KFM07C /Ask et al. 2007/ compared the classically interpreted results with the results interpreted using information from the creation of sleeve fractures (fractures below the packers). At 197 m depth the maximum horizontal stress was determined to be 11.3 MPa, using  $\sigma_h$  from conventional hydraulic fracturing and 12.0 MPa, using the tensile strength estimate from the corresponding sleeve fracturing. According to Ask these packer-induced fractures were used to verify the inversion solution. Ask concluded that their approach produced an independent check on the validity of the stress determination and regarded this check as a unique aspect of quality at drill sites 7, 8 and 9 are very consistent with respect to assurance. Ask also concluded that the results from hydraulic tests suggest that the vertical stress closely resembles the theoretical weight of the overburden of about 0.026 MPa/m. Table 6-2 presents the estimated stress magnitudes at 400 m and 500 m depth.

### ***The stress determinations based on HTPF orientation of the maximum horizontal stress***

Most orientations fall within the interval 122–133° N, and the average standard deviation is about 4°. This may also be compared with the two hydraulic fracturing tests that are judged reliable in borehole KFM07C, indicating about 125°N. Hence, there is no evidence from hydraulic stress data that significant variations in stress orientation exist between the three drill sites.

### ***Interpretation using overcoring data***

Stress measurements at Forsmark date back to the late 1970's. Stress measurements in KFK001 and KFK003 were carried out during the construction of the Forsmark nuclear plant. The results from these boreholes and stress data from the Forsmark region were summarised by /Sjöberg et al. 2005/ and formed the basis for the stress model provided in the Site Descriptive Model version 1.2. Overcoring stress measurements using the triaxial strain cell (Borre Probe) were carried out in boreholes KFM01B and KFM07C during the current Forsmark Site Investigations. The results from these boreholes were combined with overcoring results from previous Forsmark boreholes, KFK001 and KFK003, to provide the primary overcoring stress data presented in Appendix 5.

/Martin 2007/ analysed the overcoring data for orientation using 4 depth intervals (0–150 m, 150–300 m, 300–400 m, > 400 m). Figure 6-15 shows the individual orientation for the three principal stresses for each test, plotted on a lower hemisphere stereonet as well as the mean stress tensor for each depth interval. Inspection of these stereonets shows that the mean maximum and intermediate principal stresses,  $\sigma_1$  and  $\sigma_2$ , lie in essentially a horizontal plane and hence are essentially the same as the maximum and minimum horizontal stress components. The minimum principal stress ( $\sigma_3$ ) is synonymous with the vertical stress. Despite the significant scatter in the individual measurements, the mean orientation NW-SE of the maximum horizontal stress is relatively consistent with depth. At the proposed depth of the repository the trend has an azimuth of approximately 145 degrees. This trend is similar to that reported by /Ask et al. 2007/ for the hydraulic fracturing (122–133°) and by /Martin 2007/ (135°) using the borehole televiewer breakout data analysed by /Ringgaard 2007ab/.

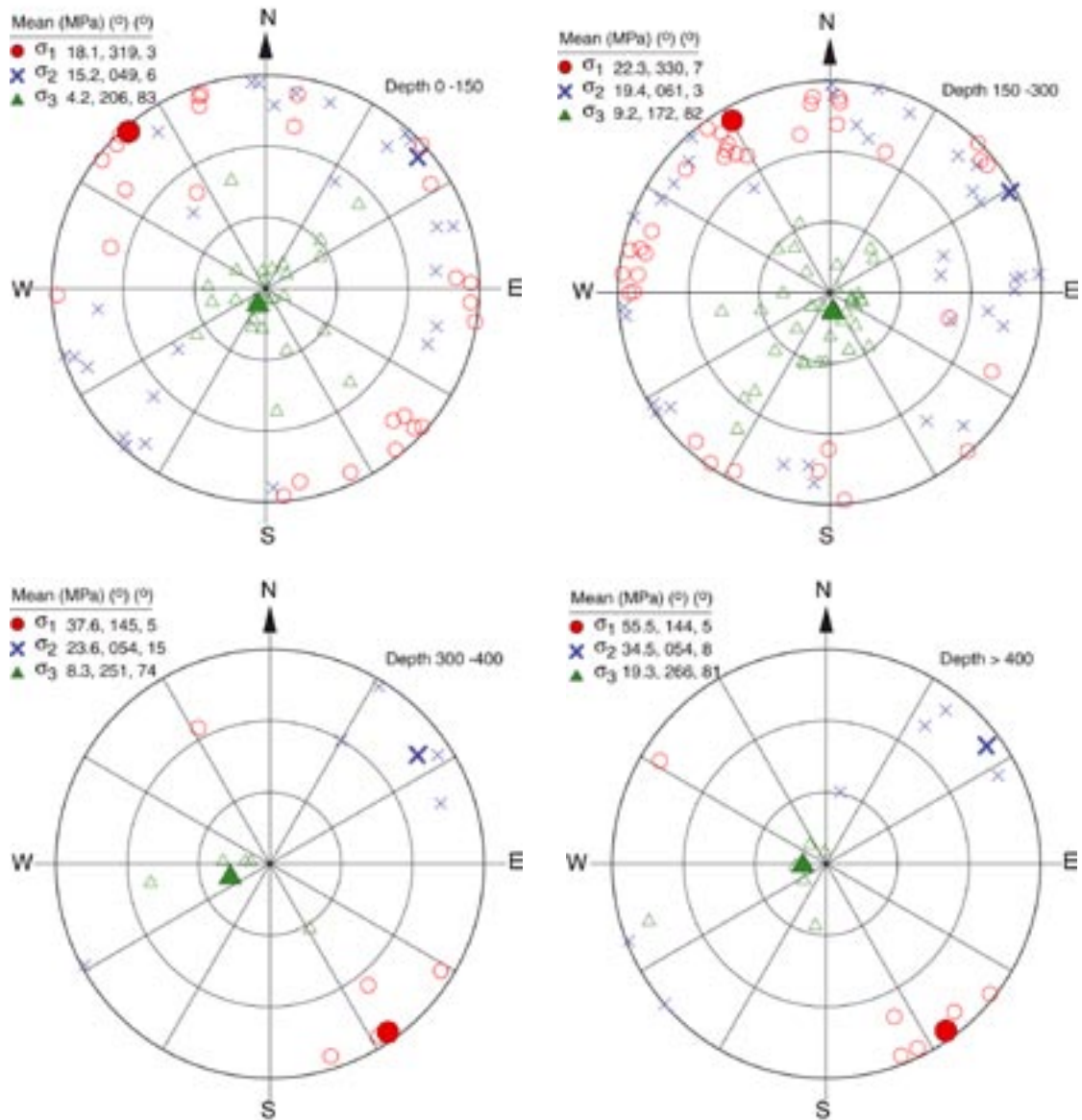


**Figure 6-15.** Principal stress orientations from overcoring tests in boreholes KFM01B, KFM07C and DBT1 and DBT3 (cf. pole plots in Appendix 5). From /Martin 2007/.

While the orientation data is relatively consistent with depth the stress magnitudes show considerable scatter. Figure 6-16 shows the results by individual borehole with depth for the minimum horizontal, maximum horizontal and vertical stresses. Also shown is the mean stress gradient recommended by /Martin 2007/. It may be noted that the deepest overcoring measurement from KFK001 (DBT1) gives maximum horizontal stress magnitudes that are higher than the recommended value at repository depth. /Martin 2007/ stated that these data are suspect because of thermal issues that were discovered during the latter stages of the stress measurement campaigns, the lack of continuous strain measurements during overcoring and that if the stress magnitudes were valid ring diskings should have occurred during overcoring. These aspects are described and discussed in detail in /Martin 2007/. Further, /Sjöberg et al. 2005/ point out the possibility that the overcoring results may have been affected by microcracks induced during the overcoring process.

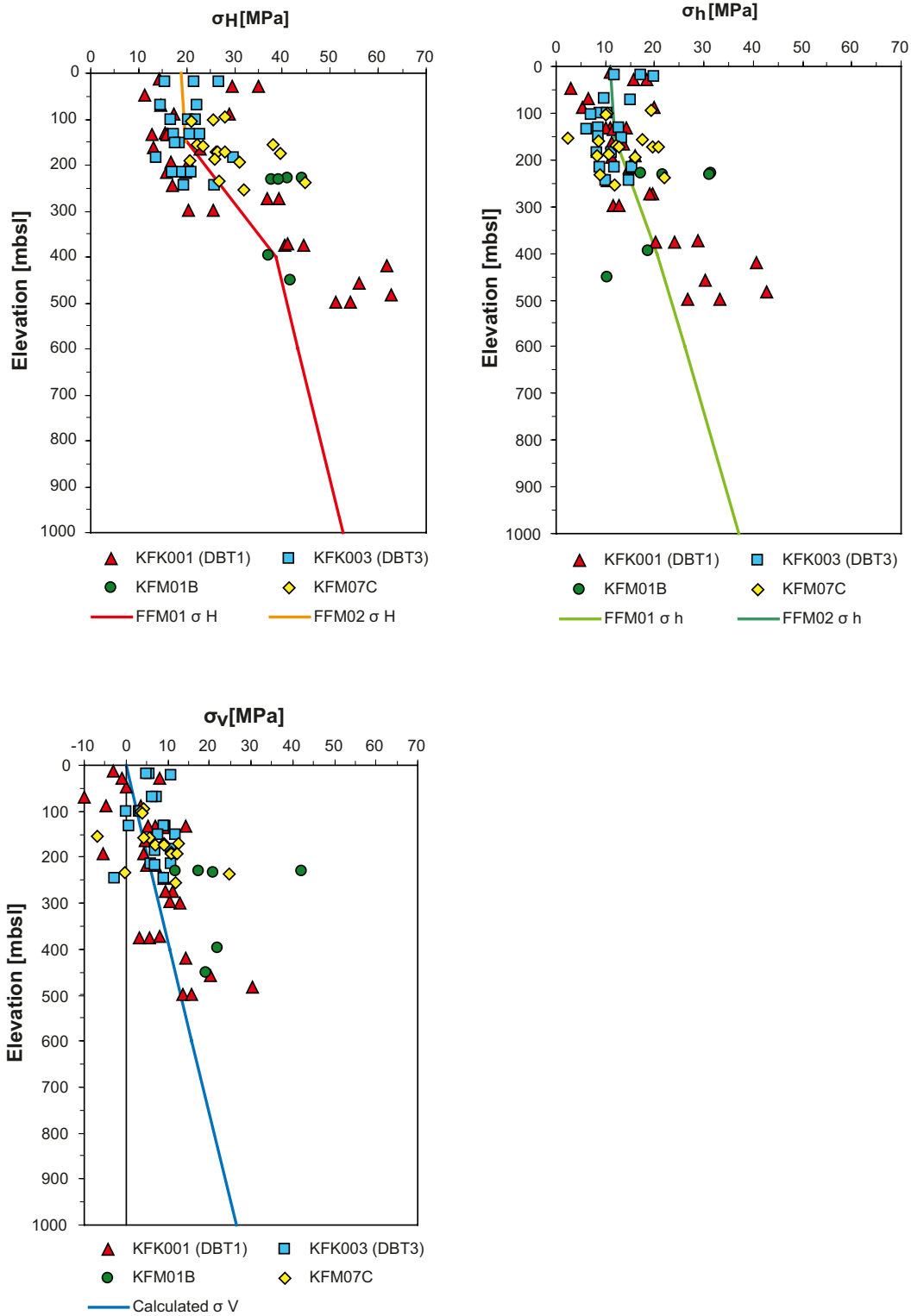


**Figure 6-16.** Estimated magnitude of the major horizontal stress, minor horizontal stress and vertical stress are shown as solid lines together with overcoring measurement data from boreholes in domains FFM01 and FFM02.



## Discussion

In addition to the in situ stress measurements discussed above, the following additional studies were undertaken to aid in assessing the stress state at Forsmark.

1. A detailed televiewer survey of approximately 6,900 m of borehole walls to depths of 1,000 m was carried out to assess borehole wall damage, i.e, borehole breakouts.
2. Evaluation of nonlinear strains in laboratory samples to artificial depths of approximately 800 m to assess if stress magnitudes were sufficient to create stress-induced microcracking.
3. Assessment of the magnitudes required to cause core dishing and a survey of core dishing observed at Forsmark.

/Martin 2007/ combined this additional information with the results of the overcoring data to develop a stress model for the site and recommended the stress magnitudes (stress gradients) and orientations with depth given in Table 6-2. For comparison purposes Table 6-2 also contains the recommended stress magnitudes by /Ask et al. 2007/ based on hydraulic fracturing. In Table 6-2 the components for the stress tensor are given as horizontal and vertical stress components. /Martin 2007/ separated the stress magnitudes into three depth ranges, 0 to 150 m corresponding to fracture domain FFM02, and two additional depth ranges occurring in fracture domain FFM01 namely 150 to 400 m and 400 to 600 m. The increase in the horizontal stress magnitudes from 150 to 400 m reflects the decreasing open fracture frequency with depth and general improvement in the rock mass quality. Below 400 m depth the rock mass is characterised as sparsely fractured and massive, and the stress gradients are expected to continue to greater depths. The findings from /Martin 2007/ were consistent with the conclusions of /Stephansson et al. 1991/ that in Fennoscandia shield both horizontal stresses tend to be greater than the vertical stress, assuming the vertical stress is equal to the weight of the overlying rock.

It is clear from inspection of Table 6-2 that at a repository depth of 500 m there is a significant difference between the maximum and minimum horizontal stress magnitudes and the likely variability proposed by /Martin 2007/ (41 and 23 MPa) and /Ask et al. 2007/ (22.7 and 10.2 MPa). /Martin 2007/ carried out a detailed comparison of the stress magnitudes from the overcoring and hydraulic fracturing data and concluded what other researchers /Evans and Engelder 1989, Doe et al. 2006/ have also reported, that the hydraulic fracturing data gives unreliable stress magnitudes in a stress regime where both horizontal stresses are greater than the vertical stress. Regardless of the reasons, the stress magnitudes from both approaches have significant implications for repository design. For example, the tangential stress magnitude on the boundary of a vertical circular opening at 500 m depth, using the horizontal stress magnitudes from /Ask et al. 2007/, are approximately 58% of those calculated using the horizontal stress magnitudes from /Martin 2007/. Because the stress measurements were taken at different locations in the target

**Table 6-2. Horizontal and vertical stress magnitudes for the Forsmark target area, where the depth below surface is z in metres. The values by /Martin 2007/ are based primarily on overcoring data while the values by /Ask et al. 2007/ are based on hydraulic fracturing and hydraulic testing of pre-existing fractures.**

Depth (m)	Maximum horizontal stress (MPa)	Trend (deg)	Minimum horizontal stress (MPa)	Trend (deg)	Vertical stress (MPa)
<i>/Martin 2007/</i>					
0–150	19+0.008z ± 20%	145 ± 20	11+0.006z ± 25%	055	0.0265z ± 2%
150–400	9:1+0.074z ± 15%	145 ± 15	6.8+0.034z ± 25%	055	0.0265z ± 2%
400–600	29.5+0.023z ± 15%	145 ± 15	9.2+0.028z ± 20%	055	0.0265z ± 2%
<i>/Ask et al. 2007/</i>					
400 mvd	19.2 ± 0.7	124 ± 6	9.3 ± 1.1	34	10.4
500 mvd	22.7 ± 1.1	124 ± 6	10.2 ± 1.6	34	13.0

area it was hypothesised that some of the differences in Table 6-2 may be attributed to spatial variability. To help resolve whether the geological conditions at the site, particularly large scale deformation zones, were contributing to the conflicting results, numerical analyses were carried out at scales ranging from the regional to the local tunnel scale. The approach and the results from those analyses are discussed in the following sections.

## **6.4 Evaluation of stress variability caused by deformation zones**

Three stages of numerical studies were carried out for the Forsmark site: Forsmark 1.2, Forsmark 2.1 and Forsmark 2.2. Investigations associated with Forsmark 1.2 and Forsmark 2.1 were reported separately, see /Mas Ivars and Hakami 2005/ and /Hakami 2006/. All 3D numerical modelling was carried out using 3DEC /Itasca 2003/. In 3DEC, faults and deformation zones are modelled as planar, through-going entities. This section summarises the results from all three modelling stages.

### **6.4.1 Modelling approaches**

Two 3D numerical modelling approaches were undertaken. In both, the numerical model block created was sufficiently large to contain the major regional deformation zones. This large model block was internally divided into a central area, encompassing the target area for the proposed repository.

The two “loading sidewalls” of the large model block were oriented at right angles to the direction of crustal shortening for the Forsmark region. During a numerical simulation, when the loading sidewalls are displaced inwards, stresses in all directions are generated within the model block. In a simulation, the sidewalls were initially displaced until the stress magnitudes at selected monitoring points within the model were in approximate agreement with local measurements. Several calibrating runs, were required to bring the numerical values close to the calibration stress values.

Two approaches were used to assess the potential stress perturbations induced by the deformation zones. In the first approach the deformation zones were initially assigned fictitious properties that caused them to remain inactive during the initial loading. Once the desired loads were reached the deformation zones were assigned realistic properties and the “push” continued, inducing shear displacements across the deformation zones. The stresses generated using this approach produced a spatial distribution of stresses within the whole model block.

In the second approach, the modelling steps from above were used to define the boundary conditions for the central area. This allowed the central area to be modelled independently, as a separate model block by applying stress boundaries that were derived from the modelling of the large model block.

The first and the second approaches, described above, both have advantages and disadvantages related model run times, numerical stability and stress path. The modelling for Forsmark stage 2.2 followed the first approach whereas the modelling for Forsmark stage 1.2 and 2.1 was based on the second approach.

### **6.4.2 In situ stress issues addressed by modelling stage**

#### ***Modelling stage 1.2***

The site investigations indicated a relatively homogeneous rock mass bounded by two NW-SE trending regional faults (Forsmark and Singö faults) and intersected by gently dipping deformation zones in the southeast region of the target area. The investigations also indicated that the

magnitudes of principal stresses increased significantly below a depth of about 300 m. The primary focus of the stage 1.2 numerical modelling was to assess:

1. If the elevated stress magnitudes within the homogeneous portion of the tectonic lens could be explained by confining a lens of good quality rock between the Forsmark and Singö faults. The strength and mechanical properties of the homogeneous tectonic lens were considered better than the rock occurring outside the lens.
2. If a gently dipping deformation zone (SHFZ), could perturb the in situ stress field?

The model block used for the computations for Forsmark 1.2 is shown in Figure 6-17. In order to study the possible effect of the tectonic lens, a central lens was made in between the Singö and the Forsmark faults. A sub horizontal deformation zone (SHFZ), striking NE-SW, was also added to the model block. Mechanical properties given in Table 6-3. were used in the numerical model and detailed results from the study are given in /Mas Ivars and Hakami 2005/. Typical results and findings from the study are summarised under Sections 6.4.3 and 6.4.4.

**Table 6-3. Mechanical properties of the rock mass, fault zones and the SHFZ, pertaining to Forsmark 1.2 analyses.**

	Rock mass	Fault zones	SHFZ
Deformation modulus (GPa)	40		
Poisson's ratio	0.24		
Density (kg/m <sup>3</sup> )	2,700		
Normal stiffness (GPa/m)		10	100
Shear stiffness (GPa/m)		5	50
Friction (°)		15	20

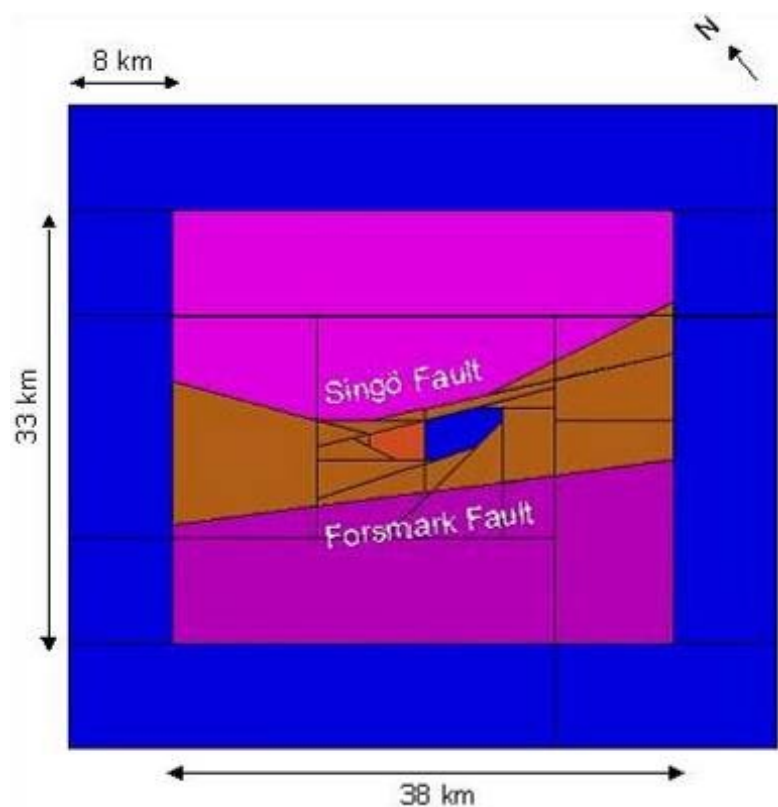


**Figure 6-17.** A top view of the model block used in the study Forsmark 1.2 /Mas Ivars and Hakami 2005/.

### Modelling stage 2.1

The Forsmark 2.1 site investigations improved the geological model for the site and identified that the gently dipping deformation ZFMA2 was a significant hydro-geological conductor across the site. These conditions suggested that this deformation zones may significantly influence the stress field and possibly lead to de-stressed conditions above ZFMA2. To examine the effect of ZFMA2 on the local stress conditions a stress boundary was used at 350 m depth, equivalent to the weight of the 350 m of rock cover. This boundary condition eliminated the numerical free surface at the top and enhanced numerical stability.

Mechanical properties given in Table 6-4 described the rock mass in the numerical model. Figure 6-18 shows the model block set up for the work carried out under Forsmark 2.1, see also /Hakami 2006/.

### Modelling stage 2.2

The focus for the numerical modelling in stage 2.2 was to establish the spatial distribution of the in situ stresses in the vicinity of the proposed repository within the target volume. The geological model for this region of the site and the geometry of deformation zones was well constrained. This geometry was used to establish a more accurate numerical model of the target volume.

**Table 6-4. Mechanical properties for the rock mass, faults and large deformation zones pertaining to Forsmark 2.1 analyses.**

	Rock mass	Faults, regional deformation zones	Deformation zones/splays
Deformation modulus (GPa)	40		
Poisson's ratio	0.24		
Density (kg/m <sup>3</sup> )	2,700		
Normal stiffness (GPa/m)		1	10
Shear stiffness (GPa/m)		0.5	5
Friction (°)		20	25

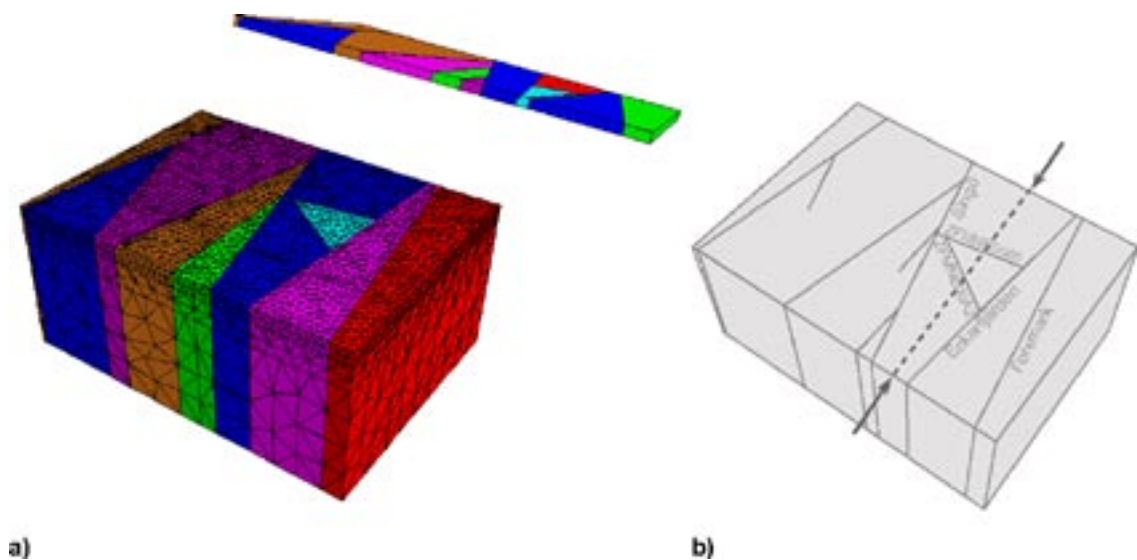
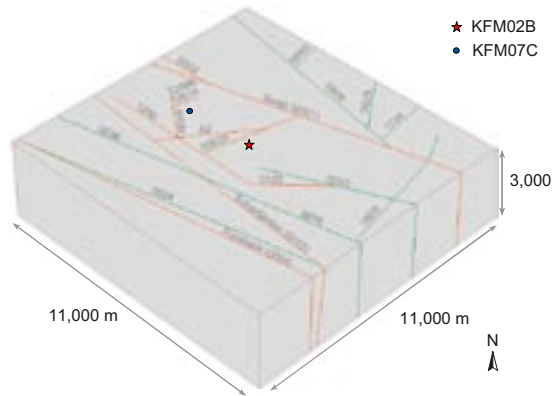


**Figure 6-18.** a) The model block used for Forsmark 2.1. The isolated slab in the figure had a thickness of 350 m and did not enter the numerical computations. b) A simplified sketch of the model block on which the approximate location of the horizontal scan line at 400 m depth is marked.

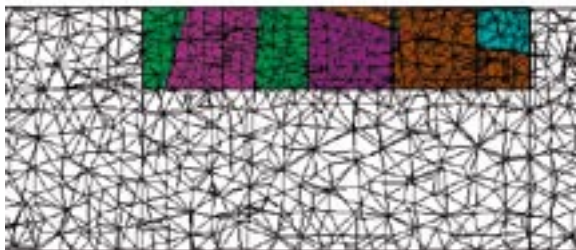
The deformation zones were modelled as through-going planar features. Figure 6-19a illustrates the model block showing the deformation zones and Figure 6-19b shows the outline of the computational tetrahedral zones. The tetrahedral zones vary in size, with a maximum edge length of 200 m in the central part of the model block and 400 m in the outer portions of the model. Figure 6-19c shows a NW-SE vertical section showing the central area in colour with the more dense computational tetrahedral zones. The approximate location of boreholes KFM02B and KFM07C are shown in Figure 6-19a. These boreholes were for comparing the measured in situ stresses with those from the numerical model.



**a)** Geometry of the model in stage 2.2



**b)** The model block discretised and meshed



**c)** NW-SE vertical cross section of the zoned model block, showing the more densely zoned part of the model in colour.

**Figure 6-19.** The numerical model block for Forsmark 2.2, showing the deformation zones. The approximate location of boreholes KFM02B and KFM07C are also shown.

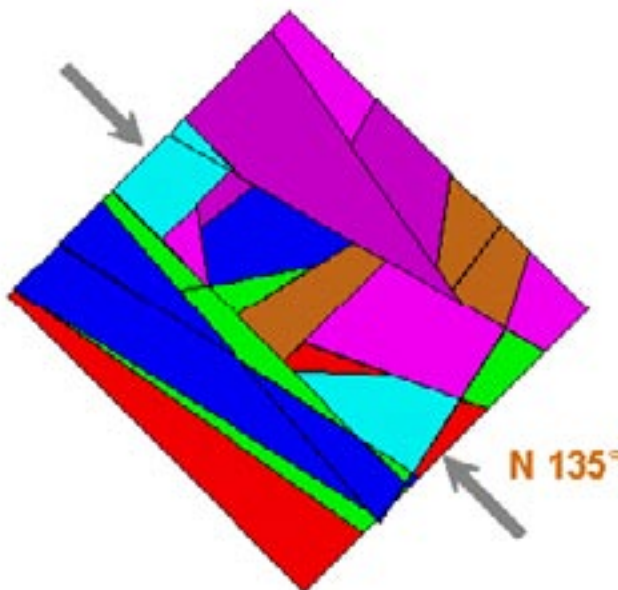
Table 5-7 (see Section 5.2.2) summarizes the mechanical properties that were assigned to the deformation zones. The direction of compression was determined for the Forsmark site to be N135deg which is in general agreement with the direction of crustal shortening (N120deg) determined by /Slunga 1991/ from seismic studies for Sweden. In the regional numerical model for Forsmark the direction of compression was set to N135deg, (Figure 6-20).

### 6.4.3 Findings from the numerical stress modelling

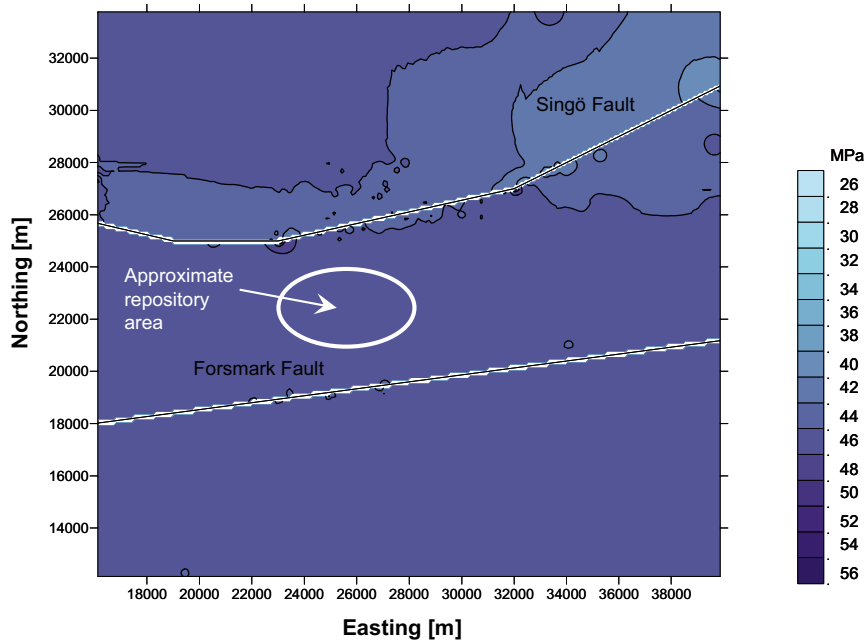
#### ***Effect of regional Singö and Forsmark Faults and subhorizontal deformation zone***

Figure 6-21 shows the contours of principal stress  $\sigma_1$  at a depth of 450 m. In the model both the Singö and Forsmark Fault have identical properties. The results show the minor perturbation to the stress field in the vicinity of the Singö fault caused by the fault geometry, i.e. a slight bending of the plane. The modelling results illustrate that despite the enormous extent and thickness of the Singö and Forsmark Faults, these regional deformation zones do not significantly perturb the stress field, except in those regions where the fault geometry changes. From Figure 6-21 it appears that at repository depth these stress perturbations associated with the Singö fault will not be observed in the vicinity of the repository.

A sub horizontal deformation zone, abbreviated as SHFZ, was included in the numerical model for Forsmark 1.2 to assess its potential effect on the stress field. These deformation zones dip towards the southeast and are bounded by the Singö and Forsmark Faults. Figure 6-22 shows the contours of  $\sigma_1$  projected on to a horizontal section of the stress field at 450 m depth. The perturbation to the maximum principal stress, is clearly seen with significant de-stressing occurring in the hanging-wall above SHFZ.



**Figure 6-20.** The direction of compression used in stage 2.2, which is in general agreement with that inferred from regional seismic studies, see /Slunga 1991/.



**Figure 6-21.** Horizontal section at 450 m depth, showing the contours of  $\sigma_1$ . Note the reduction of  $\sigma_1$  in relation to the NE-side of the Forsmark fault, see /Mas Ivars and Hakami 2005/. Note that the Northing and Easting refer to truncated model coordinates.

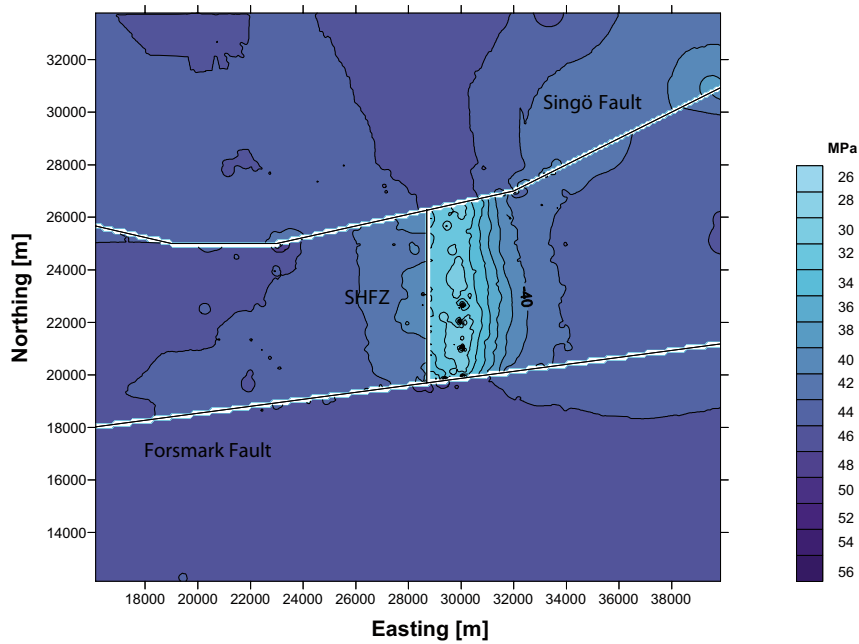


**Figure 6-22.** Horizontal section at 450 m depth showing the contours of  $\sigma_1$  around the intersection of the sub-horizontal zone SHFZ and the Forsmark and Singö faults, see /Mas Ivars and Hakami 2005/. The repository is located to the left of the SHFZ. Note that the Northing and Easting refer to truncated model coordinates.

### **Effect of a stiff central tectonic lens**

The Forsmark 1.2, geological investigations indicated that the tectonic lens may be stiffer than the rock mass outside. Figure 6-23 shows the central lens in the numerical model that was treated as a stiff inclusion with a modulus of elasticity 10% greater than the surrounding rock mass.

Two cases (Case 0 and 1) were evaluated. In Case 0, the rock mass and the tectonic lens had identical properties. In Case 1 the central tectonic lens' modulus of elasticity was increased by 10%. In both cases the properties of the Singö and Forsmark faults were identical. Figure 6-24 compares  $\sigma_1$  from scan lines DS2 and D (see Figure 6-23) for Case 0 and Case 1. As shown in Figure 6-24 the changes made to the properties of the tectonic lens did not bring about any notable change in the prevailing stress field.

### **Combined effect of stiff tectonic lens and sub horizontal deformation zone (SHFZ)**

The results of the modelling thus far showed that the sub horizontal deformation zones had a significant effect on the stress field, while essentially no effect could be attributed to a 10% stiffening of the tectonic lens.

In the analyses discussed in this section four cases were examined. Case 0 refers to the analysis in which the properties of the tectonic zone did not differ from the surrounding rock. In Case 1 the stiffness of the tectonic was increased 10% above the surrounding rock. In Case 2 the sub horizontal fracture zone (SHFZ) was allowed to slip and the stiffness of the tectonic lens below the SHFZ was increased by 10%, while the stiffness of the tectonic lens above the SHFZ was decreased 10%, relative to the surrounding rock mass. Case 3 included an SHFZ that was allowed to slip while both the properties of the tectonic lens and the surrounding rock mass were identical.

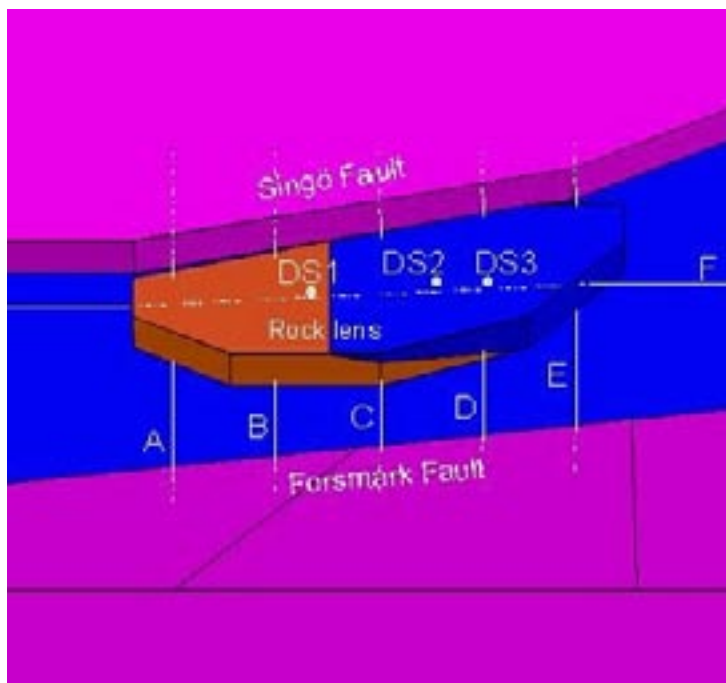
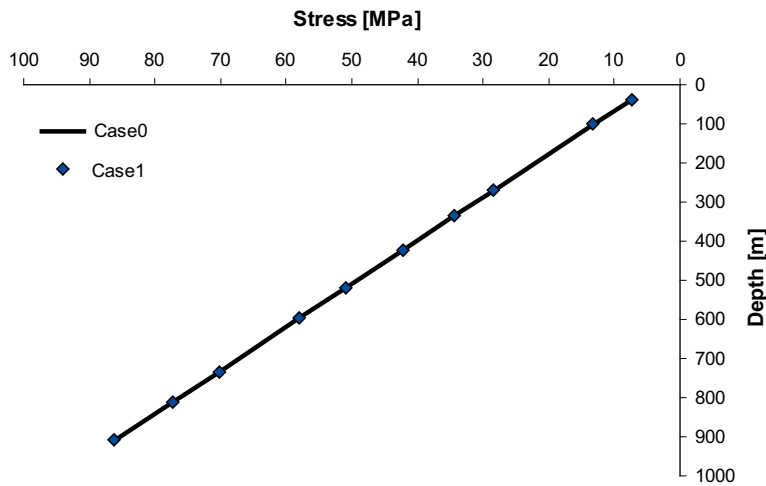
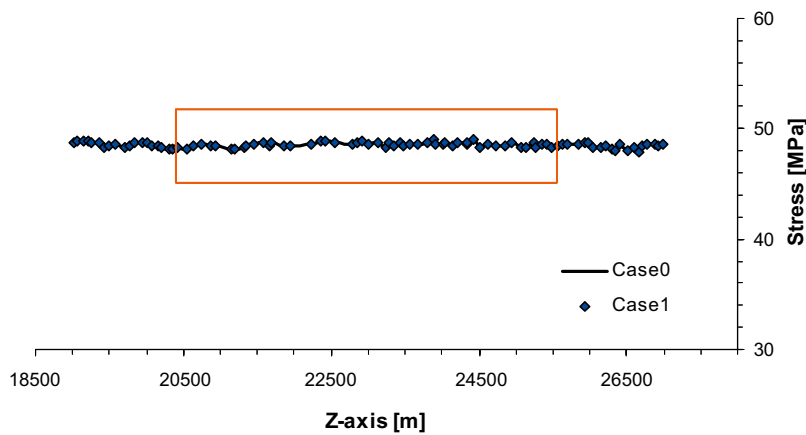


**Figure 6-23.** The locations of the tectonic lens and horizontal scan lines used to sample the principal stresses. In the figure, some rock is removed from around the tectonic lens to expose it more clearly.





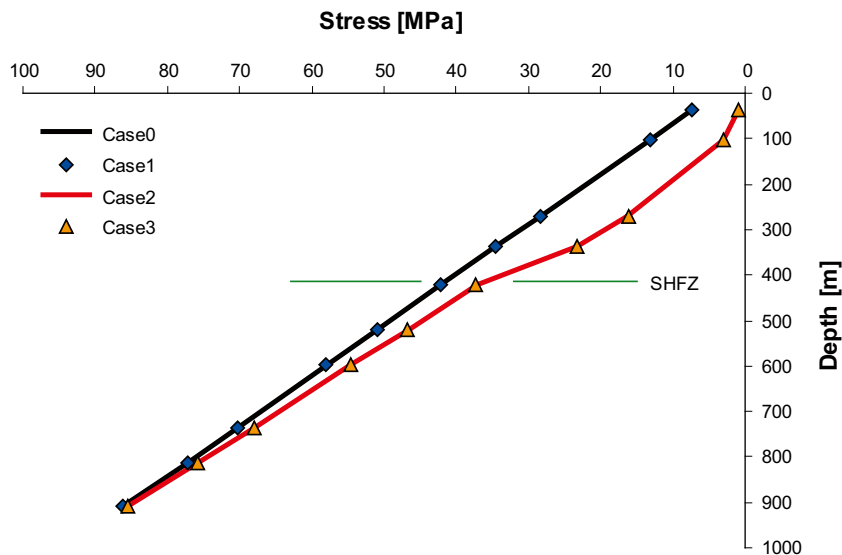
a)  $\sigma_1$  with depth along a vertical scan line DS2.



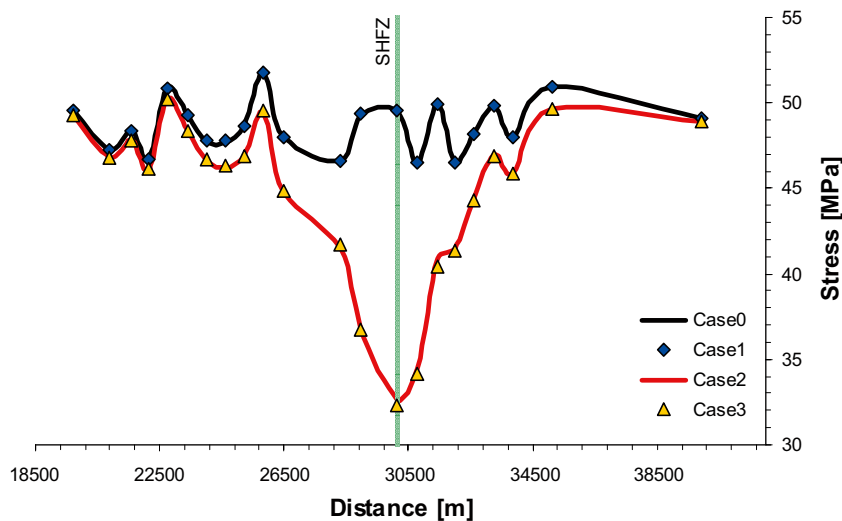
b)  $\sigma_1$  along the horizontal scan line D, at a depth of 500 m.

**Figure 6-24.** The lateral variation of  $\sigma_1$  along a vertical scan line DS2 and a horizontal scan line D at a depth of 500 m. See Figure 6-23 for the location of the scan lines. For both Cases 0 and 1 the results are identical. The box on the figure roughly marks the longitudinal limits of the tectonic lens along the scan line.

Figure 6-25a shows the variation of  $\sigma_1$  along the vertical scan line DS2, while Figure 6-25b shows the lateral variation of  $\sigma_1$  along the horizontal scan line F at a depth of 500 m. Figure 6-25a illustrates that the presence of the sub horizontal deformation zone and not the properties of tectonic lens has the most significant impact on the stress field.



a) The variation of  $\sigma_1$  along vertical scan line DS2.



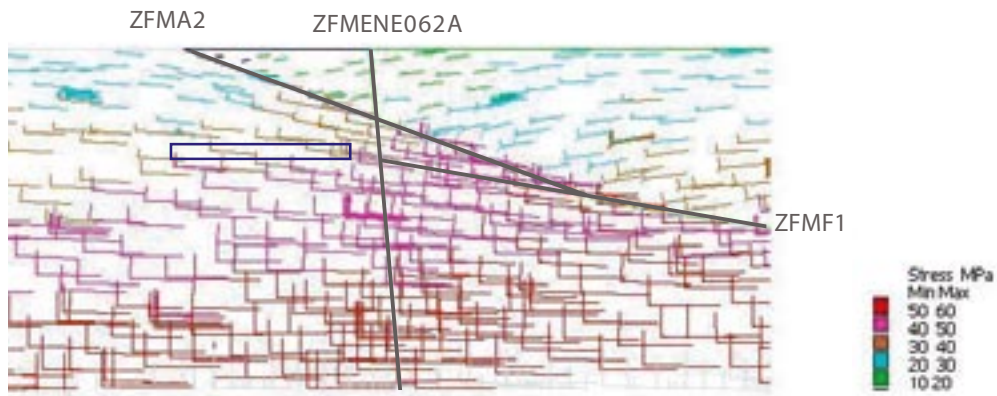
b) The variation of  $\sigma_1$  along horizontal scan-line F.

**Figure 6-25.** The variation of  $\sigma_1$  for the four cases analysed, see /Mas Ivars and Hakami 2005/. For the location of the Scan line F see Figure 6-23. The grey line indicates the point where the scan line cuts through the SHFZ.

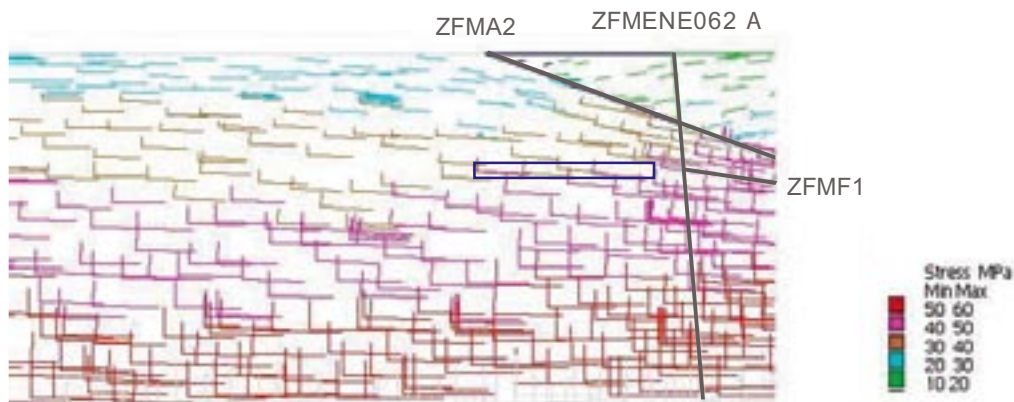
### Effect of deformation zones in the target volume

The update for the SDM 2.2, provided the best estimate for the deformation zone strength and stiffness properties as well as their spatial description. This data was used to update the numerical model and evaluate the effect of deformation zones ZFMA2, ZFMENE062A and ZFMF1 on the stress state in the target volume.

Figure 6-26 show the principal stress tensors occurring along a NW-SE vertical section cutting through the central portion of the tectonic lens. The results in Figure 6-26 show a notable rotation of the principal stresses in the hanging wall in the immediate vicinity of ZFMA2. The stress rotation appears to be less pronounced on the footwall side of the deformation zones. Nonetheless the results support the previous modelling results that the stress field at the repository depth appears relatively homogeneous.



a) General NW-SE vertical section of deformation zones in the general Target Area.

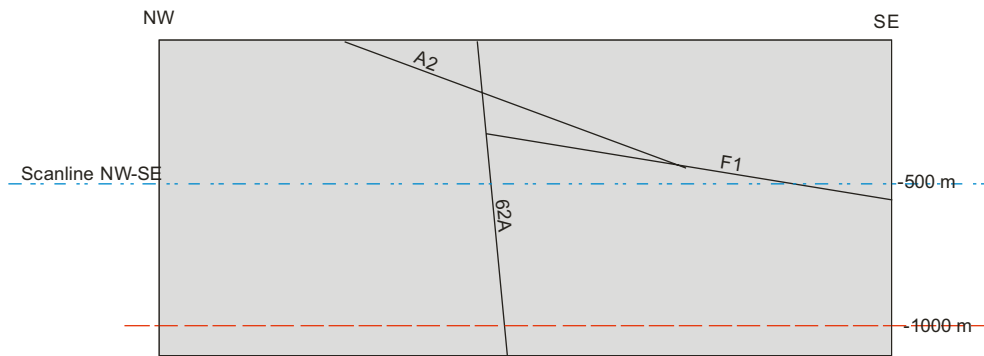


b) Close-up view showing more of the NW-side, including deformation zones ZFMA2 and ZFMENE062A and ZFMF1.

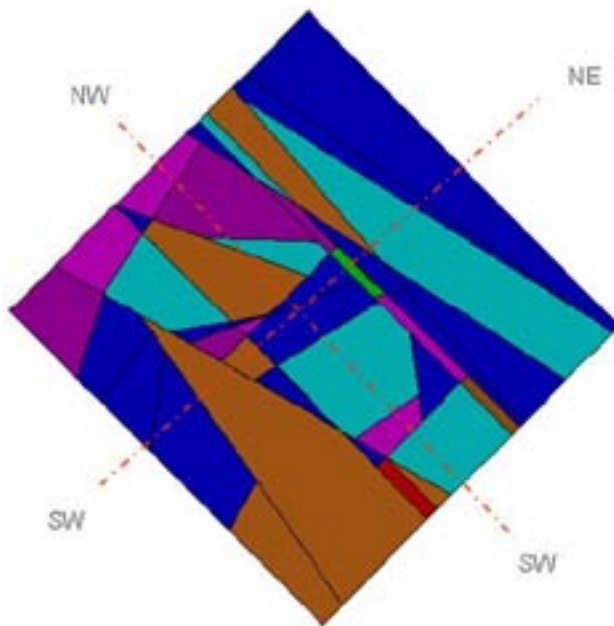
**Figure 6-26.** A NW-SE section showing deformation zones ZFMA2, ZFMENE062A and ZFMF1. Note the rotation of principal stress tensors above and around ZFMA2 and ZFMF1. The location of the Target Area is marked as a horizontal rectangle on the figure. The proposed repository extends to the left of rectangle.

### **Stress variability at repository level**

Two scan lines were used to investigate the stress magnitudes at the 500 m depth, the approximate depth of the repository (Figure 6-27). The most current rock and deformation zone properties are used in this modelling stage.



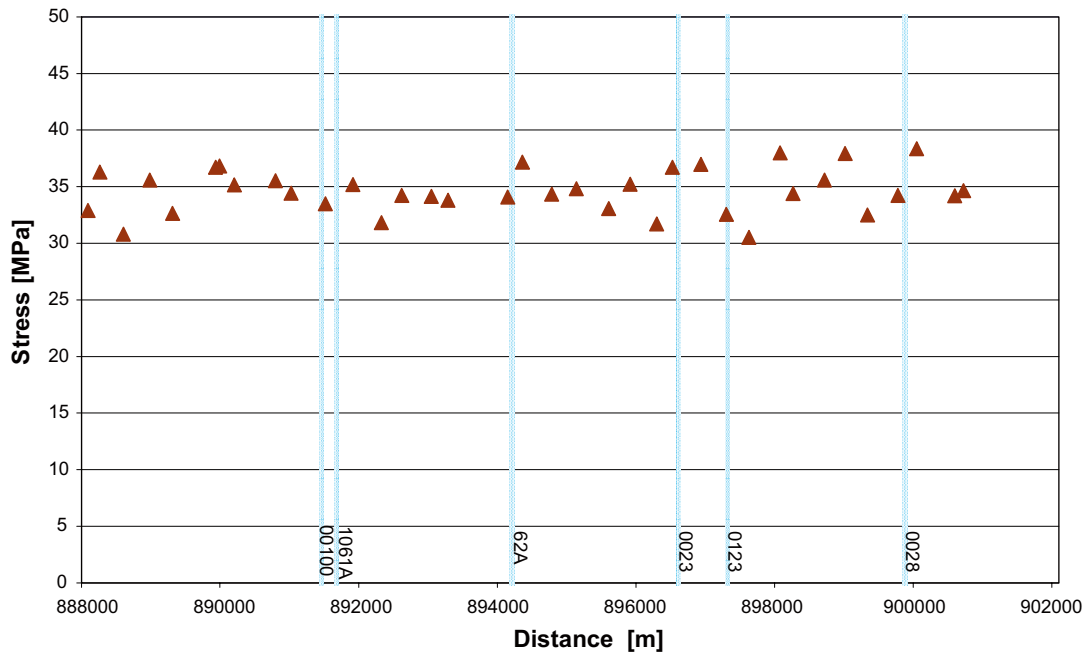
a) NW-SE vertical section showing scan line location at 500 m depth. Deformation zones ZFMA2, ZFMENE062A and ZFMF1 are also shown.



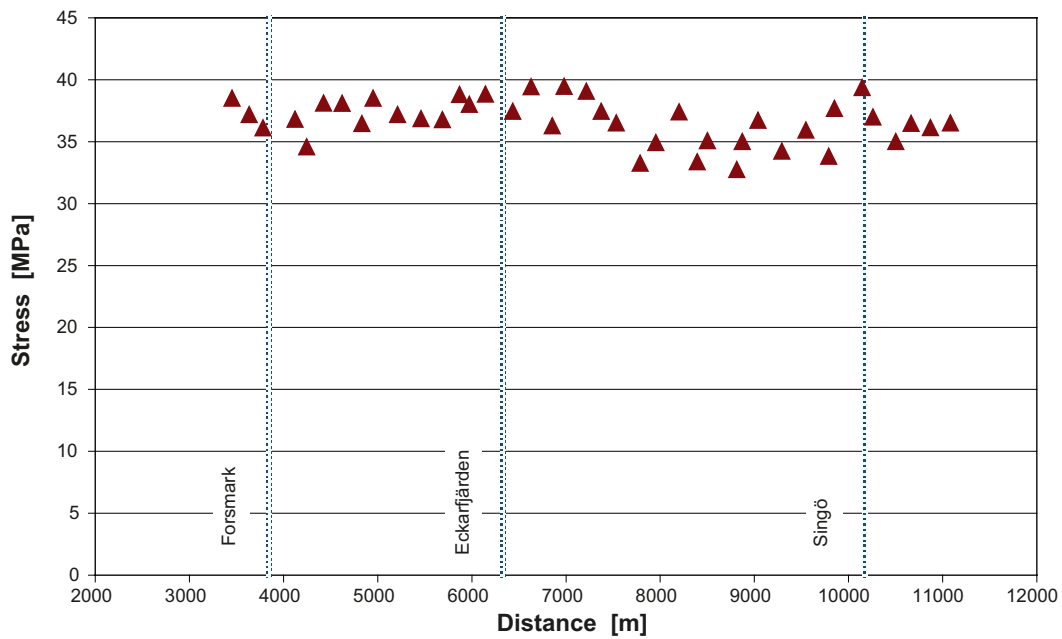
b) Plan view of the numerical model showing the location of the NW-SE and NE-SW scan lines

**Figure 6-27.** Location of the scan lines used to examine the stress variation at the 500 m depth, the approximate depth of the repository, in stage 2.2.

The lateral variation of the maximum principal stress  $\sigma_1$  along the NE-SW and NW-SE scan lines is shown in Figure 6-28. The results for  $\sigma_2$  and  $\sigma_3$  along the same scan lines are given in Appendix 7. The results along the two perpendicular scan lines illustrate that the variation of the maximum principal stresses is approximately  $\pm 4$  MPa. Note that the scan lines, taken at the repository level, sample the stresses directly beneath deformation zones ZFMA2 and ZFMF1. Hence the more pronounced variation at shallower depths, associated with the deformation zones, is not reflected in the scan line results. It should also be mentioned that some of the variation is likely caused by the non-uniform size of the tetrahedral zones used to sample the stress magnitudes in the model.



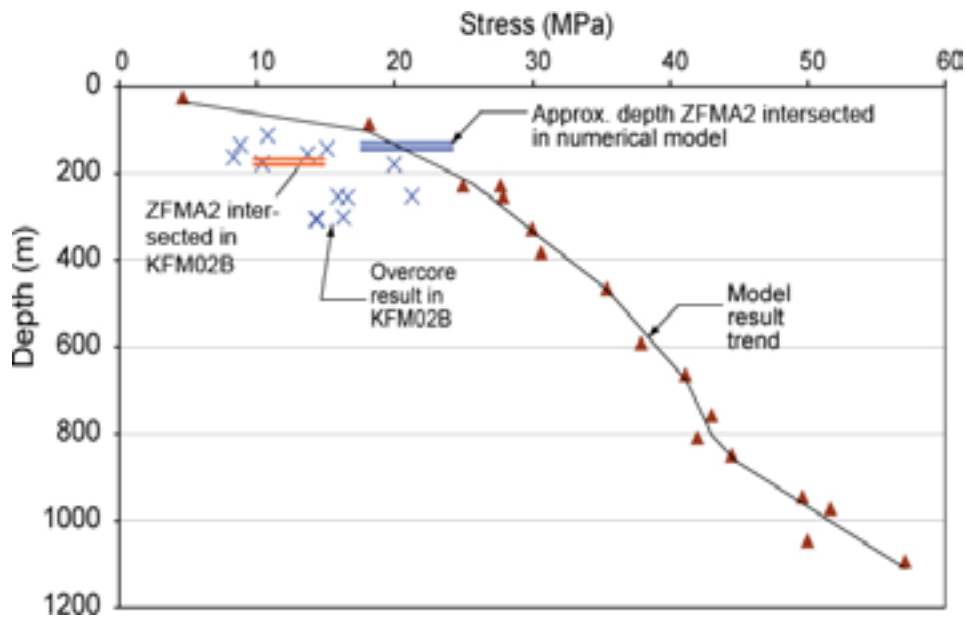
a) NW-SE scan line.



b) NE-SW scan line.

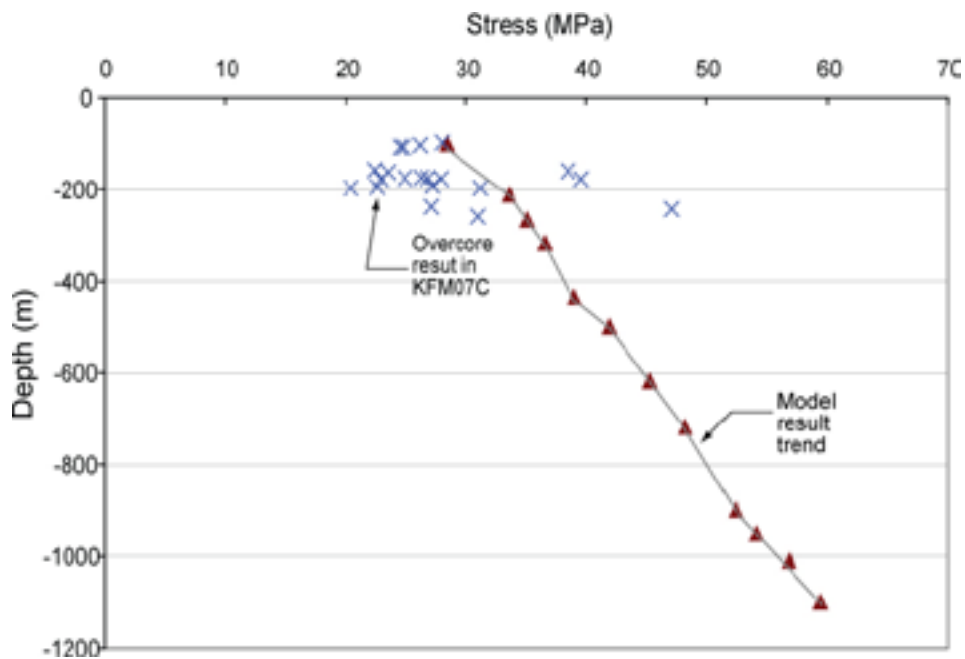
**Figure 6-28.** The variation of  $\sigma_1$  magnitudes along a NW-SE and NE-SW scan line at the depth of 500 m.

Figure 6-29 shows the variation in the magnitude of the major principal stress along a vertical scan line located near the borehole KFM02B. In situ stress measurements carried out in borehole KFM02B are also plotted in the figure for comparison. The vertical stress profiles clearly show a substantial change in stress magnitudes below deformation zone ZFMA2. The depths at which the numerical borehole and KFM02B cut through deformation zone ZFMA2 are marked on the figure. Plots showing the vertical variation in the magnitudes of  $\sigma_2$  and  $\sigma_3$ , close to borehole KFM02B, are given in Appendix 7.



**Figure 6-29.** The vertical variation of  $\sigma_1$  along a numerical scan line, in close proximity to borehole KFM02B, compared to the overcoring results from borehole KFM02B. The approximate depths where borehole KFM02B intersects the deformation zone ZFMA2 and the numerical scan line are also shown.

A second comparison was made between the principal stresses obtained numerically and those measured in borehole KFM07C. KFM07C is located towards the northwest portion of the target area. The results from this scan line should show the effect of the steeply dipping deformation zones. Figure 6-30 shows the vertical distribution of  $\sigma_1$  sampled from a numerical scan line in close vicinity to borehole KFM07C. The maximum principal stress from overcoring carried out in KFM07C is also shown in Figure 6-30. Plots showing the vertical variation of  $\sigma_2$  and  $\sigma_3$  along a scan line close to borehole KFM07C are given in Appendix 7.



**Figure 6-30.** Vertical distribution of  $\sigma_1$  along a scan line in the numerical model close to borehole KFM07C compared with the  $\sigma_1$  magnitudes from KFM07C overcoring results.

#### 6.4.4 Summary

A series of three dimensional 3DEC numerical models was carried out to assess the impact of the major deformation zones on the stress magnitudes within the target volume at the depth of the proposed repository. It must be remembered that the numerical simulations can only approximate the in situ conditions and geological history of the Forsmark Site. Numerical modelling requires striking a balance between the geological details of the site and the practical constraints of numerical modelling such as run time and model size limitations. Nonetheless the simplifications made to accomplish the modelling do not reduce the significance of the findings which can be summarised as follows:

1. The regional Forsmark and Singo faults do not significantly perturb the stresses in the target volume. Perturbation could locally increase in areas where a deformation zone bends and makes a larger angle with the applied boundary stress orientation, see /Mas Ivars and Hakami 2005/.
2. Significant perturbations of the stress field are caused by the gently dipping deformation zones, striking at a wide range of angles with respect to the orientation of the maximum horizontal stress. Deformation zone ZFMA2 is the most prominent gently dipping deformation zone in the target volume.
3. It appears that the two gently dipping deformation zones ZFMA2 and ZFMF1 are responsible for reducing the stress magnitudes above ZFMA2. Also, de-stressing in the model has clearly reached deeper levels compared with the NW-side of ZFMA2. The dominant mechanism behind the stress perturbation here is probably “unloading from the top” (uplifting) and not only due to shearing across the linked deformation zones.
4. In numerical analyses, the stress gradients with depth depend on the input parameters such as Poisson’s ratio, the rock mass modulus of elasticity and interaction of the geological structures with the inward movement due to the loading of the sidewalls. An approximate stress gradient of 0.029 MPa/m for  $\sigma_1$ , was determined from the numerical analyses for depths greater than 400 m. /Martin 2007/ suggested a stress gradient of 0.074 MPa/m between 150 m and 400 m and 0.023 MPa/m between 150 and 600 m depth. The difference in the predicted magnitudes of  $\sigma_1$  using either the numerical model stress gradient or the stress gradient proposed by /Martin 2007/ is practically negligible at the depth range of the repository.
5. Estimating the stress magnitudes near a free boundary is always problematic in a numerical model. No attempt was made in the model to represent the actual surface topography or the many near horizontal open fractures found in FFM02. Hence the stress magnitudes in the numerical models between 0 and 200 m depth are not considered representative of the actual in situ stresses.
6. The analyses for stages 1.2 and 2.1 used low friction angles, zero cohesion and zero tensile strength for the deformation zones. These “apparent properties” caused large shear displacements along the deformation zones. As a consequence the local perturbation of stress field in the vicinity of the deformation zones may be exaggerated. Nonetheless such exaggerations unambiguously reveal the areas for potential perturbations, small or large.

In the Forsmark 2.2 study, deformation zones were assigned more realistic properties. As a result a number of the deformation zones, which slipped in the previous models, did not reach a yield state resulting in less local stress perturbations.

#### 6.5 Evaluation of local stress spatial variability

The regional numerical model in Section 6.4 was used to assess the impact of the major deformation zones on the stress magnitudes within the target volume at the repository depth. In this section numerical models are used to evaluate the stress variability that could be expected from: (1) the decreasing fracture frequency with depth, and (2) fractures at a tunnel scale and depth of 450 m. These scenarios are discussed in the following sections.

### 6.5.1 Stress variability with depth due to varying modulus

At the Forsmark site it has been shown that the fracture frequency, i.e. rock mass quality, gradually improves below a depth of 100 m, see Section 6.2.3. It is well known that as fracture frequency decreases the rock mass deformation modulus increases. /Cartwright 1997/ showed how the deformation modulus could influence the in situ stress field in a rock mass. A two dimensional elastic finite element program was used to explore the effect of varying deformation modulus on the maximum horizontal in situ stress magnitude with depth.

The finite element model was constructed in the NW-SE orientation aligned with the general direction of the maximum horizontal stress. The Young's modulus values in the model were varied with depth and reflect the shear modulus profile given in Figure 6-7. A displacement boundary condition was applied until the stress magnitudes at the ground surface equalled the measured maximum horizontal stress magnitude of approximately 20 MPa. Figure 6-31 illustrates the model used to predict the maximum horizontal stress gradient with depth.

Figure 6-32 shows the comparison of the measured maximum horizontal stress magnitudes with stress gradients from the two-dimensional elastic finite element model. Also shown on Figure 6-32 is the mean maximum horizontal stress magnitude for the depth intervals: 0–150 m, 150–300 m, 300–400 m and 400–500 m. The predicted stress magnitudes are in reasonable agreement with the measured data. It should be noted that the Young's modulus values in the finite element model were not optimised to force agreement with the measured data. Optimisation was not attempted at this stage since the seismic profile needs re-evaluating as additional data is now available since the profile was published in 2002.

The results from the relatively simple finite element model illustrate that as the rock mass quality improves with depth the increase in stress magnitudes should reflect this improvement.

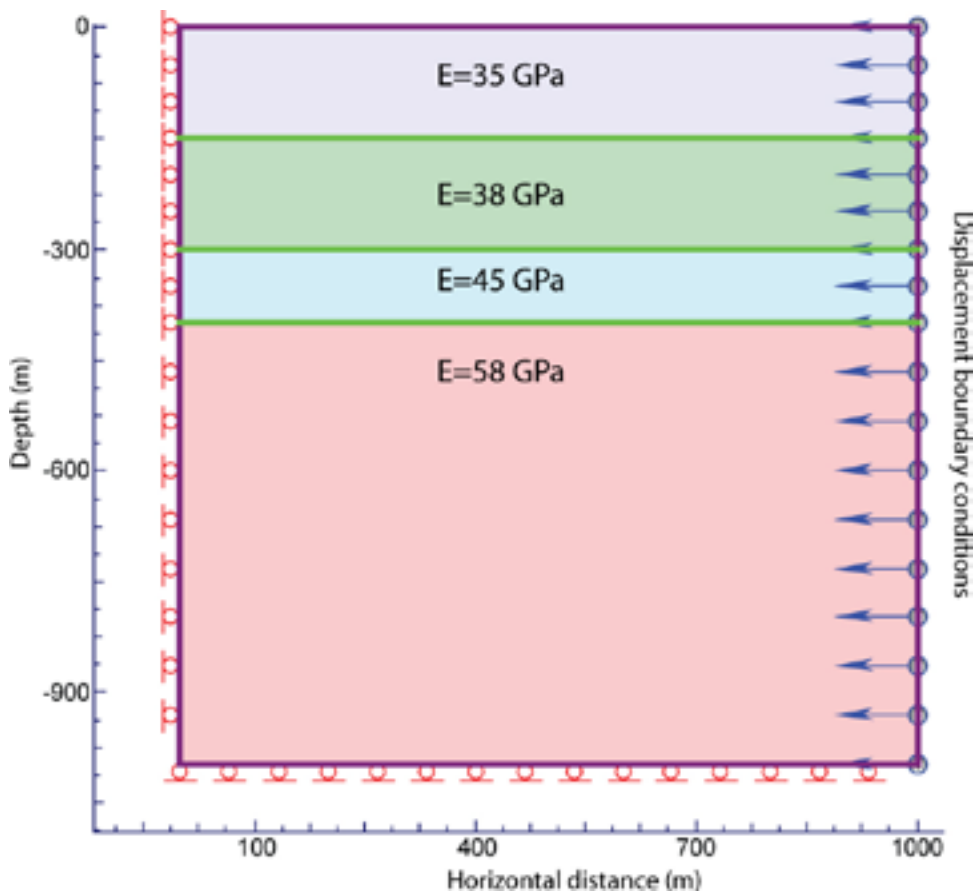
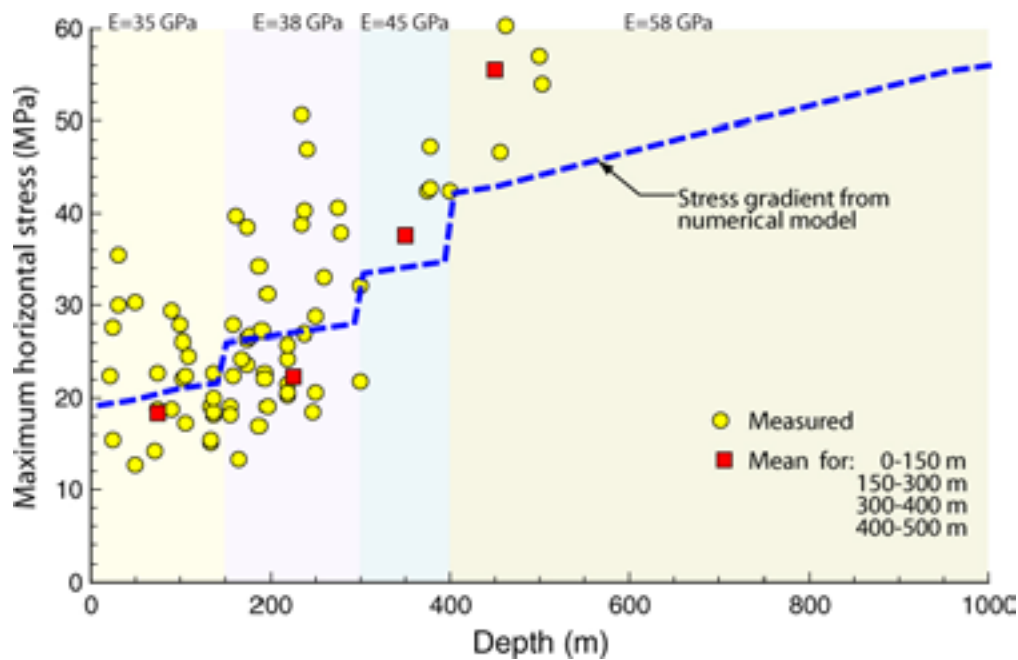


Figure 6-31. The Young's modulus used in the two dimensional finite element numerical model.





*Figure 6-32. Comparison of the maximum horizontal stress from the overcoring measurements with the stress gradient from the two dimensional finite element model.*

### 6.5.2 Stress variability due to discrete fractures

The potential variation in magnitude of the principal stresses, at the scale of a 5-m-diameter deposition tunnel, was examined by applying the mean principal stresses at repository depth to a 3DEC model containing a discrete fracture network model. The methodology used in these analyses is similar to that given in Section 5.2. A 20 m × 20 m × 1 m plane strain block model was populated with fractures based on DFN-model representing the “Tectonic Continuum model” described by /Fox et al. 2007/. The sides of the box were parallel with the principal stresses. The fractures and the intact rock in this 3DEC model were given mean properties described in Section 3 and 4. The mean principal stresses were applied to the boundaries of the model and the program was iterated to equilibrium.

The 3DEC model was divided into approximately 560 intact rock blocks. The mesh generated in these blocks produced some 15,000 sampling points equating to a sampling volume of approximately 0.03 m<sup>3</sup>. This volume is approximately the same as that associated with an overcoring test (0.01–0.08 m<sup>3</sup>). Hence, the variability in magnitude and orientation at these sampling points (see Figure 6-33 and Figure 6-34) is approximately what could be expected from overcore stress measurements in FFM01. The variation in the stress magnitudes and orientations is attributed to stress perturbations caused by the discrete fractures in the sampled volume.

Figure 6-33 and Figure 6-34 show the variation in magnitude and orientation of the major principal stress due to the discrete fractures at 400–500 m depth in the 3DEC model. The variation in magnitudes and orientation for all three principal stresses are presented in Table 6-5 and Table 6-6. The analyses indicate that for the rock mass conditions expected at Forsmark  $\sigma_1$  obtained from overcore tests, could be expected to vary spatially by  $\pm 5$  MPa in magnitude and  $\pm 9$  degrees in orientation. /Martin et al. 1990/ clearly showed that as the sampling volume increased from a 96-mm-diameter overcoring test to the tunnel scale, the mean stress remained relatively constant while the variability in the magnitudes decreased dramatically. Hence, the variability in the stress magnitudes and orientations from this 3DEC simulation, is considered an upper bound for the Forsmark rock mass, at the repository depth containing a discrete fracture network.

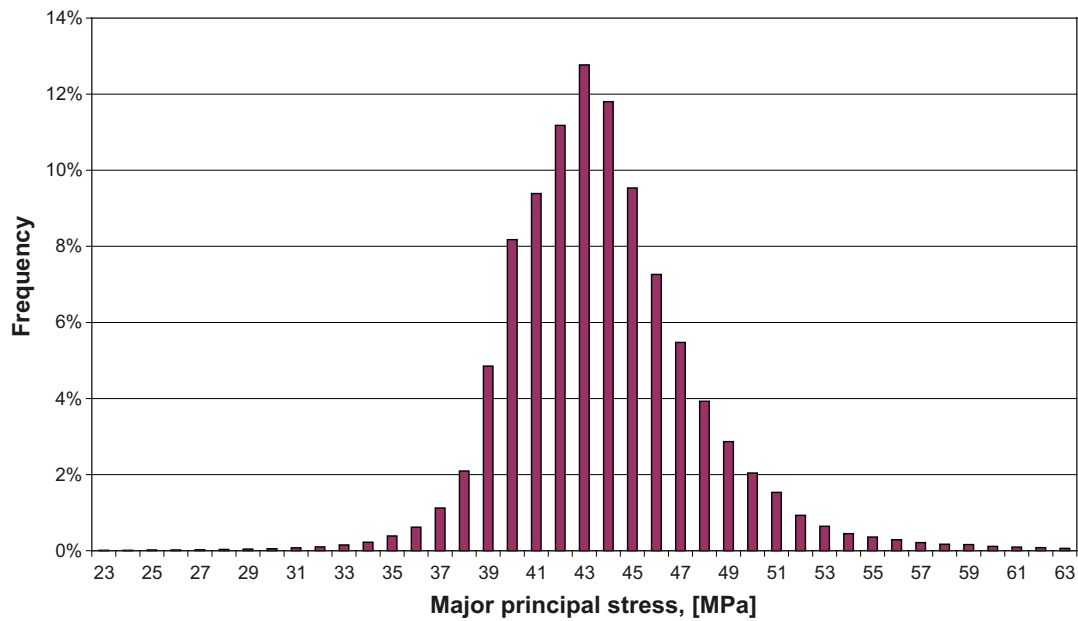


Figure 6-33. Variation of the major principal stress in the zones of the model.

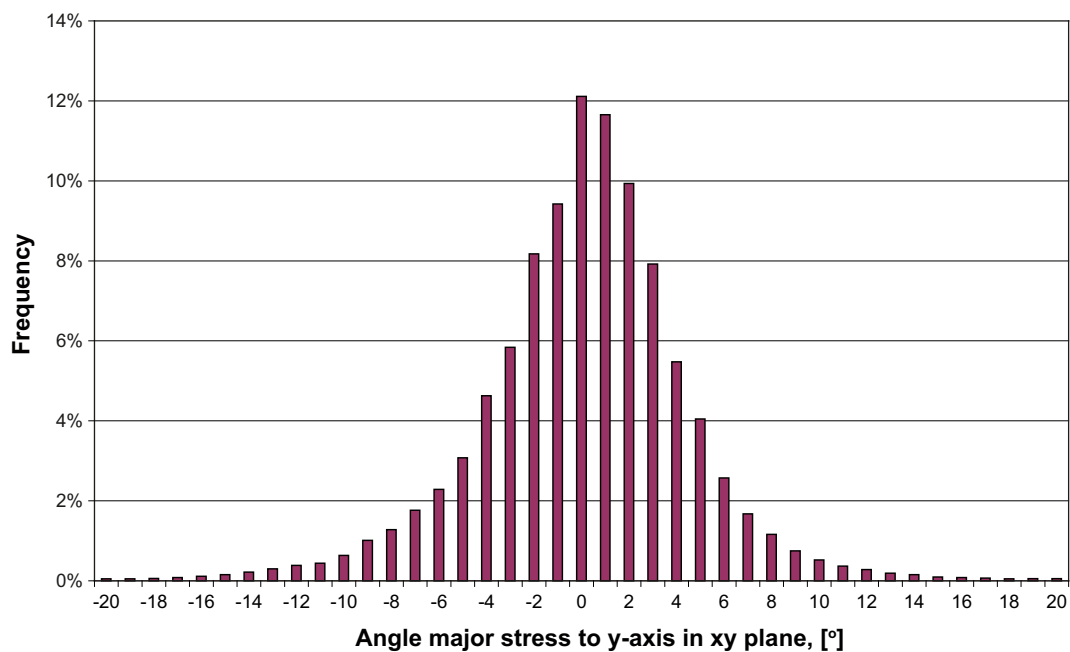


Figure 6-34. Variation in orientation of the major principal stress in the zones of the model.

Table 6-5. Summary of the results regarding variation in magnitude of the principal stresses.

Principal stress component	Mean magnitude (MPa)	Standard deviation (MPa)
$\sigma_1$	40.4	3.2
$\sigma_2$	28.1	2.1
$\sigma_3$	15.8	2.1

**Table 6-6. Summary of the results regarding variation in orientation of the principal stresses in relation to applied boundary stresses.**

Principal stress component	Mean orientation (°)	Standard deviation (°)
$\sigma_1$ – y-axis in xy plane	-0.5	5.6
$\sigma_2$ – x-axis in xy plane	0.3	5.5
$\sigma_1$ – y-axis in yz plane	0.1	3.5
$\sigma_3$ – z-axis in yz plane	-0.3	3.9
$\sigma_2$ – x-axis in xz plane	0.3	4.5
$\sigma_3$ – z-axis in xz plane	-0.2	4.5

## 6.6 Assessment of in situ stress state at repository depth

The results from in situ stress measurements may contain both systematic and/or non-systematic errors, and variability related to the state of stress. It is difficult, if not impossible, to quantify and separate the errors from the variability by simply analysing the measurement data. Yet, it may be important to distinguish the two components contributing to the results. The following example illuminates the situation and defines the terms used in this section.

Assume that the actual value of the major horizontal stress, at a particular depth in a fracture domain, is 30 MPa for a block of rock that is 20 m × 20 m × 20 m. If the small scale measurements within the block contained no errors only the spatial variability would be observed in the data. This expected small scale spatial variation would be caused by local fractures and material heterogeneity and is denoted *local scale variability*. Simply averaging that data would recover the actual value of ~ 30 MPa and the spatial variability could be quantified using statistics appropriate for 2<sup>nd</sup> order stress tensors. However, we know from the analysis by /Martin 2007/ that there are systematic and non systematic errors associated with the data that are difficult to quantify. Hence the interpretation of the measured data is expressed as the most likely value for  $\sigma_H$  and it may or may not be 30 MPa. If we know the fracture frequency we can estimate part of the *local scale variability* attributed to the fractures using the approach discussed in Section 6.5.2. However, this still does not account for material heterogeneity. As shown in Section 6.5.2 this local scale variability caused by the discrete fracture network is relatively small. But of course estimating this local scale variability using this approach assumes that the discrete fracture network which is developed from widely spaced boreholes is appropriate for the 20 m cube at depth.

The most likely values given in Table 6-7 to 6-10 were established by /Martin 2007/ using the data integration methodology illustrated in Figure 6-35. There is no doubt that these most likely values contain uncertainty. In addition to large-scale spatial variability, local scale variability and systematic and non systematic errors, there are also only limited measurement data that decreases with depth. However, experience and measurements from underground excavations in crystalline rock have shown that as the rock mass quality improves the spatial variability in in situ stress decreases. In addition, the errors in magnitude cannot be so large that there is a potential swapping of  $\sigma_2$  and  $\sigma_1$ , because the orientation of the maximum stress is well constrained at Forsmark. So there is additional information that reduces the uncertainty in the most likely values. The approach used to constrain the uncertainty in the stress magnitudes at the repository depth (450–500 m) is discussed below.

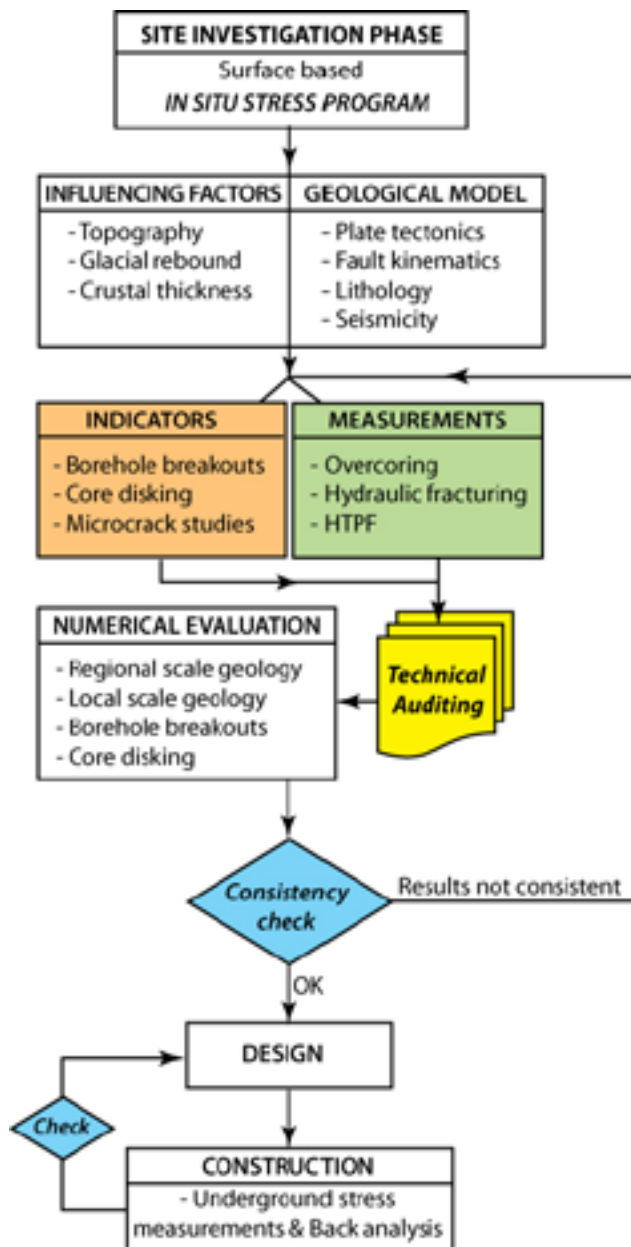
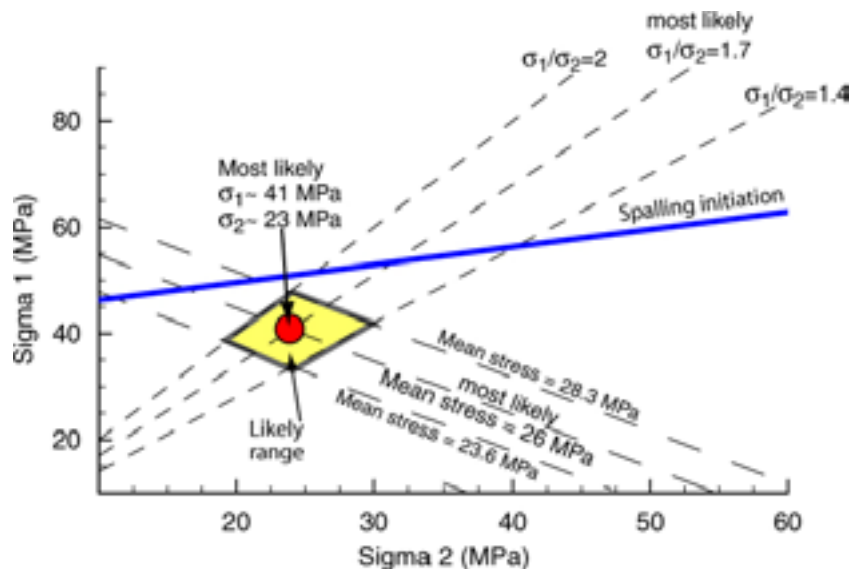


Figure 6-35. Flow chart illustrating the data integration methodology used by /Martin 2007/ to reduce uncertainty and establish the most likely stress magnitudes and orientations.

### 6.6.1 Uncertainty and spatial variability in the stress model

The methodology developed by /Martin 2007/ to evaluate the stress magnitudes at Forsmark is a function of the mean stress magnitude ( $M$ ) and the  $\sigma_1/\sigma_2$  ratio ( $R$ ). It was further constrained by keeping the tangential stress magnitude ( $3\sigma_1 - \sigma_2$ ) below the limit for spalling around a circular vertical borehole, since spalling was not observed in the site investigation boreholes at depths of 1,000 m. Martin showed that the stress magnitudes were reasonably well constrained using this methodology (Figure 6-36). Inspection of Figure 6-36 shows that in order for  $\sigma_1$  to be significantly higher than 41 MPa,  $\sigma_2$  would have to be significantly higher than 23 MPa. The hydraulic fracturing data which should provide  $\sigma_2$  was rejected because it gave values lower than the overcoring data. Hence, the possibility that  $\sigma_2$  should be higher than the value given here is not supported by any data. Alternatively, it could be suggested that the  $\sigma_1/\sigma_2$  ratio should be greater than 1.7. /Martin 2007/ compiled  $\sigma_1/\sigma_2$  ratios for various countries and sites and found that the ratio ranged from 1.25 to 2.0. Hence a  $\sigma_1/\sigma_2 > 2$  seems unlikely.



**Figure 6-36.** The likely range in Sigma 1 (Maximum horizontal stress) and Sigma 2 (Minimum horizontal stress) stress magnitudes for 500 m depth from /Martin 2007/.

In addition the stage 2.2 regional 3DEC numerical modelling discussed in Section 6.4 was used to evaluate the  $\sigma_1/\sigma_2$  (maximum horizontal/minimum horizontal) stress ratio that developed in the model. In the 3DEC model no stress ratios are specified, gravity is imposed and model boundaries are displaced (compressed) in one direction, while the other boundary remains fixed. The compression is stopped once the maximum horizontal stress in the model approaches the measured values from the stress measurement campaigns. Because most of the measurements were recorded above 300 m depth, there is no match with repository depth and there was no attempt to match the stress ratios. The minimum horizontal stress that develops using this modelling approach is a function of the friction free boundary used to represent the ground surface; Poisson's ratio; displacements along the regional and local deformation zones; and the properties of the rock mass and deformation zones. Figure 6-37 shows the ratio of the maximum horizontal to the minimum horizontal stress from a scan line in the 3DEC numerical model close to KFM07C. The stress ratio shows a general decrease in horizontal stress ratio that is consistent with trends in stress measurements /Brown and Hoek 1978/. Hence the horizontal stress ratios are also well constrained.

The uncertainty in the mean stress was constrained by the limit for the initiation for spalling. The spalling limit used by /Martin 2007/ to constrain the upper bound for the stress magnitudes was based on the results back calculated by /Andersson 2007/ for a full scale vertical deposition hole (1.8 m diameter) in crystalline rock. This in situ spalling limit was given by /Andersson 2007/ as  $0.58\% \pm 4\%$  of the laboratory uniaxial compressive strength. Hence the magnitude for this upper bound is also reasonably well constrained.

### 6.6.2 Proposed in situ stress models

The in situ stress state at Forsmark has been evaluated by stress measurements, indirect methods and by numerical analysis based on the current geological model. All results suggest that at the repository level the magnitudes and orientations are expected to be relatively consistent over the repository footprint and that the Azimuth of the maximum horizontal stress is expected to vary between 130 and 160 degrees. However, despite this confidence there is uncertainty in the stress magnitudes, particularly the horizontal stress magnitudes. Table 6-2 highlighted two stress models for Forsmark, one based on overcoring and indirect data, and the other based on hydraulic fracturing data. While there is uncertainty in both models, the stress model based on the overcoring data and indirect measurements is more consistent with the geological understanding of the site, and the general understanding of in situ stresses in the Fennoscandian Shield.

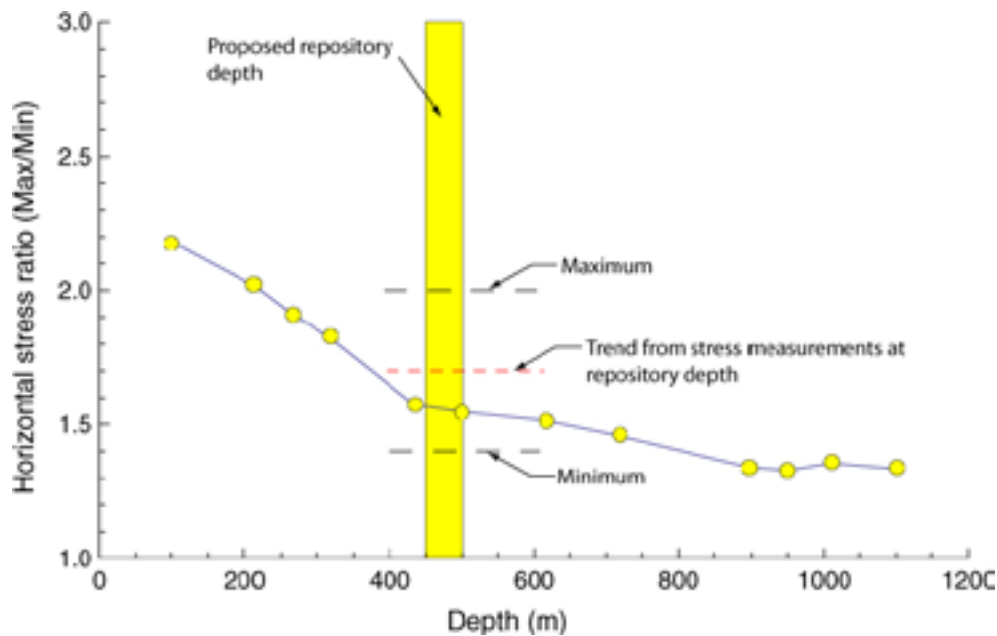


**Figure 6-37.** Horizontal stress ratio captured from the 3DEC numerical model stage 2.2, near borehole KFM07C. See Figure 6-30 for the  $\sigma_1$  values. The minimum and maximum lines represent the limits used in Figure 6-36 to establish the most likely range in Maximum and Minimum Horizontal stress.

The stress model for Forsmark is described in Table 6-7 to Table 6-10 for fracture domains FFM01, FFM02, FFM03 and FFM06. While no stress measurements were carried out in FFM06 it is expected to have a similar in situ stress state as FFM01 since it consists of a rock mass with similar stiffness properties and is located next to FFM01 below deformation zone ZFMA2 (Figure 2-9). The in situ stress gradient for fracture domain FFM03 is based primarily on the measurements in KFM02 and the numerical modelling results. The uncertainty in the estimation of the most likely stress value and expected uncertainty attributed to the local variability are also given in Table 6-7 to Table 6-10.

The term “most likely value” in Table 6-7 to Table 6-10 is preferred over the term “mean value”, as referring to a mean value implies a formal mathematical procedure to arrive at the mean value. As stated previously the “most likely value” was determined using the approach described in the flow chart in Figure 6-35. The “estimated uncertainty” in Tables 6-7 to 6-10 reflects the total uncertainty in the “most likely value” and it too was assessed in the same manner as the “most likely value”. The “uncertainty due to local variability” was assessed using the numerical modelling results discussed in Section 6.5.2. This “uncertainty due to local variability” is included in the “estimated uncertainty”.

**Table 6-7. Stress model for domains FFM01 and FFM06, ca 150–400 m.**

Parameter	Most likely value	Estimated uncertainty <sup>2</sup>	Uncertainty due to local variability
<b>Magnitude</b>			
Major horizontal stress, $\sigma_H$	$9.1 + 0.074z$ MPa	$\pm 15\%$	4%
Minor horizontal stress, $\sigma_h$	$6.8 + 0.034z$ MPa	$\pm 25\%$ <sup>1</sup>	6%
Vertical stress, $\sigma_v$	$0.0265z$ MPa	$\pm 2\%$	4%
<b>Orientation</b>			
Major horizontal stress trend, $\sigma_H$	145°	$\pm 15^\circ$	$\pm 3^\circ$

<sup>1</sup> The uncertainty in  $\sigma_h$  is correlated to uncertainty in  $\sigma_H$ . The ratio  $\sigma_H/\sigma_h$  at the depth of the repository range between 1.4 and 2.0 (i.e. other combinations are not expected).

<sup>2</sup> The “uncertainty due to local variability” is included in the “estimated uncertainty”.

**Table 6-8. Stress model for domains FFM01 and FFM06, 400–600 m.**

	Most likely value	Estimated uncertainty <sup>2</sup>	Uncertainty due to local variability
<b>Magnitude</b>			
Major horizontal stress, $\sigma_H$	29.5 + 0.023z MPa	± 15%	4%
Minor horizontal stress, $\sigma_h$	9.2 + 0.028z MPa	± 20% <sup>1</sup>	6%
Vertical stress, $\sigma_v$	0.0265z MPa	± 2%	–
<b>Orientation</b>			
Major horizontal stress trend, $\sigma_H$	145°	± 15°	± 3°

<sup>1</sup> The uncertainty in  $\sigma_h$  is correlated to uncertainty in  $\sigma_H$ . The ratio  $\sigma_H/\sigma_h$  at the depth of the repository range between 1.4 and 2.0 (i.e. other combinations are not expected).

<sup>2</sup> The “uncertainty due to local variability” is included in the “estimated uncertainty”.

**Table 6-9. Stress model for domain FFM02, 0 – ca 150 m.**

	Most likely value	Estimated uncertainty <sup>2</sup>	Uncertainty due to local variability
<b>Magnitude</b>			
Major horizontal stress, $\sigma_H$	19 + 0.008z MPa	± 20%	8%
Minor horizontal stress, $\sigma_h$	11 + 0.006z MPa	± 25% <sup>1</sup>	12%
Vertical stress, $\sigma_v$	0.0265z MPa	± 10%	4%
<b>Orientation</b>			
Major horizontal stress trend, $\sigma_H$	145°	± 15°	± 6°

<sup>1</sup> The uncertainty in  $\sigma_h$  is correlated to uncertainty in  $\sigma_H$ . The ratio  $\sigma_H/\sigma_h$  at the depth of the repository range between 1.4 and 2.0 (i.e. other combinations are not expected).

<sup>2</sup> The “uncertainty due to local variability” is included in the “estimated uncertainty”.

**Table 6-10. Stress model for domain FFM03.**

	Most likely value	Estimated uncertainty <sup>2</sup>	Uncertainty due to local variability
<b>Magnitude</b>			
Major horizontal stress, $\sigma_H$	5 + 0.075z MPa	± 20%	8%
Minor horizontal stress, $\sigma_h$	2.5 + 0.0375z MPa	± 25% <sup>1</sup>	12%
Vertical stress, $\sigma_v$	0.0265z MPa	± 10%	4%
<b>Orientation</b>			
Major horizontal stress trend, $\sigma_H$	145°	± 15°	± 6°

<sup>1</sup> The uncertainty in  $\sigma_h$  is correlated to uncertainty in  $\sigma_H$ . The ratio  $\sigma_H/\sigma_h$  at the depth of the repository range between 1.4 and 2.0 (i.e. other combinations are not expected).

<sup>2</sup> The “uncertainty due to local variability” is included in the “estimated uncertainty”.

## 7 Summary of the rock mechanics model

### 7.1 Intact rock properties

The results of the dominant rock type and tested subordinate rock type within fracture domain FFM01 and FFM06 show high values of compressive strength. The uniaxial compressive strength of the dominant rock type within FFM01 ranged between 157 and 289 MPa with a mean value of 226 MPa. The uniaxial compressive strength of the dominant rock type within fracture domain FFM06 ranged between 229 and 371 MPa with a mean value of 320 MPa. While fewer samples from FFM06 were tested the results clearly show a significant strength increase.

The tensile strength, based on indirect tests of the dominant rock type within fracture domain FFM01, ranged between 10 and 18 MPa with a mean of 13 MPa. As expected, direct tensile tests on the same rock type showed lower values. The ratio between the mean direct and mean indirect tensile strength was 0.6. No samples were tested from FFM06.

A difference of 1 MPa between indirect tensile tests carried out perpendicular and parallel to the foliation indicates essentially isotropic rock conditions in the target volume.

The Young's modulus of the dominant rock type within fracture domain FFM01 ranged between 69 and 83 MPa with a mean of 76 MPa. The Young's modulus of the dominant rock type within fracture domain FFM06 ranged between 80 and 86 MPa with a mean of 82 MPa. Again, the limited sampling in FFM06 may impact the range in the values reported.

The laboratory results on samples inside or in the vicinity of deformation zones are in the same range as the results on samples taken in the host rock outside deformation zones. The results are in accordance with the geological description of the deformation zones being composed of mainly sealed fractures.

The uniaxial compressive strength, the indirect tensile strength and Young's modulus for the dominant rock type all display a slight decrease in the values with depth. The decrease in these values with depth is assumed to be related to an increasing volume of microcracks in the samples. The release of rock stresses may create a larger volume of microcracks in the samples with depth. Support for the proposed explanation is provided by the microcrack volume measurements and the P-wave measurements on laboratory samples.

The estimated microcrack volume for samples of the main rock type indicates that the microcracking due to stress relaxation and mechanical effects during the drilling corresponds to 5–10% of the measured mean porosity.

### 7.2 Fracture properties

Based on a large number of direct shear tests within fracture domain FFM01, the mean peak friction angle was  $37^\circ$ , the mean peak cohesion 0.8 MPa and the mean normal stiffness 656 GPa/m. The shear stiffness and dilation angle that are dependent on the normal stress were determined to be 34 GP/m and  $3.2^\circ$  for a normal stress of 20 MPa.

Samples from the adjacent domains FFM02, FFM03, FFM04 and FFM05 on the whole show similar results as for FFM01. The same is also true for the samples examined from the deformation zones. The differences that exist chiefly concern the normal stiffness that is less in fracture domain FFM02 and FFM03, and higher in fracture domain FFM04.



Comparisons with the results obtained from tilt tests show a slightly higher peak cohesion and peak friction angle from the direct shear tests. For design and safety assessments it is recommended to use the values from the direct shear tests since they are based on direct measurements with a stress magnitude comparable to what is expected to be found at the tentative repository depth in the Forsmark target volume.

The results for sealed fractures are similar to those of open fractures excepting the peak friction angle and peak cohesion that are larger for sealed fractures ( $\phi_p = 52.6^\circ$  and  $c_p = 4.1$  MPa).

Depth dependence was examined and it is difficult to see any clear trends, except for the friction angle from the tilt tests on samples within fracture domain FFM02, that seem to be smaller than in other domains.

It should be noted that the large-scale mechanical properties of fractures are expected to deviate from the results reported here on small specimens. Most likely the shear strength of the large-scale fractures will be reduced as compared to the results from the tested samples. There is also a possibility that the large-scale fractures will show differences between the fracture sets, although the differences in the small scale were insignificant.

### 7.3 Rock mass properties

The rock mass quality in the target volume appears to be of high and uniform quality. The rock mass quality is classified as “good” to “very good” with minor occurrence of “fair” rock quality and rare occurrence of sections with “poor” rock. The portions with reduced rock mass quality are in the main related to sections with increased fracture frequency.

The rock mass strength and deformation properties estimated from the empirical approach were in reasonable agreement with the strength and deformation properties estimated using the theoretical (numerical modelling) approach. Fracture domains FFM01 and FFM06, which show the highest rock mass quality of the examined domains, have almost equal evaluated mechanical properties. The higher fracture density in FFM06 is compensated for by higher strength and deformation modulus of the intact rock compared to FFM01. The rock mass compressive strength is predicted as a mean of 92 MPa in fracture domain FFM01 and 95 MPa in fracture domain FFM06. The deformation modulus was assessed as a mean value of 70 GPa in FFM01 and a mean value of 69 GPa in FFM06.

Adjacent rock domains and fracture domains of the target volume were only analysed by the empirical approach. The results show that all rock domains covered by the analysis have rock of good competent quality. Rock domain RFM017 has the lowest estimate of the compressive strength with a mean value 46 MPa. The lowest estimate of the deformation modulus is for rock domain RFM018.

The theoretical analyses of the rock mass properties, in directions parallel and perpendicular to the major principal stress, result in almost the same parameter values for strength and deformation properties. This indicates that the rock mass in the target volume is isotropic.

The empirically evaluated compressive strength and deformation modulus for rock in fracture domain FFM02 is very close to the mean values estimated for deformation zones. The estimated strength and deformation modulus for rock in fracture domain FFM03 falls between FFM01 and FFM02.

The rock mass deformation modulus has in the empirical approach been estimated based on the relationship developed by /Serafim and Pereira 1983/. The equation is based on the analyses of a number of case histories, mostly shallow depth facilities such as dam foundations, for which the deformation modulus was evaluated by back analysis of measured deformation /Hoek et al. 1995/. In the application of the formula using data from Forsmark, the formula has a cut-off at the value of the intact rock, which results in an unequal distribution of Young's modulus

around the mean. It should also be noted that most of the projects included in the database are of rock masses that had a quality corresponding to  $RMR < 75$ . The applicability of the equation to a repository constructed in a massive, high quality rock mass of  $RMR > 75$ , at 500 m depth, is consequently somewhat uncertain and it is likely that the estimated Young's modulus of the rock mass is somewhat over estimated.

The mechanical properties of the deformation zones were evaluated in an isotropic manner in the empirical approach and in an anisotropic manner in the theoretical approach. This means that the results from the two approaches are not fully comparable. It is therefore recommended that users who apply the results evaluated for the deformation zones should consider which one of the two approaches is the most appropriate for the case being analysed.

The empirical estimate of mechanical properties of the deformation zones provided no clear correlation between characteristics such as orientation or thickness of the zones. However, the gently dipping zones tend to have somewhat lower compressive strength and deformation moduli than the steeply dipping zones. The evaluated mechanical properties of the deterministic deformation zones are on the whole relatively close to the properties evaluated for the fracture domains.

## 7.4 In situ state of stress

Both direct and indirect measurements of the in situ stresses end up with a stable and constant orientation of the major horizontal stress in NW-SE direction. The orientation determined by the overcoring data was given most weight and a mean of  $145^\circ$  for the major horizontal stress was chosen in the final model.

The evaluated orientation of the major horizontal stress is sub-parallel to the Singö and Forsmark deformation zones. The orientation is also sub-parallel with the expected direction of the plate movements in Scandinavia.

Compared to the major horizontal stress, there is a larger spread in the orientation for the minor horizontal stress. The relatively smaller difference in magnitude between intermediate and minor stress is presumed to cause the larger spread.

The proposed stress model establishes separate functions of the stress gradient in respective fracture domains. Fracture domains FFM01 and FFM06 are presumed to have the same gradient, since FFM06 is located next to FFM01, below deformation zone ZFMA2, with similar rock mass properties.

The stress gradient in fracture domains FFM01 and FFM06 consists of a bilinear function with a breakpoint in the gradient at 400 m depth. The gradient above 400 m depth is based on overcoring measurements, whereas the gradient below is based on indirect observations of the stress magnitude. The magnitude at 1,000 m depth is determined by the expected upper stress limit that results from the lack of observed borehole breakouts. The choice of depth for the breakpoint in the gradient is somewhat arbitrary, which naturally may have an influence of the estimation at 500 m depth.

The adopted model results in a mean magnitude of the major horizontal stress of around 41 MPa and of the minor horizontal stress around 23 MPa for 500 m depth in FFM01. Compared to previous model versions, the present estimate corresponds to a slight reduction in magnitudes.

According to the numerical results the stress field in the target volume seems to be relatively homogeneous. The steeply dipping deformation zones cause very limited perturbation of the stress field. It is mainly the gently dipping deformation zone ZFMA2 that seems to have importance for the stress field in the target volume. However, the spatial extension of the disturbance caused by this zone is also limited.

Numerical models were used to evaluate the local stress spatial variability due to discrete fractures. The results illustrate that an improvement in rock mass quality is reflected by an increased in situ stress magnitude. Furthermore, for the rock mass conditions at Forsmark the major principal stress could be expected to vary spatially by  $\pm 5$  MPa in magnitude and  $\pm 9$  degrees in orientation.

## 7.5 Overall confidence

The number of tests within fracture domain FFM01 is much larger than for FFM06. This fact makes the confidence of the results for FFM06 larger than for FFM01.

For the dominant rock type the uncertainty of the mean values is small for both the mechanical properties of the intact rock and of the rock mass. This fact indicates homogeneous conditions in the target volume. Homogeneous conditions in this volume are also supported by the lithological model and the hydro-geological model.

The changes in the laboratory results between the modelling steps performed up to now, i.e. version 1.2, stage 2.1 and stage 2.2, are small in the target volume. This holds true both regarding the intact rock and the fractures that have been tested. In a similar way the evaluated difference in the mechanical properties, based on the empirical model, is insignificant despite a large increase in the analysed borehole length. This fact indicates that the evaluated mean values are representative and that the test data are sufficient in the target volume.

The mechanical properties of the rock mass in fracture domains FFM01 and FFM06, the orientation of in situ stresses and the magnitude of the vertical stress component are the aspects of the model that are judged to have highest confidence. With respect to the mechanical properties of the rock mass, the main reason for the confidence in the model is consistency between model versions, wealth of data and support from other disciplines. The basis for the confidence in the in situ stress orientation is the conformity in the results between measuring methods and indirect observations at different scales. Finally, the confidence in the vertical stress component is founded on the concordance between measured values and theoretical values based on the weight of the overlying rock cover.

Lowest confidence is given to the large-scale mechanical properties of the fractures and the magnitude of the horizontal stress component.

## 8 Conclusions

The work carried out during modelling stage 2.2 has increased the understanding of the Forsmark site and at the same time strengthened the confidence in the rock mechanical model. Thanks to an increased quantity of data the confidence in the rock mechanics properties, especially in the target volume, have increased compared to previous model versions. Furthermore, the confidence in the in situ state of stress has been increased by means of indirect observation of the stress field and further stress modelling.

The small change in rock mechanics properties compared to previous model versions, despite a large increase in number of samples and analysed borehole sections, indicates that the evaluated mean values are representative and that the test data are sufficient in the target volume.

The conformity in the results between indirect observations and direct stress measurements at different scales forms the basis for high confidence in the in situ stress orientation. An upper boundary of the magnitude of the maximum horizontal stress has been developed from the observed lack of stress-induced damage in drill cores and boreholes down to a depth of 1,000 m. The magnitude of the minor horizontal stress was estimated based on the measured ratio between the major and intermediate principal stress. These ratios were confirmed using three dimensional numerical models. The magnitude of the vertical stress component was measured using hydraulic fracturing and it was found to be equivalent to the calculated weight of the overburden.

## 9 References

- Andersson J, Ström A, Svemar C, Almén K-E, Ericsson L-O, 2000.** What requirements does the KBS-3 repository make on the host rock? Geoscientific suitability indicators and criteria for siting and site evaluation. SKB TR-00-12, Svensk Kärnbränslehantering AB.
- Andersson J, Christiansson R, Hudson J, 2002.** Site investigations. Strategy for Rock Mechanics Site Descriptive Model. SKB TR-02-01, Svensk Kärnbränslehantering AB.
- Andersson A C, 2007.** Äspö Pillar Stability Experiment. Rock mass response to coupled mechanical thermal loading. Ph.D. thesis, Royal institute of Technology, KTH, Stockholm.
- Ask D, Cornet F, Fontbonne F, Brunet C, 2007.** Forsmark site investigation. The state of stress at Forsmark site using hydraulic stress determination methods. SKB R-07-XX, Svensk Kärnbränslehantering AB.
- Back P-E, Wrafter J, Rosén L, Sundberg J, 2007.** Thermal properties. Site descriptive modelling Forsmark Stage 2.2. SKB R -07-XX, Svensk Kärnbränslehantering AB.
- Bandis S, 1980.** Experimental studies of scale effects on shear strength, and deformation of rock joints. Ph.D. thesis, University of Leeds.
- Barton N, Bandis S, 1982.** Effects of block size on the shear behaviour of jointed rock. 23<sup>rd</sup> U.S. symp. On rock mechanics, Berkeley pp. 739–760.
- Barton N, Bandis S, 1990.** Review of predictive capabilities of JRC-JCS model in engineering practice. In Rock joints, proc. Int. symp. On rock joints, Loen, Norway, p. 603–610. Balkema.
- Barton N, 2002.** Some new Q-value correlations to assist in site characterization and tunnel design. International Journal of Rock Mechanics & Mining Sciences 39, p. 185–216. Pergamon.
- Bieniawski Z T, 1989.** Engineering rock mass classifications. John Wiley & Sons.
- Brantberger M, Zetterqvist A, Arnbjerg-Nielsen T, Olsson T, Outters N, Syrjänen P, 2006.** Final repository for spent nuclear fuel. Underground design Forsmark, Layout D1. SKB R-06-34, Svensk Kärnbränslehantering AB.
- Brown E T, Hoek E, 1978.** Trends in relationships between measured and in situ stresses and depth. International Journal Rock Mechanics Mining Science & Geomechanics Abstracts, 15:211–215.
- Bäckström A, Lanaro F, 2007.** Forsmark modeling stage 2.2. Rock mechanics characterization of borehole KFM01B, KFM07C, KFM09A and KFM09B. SKB P-07-115, Svensk Kärnbränslehantering AB.
- Cameron-Clarke I S, Budavari S, 1981.** Correlation of rock mass classification parameters obtained from borecore an in-situ observation, Int. J. Eng. Geo., vol. 17, pp. 19–53.
- Cartwright P B, 1997.** A review of recent in-situ stress measurements in United Kingdom coal measures strata. In Proc. Int. Symp. On Rock Stress, Kumamoto, pp. 469–474, A A Balkema, Rotterdam.
- Doe T W, Zieger M, Enachescu C, Böhner J, 2006.** In-situ stress measurements in exploratory boreholes. Felsbau, 24(4):39–47.

**Evans K, Engelder T, 1989.** Some problems in estimating horizontal stress magnitude in thrust regimes. *International Journal Rock Mechanics Mining Science & Geomechanics Abstracts* 26(6):647–660.

**Follin S, Levén J, Hartley L, Jackson P, Joyce S, Roberts D, Swift B, 2007.** Hydrogeological characterisation and modelling of deformation zones and fracture domains in Forsmark, stage 2.2. SKB R-07-48, Svensk Kärnbränslehantering AB.

**Fox A, La Pointe P, Hermanson J, Öhmna J, 2007.** Statistical geological discrete fracture network model for the Forsmark site – stage 2.2. SKB R-07-46, Svensk Kärnbränslehantering AB.

**Fredriksson A, Olofsson I, 2005.** Rock mechanics site descriptive model – theoretical approach. Preliminary site description Forsmark area – version 1.2. SKB R-05-22, Svensk Kärnbränslehantering AB.

**Fälth B, Hökmark H, 2006.** Seismically induced slip on rock fractures. Results from dynamic discrete fracture modeling. SKB R-06-48, Svensk Kärnbränslehantering AB.

**Glamheden R, Hansen L M, Fredriksson A, Bergkvist L, Markström I, Elfström M, 2007.** Mechanical modelling of the Singö deformation zone. Site descriptive modelling Forsmark stage 2.1. SKB R-07-06, Svensk Kärnbränslehantering AB.

**Gorski, B, Conlon, B, Ljunggren, B, 2007.** Forsmark Site investigation – Determination of the direct and indirect tensile strength on cores from borehole KFM01D. SKB P-07-76, Svensk Kärnbränslehantering AB.

**Hakami E, Hakami H, Cosgrove J, 2002.** Strategy for a Rock Mechanics Site Descriptive Model. Development and testing of an approach to modelling the state of stress. SKB R-02-03, Svensk Kärnbränslehantering AB.

**Hakami H, 2006.** Numerical studies on spatial variation of the in situ stress field at Forsmark – a further step. Site descriptive modeling Forsmark – stage 2.1. SKB R-06-124, Svensk Kärnbränslehantering AB.

**Hicks E C, Bungum H, Lindholm C D, 2000.** Stress inversion of earthquake focal mechanism solutions from onshore and offshore Norway. *Norsk Geologisk Tidsskrift*, 80:235–250.

**Hoek E, Brown E T, 1980.** Under ground excavations in rock.

**Hoek E, Kaiser P K, Bawden W F, 1995.** Support of underground excavations in hard rock, Balkema.

**Hoek E, Carranza-Torres C, Corkum B, 2002.** The Hoek-Brown Failure Criterion – 2002 Edition. 5<sup>th</sup> North American Rock Mech. Symp. And 17<sup>th</sup> Tunneling Ass. Of Canada Conf. NARMS-TAC, p. 267–271.

**Hoek E, 2007.** Practical rock engineering, updated version. Notes that are available on the site [www.rocscience.com](http://www.rocscience.com).

**Hökmark H, Fälth B, Wallroth T, 2006.** T-H-M couplings in rock. Overview of results of importance to the SR-Can safety assessment. SKB R-06-88, Svensk Kärnbränslehantering AB.

**Itasca, 2003.** 3 Dimensional Distinct Element Code (3DEC), User's Guide. Itasca consulting group, Inc., Minneapolis.

**Jacobsson L, 2007.** Forsmark site investigation. Boreholes KFM01A and KFM02B. Microcrack volume measurements and triaxial compression tests on intact rock. SKB R-07-93, Svensk Kärnbränslehantering AB.

- Jaeger J C, Cook N G W, Zimmerman R, 2007.** Fundamentals of Rock Mechanics. Blackwell, London.
- Juhlin C, Bergman B, Palm H, 2002.** Reflection seismic studies in the Forsmark area – stage 1. SKB R-02-43, Svensk Kärnbränslehantering AB.
- Juhlin C, 2006.** Personal Communication Derek Martin.
- Kinck J J, Husebye E S, Larsson F R, 1993.** The Moho depth distribution in Fennoscandia and the regional tectonic evolution from Archean to Permian times. *Precambrian Research*, 64:23–51.
- Klee G, Rummel F, 2004.** Forsmark site investigation – rock stress measurements with hydraulic fracturing and hydraulic testing of pre-existing fractures in borehole KFM01A, KFM01B, KFM02A and KFM04A results of in-situ tests. SKB P-04-311, Svensk Kärnbränslehantering AB.
- Lanaro F, 2001.** Unpublished results from laboratory test of fracture samples collected at Äspö HRL.
- Lanaro F, Fredriksson A, 2005.** Rock Mechanics Model – Summary of the primary data. Forsmark site investigation. SKB R-05-83, Svensk Kärnbränslehantering AB.
- Martin C D, Read R S, Chandler N A, 1990.** Does scale influence in situ stress measurements? – Some findings at the Underground Research Laboratory. In Proc. First Int. Workshop on Scale Effects in Rock Masses, Loen, Norway (Ed. da Cunha AP), pp. 307–316, A.A. Balkema, Rotterdam.
- Martin C D, Stimpson B, 1994.** The effect of sample disturbance on laboratory properties of Lac du Bonnet granite. *Canadian Geotechnical Journal*, vol. 31, pp. 692–702.
- Martin C D, Christiansson R, Södehäll J, 2001.** Rock stability considerations for siting and constructing a KBS-3 repository. Based on experiences from Äspö HRL, AECL's URL, tunnelling and mining. SKB TR-01-38, Svensk Kärnbränslehantering AB.
- Martin C D, 2007.** Quantifying in-situ stress magnitudes and orientations for Forsmark Design Step D2. SKB R-07-26, Svensk Kärnbränslehantering AB.
- Mas Ivars D, Hakami H, 2005.** Effect of a sub-horizontal fracture zone and rock mass heterogeneity on the stress field in Forsmark area – A numerical study using 3DEC. Preliminary site description Forsmark area – version 1.2, SKB R-05-59, Svensk Kärnbränslehantering AB.
- Munier R, Hermanson J, 2001.** Metodik för geometrisk modellering. Presentation och administration av platsbeskrivande modeller. SKB R-01-15, Svensk Kärnbränslehantering AB.
- Munier R, Stenberg L, Stanfors R, Milnes A G, Hermanson J, Triumf C-A, 2003.** Geological Site Descriptive Model. A strategy for the model development during site investigations. SKB R-03-07, Svensk Kärnbränslehantering AB.
- Munier R, Stigsson M, 2007** (in preparation). Implementation of uncertainties in borehole geometries and geological orientation data in Sicada. SKB R-07-19, Svensk Kärnbränslehantering AB.
- Ojala V j, Kuivamäki A, Vuorela P, 2004.** Postglacial deformation of bedrock in Finland. Report YST-120, Geological Survey of Finland, Nuclear Waste Disposal Research.
- Olofsson I, Fredriksson A, 2005.** Strategy for a numerical Rock Mechanics Site descriptive Model. SKB R-05-43, Svensk Kärnbränslehantering AB.

**Olofsson I, Simeonov A, Stigsson M, Stephens M, Follin S, Nilsson A-C, Röshoff K, Lindberg U, Lanaro F, Fredriksson A, Persson L, 2007.** Site descriptive modelling Forsmark, stage 2.2. A fracture domain concept as a basis for the statistical modelling of fractures and minor deformation zones, and interdisciplinary coordination. SKB R-07-15, Svensk Kärnbränslehantering AB.

**Peebles P Z, 1993.** Probability, random variables and random signal functions, McGraw.

**Reinecker J, Heidbach O, Tingay M, Sperner B, Müller B, 2005.** The 2005 release of the World Stress Map (available online at [www.world-stress-map.org](http://www.world-stress-map.org)).

**Ringgaard J, 2007a.** Forsmark site investigation, mapping of borehole breakouts, processing of acoustical televiewer data from KFM08A, KFM08C, KFM09A, KFM09AB and KFM90B. SKB P-07-166, Svensk Kärnbränslehantering AB.

**Ringgaard J, 2007b.** Mapping of borehole breakouts. processing of acoustical televiewer data from KFM01A, KFM01B, KFM02A, KFM03A, KFM03B, KFM04A, KFM05A, KFM06A and KFM07C. SKB P-07-07, Svensk Kärnbränslehantering AB.

**Röshoff K, Lanaro F, Jing L, 2002.** Strategy for a Rock Mechanics Site Descriptive Model. Development and testing of the empirical approach. SKB R-02-01, Svensk Kärnbränslehantering AB.

**Sandström M, 2005.** Boreholes KFM01A and KSH01A. Inter-laboratory comparison of rock mechanics testing results. Forsmark and Oskarshamn site investigation. SKB P-05-239, Svensk Kärnbränslehantering AB.

**Serafim J L, Pereira J P, 1983.** Consideration of the geomechanical classification of Bieniawski. Proc. Int. Symp. On engineering geology and underground construction, Lisbon 1 (II), pp. 33–44.

**Sjöberg J, Lindfors U, Perman F, Ask D, 2005.** Evaluation of the stress at the Forsmark site. Preliminary site investigation Forsmark area – version 1.2. SKB R-05-35, Svensk Kärnbränslehantering AB.

**SKB, 2000.** Geoscientific programme for investigation and evaluation of sites for the deep repository. SKB TR-00-20, Svensk Kärnbränslehantering AB.

**SKB, 2001.** Site investigations. Investigation methods and general execution programme. SKB TR-01-29, Svensk Kärnbränslehantering AB.

**SKB, 2002.** Forsmark – site descriptive model version 0. SKB R-02-32, Svensk Kärnbränslehantering AB.

**SKB, 2004.** Preliminary site description Forsmark area – version 1.1. SKB R-04-15, Svensk Kärnbränslehantering AB.

**SKB, 2005a.** Preliminary site description Forsmark area – version 1.2. SKB R-05-18, Svensk Kärnbränslehantering AB.

**SKB, 2005b.** Preliminary safety evaluation for the Forsmark area. Based on data and site descriptions after the initial site investigation stage. SKB TR-05-16, Svensk Kärnbränslehantering AB.

**SKB, 2005c.** Programme for further investigations of geosphere and biosphere. Forsmark site investigation. SKB R-05-14, Svensk Kärnbränslehantering AB.

**SKB, 2006a.** Long-term safety for KBS-3 repositories at Forsmark and Laxemar – a first evaluation. Main Report of the SR-Can project. SKB TR-06-09, Svensk Kärnbränslehantering AB.



**SKB, 2006b.** Site descriptive modeling Forsmark stage 2.1. Feedback for completion of the site investigation including input from safety assessment and repository engineering. SKB R-06-38, Svensk Kärnbränslehantering AB.

**SKB, 2006c.** Data report for the safety assessment SR-Can. TR-06-25, Svensk Kärnbränslehantering AB.

**Slunga, 1991.** The Baltic Shield earthquakes. *Tectonophysics*, 189, pp. 323–331.

**Stephansson O, Ljunggren C, Jing L, 1991.** Stress measurements and tectonic implications for Fennoscandia. *Tectonophysics*, 189:317–322.

**Stephens M B, Isaksson H, Simenov A, 2007.** Geology – Site descriptive modelling Forsmark stage 2.2. SKB R-07-45, Svensk Kärnbränslehantering AB.

## Intact rock mechanical properties

### A1.1 Primary data on intact rock

**Table A1-1. Number of tests for P-wave velocity tests performed in rock domain RFM017, RFM018, RFM029, RFM034 and RFM045 (DZ = deformation zone).**

Borehole	Rock domain	Fracture domain	Deformation zone	Number of tests
KFM01A	RFM029	FFM01	–	29
KFM01A	RFM029	FFM02	–	2
KFM01A	RFM029	–	–	1
KFM01A	RFM029DZ	–	ZFMENE2254	2
KFM02A	RFM029	FFM01	–	45
KFM02A	RFM029	FFM03	–	15
KFM02A	RFM029DZ	–	ZFM0089	1
KFM02A	RFM029DZ	–	ZFMA1	6
KFM02A	RFM029DZ	–	ZFMA2	1
KFM02A	RFM029DZ	–	ZFMB4	1
KFM02A	–	–	–	5
KFM03A	RFM017	FFM03	–	5
KFM03A	RFM029	FFM03	–	56
KFM03A	RFM029DZ	–	ZFMA3	3
KFM03A	RFM029DZ	–	ZFMA4	3
KFM03A	RFM029DZ	–	ZFMB1	1
KFM03B	RFM029	FFM03	–	3
KFM04A	RFM018DZ	–	ZFMNW1200	3
KFM04A	RFM029	FFM01	–	21
KFM04A	RFM029DZ	–	ZFMWNW0123	1
KFM05A	RFM029	FFM01	–	24
KFM05A	RFM029	FFM02	–	4
KFM05A	RFM029DZ	–	ZFMENE2282	2
KFM05A	RFM029DZ	–	ZFMENE0401B	2
KFM06A	RFM029	FFM01	–	22
KFM06A	RFM029	–	–	1
KFM06A	RFM029DZ	–	ZFMENE0060A, ZFMB7	2
KFM06A	RFM029DZ	–	ZFMENE0060B	3
KFM06A	RFM029DZ	–	ZFMNNE2273	2
KFM07A	RFM029	FFM01	–	32
KFM07A	RFM029	–	–	1
KFM08A	RFM029	FFM1	–	25
KFM08A	RFM029	–	–	3
KFM08A	RFM029DZ	–	ZFMENE1061A	3
KFM08A	RFM029DZ	–	ZFMNNW1204	1
KFM08A	RFM029DZ	–	ZFMENE2248	1
KFM09A	RFM018	FFM04	–	3
KFM09A	RFM029	FFM01	–	1
KFM09A	RFM029DZ	–	ZFMENE0159A, ZFMNNW0100	1
KFM09A	RFM034	FFM01	–	8
<b>Total</b>				<b>345</b>

## A1.2 Uniaxial compressive strength

**Table A1-2. Results from rock domain RFM029.**

FFM	Rock type	No. of samples	Minimum UCS [MPa]	Mean UCS [MPa]	Median UCS [MPa]	Maximum UCS [MPa]	StDev
FFM01	Granite to granodiorite, metamorphic, medium-grained	47	157	226	225	289	28.8
FFM01	Pegmatite, pegmatitic granite	10	192	228	231	266	21

FFM	Rock type	No. of samples	Minimum UCS [MPa]	Mean UCS [MPa]	Median UCS [MPa]	Maximum UCS [MPa]	StDev
FFM03	Granite to granodiorite, metamorphic, medium-grained	13	203	220	221	251	12.9
FFM03	Tonalite to granodiorite, metamorphic	4	143	150	152	155	5.6

FFM	Rock type	No. of samples	Minimum UCS [MPa]	Mean UCS [MPa]	Median UCS [MPa]	Maximum UCS [MPa]	StDev
no FFM <sup>1</sup>	Granite to granodiorite, metamorphic, medium-grained	4	166	205	206	242	32.6

<sup>1</sup> The tests are on intact samples from a possible deformation zone.

**Table A1-3. Results from rock domain RFM045.**

FFM	Rock type	No. of samples	Minimum UCS [MPa]	Mean UCS [MPa]	Median UCS [MPa]	Maximum UCS [MPa]	StDev
FFM06	Granite, metamorphic, aplitic	5	229	310	320	371	66.7

**Table A1-4. Results from rock domain RFM017.**

FFM	Rock type	No. of samples	Minimum UCS [MPa]	Mean UCS [MPa]	Median UCS [MPa]	Maximum UCS [MPa]	StDev
FFM03	Tonalite to granodiorite, metamorphic	4	140	162	166	176	15.7

**Table A1-5. Results from rock domain RFM018.**

FFM	Rock type	No. of samples	Minimum UCS [MPa]	Mean UCS [MPa]	Median UCS [MPa]	Maximum UCS [MPa]	StDev
no FFM <sup>1</sup>	Granodiorite, metamorphic	4	222	236	236	249	12.0

<sup>1</sup> The tests comprises of intact samples from deformation zone ZFMNW1200.

**Table A1-6. Results from rock domain RFM034.**

FFM	Rock type	No. of samples	Minimum UCS [MPa]	Mean UCS [MPa]	Median UCS [MPa]	Maximum UCS [MPa]	StDev
FFM01	Granite to granodiorite, metamorphic, medium-grained	4	192	199	195	214	10.3
FFM01	Pegmatite, pegmatitic granite	2	153	170	170	187	23.8

### A1.3 Strength less than 160 MPa

The results of the uniaxial compressive strength show that nine of the tests gave values of less than 160 MPa. They are all listed in Table A1-7 together with information on the borehole and where the sample is located in the borehole. No information on the cause of failure is available for the samples in borehole KFM01C.

**Table A1-7. Samples with uniaxial strength less than 160 MPa.**

Rock domain	Borehole	Elevation (m)	Elevation (m)	UCS (MPa)	Rock type	Cause of failure
RFM029	KFM01C	400.10	400.26	157.6	Pegmatite, pegmatitic granite	No information
		413.08	413.26	157.9	Pegmatite, pegmatitic granite	No information
RFM029	KFM03A	280.85	280.99	140.1	Tonalite-granodiorite	Failure crack partly along foliation
		305.98	306.12	149.2	Granodiorite-tonalite	Diagonal failure crack
		306.12	306.26	143.0	Granodiorite-tonalite	Spalling on one side
		306.26	306.40	154.9	Granodiorite-tonalite	Diagonal failure crack
		308.54	308.68	154.5	Granodiorite-tonalite	Foliation
RFM045	KFM06A	449.29	449.43	157.0	Granite to granodiorite, metamorphic	Spalling and crack partly along foliation
RFM034	KFM09A	596.01	596.16	153.2	Pegmatite, pegmatitic granite	Multiple spalling along one side of the sample

## A1.4 Triaxial compressive strength

**Table A1-8. Results for rock domain RFM029.**

FFM	Rock type	No. of samples	Minimum TCS [MPa]	Mean TCS [MPa]	Median TCS [MPa]	Maximum TCS [MPa]	StDev
FFM01	Granite to granodiorite, metamorphic, medium-grained	44	222	333	323	525	73.2
FFM01	Granite, granodiorite and tonalite, metamorphic, fine- to medium-grained	4	260	369	379	457	90.3
FFM01	Pegmatite, pegmatitic granite	5	245	329	321	448	76.9

FFM	Rock type	No. of samples	Minimum TCS [MPa]	Mean TCS [MPa]	Median TCS [MPa]	Maximum TCS [MPa]	StDev
FFM03	Granite to granodiorite, metamorphic, medium-grained	12	239	310	318	372	41.7
FFM03	Tonalite to granodiorite, metamorphic	4	171	199	199	228	23.6

FFM	Rock type	No. of samples	Minimum TCS [MPa]	Mean TCS [MPa]	Median TCS [MPa]	Maximum TCS [MPa]	StDev
no FFM <sup>1</sup>	Granite to granodiorite, metamorphic, medium-grained	4	274	320	308	391	50.5

<sup>1</sup> The tests are on intact samples from a possible deformation zone.

**Table A1-9. Results for rock domain RFM017.**

FFM	Rock type	No. of samples	Minimum TCS [MPa]	Mean TCS [MPa]	Median TCS [MPa]	Maximum TCS [MPa]	StDev
FFM03	Tonalite to granodiorite, metamorphic	4	176	193	195	207	12.7

**Table A1-10. Results for rock domain RFM018.**

FFM	Rock type	No. of samples	Minimum TCS [MPa]	Mean TCS [MPa]	Median TCS [MPa]	Maximum TCS [MPa]	StDev
no FFM <sup>1</sup>	Granodiorite, metamorphic	3	226	297	307	359	66.7

<sup>1</sup> The tests are on intact samples from deformation zone ZFMNW1200.

**Table A1-11. Results for rock domain RFM034.**

FFM	Rock type	No. of samples	Minimum TCS [MPa]	Mean TCS [MPa]	Median TCS [MPa]	Maximum TCS [MPa]	StDev
FFM01	Granite to granodiorite, metamorphic, medium-grained	2	315	325	325	336	15.3
FFM01	Pegmatite, pegmatitic granite	1	359	359	359	359	–

**Table A1-12. Results for rock domain RFM044.**

FFM	Rock type	No. of samples	Minimum TCS [MPa]	Mean TCS [MPa]	Median TCS [MPa]	Maximum TCS [-]	StDev
FFM05	Pegmatite, pegmatitic granite	2	348	405	405	462	80.4

## A1.5 Tensile strength

**Table A1-13. Results for rock domain RFM029.**

FFM	Rock type	No. of samples	Minimum T [MPa]	Mean T [MPa]	Median T [MPa]	Maximum T [MPa]	StDev
FFM01	Granite to granodiorite, metamorphic, medium-grained	92	9.7	13.5	13.7	17.9	1.57
FFM01	Pegmatite, pegmatitic granite	12	8.4	11.5	11.0	16.2	2.64

FFM	Rock type	No. of samples	Minimum T [MPa]	Mean T [MPa]	Median T [MPa]	Maximum T [MPa]	StDev
FFM03	Granite to granodiorite, metamorphic, medium-grained	30	10.4	13.6	13.8	17.0	1.71
FFM03	Tonalite to granodiorite, metamorphic	10	14.4	16.0	16.1	17.5	1.11

FFM	Rock type	No. of samples	Minimum T [MPa]	Mean T [MPa]	Median T [MPa]	Maximum T [MPa]	StDev
no FFM <sup>1</sup>	Granite to granodiorite, metamorphic, medium-grained	10	11.1	13.3	12.6	16.6	1.91

<sup>1</sup> The tests are on intact samples from a possible deformation zone.

**Table A1-14. Results for rock domain RFM017.**

FFM	Rock type	No. of samples	Minimum T [MPa]	Mean T [MPa]	Median T [MPa]	Maximum T [MPa]	StDev
FFM03	Tonalite to granodiorite, metamorphic	10	13.7	15.2	15.5	16.5	1.01

**Table A1-15. Results for rock domain RFM018.**

FFM	Rock type	No. of samples	Minimum T [MPa]	Mean T [MPa]	Median T [MPa]	Maximum T [MPa]	StDev
no FFM <sup>1</sup>	Granodiorite, metamorphic	11	16.8	18.0	17.8	19.7	0.98

<sup>1</sup> The tests are on intact samples from deformation zone ZFMNW1200.

**Table A1-16. Results for rock domain RFM034.**

FFM	Rock type	No. of samples	Minimum T [MPa]	Mean T [MPa]	Median T [MPa]	Maximum T [MPa]	StDev
FFM01	Granite to granodiorite, metamorphic, medium-grained	8	14.0	15.6	15.3	17.7	1.19
FFM01	Pegmatite, pegmatitic granite	6	6.6	9.6	10.0	12.1	1.83

**Table A1-17. Results for rock domain RFM044.**

FFM	Rock type	No. of samples	Minimum T [MPa]	Mean T [MPa]	Median T [MPa]	Maximum T [MPa]	StDev
FFM05	Granite to granodiorite, metamorphic, medium-grained	4	13.6	16	15.9	18.8	2.44
FFM05	Pegmatite, pegmatitic granite	2	16.1	16.4	16.4	16.7	0.42

## A1.6 Young's modulus and Poisson's ratio

**Table A1-18. Results for rock domain RFM029 – Young's modulus, uniaxial tests.**

FFM	Rock type	No. of samples	Minimum E [GPa]	Mean E [GPa]	Median E [GPa]	Maximum E [GPa]	StDev
FFM01	Granite to granodiorite, metamorphic, medium-grained	47	69.5	75.7	75.9	82.9	2.85
FFM01	Pegmatite, pegmatitic granite	10	71.1	75.3	75.6	79.8	3.23

FFM	Rock type	No. of samples	Minimum E [GPa]	Mean E [GPa]	Median E [GPa]	Maximum E [GPa]	StDev
FFM03	Granite to granodiorite, metamorphic, medium-grained	13	70.6	75.2	75.3	80.1	2.82
FFM03	Tonalite to granodiorite, metamorphic	4	69.7	71.7	70.4	76.2	3.01

FFM	Rock type	No. of samples	Minimum E [GPa]	Mean E [GPa]	Median E [GPa]	Maximum E [GPa]	StDev
no FFM <sup>1</sup>	Granite to granodiorite, metamorphic, medium-grained	4	76.6	77.5	77.3	78.6	0.83

<sup>1</sup> The tests are on intact samples from a possible deformation zone.

**Table A1-18. cont. Results for rock domain RFM029 – Poisson’s ratio, uniaxial tests.**

FFM	Rock type	No. of samples	Minimum $\nu$ [-]	Mean $\nu$ [-]	Median $\nu$ [-]	Maximum $\nu$ [-]	StDev
FFM01	Granite to granodiorite, metamorphic, medium-grained	47	0.14	0.23	0.24	0.30	0.036
FFM01	Pegmatite, pegmatitic granite	10	0.26	0.3	0.3	0.35	0.027

FFM	Rock type	No. of samples	Minimum $\nu$ [-]	Mean $\nu$ [-]	Median $\nu$ [-]	Maximum $\nu$ [-]	StDev
FFM03	Granite to granodiorite, metamorphic, medium-grained	13	0.16	0.23	0.24	0.27	0.029
FFM03	Tonalite to granodiorite, metamorphic	4	0.25	0.29	0.29	0.34	0.037

FFM	Rock type	No. of samples	Minimum $\nu$ [-]	Mean $\nu$ [-]	Median $\nu$ [-]	Maximum $\nu$ [-]	StDev
no FFM <sup>1</sup>	Granite to granodiorite, metamorphic, medium-grained	4	0.20	0.22	0.22	0.24	0.018

<sup>1</sup> The tests are on intact samples from a possible deformation zone.

**Table A1-18. cont. Results for rock domain RFM029 – Young’s modulus, triaxial tests.**

FFM	Rock type	No. of samples	Minimum E [GPa]	Mean E [GPa]	Median E [GPa]	Maximum E [GPa]	StDev
FFM01	Granite to granodiorite, metamorphic, medium-grained	44	66.1	74.3	74.4	85.4	4.00
FFM01	Granite, granodiorite and tonalite, metamorphic, fine- to medium-grained	4	66.4	68.7	68.7	71.1	2.44
FFM01	Pegmatite, pegmatitic granite	5	65.4	70.9	69.8	76.3	4.26

FFM	Rock type	No. of samples	Minimum E [GPa]	Mean E [GPa]	Median E [GPa]	Maximum E [GPa]	StDev
FFM03	Granite to granodiorite, metamorphic, medium-grained	12	69.5	73.8	73.6	77.2	2.56
FFM03	Tonalite to granodiorite, metamorphic	4	65.4	70.9	71.6	74.8	3.94

FFM	Rock type	No. of samples	Minimum E [GPa]	Mean E [GPa]	Median E [GPa]	Maximum E [GPa]	StDev
no FFM*	Granite to granodiorite, metamorphic, medium-grained	4	71.4	71.9	71.7	73.0	0.71

\* The tests are on intact samples from a possible deformation zone.



**Table A1-18. cont. Results for rock domain RFM029 – Poisson's ratio, triaxial tests.**

FFM	Rock type	No. of samples	Minimum $\nu$ [-]	Mean $\nu$ [-]	Median $\nu$ [-]	Maximum $\nu$ [-]	StDev
FFM01	Granite to granodiorite, metamorphic, medium-grained	44	0.15	0.19	0.19	0.26	0.027
FFM01	Granite, granodiorite and tonalite, metamorphic, fine- to medium-grained	4	0.20	0.24	0.24	0.27	0.030
FFM01	Pegmatite, pegmatitic granite	5	0.20	0.24	0.25	0.28	0.036

FFM	Rock type	No. of samples	Minimum $\nu$ [-]	Mean $\nu$ [-]	Median $\nu$ [-]	Maximum $\nu$ [-]	StDev
FFM03	Granite to granodiorite, metamorphic, medium-grained	12	0.17	0.20	0.21	0.22	0.019
FFM03	Tonalite to granodiorite, metamorphic	4	0.19	0.21	0.20	0.23	0.017

FFM	Rock type	No. of samples	Minimum $\nu$ [-]	Mean $\nu$ [-]	Median $\nu$ [-]	Maximum $\nu$ [-]	StDev
no FFM*	Granite to granodiorite, metamorphic, medium-grained	4	0.17	0.19	0.20	0.20	0.015

\* The tests are on intact samples from a possible deformation zone.

**Table A1-19. Results for rock domain RFM045 – Young's modulus, uniaxial tests.**

FFM	Rock type	No. of samples	Minimum E [GPa]	Mean E [GPa]	Median E [GPa]	Maximum E [GPa]	StDev
FFM06	Granite, metamorphic, aplitic	5	80.0	81.9	81.3	85.6	2.60

**Table A1-19. cont. Results for rock domain RFM045 – Poisson's ratio, uniaxial test.**

FFM	Rock type	No. of samples	Minimum $\nu$ [-]	Mean $\nu$ [-]	Median $\nu$ [-]	Maximum $\nu$ [-]	StDev
FFM06	Granite, metamorphic, aplitic	5	0.25	0.27	0.26	0.31	0.029

**Table A1-20. Results for rock domain RFM017 – Young's modulus, uniaxial tests.**

FFM	Rock type	No. of samples	Minimum E [GPa]	Mean E [GPa]	Median E [GPa]	Maximum E [GPa]	StDev
FFM03	Tonalite to granodiorite, metamorphic	4	68.7	72.6	72.1	77.8	3.92

**Table A1-20. cont. Results for rock domain RFM017 – Poisson’s ratio, uniaxial tests.**

FFM	Rock type	No. of samples	Minimum $\nu$ [-]	Mean $\nu$ [-]	Median $\nu$ [-]	Maximum $\nu$ [-]	StDev
FFM03	Tonalite to granodiorite, metamorphic	4	0.23	0.25	0.25	0.28	0.026

**Table A1-20. cont. Results for rock domain RFM017 – Young’s modulus, triaxial tests.**

FFM	Rock type	No. of samples	Minimum E [GPa]	Mean E [GPa]	Median E [GPa]	Maximum E [GPa]	StDev
FFM03	Tonalite to granodiorite, metamorphic	4	65.9	69.9	70.7	72.2	2.80

**Table A1-20. cont. Results for rock domain RFM017 – Poisson’s ratio, triaxial tests.**

FFM	Rock type	No. of samples	Minimum $\nu$ [-]	Mean $\nu$ [-]	Median $\nu$ [-]	Maximum $\nu$ [-]	StDev
FFM03	Tonalite to granodiorite, metamorphic	4	0.18	0.19	0.19	0.21	0.015

**Table A1-21. Results for rock domain RFM018 – Young’s modulus, uniaxial tests.**

FFM	Rock type	No. of samples	Minimum E [GPa]	Mean E [GPa]	Median E [GPa]	Maximum E [GPa]	StDev
no FFM <sup>1</sup>	Granodiorite, metamorphic	4	73.4	77.2	77.4	80.7	3.04

<sup>1</sup> The tests are on intact samples from deformation zone ZFMNW1200.

**Table A1-21. cont. Results for rock domain RFM018 – Poisson’s ratio, uniaxial tests.**

FFM	Rock type	No. of samples	Minimum $\nu$ [-]	Mean $\nu$ [-]	Median $\nu$ [-]	Maximum $\nu$ [-]	StDev
no FFM <sup>1</sup>	Granodiorite, metamorphic	4	0.19	0.23	0.24	0.25	0.026

<sup>1</sup> The tests are on intact samples from deformation zone ZFMNW1200.

**Table A1-21. cont. Results for rock domain RFM018 – Young’s modulus, triaxial tests.**

FFM	Rock type	No. of samples	Minimum E [GPa]	Mean E [GPa]	Median E [GPa]	Maximum E [GPa]	StDev
no FFM <sup>1</sup>	Granodiorite, metamorphic	3	70.5	74.6	75.7	77.6	3.68

<sup>1</sup> The tests are on intact samples from deformation zone ZFMNW1200.

**Table A1-21. cont. Results for rock domain RFM018 – Poisson’s ratio, triaxial tests.**

FFM	Rock type	No. of samples	Minimum $\nu$ [-]	Mean $\nu$ [-]	Median $\nu$ [-]	Maximum $\nu$ [-]	StDev
no FFM <sup>1</sup>	Granodiorite, metamorphic	3	0.18	0.18	0.18	0.19	0.006

<sup>1</sup> The tests are on intact samples from deformation zone ZFMNW1200.

**Table A1-22. Results for rock domain RFM034 – Young’s modulus, uniaxial tests.**

FFM	Rock type	No. of samples	Minimum E [GPa]	Mean E [GPa]	Median E [GPa]	Maximum E [GPa]	StDev
FFM01	Granite to granodiorite, metamorphic, medium-grained	4	70.4	72.7	73.4	73.6	1.54
FFM01	Pegmatite, pegmatitic granite	2	71.5	72.4	72.4	73.3	1.30

**Table A1-22. cont. Results for rock domain RFM034 – Poisson’s ratio, uniaxial tests.**

FFM	Rock type	No. of samples	Minimum $\nu$ [-]	Mean $\nu$ [-]	Median $\nu$ [-]	Maximum $\nu$ [-]	StDev
FFM01	Granite to granodiorite, metamorphic, medium-grained	4	0.25	0.27	0.27	0.30	0.021
FFM01	Pegmatite, pegmatitic granite	2	0.19	0.26	0.26	0.32	0.092

**Table A1-22. cont. Results for rock domain RFM034 – Young’s modulus, triaxial tests.**

FFM	Rock type	No. of samples	Minimum E [GPa]	Mean E [GPa]	Median E [GPa]	Maximum E [GPa]	StDev
FFM01	Granite to granodiorite, metamorphic, medium-grained	2	68.7	70.1	70.1	71.4	1.88
FFM01	Pegmatite, pegmatitic granite	1	77.2	77.2	77.2	77.2	–

**Table A1-22. cont. Results for rock domain RFM034 – Poisson’s ratio, triaxial tests.**

FFM	Rock type	No. of samples	Minimum $\nu$ [-]	Mean $\nu$ [-]	Median $\nu$ [-]	Maximum $\nu$ [-]	StDev
FFM01	Granite to granodiorite, metamorphic, medium-grained	2	0.24	0.25	0.25	0.25	0.007
FFM01	Pegmatite, pegmatitic granite	1	0.17	0.17	0.17	0.17	–

**Table A1-23. Results for rock domain RFM044 – Young’s modulus, triaxial tests.**

FFM	Rock type	No. of samples	Minimum E [GPa]	Mean E [GPa]	Median E [GPa]	Maximum E [GPa]	StDev
FFM05	Pegmatite, pegmatitic granite	2	67.7	69.4	69.4	71.0	2.34

**Table A1-23. cont. Results for rock domain RFM044 – Poisson’s ratio, triaxial tests.**

FFM	Rock type	No. of samples	Minimum $\nu$ [-]	Mean $\nu$ [-]	Median $\nu$ [-]	Maximum $\nu$ [-]	StDev
FFM05	Pegmatite, pegmatitic granite	2	0.23	0.24	0.24	0.25	0.014

## A1.7 Hoek-Brown's and Coulomb's failure envelopes

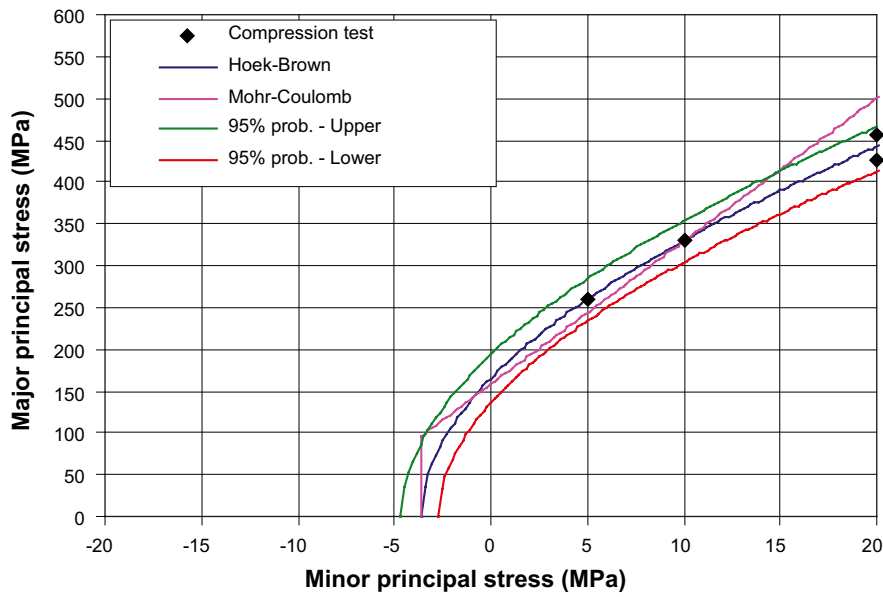


**Figure A1-1.** Hoek-Brown's and Coulomb's failure envelopes based on uniaxial and triaxial tests on samples from RFM029, FFM01 of Granite, granodiorite and tonalite, metamorphic, fine- to medium-grained. No data from tensile tests were available.

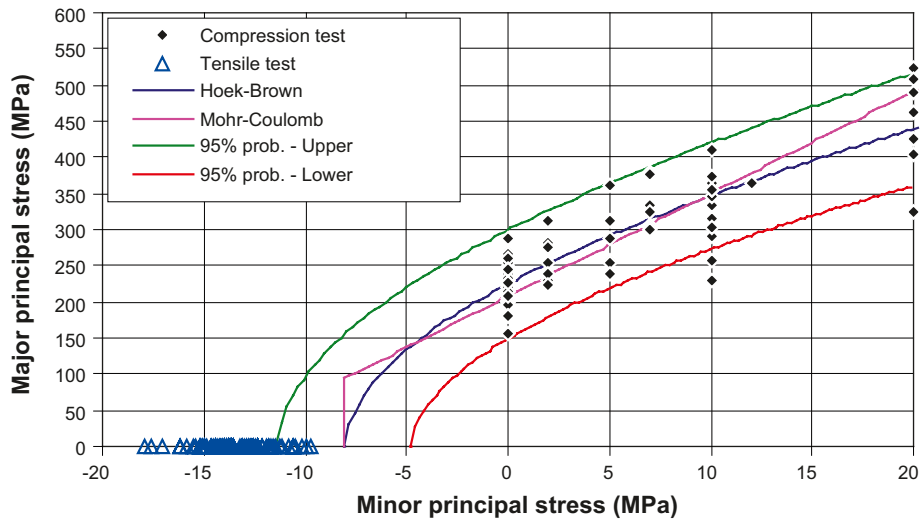


**Figure A1-2.** Hoek-Brown's and Coulomb's failure envelopes based on uniaxial and triaxial tests on samples from RFM029, FFM01 of Granite to granodiorite, metamorphic, medium-grained. Tensile strength from test data.

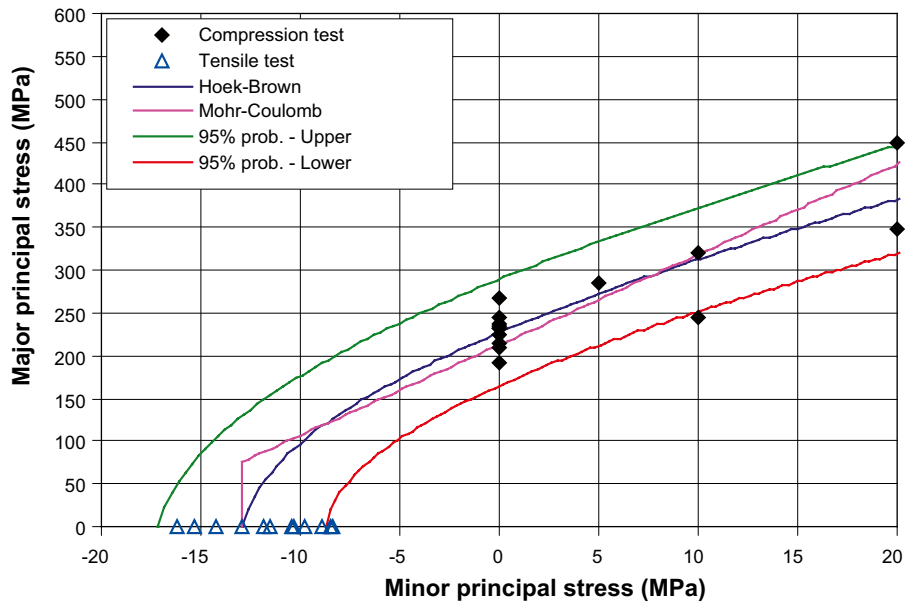


Figure A1-3. Hoek-Brown's and Coulomb's failure envelopes based on uniaxial and triaxial tests on samples from RFM029, FFM01 of Pegmatite, pegmatitic granite. Tensile strength from test data.

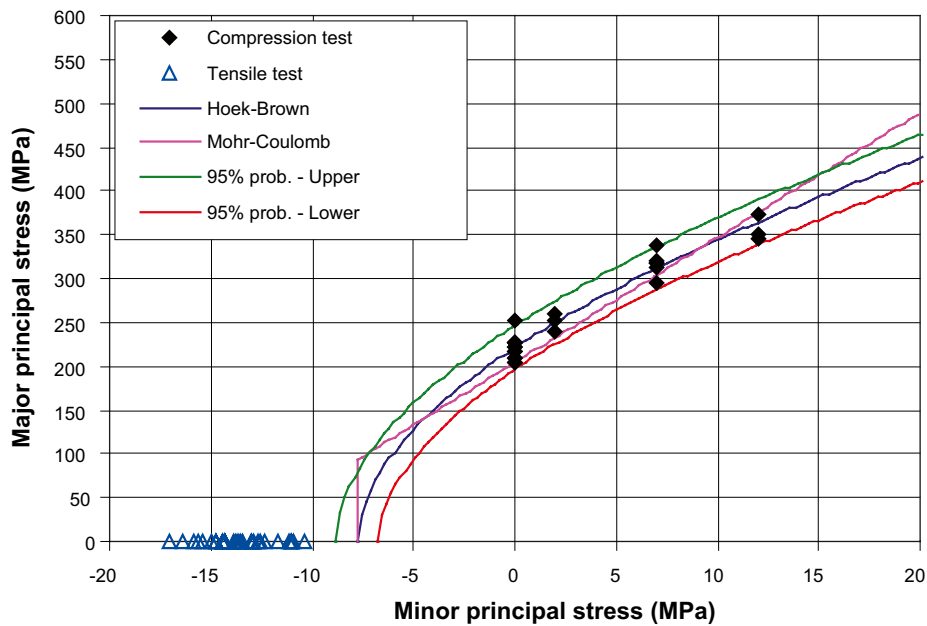
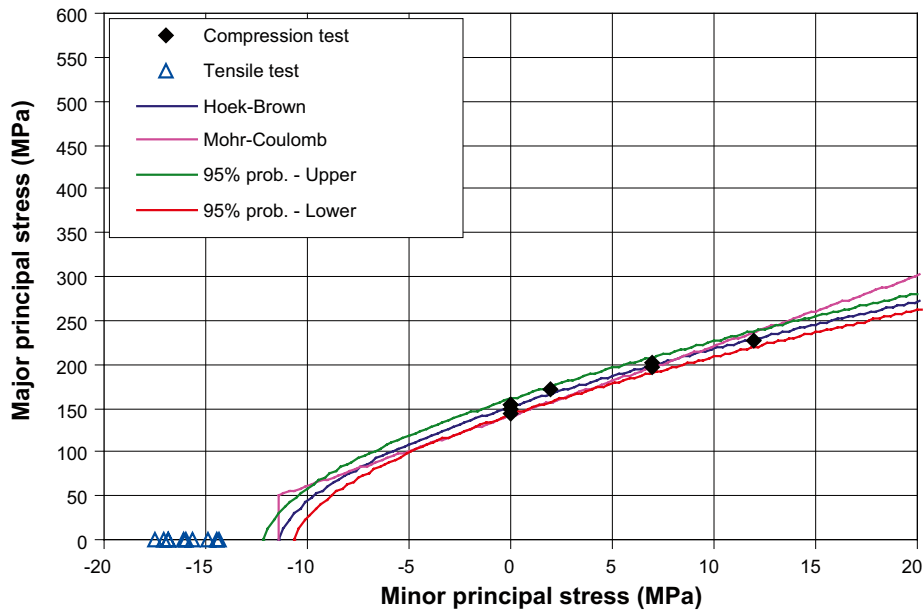
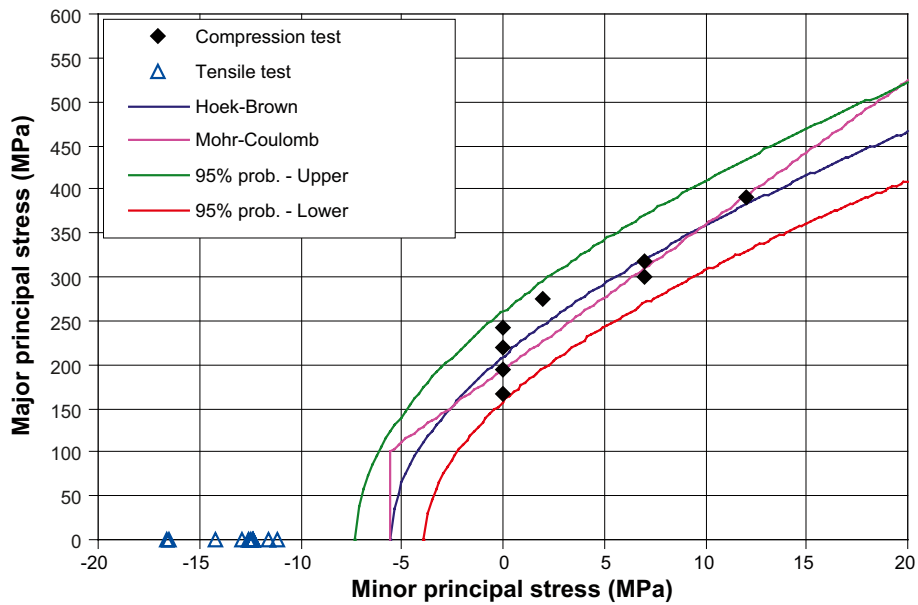


Figure A1-4. Hoek-Brown's and Coulomb's failure envelopes based on uniaxial and triaxial tests on samples from RFM029, FFM03 of Granite to granodiorite, metamorphic, medium-grained. Tensile strength from test data.



*Figure A1-5. Hoek-Brown's and Coulomb's failure envelopes based on uniaxial and triaxial tests on samples from RFM029, FFM03 of Tonalite to granodiorite, metamorphic. Tensile strength from test data.*



*Figure A1-6. Hoek-Brown's and Coulomb's failure envelopes based on uniaxial and triaxial tests on samples from RFM029, no FFM, (ZFMNW1200 and PDZ) Granite to granodiorite, metamorphic, medium-grained. Tensile strength from test data.*

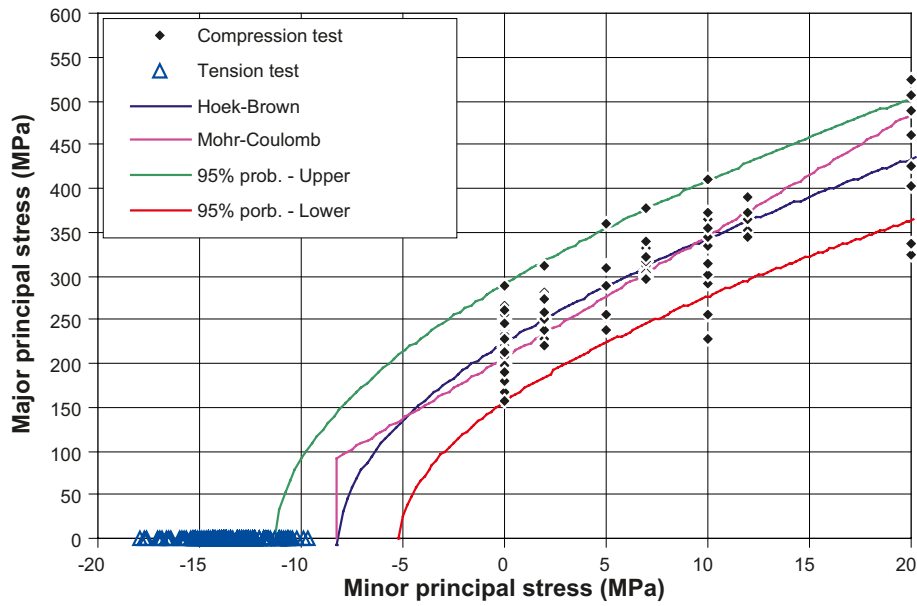


Figure A1-7. Hoek-Brown's and Coulomb's failure envelopes based on uniaxial and triaxial tests on granite to granodiorite metamorphic, medium grained. Tensile strength from test data.

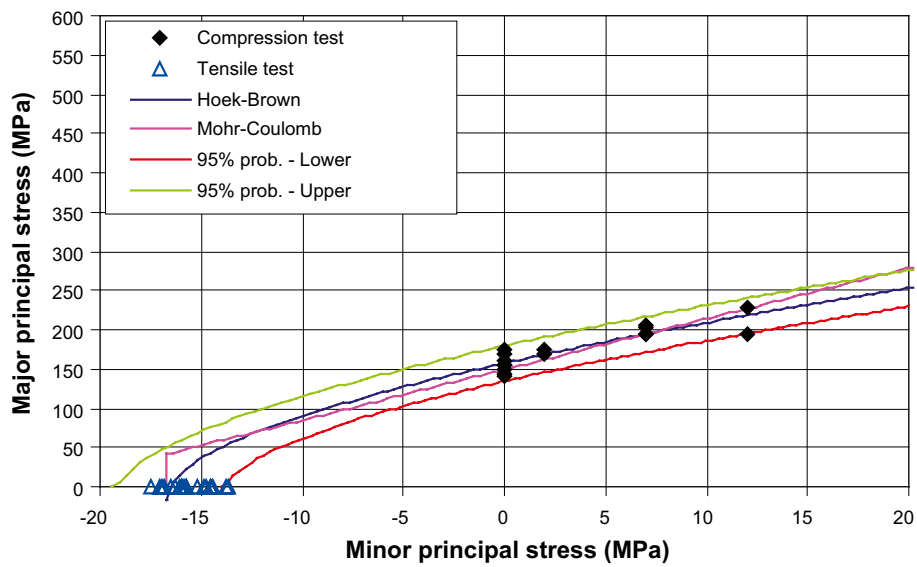


Figure A1-8. Hoek-Brown's and Coulomb's failure envelopes based on uniaxial and triaxial tests on tonalite to granodiorite. Tensile strength from test data.

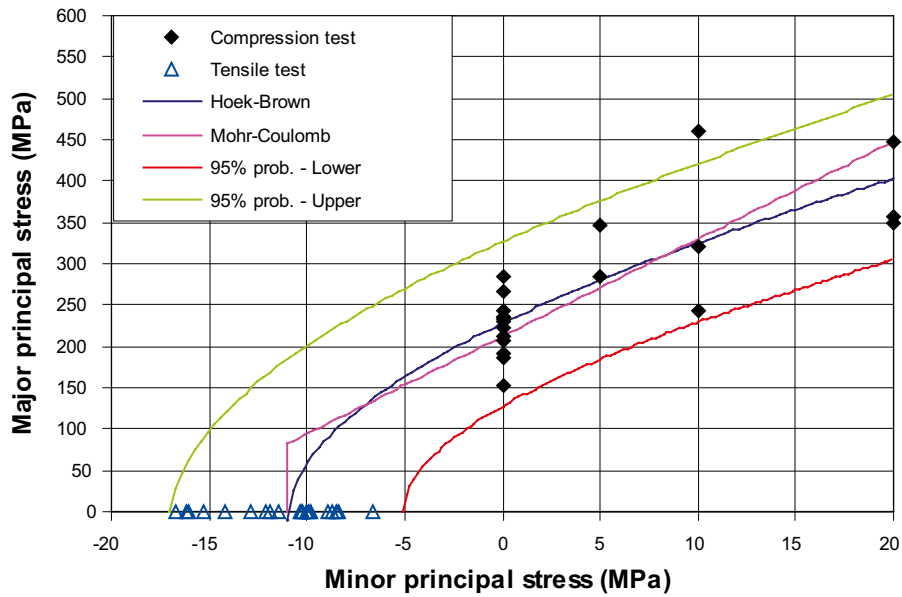


Figure A1-9. Hoek-Brown's and Coulomb's failure envelopes based on uniaxial and triaxial tests on pegmatite. Tensile strength from test data.

Table A1-22. Parameters for Hoek-Brown's Criterion based on results of uniaxial and triaxial tests on intact rock based on all rock types.

Rock type	Number of samples	Lower envelope 95% probability		Mean		Upper envelope 95% probability	
		UCS (MPa)	$m_i$	UCS (MPa)	$m_i$	UCS (MPa)	$m_i$
Granite to granodiorite, metamorphic, medium grained	130	156	30.0	223	27.2	291	25.6
Granite, granodiorite and tonalite	4	135	50.0	166	45.4	164	41.4
Granodiorite, metamorphic	7	184	31.5	230	30.4	275	29.7
Pegmatite, pegmatitic granite	21	128	24.9	228	20.8	327	19.1
Tonalite to granodiorite, metamorphic	16	134	9.6	157	9.4	180	9.2
<b>All intact samples</b>	<b>182</b>	<b>130</b>	<b>28.2</b>	<b>221</b>	<b>24.3</b>	<b>313</b>	<b>22.7</b>



**Table A1-23. Parameters for the Coulomb's criteria based on results of uniaxial and triaxial tests on intact rock samples on all rock types.**

Rock type	Number of samples	Lower envelope 95% probability		Mean		Upper envelope 95% probability	
		C (MPa)	$\phi$ [°]	C (MPa)	$\phi$ [°]	C (MPa)	$\phi$ [°]
Granite to granodiorite, metamorphic, medium grained	130	20.0	59.2	27.6	60.0	35.6	60.5
Granite, metamorphic, aplitic	4	16.5	62.4	19.2	62.8	22.0	62.9
Granodiorite, metamorphic	7	22.5	60.4	27.3	61.1	32.1	61.7
Pegmatite, pegmatitic granite	21	17.9	56.5	30.9	57.5	44.4	58.0
Tonalite to granodiorite, metamorphic	16	25.1	46.7	29.4	47.1	33.5	47.3
<b>All intact samples</b>	<b>182</b>	<b>17.6</b>	<b>57.7</b>	<b>28.5</b>	<b>59.0</b>	<b>39.9</b>	<b>59.6</b>

## A1.8 Depth dependency intact properties

### A1.8.1 Uniaxial compressive strength and tensile strength

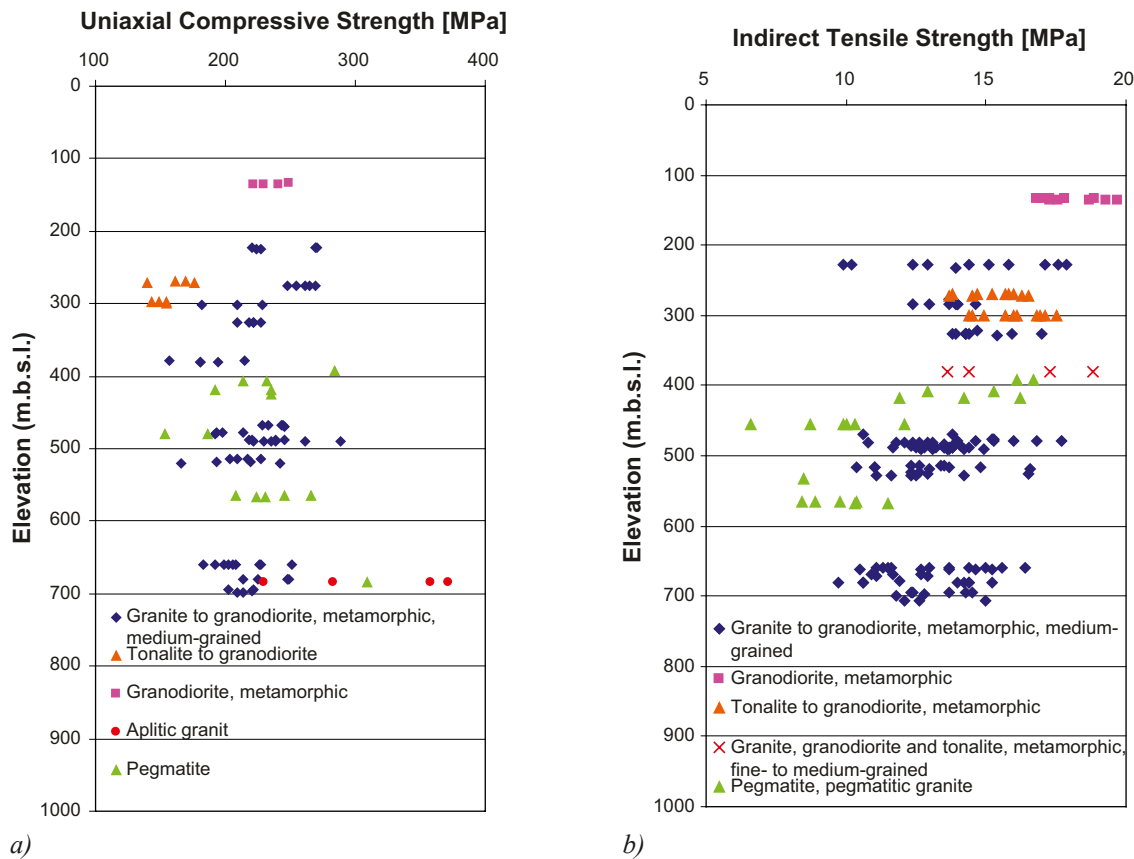


**Figure A1-10. Uniaxial compressive strength a) and tensile strength b) versus elevation and sorted by rock type.**

### A1.8.2 Young's Modulus and Poisson's Ratio

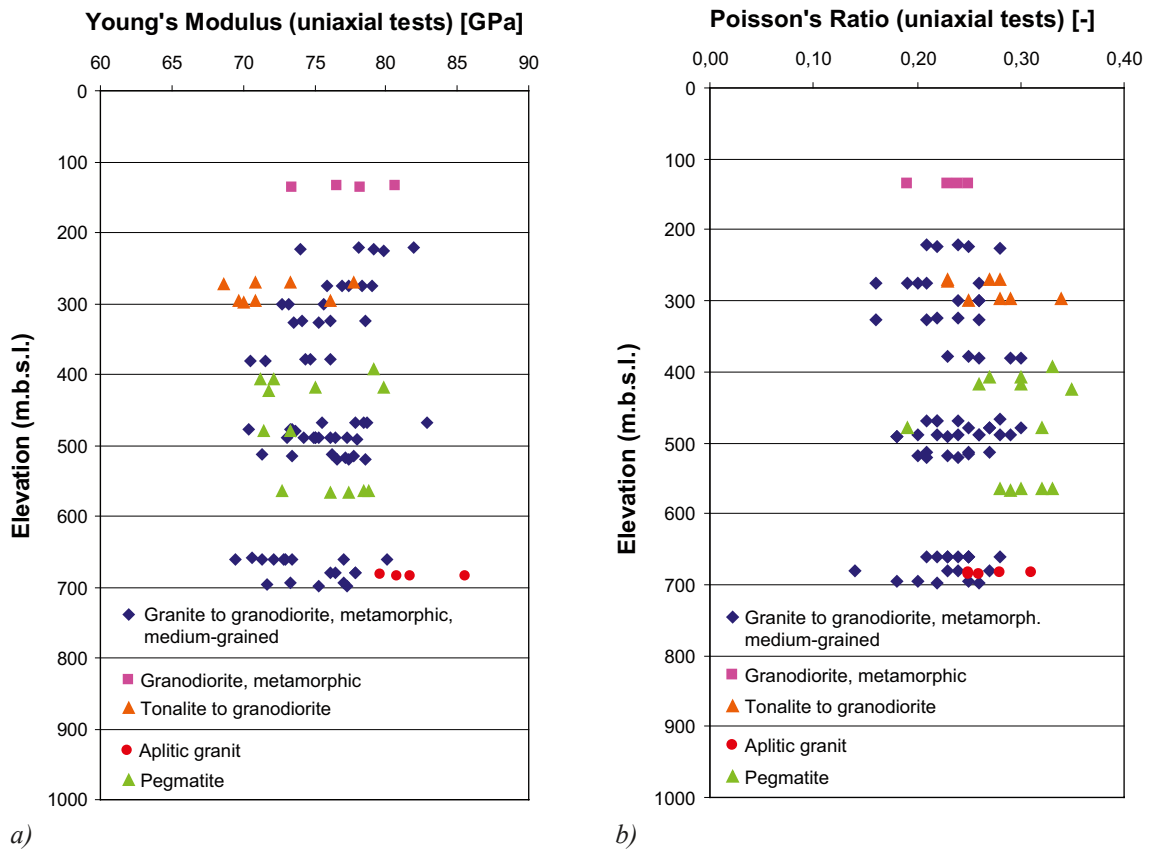


Figure A1-11. Young's modulus a) and Poisson's ratio b) versus elevation.

### A1.9 Estimated uncertainties

Table A1-24. Uncertainties of the predicted mechanical properties. The uncertainties are given as range of variation of the possible mean value.

RFM	FFM	Rock type	No. of samples	Uniaxial compressive strength	Young's modulus	Poisson's ratio
RFM017	FFM03	Tonalite to granodiorite, metamorphic	4	± 9.5%	± 5.3%	± 10.2%
RFM018DZ	–	Granodiorite, metamorphic	4	± 5.0%	± 3.9%	± 11.3%
RFM029	FFM01	Granite to granodiorite, metamorphic, medium-grained	47	± 3.5%	± 1.1%	± 4.3%
RFM029	FFM01	Pegmatite, pegmatitic granite	10	± 5.6%	± 2.7%	± 5.7%
RFM029	FFM03	Granite to granodiorite, metamorphic, medium-grained	13	± 3.2%	± 2.0%	± 6.7%
RFM029	FFM03	Tonalite to granodiorite, metamorphic	4	± 3.6%	± 4.1%	± 1.6%
RFM029	–	Granite to granodiorite, metamorphic, medium-grained	4	± 15.6%	± 1.1%	± 8.1%
RFM034	FFM01	Granite to granodiorite, metamorphic, medium-grained	4	± 5.1%	± 2.1%	± 7.4%
RFM034	FFM01	Pegmatite, pegmatitic granite	2	± 19.4%	± 2.5%	± 50.0%
RFM045	FFM06	Granite, metamorphic, aplitic	5	± 21.1%	± 3.1%	± 10.5%

**Table A1-24. cont. Uncertainties of the predicted mechanical properties. The uncertainties are given as range of variation of the possible mean value.**

<b>RFM</b>	<b>FFM</b>	<b>Rock type</b>	<b>No. of samples</b>	<b>Triaxial compressive strength</b>	<b>Young's modulus</b>	<b>Poisson's ratio</b>
RFM017	FFM03	Tonalite to granodiorite, metamorphic	4	± 6.4%	± 3.9%	± 7.6%
RFM018DZ	–	Granodiorite, metamorphic	3	± 25.4%	± 5.6%	± 3.6%
RFM029	FFM01	Granite to granodiorite, metamorphic, medium-grained	44	± 6.5%	± 1.6%	± 4.1%
RFM029	FFM01	Granite, granodiorite and tonalite, metamorphic, fine- to medium-grained	4	± 24.0%	± 3.5%	± 12.3%
RFM029	FFM01	Pegmatite, pegmatitic granite	5	± 20.5%	± 5.3%	± 12.9%
RFM029	FFM03	Granite to granodiorite, metamorphic, medium-grained	12	± 7.6%	± 2.0%	± 5.3%
RFM029	FFM03	Tonalite to granodiorite, metamorphic	4	± 11.6%	± 5.5%	± 8.3%
RFM029	–	Granite to granodiorite, metamorphic, medium-grained	4	± 15.4%	± 1.0%	± 7.6%
RFM034	FFM01	Granite to granodiorite, metamorphic, medium-grained	2	± 6.5%	± 3.7%	± 4.0%
RFM034	FFM01	Pegmatite, pegmatitic granite	1	–	–	–
RFM044	FFM05	Pegmatite, pegmatitic granite	2	± 27.5%	± 4.7%	± 8.2%

<b>RFM</b>	<b>FFM</b>	<b>Rock type</b>	<b>No. of samples</b>	<b>Indirect tensile strength</b>
RFM017	FFM03	Tonalite to granodiorite, metamorphic	10	± 4.1%
RFM018DZ	–	Granodiorite, metamorphic	11	± 3.2%
RFM029	FFM01	Granite to granodiorite, metamorphic, medium-grained	92	± 2.5%
RFM029	FFM01	Pegmatite, pegmatitic granite	12	± 13.0%
RFM029	FFM03	Granite to granodiorite, metamorphic, medium-grained	30	± 4.5%
RFM029	FFM03	Tonalite to granodiorite, metamorphic	10	± 4.3%
RFM029	–	Granite to granodiorite, metamorphic, medium-grained	10	± 8.9%
RFM034	FFM01	Granite to granodiorite, metamorphic, medium-grained	8	± 5.3%
RFM034	FFM01	Pegmatite, pegmatitic granite	6	± 15.3%
RFM044	FFM05	Granite to granodiorite, metamorphic, medium-grained	4	± 24.2%
RFM044	FFM05	Pegmatite, pegmatitic granite	2	± 23.2%

## Mechanical properties of fractures

### A2.1 Results from tilt tests

**Table A2-1. Calculated results from tilt tests in FFM01, total 63 tests.**

Test	Minimum	Mean	Median	Maximum	Standard deviation
Peak friction angle, $\phi_p^{MC}$ [°]	29.5	33.9	33.9	36.6	1.7
Peak cohesion, $c_p^{MC}$ [MPa]	0.2	0.4	0.4	0.7	0.1
Residual friction angle, $\phi_r^{MC}$ [°]	22.6	29.7	30.1	37.9	2.9
Residual cohesion, $c_r^{MC}$ [MPa]	0.2	0.4	0.4	0.6	0.1

**Table A2-2. Calculated results from tilt tests in FFM02, total 7 tests.**

Test	Minimum	Mean	Median	Maximum	Standard deviation
Peak friction angle, $\phi_p^{MC}$ [°]	25.8	30.8	30.9	34.9	3.1
Peak cohesion, $c_p^{MC}$ [MPa]	0.2	0.5	0.5	0.7	0.1
Residual friction angle, $\phi_r^{MC}$ [°]	20.3	26.2	26.8	32.8	3.9
Residual cohesion, $c_r^{MC}$ [MPa]	0.2	0.4	0.4	0.6	0.1

**Table A2-3. Calculated results from tilt tests in FFM03, total 41 tests.**

Test	Minimum	Mean	Median	Maximum	Standard deviation
Peak friction angle, $\phi_p^{MC}$ [°]	32.2	34.5	34.2	37.7	1.5
Peak cohesion, $c_p^{MC}$ [MPa]	0.2	0.5	0.5	0.8	0.1
Residual friction angle, $\phi_r^{MC}$ [°]	23.7	29.3	29.6	33.5	2.5
Residual cohesion, $c_r^{MC}$ [MPa]	0.2	0.4	0.4	0.7	0.1

**Table A2-4. Calculated results from tilt tests in FFM04, total 2 tests.**

Test	Minimum	Mean	Median	Maximum	Standard deviation
Peak friction angle, $\phi_p^{MC}$ [°]	33.1	34.5	34.5	35.8	1.9
Peak cohesion, $c_p^{MC}$ [MPa]	0.3	0.5	0.5	0.6	0.2
Residual friction angle, $\phi_r^{MC}$ [°]	32.3	33.0	33.0	33.7	1.0
Residual cohesion, $c_r^{MC}$ [MPa]	0.3	0.5	0.5	0.6	0.2

**Table A2-5. Calculated results from tilt tests in FFM05, total 5 tests.**

Test	Minimum	Mean	Median	Maximum	Standard deviation
Peak friction angle, $\phi_p^{MC}$ [°]	31.4	33.4	33.4	34.8	1.3
Peak cohesion, $c_p^{MC}$ [MPa]	0.3	0.4	0.4	0.6	0.1
Residual friction angle, $\phi_r^{MC}$ [°]	24.3	27.8	27.3	32.4	3.4
Residual cohesion, $c_r^{MC}$ [MPa]	0.2	0.4	0.4	0.5	0.1

## A2.2 Results from direct shear test on open fractures

Table A2-6. Shear stiffness  $K_{S0.5}$  for each fracture domain, 57 tests.

FFM	Number of samples	Minimum $K_{S0.5}$ (MPa/mm)	Mean $K_{S0.5}$ (MPa/mm)	Median $K_{S0.5}$ (MPa/mm)	Maximum $K_{S0.5}$ (MPa/mm)	Std. dev. $K_{S0.5}$ (MPa/mm)
FFM01	29	1	10	9	23	6
FFM02	4	4	8	8	12	4
FFM03	9	4	8	7	15	4
FFM04	3	1	8	10	12	6
FFM05	2	4	6	6	8	3
DZ	10	3	12	10	35	10
<b>All</b>	<b>57</b>	<b>1</b>	<b>10</b>	<b>9</b>	<b>35</b>	<b>6</b>

Table A2-7. Shear stiffness  $K_{S5}$  for each fracture domain, 57 tests.

FFM	Number of samples	Minimum $K_{S5}$ (MPa/mm)	Mean $K_{S5}$ (MPa/mm)	Median $K_{S5}$ (MPa/mm)	Maximum $K_{S5}$ (MPa/mm)	Std. dev. $K_{S5}$ (MPa/mm)
FFM01	29	7	26	25	46	9
FFM02	4	21	26	27	31	4
FFM03	9	23	31	29	43	7
FFM04	3	12	16	14	22	5
FFM05	2	14	20	20	25	7
DZ	10	7	26	26	41	9
<b>All</b>	<b>57</b>	<b>7</b>	<b>26</b>	<b>25</b>	<b>46</b>	<b>8</b>

Table A2-8. Shear stiffness  $K_{S20}$  for each fracture domain, 57 tests.

FFM	Number of samples	Minimum $K_{S20}$ (MPa/mm)	Mean $K_{S20}$ (MPa/mm)	Median $K_{S20}$ (MPa/mm)	Maximum $K_{S20}$ (MPa/mm)	Std. dev. $K_{S20}$ (MPa/mm)
FFM01	29	18	34	33	52	10
FFM02	4	25	33	32	41	8
FFM03	9	20	35	36	49	10
FFM04	3	18	23	22	29	5
FFM05	2	23	25	25	26	2
DZ	10	19	31	33	44	8
<b>All</b>	<b>57</b>	<b>18</b>	<b>33</b>	<b>32</b>	<b>52</b>	<b>10</b>

Table A2-9. Dilatancy angle  $\psi_{0.5}$  for each fracture domain, 57 tests.

FFM	Number of samples	Minimum $\psi_{0.5}$ (°)	Mean $\psi_{0.5}$ (°)	Median $\psi_{0.5}$ (°)	Maximum $\psi_{0.5}$ (°)	Std. dev. $\psi_{0.5}$ (°)
FFM01	29	7.8	14.6	14.4	27.1	4.1
FFM02	4	11.5	15.2	15.9	17.6	2.9
FFM03	9	14.0	16.4	15.4	20.2	2.2
FFM04	3	9.5	10.1	10.0	10.9	0.7
FFM05	2	14.4	14.7	14.7	15.0	0.4
DZ	10	0.3	14.4	16.4	22.8	6.4
<b>All</b>	<b>57</b>	<b>0.3</b>	<b>14.6</b>	<b>14.9</b>	<b>27.1</b>	<b>4.2</b>

**Table A2-10. Dilatancy angle  $\psi_5$  for each fracture domain, 57 tests.**

FFM	Number of samples	Minimum $\psi_5$ (°)	Mean $\psi_5$ (°)	Median $\psi_5$ (°)	Maximum $\psi_5$ (°)	Std. dev. $\psi_5$ (°)
FFM01	29	2.5	7.7	7.6	13.7	2.7
FFM02	4	1.6	2.2	2.2	2.6	0.5
FFM03	9	0.5	3.1	3.4	6.3	2.1
FFM04	3	5.4	6.6	6.4	7.9	1.3
FFM05	2	8.7	8.8	8.8	8.8	0.1
DZ	10	1.0	5.7	4.2	13.0	4.3
<b>All</b>	<b>57</b>	<b>0.5</b>	<b>6.2</b>	<b>6.1</b>	<b>13.7</b>	<b>3.4</b>

**Table A2-11. Dilatancy angle  $\psi_{20}$  for each fracture domain, 57 tests.**

FFM	Number of samples	Minimum $\psi_{20}$ (°)	Mean $\psi_{20}$ (°)	Median $\psi_{20}$ (°)	Maximum $\psi_{20}$ (°)	Std. dev. $\psi_{20}$ (°)
FFM01	29	0.2	3.2	3.1	9.6	2.1
FFM02	4	0.2	2.1	1.9	4.3	2.2
FFM03	9	0.2	2.3	1.9	6.1	1.7
FFM04	3	0.3	1.3	1.5	2.2	1.0
FFM05	2	1.9	2.3	2.3	2.6	0.5
DZ	10	0.5	3.0	3.2	4.6	1.3
<b>All</b>	<b>57</b>	<b>0.2</b>	<b>2.8</b>	<b>2.6</b>	<b>9.6</b>	<b>1.9</b>

**Table A2-12. Residual friction angle,  $\phi_r$ , for each fracture domain, 57 tests. Values from test type I and type II are converted to test type III.**

FFM	Number of samples	Minimum $\phi_r$ (°)	Mean $\phi_r$ (°)	Median $\phi_r$ (°)	Maximum $\phi_r$ (°)	Std. dev. $\phi_r$ (°)
FFM01	29	27.9	34.9	34.6	41.9	3.4
FFM02	4	24.1	34.8	37.3	40.3	7.3
FFM03	9	25.7	34.2	36.1	41.5	6.2
FFM04	3	29.6	32.2	32.4	34.6	2.5
FFM05	2	32.2	34.3	34.3	36.4	3.0
DZ	10	30.3	34.8	35.1	36.8	2.0
<b>All</b>	<b>57</b>	<b>24.1</b>	<b>34.6</b>	<b>35.1</b>	<b>41.9</b>	<b>4.0</b>

**Table A2-13. Residual cohesion,  $c_r$ , for each fracture domain, 57 tests.**

FFM	Number of samples	Minimum $c_r$ (MPa)	Mean $c_r$ (MPa)	Median $c_r$ (MPa)	Maximum $c_r$ (MPa)	Std. dev. $c_r$ (MPa)
FFM01	29	0.1	0.3	0.3	0.8	0.2
FFM02	4	0.1	0.4	0.2	1.3	0.6
FFM03	9	0.2	0.5	0.3	1.1	0.4
FFM04	3	0.2	0.3	0.3	0.4	0.1
FFM05	2	0.4	0.4	0.4	0.5	0.1
DZ	10	0.0	0.3	0.3	0.6	0.2
<b>All</b>	<b>57</b>	<b>0.0</b>	<b>0.4</b>	<b>0.3</b>	<b>1.3</b>	<b>0.2</b>

### A2.3 Results from direct shear test on sealed fractures

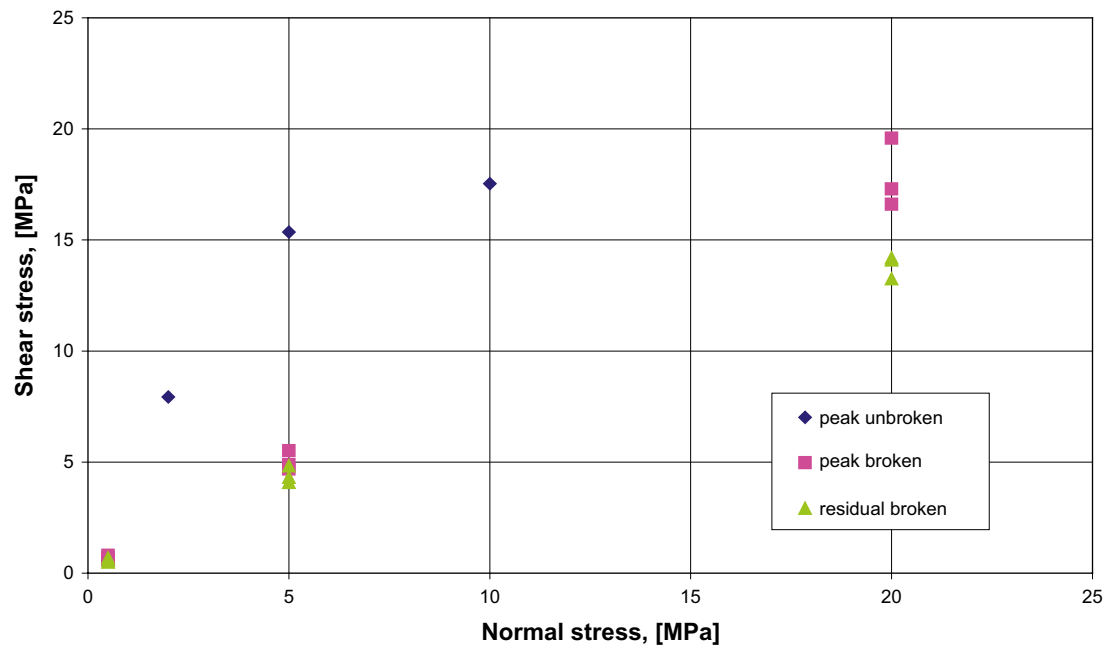


Figure A2-1. Shear test on sealed fracture from borehole KFM01D, secup 482.83.

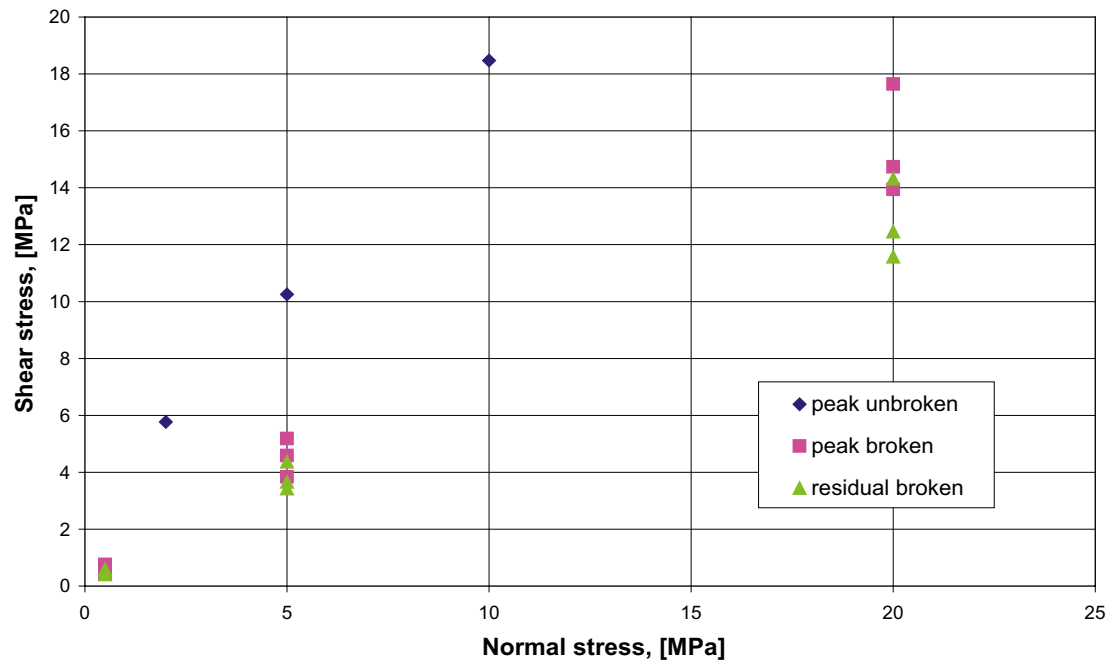


Figure A2-2. Shear test on sealed fracture from borehole KFM01D, secup 588.28.

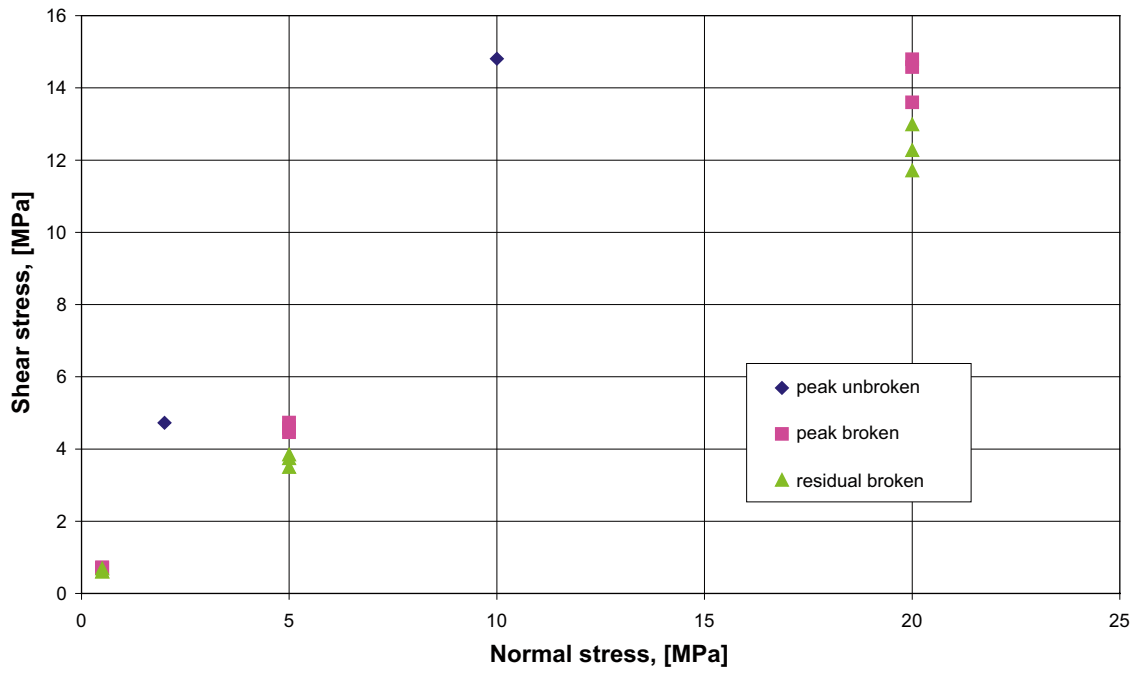


Figure A2-3. Shear test on sealed fracture from borehole KFM01D, secup 658.34.

#### A2.4 Results from tilt tests versus depth

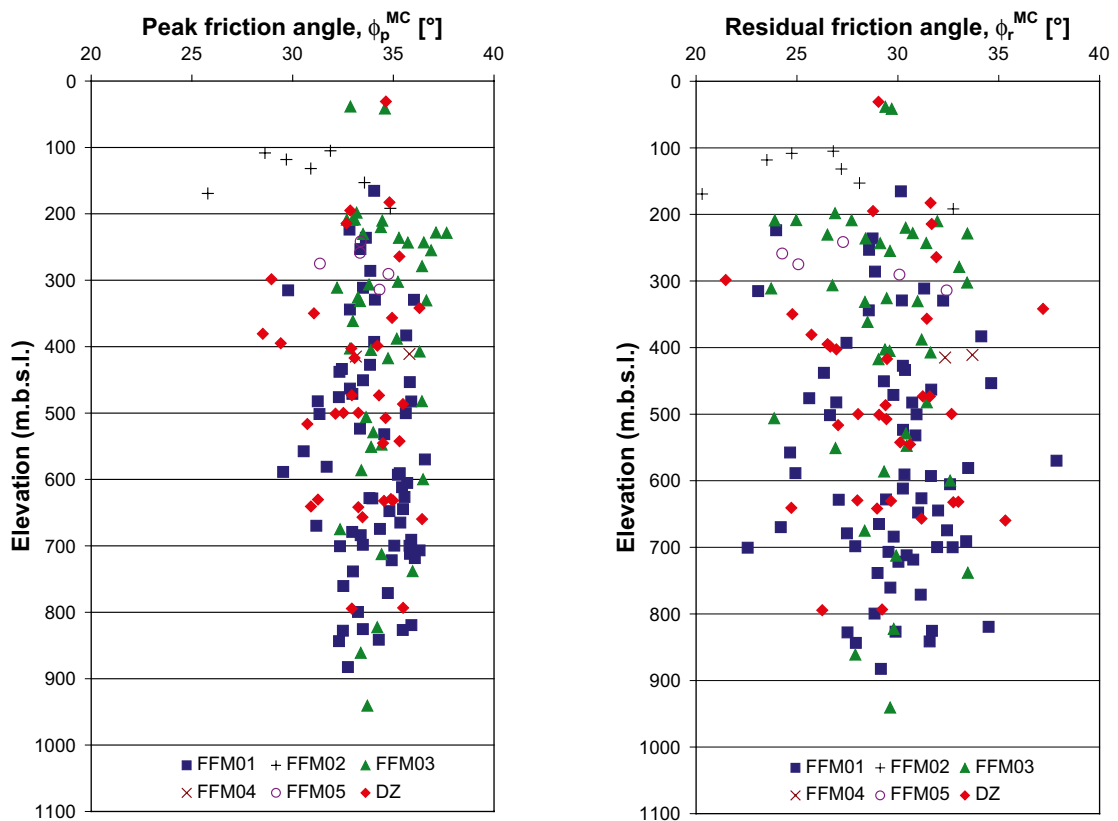


Figure A2-4. Peak friction angle  $\phi_p^{MC}$  and residual friction angle  $\phi_r^{MC}$  versus depth.



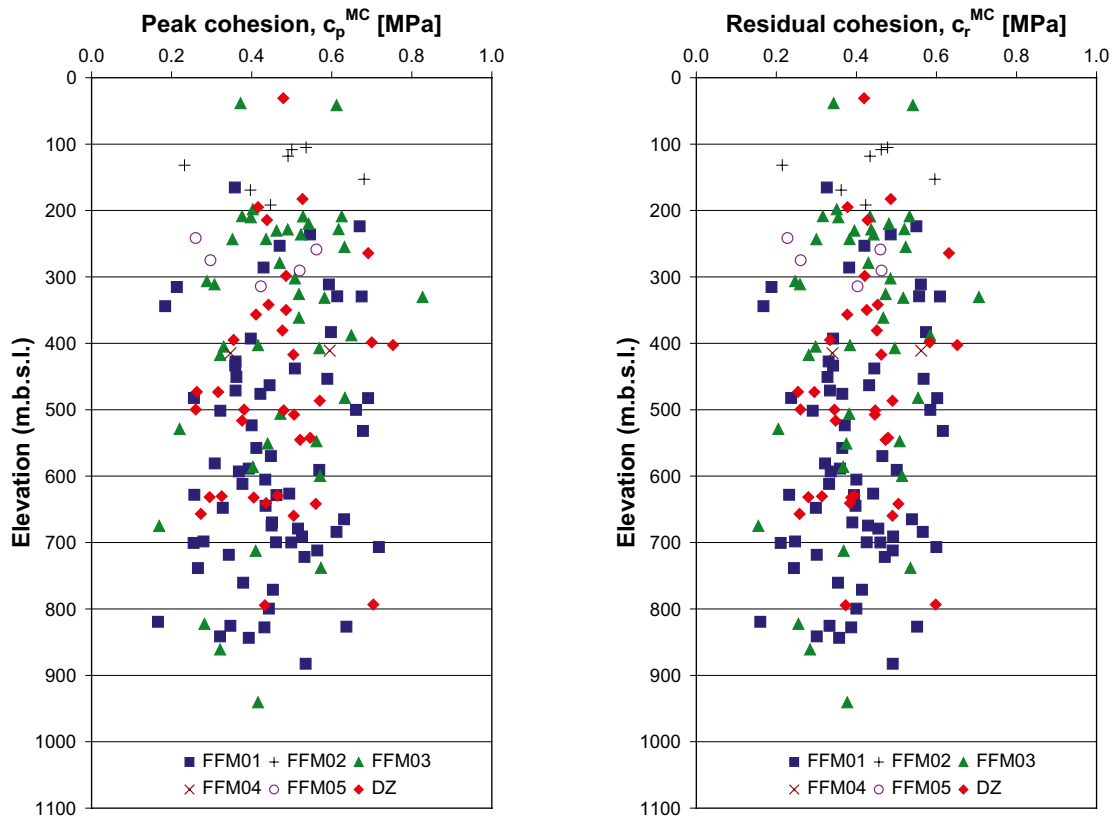


Figure A2-5. Peak cohesion  $c_p^{MC}$  and residual cohesion  $c_r^{MC}$  versus depth.

## A2.5 Results from direct shear tests versus depth

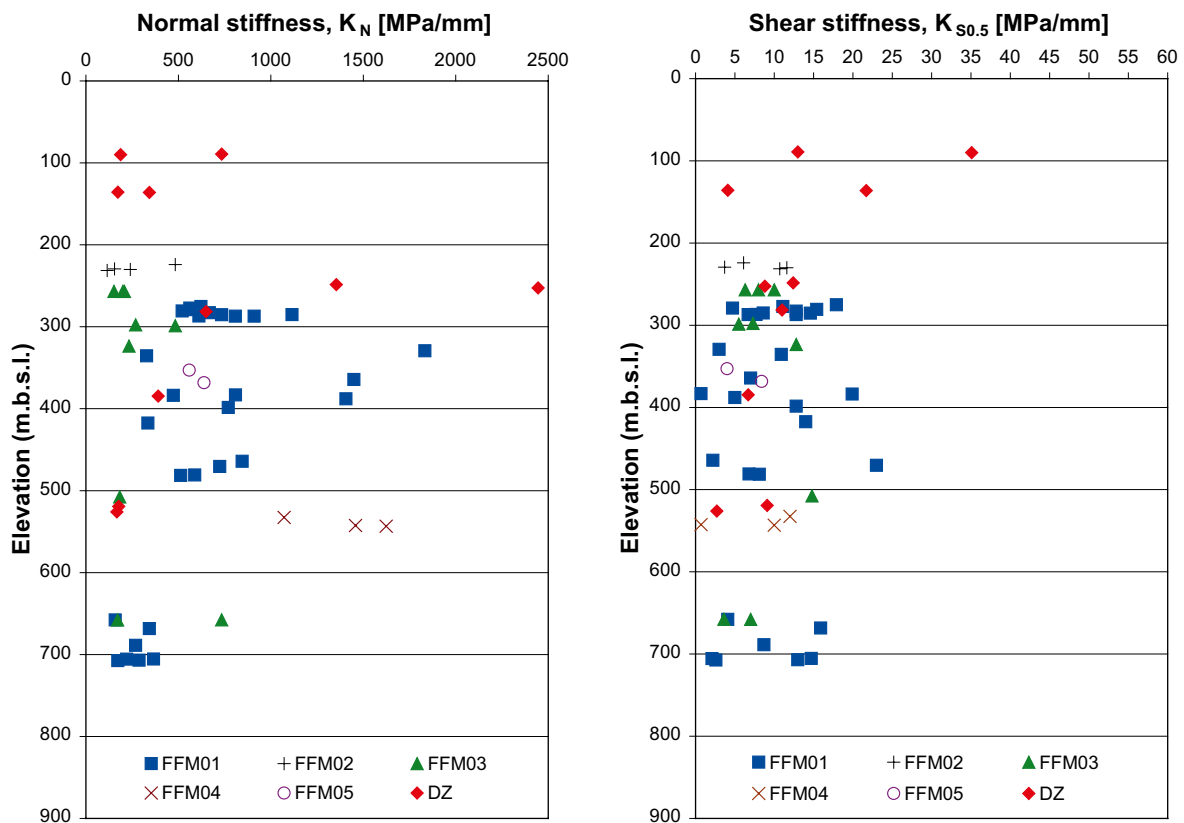


Figure A2-6. Normal stiffness  $K_N$  and shear stiffness  $K_{S0.5}$  versus depth.

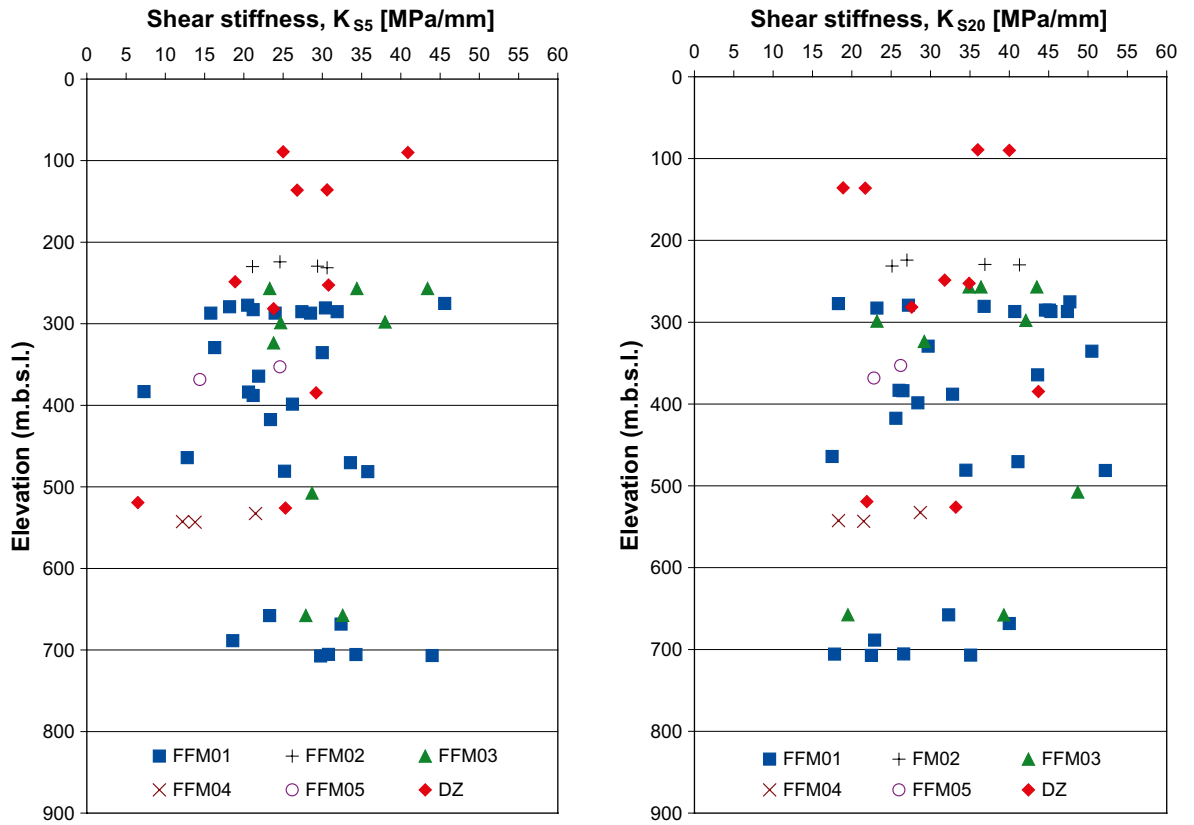


Figure A2-7. Shear stiffness  $K_{S5}$  and shear stiffness  $K_{S20}$  versus depth

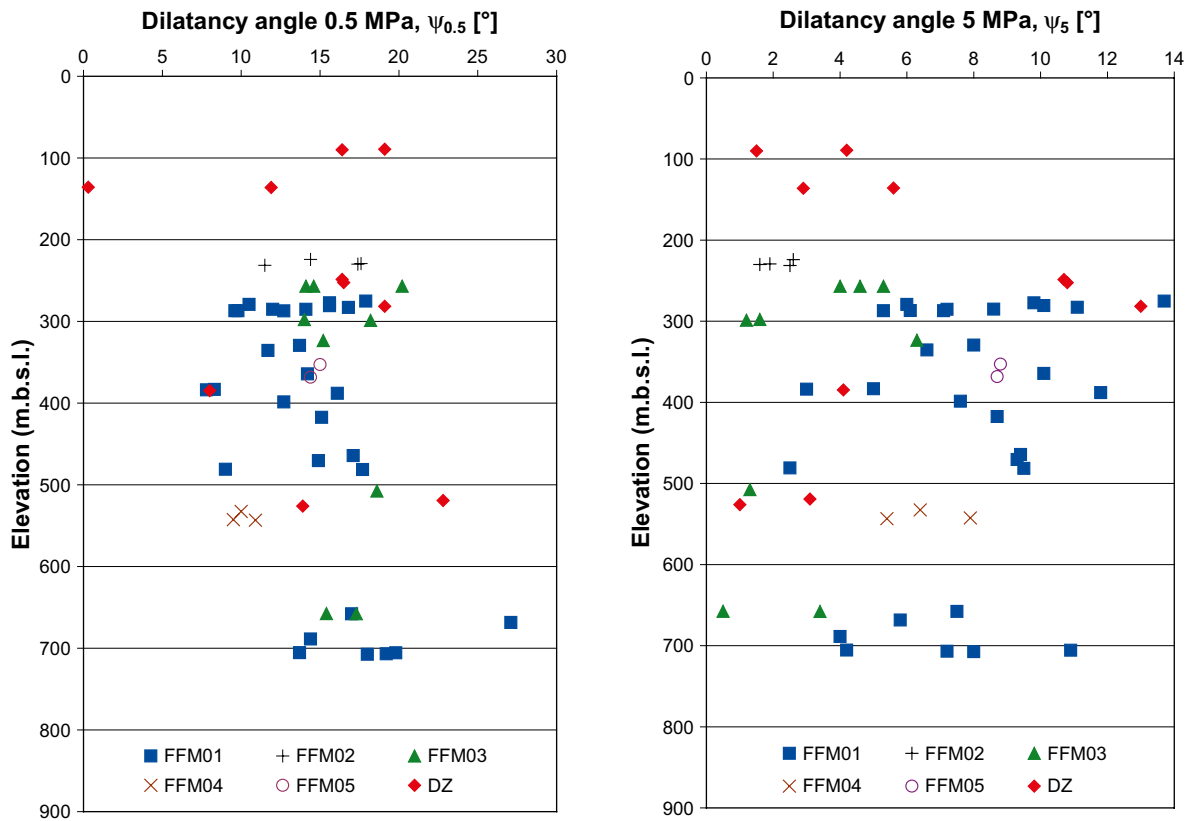


Figure A2-8. Dilatancy angle at 0.5 MPa and dilatancy angle at 5 MPa versus depth.

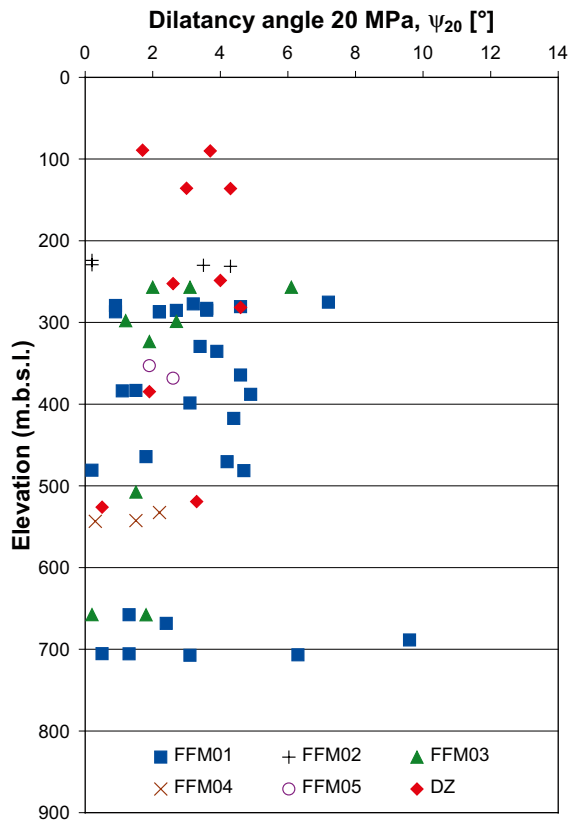


Figure A2-9. Dilatancy angle at 20 MPa versus depth.

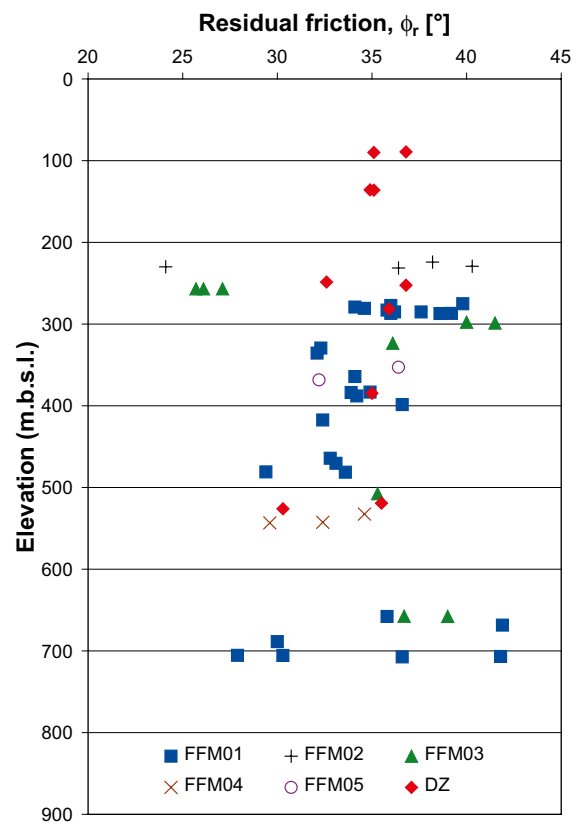
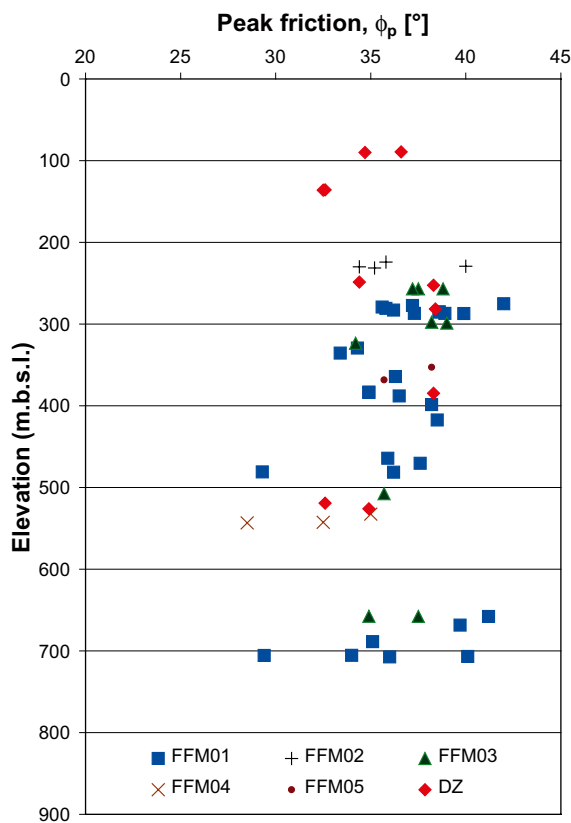


Figure A2-10. Peak and residual friction angle versus depth.

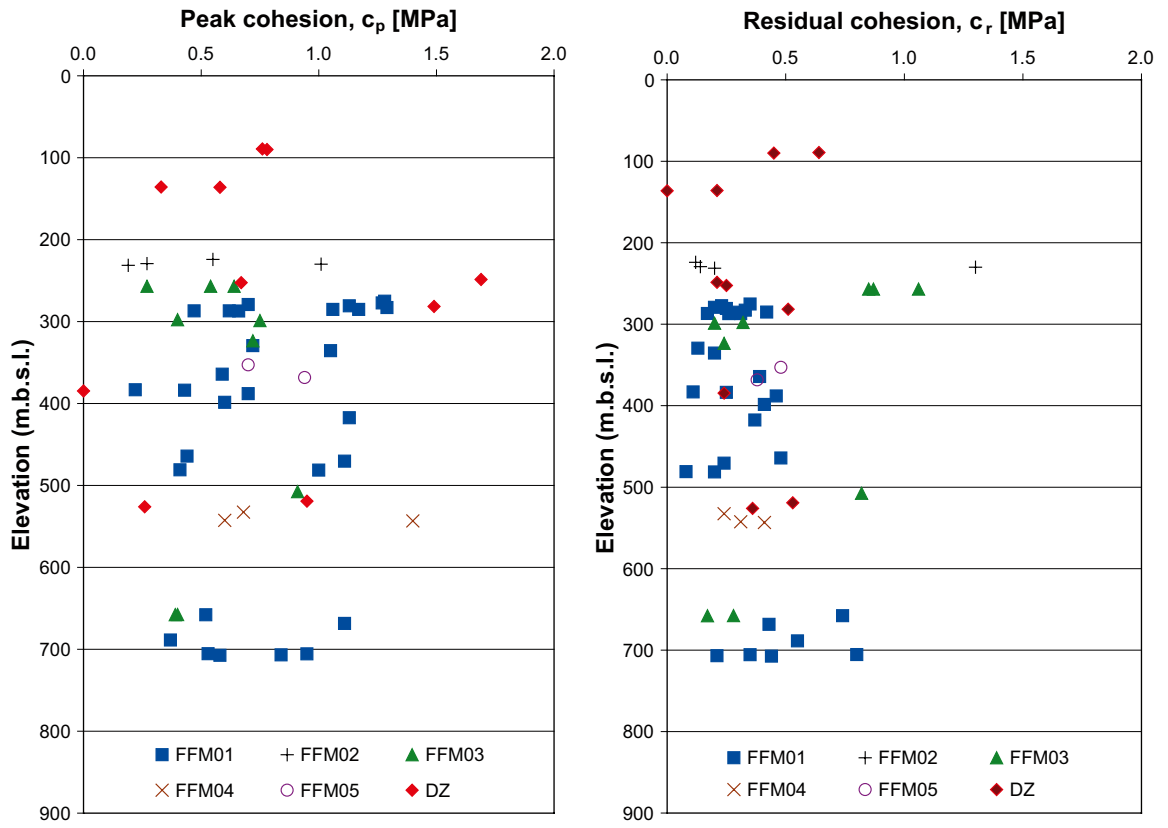
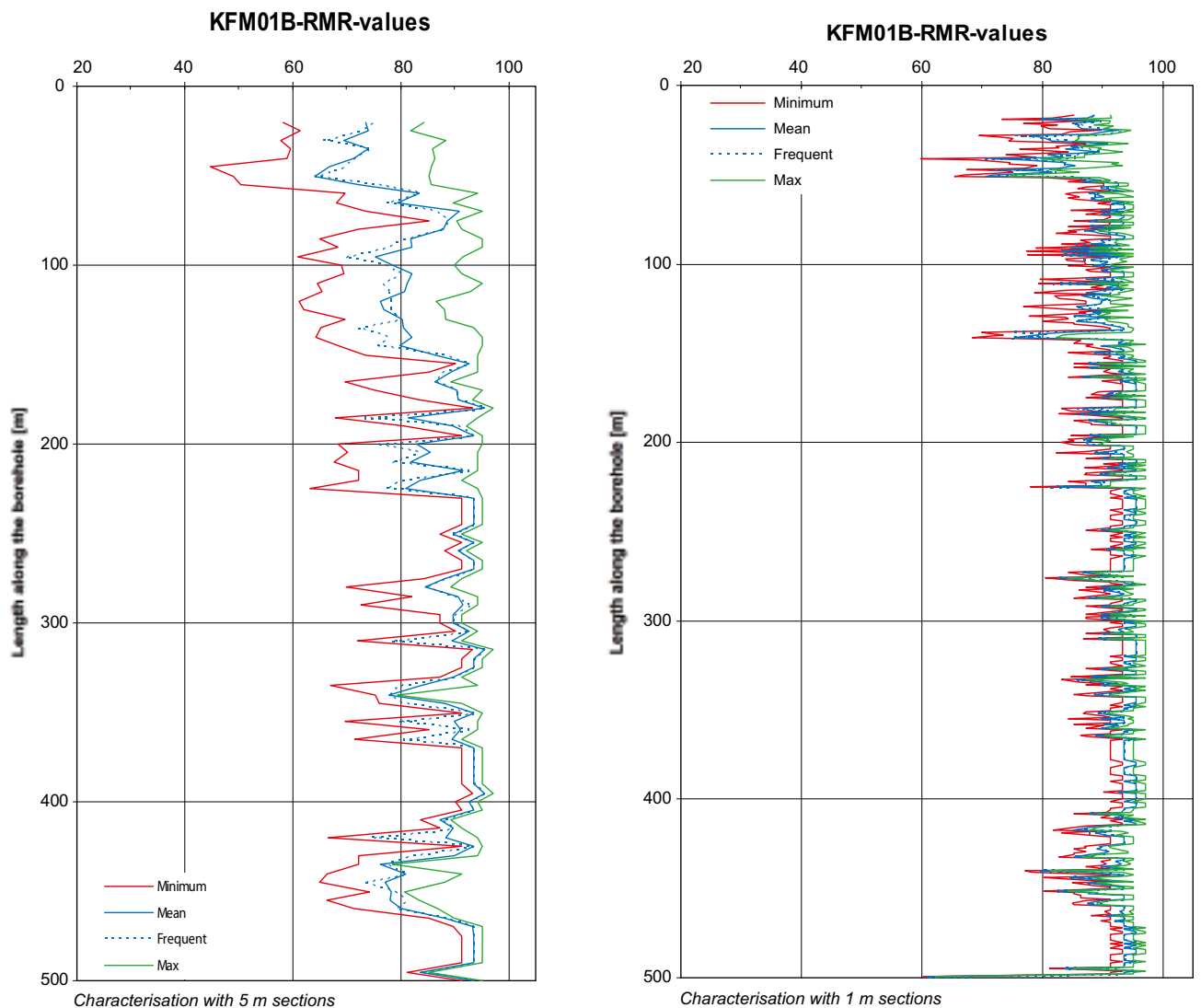


Figure A2-11. Peak and residual cohesion versus depth.

## Results from empirical modelling

### A3.1 Influence of characterisation length

The characterisations were performed for borehole sections of 5 metres according to the empirical methods of the Q-system and RMR (Rock Mass Rating) and the methodology developed for the Äspö Test Case /Andersson et al. 2002, Röshoff et al. 2002/. The influence of the characterisation scale has been examined by comparisons of results obtained for characterisation at 1 and 5 metre sections /Bäckström and Lanaoro 2007/. The comparison shows that the analysed difference in scale has no significant impact on the results, see Figure A3-1 and Figure A3-2.



**Figure A3-1.** Comparison of RMR values obtained for characterisation at 5 and 1 m sections along KFM01B. Adapted from /Bäckström and Lanaoro 2007/.

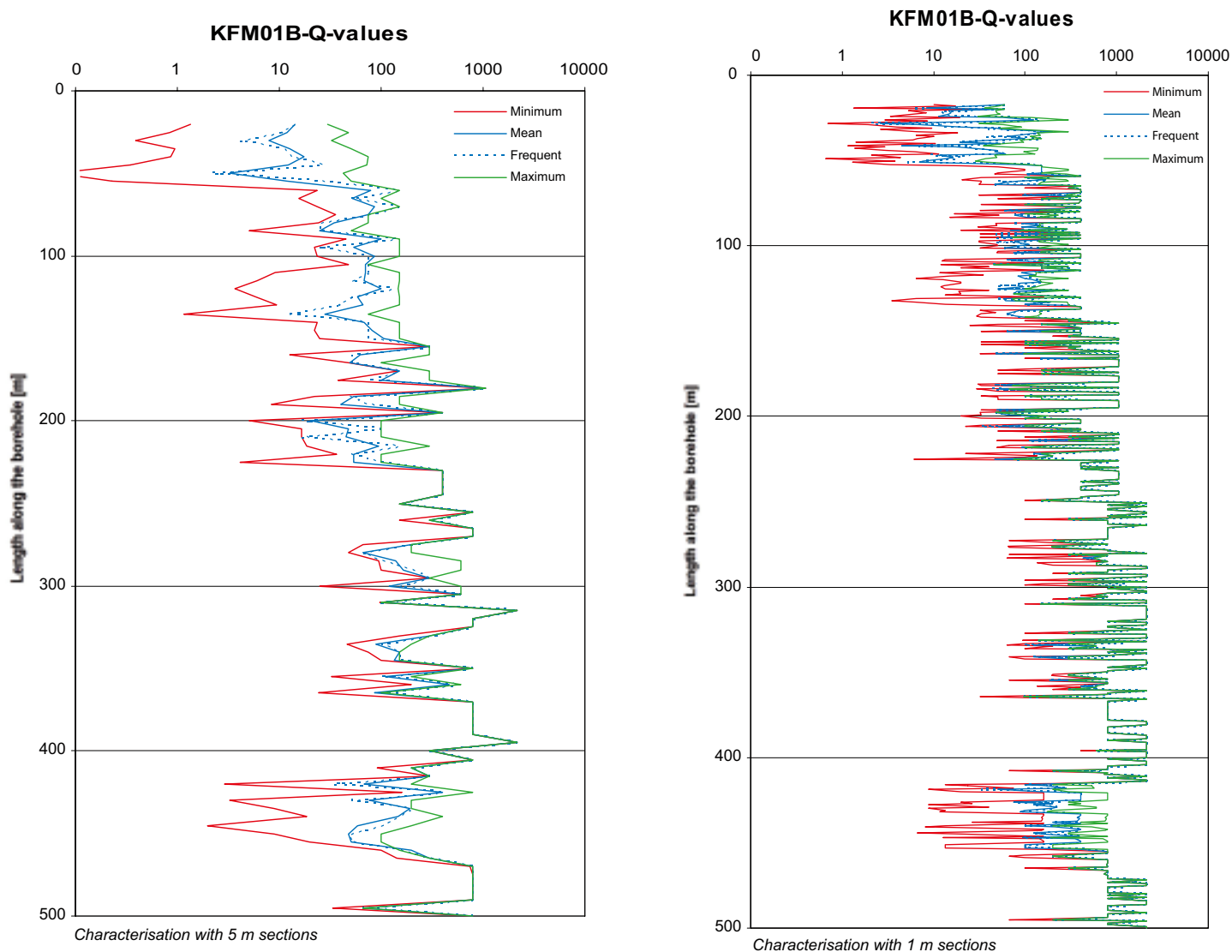


**Figure 3-2.** Comparisons of  $Q$  values obtained for characterisation at 5 and 1 m sections along borehole KFM01B. Adapted from /Bäckström and Lanaro 2007/.

### A3.2 Correlation between $Q$ and RMR

In Figure A3-3 and Figure A3-4 the  $Q$ - and RMR-values of the rock in RFM029 respective RFM045 are plotted together with several generally accepted relations. The results show that the correlation that seems to fit the results best is the one published by /Cameron-Clarke and Budavari 1981/:

$$RMR = 5 \ln Q + 60.8$$

Equation A3-1

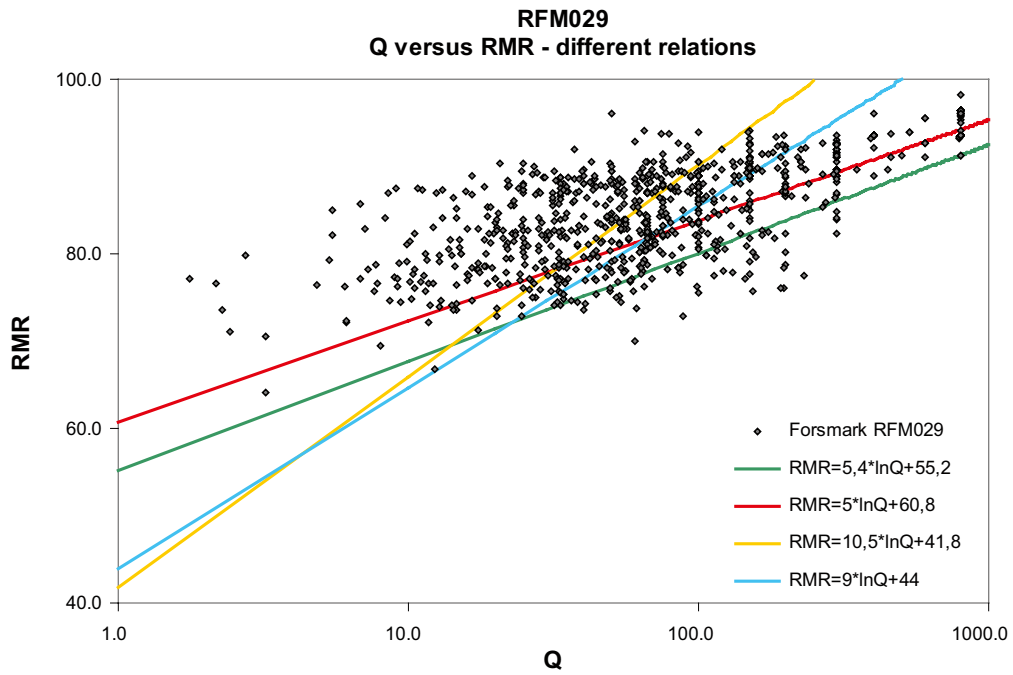


**Figure A3-3.** Correlation between RMR and  $Q$  for core sections of 5 m along boreholes in rock domain RFM029. The characterisation results are compared with some relations from the literature.

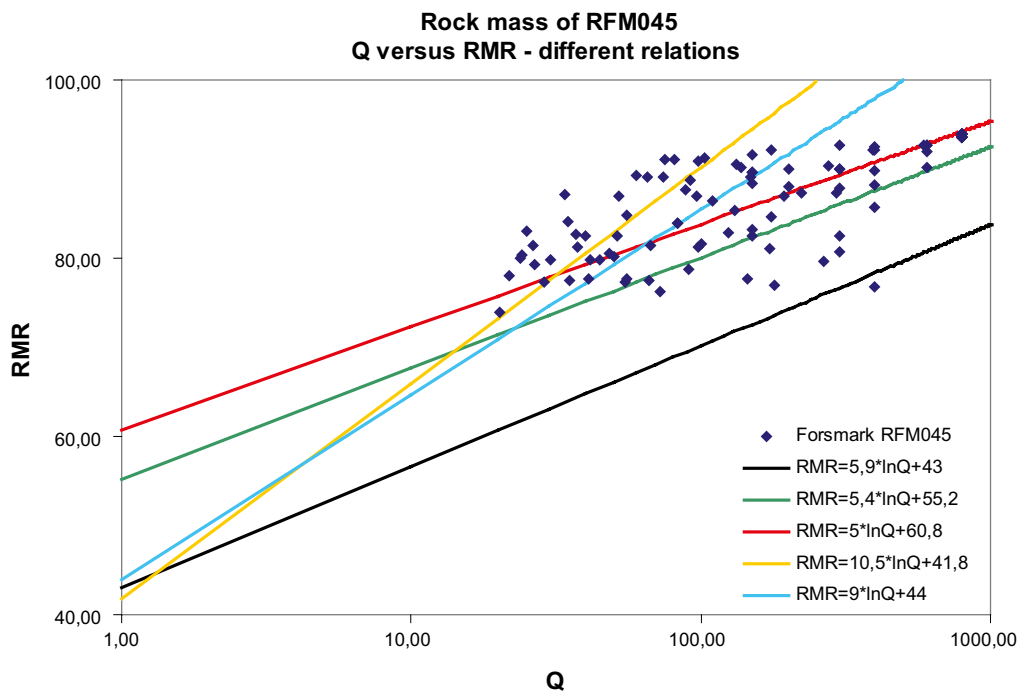


**Figure A3-4.** Correlation between RMR and  $Q$  for core sections of 5 m along boreholes in rock domain RFM045. The characterisation results are compared with some relations from the literature.

### A3.3 Comparison between boreholes

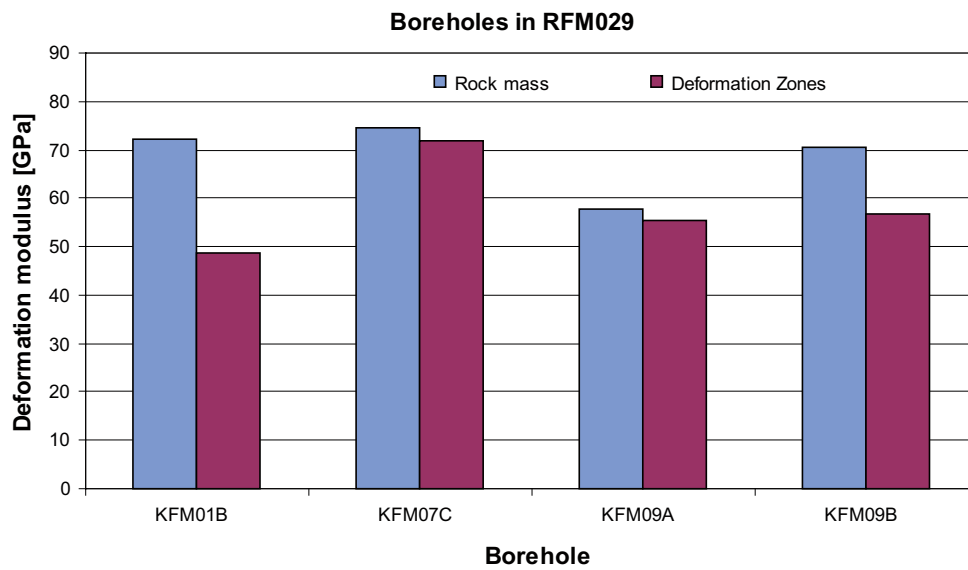


*Figure A3-5. Mean deformation modulus  $E_m$  of the rock mass for the analysed boreholes in RFM029. The mean values for the rock mass outside and within the deformation zones are shown.*

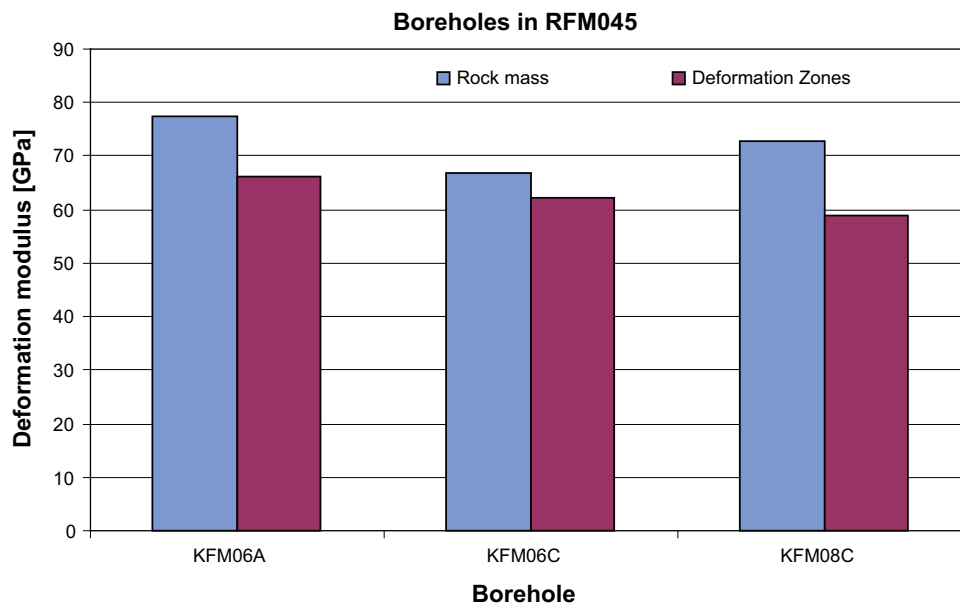


*Figure A3-6. Mean deformation modulus  $E_m$  of the rock mass for the analysed boreholes in RFM029. The mean values for the rock mass outside and within the deformation zones are shown.*



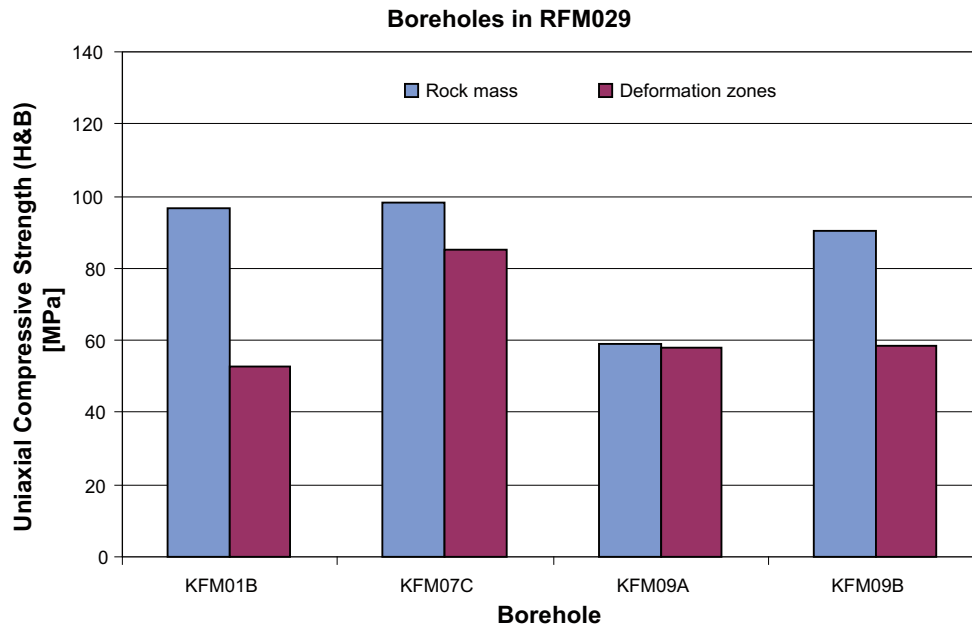


*Figure A3-7. Mean uniaxial compressive strength  $UCS_m$  of the rock mass for the analysed boreholes in RFM029. The mean values for the rock mass outside and within the deformation zones are shown.*

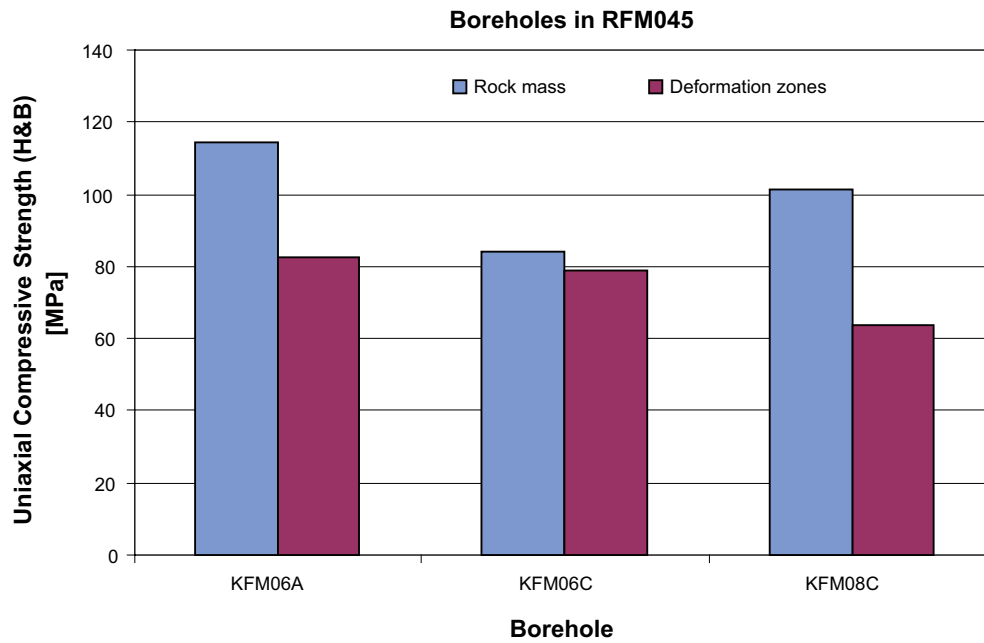


*Figure A3-8. Mean uniaxial compressive strength  $UCS_m$  of the rock mass for the analysed boreholes in RFM045. The mean values for the rock mass outside and within the deformation zones are shown.*

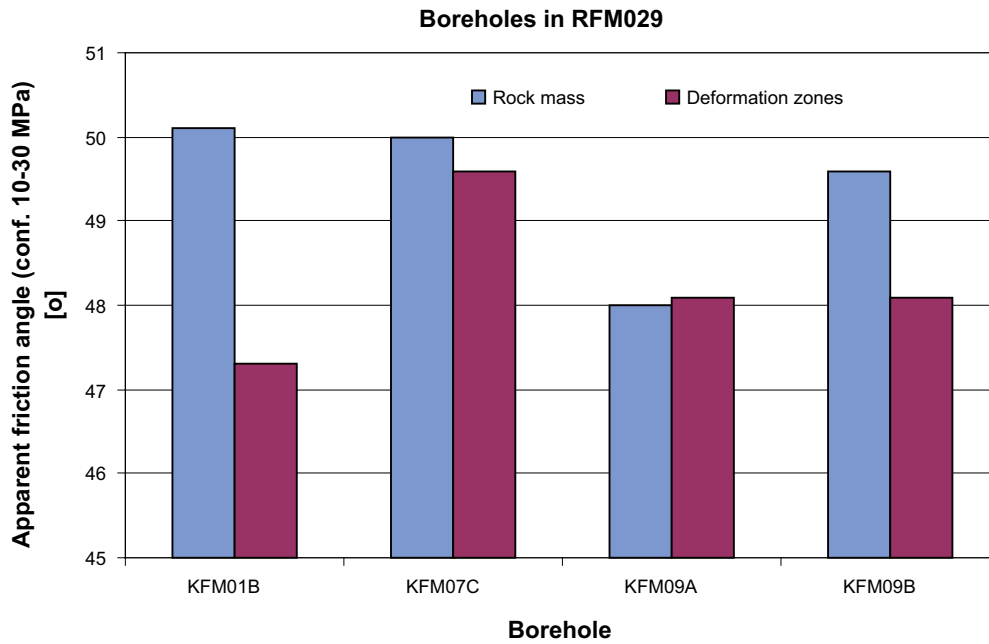


*Figure A3-9. Mean apparent friction angle of the rock mass for the analysed boreholes in RFM029. The mean values for the rock mass outside and within the deformation zones are shown. The confinement stress is between 10 and 30 MPa.*

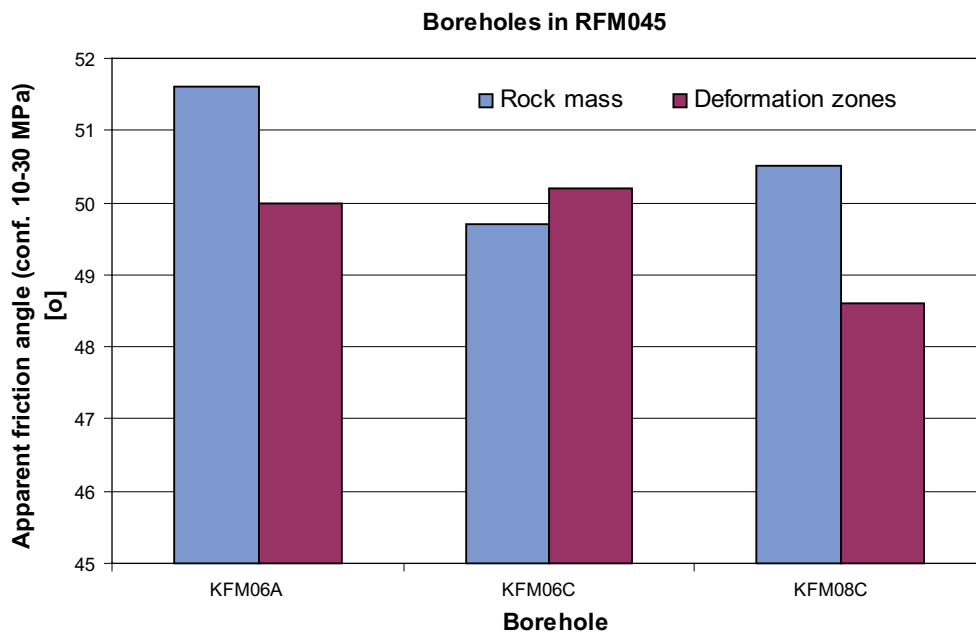


*Figure A3-10. Mean apparent friction angle of the rock mass for the analysed boreholes in RFM045. The mean values for the rock mass outside and within the deformation zones are shown respectively. The confinement stress is between 10 and 30 MPa.*

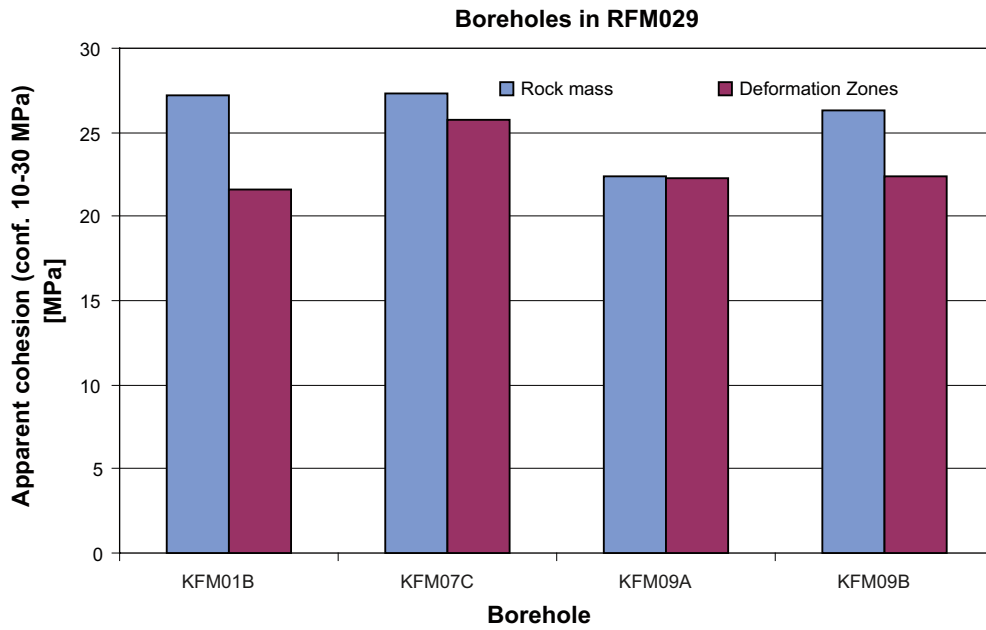


*Figure A3-11. Mean apparent cohesion of the rock mass for the analysed boreholes in RFM029. The mean values for the rock mass outside and within the deformation zones are shown respectively. The confinement stress is between 10 and 30 MPa.*

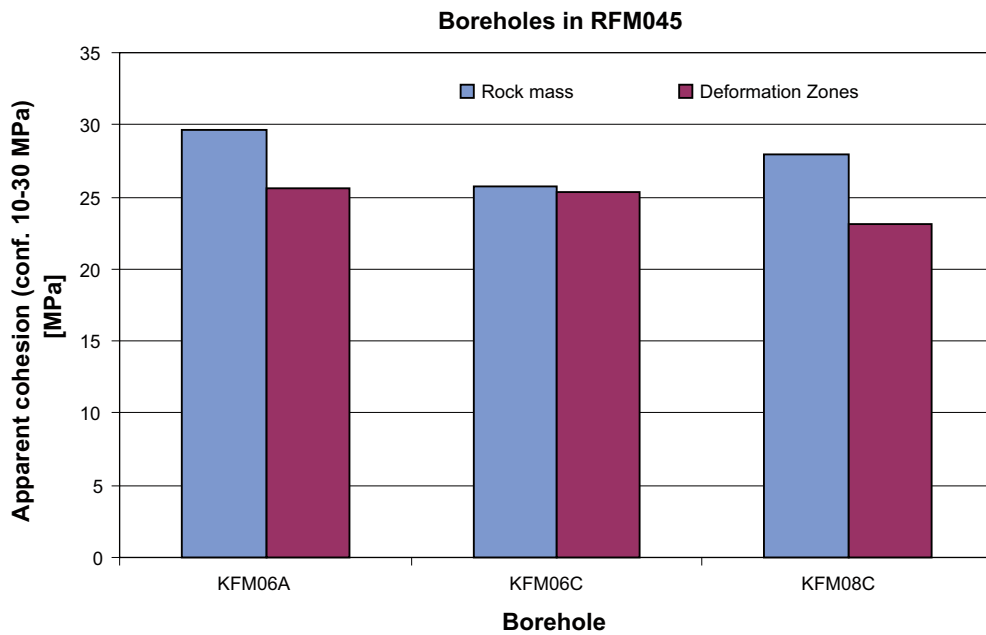


*Figure A3-12. Mean apparent cohesion of the rock mass for the analysed boreholes in RFM045. The mean values for the rock mass outside and within the deformation zones are shown respectively. The confinement stress is between 10 and 30 MPa.*

### A3.4 Variation along the boreholes

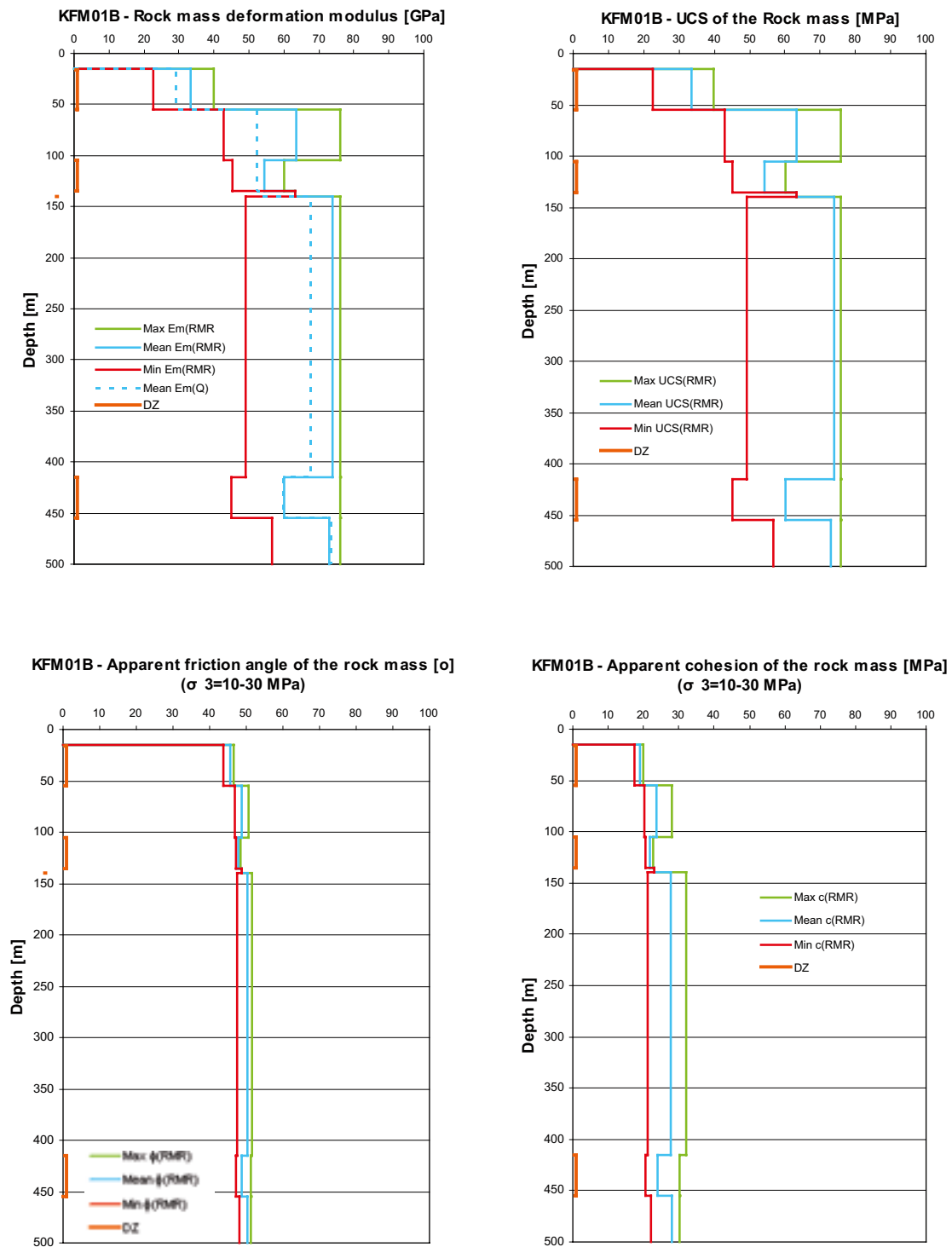
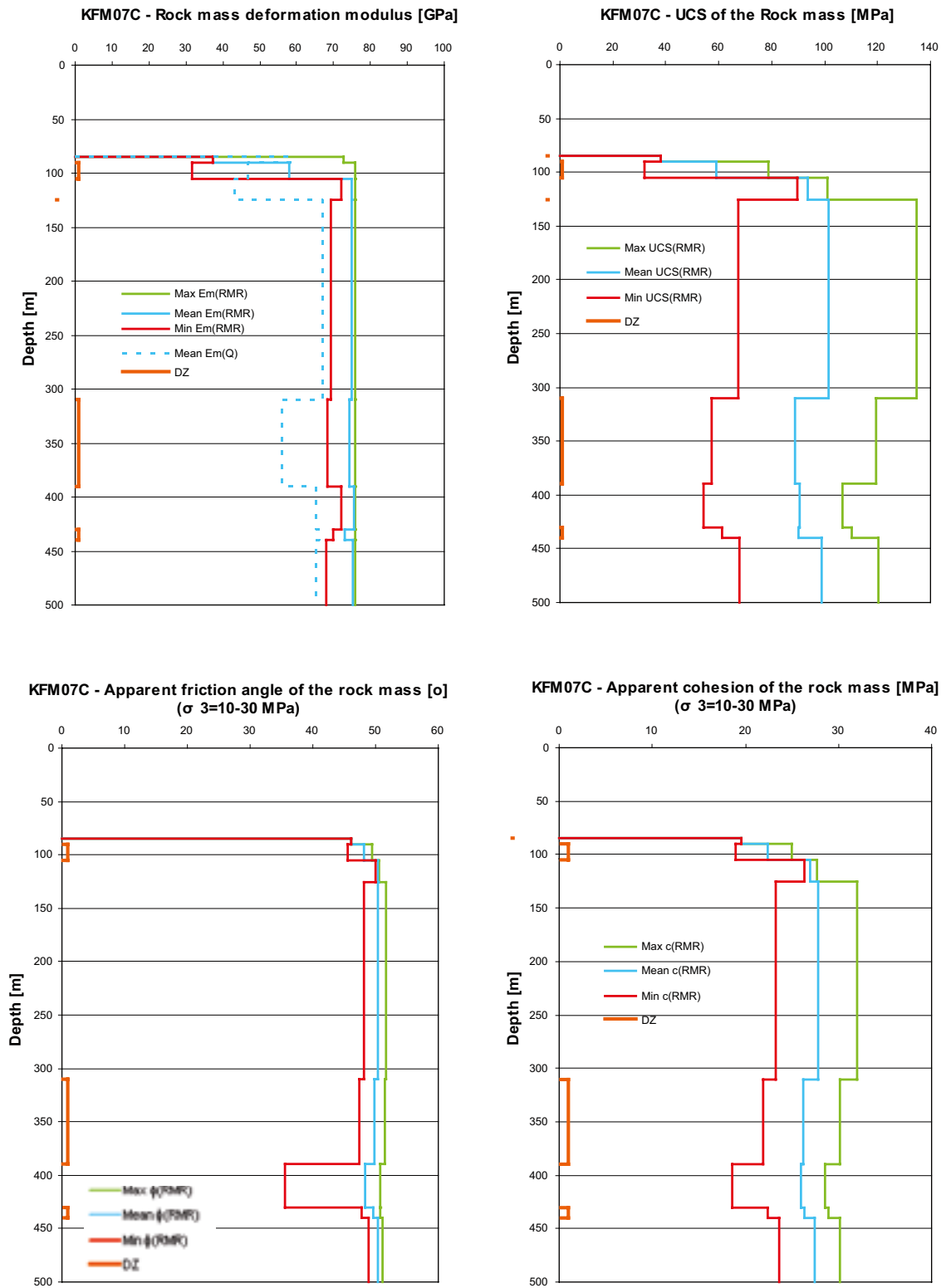
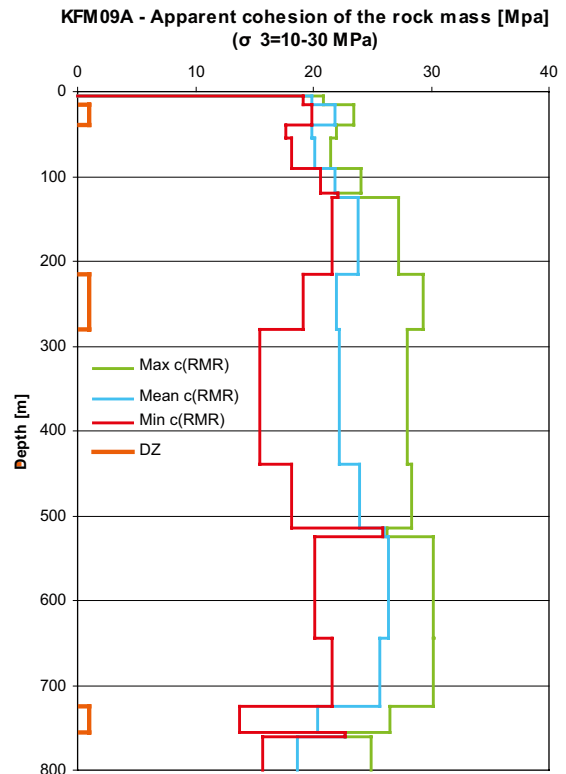
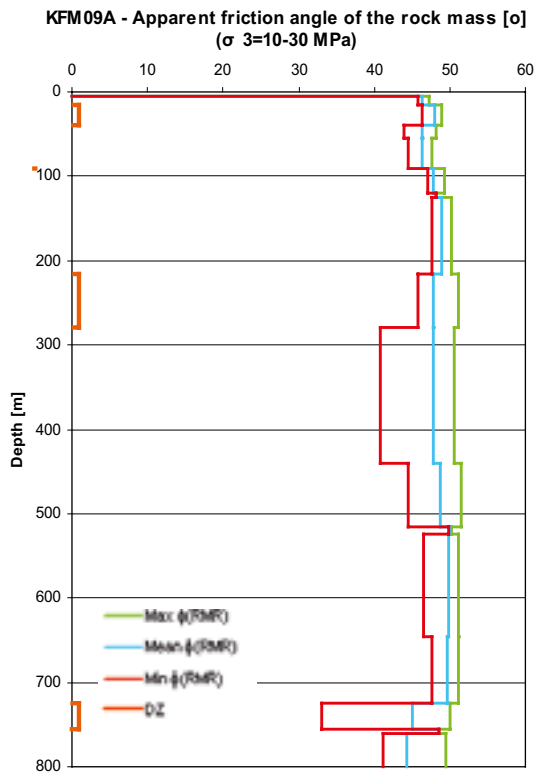
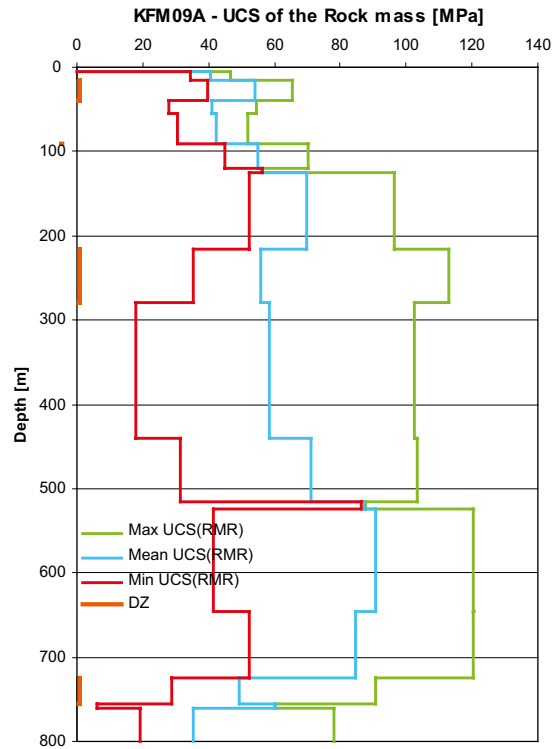
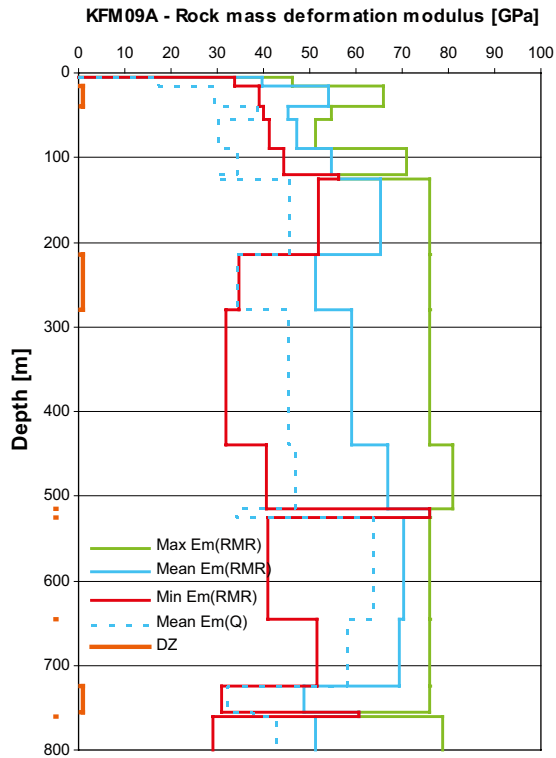


Figure A3-13. KFM01B. Variation of the deformation modulus, uniaxial strength, apparent friction angle and apparent cohesion of the rock mass with depth. The minimum, mean and maximum values are shown.



**Figure A3-14.** KFM07C. Variation of the deformation modulus, uniaxial strength, apparent friction angle and apparent cohesion of the rock mass with depth. The minimum, mean and maximum values are shown.



**Figure A3-15.** KFM09A. Variation of the deformation modulus, uniaxial strength, apparent friction angle and apparent cohesion of the rock mass with depth. The minimum, mean and maximum values are shown.

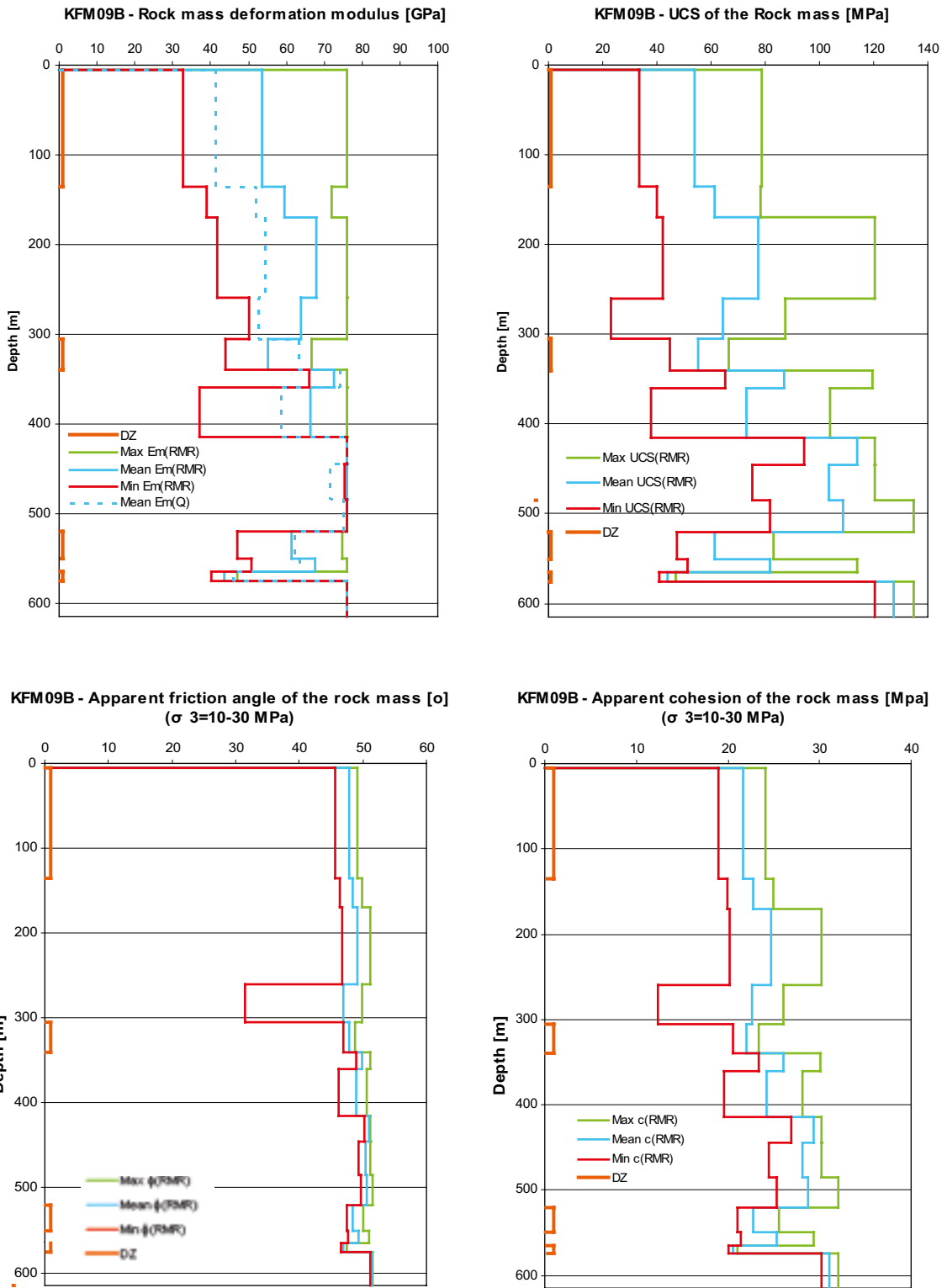


*Figure A3-16. KFM09B. Variation of the deformation modulus, uniaxial strength, apparent friction angle and apparent cohesion of the rock mass with depth. The minimum, mean and maximum values are shown.*

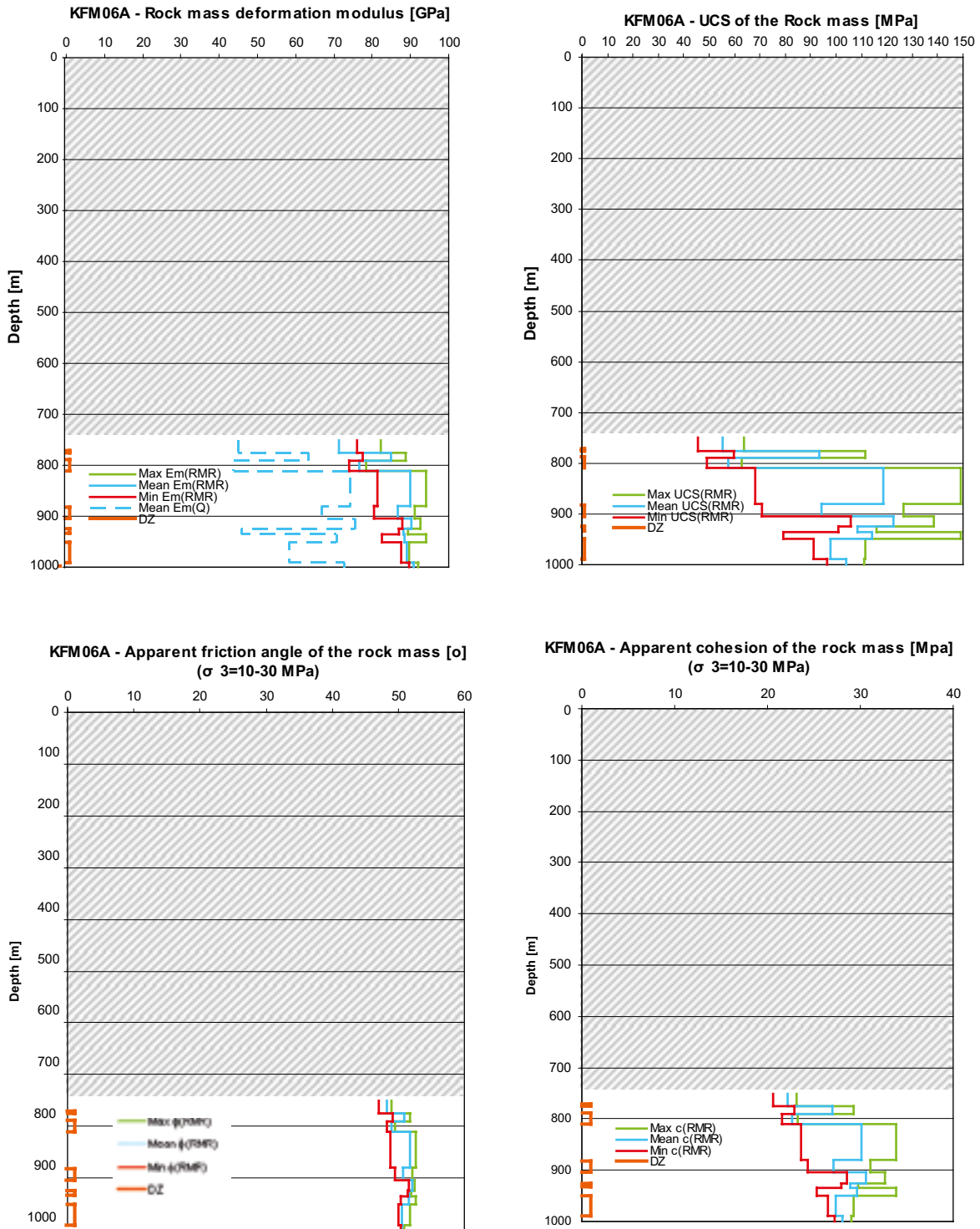


**Figure A3-17.** KFM06A. Variation of the deformation modulus, uniaxial strength, apparent friction angle and apparent cohesion of the rock mass with depth in rock domain RFM045. The minimum, mean and maximum values are shown.



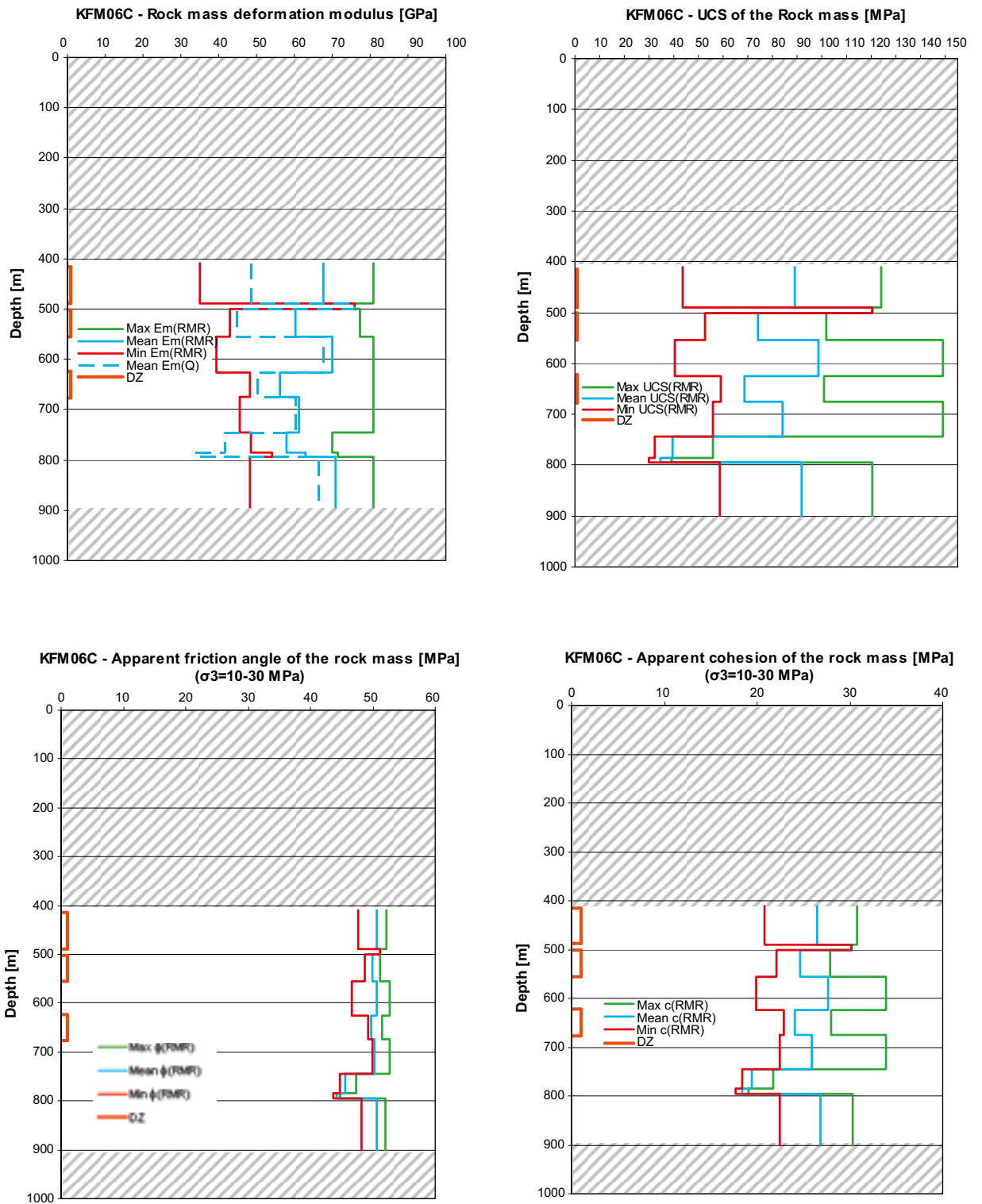


**Figure A3-18.** KFM06C. Variation of the deformation modulus, uniaxial strength, apparent friction angle and apparent cohesion of the rock mass with depth in rock domain RFM045. The minimum, mean and maximum values are shown.

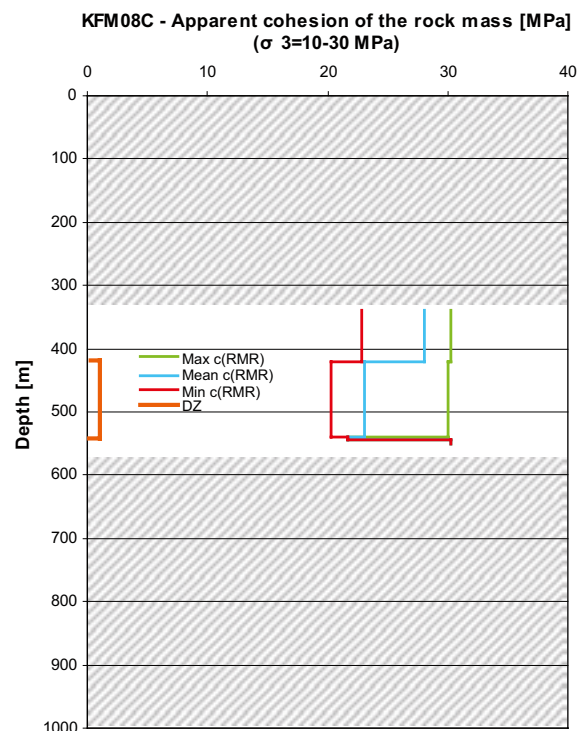
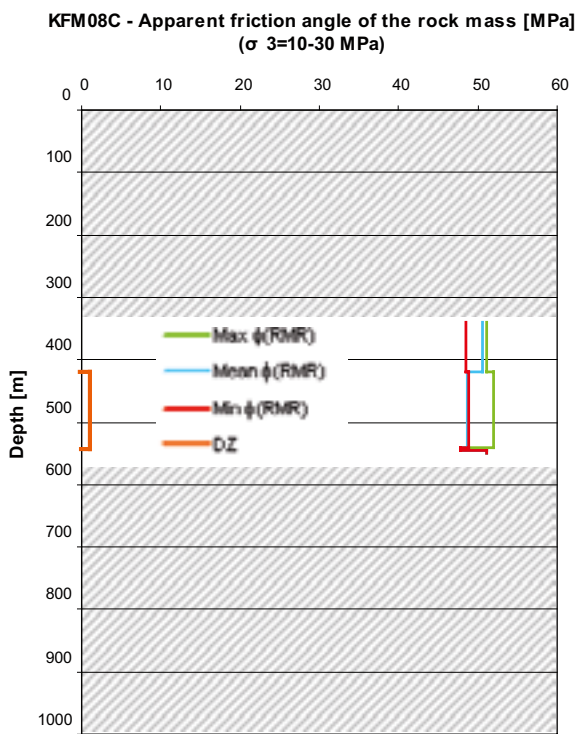
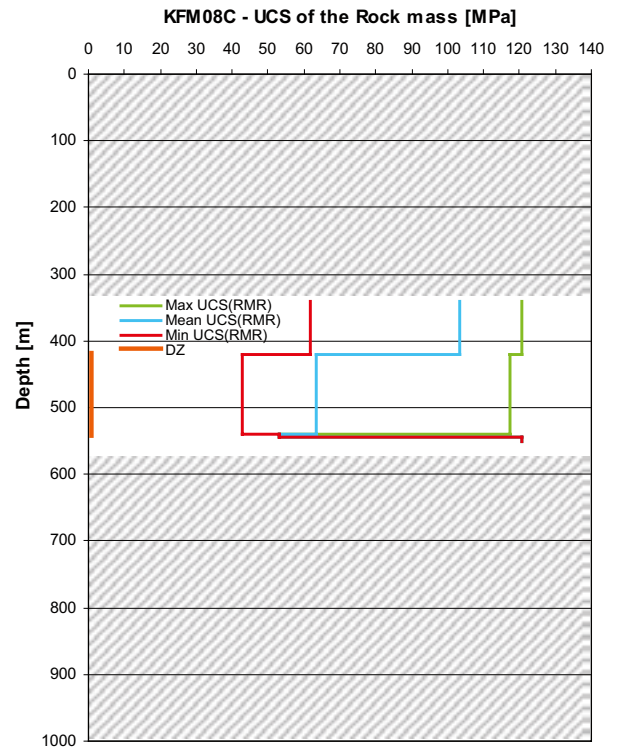
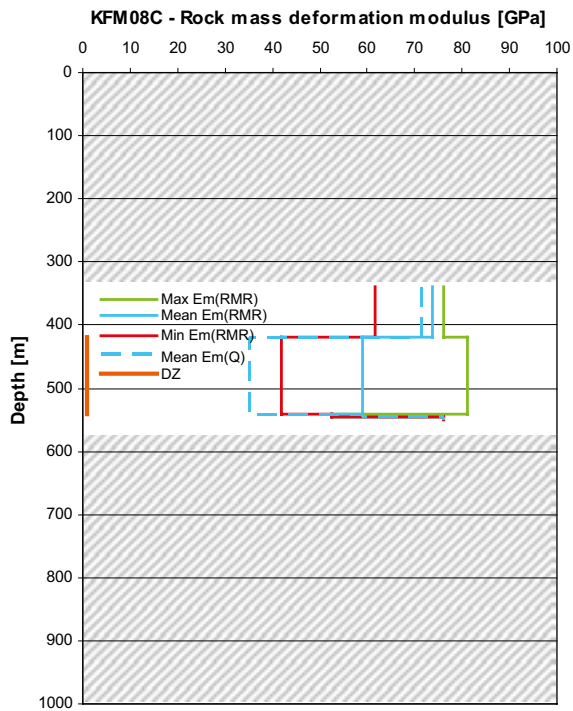


**Figure A3-19.** KFM08C. Variation of the deformation modulus, uniaxial strength, apparent friction angle and apparent cohesion of the rock mass with depth in rock domain RFM045. The minimum, mean and maximum values are shown.

### A3.5 Rock domains

In the following sections, summary tables with the Q index, RMR, and the properties of the rock mass seen as an equivalent continuum are provided. In particular, for each rock domain, the deformation modulus, Poisson's ratio, uniaxial compressive strength (from Hoek-Brown's Criterion and Coulomb's Criterion), tensile strength, apparent friction angle and cohesion are listed.

Besides the mean value and standard deviation, the absolute minimum and absolute maximum values are given in the tables.

#### A3.5.1 Rock Quality Index (Q)

The rock quality of the rock mass is evaluated by means of the Q system. A summary is given in Table A3-1.

**Table A3-1. Q values for rock domains RFM029 and RFM045.**

Q [-]	Outside deformation zones			Within deformation zones		
	Min	Mean [mode]	Max	Min	Mean [mode]	Max
RFM029	2.2	363.4 [100.0]	2,133.3	1.8	80.8 [46.2]	1,066.7
RFM045	20.1	287.5 [150.0]	800.0	3.9	48.4 [33.2]	225.0

#### A3.5.2 Rock Mass Rating (RMR)

**Table A3-2. RMR values for rock domains RFM029 and RFM045.**

RMR [-]	Outside deformation zones			Within deformation zones		
	Min	Mean/St dev	Max	Min	Mean/St dev	Max
RFM029	71.0	87.4/6.1	98.5	64.2	81.1/5.6	94.0
RFM045	73.9	86.7/5.8	94.0	71.8	82.3/5.1	91.1

#### A3.5.3 Uniaxial compressive strength of the rock mass

**Table A3-3. Estimated uniaxial compressive strength  $UCS_m$  (equivalent strength for zero confinement pressure) according to the Hoek-Brown's Criterion for rock domains RFM029 and RFM045.**

$UCS_m$ [MPa]	Outside deformation zones			Within deformation zones		
	Min	Mean/St dev	Max	Min	Mean/St dev	Max
RFM029	22.9	83.7/28.0	153.3	13.9	59.1/19.7	120.5
RFM045	30.1	94.5/32.2	149.3	42.7	75.6/22.8	126.3

### A3.5.4 Deformation modulus of the rock mass

**Table A3-4. Estimated deformation modulus,  $E_m$ , from RMR for rock domains RFM029 and RFM045.**

$E_m$ [GPa] Rock domain/ Deformation zone	Outside deformation zones			Within deformation zones		
	Min	Mean/St dev	Max	Min	Mean/St dev	Max
RFM029	33.6	69.4/9.9	76.0	22.6	58.6/13.5	76.0
RFM045	39.5	70.3/11.7	81.0	35.1	62.5/13.7	81.0

### A3.5.5 Poisson's ratio of the rock mass

**Table A3-5. Estimated Poisson's ratio from RMR for rock domains RFM029 and RFM045.**

$\nu_m$ [-] Rock domain/ Deformation zone	Outside deformation zones			Within deformation zones		
	Min	Mean/St dev	Max	Min	Mean/St dev	Max
RFM029	0.11	0.22/0.03	0.30	0.07	0.21/0.07	0.55
RFM045	0.12	0.23/0.04	0.33	0.11	0.20/0.04	0.27

### A3.5.6 Coulomb's strength criterion of the rock mass

The Coulomb's Criterion is fitted to the Hoek-Brown's Criterion to determine the apparent cohesion  $c$ , friction angle  $\phi$  and the extrapolated uniaxial compressive strength. This fitting is performed for confinement stresses between 10 and 30 MPa.

**Table A3-6. Estimated cohesion of the rock mass according to the Mohr-Coulomb criterion for rock domains RFM029 and RFM045.**

$c_m$ [MPa]* Rock domain/ Deformation zone	Outside deformations zones			Within deformation zones		
	Min	Mean/St dev	Max	Min	Mean/St dev	Max
RFM029	12.4	25.5/3.6	34.6	14.0	22.4/2.6	30.2
RFM045	17.7	27.0/4.2	33.9	20.3	24.7/2.9	31.1

\* Linear envelope between 10 and 30 MPa.

**Table A3-7. Estimated friction angle of the rock mass according to the Mohr-Coulomb criterion for rock domains RFM029 and RFM045.**

$\phi_m$ [°]* Rock domain/ Deformation zone	Outside deformations zones			Within deformation zones		
	Min	Mean/St dev	Max	Min	Mean/St dev	Max
RFM029	31.5	49.2/1.6	51.7	38.2	47.9/1.6	51.4
RFM045	43.5	50.3/2.0	52.7	46.8	49.7/1.4	52.2

\* Linear envelope between 10 and 30 MPa.

**Table A3-8. Estimated apparent uniaxial compressive strength UCS<sub>m</sub> according to the Mohr-Coulomb criterion for rock domains RFM029 and RFM045.**

UCS <sub>m</sub> * (Mohr-Coulomb) Rock domain/ Deformation zone	Outside deformations zones			Within deformation zones		
	Min	Mean/St dev	Max	Min	Mean/St dev	Max
RFM029	44.3	138.3/24.6	195.6	57.8	117.0/18.4	171.9
RFM045	82.1	151.2/29.9	201.2	102.3	135.4/20.9	181.6

\* Linear envelope between 10 and 30 MPa.

### A3.5.7 Tensile strength of the rock mass

By using the Hoek-Brown's Criterion, the tensile strength of the rock mass, assumed as a continuous medium, can be determined. Results are presented in Table A3-9. These values should, however, be used with caution when applied to relatively fracture-free rock such as the rock at the Forsmark site.

**Table A3-9. Estimated tensile strength, T<sub>m</sub>, according to the Mohr-Coulomb criterion for rock domains RFM029 and RFM045.**

T <sub>m</sub> [MPa] Rock domain/ Deformation zone	Outside deformation zones			Within deformation zones		
	Min	Mean/St dev	Max	Min	Mean/St dev	Max
RFM029	0.49	2.12/0.96	4.99	0.24	1.30/0.59	3.31
RFM045	0.60	2.31/0.99	4.00	0.75	1.68/0.67	3.19

## A3.6 Uncertainties

### A3.6.1 Background

It was decided to correlate the uncertainty of each mechanical parameter P to the range of its possible values obtainable for a certain depth (e.g. location of each core section of 5 m). This range of variation might depend on: i) uncertainty in the input data; ii) opinion of different operators characterising the rock mass; iii) estimation of missing parameters; iv) biases due to sampling direction; v) intrinsic uncertainties of the methods used for the characterisation.

The range of variation of the parameter P at each depth is inferred from the width of the interval between the possible minimum and maximum occurring value of the parameter. For Q and RMR, the range of the possible minimum and maximum values of RMR and Q is obtained by combining the indices and ratings in the most unfavourable and favourable way, respectively. For the other parameters, the range of variation might depend on the variation of Q and RMR, or on that of other mechanical properties (e.g. from the laboratory).

The spatial variability of the geological parameters has to be filtered out because it should not affect the uncertainty on the mean value of P at a certain depth. To filter the spatial variability out, the differences between the maximum and mean P, and the minimum and mean P are evaluated at each depth. These differences are then normalised by the mean value of P itself. Each obtained normalised difference is considered as a sample from a statistical population of variation intervals. The concept of "confidence interval of a population mean" can then be applied to quantify the uncertainty. According to the "Central Limit Theorem" /Peebles 1993/, the 95% confidence interval of the mean  $\Delta_{\text{conf mean}}$  is obtained as:

$$\Delta_{\text{conf mean of } P} = \pm \frac{1.96 \sigma}{\sqrt{n}} \quad \text{Equation A3-2}$$

where  $\sigma$  is the standard deviation of the parameter population and  $n$  is the number of values composing the sample.  $n$  is also the number of values on which the mean can be calculated for each rock domain/deformation zone.

For rock domain RFM029, the number of values,  $n$ , provided by each borehole is around 785. For RFM012, RFM017 and RFM018,  $n$  is around 42, 15 and 12, respectively.

In practice, two confidence intervals are determined by means of the proposed technique, one related to the maximum value of P, and the other related to the minimum value of P:

$$\Delta P_{+conf\ mean} = \frac{P_{MAX} - P_{MEAN}}{\sqrt{n}}$$

$$\Delta P_{-conf\ mean} = \frac{P_{MEAN} - P_{MIN}}{\sqrt{n}}$$

Equation A3-3

Where, P is the parameter with its possible maximum, minimum and mean values.

### A3.6.2 Uncertainty in the rock mass quality and properties

**Table A3-10. Uncertainties in the predicted mechanical properties of rock domains RFM029 and RFM045. The uncertainties are given as the range of variation of the possible mean value.**

Rock domain	RFM029	RFM045
Properties of the rock mass	Uncertainty of the mean	Uncertainty of the mean
Q [-]	-1% +4%	-5% +19%
RMR [-]	-1% +0%	-1% +1%
$E_m$ [GPa] <sup>1</sup>	-2% +1%	-3% +2%
$\nu_m$ [-] <sup>1</sup>	-2% +2%	-2% +4%
UCS <sub>m</sub> (H-B) [MPa] <sup>2</sup>	-3% +3%	-6% +8%
$\phi_m$ [°] <sup>3</sup>	-1% +0%	-1% +1%
$c_m$ [MPa] <sup>3</sup>	-1% +1%	-3% +3%
UCS <sub>m</sub> (M-C) [MPa] <sup>3</sup>	-2% +2%	-4% +4%
$T_m$ [MPa] <sup>2</sup>	-3% +4%	-6% +10%

<sup>1</sup>) The deformation modulus and the Poisson's ratio of the rock mass are assumed to be independent of the state of stress due to their high values.

<sup>2</sup>) The uniaxial compressive and tensile strength is obtained from the Hoek-Brown's envelope of the rock mass.

<sup>3</sup>) The apparent uniaxial compressive strength, cohesion and friction angle are obtained from the Coulomb's Strength Criterion between 10 and 30 MPa confinement stress.

It can be observed that the size of the available dataset affects the uncertainty in the determination. RFM029 has lower values due to the larger amount of data available.

In particular, the uncertainty in the Q determination is the largest. This is because the Q system is structured in a logarithmic fashion, and this is not well captured by the technique for estimating the uncertainties.

RMR seems to be characterised with very high accuracy. The uncertainty in the mean varies between  $\pm 0\%$  to about  $\pm 1\%$ .

### A3.7 Fracture domains

A fracture domain refers to a rock volume outside deformation zones in which rock units show similar fracture frequency characteristics. Rock domain RFM029 contains three fracture domains, FFM01, FFM02 and FFM03, while rock domain RFM045 consists of one fracture domain, FFM06.

The same empirical relationships were used as for the rock domains and deformation zones. Below is a summary of the results and the statistical spread of the data.

Rock domain	FFM01	FFM02	FFM03	FFM06
Properties of the rock mass	Mean/st. dev. Min-max Uncertainty of mean	Mean/st. dev. Min-max Uncertainty of mean	Mean/st. dev. Min-max Uncertainty of mean	Mean/st. dev. Min-max Uncertainty of mean
Deformation Modulus <sup>1</sup>	72/8 39–76 ± 1%	59/13 34–76 ± 5%	67/8 40–75 ± 2%	70/12 40–81 ± 3%
Poisson's ratio <sup>1</sup>	0.23/0.03 0.12–0.30 ± 1%	0.19/0.04 0.11–0.29 ± 5%	0.21/0.03 0.13–0.24 ± 2%	0.23/0.04 0.12–0.33 ± 3%
Uniaxial compressive strength (Hoek-Brown) <sup>2</sup>	92/27 23–153 ± 3%	62/24 28–135 ± 9%	68/20 36–121 ± 4%	95/32 30–149 ± 7%
Friction angle <sup>3</sup>	50/2 32–52 ± 0%	48/2 44–52 ± 1%	49/1 46–51 ± 0%	50/2 43–53 ± 1%
Cohesion <sup>3</sup>	27/4 12–35 ± 1%	23/3 18–32 ± 3%	24/4 19–30 ± 2%	27/4 18–34 ± 3%
Uniaxial compressive strength (Mohr-Coulomb) <sup>3</sup>	146/24 44–196 ± 1%	120/22 83–183 ± 4%	125/18 95–171 ± 2%	151/30 82–201 ± 4%
Tensile strength <sup>2</sup>	2.4/1.0 0.6–5.0 ± 3%	1.4/0.7 0.6–3.9 ± 12%	1.6/0.6 0.7–3.4 ± 6%	2.3/1.0 0.6–4.0 ± 8%

<sup>1</sup>) The deformation modulus and the Poisson's ratio of the rock mass are assumed to be independent of the state of stress due to their high values.

<sup>2</sup>) The uniaxial compressive and tensile strength is obtained from the Hoek-Brown's envelope of the rock mass.

<sup>3</sup>) The apparent uniaxial compressive strength, cohesion and friction angle are obtained from the Coulomb's Strength Criterion between 10 and 30 MPa confinement stress.

### A3.8 Deformation zones

23 deterministic deformation zones were found to intercept the boreholes in rock domain RFM029 and RFM045 /Stephens et al. 2007/.

The deformation zones are divided into groups based on orientation. These groups are:

- “Vertical and steeply-dipping brittle deformation zones with ENE, NNE (and NE) strike.”
- “Gently-dipping brittle deformation zones.”
- “Vertical and steeply-dipping brittle deformation zones with NNW strike.”
- “Vertical and steeply, SSW- (and SW-dipping) deformation zones with WNW (and NW strike).”

**Table A3-11. The deterministic deformation zones in RFM029 and RFM045.**

Deformation zone	Length (m)	Thickness (m)	Strike/dip	Group
ZFMENE0159A	909	16	239/80	ENE, NNE and NE strike
ZFMENE1208A	1,081	20	238/81	ENE, NNE and NE strike
ZFMA2	987	35	080/24	Gently-dipping brittle zone
ZFMNNW0404	947	10	150/90	NNW and EW strike
ZFM1203	881	10	180/7	Gently-dipping brittle zone
ZFMENE2320	1,251	21	244/81	ENE, NNE and NE strike
ZFMENE2325A	963	23	246/82	ENE, NNE and NE strike
ZFMENE2325B	553	10	245/81	ENE, NNE and NE strike
ZFMENE1208B	1,112	13	238/81	ENE, NNE and NE strike
ZFMENE0061	2,081	11	252/85	ENE, NNE and NE strike
ZFMNNE0725	1,274	12	196/84	ENE, NNE and NE strike
ZFMNNE2280	1,035	14	206/84	ENE, NNE and NE strike
ZFMNNE2263	446	30	197/63	ENE, NNE and NE strike
ZFMWNW0044	834	39	118/77	Steeply dipping with WNW strike.
ZFMNNE2312	742	43	202/84	ENE, NNE and NE strike
ZFMENE1192	1,090	3	064/88	ENE, NNE and NE strike
ZFMA3	3,234	17	046/22	Gently-dipping brittle zone
ZFM866	1,724	11	080/23	Gently-dipping brittle zone
ZFMB4	–	12	050/29	Gently-dipping brittle zone
ZFMB1	3,224	7	032/27	Gently-dipping brittle zone
ZFMA7	3,510	7	055/23	Gently-dipping brittle zone
ZFMA4	3,641	25	061/25	Gently-dipping brittle zone
ZFMENE2254	1,021	3	238/83	ENE, NNE and NE strike

Q and RMR are listed below for each deformation zone as well as:

- The deformation modulus and the Poisson's ratio.
- The uniaxial compressive and tensile strength according to the Hoek-Brown's Criterion.
- The apparent friction angle, cohesion and uniaxial compressive strength according to the Coulomb's Criterion.

Presented in the tables below are the mean value and standard deviation along with the absolute minimum and maximum values.

**Table A3-12. Rock mass properties for the vertical and steeply-dipping brittle deformation zones with ENE, NNE (and NE) strike.**

Def. zone Properties of the rock mass	ZFMENE0159A			ZFMENE1208A			ZFMENE2320		
	min	Mean/st dev	max	min	Mean/st dev	max	min	Mean/st dev	max
Q [-]	5.2	34.9 [25.1]	117.4	2.3	25.0 [17.5]	75.2	15.8	128.7 [93.7]	800.0
RMR [-]	71.5	79.4/ 5.6	92.6	70.5	78.0/ 4.0	85.9	72.8	86.6/ 4.6	93.6
E <sub>m</sub> [GPa]	34.6	54.0/ 13.7	76.0	32.6	51.2/ 11.5	76.0	37.2	71.2/ 9.9	76.0
ν <sub>m</sub> [-]	0.11	0.19/ 0.06	0.29	0.10	0.18/ 0.05	0.27	0.12	0.23/ 0.04	0.30
UCS <sub>m</sub> (H-B) [MPa]	35.4	57.1/ 19.5	113.0	33.4	51.7/ 11.7	78.7	38.0	82.0/ 19.1	119.4
φ <sub>m</sub> [°]	45.8	48.0/ 1.4	51.2	45.6	47.6/ 1.1	49.5	46.2	49.5/ 1.2	51.4
c <sub>m</sub> [MPa]	19.2	22.2/ 2.5	29.3	18.9	21.5/ 1.6	24.9	19.6	25.3/ 2.5	30.1
UCS <sub>m</sub> (M-C) [MPa]	94.8	116.1/ 18.0	166.4	92.7	111.1/ 11.2	135.2	97.5	137.8/ 17.4	171.9
T <sub>m</sub> [MPa]	0.63	1.21/ 0.57	2.94	0.58	1.05/ 0.32	1.86	0.69	1.99/ 0.59	3.18



**Table A3-13. Rock mass properties for the vertical and steeply-dipping brittle deformation zones with ENE, NNE (and NE) strike.**

Def. zone Properties of the rock mass	ZFMENE1208B			ZFMENE0061			ZFMNNE0725		
	min	Mean/st dev	max	min	Mean/st dev	max	min	Mean/st dev	max
Q [-]	7.3	20.8 [17.5]	44.5	25.2	31.1 [26.5]	46.3	20.4	41.0 [30.8]	69.7
RMR [-]	75.9	78.7/ 2.2	84.0	74.0	76.8/ 2.0	78.4	76.0	78.2/ 2.7	82.2
E <sub>m</sub> [GPa]	44.3	52.5/ 7.2	70.8	39.8	46.9/ 5.3	51.2	44.7	51.2/ 8.4	64.0
v <sub>m</sub> [-]	0.14	0.18/ 0.04	0.27	0.13	0.15/ 0.02	0.16	0.14	0.17/ 0.04	0.26
UCS <sub>m</sub> (H-B) [MPa]	45.0	52.8/ 6.9	70.1	49.1	57.6/ 6.3	62.6	45.4	55.5/ 6.6	63.6
φ <sub>m</sub> [°]	47.0	47.8/ 0.6	49.3	48.3	49.0/ 0.5	49.4	47.1	48.4/ 0.8	49.1
c <sub>m</sub> [MPa]	20.6	21.7/ 0.9	24.0	21.6	22.7/ 0.8	23.3	20.6	22.2/ 0.9	23.1
UCS <sub>m</sub> (M-C) [MPa]	104.5	112.3/ 6.7	129.2	113.3	121.3/ 5.9	126.1	104.9	116.7/ 7.3	123.3
T <sub>m</sub> [MPa]	0.87	1.08/ 0.19	1.54	0.88	1.10/ 0.16	1.23	0.88	1.11/ 0.17	1.35

**Table A3-14. Rock mass properties for the vertical and steeply-dipping brittle deformation zones with ENE, NNE (and NE) strike.**

Def. zone Properties of the rock mass	ZFMNNE2280			ZFMENE2325A			ZFMENE2325B		
	min	Mean/st dev	max	min	Mean/st dev	max	min	Mean/st dev	max
Q [-]	37.5	86.4 [77.2]	150.0	33.0	128.9 [127.2]	240.0	31.7	59.9 [57.8]	90.3
RMR [-]	87.5	89.0/ 0.7	89.6	76.9	82.4/ 4.9	88.0	74.2	76.4/ 2.1	78.2
E <sub>m</sub> [GPa]	76.0	77.3/ 2.3	81.0	47.0	61.5/ 12.3	74.8	40.2	46.0/ 5.3	50.8
v <sub>m</sub> [-]	0.24	0.25/ 0.01	0.26	0.19	0.24/ 0.05	0.30	0.13	0.16/ 0.03	0.19
UCS <sub>m</sub> (H-B) [MPa]	91.3	97.8/ 6.8	111.6	47.2	61.4/ 14.4	83.0	41.0	46.5/ 5.2	51.3
φ <sub>m</sub> [°]	50.1	50.6/ 0.7	51.8	47.5	48.4/ 1.0	50.0	46.6	47.2/ 0.60	47.6
c <sub>m</sub> [MPa]	26.5	27.4/ 0.9	29.3	21.0	22.8/ 1.8	25.6	20.0	20.8/ 0.7	21.4
UCS <sub>m</sub> (M-C) [MPa]	146.2	153.1/ 8.1	169.0	108.1	120.0/ 13.1	140.6	100.6	106.4/ 5.2	110.6
T <sub>m</sub> [MPa]	2.27	2.43/ 0.13	2.70	0.90	1.33/ 0.42	1.94	0.77	0.90/ 0.14	1.04

**Table A3-15. Rock mass properties for the vertical and steeply-dipping brittle deformation zones with ENE, NNE (and NE) strike.**

Def. zone Properties of the rock mass	ZFMNNE2263			ZFMNNE2312		
	min	Mean/st dev	max	min	Mean/st dev	max
Q [-]	11.6	41.3 [45.5]	99.4	7.73	20.6 [15.5]	54.0
RMR [-]	71.8	83.5/ 6.4	90.7	74.9	80.8/ 3.6	89.7
E <sub>m</sub> [GPa]	35.1	66.6/ 17.0	81.0	42.0	59.1/ 10.7	81.0
v <sub>m</sub> [-]	0.11	0.21/ 0.05	0.26	0.13	0.19/ 0.03	0.26
UCS <sub>m</sub> (H-B) [MPa]	43.5	86.9/ 28.1	123.9	42.7	63.5/ 17.6	117.4
φ <sub>m</sub> [°]	47.7	50.4/ 1.5	52.1	46.7	48.6/ 1.29	52.0
c <sub>m</sub> [MPa]	20.8	26.2/ 3.5	30.8	20.3	23.1/ 2.3	30.0
UCS <sub>m</sub> (M-C) [MPa]	107.7	146.8/ 25.2	179.5	102.3	122.6/ 17.1	173.9
T <sub>m</sub> [MPa]	0.75	1.98/ 0.83	3.11	0.81	1.37/ 0.49	2.89

**Table A3-16. Rock mass properties for the vertical and steeply-dipping brittle deformation zones with ENE, NNE (and NE) strike.**

Def. zone Properties of the rock mass	ZFMENE1192			ZFMENE2254		
	min	Mean/st dev	max	min	Mean/st dev	max
Q [-]	15.0	32.3 [25.8]	66.7	15.2	169.6 [64.9]	1,066.7
RMR [-]	78.6	80.6/ 1.7	82.6	77.1	82.1/ 5.3	94.0
E <sub>m</sub> [GPa]	52.0	58.4/ 5.5	65.2	47.6	59.9/ 10.1	75.0
v <sub>m</sub> [-]	0.17	0.19/ 0.02	0.21	0.15	0.19/ 0.03	0.24
UCS <sub>m</sub> (H-B) [MPa]	46.3	51.7/ 4.7	57.6	42.5	58.6/ 20.9	108.5
φ <sub>m</sub> [°]	47.0	47.5/ 0.4	48.1	46.6	47.9/ 1.3	50.7
c <sub>m</sub> [MPa]	20.7	21.4/ 0.6	22.2	20.2	22.3/ 2.7	28.7
UCS <sub>m</sub> (M-C) [MPa]	105.2	110.4/ 4.5	115.9	101.6	116.42/ 18.6	160.5
T <sub>m</sub> [MPa]	0.91	1.06/ 0.13	1.23	0.81	1.29/ 0.66	2.91

**Table A3-17. Rock mass properties for the gently-dipping brittle deformation zones.**

Def. zone Properties of the rock mass	ZFMA2			ZFMA3			ZFMA4		
	min	Mean/st dev	max	min	Mean/st dev	max	min	Mean/st dev	max
Q [-]	3.22	29.9 [12.80]	131.47	5.5	17.6 [15.8]	33.0	6.1	14.9 [11.1]	32.7
RMR [-]	64.2	76.7/ 8.6	90.6	73.6	81.1/ 4.7	85.6	72.1	77.0/ 3.1	83.1
E <sub>m</sub> [GPa]	22.6	48.5/ 20.6	75.0	39.0	61.1/ 14.5	75.0	35.7	48.0/ 9.0	67.3
v <sub>m</sub> [-]	0.07	0.15/ 0.07	0.24	0.12	0.20/ 0.05	0.24	0.11	0.15/ 0.03	0.22
UCS <sub>m</sub> (H-B) [MPa]	23.5	48.8/ 21.0	89.8	35.0	54.4/ 12.9	68.2	32.1	42.8/ 7.7	59.3
φ <sub>m</sub> [°]	43.8	46.9/ 1.93	49.9	45.7	47.6/ 1.2	48.8	45.3	46.6/ 0.8	48.2
c <sub>m</sub> [MPa]	17.3	21.0/ 2.8	26.3	19.1	21.8/ 1.7	23.6	18.7	20.2/ 1.1	22.4
UCS <sub>m</sub> (M-C) [MPa]	81.1	107.0/ 19.8	144.30	93.6	112.6/ 12.2	125.5	90.8	101.7/ 7.6	117.5
T <sub>m</sub> [MPa]	0.36	1.02/ 0.60	2.25	0.63	1.15/ 0.36	1.55	0.56	0.83/ 0.21	1.28

**Table A3-18. Rock mass properties for the gently-dipping brittle deformation zones.**

Def. zone Properties of the rock mass	ZFMA7			ZFMB1			ZFMB4		
	min	Mean/st dev	max	min	Mean/st dev	max	min	Mean/st dev	max
Q [-]	1.8	15.2 [15.2]	28.7	7.7	9.2 [9.2]	10.8	2.8	5.6/ 4.0	8.5
RMR [-]	77.2	78.1/ 1.3	79.1	78.7	83.1/ 6.3	87.5	79.7	83.3/ 5.1	86.9
E <sub>m</sub> [GPa]	47.9	50.6/ 3.8	53.3	52.2	63.6/ 16.1	75.0	55.4	65.2/ 13.9	75.0
v <sub>m</sub> [-]	0.15	0.16/ 0.01	0.17	0.17	0.20/ 0.05	0.24	0.18	0.21/ 0.04	0.24
UCS <sub>m</sub> (H-B) [MPa]	42.7	45.0/ 3.3	47.4	46.4	61.1/ 20.8	75.8	49.2	61.2/ 17.0	73.2
φ <sub>m</sub> [°]	46.7	46.9/ 0.4	47.2	47.1	48.2/ 1.6	49.3	47.3	48.2/ 1.3	49.1
c <sub>m</sub> [MPa]	20.2	20.5/ 0.5	20.9	20.7	22.6/ 2.7	24.5	21.1	22.7/ 2.2	24.2
UCS <sub>m</sub> (M-C) [MPa]	101.8	104.0/ 3.2	106.3	105.4	118.8/ 18.9	132.2	108.0	118.9/ 15.4	129.8
T <sub>m</sub> [MPa]	0.82	0.88/ 0.09	0.94	0.92	1.35/ 0.61	1.79	0.99	1.35/ 0.50	1.70

**Table A3-19. Rock mass properties for the gently-dipping brittle deformation zones.**

Def. zone Properties of the rock mass	ZFM866			ZFM1203		
	min	Mean/st dev	max	min	Mean/st dev	max
Q [-]	9.1	12.7 [12.7]	16.2	7.1	60.4 [60.4]	113.6
RMR [-]	77.2	77.3/ 0.2	77.5	70.0	79.6/ 8.5	86.0
E <sub>m</sub> [GPa]	47.9	48.3/ 0.5	48.6	31.6	58.0/ 23.4	76.0
v <sub>m</sub> [-]	0.15	0.15/ 0.00	0.16	0.13	0.21/ 0.07	0.27
UCS <sub>m</sub> (H-B) [MPa]	42.7	43.0/ 0.5	43.3	32.1	59.0/ 24.1	78.8
φ <sub>m</sub> [°]	46.7	46.7/ 0.1	46.7	45.6	48.1/ 2.12	49.5
c <sub>m</sub> [MPa]	20.2	20.3/ 0.1	20.3	18.9	22.4/ 3.2	25.0
UCS <sub>m</sub> (M-C) [MPa]	101.8	102.1/ 0.4	102.4	92.5	117.8/ 22.4	135.3
T <sub>m</sub> [MPa]	0.82	0.83/ 0.01	0.84	0.53	1.27/ 0.68	1.86

**Table A3-20. Rock mass properties for the vertical and steeply-dipping brittle deformation zones with NNW strike (ZFMNNW0404) and the vertical and steeply, SSW- (and SW-dipping) deformation zones with WNW strike (ZFMWNW0044).**

Def. zone Properties of the rock mass	ZFMWNW0044			ZFMNNW0404		
	min	Mean/st dev	max	min	Mean/st dev	max
Q [-]	3.9	49.0 [29.6]	175.0	48.1	130.1 [72.2]	400.0
RMR [-]	75.3	81.3/ 4.4	90.6	76.1	82.8/ 6.8	93.6
E <sub>m</sub> [GPa]	42.8	60.2/ 12.0	77.4	45.0	60.1/ 13.8	76.0
v <sub>m</sub> [-]	0.14	0.19/ 0.04	0.25	0.14	0.19/ 0.04	0.24
UCS <sub>m</sub> (H-B) [MPa]	52.7	74.1/ 15.7	101.8	45.7	70.4/ 28.3	120.5
φ <sub>m</sub> [°]	48.6	50.0/ 0.8	51.1	47.1	48.7/ 1.6	51.1
c <sub>m</sub> [MPa]	22.0	24.7/ 1.9	27.8	20.7	23.9/ 3.6	30.2
UCS <sub>m</sub> (M-C) [MPa]	116.8	135.7/ 13.1	155.2	105.2	127.4/ 25.0	171.3
T <sub>m</sub> [MPa]	0.97	1.58/ 0.50	2.64	0.89	1.65/ 0.91	3.31

### A3.10 Uncertainties

Uncertainties were calculated for both major and minor deterministically modeled deformation zones as well as possible (not deterministically modeled) deformation zones.

**Table A3-21. Uncertainties calculated according to the same principles as for the rock domains.**

Type of deformation zone Properties of the rock mass	Possible DZ Uncertainty of the mean	Major deformation zones Uncertainty of the mean	Minor deformation zones Uncertainty of the mean
Q [-]	-11% +39%	-6% +39%	-11% +76%
RMR [-]	-2% +2%	-1% +1%	-2% +1%
E <sub>m</sub> [GPa]	-7% +6%	-4% +4%	-6% +4%
v <sub>m</sub> [-]	-6% +9%	-5% +7%	-7% +8%
UCS <sub>m</sub> (H-B) [MPa]	-10% +19%	-6% +11%	-8% +12%
φ <sub>m</sub> [°]	-3% +1%	-2% +1%	-2% +1%
c <sub>m</sub> [MPa]	-5% +6%	-3% +3%	-4% +4%
UCS <sub>m</sub> (M-C) [MPa]	-7% +9%	-4% +5%	-5% +6%
T <sub>m</sub> [MPa]	-11% +24%	-6% +15%	-9% +17%

## Results from theoretical modelling

### A4.1 Data for DFN-model based on the draft report

The input to the DFN realisations was taken from the draft report in June by /Fox et al. 2007/. The primary geological DFN model ('Base Case') was used. The input parameters for the DFN realisations in fracture domain FFM01 and FFM06 are shown in Table A4-1 to Table A4-3. The intensity,  $P_{32}$ , in the "Base model" is corrected for lithology and for the ratio (open and partly open)/total number of fractures, see Table A4-4 and Table A4-5.

**Table A4-1. Orientation model for fracture domain FFM01.**

Fracture Set	Mean Pole (°)		Mean Fisher K
	Trend	Plunge	
<b>Global Sets</b>			
NE	314.7	1.4	20.0
NS	269.0	4.8	20.9
NW	229.1	4.8	13.8
SH	340.2	86.9	15.7
EW	0.1	14.8	15.0
<b>Local Sets</b>			
ENE	158.1	5.0	28.6
NNE	109.6	7.2	16.6

**Table A4-2. Orientation model for fracture domain FFM06.**

Fracture Set	Mean Pole (°)		Mean Fisher K
	Trend	Plunge	
<b>Global Sets</b>			
NE	125.7	10.1	45.1
NS	91.0	4.1	19.5
NW	34.1	0.8	16.1
SH	84.3	71.3	10.8
<b>Local Sets</b>			
ENE	155.4	8.3	20.8

**Table A4-3. Base Case coupled size-intensity model for fracture domain FFM01 and FFM06.**

Fracture Set	Distribution	Mean Min. radius ( $r_{min}$ )	Std. Dev. Exponent ( $k_r$ )	Intensity $P_{32}$
<b>Global Sets</b>				
NE	Lognormal	0.536	0.62	1.250
NS	Power Law	0.353	2.12	0.333
NW	Lognormal	0.729	0.85	0.910
SH	Power Law	0.283	2.10	1.820
EW	Power Law	0.330	2.54	0.526
<b>Local Sets</b>				
ENE	Power Law	0.384	1.74	0.500
NNE	Power Law	0.313	1.44	0.303

**Table A4-4. Lithology correction factor,  $D_{lith}$ .**

Fracture Set	Granite to granodiorite, metamorphic, medium-grained in FFM01	Granite, metamorphic, aplitic in FFM06
NW	0.69	0.71
NS	0.66	1.07
NE	0.80	0.64
SH	0.44	0.43
ENE	1.36	4.46
NNE	0.22	
EW	0.53	

**Table A4-5. Correction factor for Open/total fractures.**

Fracture Set	Ratio Open/total in FFM01	Ratio Open/total in FFM06
NW	0.207	0.154
NS	0.080	0.031
NE	0.151	0.133
SH	0.383	0.341
ENE	0.113	0.346
NNE	0.106	
EW	0.218	

**Table A4-6. Mean material properties.**

Property	FFM01	FFM06
<b>Intact rock</b>		
Young's modulus, (GPa)	76.0	82.0
Poisson's ratio	0.23	0.27
Cohesion, (MPa)	27.6	41.5
Friction angle, (°)	60.0	60.0
Tensile strength, (MPa)	13.0	18.0
<b>Fracture</b>		
Normal stiffness, (GPa/m)	656.0	607.0
Shear stiffness, (GPa/m)	34.0	33.0
Cohesion, (MPa)	0.8	0.7
Friction angle, (°)	36.6	36.2
Dilatancy, (°)	3.2	2.8

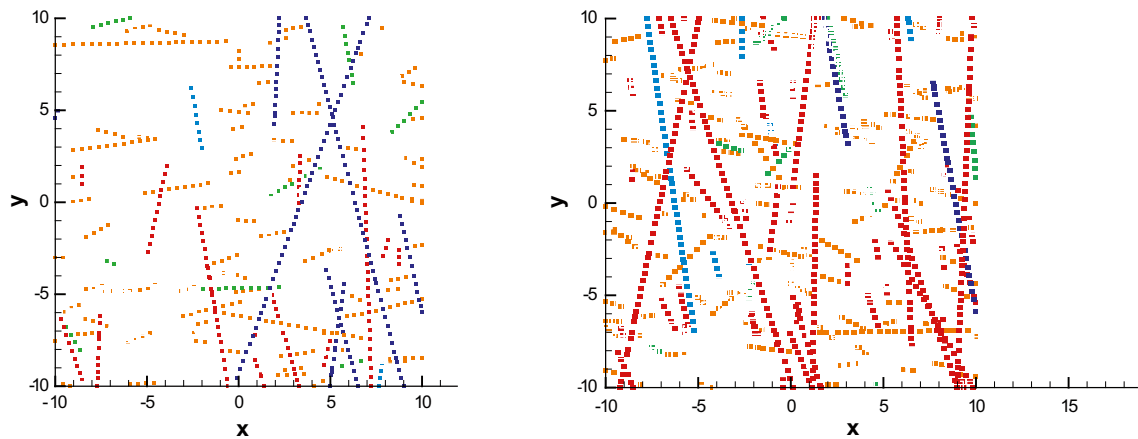


**Figure A4-1.** Example of fracture traces. FFM01 to left and FFM06 to right.

#### **A4.2 Comparison of results based on the draft model in June and the final DFN-model in October 2007**

The difference between the Basic DFN-model reported in the draft in June 2007 and the Tectonic Continuum model reported in the final model in October 2007 has been analysed by calculating the Poisson's ratio, the deformation modulus and the vertical stress at failure for one realisation for fracture domain FFM01. The data for the Tectonic Continuum model are given in Table A4-7 to Table A4-9.

The results from the Tectonic Continuum model are compared with the results from the Base Case model reported in the draft in Table A4-10. The calculated values for Poisson's ratio, deformation modulus and vertical stress at failure from the Tectonic Continuum model are of the same order as the values calculated from the Base Case model presented in the draft.

**Table A4-7. Orientation model for fracture domain FFM01 based on the Tectonic Continuum model presented in the final DFN-model.**

Fracture Set	Mean Pole (°) Trend	Plunge	Mean Fisher K
<b>Global Sets</b>			
NE	314.9	1.3	20.9
NS	270.1	5.3	21.3
NW	230.1	4.6	15.7
SH	0.8	87.3	17.4
EW	0.4	11.9	13.9
<b>Local Sets</b>			
ENE	157.5	3.1	34.1
NNE	293.8	0.0	21.8
SH2	164.0	52.6	35.4
SH3	337.9	52.9	17.1

**Table A4-8. Mean P32 Intensity based on the Tectonic Continuum model presented in the final DFN-model.**

Fracture Set	Distribution	Min. radius ( $r_{min}$ )	Exponent ( $k_r$ )	Intensity $P_{32}$ (0.5–564 m)
<b>Global Sets</b>				
NE	Power Law	0.5	3.02	2.30
NS	Power Law	0.5	2.78	0.24
NW	Power Law	0.5	2.85	1.10
SH	Power Law	0.5	2.85	0.95
<b>Local Sets</b>				
ENE	Power Law	0.5	3.25	1.60
EW	Power Law	0.5	3.10	0.34
NNE	Power Law	0.5	3.00	0.34
SH2	Power Law	0.5	2.61	0.19
SH3	Power Law	0.5	2.61	0.17

**Table A4-9. Correction factors based on the Tectonic Continuum model presented in the final DFN-model.**

Fracture Set	Correction factor for Lithology	Correction factor for open/total fractures	Corrected intensity $P_{32}$ (0.5–564 m)
<b>Global Sets</b>			
NE	1.22	0.152	0.423
NS	0.66	0.080	0.013
NW	1.37	0.207	0.311
SH	1.92	0.383	0.382
<b>Local Sets</b>			
ENE	1.77	0.113	0.322
EW	2.17	0.218	0.161
NNE	0.0	0.106	0.0
SH2	0.0		0.0
SH3	0.0		0.0

**Table A4-10. Comparison of calculated results based on the Tectonic Continuum model presented in the final DFN-model and the Basic model in the draft.**

Parameter	Values based on the final DFN-model	Variation in values based on the draft DFN-model
<b><math>\sigma_H = 39.0</math> MPa</b>		
Poisson's ratio	0.26	0.24 – 0.27
Deformation modulus, (GPa)	64.5	64.2 – 72.0
Vertical stress at failure, (MPa)	394.3	354.9 – 506.9
<b><math>\sigma_H = 9.75</math> MPa</b>		
Poisson's ratio	0.27	0.24 – 0.28
Deformation modulus, (GPa)	61.1	60.5 – 70.9
Vertical stress at failure, (MPa)	181.3	143.5 – 246.4
<b><math>\sigma_H = 2.0</math> MPa</b>		
Poisson's ratio	0.25	0.23 – 0.33
Deformation modulus, (GPa)	59.8	50.6 – 67.6
Vertical stress at failure, (MPa)	86.5	75.7 – 177.8

### A4.3 Results from the theoretical model

In this section the results from the theoretical model based on the Base Case model reported in the draft DFN-model are presented in detail.

**Table A4-11. Poisson's ratio, deformation modulus and vertical stress at failure for all DFN realisations, FFM01 parallel to  $\sigma_H$ , stress level 39 MPa.**

DFN realisation	P <sub>10</sub>	Poisson's ratio, v <sub>m</sub>	Deformation modulus, E <sub>m</sub> , (GPa)	Vertical stress at failure, σ <sub>vf</sub> , (MPa)
1	0.42	0.27	64.21	371.78
2	0.31	0.24	70.82	460.23
3	0.55	0.24	69.97	364.88
4	0.32	0.25	70.29	466.76
5	0.24	0.25	66.65	494.66
6	0.36	Initial stress calculations do not converge		
7	0.42	0.25	69.87	418.79
8	0.46	0.25	68.43	506.36
9	0.41	0.25	67.47	404.90
10	0.28	0.25	67.84	434.11
11	0.29	0.24	67.51	445.43
12	0.46	0.25	67.64	392.88
13	0.29	0.24	68.92	506.90
14	0.23	0.25	68.31	448.20
15	0.36	Initial stress calculations do not converge		
16	0.36	0.24	72.03	474.22
17	0.41	0.25	69.55	403.37
18	0.31	0.25	67.91	389.78
19	0.4	0.26	68.03	447.99
20	0.33	0.25	68.37	457.84
<b>Mean</b>	<b>0.36</b>	<b>0.25</b>	<b>68.54</b>	<b>438.28</b>
<b>Standard dev.</b>	<b>0.08</b>	<b>0.01</b>	<b>1.75</b>	<b>43.85</b>
<b>Min.</b>	<b>0.23</b>	<b>0.24</b>	<b>64.21</b>	<b>364.88</b>
<b>Max</b>	<b>0.55</b>	<b>0.27</b>	<b>72.03</b>	<b>506.90</b>



**Table A4-12. Poisson's ratio, deformation modulus and vertical stress at failure for all DFN realisations, FFM01 parallel to  $\sigma_H$ , stress level 9.75 MPa.**

DFN realisation	$P_{10}$	Poisson's ratio, $\nu_m$	Deformation modulus, $E_m$ , (GPa)	Vertical stress at failure, $\sigma_{vf}$ , (MPa)
1	0.42	0.27	61.46	194.74
2	0.31	0.25	69.07	210.11
3	0.55	0.25	67.89	143.54
4	0.32	0.27	64.26	243.38
5	0.24	0.28	60.48	220.13
6	0.36	Initial stress calculations do not converge		
7	0.42	0.25	70.33	177.62
8	0.46	0.25	63.97	221.54
9	0.41	0.25	69.41	153.68
10	0.28	0.27	65.95	214.39
11	0.29	0.25	65.83	209.27
12	0.46	0.24	62.60	185.93
13	0.29	0.26	66.89	241.83
14	0.23	0.26	65.71	227.41
15	0.36	Initial stress calculations do not converge		
16	0.36	0.25	70.92	217.83
17	0.41	0.25	69.60	149.46
18	0.31	0.24	65.49	164.15
19	0.4	0.28	63.29	173.35
20	0.33	0.26	62.85	246.44
<b>Mean</b>		<b>0.26</b>	<b>65.89</b>	<b>199.71</b>
<b>Standard dev.</b>		<b>0.01</b>	<b>3.15</b>	<b>33.19</b>
<b>Min.</b>		<b>0.24</b>	<b>60.48</b>	<b>143.54</b>
<b>Max</b>		<b>0.28</b>	<b>70.92</b>	<b>246.44</b>

**Table A4-13. Poisson's ratio, deformation modulus and vertical stress at failure for all DFN realisations, FFM01 parallel to  $\sigma_H$ , stress level 2.0 MPa.**

DFN realisation	$P_{10}$ Mean value	Poisson's ratio, $\nu_m$	Deformation modulus, $E_m$ , (GPa)	Vertical stress at failure, $\sigma_{vf}$ , (MPa)
1	0.42	0.27	63.32	110.69
2	0.31	0.25	66.98	122.19
3	0.55	0.23	67.61	75.72
4	0.32	0.30	59.05	177.81
5	0.24	0.31	60.09	146.47
6	0.36	Initial stress calculations do not converge		
7	0.42	0.29	58.28	106.50
8	0.46	0.29	53.89	127.14
9	0.41	0.33	52.09	83.89
10	0.28	0.30	61.76	137.31
11	0.29	0.30	58.45	116.31
12	0.46	0.23	50.62	112.69
13	0.29	0.29	63.25	164.75
14	0.23	0.30	62.08	125.28
15	0.36	0.28	56.87	102.67

DFN realisation	$P_{10}$ Mean value	Poisson's ratio, $\nu_m$	Deformation modulus, $E_m$ , (GPa)	Vertical stress at failure, $\sigma_{vf}$ , (MPa)
16	0.36	0.30	59.53	133.14
17	0.41	0.24	61.17	90.29
18	0.31	0.32	57.16	76.41
19	0.4	0.27	62.50	97.61
20	0.33	0.31	61.63	133.20
<b>Mean</b>		<b>0.28</b>	<b>59.81</b>	<b>117.90</b>
<b>Standard dev.</b>		<b>0.03</b>	<b>4.46</b>	<b>27.77</b>
<b>Min.</b>		<b>0.23</b>	<b>50.62</b>	<b>75.72</b>
<b>Max</b>		<b>0.33</b>	<b>67.61</b>	<b>177.81</b>

Table A4-14. Friction angle (MC), cohesion (MC) for FFM01 parallel to  $\sigma_H$ .

DFN realisation	Friction angle, (°)	Cohesion, (MPa)
1	50.28	19.20
2	53.08	18.75
3	50.48	11.44
4	50.50	29.45
5	53.88	20.87
6	Initial stress calculations do not converge	
7	51.90	15.96
8	55.06	17.95
9	52.45	11.53
10	50.79	22.91
11	52.48	18.74
12	49.74	19.11
13	53.50	24.55
14	51.93	21.53
15	Initial stress calculations do not converge	
16	53.31	20.10
17	52.18	12.03
18	51.63	12.24
19	53.96	12.99
20	51.82	23.87
<b>Mean</b>	<b>52.16</b>	<b>18.51</b>
<b>Standard dev.</b>	<b>1.46</b>	<b>5.09</b>
<b>Min.</b>	<b>49.74</b>	<b>11.44</b>
<b>Max</b>	<b>55.06</b>	<b>29.45</b>

**Table A4-15. Poisson's ratio, deformation modulus and vertical stress at failure for all DFN realisations, FFM01 parallel to  $\sigma_n$ , stress level 26 (MPa).**

DFN realisation	P <sub>10</sub> Mean value	Poisson's ratio, v <sub>m</sub>	Deformation modulus, E <sub>m</sub> , (GPa)	Vertical stress at failure, $\sigma_{vf}$ , (MPa)
1	0.42	Initial stress calculations do not converge		
2	0.31	0.25	70.07	382.69
3	0.55	0.25	68.72	323.43
4	0.32	0.25	68.33	396.00
5	0.24	0.24	66.97	337.90
6	0.36	0.25	68.96	347.47
7	0.42	0.25	69.26	300.28
8	0.46	0.25	67.09	338.53
9	0.41	0.26	65.43	260.95
10	0.28	0.25	67.84	401.71
11	0.29	Initial stress calculations do not converge		
12	0.46	0.26	65.25	324.96
13	0.29	0.24	69.54	387.26
14	0.23	0.24	69.14	316.16
15	0.36	0.25	69.64	404.98
16	0.36	0.25	67.55	304.30
17	0.41	0.25	69.35	375.06
18	0.31	0.24	67.46	243.66
19	0.4	0.25	70.53	288.28
20	0.33	0.26	67.69	296.00
<b>Mean</b>	<b>0.36</b>	<b>0.25</b>	<b>68.27</b>	<b>334.98</b>
<b>Standard dev.</b>	<b>0.08</b>	<b>0.01</b>	<b>1.48</b>	<b>48.58</b>
<b>Min.</b>	<b>0.23</b>	<b>0.24</b>	<b>65.25</b>	<b>243.66</b>
<b>Max</b>	<b>0.55</b>	<b>0.26</b>	<b>70.53</b>	<b>404.98</b>

**Table A4-16. Poisson's ratio, deformation modulus and vertical stress at failure for all DFN realisations, FFM01 parallel to  $\sigma_n$ , stress level 6.5 (MPa).**

DFN realisation	P <sub>10</sub> Mean value	Poisson's ratio, v <sub>m</sub>	Deformation modulus, E <sub>m</sub> , (GPa)	Vertical stress at failure, $\sigma_{vf}$ , (MPa)
1	0.42	Initial stress calculations do not converge		
2	0.31	0.25	67.85	234.06
3	0.55	0.31	59.39	174.36
4	0.32	0.26	67.74	200.04
5	0.24	0.25	60.93	167.78
6	0.36	0.25	67.34	169.47
7	0.42	0.24	66.05	130.06
8	0.46	0.31	56.77	143.02
9	0.41	0.30	57.69	127.75
10	0.28	0.25	66.46	219.38
11	0.29	Initial stress calculations do not converge		
12	0.46	0.28	61.04	144.37
13	0.29	0.25	66.30	203.16
14	0.23	0.28	70.08	143.79
15	0.36	0.25	66.78	210.49

DFN realisation	P <sub>10</sub> Mean value	Poisson's ratio, ν <sub>m</sub>	Deformation modulus, E <sub>m</sub> , (GPa)	Vertical stress at failure, σ <sub>vf</sub> , (MPa)
16	0.36	0.29	59.54	138.19
17	0.41	0.28	62.68	170.21
18	0.31	0.29	62.15	109.83
19	0.4	0.26	71.45	154.41
20	0.33	0.28	65.99	129.05
<b>Mean</b>		<b>0.27</b>	<b>64.23</b>	<b>164.97</b>
<b>Standard dev.</b>		<b>0.02</b>	<b>4.31</b>	<b>35.77</b>
<b>Min.</b>		<b>0.24</b>	<b>56.77</b>	<b>109.83</b>
<b>Max</b>		<b>0.31</b>	<b>71.45</b>	<b>234.06</b>

**Table A4-17. Poisson's ratio, deformation modulus and vertical stress at failure for all DFN realisations, FFM01 parallel to σ<sub>n</sub>, stress level 2.0 MPa.**

DFN realisation	P <sub>10</sub> Mean value	Poisson's ratio, ν <sub>m</sub>	Deformation modulus, E <sub>m</sub> , (GPa)	Vertical stress at failure, σ <sub>vf</sub> , (MPa)
1	0.42	Initial stress calculations do not converge		
2	0.31	0.28	66.88	168.15
3	0.55	0.31	58.82	124.89
4	0.32	0.26	68.14	146.00
5	0.24	0.29	61.76	121.60
6	0.36	0.25	66.48	110.11
7	0.42	0.23	58.75	87.46
8	0.46	0.33	51.70	92.80
9	0.41	0.38	47.25	76.25
10	0.28	0.26	66.05	145.02
11	0.29	Initial stress calculations do not converge		
12	0.46	0.28	60.49	123.96
13	0.29	0.24	69.30	139.61
14	0.23	0.30	60.33	101.30
15	0.36	0.26	67.09	139.74
16	0.36	0.32	64.79	85.51
17	0.41	0.33	58.61	131.14
18	0.31	0.25	69.82	62.89
19	0.4	0.26	63.26	104.03
20	0.33	0.29	63.18	75.81
<b>Mean</b>		<b>0.28</b>	<b>62.37</b>	<b>113.13</b>
<b>Standard dev.</b>		<b>0.04</b>	<b>5.98</b>	<b>29.24</b>
<b>Min.</b>		<b>0.23</b>	<b>47.25</b>	<b>62.89</b>
<b>Max</b>		<b>0.38</b>	<b>69.82</b>	<b>168.15</b>

**Table A4-18. Friction angle (MC), cohesion (MC) for FFM01 parallel to  $\sigma_h$ .**

DFN realisation	Friction angle, (°)	Cohesion, (MPa)
1	Initial stress calculations do not converge	
2	52.23	27.94
3	51.25	20.15
4	55.40	20.06
5	52.99	17.81
6	54.33	15.75
7	52.79	11.97
8	55.19	11.67
9	49.72	12.74
10	55.38	21.35
11	Initial stress calculations do not converge	
12	52.42	16.74
13	55.00	20.14
14	52.97	14.15
15	56.05	19.59
16	52.98	12.26
17	55.33	16.76
18	49.46	10.06
19	49.72	17.74
20	53.11	10.60
<b>Mean</b>	<b>53.1</b>	<b>16.5</b>
<b>Standard dev.</b>	<b>2.1</b>	<b>4.6</b>
<b>Min.</b>	<b>49.5</b>	<b>10.1</b>
<b>Max</b>	<b>56.0</b>	<b>27.9</b>

**Table A4-19. Poisson's ratio, deformation modulus and vertical stress at failure for all DFN realisations, FFM06 parallel to  $\sigma_h$ , stress level 39 MPa.**

DFN realisation	P <sub>10</sub> Mean value	Poisson's ratio, $\nu_m$	Deformation modulus, E <sub>m</sub> , (GPa)	Vertical stress at failure, $\sigma_{vf}$ , (MPa)
1	0.72	0.29	69.39	435.82
2	0.54	0.29	73.04	584.50
3	0.59	0.30	69.66	391.25
4	0.62	0.30	68.82	340.95
5	0.58	0.30	68.58	368.83
6	0.61	0.30	73.31	475.98
7	0.54	0.30	71.68	354.91
8	0.77	0.29	71.62	358.09
9	0.63	0.29	70.38	360.21
10	0.52	0.29	73.06	402.35
11	0.61	0.30	69.02	302.51
12	0.7	0.30	68.88	302.61
13	0.66	0.29	72.17	493.75
14	0.58			
15	0.69	0.29	68.44	386.07

DFN realisation	P <sub>10</sub> Mean value	Poisson's ratio, ν <sub>m</sub>	Deformation modulus, E <sub>m</sub> (GPa)	Vertical stress at failure, σ <sub>vf</sub> (MPa)
16	0.64	0.30	69.87	411.20
17	0.57	0.30	64.29	343.70
18	0.62	0.29	68.19	444.89
19	0.68	0.30	69.63	338.33
20	0.66			
<b>Mean</b>	<b>0.63</b>	<b>0.30</b>	<b>70.00</b>	<b>394.22</b>
<b>Standard dev.</b>	<b>0.06</b>	<b>0.00</b>	<b>2.23</b>	<b>71.74</b>
<b>Min.</b>	<b>0.52</b>	<b>0.29</b>	<b>64.29</b>	<b>302.51</b>
<b>Max</b>	<b>0.77</b>	<b>0.30</b>	<b>73.31</b>	<b>584.50</b>

**Table A4-20. Poisson's ratio, deformation modulus and vertical stress at failure for all DFN realisations, FFM06 parallel to σ<sub>ff</sub>, stress level 9.75 MPa.**

DFN realisation	P <sub>10</sub> Mean value	Poisson's ratio, ν <sub>m</sub>	Deformation modulus, E <sub>m</sub> (GPa)	Vertical stress at failure, σ <sub>vf</sub> (MPa)
1	0.72	0.32	62.42	195.49
2	0.54	0.29	73.99	276.00
3	0.59	0.29	63.92	184.70
4	0.62	0.29	70.20	123.16
5	0.58	0.31	68.69	135.23
6	0.61	0.34	66.84	204.97
7	0.54	0.32	66.28	157.40
8	0.77	0.28	70.85	162.29
9	0.63	0.29	66.37	143.62
10	0.52	0.31	65.87	177.29
11	0.61	0.31	80.66	108.63
12	0.7	0.29	65.19	131.24
13	0.66	0.31	69.44	259.81
14	0.58			
15	0.69	0.27	67.91	163.37
16	0.64	0.29	70.29	164.28
17	0.57	0.29	68.25	137.41
18	0.62	0.29	69.60	223.38
19	0.68	0.29	72.26	156.80
20	0.66			
<b>Mean</b>		<b>0.30</b>	<b>68.84</b>	<b>172.50</b>
<b>Standard dev.</b>		<b>0.02</b>	<b>4.15</b>	<b>45.43</b>
<b>Min.</b>		<b>0.27</b>	<b>62.42</b>	<b>108.63</b>
<b>Max</b>		<b>0.34</b>	<b>80.66</b>	<b>276.00</b>

**Table A4-21. Poisson's ratio, deformation modulus and vertical stress at failure for all DFN realisations, FFM06 parallel to  $\sigma_H$ , stress level 2.0 MPa.**

DFN realisation	P <sub>10</sub> Mean value	Poisson's ratio, v <sub>m</sub>	Deformation modulus, E <sub>m</sub> (GPa)	Vertical stress at failure, $\sigma_{vf}$ , (MPa)
1	0.72	0.36	54.71	106.58
2	0.54	0.31	67.33	200.92
3	0.59	0.25	75.07	97.04
4	0.62	0.36	72.41	76.03
5	0.58	0.35	66.15	72.98
6	0.61	0.40	58.16	122.25
7	0.54	0.35	58.18	83.02
8	0.77	0.30	71.68	80.72
9	0.63	0.25	73.44	60.15
10	0.52	0.27	73.46	100.59
11	0.61	0.25	79.39	46.14
12	0.7	0.34	56.33	56.63
13	0.66	0.37	58.63	115.80
14	0.58			
15	0.69	0.26	75.59	72.33
16	0.64	0.38	53.57	90.26
17	0.57	0.30	71.30	71.46
18	0.62	0.34	57.56	127.83
19	0.68	0.39	49.70	67.21
20	0.66			
<b>Mean</b>		<b>0.32</b>	<b>65.15</b>	<b>91.55</b>
<b>Standard dev.</b>		<b>0.05</b>	<b>9.22</b>	<b>35.61</b>
<b>Min.</b>		<b>0.25</b>	<b>49.70</b>	<b>46.14</b>
<b>Max</b>		<b>0.40</b>	<b>79.39</b>	<b>200.92</b>

**Table A4-22. Friction angle (MC), cohesion (MC) for FFM06 parallel to  $\sigma_H$ .**

DFN realisation	Friction angle, (°)	Cohesion, (MPa)
1	52.66	16.71
2	55.57	27.51
3	50.38	16.92
4	49.22	10.70
5	51.06	10.05
6	54.01	17.44
7	49.08	14.35
8	49.32	14.43
9	50.87	9.61
10	51.12	16.05
11	48.17	7.00
12	46.96	11.79
13	54.23	20.54
14		
15	51.59	11.82

DFN realisation	Friction angle, (°)	Cohesion, (MPa)
16	52.36	12.99
17	49.31	11.33
18	51.71	21.71
19	48.64	12.97
20		
<b>Mean</b>	<b>50.90</b>	<b>14.66</b>
<b>Standard dev.</b>	<b>2.28</b>	<b>4.99</b>
<b>Min.</b>	<b>46.96</b>	<b>7.00</b>
<b>Max</b>	<b>55.57</b>	<b>27.51</b>

**Table A4-23. Poisson's ratio, deformation modulus and vertical stress at failure for all DFN realisations, FFM06 parallel to  $\sigma_h$ , stress level 26 MPa.**

DFN realisation	P <sub>10</sub> Mean value	Poisson's ratio, $\nu_m$	Deformation modulus, E <sub>m</sub> , (GPa)	Vertical stress at failure, $\sigma_{vfz}$ (MPa)
1	0.72			
2	0.54	0.32	65.96	330.79
3	0.59	0.29	71.27	403.99
4	0.62	0.31	66.99	363.85
5	0.58	0.32	61.33	303.90
6	0.61	0.31	67.07	401.00
7	0.54	0.31	63.99	319.97
8	0.77	0.31	63.67	290.28
9	0.63	0.30	68.95	371.49
10	0.52	0.30	69.46	367.35
11	0.61	0.31	63.52	312.03
12	0.70	0.31	63.71	229.20
13	0.66	0.30	67.24	353.19
14	0.58	0.31	64.44	239.59
15	0.69	0.30	66.92	282.16
16	0.64	0.32	63.69	275.15
17	0.57	0.32	63.51	201.61
18	0.62	0.29	73.89	386.63
19	0.68	0.30	67.56	371.20
20	0.66	0.29	64.85	350.30
<b>Mean</b>		<b>0.31</b>	<b>66.21</b>	<b>323.88</b>
<b>Standard dev.</b>		<b>0.01</b>	<b>3.12</b>	<b>59.03</b>
<b>Min.</b>		<b>0.29</b>	<b>61.33</b>	<b>201.61</b>
<b>Max</b>		<b>0.32</b>	<b>73.89</b>	<b>403.99</b>



**Table A4-24. Material combinations used to investigate the influence of material variation.**

Combination of material properties	Intact rock		$\phi$ , (°)	$c$ , (MPa)	$T$ , (MPa)	Fractures				
	$E$ , (GPa)	$\nu$				$K_N$ , (GPa/m)	$K_S$ , (GPa/m)	$c_p$ (MPa)	$\phi_p$ , (°)	$\psi$ , (°)
1	75.1	0.194	60.2	32.44	13.23	1,262.7	34.5	0.78	29.81	9.55
2	72.2	0.252	60.2	20.24	14.57	732.3	30.9	0.79	36.00	0.99
3	76.7	0.255	59.7	31.74	11.47	886.8	50.5	0.82	38.74	2.64
4	79.8	0.251	60.0	24.33	13.30	1,320.0	50.6	0.44	39.16	5.22
5	79.6	0.201	59.9	28.55	13.50	350.1	44.9	0.67	36.01	4.39
6	81.2	0.202	59.9	32.84	14.82	237.1	38.4	0.29	39.54	4.66
7	69.4	0.244	60.2	28.43	11.04	1,018.9	28.5	0.90	35.84	1.59
8	75.3	0.217	60.1	31.82	13.40	270.9	42.8	0.90	32.45	3.66
9	79.3	0.200	59.7	24.19	10.45	1,307.5	19.4	0.77	37.04	0.84
10	72.7	0.195	60.1	21.91	12.34	718.4	31.6	0.91	33.42	2.26
11	73.9	0.190	60.1	25.08	10.61	354.3	42.5	0.92	36.49	3.29
12	70.9	0.228	59.6	26.10	13.09	375.3	38.5	0.94	34.88	1.94
13	70.5	0.219	59.7	24.27	10.31	590.2	36.9	0.80	36.77	3.22
14	73.1	0.228	60.0	28.41	13.85	1,194.5	31.4	0.71	33.65	2.66
15	73.7	0.266	60.1	25.70	13.18	563.8	50.8	0.52	38.16	1.62
16	69.6	0.247	60.0	34.71	13.55	400.3	49.6	0.71	34.42	5.90
17	74.3	0.222	60.1	27.02	12.50	989.9	31.4	0.95	32.13	5.10
18	74.8	0.182	59.9	25.56	11.85	602.7	20.7	0.76	32.79	3.38
19	76.4	0.247	60.0	28.78	12.78	598.6	30.5	0.51	37.92	3.87
20	74.9	0.188	60.1	24.60	11.38	692.2	29.7	0.78	36.70	1.57
21	75.0	0.250	60.1	27.47	12.89	629.5	19.0	0.83	40.11	3.41
22	74.9	0.233	59.8	30.11	13.34	175.3	27.3	0.99	38.21	4.03
23	80.0	0.191	60.1	27.99	13.85	939.1	25.8	0.68	32.83	2.96
24	75.7	0.191	59.6	31.25	13.54	907.7	30.5	0.51	38.95	8.09
25	75.4	0.201	60.2	25.67	13.36	1,182.0	38.2	0.96	35.64	6.76
26	74.5	0.288	60.0	23.50	12.14	784.0	32.4	0.96	36.55	4.22
27	81.9	0.216	60.0	25.69	12.87	903.7	38.7	0.88	36.64	0.59
28	78.6	0.186	59.9	29.15	10.54	396.9	51.6	0.82	40.83	1.50
29	74.0	0.243	60.1	20.14	13.21	919.3	31.5	0.67	41.85	2.21
30	81.0	0.202	59.9	27.13	11.29	1,033.6	44.0	0.74	35.95	4.35
31	71.2	0.273	60.1	30.92	17.07	375.8	34.3	0.81	36.68	4.52
32	77.6	0.268	59.9	28.67	10.28	725.7	40.4	1.17	32.05	6.73
33	78.7	0.233	60.0	33.55	14.68	984.3	20.3	0.70	40.18	1.77
34	81.8	0.241	60.4	25.20	14.88	420.6	39.8	0.82	36.00	2.99
35	75.7	0.236	60.1	23.78	16.11	579.4	31.0	0.50	40.21	1.55
36	74.4	0.227	59.7	30.50	12.79	687.4	33.2	1.19	35.82	1.76
37	78.0	0.276	59.9	29.26	13.03	214.6	29.2	0.64	35.40	2.40
38	74.9	0.199	60.2	28.26	13.03	477.1	30.1	0.64	37.83	4.05
39	78.3	0.181	60.3	26.80	14.15	1,269.3	45.6	0.55	34.05	4.46
40	71.7	0.272	59.9	30.55	11.73	631.7	41.1	0.80	34.07	3.19

**Table A4-25. Poisson's ratio, deformation modulus and vertical stress at failure for different material combinations in one DFN-realisation.**

Combination of material properties	Poisson's ratio, $\nu_m$	Deformation modulus, $E_m$ , GPa	Vertical stress at failure, $\sigma_{v,f}$ , MPa
1	0.22	68.24	388.08
2	0.27	64.92	391.96
3	0.26	71.03	436.36
4	0.26	73.60	423.15
5	0.21	71.14	410.26
6	0.21	70.09	462.57
7	0.26	62.99	420.74
8	0.22	66.25	409.17
9	0.24	71.11	393.01
10	0.22	65.68	377.95
11	0.20	66.19	428.62
12	0.24	63.46	421.72
13	0.23	64.18	407.46
14	0.25	66.17	427.25
15	0.27	67.49	452.31
16	0.25	63.11	421.11
17	0.24	66.69	426.33
18	0.21	65.38	396.97
19	0.26	68.15	435.94
20	0.21	67.11	425.68
21	0.27	65.33	436.88
22	0.23	62.55	453.14
23	0.22	71.66	408.72
24	0.21	68.52	432.77
25	0.22	69.08	445.40
26	0.30	67.60	408.00
27	0.23	74.86	435.71
28	0.19	70.78	477.68
29	0.26	67.33	439.11
30	0.22	74.18	464.21
31	0.28	63.14	432.36
32	0.28	70.99	396.06
33	0.26	68.56	458.09
34	0.25	72.34	425.22
35	0.25	67.31	438.56
36	0.24	67.45	429.76
37	0.27	65.98	444.76
38	0.22	66.86	439.57
39	0.20	71.60	436.28
40	0.28	65.54	421.19

#### A4.4 Modelling of deformation zones

The fracture set orientations have been examined in the deformation zones, see Figure A4-2. In all zones one fracture set is near parallel to the strike of the zone. The fracture intensity varies across the zones and most of the fractures are sealed, see Figure A4-3.

DFN-realizations have been generated with different fracture intensity. Only open fractures are modelled. The realisation box is perpendicular to the zone. A slice is taken from the box and exported to 3DEC. Two numerical load tests are performed on the model. First the model is loaded under confinement to get the constrained modulus,  $M$ , see Figure A4-4, second the model is sheared to get the shear modulus,  $G$ , and the shear strength of the model, see Figure A4-5. The strength of the intact rock is reduced to take in to account the effect of the sealed fractures.

The deformation zone is then divided in sections with constant fracture frequency and the normal stiffness,  $K_N$ , and shear stiffness,  $K_S$ , are calculated using Equation A4-1 and Equation A4-2. For each section the constrained modulus,  $M_i$ , and shear modulus,  $G_i$ , are taken from the 3DEC simulations. The shear strength of the deformation zone is set as being equal to the section with the smallest shear strength.

$$K_N = \frac{\sum_{i=1}^n b_i}{\sum_{i=1}^n \frac{b_i}{M_i}} \quad \text{Equation A4-1}$$

$$K_S = \frac{\sum_{i=1}^n b_i}{\sum_{i=1}^n \frac{b_i}{G_i}} \quad \text{Equation A4-2}$$

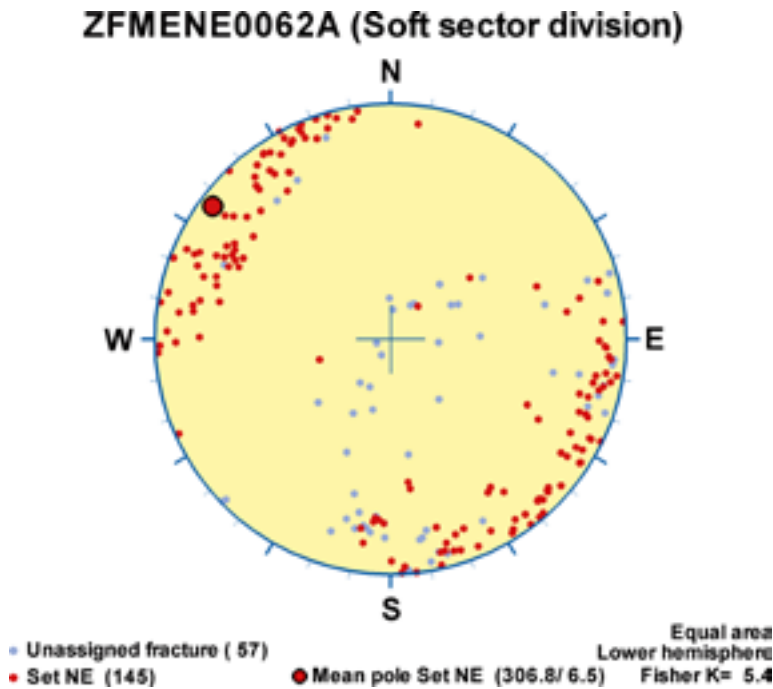


Figure A4-2. Fractures in deformation zone ZFMENE0062A.

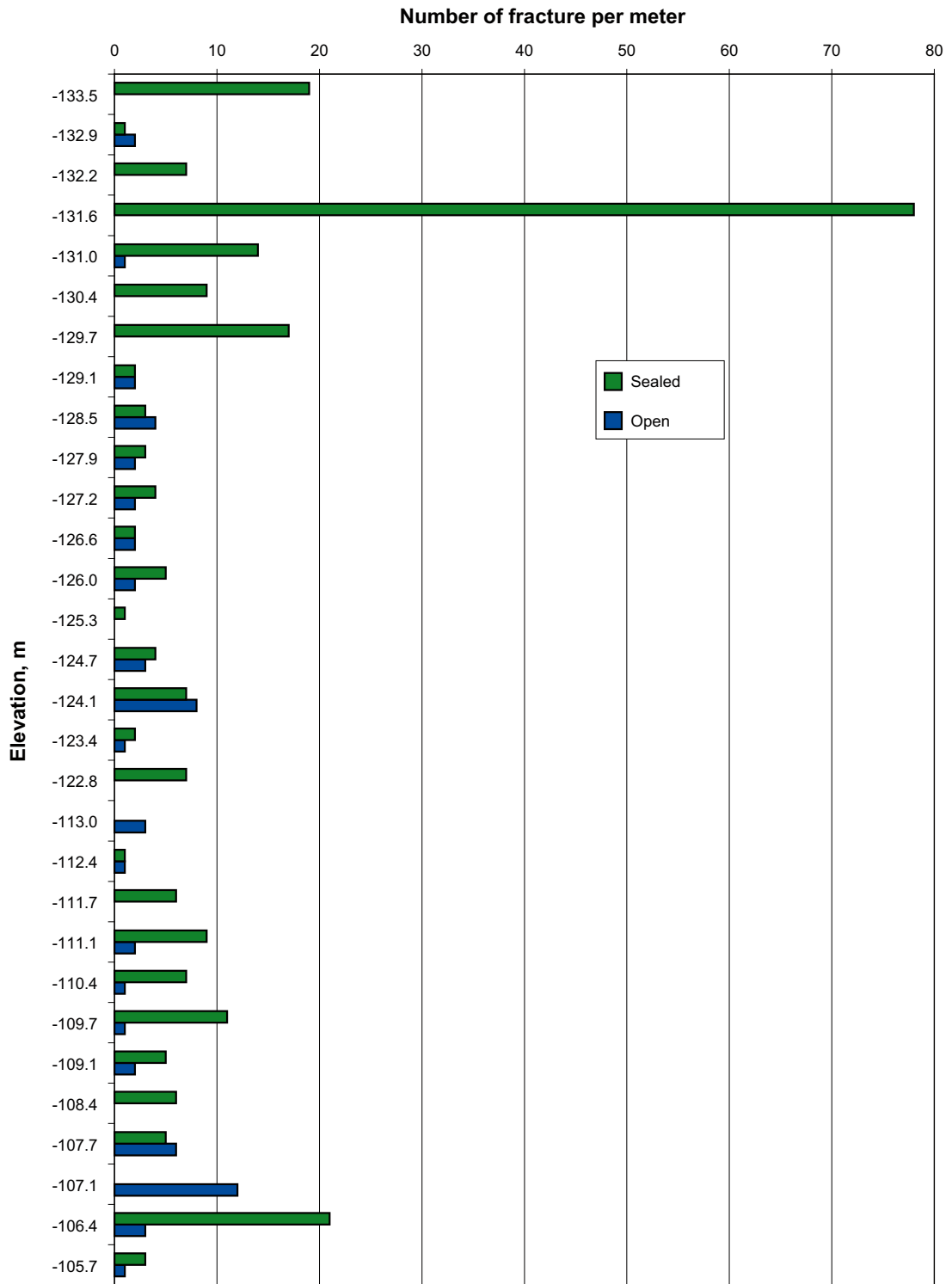


Figure A4-3. Fracture frequency in deformation zone ZFMENE0062A.

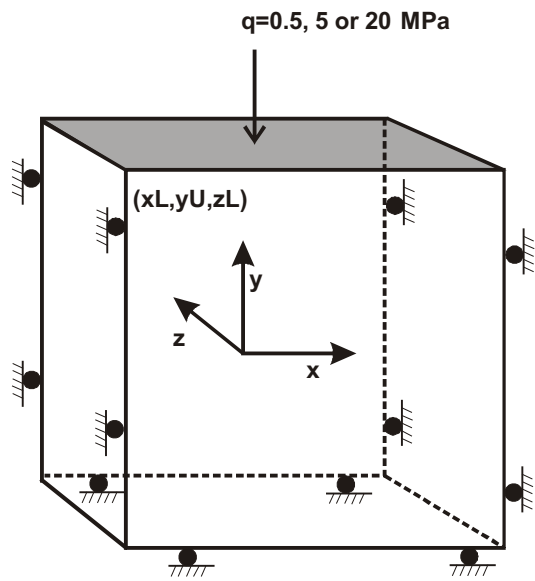


Figure A4-4. Loading to determine the constrained modulus.

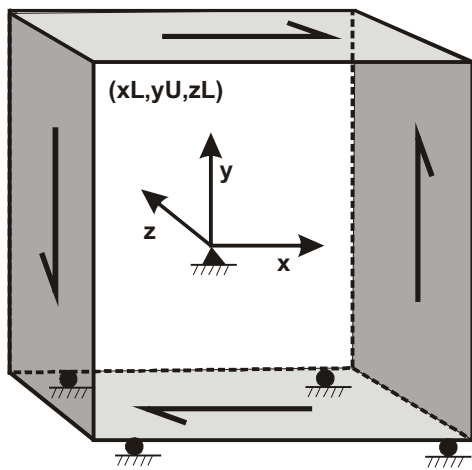


Figure A4-5. Loading to determine the shear modulus and shear strength.

### WellCad plots stress observations

To facilitate the reading and understanding of these diagrams a short description of the diagrams are given here.

The first two columns give the location of the data. Borehole length is calculated from the top of the casing downwards along the borehole. The starting point and the orientation of the hole are given in the top of the legend. The elevation is calculated as the true vertical distance below sea level (m.b.s.l.) and thus gives negative values. In some cases the boreholes are quite inclined and therefore the elevation parameter must be used to infer depth dependence of the stress magnitude.

A complete description of the geology and the geological modelling is found in /Stephens et al. 2007/, which should be consulted if a deeper understanding of the geological model is desired. However, the third and fourth columns indicates the rock types along the borehole (rock types occurring with section length > 1 m). Most important for the stress interpretation are the deformation zones that intersect the hole. The zones marked are the ones identified in the so called single-hole interpretation (SHI). A description of each such interpretation is given in separate P-reports. The deformation zone sections are determined only when the width of the zone is at least 25 m long in the borehole.

The fifth column in the WellCad plot shows the P-wave velocities measured along the borehole using a sonic logging tool. A low P-wave velocity indicates a lower rock deformation modulus. Therefore, there is often a correlation between the low P-wave sections and the identified deformation zones in the single-hole interpretation. When there is no correlation this may be explained by the fact that a deformation zone is identified based on a number of observed parameters that are dominated by borehole mapping data.

In the sixth, seventh and eighth columns, overcoring measurement results are presented as the magnitude of the three principal stress components. The scale magnification of the three columns is the same but note that the total interval span shown in the columns differs. The circle shaped symbol is red or pink for the major principal stress (denoted Sigma 1). The difference between red and pink involves a measurement quality rating, where rating A (red) is a fully successful test and rating B (pink) is a partly successful test. Tests with rating C are failed tests and are not included in the SICADA database or WellCad plots. One symbol represents one single overcoring point. Normally 3–4 measurements are made close to each other in at any one measurement “level”. Correspondingly the intermediate and minor principal stress magnitudes are shown with dark and light, green and blue, respectively. The ninth column shows the mean principal stress  $(\sigma_1 + \sigma_2 + \sigma_3)/3$ , which gives a measure of the general stress level at the point.

In the tenth column a hemispherical plot shows the orientation data for all stress data. The overcoring principal stress tensors are given with exactly the same symbols as for the magnitudes. Lower hemisphere plots are presented. By looking at the compiled orientation in the pole plot it is easy to see whether there is a correspondence between methods and also if there is a large or small spread between different points. The data given in one single plot belongs to the borehole interval indicated above the pole plot diagram. For overcoring and hydraulic fracturing every single point is given, while for HTPF and breakout in general only one symbol for the interval is plotted.

In the 11th column the magnitude of the HF measurements are plotted, using the same scale as for overcoring. The HTPF interpreted stress function is given as lines in column 12. The lines start at the upper tested fracture and end at the lower fracture. If the interpretation is made separately for several fracture clusters, the result will be shown by separate sets of corresponding lines in the plot.

Column 13 and 14 give the indirect stress data. Column 13 consists of the results from the interpretation of televiewer data that gives the actual geometry of the borehole. At points where the borehole periphery deviates from the pure circle shape this may be caused by different

mechanisms, namely so called borehole breakout (BB), key seats (KS), micro-fracturing (MF) and washouts (WO). The colour in the column indicates which type of geometry change that is interpreted. Only the breakouts (red) are used to infer the orientation of the minor principal stress, plotted in column 9 with a red rhomboidal symbol.

The occurrence of core disking is shown in column 14. The observations have been sorted into three classes: core disking (solid), ring disking (overcoring) and saddle petal. The colour and the subordinated columns indicate which class that is interpreted. The number of disks in the sections is indicated by two different shades of colours. Portions with less than 4 disks in the section are marked with light colour and portions with more than 4 disks in the section with dark colour.

In a borehole where one of the parameters is absent, this is indicated in the corresponding column by the text *No data*. Only boreholes where some stress data is available are presented, which means that in non-presented boreholes there is no measurements or no occurrences of core disking from the core mapping.

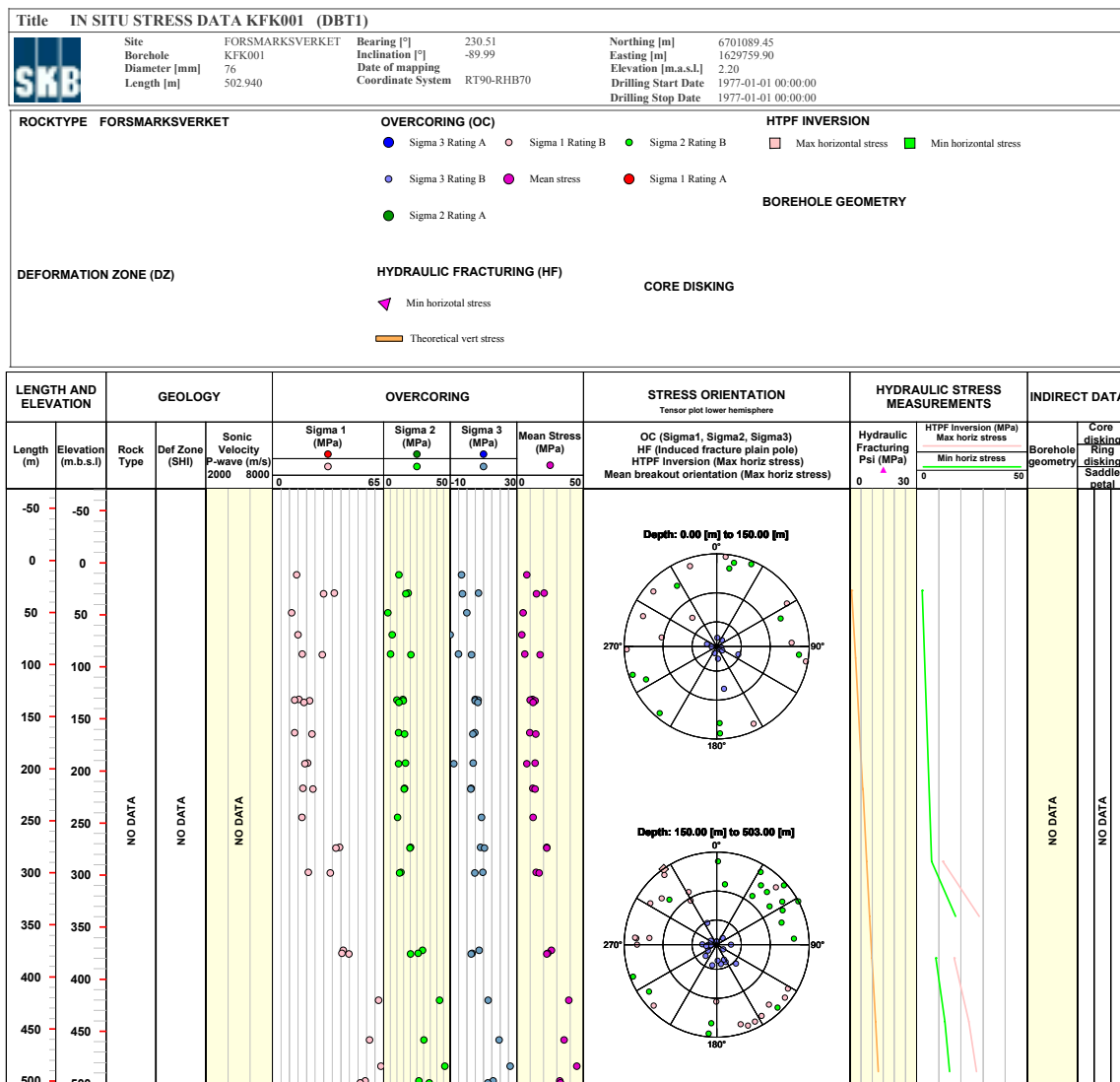


Figure A5-1. WellCad diagram for borehole KFK001 (DBT1).

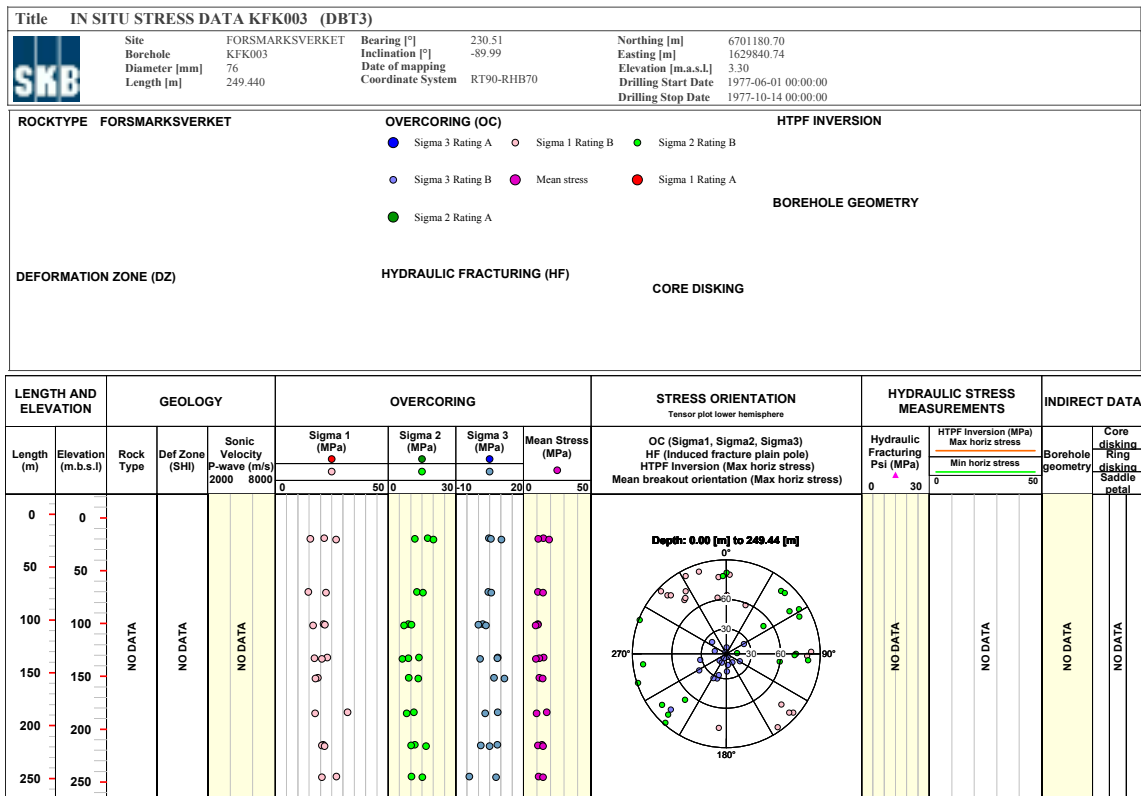


Figure A5-2. WellCad diagram for borehole KFK003 (DBT3).



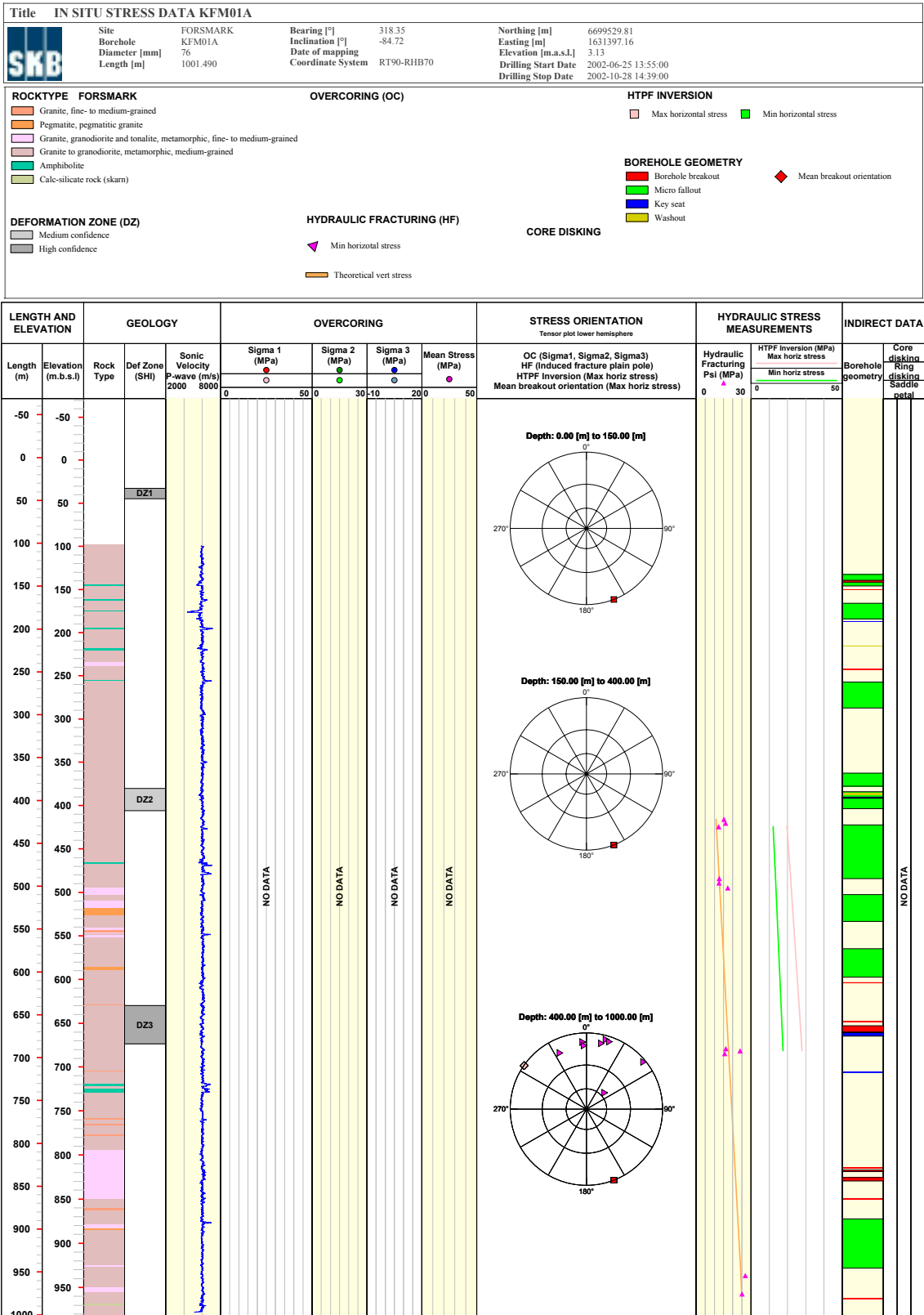


Figure A5-3. WellCad diagram for borehole KFM01A.

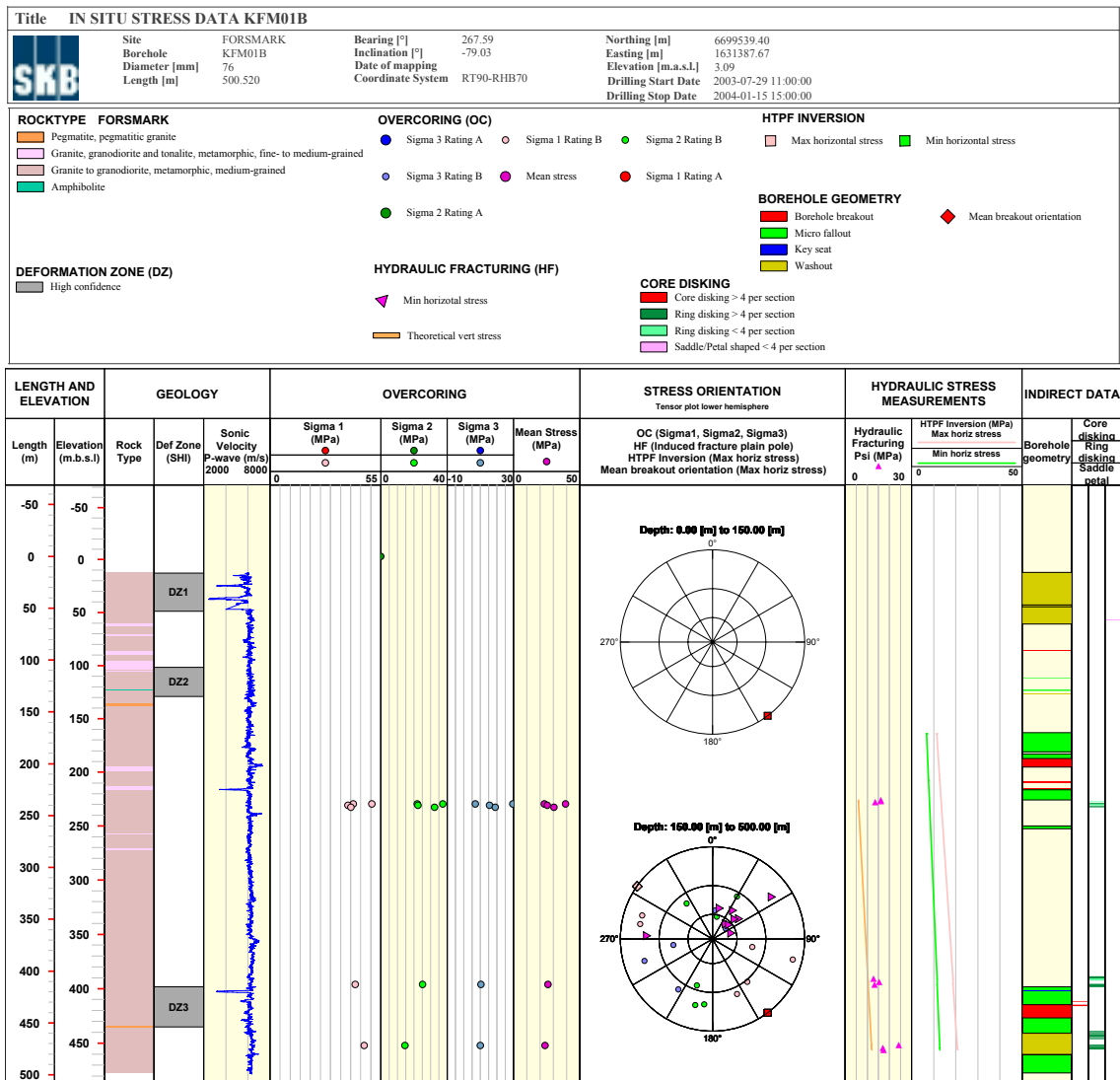


Figure A5-4. WellCad diagram for borehole KFM01B.

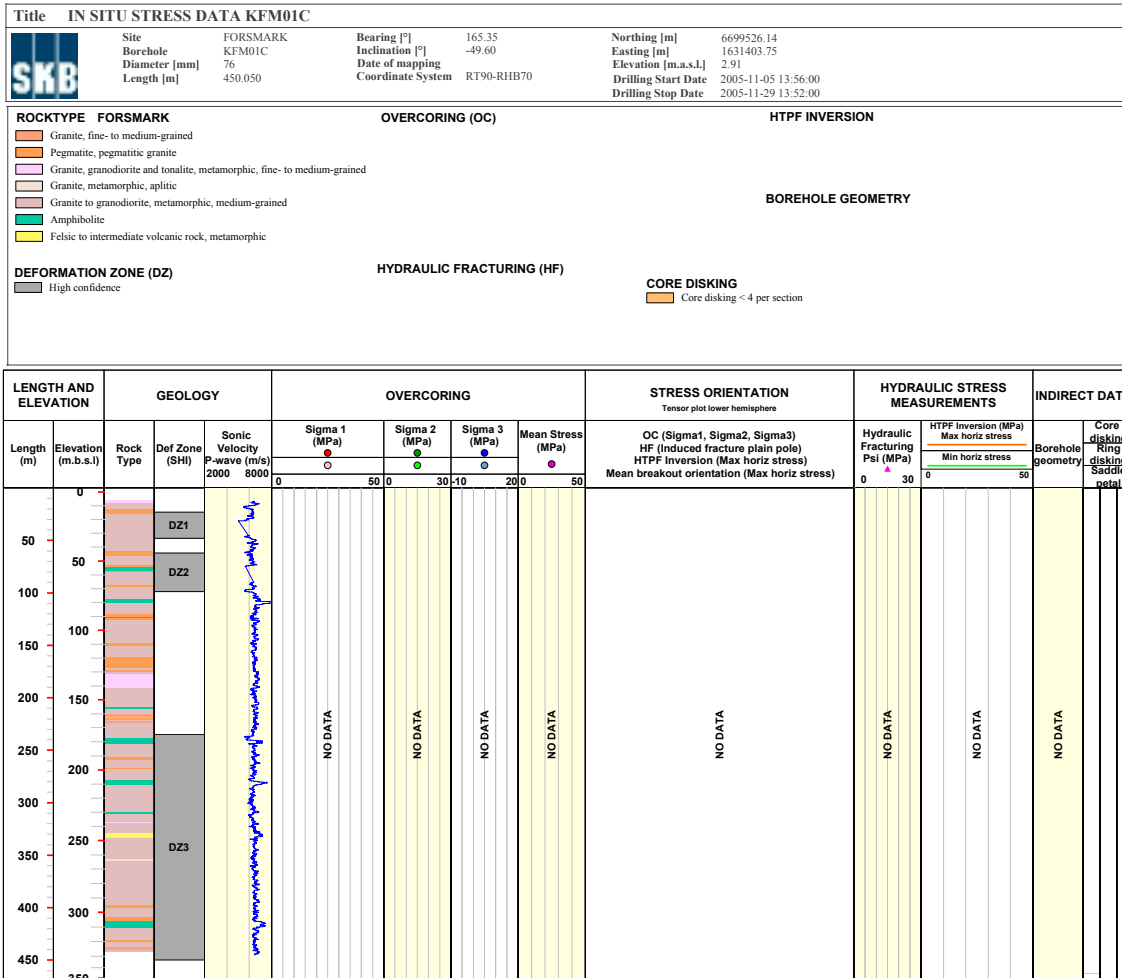


Figure A5-5. WellCad diagram for borehole KFM01C.

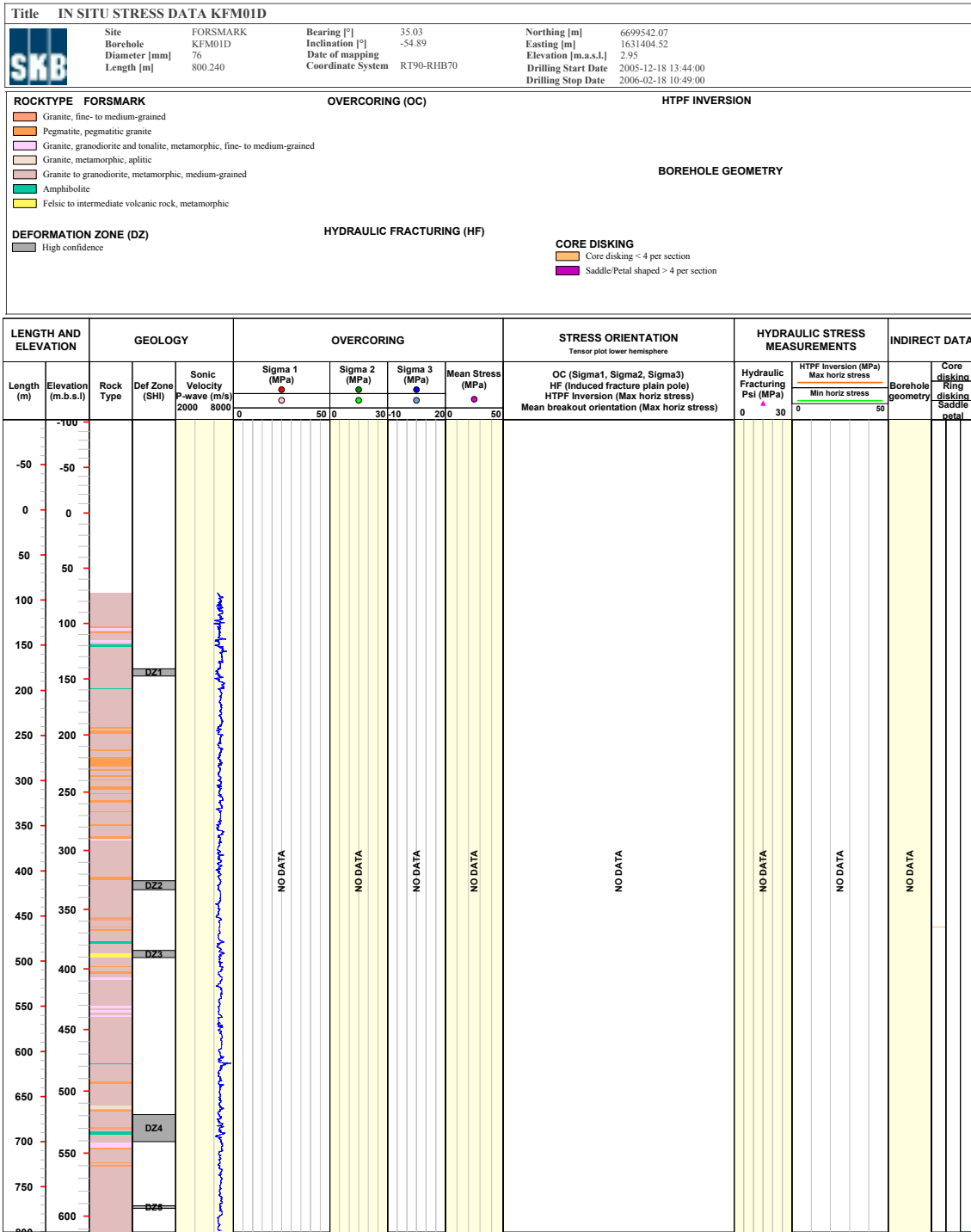


Figure A5-6. WellCad diagram for borehole KFM01D.

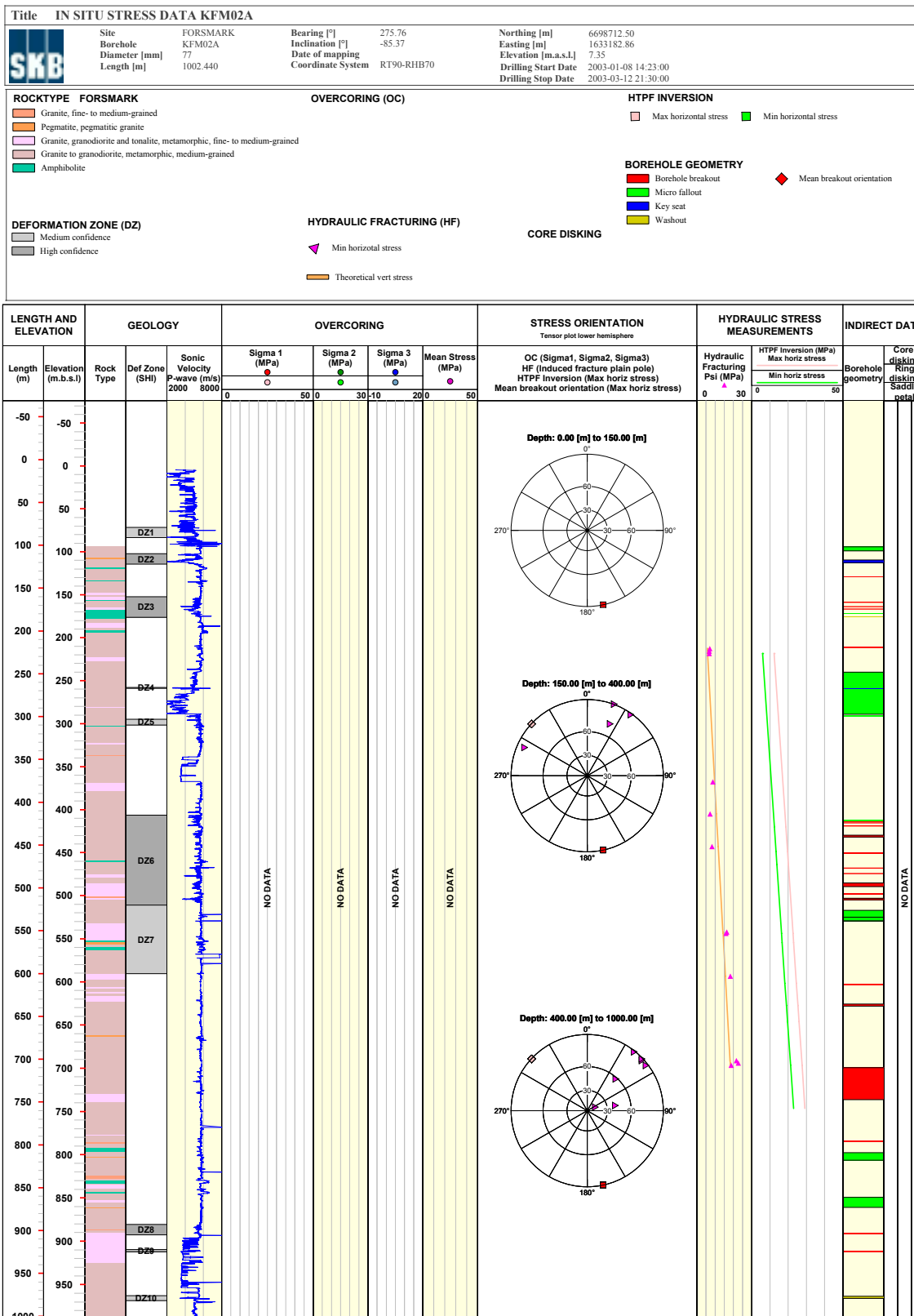


Figure A5-7. WellCad diagram for borehole KFM02A.

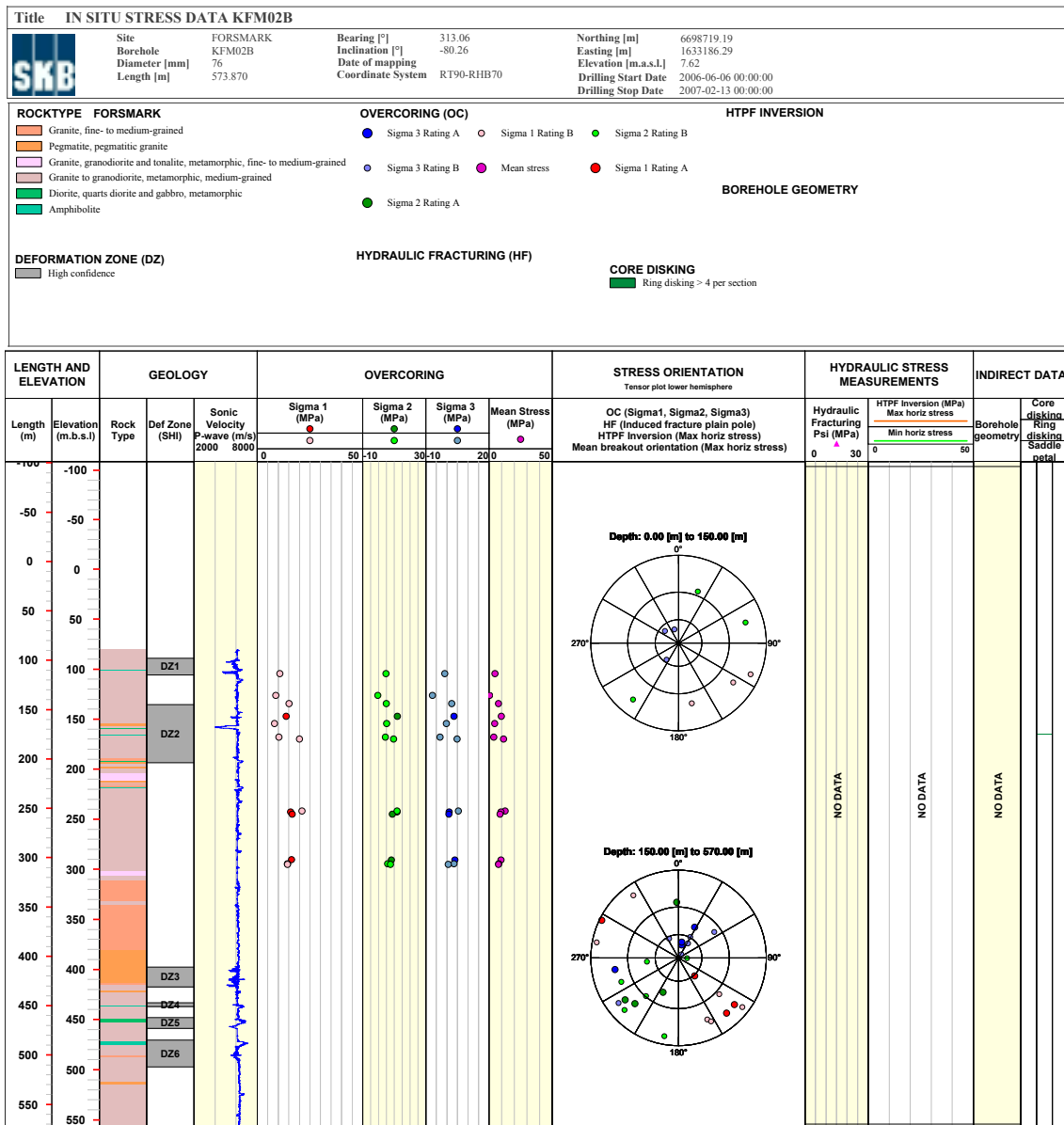


Figure A5-8. WellCad diagram for borehole KFM02B.

<b>Title</b> IN SITU STRESS DATA KFM03A		Site FORSMARK		Bearing [°]	271.52	Northing [m]	6697852.10
	Borehole	KFM03A	Inclination [°]	-83.74	Easting [m]		1634630.74
	Diameter [mm]	77	Date of mapping		Elevation [m.a.s.l.]		8.29
	Length [m]	1001.190	Coordinate System	RT90-RHB70	Drilling Start Date		2003-04-16 11:33:00
					Drilling Stop Date		2003-06-23 16:15:00

<b>ROCKTYPE FORSMARK</b>	<b>OVERCORING (OC)</b>	<b>HTPF INVERSION</b>
<ul style="list-style-type: none"> <li><span style="display: inline-block; width: 15px; height: 10px; background-color: #f4a460; border: 1px solid black; margin-right: 5px;"></span> Granite, fine- to medium-grained</li> <li><span style="display: inline-block; width: 15px; height: 10px; background-color: #e67e22; border: 1px solid black; margin-right: 5px;"></span> Pegmatite, pegmatitic granite</li> <li><span style="display: inline-block; width: 15px; height: 10px; background-color: #f1c40f; border: 1px solid black; margin-right: 5px;"></span> Granite, granodioritic and tonalite, metamorphic, fine- to medium-grained</li> <li><span style="display: inline-block; width: 15px; height: 10px; background-color: #9b59b6; border: 1px solid black; margin-right: 5px;"></span> Granite to granodioritic, metamorphic, medium-grained</li> <li><span style="display: inline-block; width: 15px; height: 10px; background-color: #34495e; border: 1px solid black; margin-right: 5px;"></span> Tonalite to granodioritic, metamorphic</li> <li><span style="display: inline-block; width: 15px; height: 10px; background-color: #27ae60; border: 1px solid black; margin-right: 5px;"></span> Amphibolitic</li> </ul>		
<b>DEFORMATION ZONE (DZ)</b>	<b>HYDRAULIC FRACTURING (HF)</b>	<b>BOREHOLE GEOMETRY</b>
<span style="display: inline-block; width: 15px; height: 10px; background-color: #95a5a6; border: 1px solid black; margin-right: 5px;"></span> High confidence		<ul style="list-style-type: none"> <li><span style="display: inline-block; width: 15px; height: 10px; background-color: #e74c3c; border: 1px solid black; margin-right: 5px;"></span> Borehole breakout</li> <li><span style="display: inline-block; width: 15px; height: 10px; background-color: #27ae60; border: 1px solid black; margin-right: 5px;"></span> Micro fallout</li> <li><span style="display: inline-block; width: 15px; height: 10px; background-color: #3498db; border: 1px solid black; margin-right: 5px;"></span> Key seat</li> <li><span style="display: inline-block; width: 15px; height: 10px; background-color: #f1c40f; border: 1px solid black; margin-right: 5px;"></span> Washout</li> </ul>
		<span style="color: red;">◆</span> Mean breakout orientation
		<b>CORE DISKING</b>

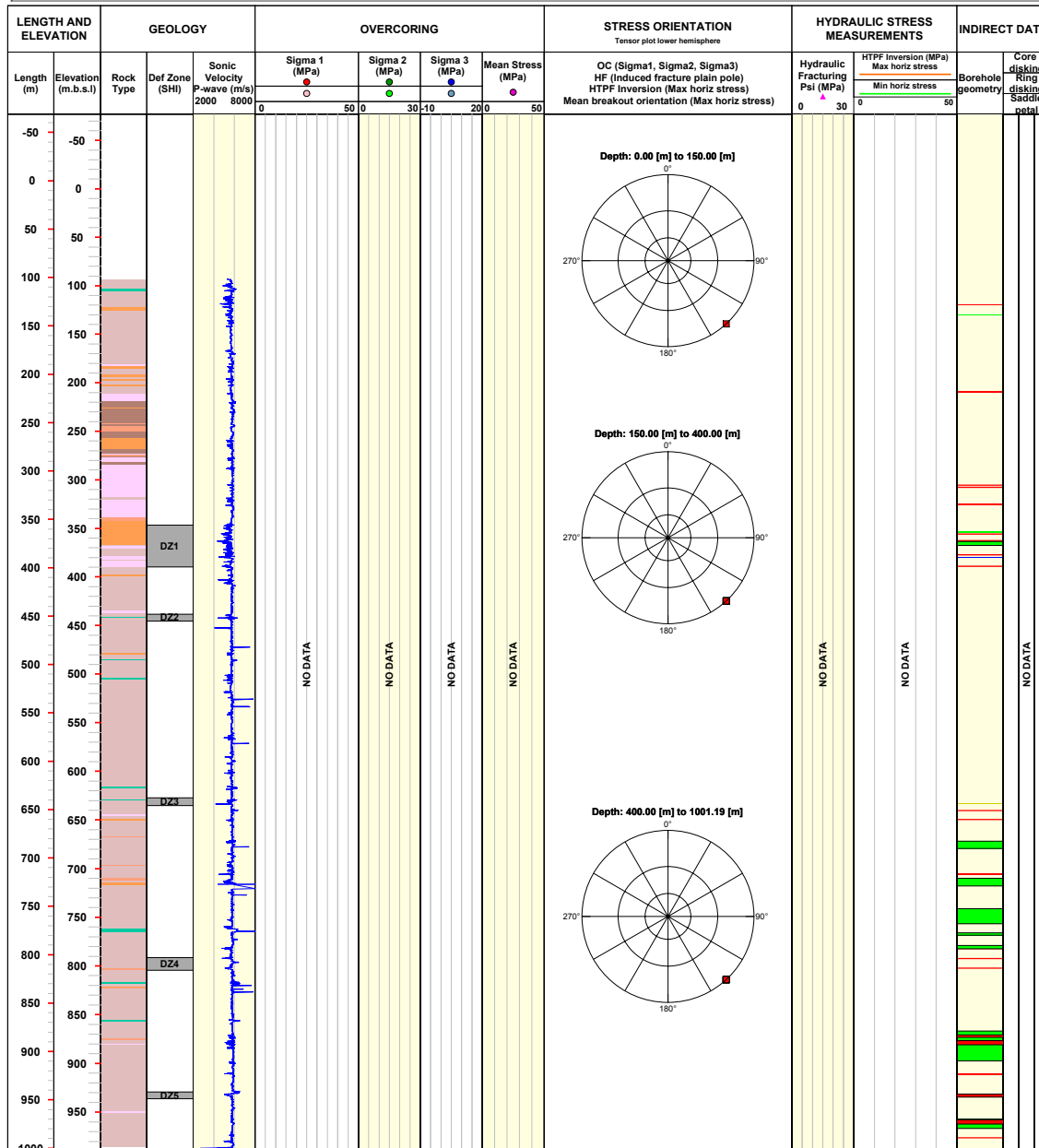


Figure A5-9. WellCad diagram for borehole KFM03A.

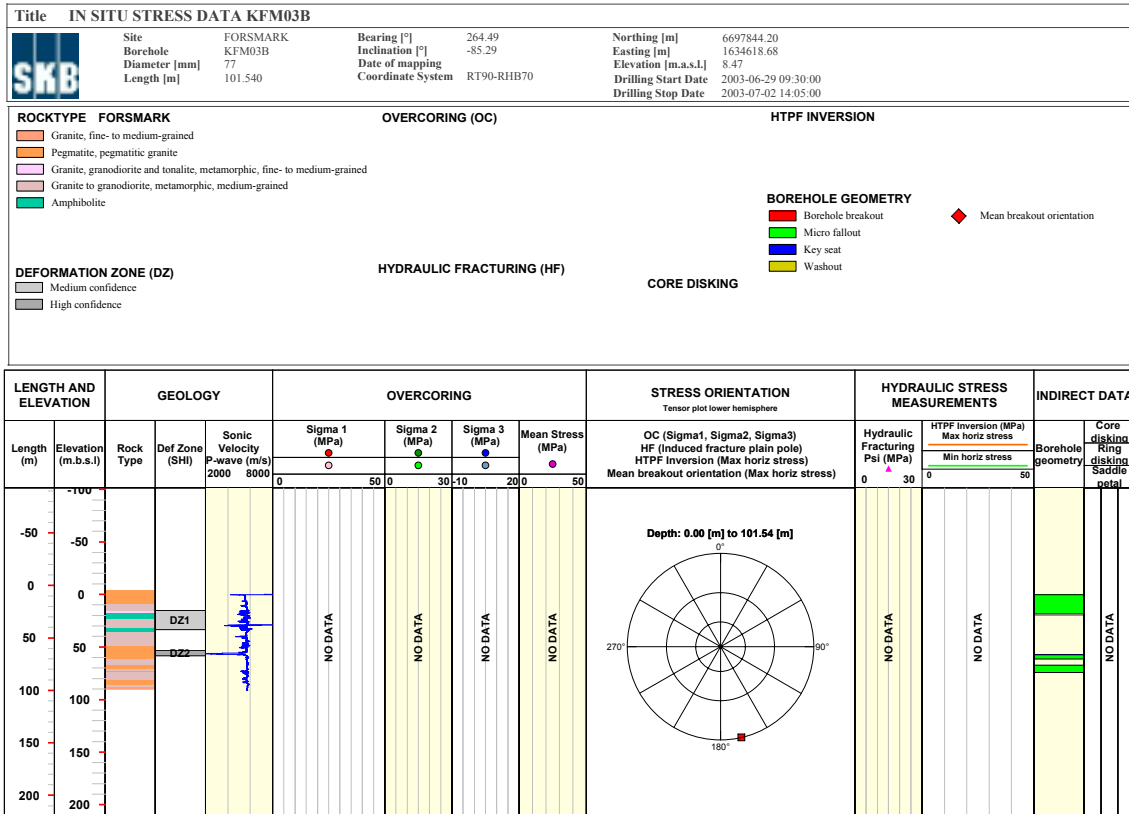


Figure A5-10. WellCad diagram for borehole KFM03B.



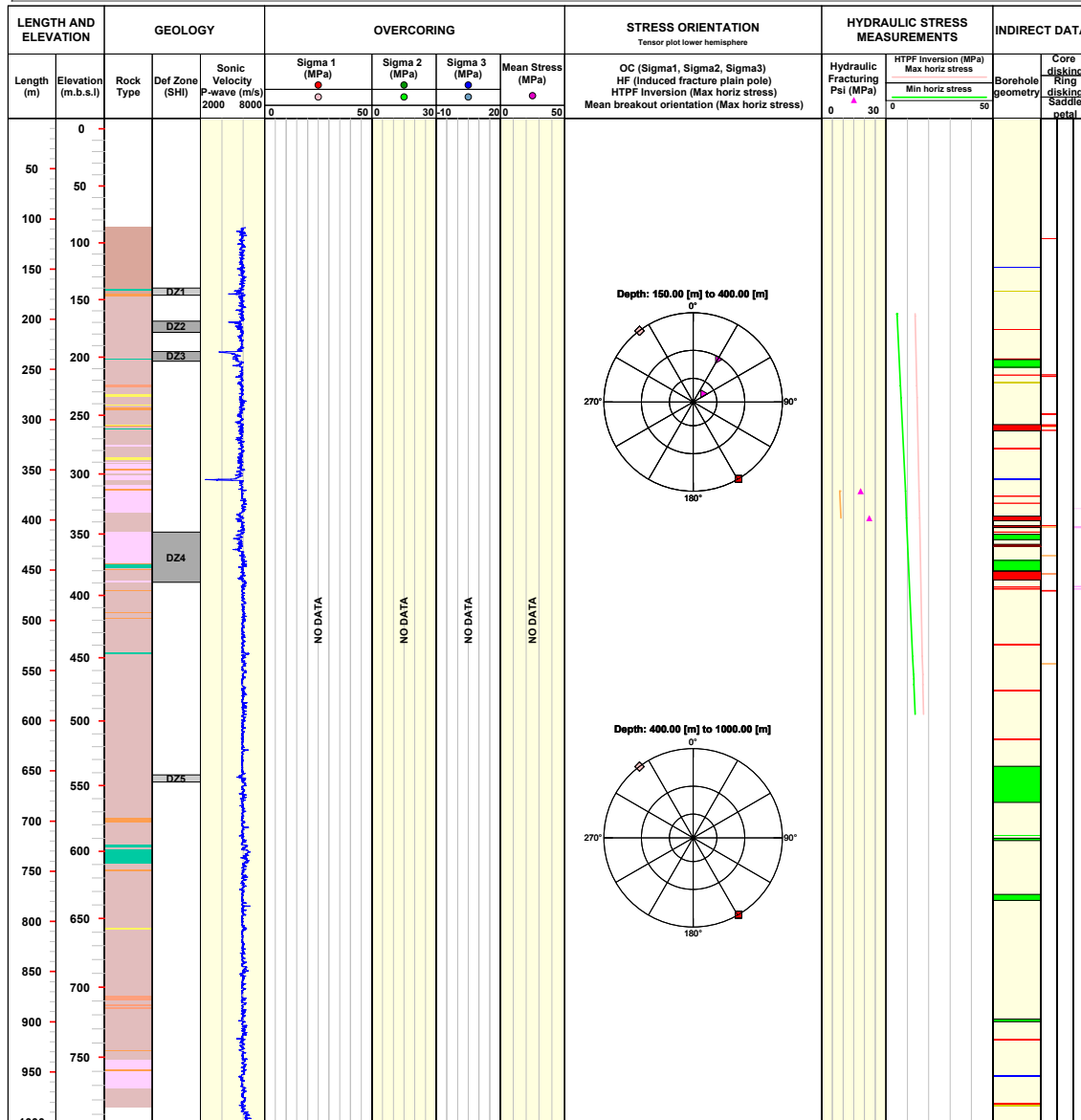
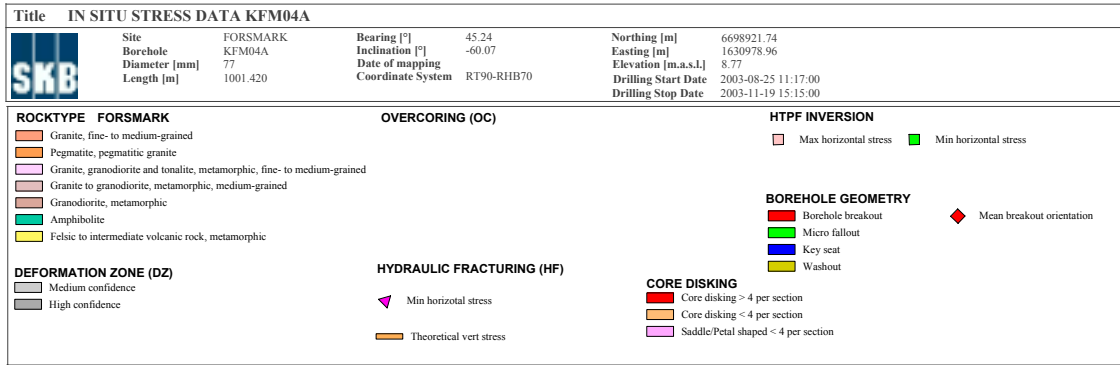


Figure A5-11. WellCad diagram for borehole KFM04A.

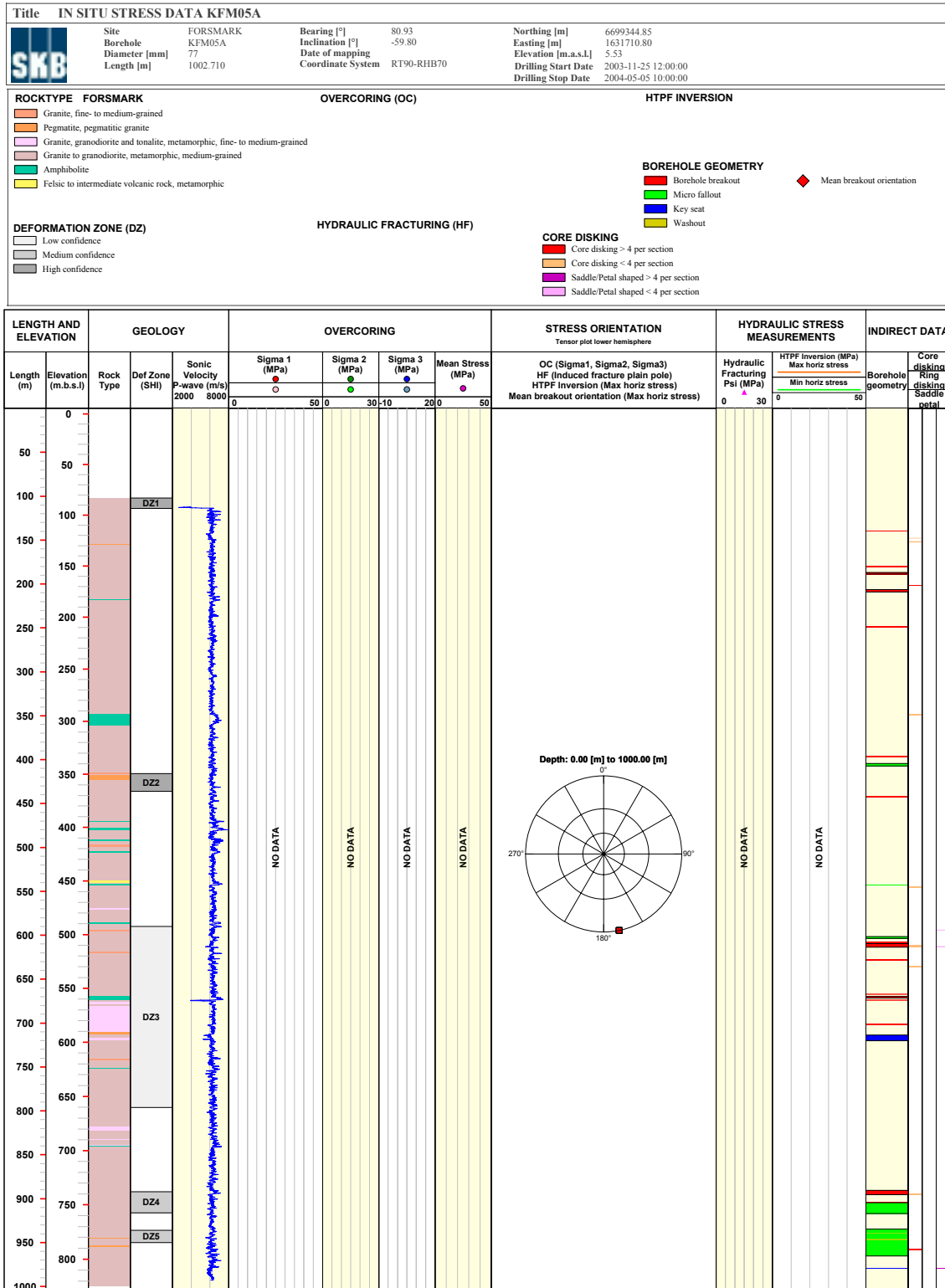


Figure A5-12. WellCad diagram for borehole KFM05A.

<b>Title</b> IN SITU STRESS DATA KFM06A		Site FORSMARK		Bearing [°]	300.92	Northing [m]	6699732.88
	Borehole	KFM06A	Inclination [°]	-60.24	Easting [m]		1632442.51
	Diameter [mm]	77	Date of mapping		Elevation [m.a.s.l.]		4.10
	Length [m]	1000.640	Coordinate System	RT90-RHB70	Drilling Start Date		2004-06-14 14:00:00
					Drilling Stop Date		2004-09-21 03:37:00

<b>ROCKTYPE FORSMARK</b>	<b>OVERCORING (OC)</b>	<b>HTPF INVERSION</b>
<ul style="list-style-type: none"> <li><span style="display: inline-block; width: 15px; height: 10px; background-color: #f4a460; border: 1px solid black; margin-right: 5px;"></span> Granite, fine- to medium-grained</li> <li><span style="display: inline-block; width: 15px; height: 10px; background-color: #e67e22; border: 1px solid black; margin-right: 5px;"></span> Pegmatite, pegmatitic granite</li> <li><span style="display: inline-block; width: 15px; height: 10px; background-color: #f1c40f; border: 1px solid black; margin-right: 5px;"></span> Granite, granodioritic and tonalite, metamorphic, fine- to medium-grained</li> <li><span style="display: inline-block; width: 15px; height: 10px; background-color: #d9ead3; border: 1px solid black; margin-right: 5px;"></span> Granite, metamorphic, aplitic</li> <li><span style="display: inline-block; width: 15px; height: 10px; background-color: #d9534f; border: 1px solid black; margin-right: 5px;"></span> Granite to granodioritic, metamorphic, medium-grained</li> <li><span style="display: inline-block; width: 15px; height: 10px; background-color: #c93025; border: 1px solid black; margin-right: 5px;"></span> Granodioritic, metamorphic</li> <li><span style="display: inline-block; width: 15px; height: 10px; background-color: #27ae60; border: 1px solid black; margin-right: 5px;"></span> Amphibolite</li> </ul>		
<b>DEFORMATION ZONE (DZ)</b>	<b>HYDRAULIC FRACTURING (HF)</b>	<b>BOREHOLE GEOMETRY</b>
<ul style="list-style-type: none"> <li><span style="display: inline-block; width: 15px; height: 10px; background-color: #d9ead3; border: 1px solid black; margin-right: 5px;"></span> Medium confidence</li> <li><span style="display: inline-block; width: 15px; height: 10px; background-color: #d9534f; border: 1px solid black; margin-right: 5px;"></span> High confidence</li> </ul>		<ul style="list-style-type: none"> <li><span style="display: inline-block; width: 15px; height: 10px; background-color: #e74c3c; border: 1px solid black; margin-right: 5px;"></span> Borehole breakout</li> <li><span style="display: inline-block; width: 15px; height: 10px; background-color: #27ae60; border: 1px solid black; margin-right: 5px;"></span> Micro fallout</li> <li><span style="display: inline-block; width: 15px; height: 10px; background-color: #2980b9; border: 1px solid black; margin-right: 5px;"></span> Key seat</li> <li><span style="display: inline-block; width: 15px; height: 10px; background-color: #f1c40f; border: 1px solid black; margin-right: 5px;"></span> Washout</li> </ul>
		<span style="color: red;">◆</span> Mean breakout orientation
		<b>CORE DISKING</b>
		<ul style="list-style-type: none"> <li><span style="display: inline-block; width: 15px; height: 10px; background-color: #e74c3c; border: 1px solid black; margin-right: 5px;"></span> Core disking &gt; 4 per section</li> <li><span style="display: inline-block; width: 15px; height: 10px; background-color: #f1c40f; border: 1px solid black; margin-right: 5px;"></span> Core disking &lt; 4 per section</li> <li><span style="display: inline-block; width: 15px; height: 10px; background-color: #9b59b6; border: 1px solid black; margin-right: 5px;"></span> Saddle/Petal shaped &gt; 4 per section</li> </ul>

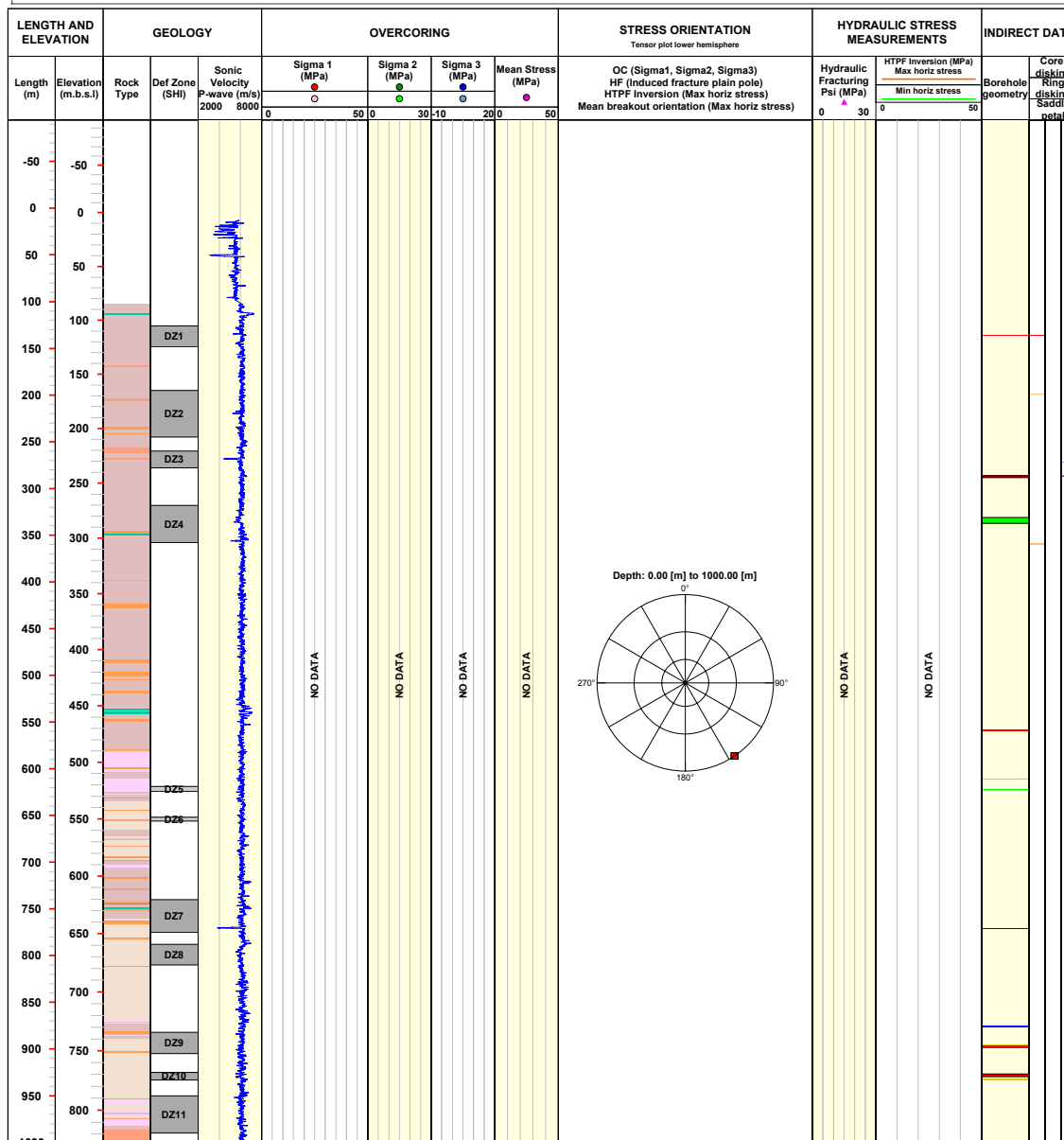


Figure A5-13. WellCad diagram for borehole KFM06A.

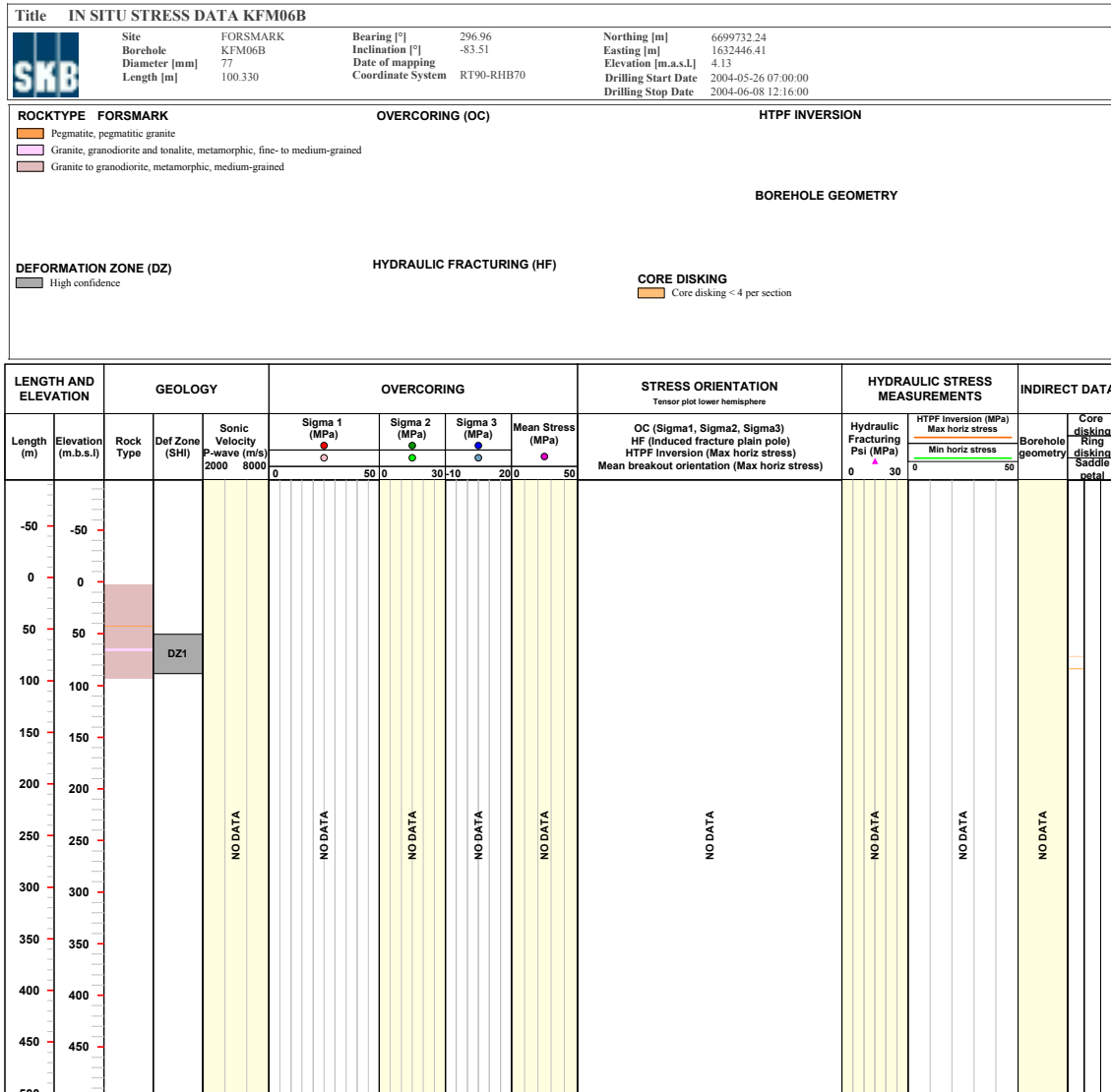



Figure A5-14. WellCad diagram for borehole KFM06B.

<b>Title</b> IN SITU STRESS DATA KFM06C		Bearing [°] 26.07		Northing [m] 6699740.96	
	Site FORSMARK	Inclination [°] -60.11	Easting [m] 1632437.03		
	Borehole KFM06C	Date of mapping	Elevation [m.a.s.l.] 4.09		
	Diameter [mm] 76	Coordinate System RT90-RHB70	Drilling Start Date 2005-04-26 14:30:00		
	Length [m] 1000.910		Drilling Stop Date 2006-06-05 00:00:00		
<b>ROCKTYPE FORSMARK</b>		<b>OVERCORING (OC)</b>		<b>HTPF INVERSION</b>	
<ul style="list-style-type: none"> <li><span style="display: inline-block; width: 15px; height: 10px; background-color: #e67e22; border: 1px solid black; margin-right: 5px;"></span> Granite, fine- to medium-grained</li> <li><span style="display: inline-block; width: 15px; height: 10px; background-color: #f1c40f; border: 1px solid black; margin-right: 5px;"></span> Pegmatite, pegmatitic granite</li> <li><span style="display: inline-block; width: 15px; height: 10px; background-color: #f08080; border: 1px solid black; margin-right: 5px;"></span> Granite, granodioritic and tonalite, metamorphic, fine- to medium-grained</li> <li><span style="display: inline-block; width: 15px; height: 10px; background-color: #d9ead3; border: 1px solid black; margin-right: 5px;"></span> Granite, metamorphic, aplitic</li> <li><span style="display: inline-block; width: 15px; height: 10px; background-color: #d9ead3; border: 1px solid black; margin-right: 5px;"></span> Granite to granodioritic, metamorphic, medium-grained</li> <li><span style="display: inline-block; width: 15px; height: 10px; background-color: #27ae60; border: 1px solid black; margin-right: 5px;"></span> Diorite, quartz diorite and gabbro, metamorphic</li> <li><span style="display: inline-block; width: 15px; height: 10px; background-color: #27ae60; border: 1px solid black; margin-right: 5px;"></span> Amphibolite</li> <li><span style="display: inline-block; width: 15px; height: 10px; background-color: #f1c40f; border: 1px solid black; margin-right: 5px;"></span> Felsic to intermediate volcanic rock, metamorphic</li> </ul>					
<b>DEFORMATION ZONE (DZ)</b>		<b>HYDRAULIC FRACTURING (HF)</b>		<b>BOREHOLE GEOMETRY</b>	
<ul style="list-style-type: none"> <li><span style="display: inline-block; width: 15px; height: 10px; background-color: #d9ead3; border: 1px solid black; margin-right: 5px;"></span> Medium confidence</li> <li><span style="display: inline-block; width: 15px; height: 10px; background-color: #f4cccc; border: 1px solid black; margin-right: 5px;"></span> High confidence</li> </ul>		<ul style="list-style-type: none"> <li><span style="display: inline-block; width: 15px; height: 10px; background-color: #e74c3c; border: 1px solid black; margin-right: 5px;"></span> Core diskling &gt; 4 per section</li> <li><span style="display: inline-block; width: 15px; height: 10px; background-color: #f1c40f; border: 1px solid black; margin-right: 5px;"></span> Core diskling &lt; 4 per section</li> <li><span style="display: inline-block; width: 15px; height: 10px; background-color: #f08080; border: 1px solid black; margin-right: 5px;"></span> Saddle/Petal shaped &lt; 4 per section</li> </ul>			

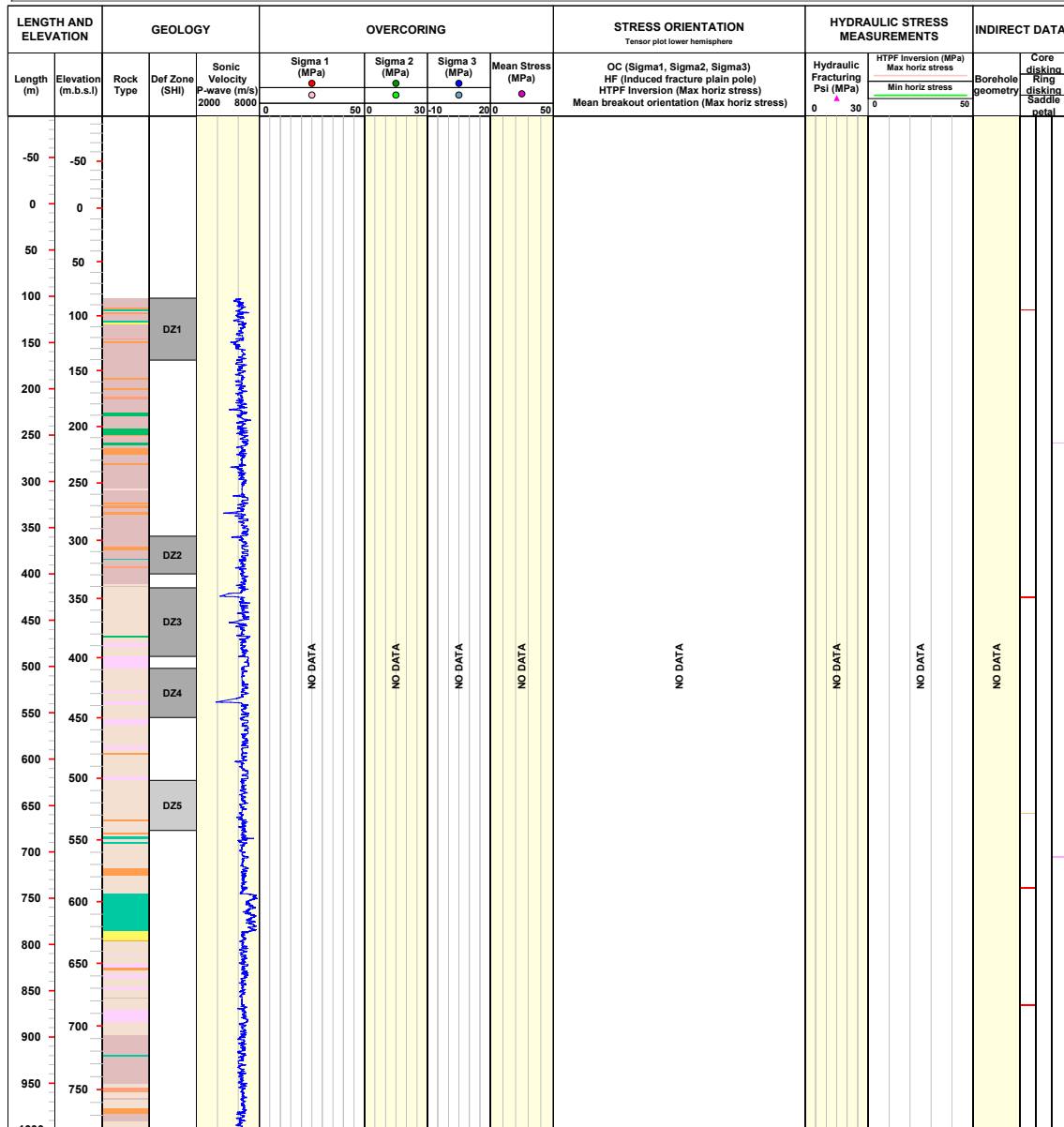


Figure A5-15. WellCad diagram for borehole KFM06C.

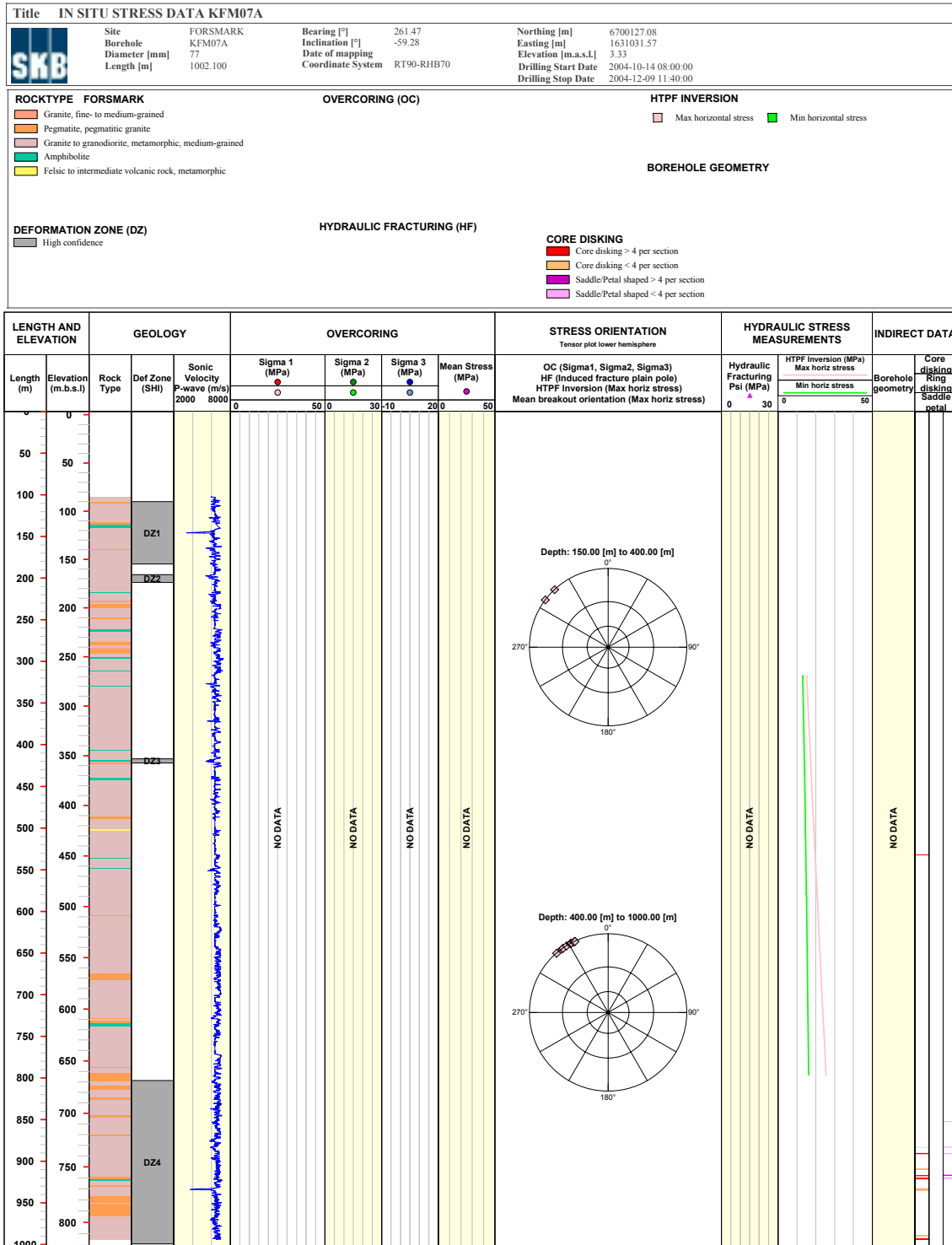


Figure A5-16. WellCad diagram for borehole KFM07A.

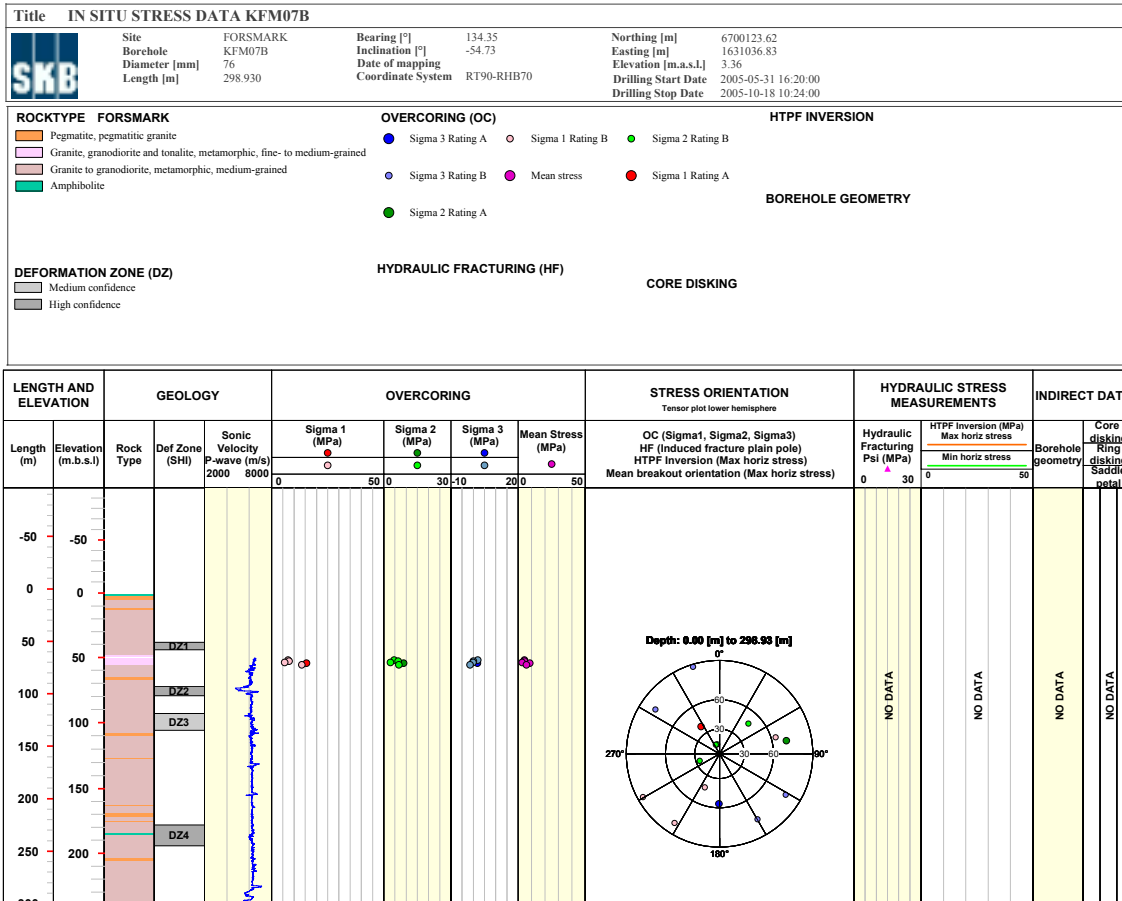


Figure A5-17. WellCad diagram for borehole KFM07B.

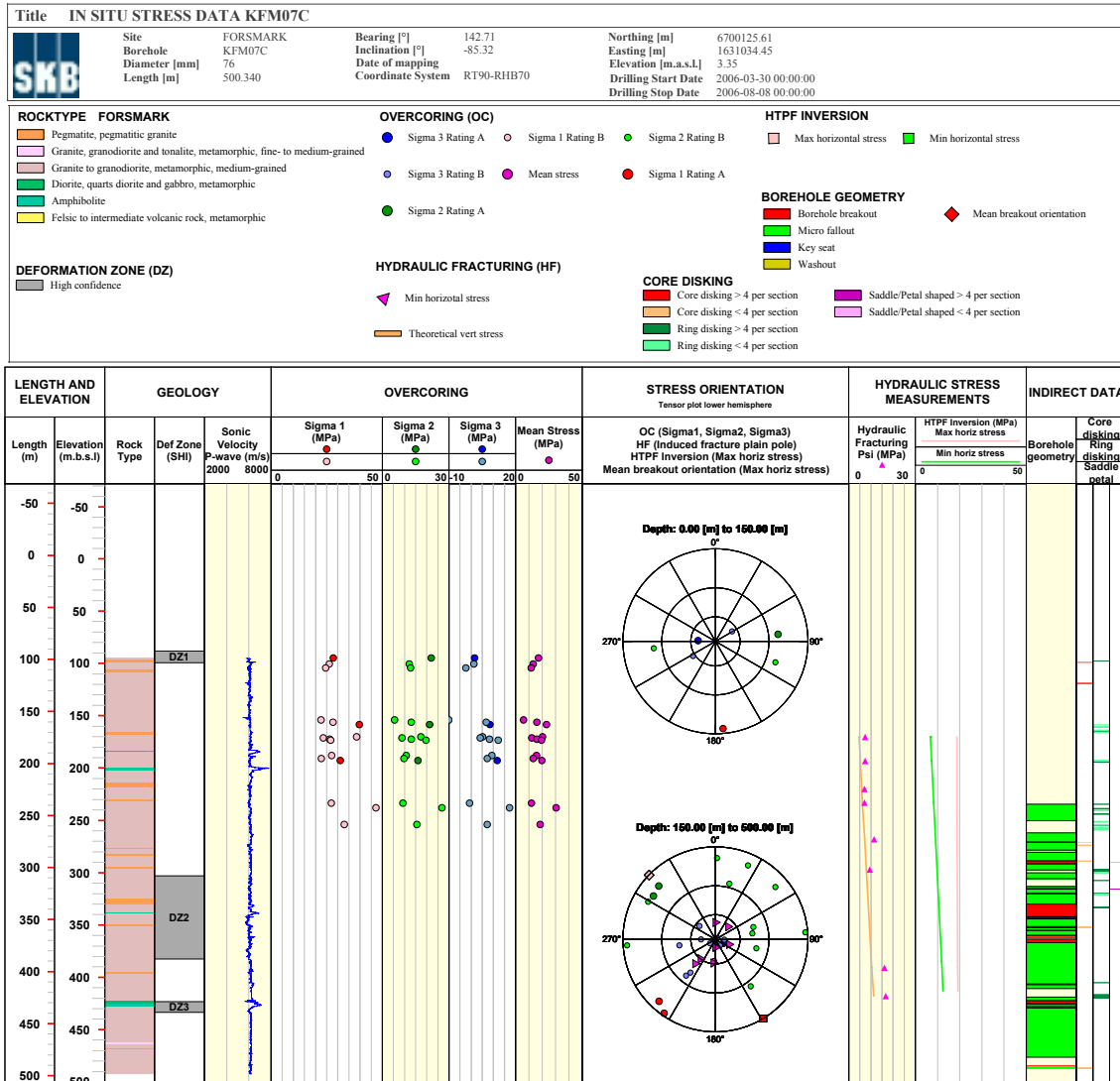


Figure A5-18. WellCad diagram for borehole KFM07C.



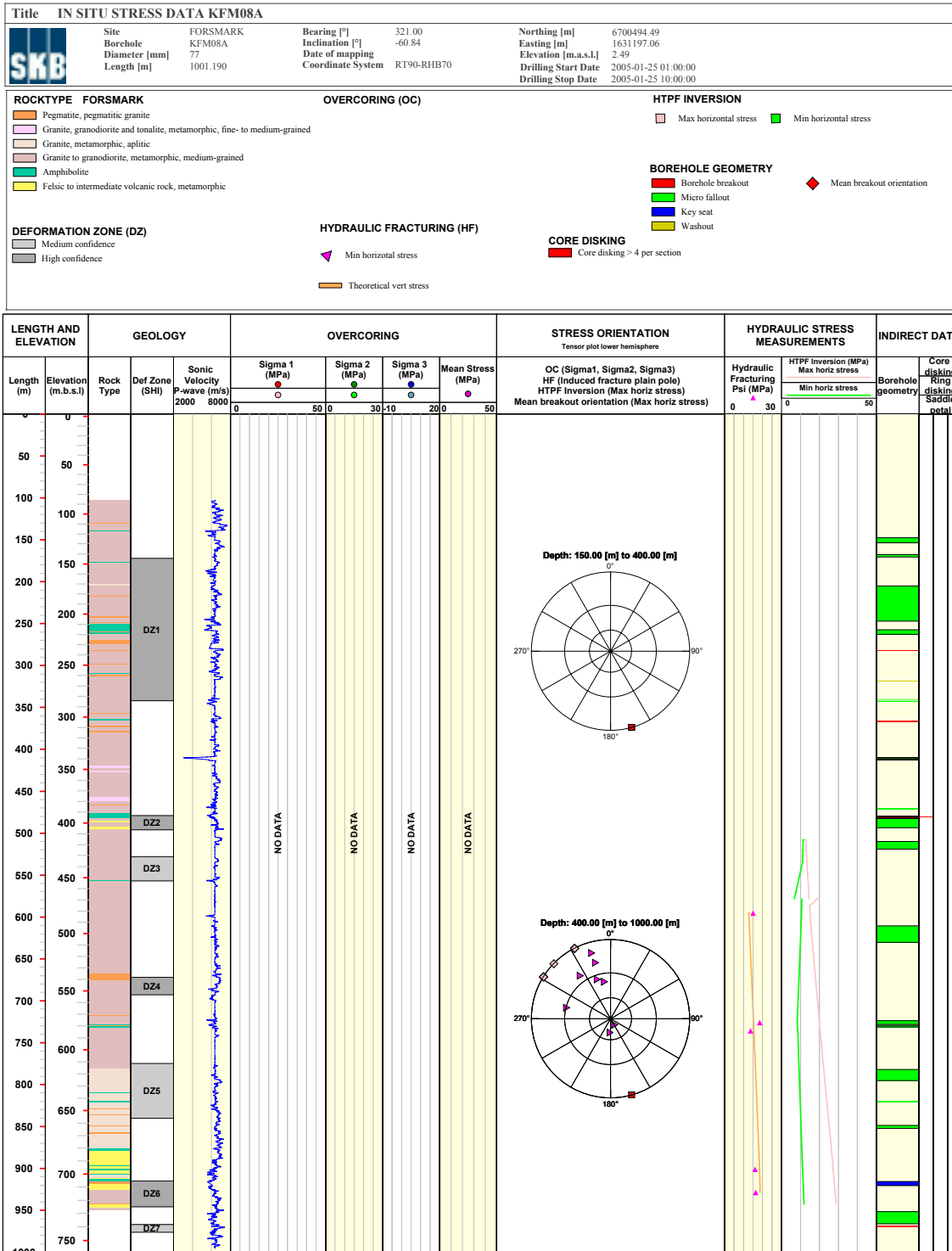


Figure A5-19. WellCad diagram for borehole KFM08A.

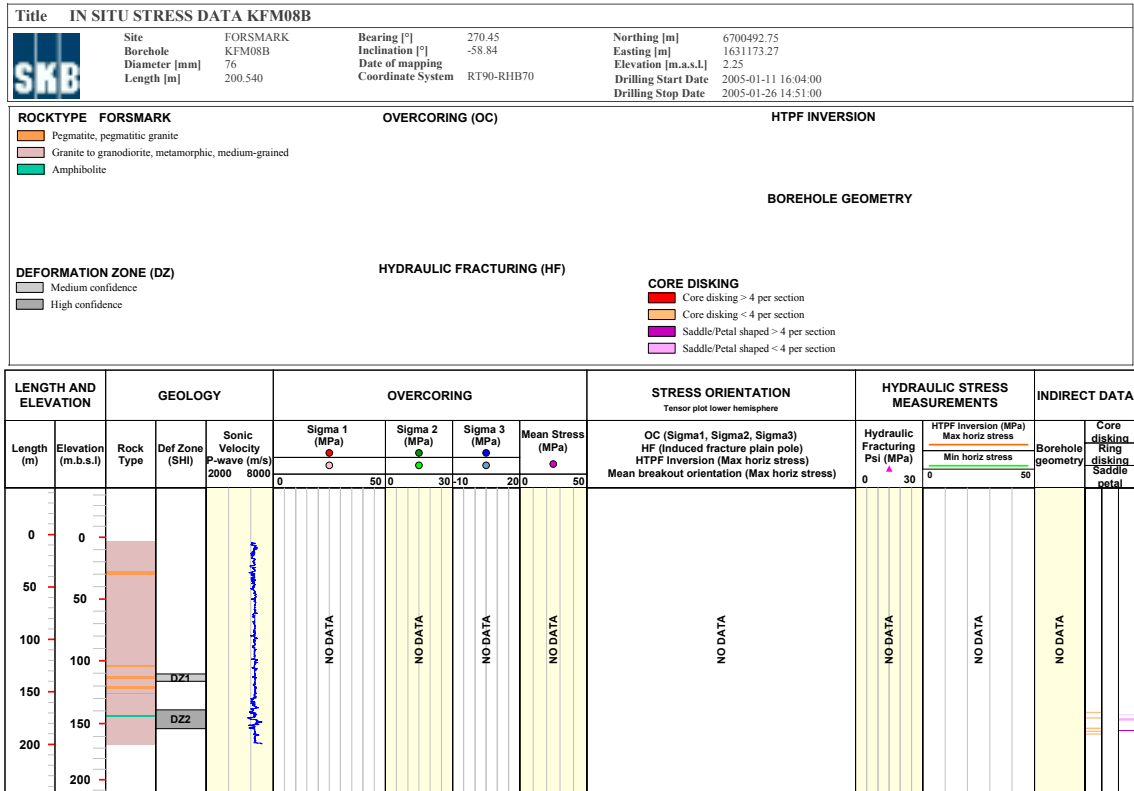


Figure A5-20. WellCad diagram for borehole KFM08B.

<b>Title</b> INSITU STRESS DATA KFM08C						
	Site	FORSMARK	Bearing [°]	35.88	Northing [m]	6700495.88
	Borehole	KFM08C	Inclination [°]	-60.47	Easting [m]	1631187.57
	Diameter [mm]	77	Date of mapping		Elevation [m.a.s.l.]	2.47
	Length [m]	951.080	Coordinate System	RT90-RHB70	Drilling Start Date	2006-01-30 16:00:00
					Drilling Stop Date	2006-05-09 06:00:00
<b>ROCKTYPE FORSMARK</b>		<b>OVERCORING (OC)</b>		<b>HTPF INVERSION</b>		
<ul style="list-style-type: none"> <li><span style="display: inline-block; width: 15px; height: 10px; background-color: #f08080; border: 1px solid black; margin-right: 5px;"></span> Pegmatite, pegmatitic granite</li> <li><span style="display: inline-block; width: 15px; height: 10px; background-color: #d2b48c; border: 1px solid black; margin-right: 5px;"></span> Granite, granodioritic and tonalite, metamorphic, fine- to medium-grained</li> <li><span style="display: inline-block; width: 15px; height: 10px; background-color: #c0c0c0; border: 1px solid black; margin-right: 5px;"></span> Granite, metamorphic, aplitic</li> <li><span style="display: inline-block; width: 15px; height: 10px; background-color: #a0a0a0; border: 1px solid black; margin-right: 5px;"></span> Granite to granodioritic, metamorphic, medium-grained</li> <li><span style="display: inline-block; width: 15px; height: 10px; background-color: #90ee90; border: 1px solid black; margin-right: 5px;"></span> Amphibolite</li> <li><span style="display: inline-block; width: 15px; height: 10px; background-color: #90ee90; border: 1px solid black; margin-right: 5px;"></span> Calc-silicate rock (skarn)</li> </ul>				<ul style="list-style-type: none"> <li><span style="display: inline-block; width: 15px; height: 10px; background-color: #ff0000; border: 1px solid black; margin-right: 5px;"></span> Borehole breakout</li> <li><span style="display: inline-block; width: 15px; height: 10px; background-color: #00ff00; border: 1px solid black; margin-right: 5px;"></span> Micro fallout</li> <li><span style="display: inline-block; width: 15px; height: 10px; background-color: #0000ff; border: 1px solid black; margin-right: 5px;"></span> Key seat</li> <li><span style="display: inline-block; width: 15px; height: 10px; background-color: #ffff00; border: 1px solid black; margin-right: 5px;"></span> Washout</li> </ul>		
<b>DEFORMATION ZONE (DZ)</b>		<b>HYDRAULIC FRACTURING (HF)</b>		<b>CORE DISKING</b>		
<ul style="list-style-type: none"> <li><span style="display: inline-block; width: 15px; height: 10px; background-color: #d3d3d3; border: 1px solid black; margin-right: 5px;"></span> Medium confidence</li> <li><span style="display: inline-block; width: 15px; height: 10px; background-color: #808080; border: 1px solid black; margin-right: 5px;"></span> High confidence</li> </ul>				<ul style="list-style-type: none"> <li><span style="display: inline-block; width: 15px; height: 10px; background-color: #ff0000; border: 1px solid black; margin-right: 5px;"></span> Core disking &gt; 4 per section</li> <li><span style="display: inline-block; width: 15px; height: 10px; background-color: #ffa500; border: 1px solid black; margin-right: 5px;"></span> Core disking &lt; 4 per section</li> <li><span style="display: inline-block; width: 15px; height: 10px; background-color: #800080; border: 1px solid black; margin-right: 5px;"></span> Saddle/Petal shaped &gt; 4 per section</li> </ul>		

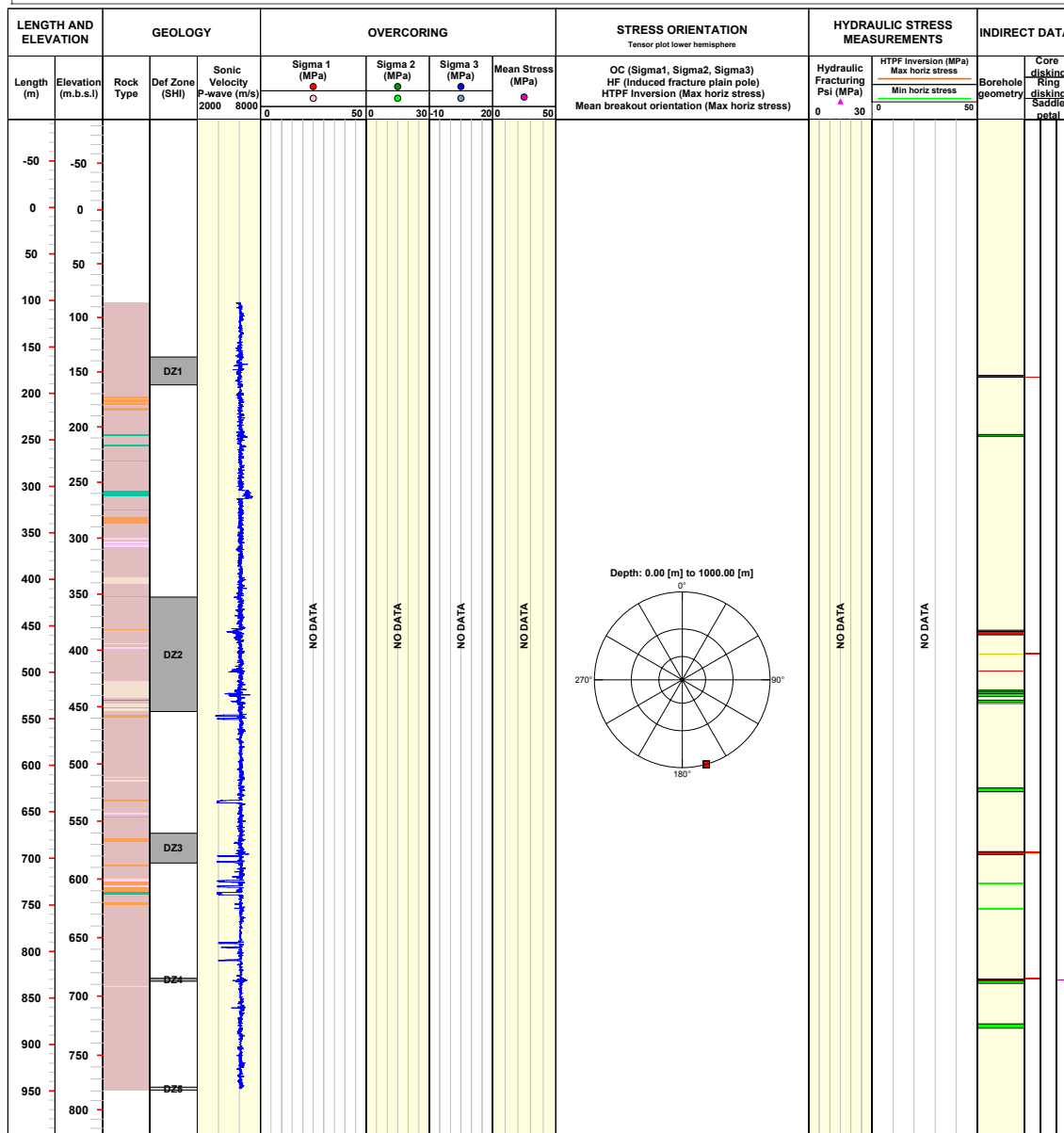


Figure A5-21. WellCad diagram for borehole KFM08C.

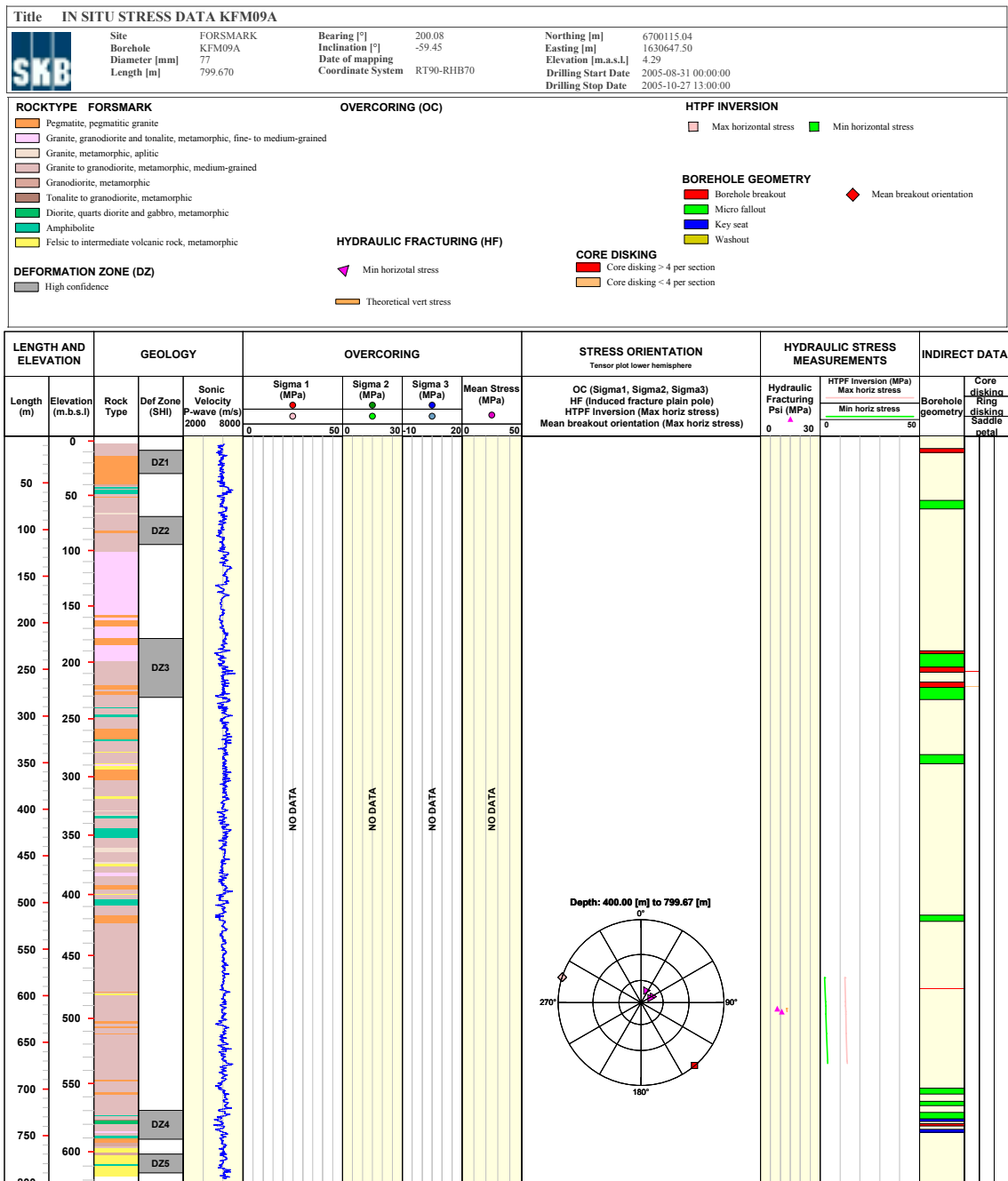


Figure A5-22. WellCad diagram for borehole KFM09A.

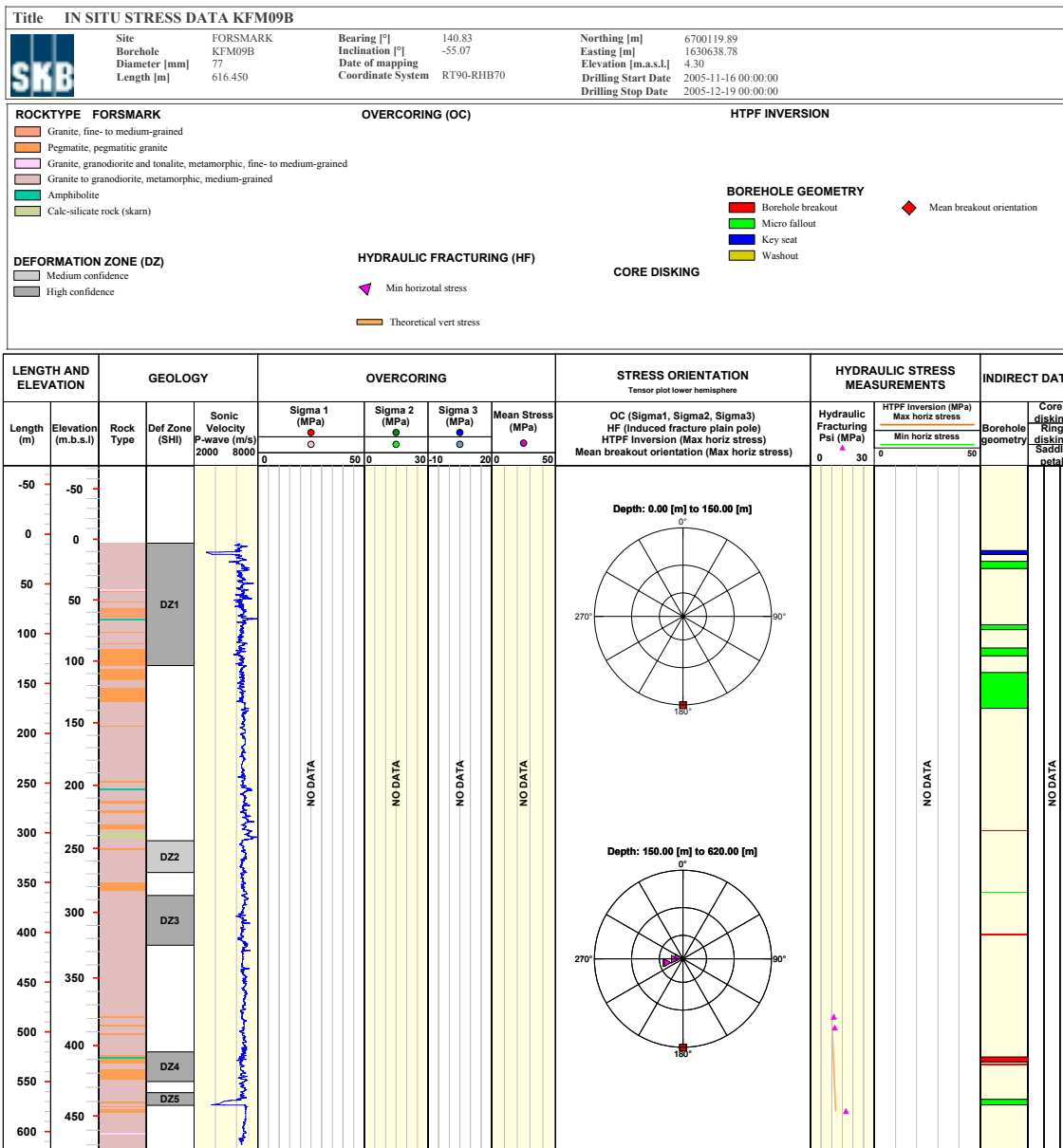


Figure A5-23. WellCad diagram for borehole KFM09B.

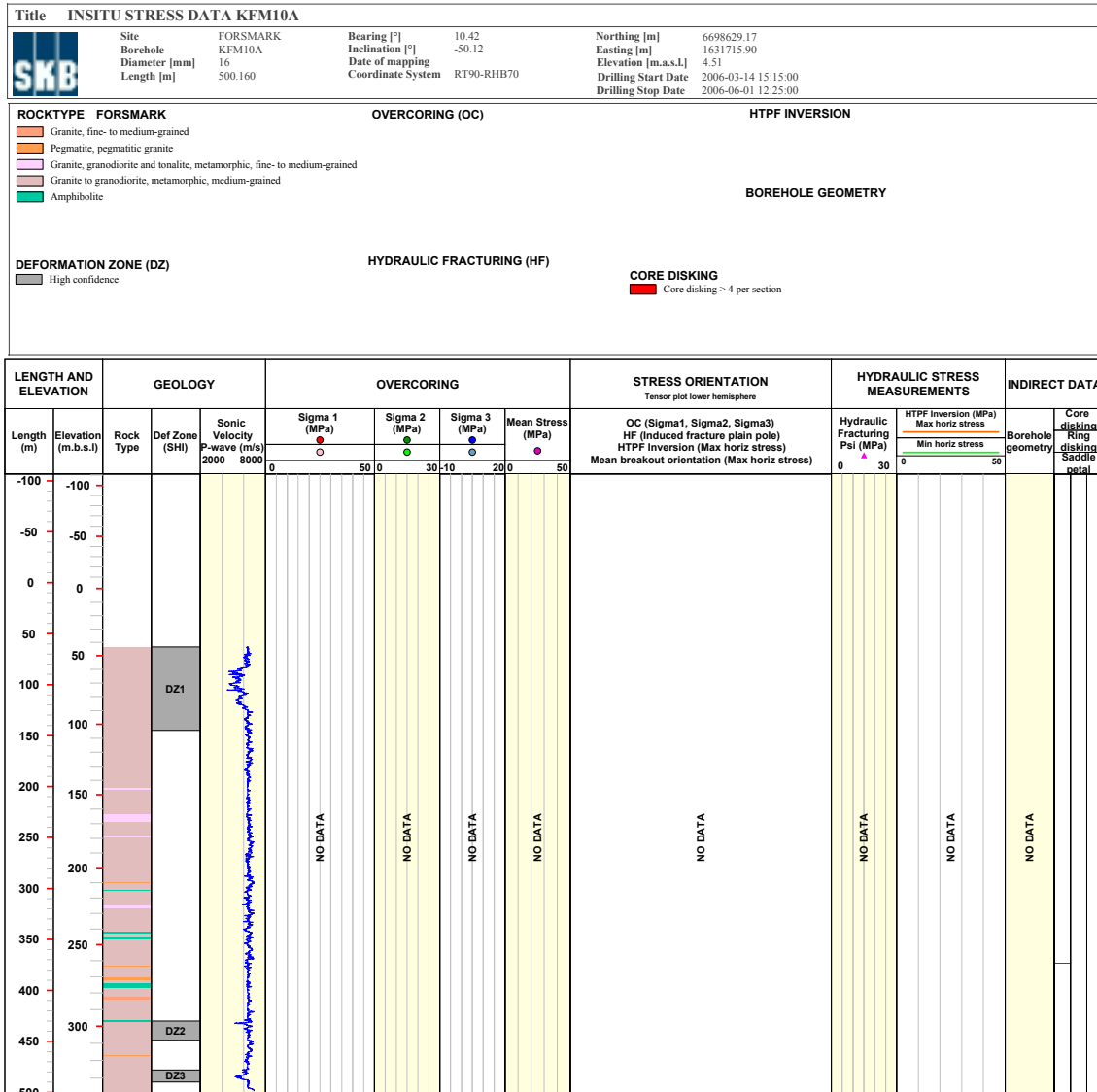


Figure A5-24. WellCad diagram for borehole KFM10A.

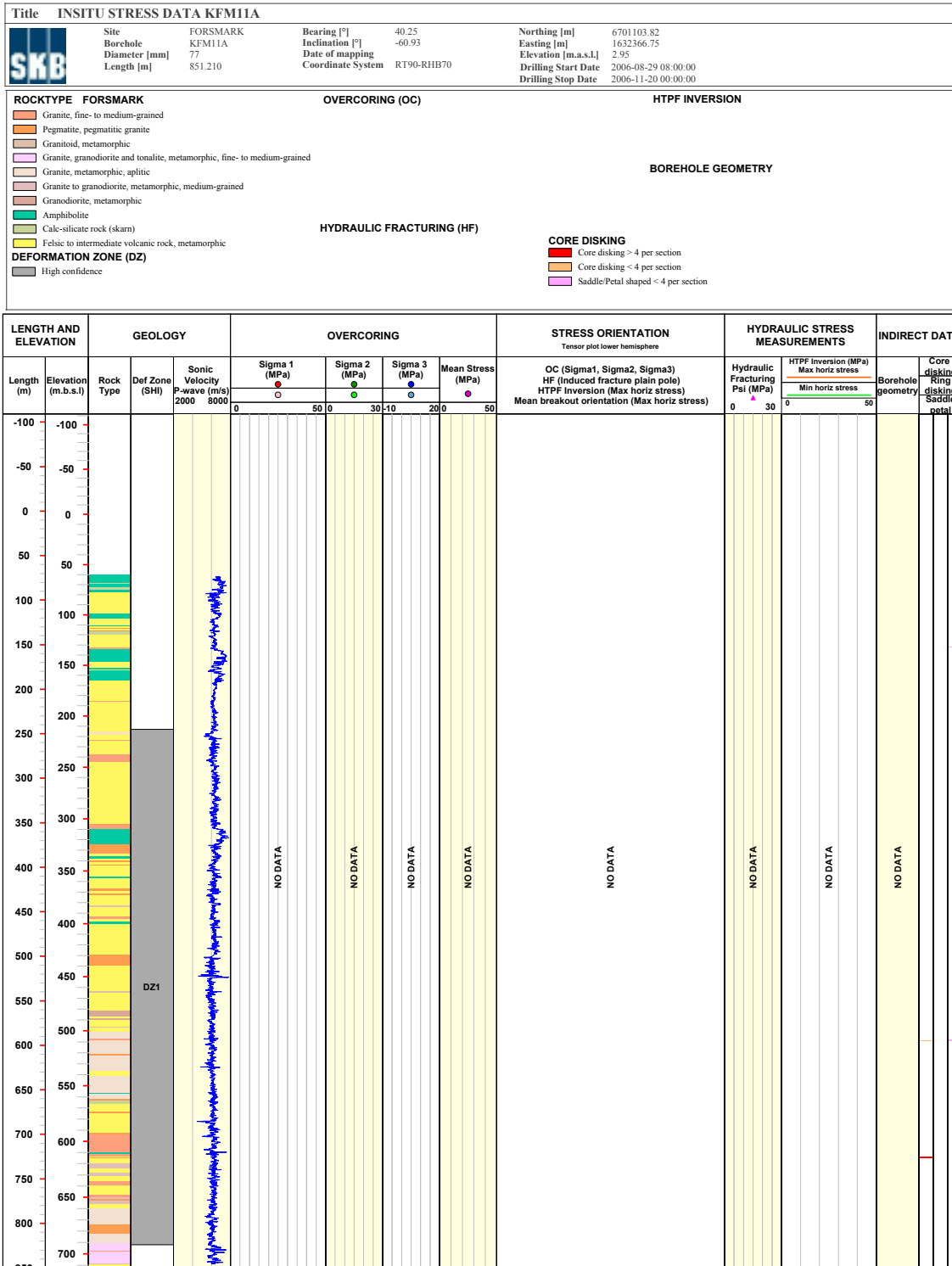


Figure A5-25. WellCad diagram for borehole KFM11A.

Evaluated principal stresses

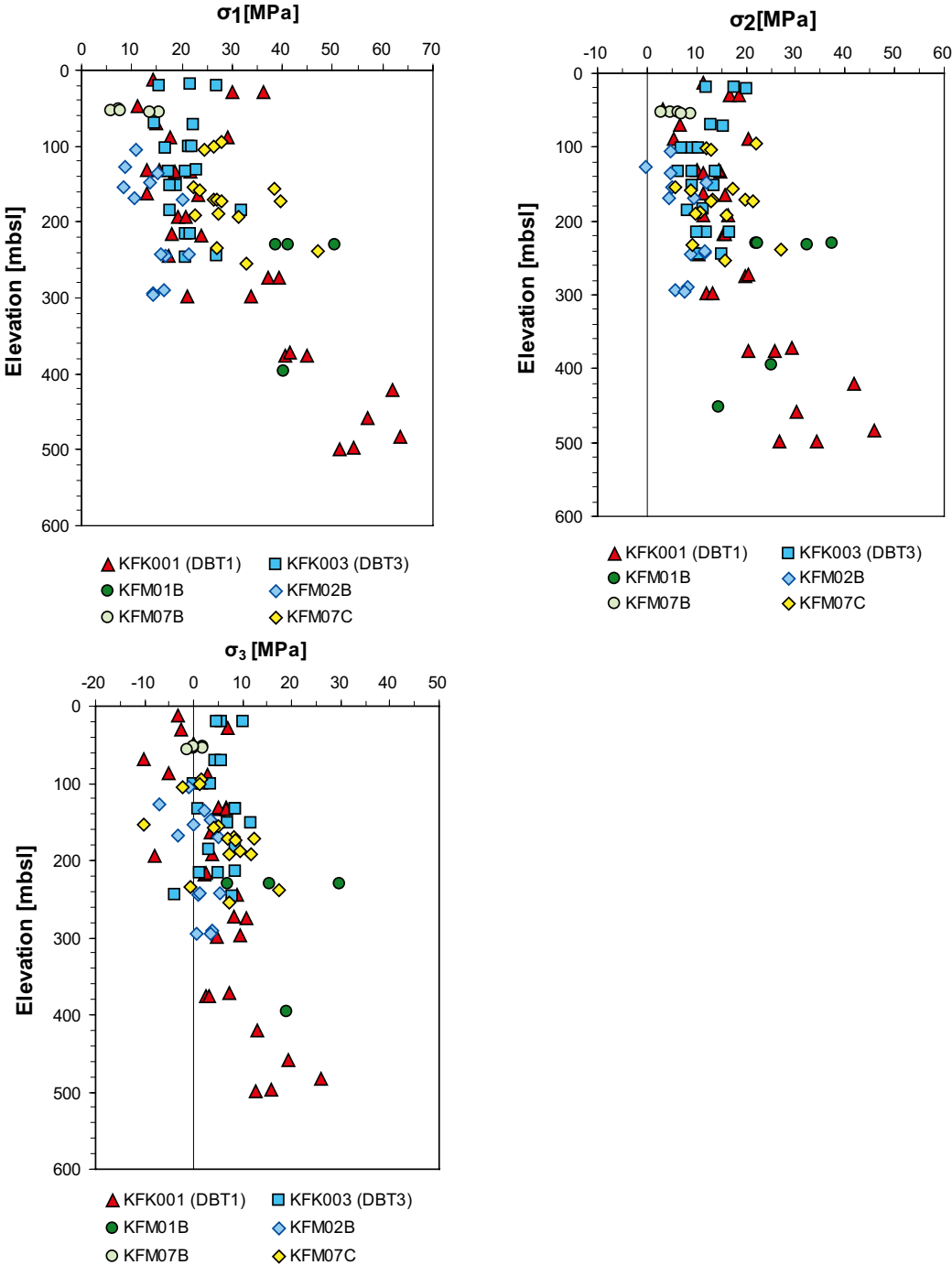


Figure A6-1. Principal stresses versus depth.



## Numerical modelling of in situ stresses

### A7.1 Deformation zones included in the numerical modelling

Table A7-1. Deformation zones included in the model block.

Zone	Strike	Dip	Thickness [m]	Thickness span [m]	Thickness confidence	Length [m]	Comment
<b>Gently-dipping brittle deformation zones</b>							
ZFMA2	80 ± 15	24 ± 10	35	23–48	High	3,987	Type intersections in upper part of DZ6 in KFM02A and along DZ2 and DZ3 in KFM10A, vuggy rock
ZFMF1	70	10 ± 10	44	23–48	Medium		Borehole interval 476–520 m along part of DZ6 in KFM02A
<b>Vertical and steeply-dipping brittle deformation zones with ENE strike</b>							
ZFMENE0062A	58 ± 5	85 ± 10	44	10–64	Low	3,543	DZ4 and DZ5 in HFM25
ZFMENE1061A	56 ± 5	81 ± 10	45	3–45	Medium	1,158	Borehole interval 244–315 m along part of DZ1 in KFM08A, DZ4 and DZ5 in KFM08C
ZFMENE2248	234 ± 5	80 ± 10	38	3–45	Medium	1,298	DZ5 and extension along borehole interval 840–843 m in KFM08A
<b>Vertical and steeply-dipping brittle deformation zones with NNE strike</b>							
ZFMNNE0828	213 ± 5	80 ± 10	35	10–64	Low	5,932	
ZFMNNE0860	198 ± 10	80 ± 10	35	10–64	Low	5,922	
ZFMNNE0929	193 ± 10	80 ± 10	35	10–64	Low	5,203	
ZFMNNE1134	192 ± 10	90 ± 10	40	10–64	Low	7,284	
<b>Vertical and steeply-dipping deformation zone with NNW strike</b>							
ZFMNNW0100	172 ± 5	88 ± 10	41	3–45	Medium	1,673	Borehole interval 920–999 m along part of DZ4 in KFM07A and DZ3 in KFM09A
<b>Vertical and steeply, SSW- (and SW-dipping) deformation zones with NW strike</b>							
ZFMNW0002	135 ± 10	90 ± 10	75	53–200	Medium	18,000	Splay from Singö deformation zone through tunnel 3
ZFMNW0003	139 ± 10	85 ± 10	53	53–200	Medium	30,000	Eckarfjärden deformation zone
ZFMNW0806	145 ± 10	90 ± 10	80	53–200	Low	22,000	Splay from Singö deformation zone
ZFMNW1200	138 ± 5	85 ± 10	47	10–64	Medium	3,121	Surface, DZ1 and extension along 110–169 m in KFM04A, DZ4 and DZ5 in KFM09A
<b>Vertical and steeply, SSW- (and SW-dipping) deformation zones with WNW strike</b>							
ZFMWNW0001	120 ± 10	90 ± 10	165	53–200	Medium	30,000	Singö deformation zone
ZFMWNW0004	125 ± 10	90 ± 10	160	53–200	Low	70,000	Forsmark deformation zone
ZFMWNW0016	123 ± 5	90 ± 10	45	10–64	Low	8,060	
ZFMWNW0023	111 ± 5	90 ± 10	45	10–64	Low	7,665	
ZFMWNW0024	124 ± 5	90 ± 10	45	10–64	Low	7,986	
ZFMWNW0036	123 ± 10	90 ± 10	55	53–200	Low	11,000	
ZFMWNW0123	117 ± 5	82 ± 10	52	10–64	Medium	5,086	DZ1 in KFM10A, DZ1, DZ2 and DZ3 in HFM24, DZ1, DZ2 and DZ3 in HFM29 and DZ5 in KFM04A; vuggy rock

## A7.2 Results from the numerical modelling

Section 6.4.3 in the report gives an account of the stress variability at the repository level. The results regarding the major principal stress,  $\sigma_1$ , are presented under that section. Here the results from sampling of  $\sigma_2$  and  $\sigma_3$  are presented. The results are given in the following order:

- Lateral variation of  $\sigma_2$  and  $\sigma_3$  along a NW-SE horizontal scan line, see Figure A7-1 and Figure A7-2.
- Lateral variation of  $\sigma_2$  and  $\sigma_3$  along a NE-SW horizontal scan line, see Figure A7-3 and Figure A7-4.
- Along a vertical numerical scan line in close vicinity of borehole KFM02B, see Figure A7-5 and Figure A7-6.
- Along a vertical numerical scan line in close vicinity of borehole KFM07C, see Figure A7-7 and Figure A7-8.

Where the horizontal scan line cuts across a deformation zone, the position is marked on the figures as a vertical bar. In situ measurement results carried out in borehole KFM02B and KFM07C, towards which the calibration of the numerical model was performed, are also plotted in the figures for comparison.

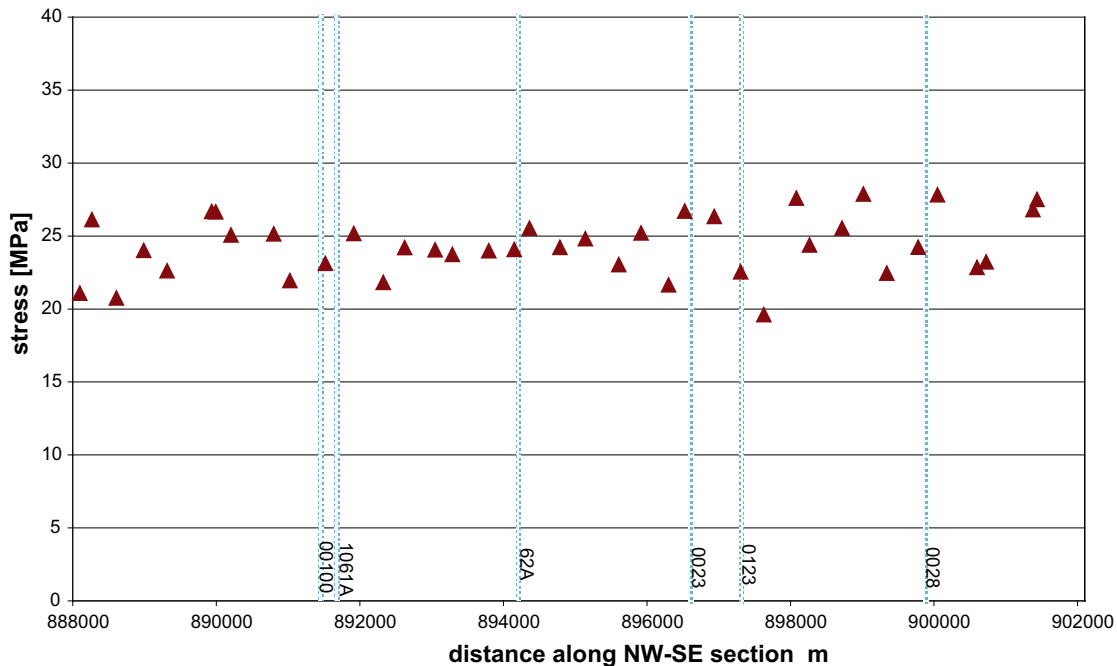


**Figure A7-1.** The lateral variation of  $\sigma_2$  along a NW-SE scan line (see Figure 6-27) drawn at a depth of 500 m.

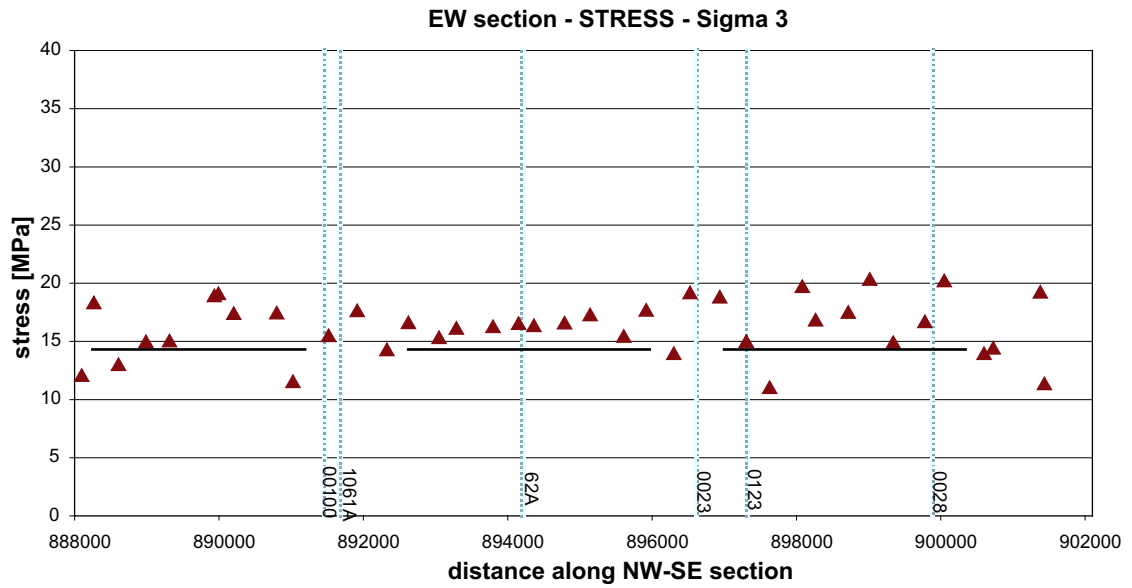


*Figure A7-2.* The lateral variation of  $\sigma_3$  along a NW-SE scan line (see Figure 6-27) drawn at a depth of 500 m. The broken line in grey shows the vertical stress due to the weight of rock overburden at 500 m depth.

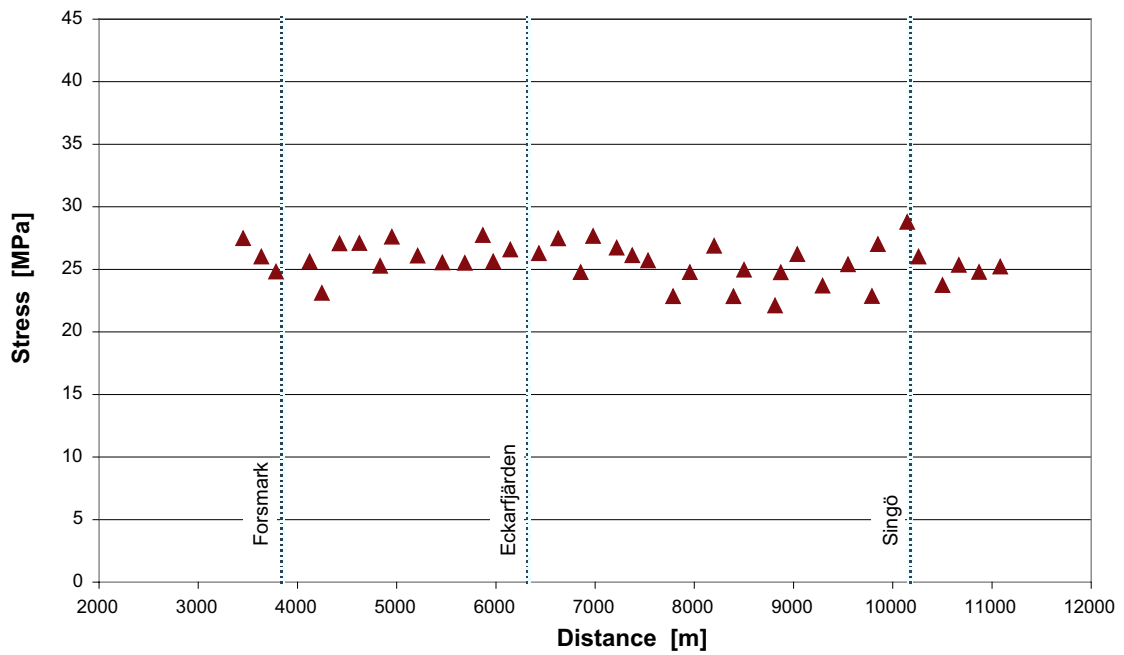


*Figure A7-3.* The lateral variation of  $\sigma_2$  along a NE-SW scan line (see Figure 6-27) drawn at a depth of 500 m.

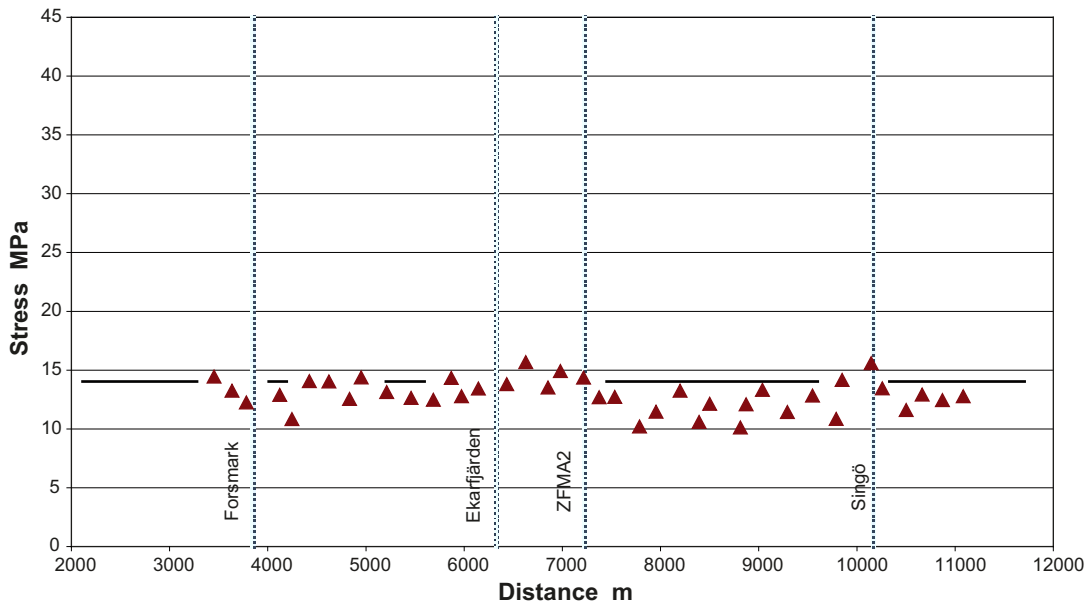


**Figure A7-4.** The lateral variation of  $\sigma_3$  sampled along a NE-SW scan line (see Figure 6-27) drawn at a depth of 500 m. The broken line in grey shows the vertical stress due to the weight of rock overburden at 500 m depth.

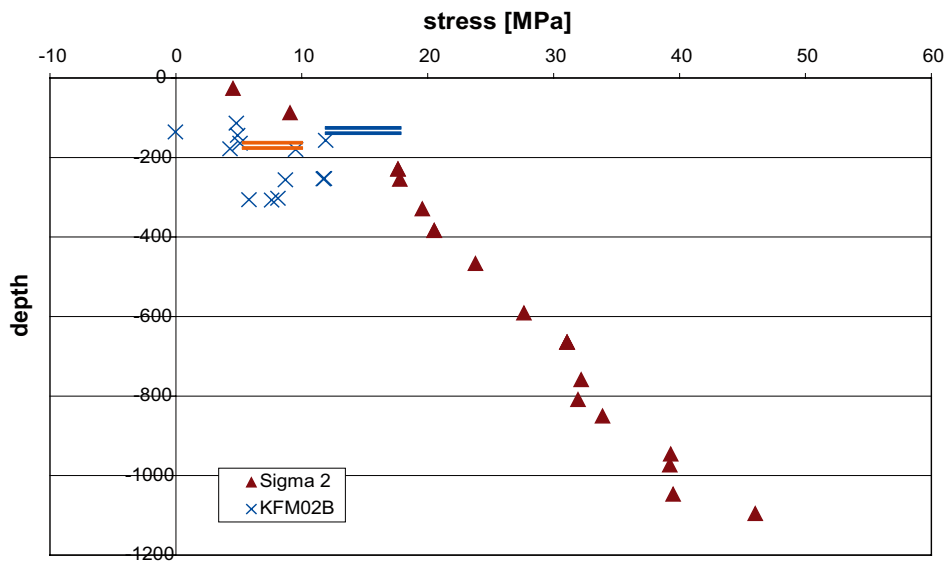


**Figure A7-5.** The vertical variation of  $\sigma_2$  along a numerical scan line in close proximity to borehole KFM02B compared to overcoring results from the KFM02B. The red parallel lines show roughly where borehole KFM02B intersects the deformation zone ZFMA2 and the blue parallel lines shows where the numerical borehole intersects.

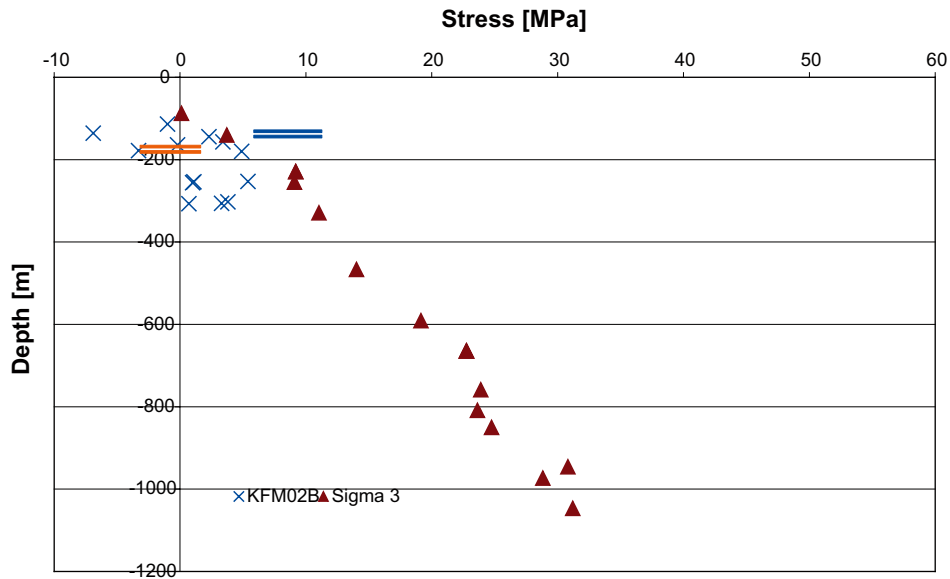


**Figure A7-6.** The vertical variation of  $\sigma_3$  along a numerical scan line in close proximity to borehole KFM02B compared to overcore results from the KFM02B. The red parallel lines show roughly where borehole KFM02B intersects the deformation zone ZFMA2 and the blue parallel lines shows where the numerical borehole intersects.

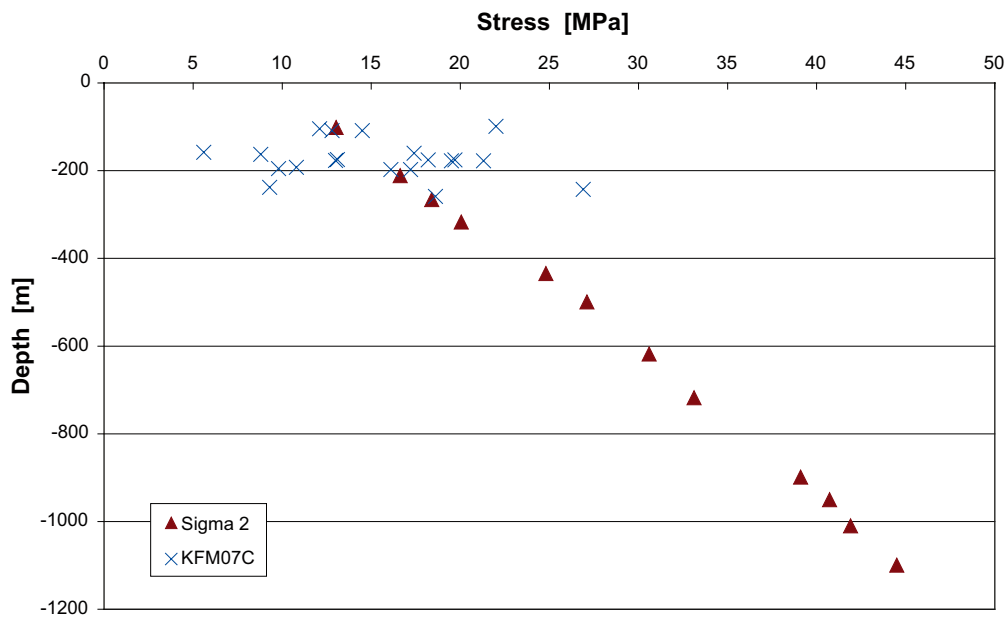


**Figure A7-7.** Vertical distribution of  $\sigma_2$  sampled from a numerical scan line in close proximity to borehole KFM07C compared with overcoring results from KFM07C.

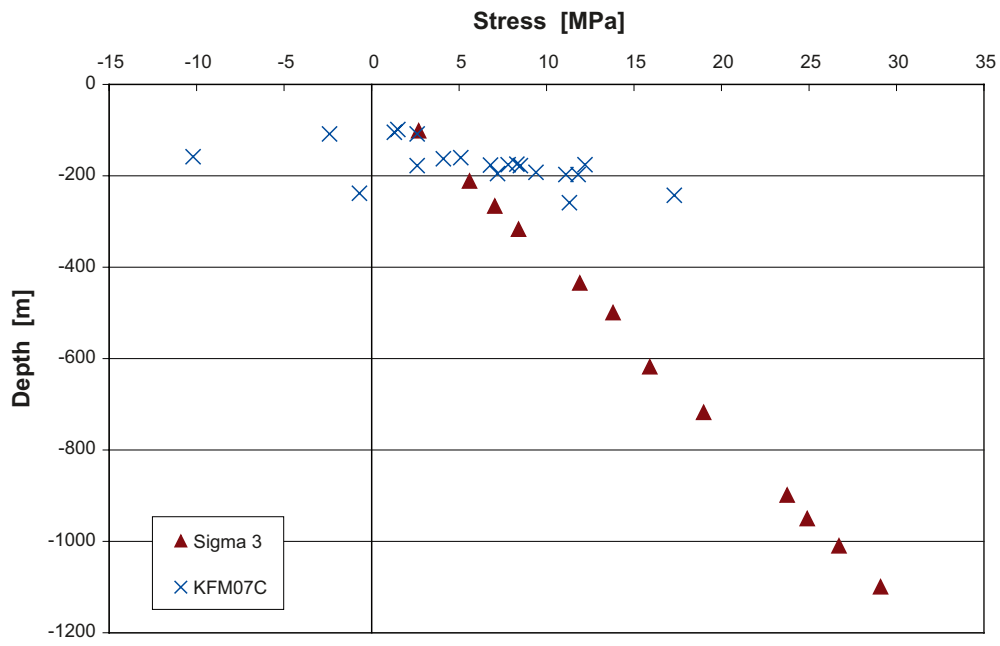


**Figure A7-8.** Vertical distribution of  $\sigma_3$  sampled from a numerical scan line in close proximity to borehole KFM07C compared with overing results from KFM07C.

### Visualization of rock mechanics data

Selected data from rock mechanics sampling, characterisation and rock stress measurements (borehole locations) are visualized in relation to fracture domains and deformation zones. The base of the visualizations is the Container presented on the appended CD in /Olofsson et al. 2007/, in which the primary data is also presented in WellCad-plots. Additional RVS visualizations are based on both official Sicada-data and working material for the rock mass characterization, used for the empirical modelling described in this report.

Each three-dimensional image is presented from three different angles: from above, tilted towards east and tilted towards west. The last shows FFM01, FFM02, FFM03, FFM06 and deformation zones, while the first two show FFM04, FFM05 and FFM06 and only the steeply dipping deformation zones.

#### A8.1 Rock mechanics sampling

Source: /Olofsson et al. 2007/ RVS container (Sicada\_07\_207). Selection as for the WellCad plots in the Fracture Domain Report /Olofsson et al. 2007/. The visualized data is the primary data selection presented in the WellCad-plots in /Olofsson et al. 2007/, hence it does not include data from independent laboratories nor from tests on sealed fractures.

The sampling for rock mechanics tests are conducted on core samples that are situated close to one another. In a visualization of the samples in the modelling volume (Forsmark 2.2 local model measures 3,776×3,200×1,200 m), some samples will be hidden by others. This is illustrated in Figure A8-1, where sampling for uniaxial tests in KFM01A is shown.

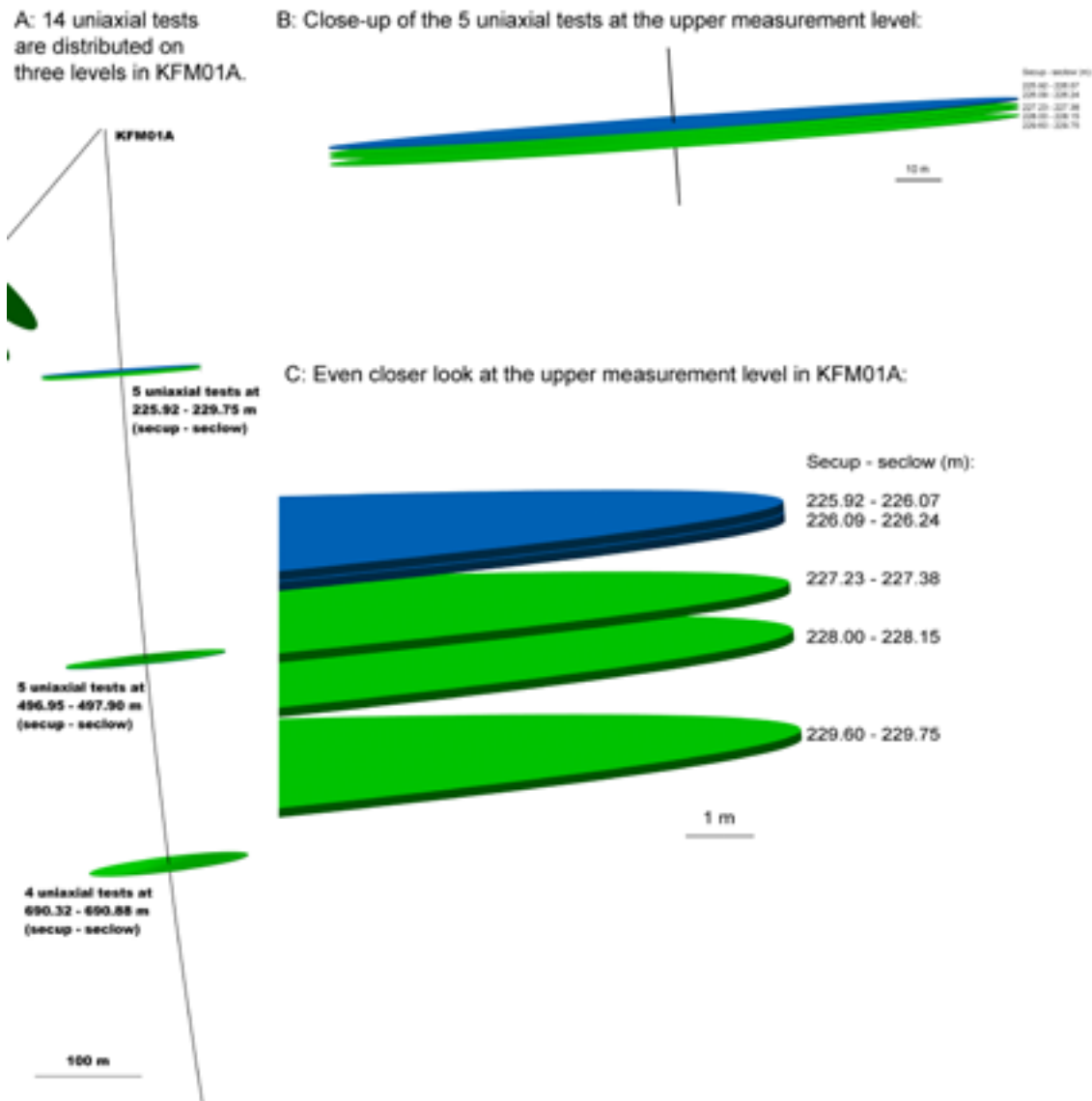


**Figure A8-1.** Example of the distribution of uniaxial measurement tests in KFM01A. The blue cylinders symbolize uniaxial compressive test results in the interval 250–600 MPa, while the green ones symbolize 200–250 MPa. Each uniaxial test is made on a 15 cm long core sample, which is visualized in natural scale.

## A8.2 Uniaxial compressive strength

Uniaxial compressive strength (UCS) is shown in subdivisions of intervals according to the legend in Figure A8-2. Included in the figure is also a legend showing the division of fracture domains and deformation zones along the boreholes. The visualized data is the primary data selection presented in the WellCad-plots in /Olofsson et al. 2007/, hence it does not include data from independent laboratories nor from tests on sealed fractures. Data from KFM01C is presented, but the data was not considered in this report.



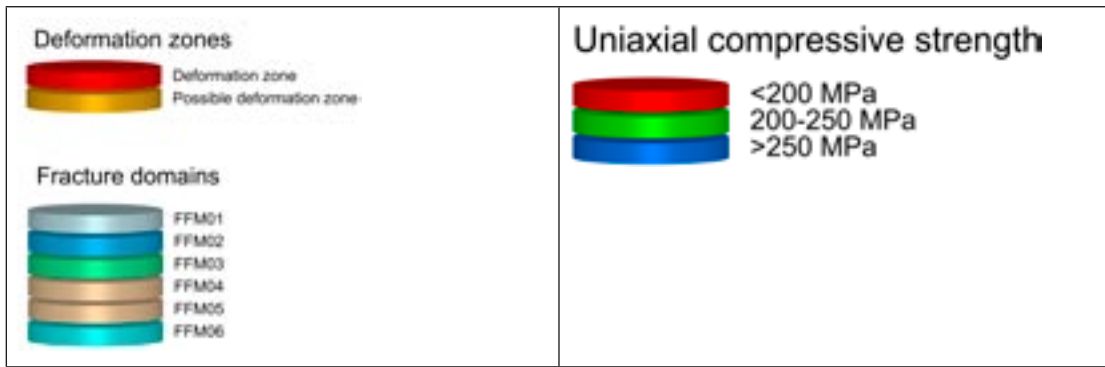


*Figure A8-2. Legend for the division of fracture domains and deformation zones along the boreholes and for uniaxial compressive strength.*

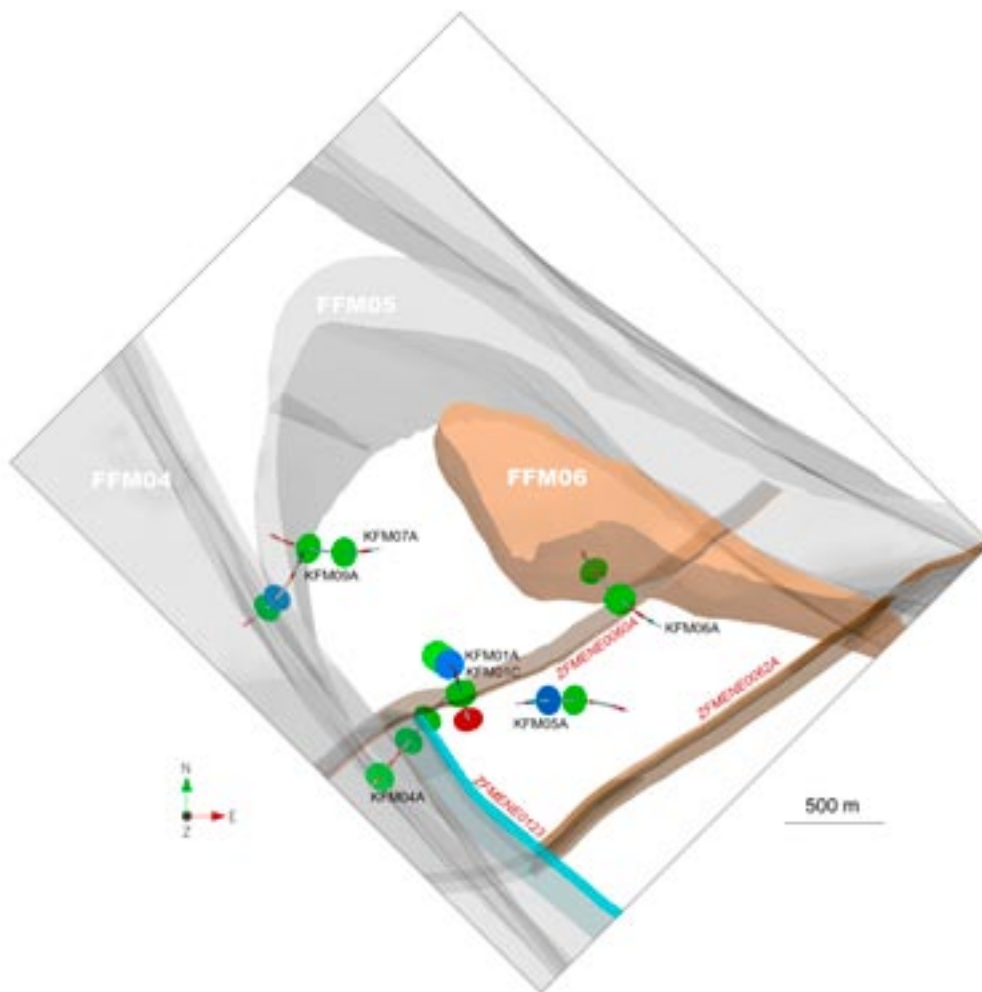


*Figure A8-3. Location and results of sampling for uniaxial compressive tests, viewed from above.*

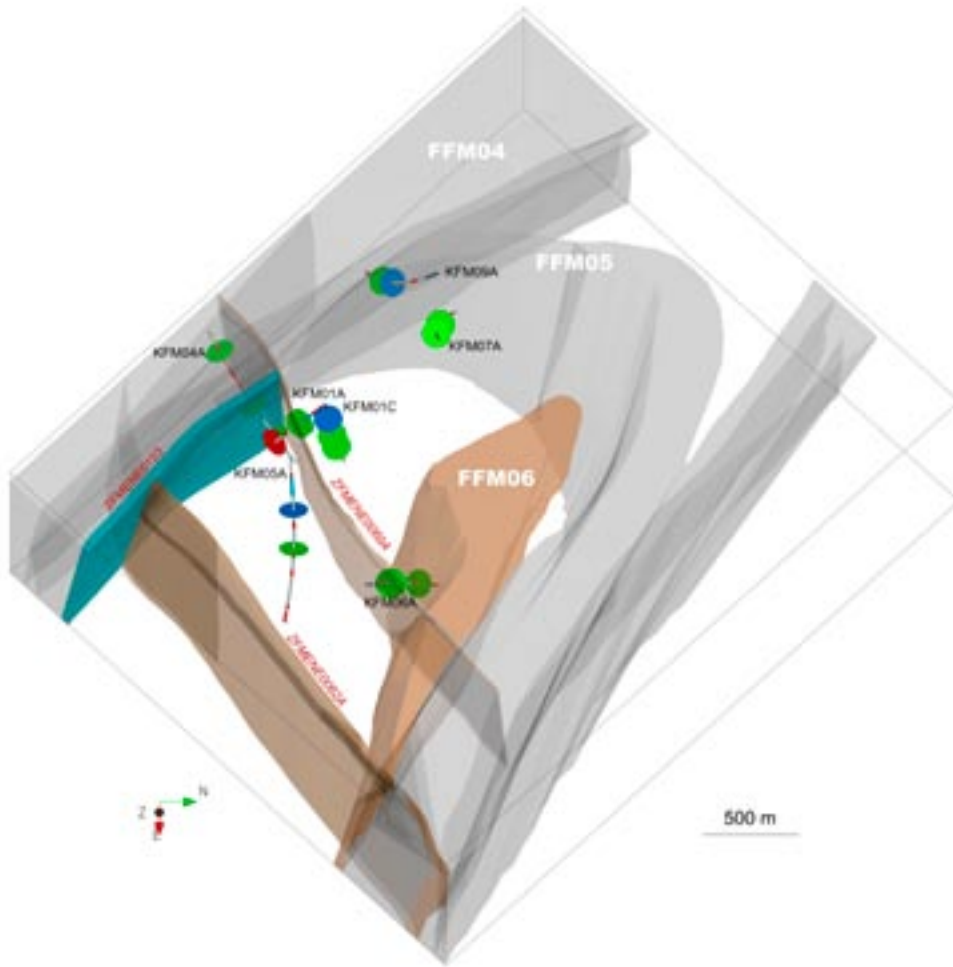


Figure A8-4. Location and results of sampling for uniaxial compressive tests, viewed towards west.

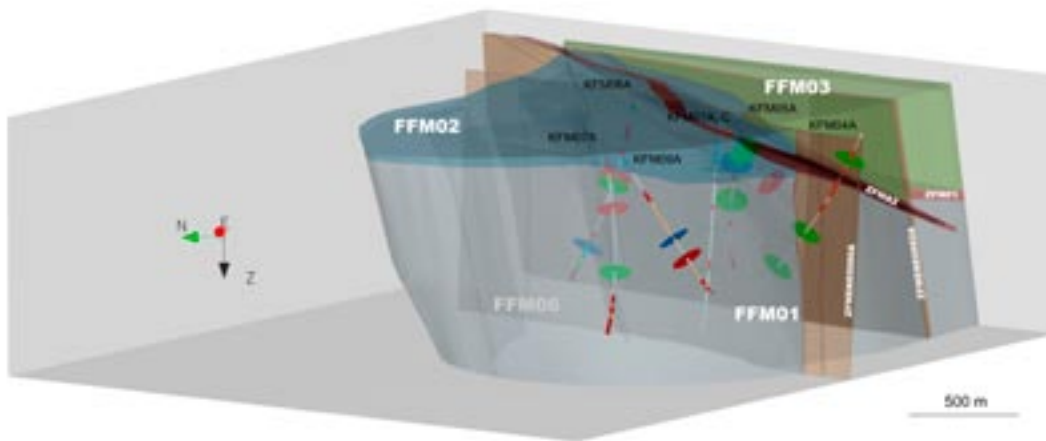
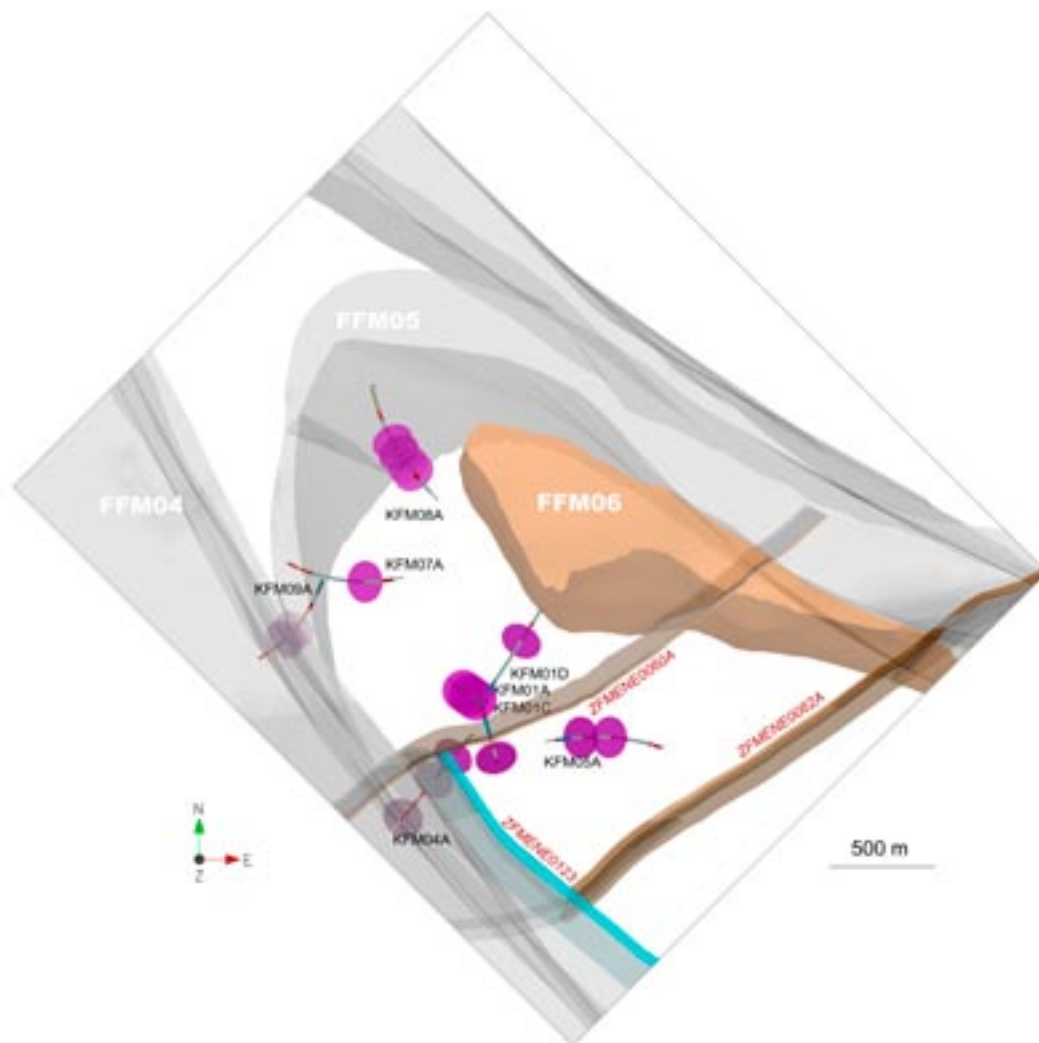


Figure A8-5. Location and results of sampling for uniaxial compressive tests, viewed towards east.

### A8.3 Triaxial compressive strength, sampling position

Source: /Olofsson et al. 2007/, RVS container (Sicada\_07\_207)



*Figure A8-6. Sampling position of triaxial compressive tests, viewed from above.*

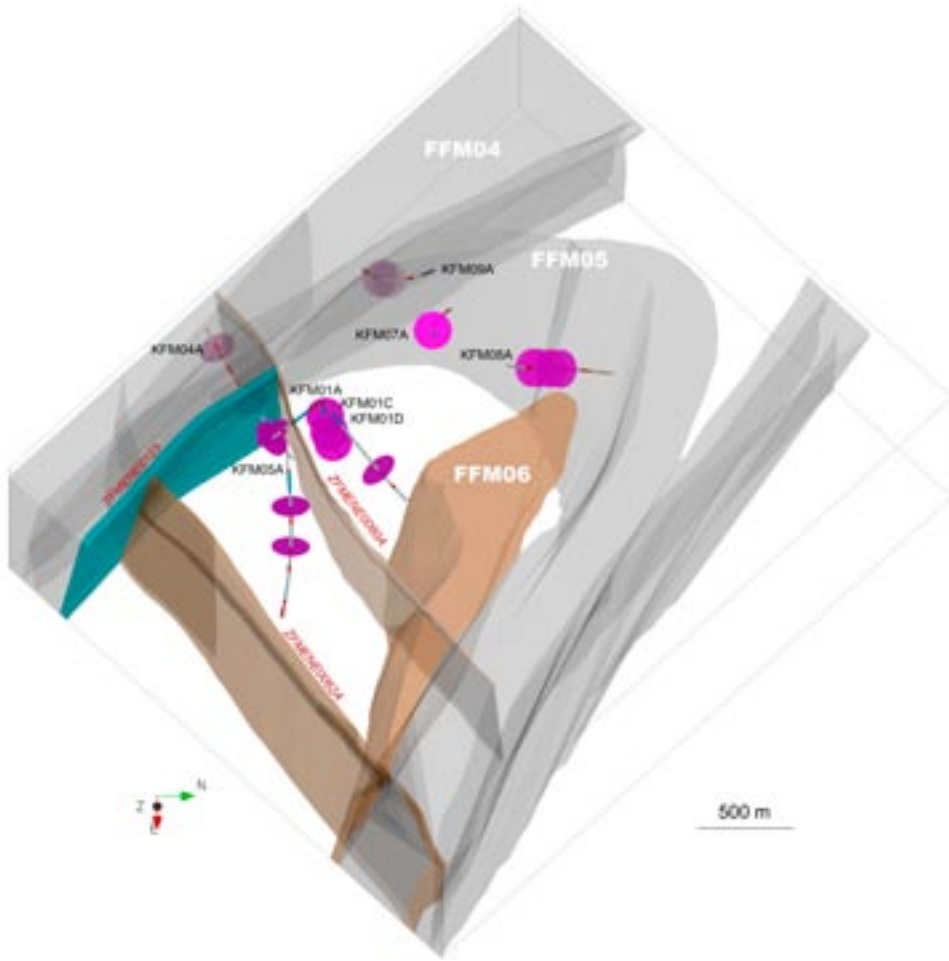


*Figure A8-7. Sampling position of triaxial compressive tests, viewed towards west.*

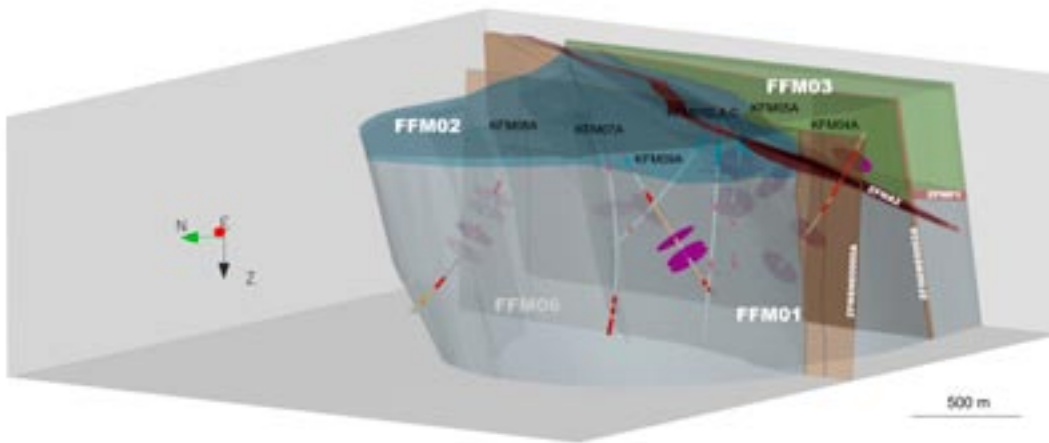


*Figure A8-8. Sampling position of triaxial compressive tests, viewed towards east.*

#### A8.4 Indirect tensile strength (Brazilian test) and direct tensile strength, sampling position

Source data: Indirect tensile tests (Brazilian): /Olofsson et al. 2007/ RVS container (Sicada\_07\_207). Direct tensile tests: Sicada\_07\_175

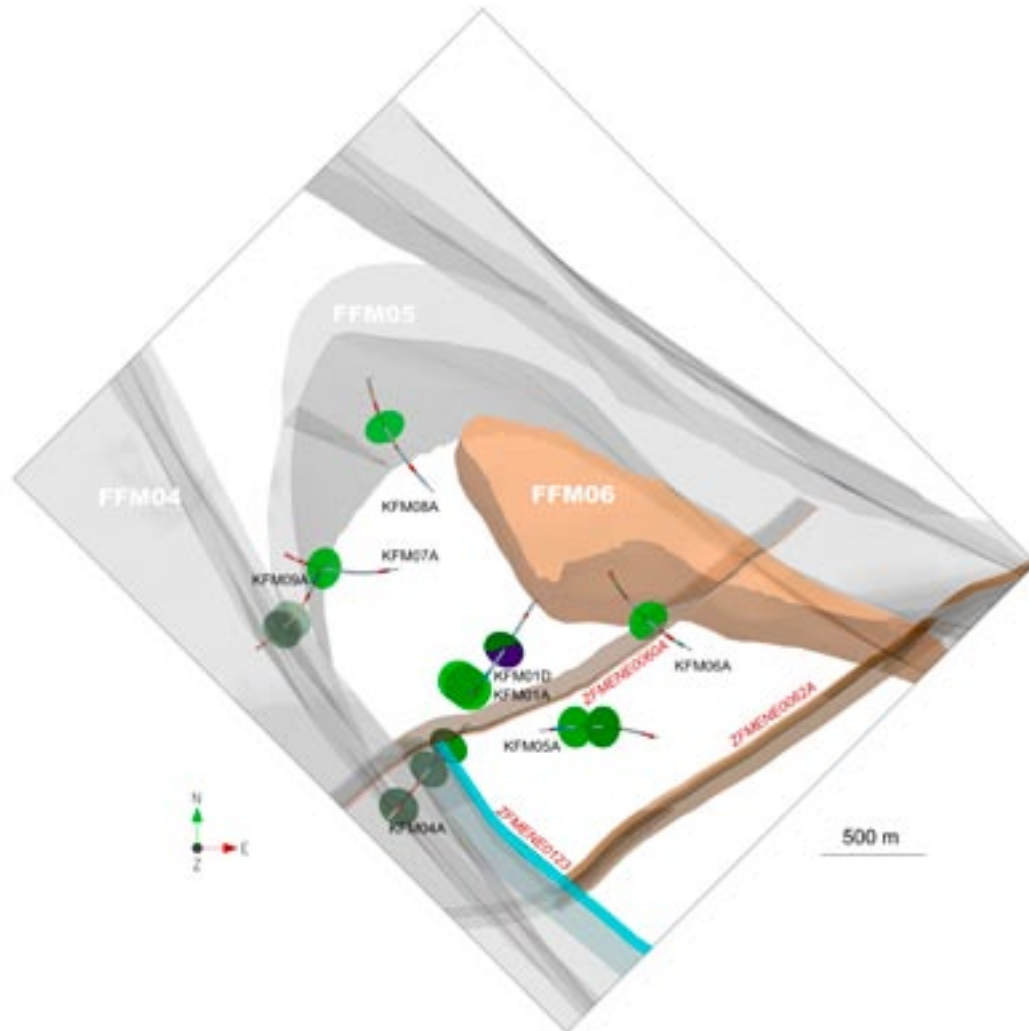


*Figure A8-9. Sampling position of indirect (green) and direct (blue) tensile tests, viewed from above.*

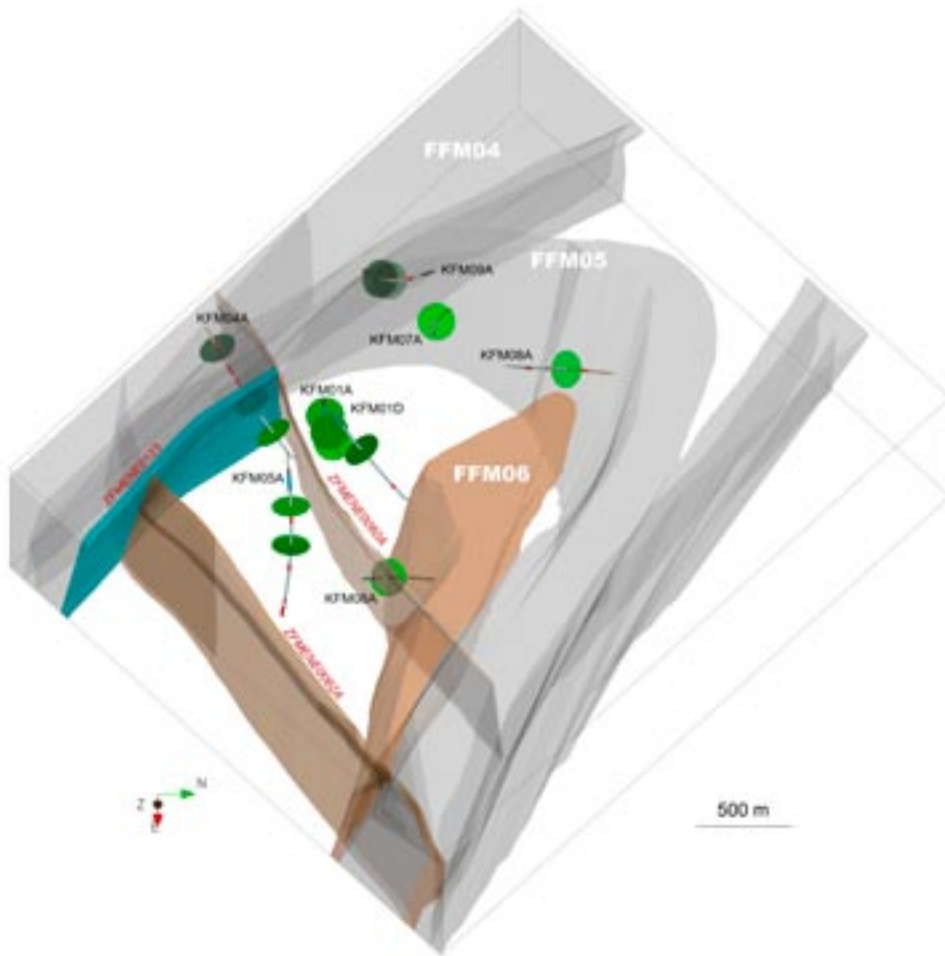


*Figure A8-10. Sampling position of indirect (green) and direct (blue) tensile tests, viewed towards west.*

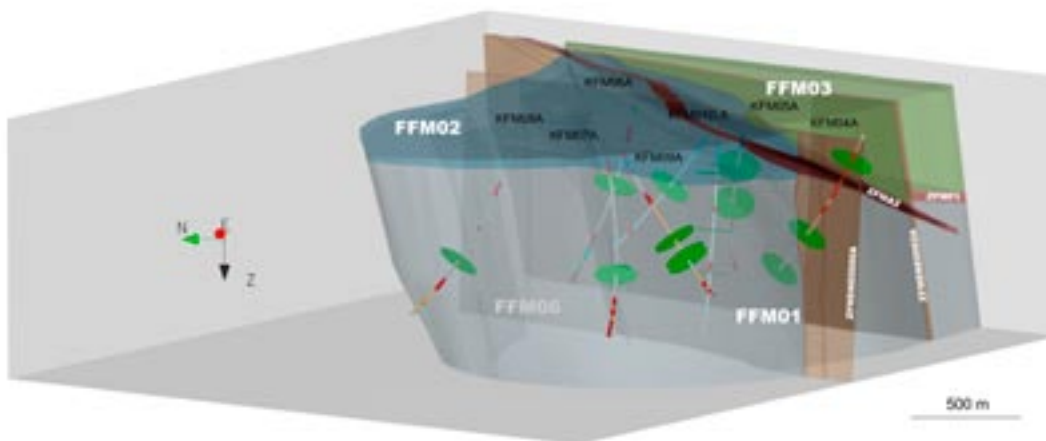


*Figure A8-11. Sampling position of indirect (green) and direct (blue) tensile tests, viewed towards east. The direct tests are not visible in this view since the samples are obscured by the indirect test samples.*

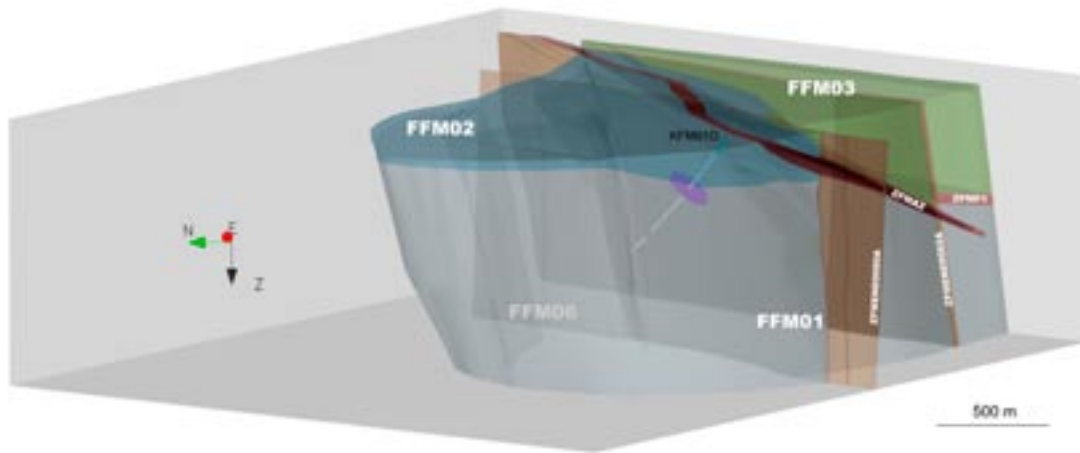


*Figure A8-12. Sampling position of direct (blue) tensile tests, viewed towards east.*

### **A8.5 Direct shear tests on open fractures, sampling position**

Source: /Olofsson et al. 2007/ RVS container (Sicada\_07\_207)

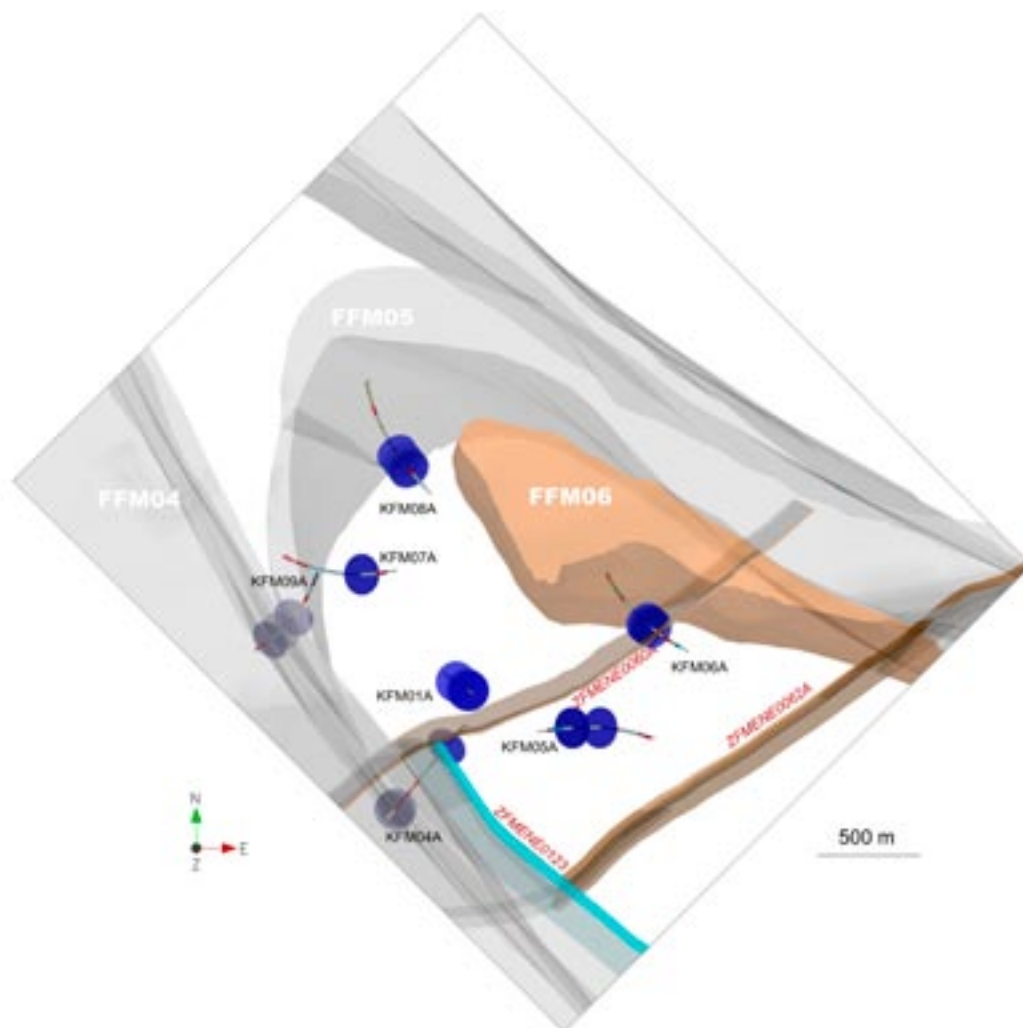


*Figure A8-13. Sampling position of direct shear tests on open fractures, viewed from above.*

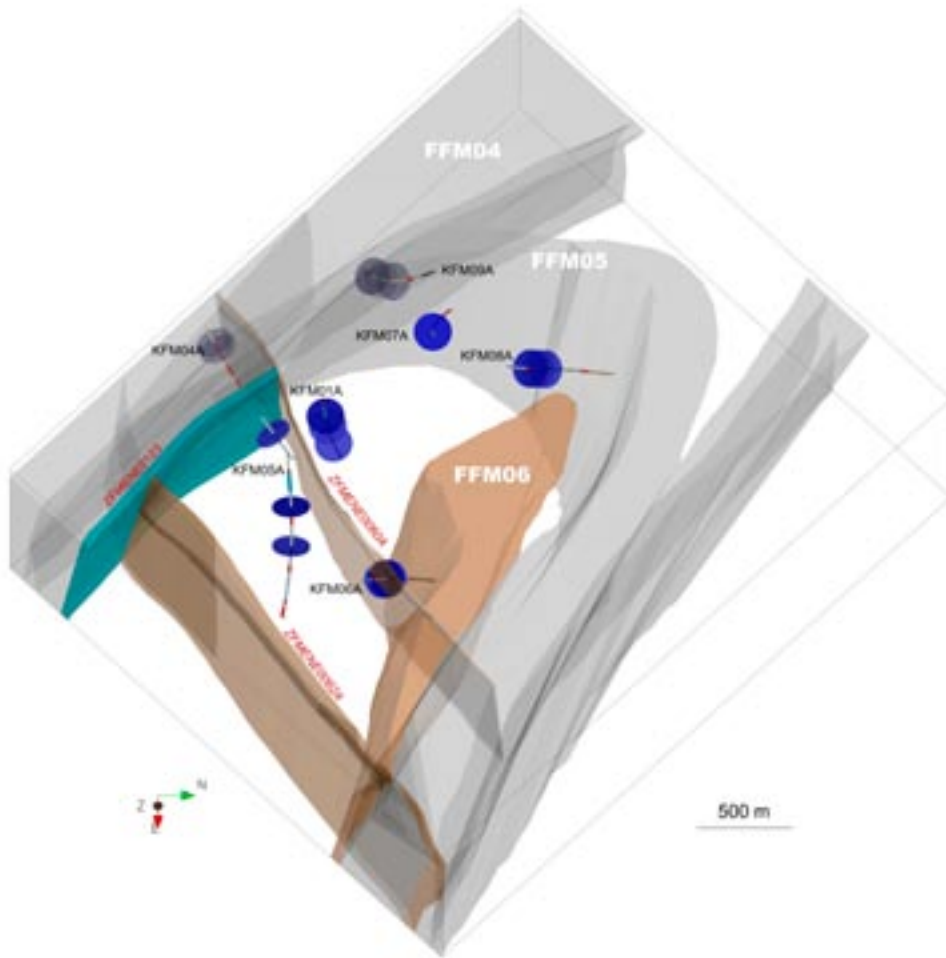


Figure A8-14. Sampling position of direct shear tests on open fractures, viewed towards west.

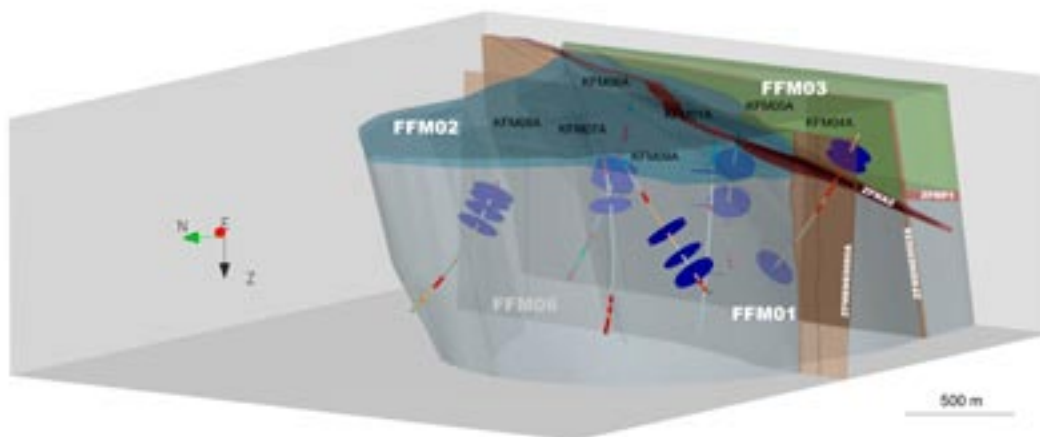


Figure A8-15. Sampling position of direct shear tests on open fractures, viewed towards east.

## A8.6 Rock mass characterization

Source: /Olofsson et al. 2007/ RVS container (Sicada\_07\_207), appended data compilation, and working material for 5 m intervals of Q and RMR in KFM06A, KFM06C and KFM08C.



RQD (rock quality designation) is used for measuring the fracture frequency along a core length, here 1 m. It is also one of the parameters defining RMR (rock mass rating) and Q (tunnelling quality index).

Q and RMR are calculated on cores at intervals of 5 m for all boreholes characterized. The mean RMR and Q values are then evaluated for the rock units and deformation zones identified by single-hole interpretation, which are available in Sicada. This appendix presents the RMR and Q results from both single-hole interpretation and the 5 m intervals. For RMR the mean value for each 5 m is used. As Q follows a logarithmic scale, the mode (most frequent) value is presented. In /Olofsson et al. 2007/, the Q mean value was presented.

The RQD, RMR and Q data are presented in the appended CD in /Olofsson et al. 2007/, with the exception of the RMR and Q for KFM06A, -06C and -08C as these boreholes were not evaluated at the time of preparing the report.

### A8.6.1 RQD – Rock quality designation

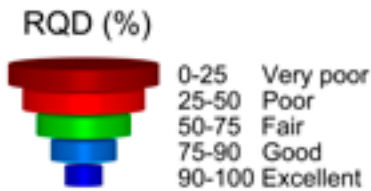


Figure A8-16. Legend for Rock quality designation.

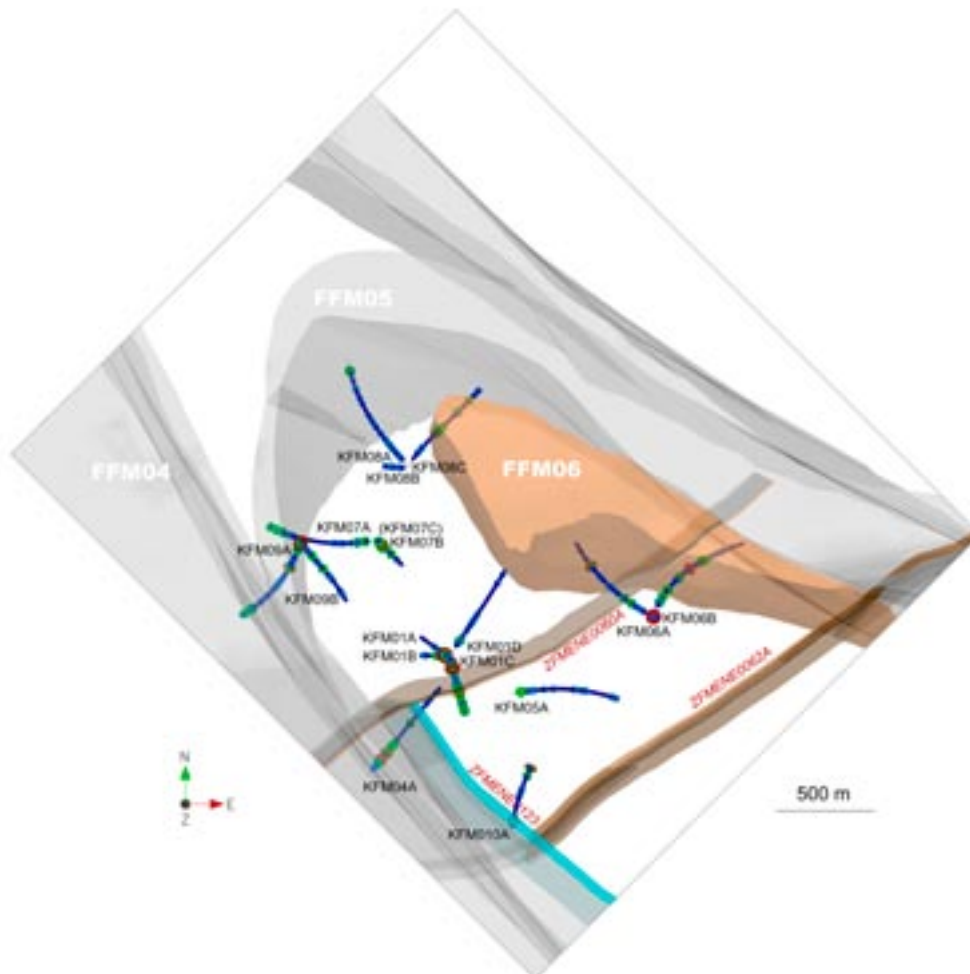


Figure A8-17. RQD along the boreholes, viewed from above.

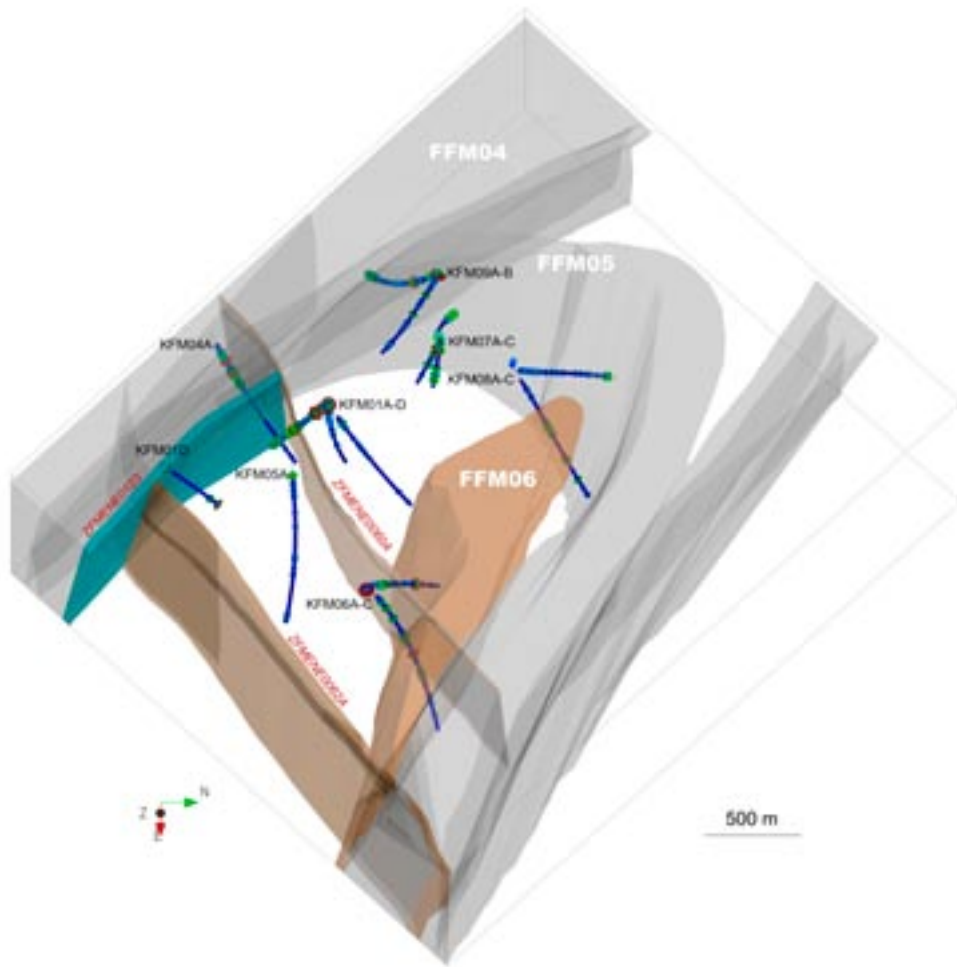


Figure A8-18. RQD along the boreholes, viewed towards west.

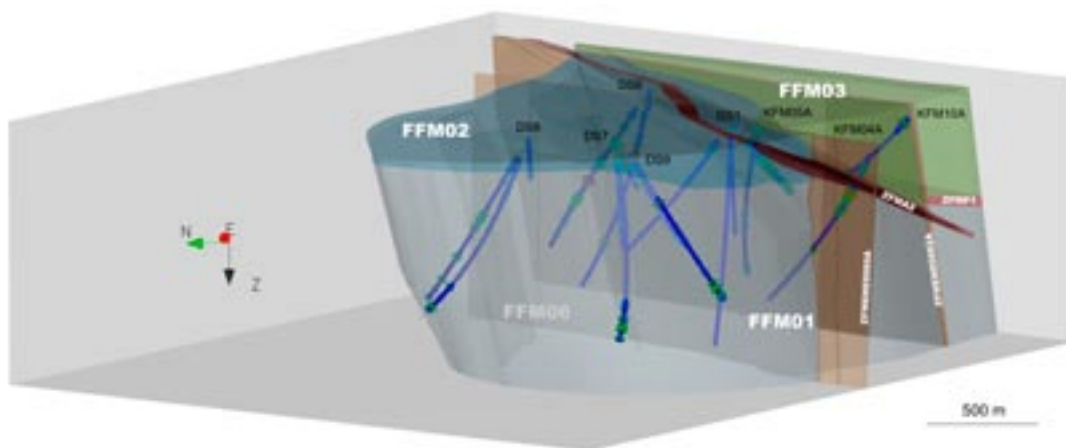
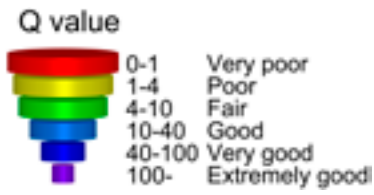


Figure A8-19. RQD along the boreholes, viewed towards east.

**A8.6.2 Q – Rock mass quality, by SHI and 5 metre interval**



*Figure A8-20. Legend for the Q-system.*

**Q – 5 metre interval**

The mode Q value (most frequent) is presented for each 5 metre interval.

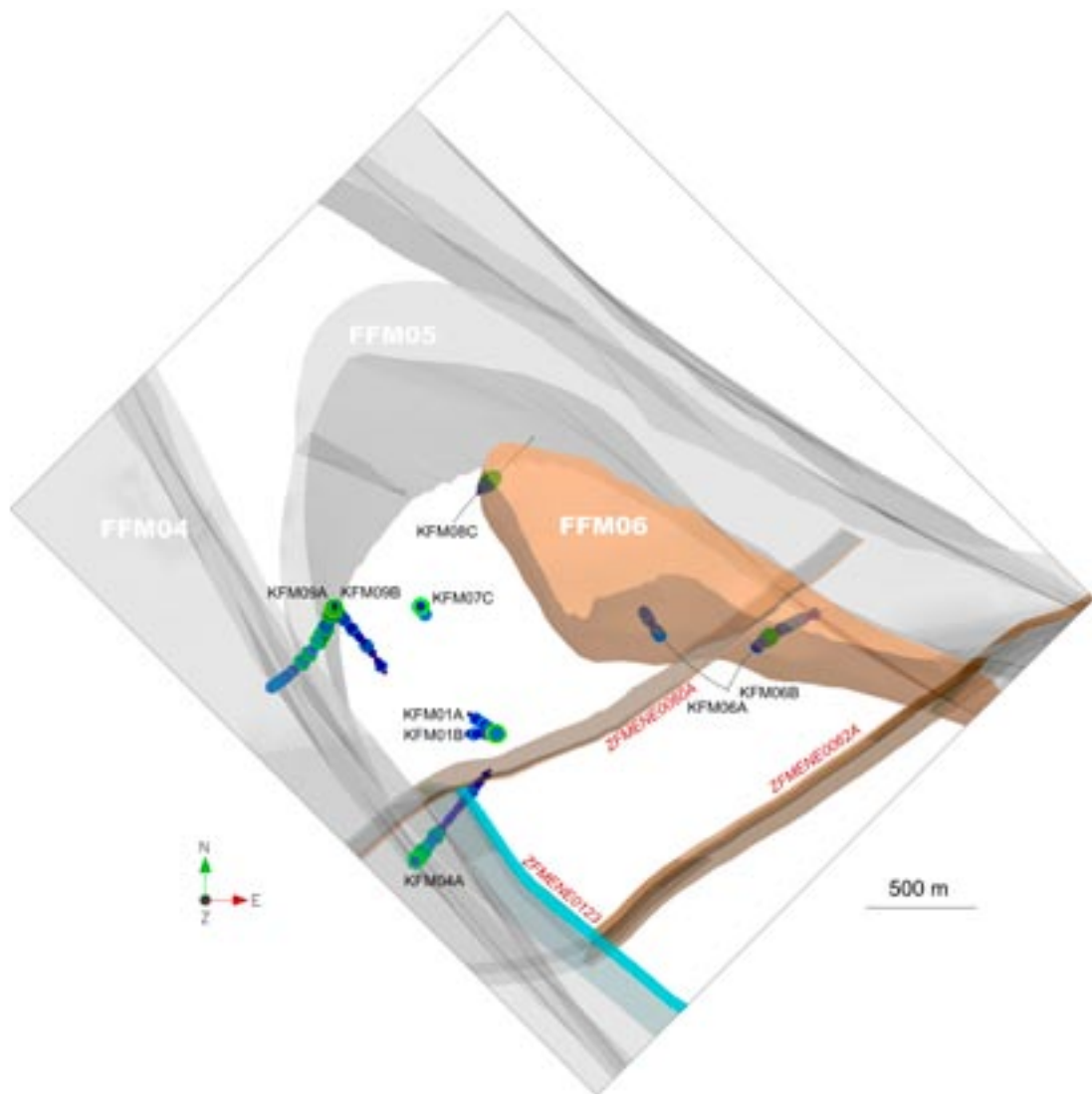


*Figure A8-21. Q value (mode) for each 5 m interval, viewed from above. In KFM06A, -06C and -08C, only sections in FFM06 were characterised.*

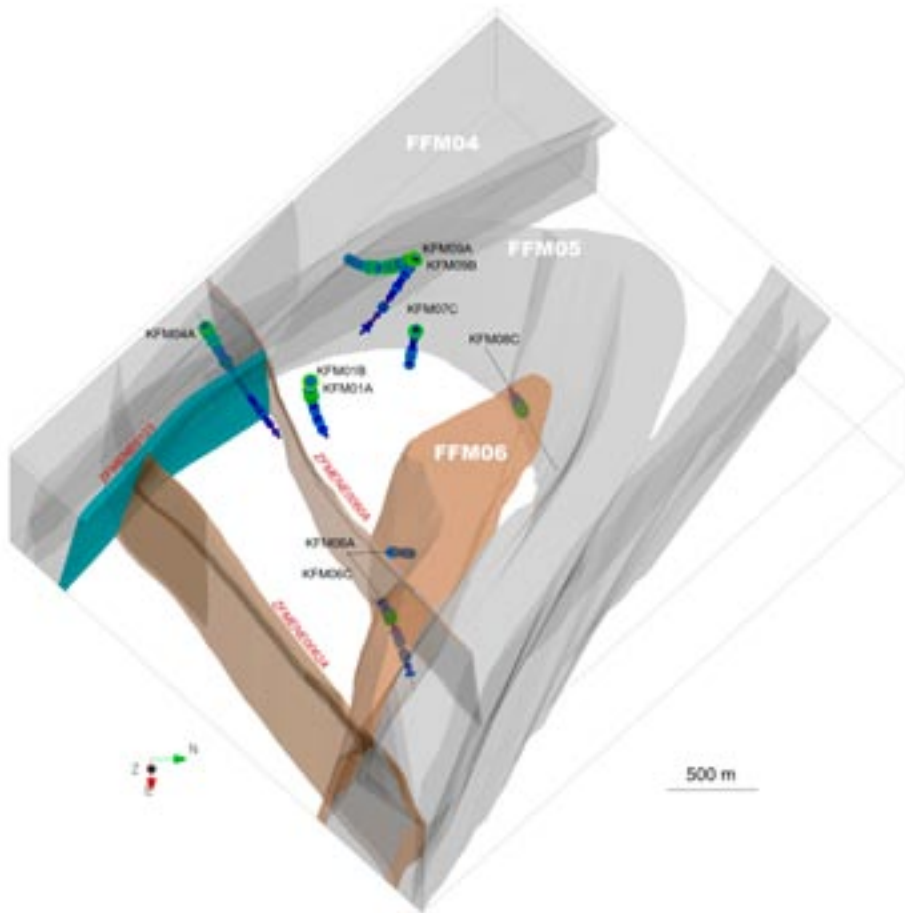


*Figure A8-22. Q value (mode) for each 5 m interval, viewed towards west. In KFM06A, -06C and -08C, only sections in FFM06 were characterised.*

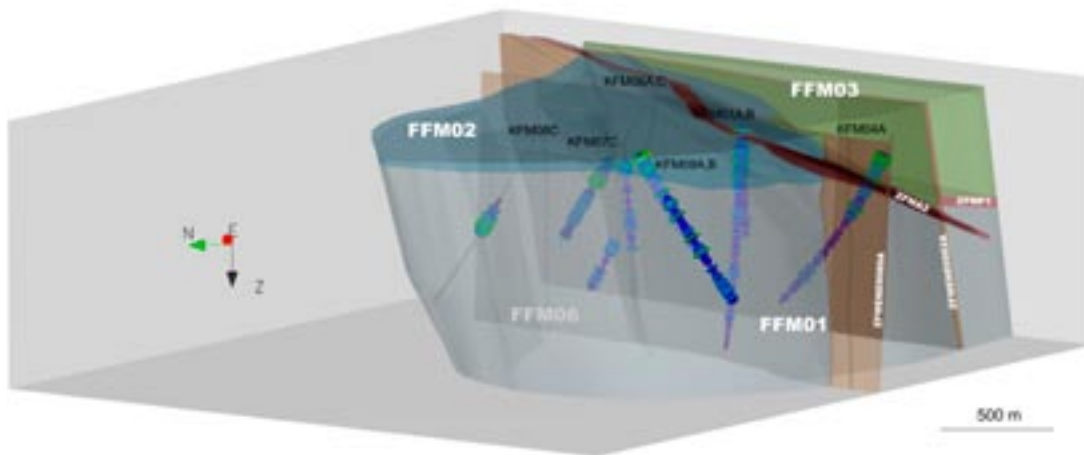


*Figure A8-23. Q value (mode) for each 5 m interval, viewed towards east. In KFM06A, -06C and -08C, only sections in FFM06 were characterised.*

**Q – Single hole interpretation**

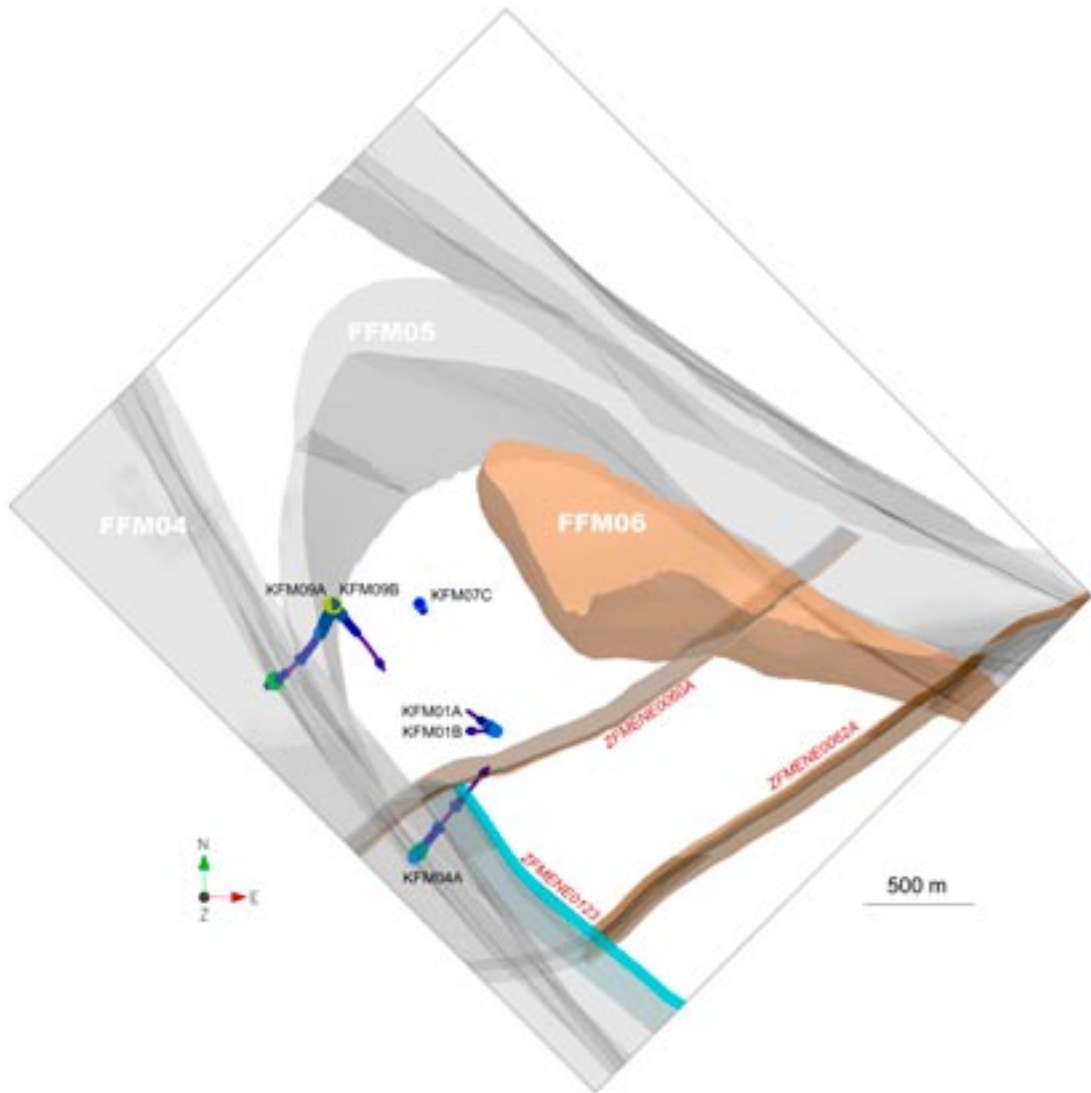


**Figure A8-24.** *Q value (mode) for rock domains and deformation zones identified by the single-hole interpretation, viewed from above.*

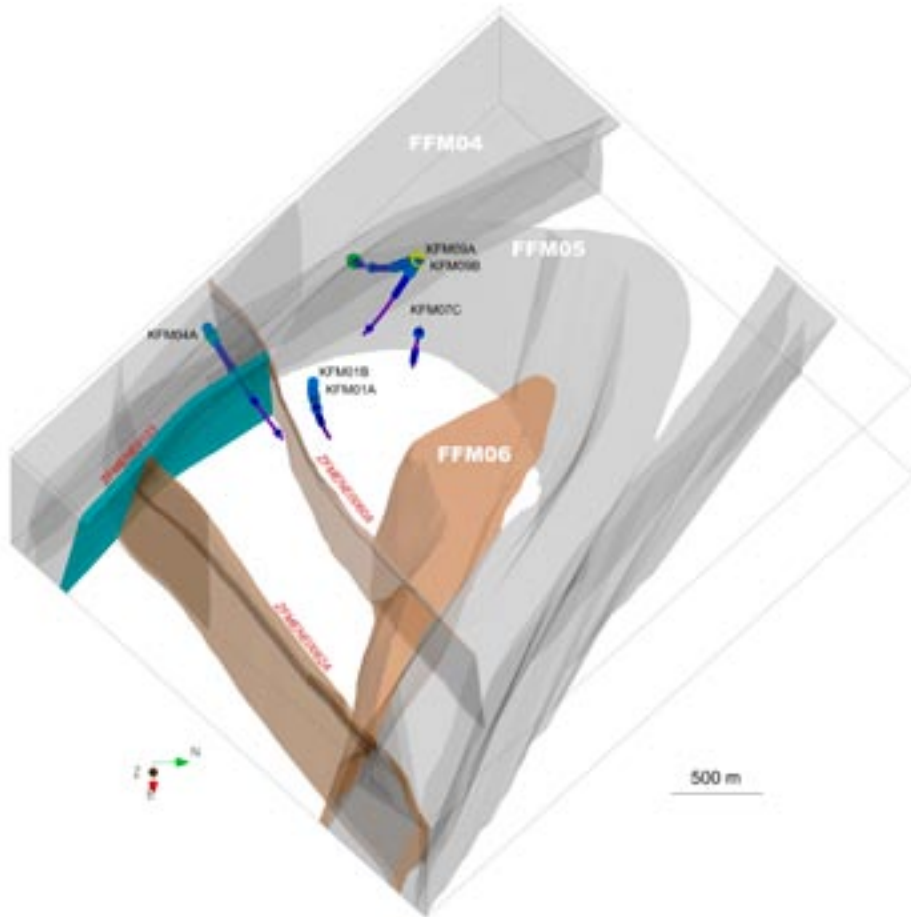


*Figure A8-25. Q value (mode) for rock domains and deformation zones identified by the single-hole interpretation, viewed towards west.*

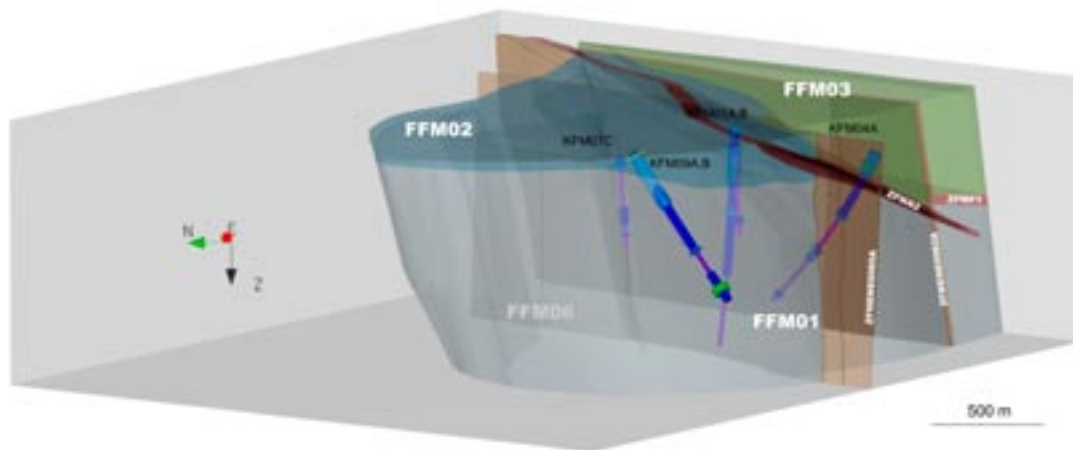


*Figure A8-26. Q value (mode) for rock domains and deformation zones identified by the single-hole interpretation, viewed towards east.*

### A8.6.3 RMR – Rock mass rating, SHI and 5 m intervals

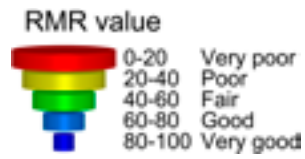


Figure A8-27. Legend for RMR system.

#### RMR – 5 metre interval

The mean RMR value is shown for each 5 metre interval.

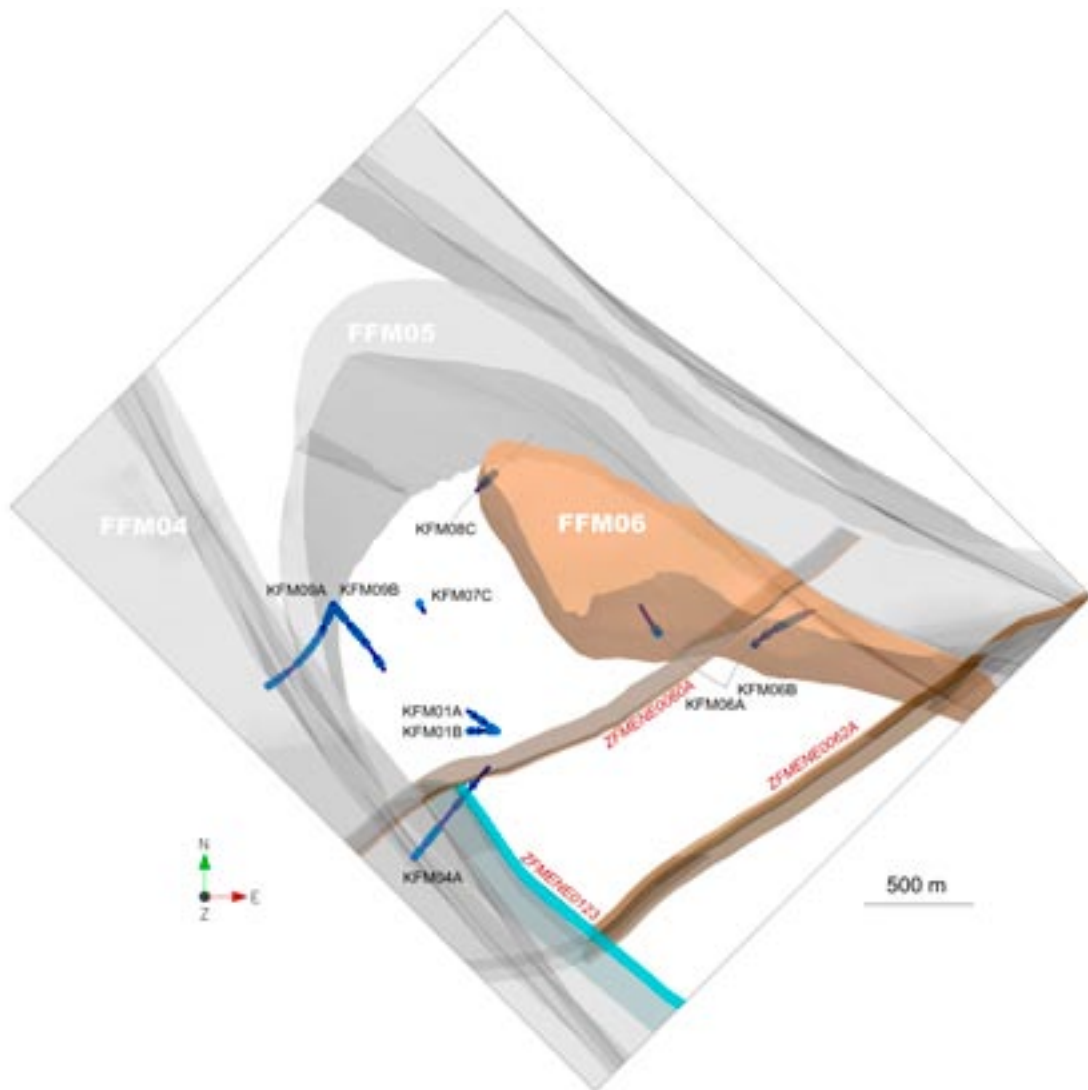
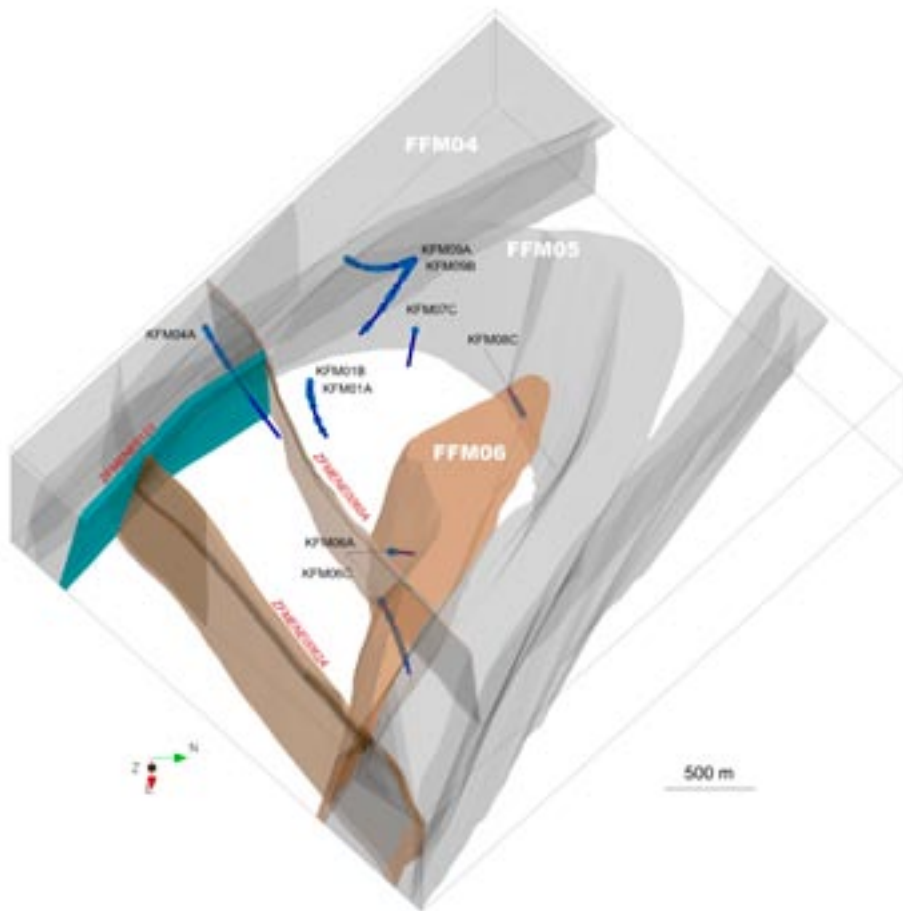
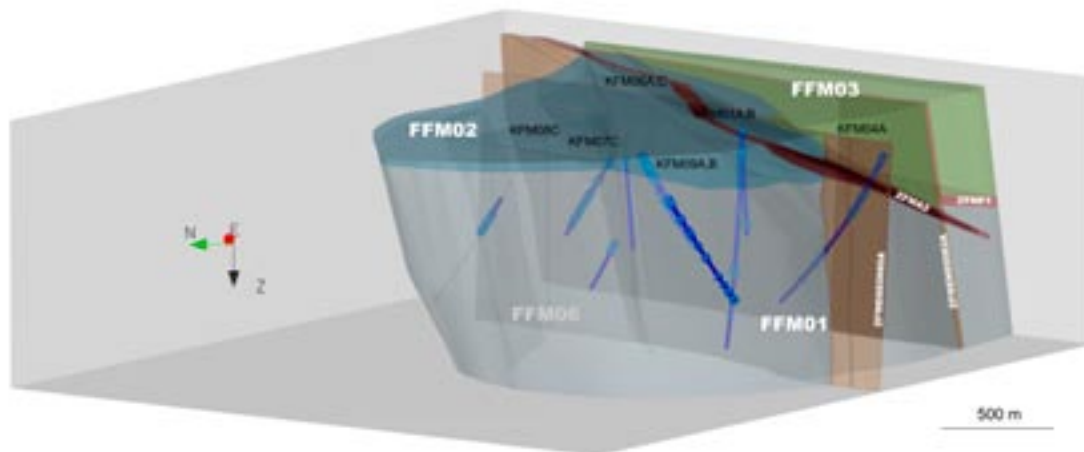


Figure A8-28. RMR value for each 5 m interval, viewed from above. In KFM06A, -06C and -08C, only sections in FFM06 were characterised.



*Figure A8-29. RMR value for each 5 m interval, viewed towards west. In KFM06A, -06C and -08C, only sections in FFM06 were characterised.*



*Figure A8-30. RMR value for each 5 m interval, viewed towards east. In KFM06A, -06C and -08C, only sections in FFM06 were characterised.*



**RMR – Single hole interpretation**

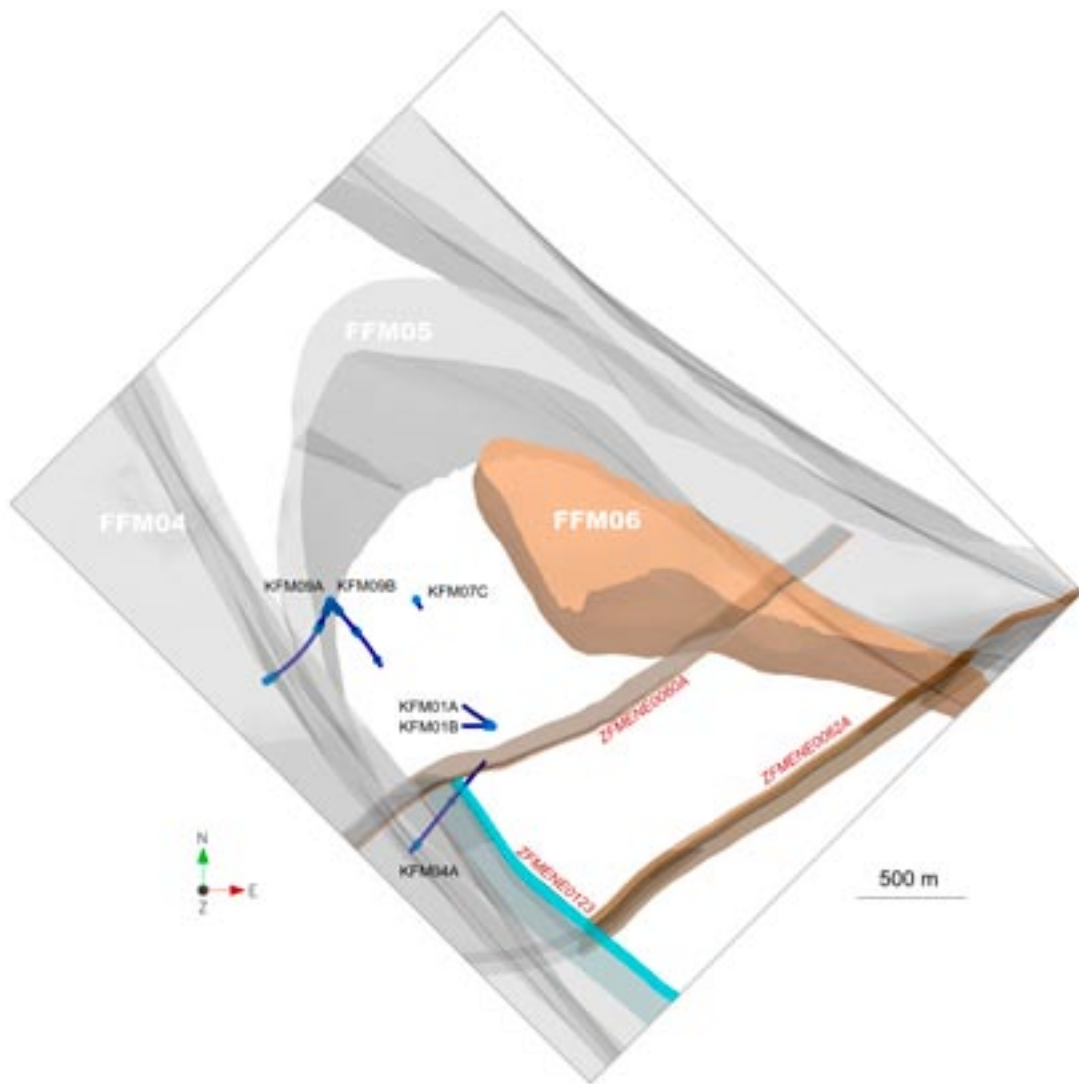


**Figure A8-31.** RMR value for rock domains and deformation zones identified by the single-hole interpretation, viewed from above.

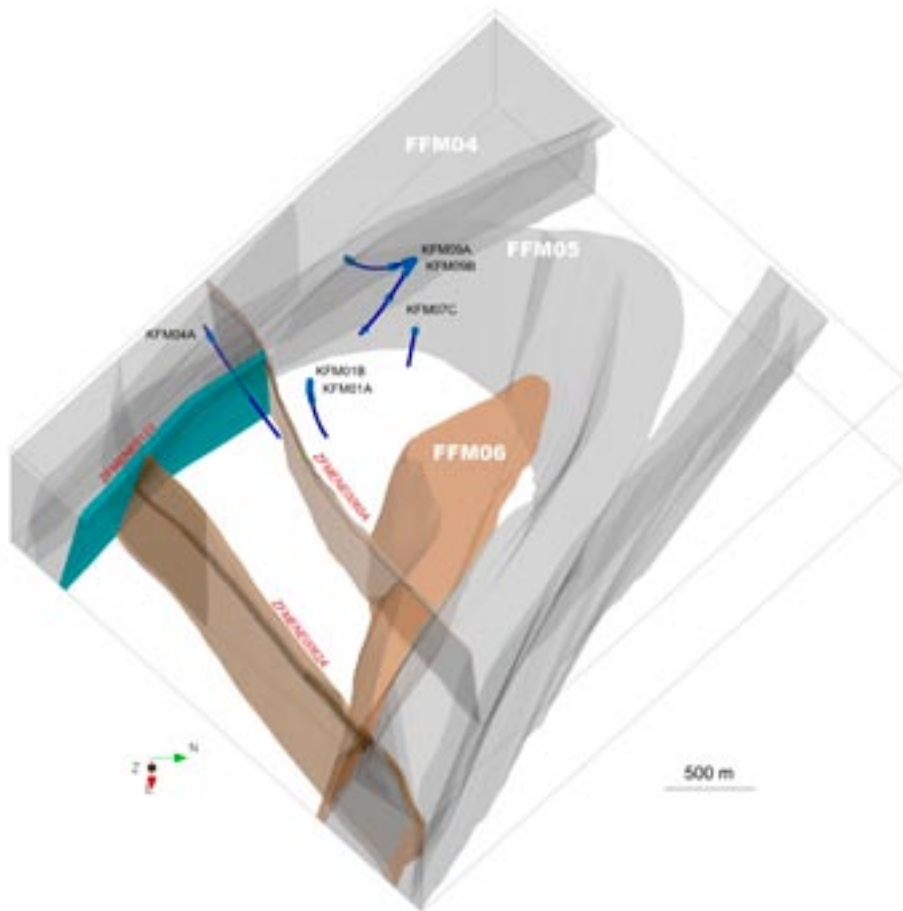


**Figure A8-32.** RMR value for rock domains and deformation zones identified by the single-hole interpretation, viewed towards west.

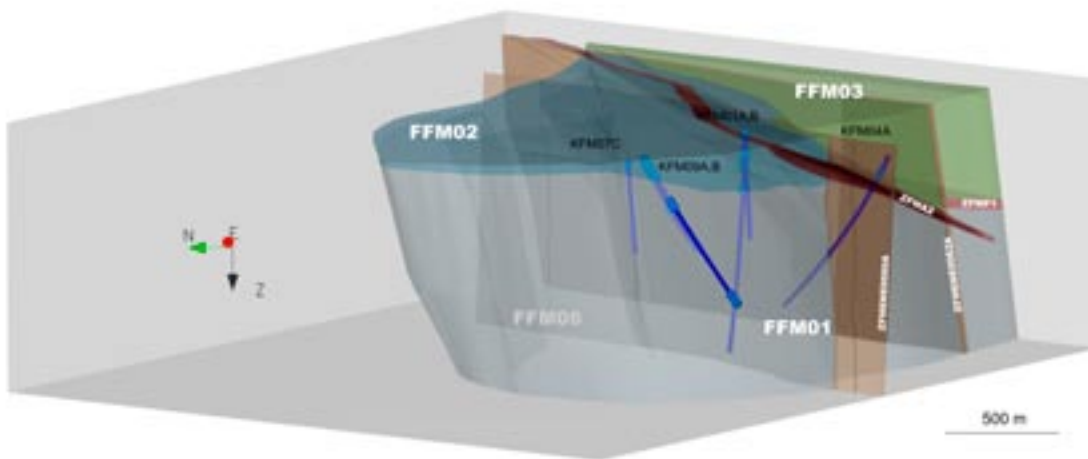


**Figure A8-33.** RMR value for rock domains and deformation zones identified by the single-hole interpretation, viewed towards east.

## A8.7 Rock stress measurements

Source: Sicada\_07-354 (2007-10-01) and Sicada\_08-029 (2008-02-13)

The positions subjected to rock stress measurements are visualized by blue discs where overcoring was conducted and by green and red discs where the hydraulic fracturing methods were used.

### A8.7.1 Overcoring

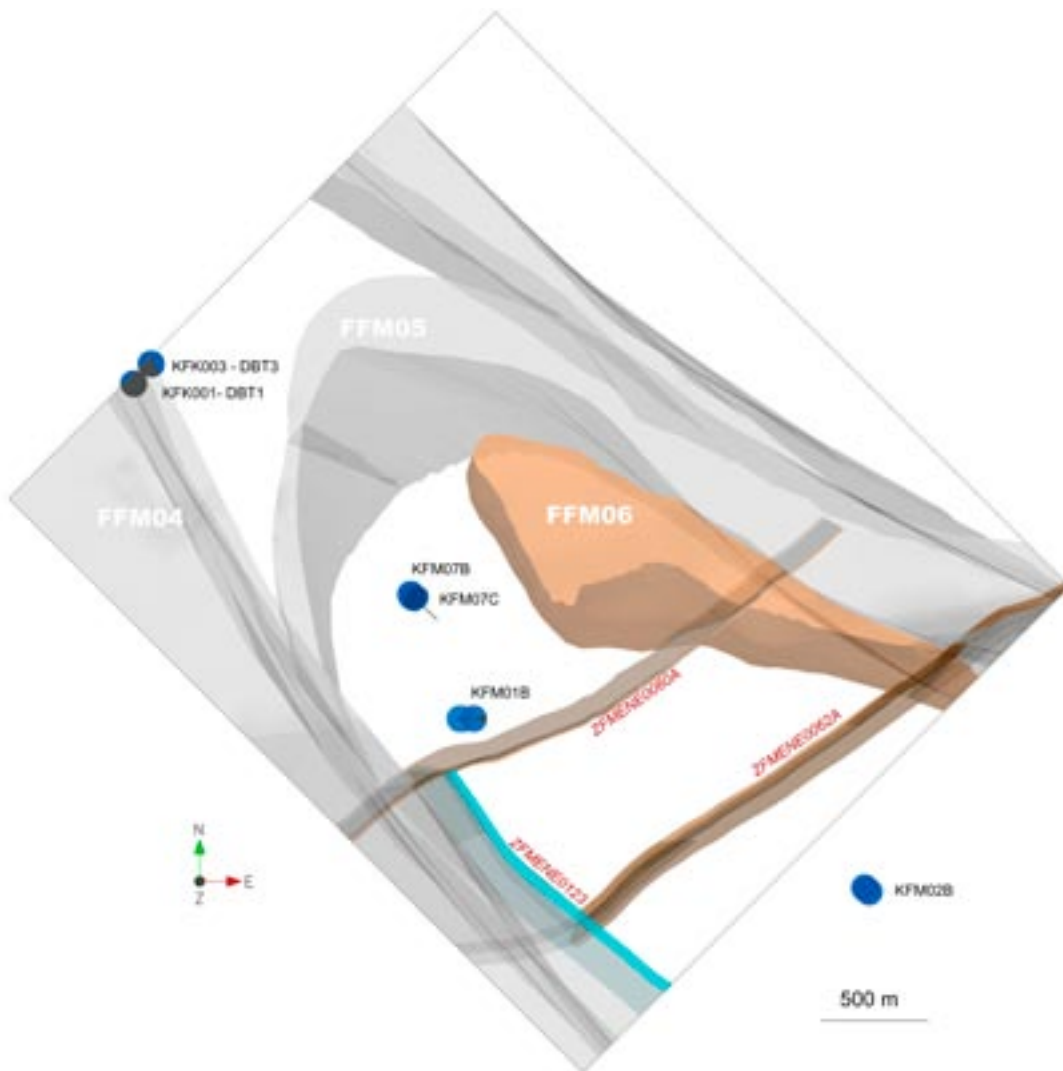


**Figure A8-34.** Three-dimensional image of the boreholes and the positions (blue discs) subjected to rock stress measurements by the overcoring method, viewed from above.

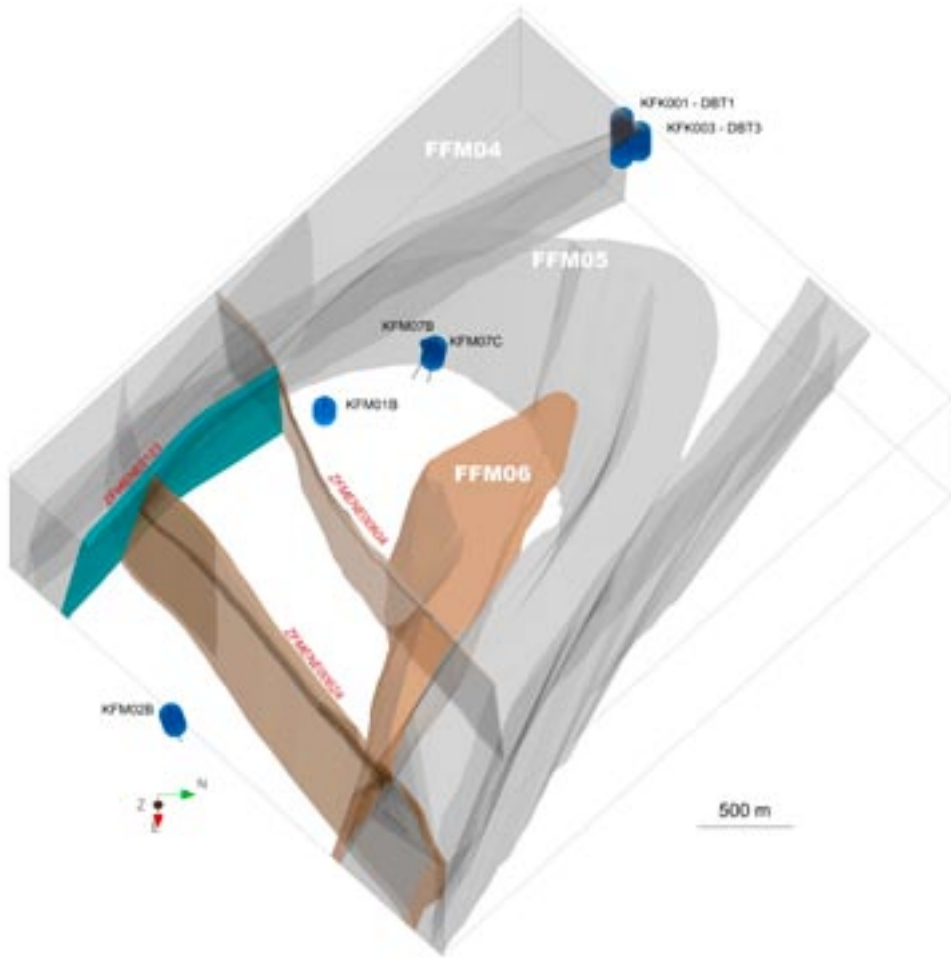


*Figure A8-35. Three-dimensional image of the boreholes and the positions (blue discs) subjected to rock stress measurements by the overcoring method, viewed towards west.*

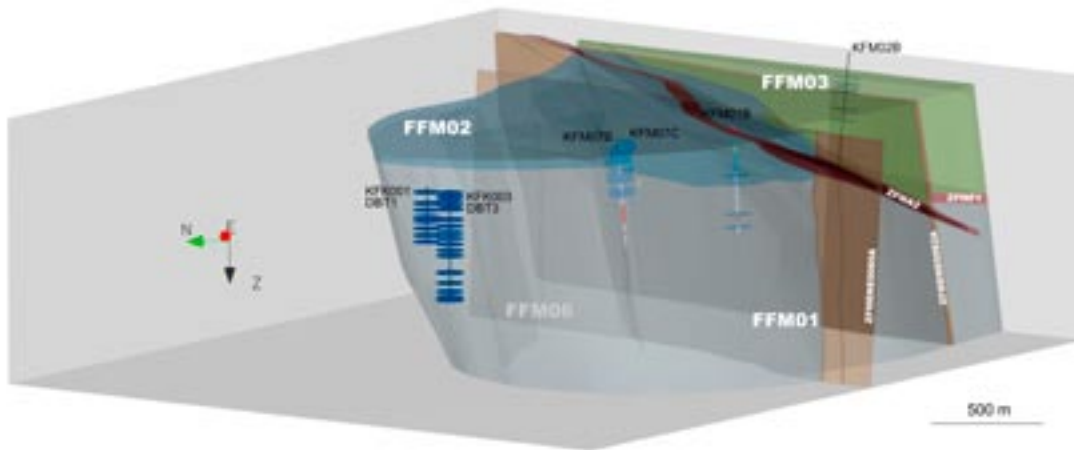


*Figure A8-36. Three-dimensional image of the boreholes and the positions (blue discs) subjected to rock stress measurements by the overcoring method, viewed towards east.*

### A8.7.2 Hydraulic fracturing

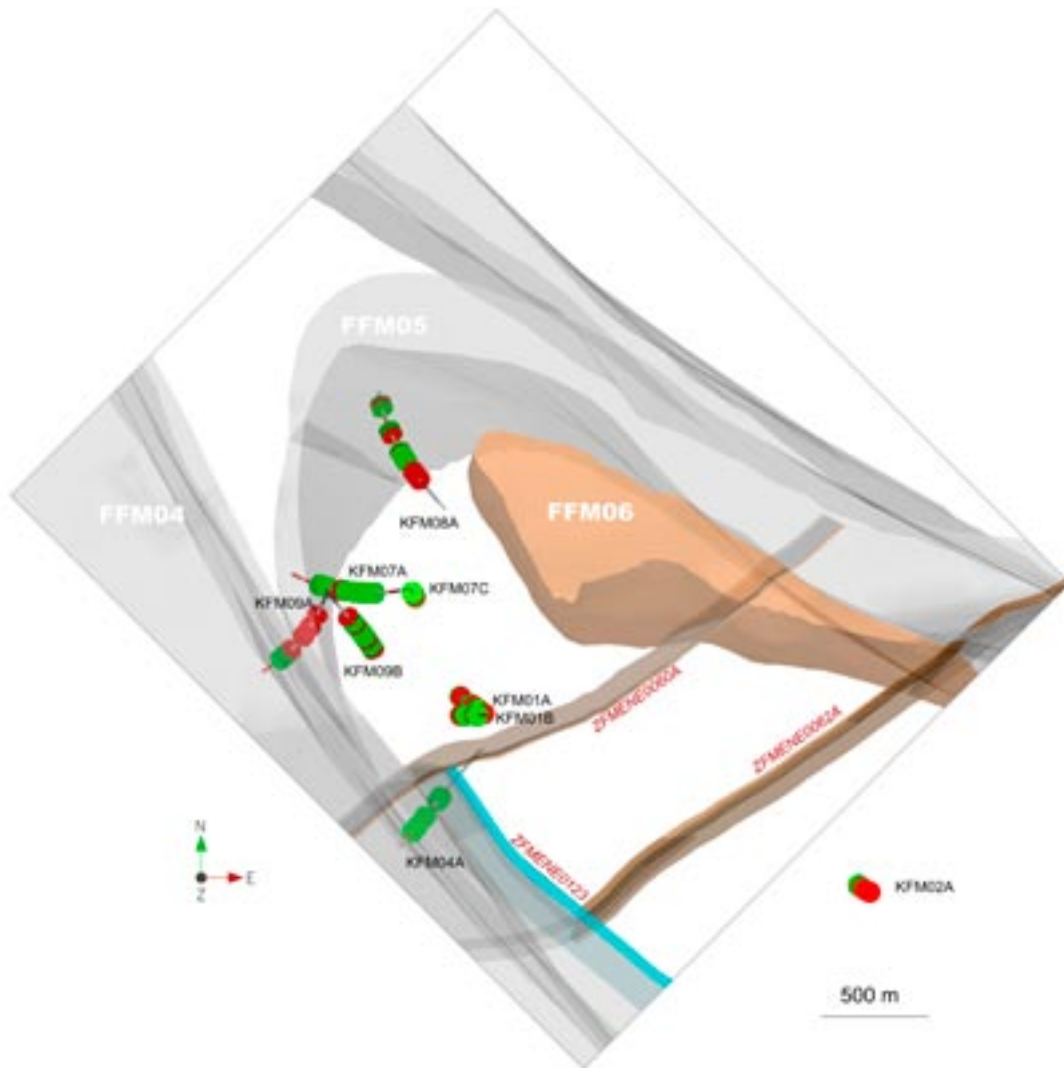


*Figure A8-37. Three-dimensional image of the boreholes and the positions (green and red discs) subjected to rock stress measurements by the hydraulic fracturing method, viewed from above. The green discs indicate successful attempts and the red ones failed attempts.*

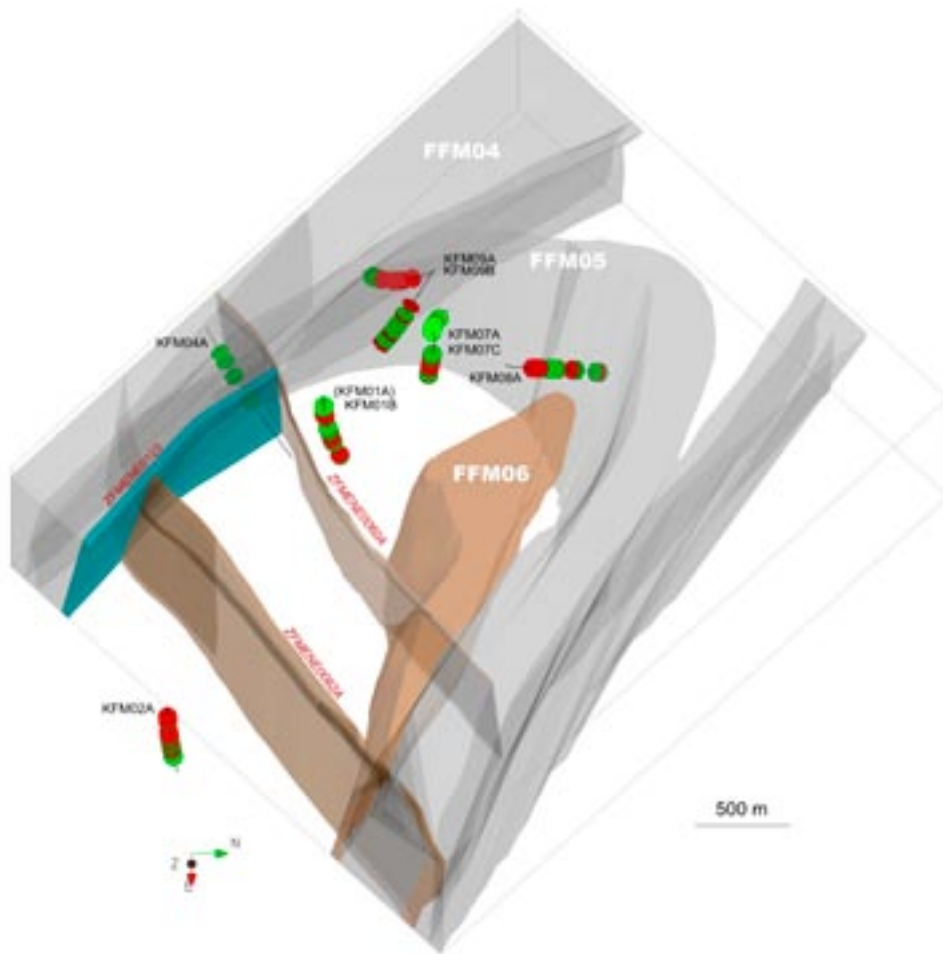


**Figure A8-38.** Three-dimensional image of the boreholes and the positions (green and red discs) subjected to rock stress measurements by the hydraulic fracturing method, viewed towards west. The green discs indicate successful attempts and the red ones failed attempts.

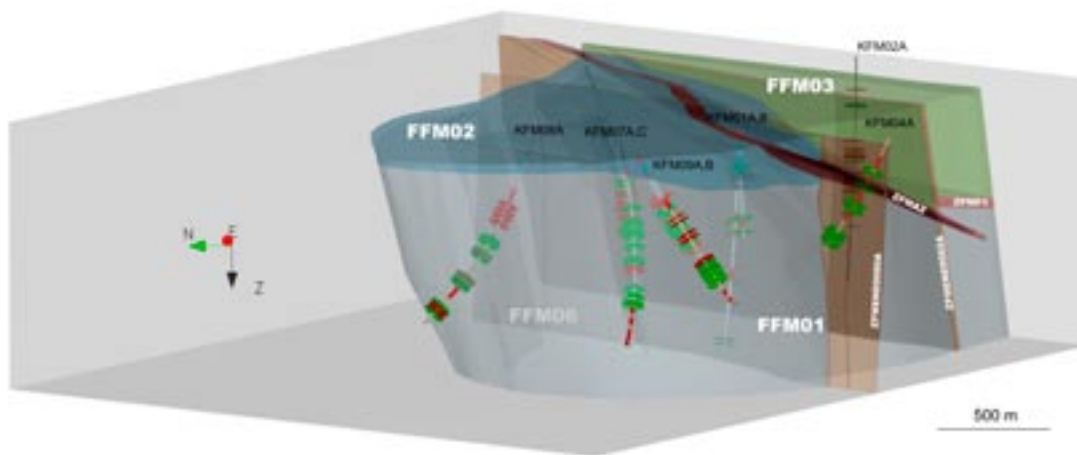


**Figure A8-39.** Three-dimensional image of the boreholes and the positions (green and red discs) subjected to rock stress measurements by the hydraulic fracturing method, viewed towards east. The green discs indicate successful attempts and the red ones failed attempts.

## Rock mechanics symbols

Rock mechanics symbols utilised in the report are listed here.

### Roman letters

$c$	Intact rock cohesion, (MPa)
$c_m$	Rock mass cohesion
$c_p$	Peak cohesion
$c_r$	Residual cohesion
$c_p^{MC}$	Peak cohesion related to Mohr-Coulomb model
$c_r^{MC}$	Residual cohesion related to Mohr-Coulomb model
$E$	Intact rock Young's modulus, (GPa)
$E_m$	Rock mass Young's modulus
$g$	Gravitation ( $\text{kg/s}^2$ )
$G$	Intact rock shear modulus, (GPa)
$G_d$	Dynamic shear modulus
$G_m$	Rock mass shear modulus
$GSI$	Geological Strength Index. Pre-1990 $GSI=RMR_{76}$ , Post-1990 $GSI=RMR_{89-5}$
$JCS$	Joint Compressive Strength, (MPa)
$JCS_{100}$	Joint Compressive Strength of a 100 mm fracture length
$JRC$	Joint Roughness Coefficient
$JRC_{100}$	Joint Roughness Coefficient of a 100 mm fracture length
$m$	Hoek-Brown constant
$m_i$	Hoek-Brown constant for intact rock
$K$	Intact rock bulk modulus, (GPa)
$K_m$	Rock mass bulk modulus
$K_N$	Secant normal stiffness, (MPa/mm)
$K_{NF}$	True normal stiffness
$K_{NM}$	Measured normal stiffness
$K_{NT}$	Holder and grout normal stiffness
$K_S$	Secant shear stiffness, (MPa/mm)
$K_{S0.5, 5, 20}$	Secant shear stiffness at 0.5, 5 and 20 MPa
$n$	Porosity
$p$	Confining pressure, (MPa)
$t$	Thickness of the deformation zone, (m)
$T$	Indirect tensile strength of intact rock, (MPa)
$T_d$	Direct tensile strength of intact rock
$T_m$	Rock mass tensile strength
$TCS$	Intact rock triaxial compressive strength, (MPa)
$TCS_m$	Rock mass triaxial compressive strength
$UCS$	Intact rock uniaxial compressive strength, (MPa)
$UCS_m$	Rock mass uniaxial compressive strength
$V_p$	P-wave velocity, (m/s)
$V_s$	S-wave velocity, (m/s)

## Greek letters

$\delta_F$	Fracture normal deformation, (mm)
$\delta_T$	Holder and grout normal deformation
$\phi$	Intact rock friction angle, ( $^{\circ}$ )
$\phi_b$	Basic friction angle
$\phi_p$	Peak friction angle
$\phi_r$	Residual friction angle
$\phi_b^{BB}$	Basic friction angle related to Barton-Bandis model
$\phi_p^{BB}$	Peak friction angle related to Barton-Bandis model
$\phi_r^{BB}$	Residual friction angle related to Barton-Bandis model
$\phi_p^{MC}$	Peak friction angle related to Mohr-Coulomb model
$\phi_r^{MC}$	Residual friction angle related to Mohr-Coulomb model
$\gamma$	Unit weight, (kN/m <sup>3</sup> )
$\nu$	Intact rock Poisson's ratio
$\nu_m$	Rock mass Poisson's ratio
$\rho$	Density, (kg/m <sup>3</sup> )
$\sigma_{ci}$	Crack initiation stress, (MPa)
$\sigma_c$	Intact rock uniaxial compressive strength
$\sigma_{cm}$	Rock mass uniaxial compressive strength
$\sigma_t$	Indirect tensile strength of intact rock
$\sigma_{td}$	Direct tensile strength of intact rock
$\sigma_{tm}$	Rock mass tensile strength
$\sigma_{H, h}$	Major and minor horizontal in situ stress, (MPa)
$\sigma_v$	Vertical in situ stress
$\sigma_{1, 2, 3}$	Major, intermediate and minor principal stress
$\sigma_n$	Normal stress, (MPa)
$\sigma_r$	Radial stress, (MPa)
$\sigma_{s, max}$	Peak shear stress
$\tau$	Fracture shear strength, (MPa)
$\psi$	Intact rock dilation angle, ( $^{\circ}$ )
$\psi_{0.5, 5, 20}$	Fracture dilation angle at 0.5, 5 and 20 (MPa)



## Delivery date of primary data from SICADA

The primary data used in this report is in the main included in the Fracture domain report /Olofsson et al. 2007/. A compilation of laboratory results, RQD, Q, RMR values divided into rock domains (RFMs) and fracture domains (FFMs) is also available at SKB model database SIMON (Rock\_mechanics\_test\_results\_compilation\_R0715.xls).

Additional data presented in this report consist of empirical characterisation by means of Q and RMR in borehole sections penetrating FFM06 in borehole KFM06A, KFM06B and KFM08C, and characterisations per 1 m-interval for boreholes KFM01B, KFM07C, KFM09A and KFM09B.

The date of delivery of the primary data from SICADA in the rock mechanics modelling is presented in Table A10-1.

**Table A10-1. Delivery date of primary data from SICADA in the rock mechanics modelling.**

Parameter	Activity	File name	Date of delivery from SICADA
Strength_uniaxial	RM113 – Strength_uniaxial	SICADA-06-239	2006-10-06
Strength_uniaxial Poisson_and_young	RM113 – Poisson_and_young	SICADA_06-239	2006-10-06
Strength_triaxial	RM115 – Strength_triaxial	SICADA_06-239	2006-10-06
Strength_triaxial Poisson_and_young	RM115 – Poisson_and_young	SICADA_06-239	2006-10-06
Tensile Strength brazil_test	RM110 – Tensile Strength Brazil_test	SICADA_06-239	2006-10-06
P-wave	RM100 – P-wave	SICADA_06-239	2006-10-06
Dir_sheartest_sealed	RM117 – Shear test	SICADA-07-028 (0:1)	2007-02-09
Dir_shear test_open	RM117– shear test	SICADA-07-028 (0:1)	2007-02-09
Tilt_test	RM118 – Tilt test	SICADA-07-028 (0:2)	2007-02-09
KFM01A	GE041 and GE300	Sicada_03_76	2003-08-12
KFM02A	GE041 and GE300	Sicada_04_17	2004-01-22
KFM03A	GE041 and GE300	Sicada_04_46 Sicada_04_68	2004-03-05 2004-04-01
KFM04A	GE041 and GE300	Sicada_04_117	2004-05-25
KFM01B, KFM09A, KFM09B	GE041 and GE300	Sicada_06_134_1	2006-07-21
KFM07C	GE041 and GE300	Sicada_07_002	2007-01-03
KFM06A, KFM06C, KFM08C	GE041 and GE300	Sicada_07_156	2007-04-03